Politecnico di Milano
Dipartimento di Matematica
Doctoral Programme In Mathematical Models and Methods in Engineering

---

Modelling and simulations of two-phase flows including geometric variables

Supervisor:
Prof. Luca Bonaventura

Co-supervisor:
Dr. Paolo Francesco Barbante

The Chair of the Doctoral Program:
Prof. Michele Correggi

Doctoral Dissertation of:
Giuseppe Orlando

XXXV Cycle

Ringraziamenti

Ed ecco qua, siamo arrivati alla fine di questa lunga maratona ed è dunque giunto il momento di tirare le somme di questo viaggio. È stata un'esperienza intensa, unica, che mi ha sicuramente formato e cambiato tanto, anche in virtù di tutti gli avvenimenti esterni ed imponderabili che si sono succeduti in questi tre anni, e che l'hanno resa decisamente diversa da come l'avevo inizialmente immaginata. Chi mi conosce sa quanto sia difficile per me esternare pensieri ed emozioni, però desidero ringraziare coloro che mi hanno accompagnato in questa avventura (sperando di non dimenticare nessuno e scusandomi in anticipo nel caso ciò accadesse).

Prima di tutto, un sentito ringraziamento al mio supervisor Luca Bonaventura ed al mio co-supervisor Paolo Barbante per avermi dato l'opportunità di lavorare su queste tematiche e per avermi seguito, nonostante le limitazioni e le varie problematiche, giorno dopo giorno, passo dopo passo, verso il completamento di questo lavoro di tesi. Grazie per il supporto e per la fiducia dimostrata nei miei confronti.
Un grazie speciale va poi a Marc Massot e a tutta l' équipe del CMAP, in particolar modo a Thomas ed Arthur, per avermi accolto per otto mesi e per avermi fatto sentire uno di loro, nonostante il mio francese un po' (tanto) stentato e, ancora una volta purtroppo, le difficoltà legate alla pandemia. Merci beacoup, c'était encroyable.
Un grazie enorme va anche a tutte le persone del personale tecnico amministrativo del Dipartimento di Matematica, in particolare ad Anna, Laura ed Esperia, che ascoltano pazientemente le nostre richieste ogni giorno (le mie soprattutto) e ci permettono di lavorare nella massima tranquillità.

Oltre all'aspetto prettamente scientifico e professionale, diverse persone hanno contribuito alla realizzazione di questo lavoro. Il primo pensiero va ovviamente al gruppo Tender, che ha rappresentato molto di più di un semplice luogo di lavoro. Inizialmente, avevo pensato di ringraziare e menzionare singolarmente coloro che hanno trascorso qui un periodo di tempo più o meno lungo in questi tre anni; tuttavia, ho poi realizzato che, oltre alla mia constante ed ingombrante (in tutti i sensi) presenza, altre 48 persone sono transitate da qui (sperando di non aver sbagliato questo calcolo, anche se dubito ci sarà mai una controverifica). Quindi, per evitare che questi ringraziamenti superino in lunghezza la tesi e diventino

una fitta sequela di nomi, mi limiterò ad un semplice, ma sentitissimo, grazie. Il Tender è un posto elettrico (anche nel senso letterale del termine) e chiunque entri a far parte di questa galassia, ne viene immediatamente assorbito e viene guidato verso esperienze imprevedebili ed indimenticabili. Ho potuto incontrare tante persone e stringere amicizie, che sento saranno durature nel tempo, e che sono state essenziali nell'affrontare i periodi più difficili.
Grazie poi ai miei amici di più lunga data Andrea, Giovanni, Jacopo, Michele A., Michele P., Michele T. e Paolo, che mi sono stati vicino durante tutto il mio percorso di studi e con cui abbiamo trascorso tanti bei momenti insieme.

Infine ringrazio infinitamente tutta la mia famiglia, in particolare i miei genitori e mia sorella, per avermi sostenuto ed incoraggiato in ogni singolo istante con la loro costante presenza, anche se geograficamente lontani.

Qui si chiude un importante capitolo: non so cosa mi aspetta nel medio-lungo periodo, ma sono sicuro che il bagaglio di esperienze che ho accumulato in questo percorso farà per sempre parte di me.

Milano, 31 Marzo 2023

Abstract

In this thesis, we analyze two-phase flows with emphasis on geometric variables that arise in their description. Two-phase flows play an important role in several natural processes and engineering systems and their modelling is thus a highly interdisciplinary research topic. They are characterized by the presence of an interface which separates the bulk regions of the single phases. Two-phase flows are classified into two main regimes: separated and disperse flows. However, independently of the specific regime, the exchanges between two phases occur at the interface and phase exchange terms are proportional to the interface area. Hence, the computation of this quantity is a prerequisite in order to obtain an accurate description of the phase exchanges themselves.

Evolution equations for the interface area density are typically obtained by means of empirical approaches. One of the main goals of this thesis is the derivation of dynamic equations for the interface area density through the Stationary Action Principle (SAP). Moreover, the addition of source terms compatible with the second principle of thermodynamics allows to obtain, in appropriate limiting regimes, the classical pressure relaxation associated to the transport of the volume fraction. Furthermore, thanks to a suitable interpretation of some parameters, it is also possible to derive semi-empirical relationships for the interface area density already known in the literature.

The other main goal of the thesis is the development of an effective computational environment for the simulation of two-phase flows. More specifically, we propose a Discontinuous Galerkin (DG) discretization suitable for a range of fluid dynamical models in the framework of the *deal.II* library, which is based on matrix-free approach and provides Adaptive Mesh Refinement (AMR) tools. We first present an implicit solver for the incompressible Navier-Stokes equations using an artificial compressibility formulation. We then derive an extension for single-phase weakly compressible flows with an implicit coupling between momentum and energy balance. A second order IMEX scheme is employed for the time discretization, with the implicit part coinciding with the TR-BDF2 scheme used for the incompressible Navier-Stokes equations, providing thus ample guarantees of robustness in the low Mach regime. The proposed technique allows us the use of rather general Equations of State (EOS) for non-ideal gases. More specifically, we propose a non straightforward extension of existing semi-implicit approaches for the ideal gas law for the Stiffened Gas (SG-EOS) and for the general cubic equation of state

and we develop suitable refinement indicators for real gases.
Finally, we provide an extension for the full non-equilibrium two-phase Baer-Nunziato models, developing also a filtering monotonization procedure in order to avoid, or at least reduce, the under- and over-shoots that arise in presence of discontinuities using high order discretizations. The effectiveness of all the proposed methods is shown in a number of significant benchmarks.

Keywords: Two-phase flows, Baer-Nunziato model, Non-ideal gases, Discontinuous Galerkin methods, IMEX scheme, Adaptive Mesh Refinement, Filtering monotonization technique

Sommario

In questa tesi, si analizzano flussi bifase ponendo l'attenzione anche su alcune variabili geometriche che caratterizzano la loro descrizione. I flussi bifase giocano un ruolo importante in diversi processi naturali and sistemi ingegneristici e la loro modellazione è pertanto un argomento di ricerca interdisciplinare. Sono caratterizzati dalla presenza di un'interfaccia che separa le regioni bulk delle singole fasi. I flussi bifase sono classificati in due regimi: flussi separati e flussi dispersi. Indipendentemente dallo specifico regime, però, gli scambi tra le due fasi avvengono all'interfaccia e i termini di scambio tra le fasi sono proporzionali all'area dell'interfaccia. Quindi, un calcolo affidabile di questa quantità è un prerequisito per ottenere una descrizione accurata degli scambi tra le fasi.

Le equazioni di evoluzione per la densità d'area interfacciale sono tipicamente ottenute attraverso considerazioni empiriche. Uno degli obiettivi principali della tesi riguarda la derivazione di relazioni dinamiche per la densità d'area interfacciale attraverso il Principio dell'Azione Stazionaria. Opportuni termini sorgenti sono considerati compatibilmente con il secondo principio della termodinamica così da ottenere, in opportuni regimi limite, il classico rilassamento della pressione associato all'equazione di trasporto della frazione di volume e, grazie ad un'opportuna interpretazione di alcuni parametri, ritrovare relazioni semi-empiriche già note in letteratura per l'evoluzione della densità d'area interfacciale.

L'altro obiettivo della tesi riguarda lo sviluppo di un ambiente computazionale per la simulazione di fluidi bifase. Più in dettaglio, verrà proposta un'opportuna discretizzazione Discontinuous Galerkin (DG) per un range di modelli per la dinamica dei fluidi implementata nel framework della libreria *deal.II*, che è basata su un approccio di tipo matrix-free e permette di utilizzare adattazione di griglia. Lo sviluppo di un solver per le equazioni di Navier-Stokes incomprimibili utilizzando una formulazione di tipo comprimibilità artificiale costituisce il punto di partenza. In seguito, verrà derivata un'estensione per fluidi monofose debolmente comprimibili con un accoppiamento implicito tra il bilancio della quantità di moto e quello dell'energia. Uno schema IMEX del secondo ordine è utilizzato per la discretizzazione temporale, la cui parte implicita coincide con lo schema TR-BDF2 utilizzato per le equazioni incomprimibili, fornendo pertanto ampia garanzia della robustezza dell'approccio proposto nel limite di basso numero di Mach. La tecnica proposta permette di utilizzare equazioni di stato di gas non ideali. Verrà proposta un'estensione non banale per la Stiffened Gas (SG-EOS) e per l'equazione

di stato general cubic di approcci esistenti in letteratura per l'equazione di stato di gas ideali e, inoltre, verranno derivati opportuni indicatori per il raffinamento locale per gas non ideali.
Infine, verrà proposta un'estensione per il modello di non equilibrio di Baer-Nunziato per fluidi bifase, sviluppando anche una procedura di monotonizzazione tramite un filtro in modo da evitare, o quantomeno ridurre, gli under- e overshoots che sorgono in presenza di discontinuità quando vengono utilizzati metodi di discretizzazione ad alto ordine. Le potenzialità dei vari metodi proposti sono dimostrate in un numero di significativi benchmarks.

Parole chiave: Flussi bifase, modello di Baer-Nunziato, Gas non ideali, Metodi Discontinuous Galerkin, schema IMEX, Adattazione di griglia, Monotonizzazione

Contents

Abstract I

Sommario III

List of Figures IX

List of Tables XV

List of Acronyms XX

1 Introduction 1

2 Model equations for compressible two-phase flows 5

- 2.1 Local balance equations . . . 7
- 2.2 Averaged formulation . . . 10
  - 2.2.1 Ensemble average . . . 10
  - 2.2.2 Time and volume averages . . . 14
  - 2.2.3 Mixture model . . . 16
- 2.3 Evolution equations for interfacial quantities . . . 17
- 2.4 Baer-Nunziato type models for two-phase flows . . . 23
  - 2.4.1 Four-equation relaxed two-phase system . . . 28
- 2.5 Variational approach for two-phase system . . . 30
  - 2.5.1 Dissipation and second principle of thermodynamics . . . 32
  - 2.5.2 Analysis of eigenvalues and eigenvectors . . . 33
  - 2.5.3 Submodels and limiting cases . . . 37
- 2.6 The equation of state . . . 38
  - 2.6.1 Analysis of isentropic processes for the general cubic equation of state . . . 41

3 Numerical methods for two-phase flows 43

- 3.1 The Discontinuous Galerkin method . . . 44
- 3.2 Monotonization technique . . . 46
- 3.3 Discretization for the incompressible Navier-Stokes equations . . . 49

3.4 Extension to the single-phase compressible Navier-Stokes equations 55

3.5 Two-phase system 72

3.5.1 Discretization of the hyperbolic operator and preservation of uniform fields 73

3.5.2 Treatment of non-conservative terms 79

3.5.3 Discretization of four-equation relaxed system 81

4 Numerical simulations 85

4.1 Validation of the filtering monotonization technique 87

4.1.1 Solid body rotation 87

4.1.2 Sod shock tube problem 93

4.1.3 Circular explosion problem 96

4.1.4 Two-dimensional Riemann problem 99

4.2 Numerical results for the incompressible Navier-Stokes equations . 100

4.2.1 Case tests with analytical solution 102

4.2.2 Two-dimensional lid-driven cavity 106

4.2.3 Three-dimensional lid-driven cavity 110

4.2.4 Flow past a cylinder 114

4.2.5 Complex geometry 116

4.3 Numerical results for the single-phase compressible Navier-Stokes equations with ideal gas law 119

4.3.1 Isentropic vortex 121

4.3.2 2D Lid-driven cavity 125

4.3.3 Cold bubble 127

4.3.4 Warm bubble 130

4.3.5 Inertia-gravity waves 131

4.3.6 Density current 133

4.3.7 3D rising bubble 135

4.3.8 Hydrostatic flow over a hill 138

4.3.9 Nonhydrostatic flow over a hill 140

4.3.10 Schär hill 144

4.3.11 3D medium-steep bell-shaped hill 146

4.4 Numerical results for the single-phase compressible Navier-Stokes equations with non-ideal gas law 146

4.4.1 Cold bubble 147

4.4.2 Warm bubble 151

4.5 Numerical results for two-phase flow systems 155

4.5.1 No mixing water-air mixture 155

4.5.2 Pure advection test case 158

4.5.3 Solid contact 161

4.5.4 Rising bubble 161

5 Conclusions and further perspectives 165

Appendix A 167

A.1 Treating Generalized Functions 167

A.2 Evolution of geometric features 170

A.3 Eigenvalues of 1D Euler equations 175

A.4 Derivation of the two-phase model 177
A.5 Time discretization methods 179
A.6 Relaxation operator 182
A.7 HPC framework and implementation issues 188
Bibliography **205**

List of Figures

3.1 Plots of filter functions 47

4.1 Solid body rotation with polynomial degree $r = 1$ and $\varepsilon = 5h_K$ . . 88
4.2 Solid body rotation with polynomial degree $r = 1$ with $\varepsilon = 10^4 h_K$ 88
4.3 Adaptive simulation of solid body rotation with polynomial degree $r = 1$ and $\varepsilon = 10^4 h_K$ 89
4.4 Adaptive simulation of solid body rotation with polynomial degree $r = 1$ and $\varepsilon = 10^5 h_K$ 89
4.5 Solid body rotation with polynomial degree $r = 1$ and $\beta = 0.4$ . . 90
4.6 Adaptive simulation of solid body rotation with polynomial degree $r = 1$ and $\beta = 0.4$ 91
4.7 Adaptive grid for solid body rotation with polynomial degree $r = 1$ and $\beta = 0.4$ 91
4.8 Adaptive simulations of solid body rotation with polynomial degree $r = 2$ comparing the filtering approaches 92
4.9 Solid body rotation with polynomial degree $r = 3$ and $\beta = 0.4$ . . 93
4.10 Sod shock tube problem with polynomial degree $r = 1$ and Oberman-Salvador filter function 94
4.11 Sod shock tube problem with polynomial degree $r = 1$ and Froese-Oberman filter function 95
4.12 Sod shock tube problem with polynomial degree $r = 2$ and Froese-Oberman filter function 97
4.13 2D circular explosion problem with polynomial degree $r = 1$, a) density, b) pressure 98
4.14 2D circular explosion problem with polynomial degree $r = 2$, a) density, b) pressure. 99
4.15 Adaptive simulation for 2D explosion problem with polynomial degree $r = 2$ 100
4.16 Two-dimensional views of adaptive simulation for 2D explosion problem with polynomial degree $r = 2$ 101
4.17 2D Riemann problem, isolines of the density with polynomial degree $r = 2$ 101
4.18 Example of distorted mesh for the Taylor-Green vortex 107

4.19 Errors for the Taylor-Green vortex on regular and distort grids with $\mathbf{Q}_2 - Q_1$ and $\mathbf{Q}_3 - Q_2$ polynomials 107
4.20 Lid-driven cavity benchmark at $Re = 1000$, a) flow field, b) streamfunction contours 108
4.21 Lid-driven cavity benchmark at $Re = 1000$: a) u velocity component values along the middle of the cavity, b) ω values along the middle of the cavity 108
4.22 Lid-driven cavity benchmark at $Re = 1000$, adaptive simulation: a) final mesh after adaptive refinement, b) streamfunction contours 109
4.23 Lid-driven cavity benchmark at $Re = 1000$, adaptive simulation: a) u velocity component values along the middle of the cavity, b) ω values along the middle of the cavity 110
4.24 Lid-driven cavity benchmark at $Re = 1000$, difference for velocity magnitude between the fixed grid simulation and the adaptive simulation (interpolated to the fixed grid) 110
4.25 3D lid-driven cavity benchmark at $Re = 1000$, fixed mesh simulation, a) v velocity component values along the x axis b) u velocity component values along the y axis. 111
4.26 3D lid-driven cavity benchmark at $Re = 1000$, a) flow field vectors for the plane $x = 0$, b) flow field vectors for the plane $y = 0$, c) flow field vectors for the plane $z = 0$ 111
4.27 3D lid-driven cavity benchmark at $Re = 1000$, a) vorticity (ω_x) contours at $x = 0$, b) vorticity (ω_y) contours at $y = 0$, vorticity (ω_z) contours at $z = 0$ 112
4.28 3D lid-driven cavity benchmark at $Re = 1000$, a) u velocity component values along the y axis for adaptive mesh simulation, b) u velocity component values along the y axis for fixed grid simulation 112
4.29 3D lid-driven cavity benchmark at $Re = 1000$, a) v velocity component values along the x axis for adaptive mesh simulation, b) v velocity component values along the x axis for fixed grid simulation. 113
4.30 3D lid-driven cavity benchmark at $Re = 1000$, a) u velocity component comparison for the plane $x = 0, z = 0$, b) v velocity component comparison for the plane $y = 0, z = 0$ 113
4.31 Strong scaling for the 3D lid-driven cavity benchmark at $Re = 1000$ 114
4.32 Weak scaling for the 3D lid-driven cavity benchmark at $Re = 1000$ 115
4.33 Flow past a cylinder benchmark, geometry and boundary conditions 115
4.34 Flow past a cylinder benchmark, contour plot of velocity magnitude at final time 116
4.35 Flow past a cylinder benchmark, a) drag coefficient, b) lift coefficient 116
4.36 Flow past a cylinder benchmark, adaptive simulation, a) grid at final time, b) drag coefficient, c) lift coefficient 117
4.37 Picture of the complex geometry of an heat exchanger 117
4.38 Comparison between *deal.II* and *OpenFOAM* for the velocity in the case of the complex geometry 118
4.39 Comparison between *deal.II* and *OpenFOAM* on the middle section in the case of the complex geometry 119
4.40 Comparison between *deal.II* and *OpenFOAM* at three-quarters section in the case of the complex geometry 120

4.41 Comparison between *deal.II* and *OpenFOAM* on the outlet in the case of the complex geometry 121
4.42 Adaptive simulation of the inviscid isentropic vortex benchmark: a) computational mesh, b) contour plot of the density 125
4.43 Computational results for the 2D lid-driven cavity with polynomial degree $r = 1$, a) streamlines, b) comparison with reference solutions 126
4.44 Computational results for the 2D lid-driven cavity with polynomial degree $r = 2$, a) streamlines, b) comparison with reference solutions 126
4.45 Adaptive simulation for the 2D lid-driven cavity, a) mesh at steady state, b) streamlines 127
4.46 Adaptive simulation for the 2D lid-driven cavity, a) comparison with reference solutions, b) difference for velocity magnitude between the fixed grid simulation and the adaptive simulation (interpolated to the fixed grid) 127
4.47 Cold bubble test case, results at $t = T_f$, a) contour plot of potential temperature perturbation for the reference explicit simulation, b) contour plot of the potential temperature perturbation for the simulation with IMEX scheme. 129
4.48 Cold bubble test case, results at $t = T_f$, density profile at $y = 1000$. The continuous blue line represents the results for the reference explicit simulation, whereas the red dots denote the results for the IMEX scheme. 129
4.49 Cold bubble test case, adaptive simulation, a) contour plot of potential temperature perturbation, b) computational grid 130
4.50 Cold bubble test case, adaptive simulation, density profile at $y = 1000$ 130
4.51 Warm bubble test case, results at $t = 10\,\mathrm{s}$. From bottom to top: temperature, horizontal velocity and vertical velocity. 132
4.52 Warm bubble test case, results at $t = 15\,\mathrm{s}$. From bottom to top: temperature, horizontal velocity and vertical velocity. 133
4.53 Warm bubble test case, results at $t = 20\,\mathrm{s}$. From bottom to top: temperature, horizontal velocity and vertical velocity. 134
4.54 Inertia-gravity waves benchmark, potential temperature deviation a) $t = 0\,\mathrm{s}$, b) $t = 3000\,\mathrm{s}$. Contours are plotted from $0.001\,\mathrm{K}$ to $0.01\,\mathrm{K}$ with interval equal to $1 \times 10^{-3}\,\mathrm{K}$ for a) and from $-0.0015\,\mathrm{K}$ to $0.003\,\mathrm{K}$ with interval equal to $5 \times 10^{-4}\,\mathrm{K}$ for b). 135
4.55 Inertia-gravity waves benchmark, potential temperature deviation at $t = 3000\,\mathrm{s}$ along $z = 5\,\mathrm{km}$ height. 136
4.56 Current density benchmark, potential temperature deviation from background 136
4.57 3D rising bubble benchmark, adaptive simulation 137
4.58 3D rising bubble benchmark, strong scaling analysis 138
4.59 Linear hydrostatic flow over a hill, evolution of normalized momentum flux 140
4.60 Linear hydrostatic flow over a hill at $t = T_f$, a) horizontal velocity deviation, b) vertical velocity 141
4.61 Nonlinear hydrostatic flow over a hill, a) horizontal velocity deviation, b) vertical velocity 142
4.62 Nonlinear hydrostatic flow over a hill, normalized momentum flux evolution 143

4.63 Linear nonhydrostatic flow over a hill, evolution of normalized momentum flux . . . 143
4.64 Nonlinear nonhydrostatic flow over a hill, a) horizontal velocity deviation, b) vertical velocity . . . 144
4.65 Schär mountain test case at $t = T_f$, a) horizontal velocity deviation, b) vertical velocity . . . 145
4.66 Schär mountain test case at $t = T_f$, a) horizontal velocity deviation. Contour values are between $-2\,\mathrm{m\,s^{-1}}$ and $2\,\mathrm{m\,s^{-1}}$ with an interval equal to $0.2\,\mathrm{m\,s^{-1}}$, b) vertical velocity. Contour values are between $-0.5\,\mathrm{m\,s^{-1}}$ and $0.5\,\mathrm{m\,s^{-1}}$ with an interval equal to $5 \cdot 10^{-2}\,\mathrm{m\,s^{-1}}$. The black lines denote the solution with uniform grid, whereas the red lines denote the solution with the non-conforming grid. 146
4.67 3D mountain benchmark, $x - y$ slice at $z = 800\,\mathrm{m}$ of the vertical velocity . . . 147
4.68 Cold bubble test case, van der Waals EOS with $\tilde{a} = 5 \cdot 10^{-9}$ and $\tilde{b} = 5 \cdot 10^{-4}$, density profile at $y = 1000$ . . . 148
4.69 Cold bubble test case, van der Waals EOS with $\tilde{a} = 1.6 \cdot 10^{-1}$ and $\tilde{b} = 5 \cdot 10^{-4}$, contour plots of β . . . 149
4.70 Cold bubble test case, van der Waals EOS with $\tilde{a} = 1.6 \cdot 10^{-1}$ and $\tilde{b} = 5 \cdot 10^{-4}$, density profile at $y = 1000$ . . . 149
4.71 Cold bubble test case, van der Waals EOS with $\tilde{a} = 1.6 \cdot 10^{-1}$ and $\tilde{b} = 5 \cdot 10^{-4}$, adaptive simulation . . . 150
4.72 Cold bubble test case, van der Waals EOS with $\tilde{a} = 1.6 \cdot 10^{-1}$ and $\tilde{b} = 5 \cdot 10^{-4}$, adaptive simulation, density profile at $y = 1000$ . . . 150
4.73 Cold bubble test case, Peng-Robinson EOS with $\tilde{a} = 5 \cdot 10^{-9}$ and $\tilde{b} = 5 \cdot 10^{-4}$, density profile at $y = 1000$ . . . 151
4.74 Cold bubble test case, Peng-Robinson EOS with $\tilde{a} = 1.6 \cdot 10^{-1}$ and $\tilde{b} = 5 \cdot 10^{-4}$, comparison between fixed and adaptive simulations . 152
4.75 Cold bubble test case, Peng-Robinson EOS with $\tilde{a} = 1.6 \cdot 10^{-1}$ and $\tilde{b} = 5 \cdot 10^{-4}$, adaptive simulation, density profile at $y = 1000$ . . . 153
4.76 Cold bubble test case, Peng-Robinson EOS with $\tilde{a} = 1.6 \cdot 10^{-1}$ and $\tilde{b} = 5 \cdot 10^{-4}$, adaptive simulation with criterion (4.51) . . . 153
4.77 Warm bubble test case for N_2O with Peng-Robinson EOS, a) horizontal velocity, b) vertical velocity, c) temperature . . . 154
4.78 Warm bubble test case for N_2O with Peng-Robinson EOS, temperature profile for $y = 0.8$ . . . 155
4.79 Warm bubble test case for N_2O with Peng-Robinson EOS, temperature evolution . . . 156
4.80 Warm bubble test case for N_2O with Peng-Robinson EOS, vertical velocity evolution . . . 156
4.81 Warm bubble test case for N_2O with SG-EOS, temperature evolution 157
4.82 Warm bubble test case for N_2O with SG-EOS, vertical velocity evolution . . . 157
4.83 Warm bubble test case for N_2O, density deviation from background state at initial time, a) Peng-Robinson EOS, b) SG-EOS . . . 158
4.84 No mixing test case, results at final time . . . 158
4.85 No mixing test case, results at final time for velocity and pressure 159
4.86 Pure advection test case, a) velocity, b) pressure, c) volume fraction 160

4.87 Pure advection test case with monotonization, a) velocity phase 1, b) pressure phase 1 . . . 160
4.88 *Solid contact* test case, a) velocity, b) pressure, c) volume fraction 162
4.89 *Rising bubble* test case, volume fraction advection with polynomial degree $r = 0$ . . . 163
4.90 *Rising bubble* test case, volume fraction and mixture density with polynomial degree $r = 2$ . . . 163

A.1 Analysis of the explicit part of IMEX scheme: a) Radius of absolute monotonicity as function of a_{32}, b) Size of stability region along the imaginary axis as a_{32} varies. . . . 182

List of Tables

4.1 Solid body rotation, maximum and minimum values for ε-filtering approach with polynomial $r = 1$ both in case of fixed grid and adaptive simulations . . . 89
4.2 Solid body rotation, maximum and minimum values for β-filtering approach with polynomial degree $r = 1$ both in case of fixed grid and adaptive simulations . . . 90
4.3 Solid body rotation, maximum and minimum values comparing filtering approaches with polynomial degree $r = 2$ in case of adaptive simulations . . . 92
4.4 Solid body rotation, maximum and minimum values with polynomial degree $r = 3$ and $\beta = 0.4$ . . . 92
4.5 Sod shock tube problem with polynomial degree $r = 1, N_{el} = 100$ and Froese-Oberman filter function . . . 94
4.6 Sod shock tube problem with polynomial degree $r = 1, N_{el} = 250$ and Froese-Oberman filter function . . . 94
4.7 Sod shock tube problem with polynomial degree $r = 2$ and Froese-Oberman filter function . . . 96
4.8 Convergence test for the Green-Taylor vortex benchmark with $\mathbf{Q}_2 - Q_1$ elements, relative errors for the velocity in H^1 and L^2 norms. . 103
4.9 Convergence test for the Green-Taylor vortex benchmark with $\mathbf{Q}_2 - Q_1$ elements, relative errors for the pressure in L^2 norm . . . 103
4.10 Convergence test for the Green-Taylor vortex benchmark computed with $\mathbf{Q}_3 - Q_2$ elements, relative errors for the velocity in H^1 and L^2 norms . . . 104
4.11 Convergence test for the Green-Taylor vortex benchmark computed with $\mathbf{Q}_3 - Q_2$ elements, relative errors for the pressure in L^2 norm 104
4.12 Convergence test for the Green-Taylor vortex benchmark computed on a distorted mesh with $\mathbf{Q}_2 - Q_1$ elements, relative errors for the velocity in H^1 and L^2 norms . . . 104
4.13 Convergence test for the Green-Taylor vortex benchmark computed on a distorted mesh with $\mathbf{Q}_2 - Q_1$ elements, relative errors for the pressure in L^2 norm . . . 104

4.14 Convergence test for the Green-Taylor vortex benchmark with $\mathbf{Q}_2 - Q_1$ elements, relative errors for the velocity in H^1 and L^2 norms . 104
4.15 Convergence test for the Green-Taylor vortex benchmark with $\mathbf{Q}_2 - Q_1$ elements, relative errors for the pressure in L^2 norm 105
4.16 Convergence test for the ABC flow benchmark with $\mathbf{Q}_2 - Q_1$ elements, relative errors for the velocity in H^1 and L^2 norms 105
4.17 Convergence test for the ABC flow benchmark with $\mathbf{Q}_2 - Q_1$ elements, relative errors for the pressure in L^2 norm 105
4.18 Convergence test for the ABC flow benchmark with $\mathbf{Q}_3 - Q_2$ elements, relative errors for the velocity in H^1 and L^2 norms 105
4.19 Convergence test for the ABC flow benchmark with $\mathbf{Q}_3 - Q_2$ elements, relative errors for the pressure in L^2 norm 105
4.20 Convergence test for the ABC flow benchmark with $\mathbf{Q}_2 - Q_1$ elements, relative errors for the velocity in H^1 and L^2 norms 106
4.21 Convergence test for the ABC flow benchmark with $\mathbf{Q}_2 - Q_1$ elements, relative errors for the pressure in L^2 norm 106
4.22 Convergence test for the ABC flow benchmark with $\mathbf{Q}_3 - Q_2$ elements, relative errors for the velocity in H^1 and L^2 norms 106
4.23 Convergence test for the ABC flow benchmark with $\mathbf{Q}_3 - Q_2$ elements, relative errors for the pressure in L^2 norm 106
4.24 Wall-clock times in seconds for the strong scaling analysis for incompressible Naiver-Stokes equations 114
4.25 Pressure drop along the four midlines of the channels for the complex geometry 118
4.26 Convergence test for the inviscid isentropic vortex with polynomial degree $r = 1$ and $a_{32} = \frac{7-2\chi}{6}$ for the explicit part 123
4.27 Convergence test for the inviscid isentropic vortex with polynomial degree $r = 2$ and $a_{32} = \frac{7-2\chi}{6}$ for the explicit part 123
4.28 Convergence test for the inviscid isentropic vortex with polynomial degree $r = 1$ and $a_{32} = 0.5$ for the explicit part 123
4.29 Convergence test for the inviscid isentropic vortex with polynomial degree $r = 2$ and $a_{32} = 0.5$ for the explicit part 123
4.30 Convergence test for the inviscid isentropic vortex with polynomial degree $r = 1$ and $a_{32} = 0.5$ for the explicit part at higher Courant number 124
4.31 Convergence test for the inviscid isentropic vortex with polynomial degree $r = 2$ and $a_{32} = 0.5$ for the explicit part at higher Courant number 124
4.32 Adaptive simulations of the inviscid isentropic vortex at different resolutions with polynomial degree $r = 1$ 125
4.33 Values for polynomial of N_2O 154
4.34 Convergence test for the pure advection benchmark with polynomial degree $r = 0$, relative errors for the volume fraction in L^2 norm 160
4.35 Convergence test for the pure advection benchmark with polynomial degree $r = 1$, relative errors for the volume fraction in L^2 norm 161
4.36 Initial conditions for the *solid contact* test case 161

A.1 *Butcher tableaux of the explicit ARK2 method* 180
A.2 *Butcher tableaux of the implicit ARK2 method* 181

List of Acronyms

ABC Arnoldi-Beltrami-Childress

AMR Adaptive Mesh Refinement

ARK Additive Runge Kutta

BN Baer-Nunziato

DG Discontinuous Galerkin

DIRK Diagonal Implicit Runge Kutta

DOF Degrees Of Freedom

EOS Equation Of State

ESDIRK Explicit Singly Diagonal Impicit Runge Kutta

FCT Flux Corrected Transport

FV Finite Volume

GMG Geometric MultiGrid

GMRES Generalized Minimal RESidual

IMEX IMplicit-EXplicit

LLF Local Lax-Friedrichs

MOOD Multidimensional Optimal Order Detection

NWP Numerical Weather Prediction

ODE Ordinary Differential Equations

PBE Population Balance Equation

PDF Probability Density Function

PISO Pressure-Implicit with Splitting of Operators

RTT Reynolds Transport Theorem

SAP Stationary Action Principle

SG-EOS Stiffened Gas Equation Of State

SIP Symmetric Interior Penalty

SSP Strong Stability Preserving

TR-BDF2 Trapeziodal Rule-Backward Differation Formula order 2

TVD Total Variation Diminishing

WENO Weighted Essentially Non-Oscillatory

CHAPTER 1

Introduction

Multiphase flows are characterized by the presence of two or more phases with different properties and play an important role in several natural processes and engineering systems: their modelling is thus a highly interdisciplinary research topic. We mention, among many other physical and industrial applications involving multiphase flows, hybrid rocket engines (see e.g. [Gandolfi, 2019, Di Battista, 2021] and the references therein), atomization of a liquid jet [Vallet et al., 2001, Lebas et al., 2009], spray combustion [Mortensen and Bilger, 2009], flows in porous media [Whitaker, 1986], sediment transport [Chiodi et al., 2014] and pyroclastic flows [Ramos, 1995].

A two-phase flow comprises only two phases. In the present work, we will focus on liquid-gas mixtures and, therefore, we will not consider equation models for flows in porous media, sediment transport or pyroclastic flows, for which one of the two phases is solid. The full non-equilibrium Baer-Nunziato (BN) model [Baer and Nunziato, 1986] has been proposed for detonation waves in granular explosives and represents the most general formulation for compressible two-phase flows. It assumes that each phase is compressible and evolves with its own pressure, temperature and velocity, together with an evolution equation for the volume fraction of one of the two phases. Reduced models have been derived by means of asymptotic expansions of the Baer-Nunziato model with assumptions of infinitely fast relaxation towards the equilibrium for the velocity, pressure or temperature, see e.g. [Kapila et al., 2001, Pelanti, 2022].

A moving interface delimits the bulk regions of the single phases. Two descriptions are possible for the interface: a *sharp* interface configuration, in which a single discontinuity across a surface separating the two fluids is considered, and a *diffuse* interface configuration, for which the interface is assumed to be thick and the properties change continuously between the equilibrium values of the two phases. The diffuse interface approach has been employed e.g. in second gradient models [Jamet et al., 2001] and assumes that the fluid is in a subcritical regime. In the present work, we will focus on the first description, whereas we refer to [Jamet et al., 2001] for a description of methods employing the diffuse interface model. According to the sharp interface geometrical configuration, two-phase flows can then be classified into two main regimes: *separated* and *disperse* flows. A separated flow is characterized by large regions of both phases. On the contrary, a disperse flow is constituted of particles, such as bubbles or droplets, dispersed in a carrier fluid which is called the continuous phase. One can make the distinction between bubbly flows, i.e. gas inclusions in a liquid, and droplet flows, i.e. liquid inclusions in a gas or in a second liquid, as in the case of emulsions. In both separated and disperse flows, the exchanges between the two phases occur at the interface and, moreover, it is well known that phase exchange terms are proportional to the interface area [Drew and Passman, 1999]. Hence, the computation of this quantity is a prerequisite to obtain reliable values of the exchange term, especially in non-equilibrium conditions or when chemical reactions occur. The use of suitable evolution equations to predict the interface area concentration has a long tradition in the literature, see e.g. [Ishii, 1975, Drew, 1990, Drew and Passman, 1999, Hibiki and Ishii, 2002], and has been employed also in the case of flames [Candel and Poinsot, 1990]. This approach represents in the case of disperse flows a popular alternative to the Population Balance Equation (PBE) models, like that proposed in [Williams, 1958], which applies the method of moments to derive several transport equations for the moments of the considered Probability Density Function (PDF) [McGraw, 1997]. The use of an equation for the interface area evolution leads instead to a single transport equation, thus providing a significant advantage in terms of computational efficiency with respect to the alternative PBE approach. The relations for the interfacial area concentration are typically derived by means of empirical approaches under a set of assumptions which are very specific of the phenomenon under consideration [Hibiki and Ishii, 2002, Lhuillier, 2004]. In the last years, the seminal contributions [Cordesse et al., 2019, Drui et al., 2019, Di Battista, 2021] opened the way to the use of variational principles to derive equations of motion for two-phase flows including geometric variables. One of the goals of this work is to show how this methodology can be adapted to obtain dynamic relations for the interfacial area density which provide also as limiting case or as submodels well known relations present in the literature.

Any continuous model of two-phase flows must be complemented by suitable numerical methods for its discretization, so that physically relevant simulations can be performed. The efficient numerical solution of the compressible Navier-Stokes equations which stem from the classical balance laws of fluid dynamics poses several major computational challenges. In particular, for flow regimes characterized by low Mach number values, severe time step restrictions are typically required by standard explicit time discretization methods. The use of implicit and semi-implicit methods has a long tradition in low Mach number flows, see e.g the seminal papers [Robert, 1982, Casulli and Greenspan, 1984, Cullen, 1990]. The Discontinuous Galerkin (DG) discretization method has proven itself a valuable tool in fluid dynamics models, see for example [Giraldo et al., 2010] or the review in [Bonaventura et al., 2012]. However, stability concerns are even more critical in the regimes of interest for spatial discretizations based on the DG method [Karniadakis and Sherwin, 2005, Giraldo, 2020]. In the present work, we will combine, on the one hand, accurate and flexible discontinuous finite element spatial discretizations, and on the other hand, efficient time discretizations, following an approach that has been shown to be quite successful for applications to numerical weather prediction in [Tumolo et al., 2013, Tumolo and Bonaventura, 2015]. In order to prove the effectiveness of the proposed approach, we first develop a solver for the incompressible Navier-Stokes equations based on the artificial compressibility formulation and the unconditionally stable TR-BDF2 method in time [Orlando et al., 2022b]. We then propose an extension of this method to single-phase weakly compressible flows, employing an IMEX scheme for the time discretization [Orlando et al., 2022a]. The implicit part of the considered IMEX method coincides with the aforementioned TR-BDF2 method, thus providing ample guarantees of robustness in the low Mach number regime. The discretization approach is able to handle non-ideal equations of state (EOS), such as the general cubic equation of state, as well as other classical convex equations of state like the stiffened gas equation of state (SG-EOS). This leads to a non straightforward extension of many classical contributions which focus exclusively on the equations of motion of an ideal gas [Bassi et al., 2007, Bassi et al., 2015, Busto et al., 2020, Boscheri and Pareschi, 2021]. Finally, we derive an extension of the same approach to two-phase flows equations and to Baer-Nunziato models [Baer and Nunziato, 1986].

The thesis is structured as follows: in Chapter 2, we provide an overview of the different mathematical models for two-phase flows and we review the local instantaneous evolution equations for geometrical features that characterize two-phase flows. We derive through the Stationary Action Principle (SAP) an evolution equation for the interface area density which should complement the classical balance laws and we provide suitable choices for the EOS, performing also an analysis of isentropic processes. Chapter 3 is devoted to the description of the numerical methods proposed in order to discretize the model equations, giving also a general overview of the Discontinuous Galerkin method. In Chapter 4, we provide some relevant numerical results for a range of fluid dynamic models. The proposed methods are implemented in the framework of the numerical library *deal.II* [Bangerth et al., 2007, Arndt et al., 2022], which is based on a matrix-free approach and provides Adaptive Mesh Refinement (AMR) tools, for which we will employ suitable refinement indicators stemming from the analysis of isentropic processes outlined in Chapter 2. Finally, we present some conclusions and perspective for future works in Chapter 5.

CHAPTER 2

Model equations for compressible two-phase flows

In this Chapter, we derive the equations that govern compressible two-phase flows. Notice that we will consider liquid-gas mixtures. In the present work, as in most standard presentations of this topic, we represent the two fluids as interacting continua separated by an interface across which the properties may vary abruptly [Drew and Passman, 1999]. We first recall the local conservation laws which hold in each bulk region of the domain and the corresponding jump conditions at the separating interface [Gurtin, 1982]. Afterwards, we apply an averaging operation to the previously described equations of motion. We then focus on the evolution equations for geometric features which, in the case of a complex interface, could provide a better description of the phase exchange terms [Drew, 1990, Drew and Passman, 1999]. We then analyze the classical full non-equilibrium Baer-Nunziato model [Baer and Nunziato, 1986] and a relaxed version of this system with four equations. Finally, we derive through the SAP an evolution equation for the interface area density and we give an overview of some possible choices for the equations of state.

Contents

2.1 Local balance equations 7
2.2 Averaged formulation 10
  2.2.1 Ensemble average 10
  2.2.2 Time and volume averages 14
  2.2.3 Mixture model 16
2.3 Evolution equations for interfacial quantities 17
2.4 Baer-Nunziato type models for two-phase flows 23
  2.4.1 Four-equation relaxed two-phase system 28
2.5 Variational approach for two-phase system 30
  2.5.1 Dissipation and second principle of thermodynamics 32
  2.5.2 Analysis of eigenvalues and eigenvectors 33
  2.5.3 Submodels and limiting cases 37
2.6 The equation of state 38
  2.6.1 Analysis of isentropic processes for the general cubic equation of state 41

2.1 Local balance equations

Let $\Omega \subset \mathbb{R}^d, 2 \leq d \leq 3$ be a connected open bounded set with a sufficiently smooth boundary $\partial\Omega$. The canonical form of a balance equation can be written as [Drew and Passman, 1999]

$$\frac{\partial \rho \Psi}{\partial t} + \nabla \cdot (\rho \Psi \mathbf{u}) = \nabla \cdot \mathbf{J} + \rho f \qquad \text{in } \Omega. \tag{2.1}$$

Herein Ψ is the conserved quantity (either a scalar or a tensorial one), ρ is the density, $\mathbf{u}$ is the velocity, $\mathbf{J}$ is the flux (molecular or diffusion) of the variable Ψ and f is the source density. For $\Psi = 1, \mathbf{J} = 0$ and $f = 0$, we obtain the continuity equation

$$\frac{\partial \rho}{\partial t} + \nabla \cdot (\rho \mathbf{u}) = 0 \qquad \text{in } \Omega. \tag{2.2}$$

For $\Psi = \mathbf{u}, \mathbf{J} = \mathbf{T}$ and $f = \mathbf{b}$, we get the balance of momentum

$$\frac{\partial \rho \mathbf{u}}{\partial t} + \nabla \cdot (\rho \mathbf{u} \otimes \mathbf{u}) = \nabla \cdot \mathbf{T} + \rho \mathbf{b} \qquad \text{in } \Omega. \tag{2.3}$$

Here $\mathbf{T}$ is the stress tensor and $\mathbf{b}$ is the body force. Eventually, for $\Psi = E, \mathbf{J} = \mathbf{Tu} - \mathbf{q}$ and $f = \mathbf{b} \cdot \mathbf{u} + r_{heat}$, we obtain the balance of energy

$$\frac{\partial \rho E}{\partial t} + \nabla \cdot (\rho E \mathbf{u}) = \nabla \cdot (\mathbf{Tu} - \mathbf{q}) + \rho (\mathbf{b} \cdot \mathbf{u} + r_{heat}) \qquad \text{in } \Omega, \tag{2.4}$$

where E is total energy per unit of mass, $\mathbf{q}$ is the heat flux and r_{heat} is the heating source per unit mass.

The relation (2.1) is based on the Reynolds Transport Theorem (RTT) [Gurtin, 1982, Slattery et al., 2007], which we briefly recall here for a generic function ϕ:

$$\frac{d}{dt} \int_\Omega \phi d\Omega = \int_\Omega \frac{\partial \phi}{\partial t} d\Omega + \int_{\partial\Omega} \phi \mathbf{u} \cdot \mathbf{n} d\Sigma = \int_\Omega \left[\frac{\partial \phi}{\partial t} + \nabla \cdot (\mathbf{u}\phi) \right] d\Omega, \tag{2.5}$$

where $\mathbf{n}$ is the outward unit normal of $\partial\Omega$. The statement holds also for the single bulk regions corresponding to each phase. From now on, we assume that the domain Ω consists of two subdomains $\Omega_1(t)$ and $\Omega_2(t)$, separated by an interface $\Gamma(t)$. Hence, we consider a single discontinuity across a smooth surface separating two parts occupied by the fluid where the fields are smooth. Suitable jump conditions hold at the interface separating multicomponent materials [Drew and Passman, 1999]:

$$[[\rho \Psi (\mathbf{u} - \mathbf{v}_I) + \mathbf{J}]] = m, \tag{2.6}$$

with $\mathbf{v}_I$ denoting the velocity of the interface $\Gamma(t)$ and $[[\cdot]]$ being the jump across the discontinuity defined for a generic scalar function ϕ as

$$[[\phi]] = \phi_1 \mathbf{n}_1 + \phi_2 \mathbf{n}_2, \tag{2.7}$$

for a generic vector function $\boldsymbol{\varphi}$ as

$$[[\boldsymbol{\varphi}]] = \boldsymbol{\varphi}_1 \cdot \mathbf{n}_1 + \boldsymbol{\varphi}_2 \cdot \mathbf{n}_2 \tag{2.8}$$

and for a generic tensor function $\boldsymbol{\Phi}$ as

$$[[\boldsymbol{\Phi}]] = \boldsymbol{\Phi}_1 \mathbf{n}_1 + \boldsymbol{\Phi}_2 \mathbf{n}_2. \tag{2.9}$$

Notice that $\phi_k, \boldsymbol{\varphi}_k$ and $\boldsymbol{\Phi}_k, k = 1, 2$ are the values of the function ϕ, $\boldsymbol{\varphi}$ and $\boldsymbol{\Phi}$, respectively, on the interface $\Gamma(t)$ from the side $\Omega_k(t)$, and that $\mathbf{n}_1 = -\mathbf{n}_2$. We derive now the jump condition for the continuity equation. The following integral balance holds:

$$\int_{\Omega} \left[\frac{\partial \rho}{\partial t} + \nabla\cdot(\rho\mathbf{u})\right] d\Omega = \sum_{k=1}^{2} \int_{\Omega_k(t)} \left[\frac{\partial \rho}{\partial t} + \nabla\cdot(\rho\mathbf{u})\right] d\Omega = 0. \tag{2.10}$$

Applying the divergence theorem [Gurtin, 1982] for each subdomain we obtain

$$\sum_{k=1}^{2} \int_{\Omega_k(t)} \frac{\partial \rho}{\partial t} d\Omega + \sum_{k=1}^{2} \int_{\partial\Omega_k(t)} \rho\mathbf{u}\cdot\mathbf{n} d\Gamma = 0. \tag{2.11}$$

The boundaries $\partial\Omega_1$ and $\partial\Omega_2$ contain the separating interface $\Gamma(t)$ moving at velocity $\mathbf{v}_I$. Along this interface, the variables are discontinuous. Hence, thanks to a generalized RTT discussed in [Slattery et al., 2007], (2.11) is equivalent to

$$\sum_{k=1}^{2} \int_{\Omega_k(t)} \frac{\partial \rho}{\partial t} d\Omega + \sum_{k=1}^{2} \int_{\partial\Omega_k(t)\backslash\Gamma(t)} \rho\mathbf{u}\cdot\mathbf{n} d\Gamma + \int_{\Gamma(t)} [[\rho\mathbf{v}_I]]\, d\Gamma = 0, \tag{2.12}$$

The flow velocities $\mathbf{u}_1$ and $\mathbf{u}_2$ still do not appear in (2.12). Therefore, we consider the integrals computed on $\partial\Omega_k(t)\backslash\Gamma(t)$ also along $\Gamma(t)$ with $\mathbf{u}_1$ and $\mathbf{u}_2$, respectively, in the place of $\mathbf{v}_I$. This quantity must also be subtracted in order to keep the balance unaltered, so as to obtain

$$\sum_{k=1}^{2} \int_{\Omega_k(t)} \frac{\partial \rho}{\partial t} d\Omega + \sum_{k=1}^{2} \int_{\partial\Omega_k(t)} \rho\mathbf{u}\cdot\mathbf{n} d\Gamma - \int_{\Gamma(t)} [[\rho\mathbf{u}]]\, d\Gamma + \int_{\Gamma(t)} [[\rho\mathbf{v}_I]]\, d\Gamma = 0. \tag{2.13}$$

By comparing (2.11) and (2.13), since we assume that no surface excess mass is associated to the interface, the jump condition associated to the mass balance is [Drew and Passman, 1999]

$$[[\rho\left(\mathbf{u} - \mathbf{v}_I\right)]] = 0. \tag{2.14}$$

The jump condition for the momentum balance is obtained in [Trusdell and Toupin, 1960, Slattery et al., 2007] and reads as follows:

$$[[\rho\mathbf{u}\otimes\left(\mathbf{u} - \mathbf{v}_I\right) + \mathbf{T}]] = \mathbf{m}_I, \tag{2.15}$$

with $\mathbf{m}_I$ being the traction associated to the surface tension. Following [Drew and Passman, 1999], the surface traction is defined as

$$\mathbf{m}_I = H\sigma\mathbf{n} + \nabla_s\sigma, \tag{2.16}$$

where H is the mean curvature, σ is the surface tension coefficient and ∇_s is the gradient in surface coordinates whose definition will be specified later on in Section 2.3. The jump condition for the energy balance reads as follows:

$$[[\rho E\left(\mathbf{u} - \mathbf{v}_I\right) + \mathbf{T}\mathbf{u} - \mathbf{q}]] = \varepsilon_I, \tag{2.17}$$

where ε_I is the surface energy associated with the interface, which is given by

$$\varepsilon_I = H\sigma\mathbf{n}\cdot\mathbf{v}_I + \nabla\cdot\left(\sigma\mathbf{v}_I\right). \tag{2.18}$$

The aforementioned physical laws can be analyzed in a simpler way if the interface conditions are directly incorporated in the balance equations. To do so, we define the characteristic function X_k of phase k as

$$X_k(\mathbf{x}, t) = \begin{cases} 1, & \text{if } \mathbf{x} \text{ is in phase } k \text{ at time } t \\ 0 & \text{otherwise} \end{cases} \tag{2.19}$$

and we take the product of the equation (2.1) with the characteristic function (2.19) so as to obtain

$$X_k \frac{\partial \rho \Psi}{\partial t} + X_k \nabla \cdot (\rho \Psi \mathbf{u}) = X_k \nabla \cdot \mathbf{J} + X_k \rho f. \tag{2.20}$$

Products including the characteristic functions are discontinuous, so that the derivatives must be treated in a distributional sense [Drew and Passman, 1999] (see also Appendix A.1). If we take the characteristic function inside the derivative we get

$$\begin{aligned} &\frac{\partial (X_k \rho \Psi)}{\partial t} + \nabla \cdot (X_k \rho \Psi \mathbf{u}) - \nabla \cdot (X_k \mathbf{J}) - X_k \rho f = \\ &\rho \Psi \left(\frac{\partial X_k}{\partial t} + \mathbf{u} \cdot \nabla X_k \right) - \mathbf{J} \cdot \nabla X_k. \end{aligned} \tag{2.21}$$

Notice that with a slight abuse of notation we employ the same symbol for both distributional and classical derivatives and the proper operator to be considered will follow from the context. Let us briefly analyze the right-hand side of (2.21) which can be rewritten as

$$\begin{aligned} &\rho \Psi \left(\frac{\partial X_k}{\partial t} + \mathbf{u} \cdot \nabla X_k \right) - \mathbf{J} \cdot \nabla X_k = \\ &\rho \Psi \left(\frac{\partial X_k}{\partial t} + \mathbf{u} \cdot \nabla X_k + \mathbf{v}_I \cdot \nabla X_k - \mathbf{v}_I \cdot \nabla X_k \right) - \mathbf{J} \cdot \nabla X_k = \\ &[\rho \Psi (\mathbf{u} - \mathbf{v}_I) - \mathbf{J}] \cdot \nabla X_k. \end{aligned} \tag{2.22}$$

The last equality stems from the so-called topological equation for phase k, which governs the evolution of the characteristic function [Drew and Passman, 1999] (see also Appendix A.1):

$$\frac{\partial X_k}{\partial t} + \mathbf{v}_I \cdot \nabla X_k = 0. \tag{2.23}$$

We substitute (2.22) into (2.21) so as to obtain

$$\frac{\partial (X_k \rho \Psi)}{\partial t} + \nabla \cdot (X_k \rho \Psi \mathbf{u}) - \nabla \cdot (X_k \mathbf{J}) - X_k \rho f = [\rho \Psi (\mathbf{u} - \mathbf{v}_I) - \mathbf{J}] \cdot \nabla X_k. \tag{2.24}$$

Notice that, as outlined in [Junqua-Moullet, 2003, Morel, 2007], ∇X_k is the product between $\delta(\Gamma)$, the Dirac delta distribution with support on the interface, and the outward unit normal from phase k $\mathbf{n}_k$, namely

$$\nabla X_k = -\mathbf{n}_k \delta(\Gamma). \tag{2.25}$$

The distribution $\delta(\Gamma)$ is defined by the following relation:

$$< \delta(\Gamma), \phi >= \int_{\Gamma} \phi d\Sigma \qquad \forall \phi \in C_0^{\infty}(\Omega) \tag{2.26}$$

and represents an interface area density. Indeed, with a slight abuse of notation, the following relation holds:

$$\int_\Omega \delta(\Gamma) d\Omega = A, \tag{2.27}$$

where A is the interface area. Hence, the interfacial source terms are proportional to the interface area density, whose computation is therefore fundamental for an accurate estimate of these exchange terms. A conceptually similar approach for the derivation of the local balance laws in two-phase flows is followed in [Séro-Guillaume and Rimbert, 2005], which we briefly recall here. Each quantity ϕ_k associated to phase k is extended to 0 on the subdomain associated to the other phase, so that it is now defined on the whole domain Ω. Using the relations (A.23) and (A.24), one obtains the following balance equations:

$$\begin{aligned}
\frac{\partial \rho_k}{\partial t} &+ \nabla\cdot\left(\rho_k \mathbf{u}_k\right) + \rho_k\left(\mathbf{u}_k - \mathbf{v}_I\right)\cdot\mathbf{n}_k\delta(\Gamma) = 0 && (2.28)\\
\frac{\partial \rho_k \mathbf{u}_k}{\partial t} &+ \nabla\cdot\left(\rho_k \mathbf{u}_k \otimes \mathbf{u}_k\right) - \nabla\cdot\mathbf{T}_k - \rho_k \mathbf{b}_k \\
&+ \rho_k \mathbf{u}_k \otimes \left(\mathbf{u}_k - \mathbf{v}_I\right)\cdot\mathbf{n}_k\delta(\Gamma) - \mathbf{T}_k\mathbf{n}_k\delta(\Gamma) = 0 && (2.29)\\
\frac{\partial \rho_k E_k}{\partial t} &+ \nabla\cdot\left(\rho_k E_k \mathbf{u}_k + \mathbf{q}_k - \mathbf{T}_k\mathbf{u}_k\right) - \rho_k \mathbf{b}_k\cdot\mathbf{u}_k \\
&+ \left[\rho_k E_k\left(\mathbf{u}_k - \mathbf{v}_I\right) + \mathbf{q}_k - \mathbf{T}_k\mathbf{u}_k\right]\cdot\mathbf{n}_k\delta(\Gamma) = 0. && (2.30)
\end{aligned}$$

Finally, the topological equation (2.23) can be rewritten as follows:

$$\frac{\partial X_k}{\partial t} + \nabla\cdot\left(X_k \mathbf{u}_k\right) + \left(\mathbf{u}_k - \mathbf{v}_I\right)\cdot\mathbf{n}_k\delta(\Gamma) = X_k\,\nabla\cdot\mathbf{u}_k. \tag{2.31}$$

Notice that in (2.31), the advection velocity associated to the characteristic function X_k is $\mathbf{u}_k$, namely the local flow velocity of phase k. Moreover, two extra terms appear in (2.31). The first one, $\left(\mathbf{u}_k - \mathbf{v}_I\right)\cdot\mathbf{n}_k\delta(\Gamma)$, is associated to the exchange between the phases at the interface, whereas the second one, $\nabla\cdot\mathbf{u}_k$ is associated to the dilatation-contraction effects of phase k.

2.2 Averaged formulation

Most multicomponent flows display a high variability in the evolution of the different phases and, in general, a macroscopic description is sufficient if we are still able to obtain reliable results, especially for industrial applications. A microscopic description is indeed too computational expensive to be adopted and it is therefore common to apply an averaging process in order to obtain the mean values of fluid motions and properties [Nigmatulin, 1970, Drew and Passman, 1999, Kapila et al., 2001]. The three different averaging processes that are often applied to multicomponent flows are the ensemble average, the time average and the volume average [Drew and Passman, 1999], which we will briefly recall in the following.

2.2.1 Ensemble average

The *ensemble average* allows us the interpretation of the phenomena in terms of their repeatability. We denote by $\tilde{\tau}$ a single realization of the process and by $\tilde{\mathcal{E}}$

the set of all realizations, known as *ensemble.* If f is some field, the ensemble average of f is defined as:

$$\bar{f}(\boldsymbol{x},t) = \int_{\tilde{\mathcal{E}}} f(\boldsymbol{x},t;\tilde{\tau})dm(\tilde{\tau}) \tag{2.32}$$

where $dm(\cdot)$ is a probability density over the ensemble $\tilde{\mathcal{E}}$. As discussed in [Drew and Passman, 1999], even though it is rather customary in the literature to use the time and volume averages even in the case of not stationary or not uniform macroscopic processes, as it is typical in turbulence flows, this approach can be justified only when the results are the same as those obtained by means of the ensemble average. Time and volume averages are at best approximations of the ensemble average for non-stationary or non-uniform flows and, therefore, the ensemble average is fundamental, whereas time and volume averages are specific. For these reasons, we focus in detail on the derivation of averaged relations by means of the ensemble average. We define the characteristic function X_k of phase k as

$$X_k(\mathbf{x},t;\tilde{\mu}) = \begin{cases} 1, & \text{if } \mathbf{x} \text{ is in phase } k \text{ at time } t \text{ for the realization } \tilde{\mu} \\ 0 & \text{otherwise.} \end{cases} \tag{2.33}$$

We apply the average operator to (2.24) so as to obtain

$$\overline{\frac{\partial(X_k\rho\Psi)}{\partial t}} + \overline{\nabla\cdot(X_k\rho\Psi\mathbf{u})} - \overline{\nabla\cdot(X_k\mathbf{J})} - \overline{X_k\rho f} = \overline{\{\rho\Psi(\mathbf{u}-\mathbf{v}_I)-\mathbf{J}\}\cdot\nabla X_k}. \tag{2.34}$$

Inside each phase we assume a regular behaviour, so that the integration and differentiation can be interchanged. Therefore, it follows from definition (2.32) that differential operators and average commute and we obtain

$$\frac{\partial\overline{(X_k\rho\Psi)}}{\partial t} + \nabla\cdot\overline{(X_k\rho\Psi\mathbf{u})} - \nabla\cdot\overline{(X_k\mathbf{J})} - \overline{X_k\rho f} = \overline{\{\rho\Psi(\mathbf{u}-\mathbf{v}_I)-\boldsymbol{J}\}\cdot\nabla X_k}. \tag{2.35}$$

The averaged continuity equation is obtained by taking $\Psi = 1, \mathbf{J} = \mathbf{0}$ and $f = 0$:

$$\frac{\partial\overline{(X_k\rho)}}{\partial t} + \nabla\cdot\overline{(X_k\rho\mathbf{u})} = \overline{\rho(\mathbf{u}-\mathbf{v}_I)\cdot\nabla X_k}. \tag{2.36}$$

For the balance of momentum, we assume for the sake of simplicity that the only acting body force is gravity and we denote by $\mathbf{g}$ the acceleration of gravity. Hence, taking $\Psi = \mathbf{u}, \mathbf{J} = \mathbf{T}$ and $f = \mathbf{g}$ results in the following equation:

$$\begin{aligned} &\frac{\partial\overline{(X_k\rho\mathbf{u})}}{\partial t} + \nabla\cdot\overline{(X_k\rho\mathbf{u}\otimes\mathbf{u})} - \nabla\cdot\overline{(X_k\mathbf{T})} - \overline{X_k\rho\mathbf{g}} = \\ &\overline{\rho\mathbf{u}\otimes(\mathbf{u}-\mathbf{v}_I) - \mathbf{T}\cdot\nabla X_k}. \end{aligned} \tag{2.37}$$

Eventually, if we take $\Psi = E, \mathbf{J} = \mathbf{Tu} - \mathbf{q}$ and $f = \mathbf{g}\cdot\mathbf{u}$, we find the relation for the balance of energy:

$$\begin{aligned} &\frac{\partial\overline{(X_k\rho E)}}{\partial t} + \nabla\cdot\overline{(X_k\rho E\mathbf{u})} - \nabla\cdot\overline{(X_k(\mathbf{Tu}-\mathbf{q}))} - \overline{X_k\rho(\mathbf{g}\cdot\mathbf{u})} = \\ &\overline{\rho E(\mathbf{u}-\mathbf{v}_I) - (\mathbf{Tu}-\mathbf{q})\cdot\nabla X_k}. \end{aligned} \tag{2.38}$$

Now we introduce adequate average variables to describe two-phase flows. First of all, following [Drew and Passman, 1999], we define

$$\alpha_k = \overline{X_k}, \tag{2.39}$$

which represents the fraction of occurrences where point $\mathbf{x}$ at time t is in the domain occupied by phase k. It is customary to call this variable *volume fraction*, even though its more correct interpretation is that of the ratio of the volume occupied by phase k in a space-time domain centered around $\mathbf{x}, t$ to the total volume of the region itself [Drew and Passman, 1999]. The other averaged quantities are either component-weighted variables, i.e. weighted with the function X_k, and they are denoted by the symbol $\overline{\overline{\Psi}}$, or mass-weighted (Favre) variables [Garnier et al., 2009], that is weighted by $X_k\rho$, which are denoted by the symbol $\widehat{\Psi}$:

$$\overline{\overline{\rho_k}} = \frac{\overline{X_k\rho}}{\alpha_k} \tag{2.40}$$

$$\widehat{\mathbf{u}_k} = \frac{\overline{X_k\rho\mathbf{u}}}{\overline{X_k\rho}} = \frac{\overline{X_k\rho\mathbf{u}}}{\alpha_k\overline{\overline{\rho_k}}} \tag{2.41}$$

$$\widehat{E_k} = \frac{\overline{X_k\rho E}}{\overline{X_k\rho}} = \frac{\overline{X_k\rho E}}{\alpha_k\overline{\overline{\rho_k}}} \tag{2.42}$$

$$\overline{\overline{\mathbf{T}}}_k = \frac{\overline{X_k\mathbf{T}}}{\alpha_k} \tag{2.43}$$

$$\overline{\overline{\mathbf{q}_k}} = \frac{\overline{X_k\mathbf{q}}}{\alpha_k}. \tag{2.44}$$

It is also interesting to notice that, for a generic function Ψ, we obtain

$$\overline{X_k\Psi} = \frac{\overline{X_k\Psi}\alpha_k}{\alpha_k} = \overline{\overline{X_k\Psi}}\alpha_k. \tag{2.45}$$

Hence, we can also express Favre averaged variables as

$$\widehat{\mathbf{u}_k} = \frac{\overline{\overline{X_k\rho\mathbf{u}}}}{\overline{\overline{\rho_k}}} = \frac{\overline{\overline{\rho_k\mathbf{u}_k}}}{\overline{\overline{\rho_k}}} \tag{2.46}$$

$$\widehat{E_k} = \frac{\overline{\overline{X_k\rho E}}}{\overline{\overline{\rho_k}}} = \frac{\overline{\overline{\rho_k E_k}}}{\overline{\overline{\rho_k}}}. \tag{2.47}$$

At the interface, several terms appear that represent the effects of convective and molecular fluxes [Drew and Passman, 1999]. Convective fluxes across the interface are represented by

$$\Gamma_k = \overline{\rho\,(\mathbf{u}-\mathbf{v}_I)\cdot\nabla X_k} \tag{2.48}$$

$$\boldsymbol{\Gamma}_{\mathbf{u},k} = \overline{\rho\mathbf{u}\otimes(\mathbf{u}-\mathbf{v}_I)\cdot\nabla X_k} \tag{2.49}$$

$$\Gamma_{E,k} = \overline{\rho E\otimes(\mathbf{u}-\mathbf{v}_I)\cdot\nabla X_k}, \tag{2.50}$$

which represent the contribution to interfacial mass, momentum and energy sources, respectively. For what concerns the molecular fluxes we define

$$\mathbf{M}_k = -\overline{\mathbf{T}\,\nabla X_k} \tag{2.51}$$

$$\Lambda_k = \overline{\mathbf{q}\cdot\nabla X_k} \tag{2.52}$$

$$W_k = -\overline{(\mathbf{T}\mathbf{u})\cdot\nabla X_k}, \tag{2.53}$$

where $\mathbf{M}_k$ represents the interfacial momentum source due to molecular fluxes, Λ_k is the interfacial heat source and W_k is the interfacial work. The motion of interfaces gives rise to quantities, and in particular velocities, that are not generally equal to their average values. The fluctuations around mean values may be due to turbulence or to the motion of the interfaces. Whatever their source, the effects of fluctuations are taken into account introducing for a generic variable Ψ the fluctuating field Ψ'

$$\Psi' = \Psi - \overline{\Psi}. \tag{2.54}$$

For the sake of clarity, we denote by Ψ'' the fluctuations associated to the mass-weighted variables so as to obtain

$$\Psi'' = \Psi - \widehat{\Psi}. \tag{2.55}$$

Let us analyze now the term $\overline{X_k \rho \mathbf{u} \otimes \mathbf{u}}$ as a function of these new variables. We obtain

$$\begin{aligned} \overline{X_k \rho \mathbf{u} \otimes \mathbf{u}} &= \overline{X_k \rho \left(\widehat{\mathbf{u}_k} + \mathbf{u}_k''\right) \otimes \left(\widehat{\mathbf{u}_k} + \mathbf{u}_k''\right)} = \overline{X_k \rho} \widehat{\mathbf{u}_k} \otimes \widehat{\mathbf{u}_k} + \overline{X_k \rho \mathbf{u}_k'' \otimes \mathbf{u}_k''} \\ &= \alpha_k \overline{\overline{\rho_k}} \widehat{\mathbf{u}_k} \otimes \widehat{\mathbf{u}_k} - \alpha_k \mathbf{T}_k^{Re} \end{aligned} \tag{2.56}$$

where $\mathbf{T}_k^{Re} = -\overline{\overline{\rho_k \mathbf{u}_k' \otimes \mathbf{u}_k'}} = -\overline{\overline{\rho_k}} \widehat{\mathbf{u}_k'' \otimes \mathbf{u}_k''}$ is known as the Reynolds stress tensor. For what concerns the energy equation we first analyze $\overline{X_k \rho E \mathbf{u}}$:

$$\begin{aligned} \overline{X_k \rho E \mathbf{u}} &= \overline{X_k \rho \left(\widehat{E_k} + E_k''\right) \left(\widehat{\mathbf{u}_k} + \mathbf{u}_k''\right)} = \overline{X_k \rho} \widehat{E_k} \widehat{\mathbf{u}_k} + \overline{X_k \rho E_k'' \mathbf{u}_k''} \\ &= \alpha_k \overline{\overline{\rho_k}} \widehat{E_k} \widehat{\mathbf{u}_k} - \alpha_k \mathbf{q}_k^{Re}, \end{aligned} \tag{2.57}$$

where $\mathbf{q}_k^{Re} = -\overline{\overline{\rho_k E_k'' \mathbf{u}_k''}} = -\overline{\overline{\rho_k}} \widehat{E_k'' \mathbf{u}_k''}$ is known as the Reynolds total energy flux. We then consider $\overline{X_k \mathbf{T} \mathbf{u}}$:

$$\overline{X_k \mathbf{T} \mathbf{u}} = \overline{\overline{\mathbf{T}_k \mathbf{u}_k}} = \overline{\overline{\mathbf{T}_k \left(\widehat{\mathbf{u}_k} + \mathbf{u}_k''\right)}} = \overline{\overline{\mathbf{T}}}_k \widehat{\mathbf{u}_k} + \mathbf{q}_k^T, \tag{2.58}$$

where $\mathbf{q}_k^T = \overline{\overline{\mathbf{T}_k \mathbf{u}_k''}}$ is the Reynolds shear stress power. We then obtain the averaged equations:

$$\frac{\partial \left(\alpha_k \overline{\overline{\rho_k}}\right)}{\partial t} + \nabla \cdot \left(\alpha_k \overline{\overline{\rho_k}} \widehat{\mathbf{u}_k}\right) = \Gamma_k \tag{2.59}$$

$$\begin{aligned} &\frac{\partial \left(\alpha_k \overline{\overline{\rho_k}} \widehat{\mathbf{u}_k}\right)}{\partial t} + \nabla \cdot \left(\alpha_k \overline{\overline{\rho_k}} \widehat{\mathbf{u}_k} \otimes \widehat{\mathbf{u}_k}\right) - \nabla \cdot \left[\alpha_k \left(\overline{\overline{\mathbf{T}_k}} + \mathbf{T}_k^{Re}\right)\right] = \\ &\alpha_k \overline{\overline{\rho_k}} \mathbf{g} + \mathbf{M}_k + \mathbf{\Gamma}_{\mathbf{u},k} \end{aligned} \tag{2.60}$$

$$\begin{aligned} &\frac{\partial \left(\alpha_k \overline{\overline{\rho_k}} \widehat{E_k}\right)}{\partial t} + \nabla \cdot \left(\alpha_k \overline{\overline{\rho_k}} \widehat{E_k} \widehat{\mathbf{u}_k}\right) - \nabla \cdot \left[\alpha_k \left(\overline{\overline{\mathbf{T}_k}} \widehat{\mathbf{u}_k} - \overline{\overline{\mathbf{q}_k}} + \mathbf{q}_k^{Re} + \mathbf{q}_k^T\right)\right] = \\ &\alpha_k \overline{\overline{\rho_k}} \widehat{\mathbf{u}_k} \cdot \mathbf{g} + \Lambda_k + W_k + \Gamma_{E,k}. \end{aligned} \tag{2.61}$$

The average stress can be written as

$$\overline{\overline{\mathbf{T}_k}} = -\overline{\overline{p_k}} \mathbf{I} + \overline{\overline{\boldsymbol{\tau}_k}}. \tag{2.62}$$

We want to separate mean field effects from local effects in the interfacial terms; for this reason we introduce the interfacial pressure p_{kI} and shear stress $\boldsymbol{\tau}_{kI}$:

$$\begin{aligned} p_{kI} &= \frac{\overline{p\mathbf{n}_k \cdot \nabla X_k}}{\Sigma} = -\frac{\overline{p\delta(\Gamma)}}{\Sigma} && (2.63) \\ \boldsymbol{\tau}_{kI} &= \frac{\overline{\boldsymbol{\tau}\left(\nabla X_k \cdot \mathbf{n}_k\right)}}{\Sigma} = -\frac{\overline{\boldsymbol{\tau}\delta(\Gamma)}}{\Sigma}, && (2.64) \end{aligned}$$

where $\Sigma = \overline{\delta(\Gamma)}$ is the average interfacial area concentration [Drew and Passman, 1999] and the values of p and $\boldsymbol{\tau}$ are considered as limit values taken in each subdomain $\Omega_k(t)$. The interfacial force density $\mathbf{M}_k$ can be therefore rewritten as follows:

$$\begin{aligned} \mathbf{M}_k &= -\overline{\mathbf{T}\nabla X_k} = \overline{p\nabla X_k} - \overline{\boldsymbol{\tau}\nabla X_k} = p_{kI}\overline{\nabla X_k} - \boldsymbol{\tau}_{kI}\overline{\nabla X_k} - \overline{\mathbf{T}^{'}_{kI}\nabla X_k} \\ &= p_{kI}\nabla\alpha_k - \boldsymbol{\tau}_{kI}\nabla\alpha_k - \overline{\mathbf{T}^{'}_{kI}\nabla X_k}, && (2.65) \end{aligned}$$

where $\mathbf{T}_{kI} = -p^{'}_{kI}\mathbf{I} + \boldsymbol{\tau}_{kI}$. Similarly, the interfacial work can be rearranged to read:

$$W_k = -\overline{\mathbf{T}\mathbf{u} \cdot \nabla X_k} = -\overline{\mathbf{T}\widehat{\mathbf{u}_k} \cdot \nabla X_k} - -\overline{\mathbf{T}\mathbf{v}^{'}_k \cdot \nabla X_k} = \mathbf{M}_k \cdot \widehat{\mathbf{u}_k} + W^{'}_k, \qquad (2.66)$$

where $W^{'}_k = -\overline{\mathbf{T}\mathbf{v}^{'}_k \cdot \nabla X_k}$.

2.2.2 Time and volume averages

In this Section, we briefly present the time and volume averages. For a more complete presentation of these techniques for two-phase flows, the reader is referred to [Ishii, 1975] and [Kolev, 2002], respectively. Notice that with a slight abuse of notation we employ the same symbol for the different averages and the proper operator to be considered will follow from the context, even though the averages are intrinsically different one from the other. Given a function $f\left(\mathbf{x}, t\right)$, we define the time mean value as

$$\frac{1}{\Delta t}\int_{t_0-\frac{\Delta t}{2}}^{t_0+\frac{\Delta t}{2}} f\left(\mathbf{x}, t\right) dt, \qquad (2.67)$$

where Δt is the time interval used for sampling and t_0 is a reference instant. For a fixed point $\mathbf{x}_0$, the various properties are subjected to jump discontinuities during the time interval. Hence, in order to obtain averaged relations, we first take a fixed time interval Δt large enough to smooth out local variations of properties but small compared to the characteristic time of unsteadiness of the flow; this is a key point in the averaging process, because in some cases the relevant duration of the phenomenon is in the order of some milliseconds and the time interval considered has to be really small. After choosing a particular reference point and time $(\mathbf{x}_0, t_0)$, the time interval goes from $\left(t_0 - \frac{\Delta t}{2}\right)$ to $\left(t_0 + \frac{\Delta t}{2}\right)$ and there are well definite times $t_1, t_2, ..., t_j, ...$ when the point $\mathbf{x}_0$ actually belongs to the interface. The effect of the interface on the physical variables is limited only to the neighbourhood of the surface and the domain of influence is given by a thin layer of thickness δ. Hence, we can define the time intervals τ_j as

$$\tau_j = \frac{\delta}{2\left|v_{nI,j}\right|}, \qquad (2.68)$$

where $v_{nI,j}$ denotes the normal component of the interfacial velocity at time t_j. The assumption that the interface is a surface reduces to

$$\lim_{\delta \to 0} \tau_j = 0 \qquad \text{if } |v_{nI,j}| \neq 0. \tag{2.69}$$

At this point we can extract from the time interval Δt a set of subintervals in which the characteristic of interface dominates denoted by $[\Delta t]_S$, namely

$$[\Delta t]_S = \{t : t \in [t_j - \tau_j, t_j + \tau_j], j = 1, ..., n\}. \tag{2.70}$$

The remaining part is denoted by $[\Delta t]_T$ which in turn can be decomposed into intervals of phase 1 and 2, namely

$$[\Delta t]_T = [\Delta t]_1 + [\Delta t]_2 . \tag{2.71}$$

By introducing the sampling interval $[\Delta t], t \in \left(t_0 - \frac{\Delta t}{2}, t_0 + \frac{\Delta t}{2}\right)$ we obtain therefore

$$[\Delta t] = [\Delta t]_S + \sum_{k=1}^{2} [\Delta t]_k . \tag{2.72}$$

We consider the characteristic function (2.19) to distinguish between the two phases. It is worth to notice that, in view of (2.72), $X_k(\mathbf{x}, t) = 0, k = 1, 2$ if the point $\mathbf{x}$ at time t is on the interface. A general function $f(\mathbf{x}, t)$ associated with the two-phase flow is assumed to be continuously differentiable everywhere except in regions of thickness delta covering the interface. We introduce a general function of the k-th phase at the averaging point $\mathbf{x}_0$:

$$f_k(\mathbf{x}_0, t) = X_k(\mathbf{x}_0, t) f(\mathbf{x}_0, t) = \begin{cases} f(\mathbf{x}_0, t), & \text{if } t \in [\Delta t]_k \\ 0, & \text{otherwise.} \end{cases} \tag{2.73}$$

We are now ready to introduce the time average values of functions associated with two-phase flows. The time average of a generic function f is defined as

$$\overline{f}(\mathbf{x}_0, t_0) = \lim_{\delta \to 0} \frac{1}{\Delta t} \int_{[\Delta t]_T} f(\mathbf{x}_0, t)\, dt. \tag{2.74}$$

Analogously the mean value of the generic function f_k for the phase k is defined as

$$\overline{f_k}(\mathbf{x}_0, t_0) = \lim_{\delta \to 0} \frac{1}{\Delta t} \int_{[\Delta t]_T} f_k(\mathbf{x}_0, t)\, dt. \tag{2.75}$$

Thanks to the definition (2.73) of f_k, we find $f(\mathbf{x}, t) = f(\mathbf{x}, t) \sum\limits_k X_k(\mathbf{x}, t) = \sum\limits_k f_k(\mathbf{x}, t)$ if $t \in [\Delta t]_T$; hence we obtain the following important relation:

$$\overline{f}(\mathbf{x}_0, t_0) = \sum_{k=1}^{2} \overline{f_k}(\mathbf{x}_0, t_0). \tag{2.76}$$

We now focus instead on the volume average technique. Consider a control volume V fixed in time and space. First of all we introduce a general function of the k-th phase at the averaging instant t_0 as

$$f_k(\mathbf{x}, t_0) = X_k(\mathbf{x}, t_0) f(\mathbf{x}, t_0) = \begin{cases} f(\mathbf{x}, t_0), & \text{if } \mathbf{x} \in V_k \\ 0, & \text{otherwise.} \end{cases} \tag{2.77}$$

We define the volume average as

$$\overline{f} = \frac{1}{|V|}\int_V f d\Omega, \tag{2.78}$$

where $|V|$ is the measure of the control volume. Afterwards, we define the local volume average for the function f_k (2.77) as

$$\overline{f_k} = \frac{1}{|V|}\int_{V_k} f_k d\Omega, \tag{2.79}$$

where V_k is the volume occupied by phase k. Moreover we define the intrinsic phase average as

$$\overline{f_k}^k = \frac{1}{|V_k|}\int_{V_k} f_k d\Omega, \tag{2.80}$$

where $|V_k|$ is the measure of V_k. The following relations hold:

$$\begin{aligned} \overline{f_k} &= \frac{1}{|V|}\int_{V_k} f_k d\Omega = \frac{1}{|V|}\int_V f_k d\Omega & (2.81) \\ \overline{f_k}^k &= \frac{1}{|V_k|}\int_{V_k} f_k d\Omega = \frac{1}{|V_k|}\int_V f_k d\Omega. & (2.82) \end{aligned}$$

The two averages are therefore related by the relation

$$\overline{f_k}^k = \alpha_k \overline{f_k}, \tag{2.83}$$

where $\alpha_k = \frac{V_k}{V}$ is the volume fraction. This term represents the fraction of volume occupied by phase k with respect to the whole control volume. Notice that here the term volume fraction has a different meaning with respect to (2.39) due to the intrinsic differences between the averages. We refer to [Ishii, 1975, Drew and Passman, 1999, Kolev, 2002] on how differential operators and averages commute dealing with distributional derivatives in order to derive the averaged balance laws from (2.20).

2.2.3 Mixture model

The mixture model (or drift-flux model) is an alternative formulation to study two-phase flows [Ishii, 1975]. The basic assumption is to consider the fluid as a mixture of the two phases. Hence, the mixture model is simpler, even though it requires strong constitutive assumptions, because we lose some important characteristics of two-phase flows, such as the interfacial variables. The mixture model equations are obtained by summing up (2.59), (2.60) and (2.61). We start by considering the continuity equation, which reads as follows:

$$\frac{\partial \rho_{mix}}{\partial t} + \nabla\cdot\left(\rho_{mix}\mathbf{u}_{mix}\right) = \sum_{k=1}^{2}\Gamma_k. \tag{2.84}$$

Here ρ_{mix} is the mixture density defined as

$$\rho_{mix} = \sum_{k=1}^{2}\alpha_k \overline{\overline{\rho_k}}, \tag{2.85}$$

with $\overline{\overline{\rho_k}}$ defined in (2.40), and the mixture velocity $\mathbf{u}_{mix}$ is equal to

$$\mathbf{u}_{mix} = \frac{\sum\limits_{k=1}^{2} \alpha_k \overline{\overline{\rho_k}} \widehat{\mathbf{u}_k}}{\rho_{mix}}, \tag{2.86}$$

where $\widehat{\mathbf{u}_k}$ is defined in (2.41). Notice that $\mathbf{u}_{mix}$ corresponds to the velocity of the center of mass of the mixture. Since the total mass is conserved, we obtain

$$\sum_{k=1}^{2} \Gamma_k = 0. \tag{2.87}$$

The mixture momentum balance is obtained by summing up (2.60) so as to obtain

$$\frac{\partial \rho_{mix} \mathbf{u}_{mix}}{\partial t} + \nabla \cdot \left(\rho_{mix} \mathbf{u}_{mix} \otimes \mathbf{u}_{mix}\right) - \nabla \cdot \left(\mathbf{T}_{mix} + \mathbf{T}_{mix}^{Re}\right) = \rho_{mix} \mathbf{g} + \mathbf{m}_{mix}, \tag{2.88}$$

where $\mathbf{T}_{mix} = \sum\limits_{k=1}^{2} \alpha_k \overline{\overline{\mathbf{T}_k}}$ is the mixture stress tensor, $\mathbf{T}_{mix}^{Re} = \sum\limits_{k=1}^{2} \alpha_k \mathbf{T}_k^{Re}$ is the mixture Reynolds stress tensor and $\mathbf{m}_{mix} = \sum\limits_{k=1}^{2} \left(\mathbf{M}_k + \mathbf{\Gamma}_{k,\mathbf{u}}\right)$ is the surface tension source [Drew and Passman, 1999]. Finally, the mixture energy balance reads as follows:

$$\begin{aligned} &\frac{\partial \rho_{mix} E_{mix}}{\partial t} + \nabla \cdot \left(\rho_{mix} E_{mix} \mathbf{u}_{mix}\right) - \nabla \cdot \left(\mathbf{T}_{mix} \mathbf{u}_{mix} - \mathbf{q}_{mix} + \mathbf{q}_{mix}^{Re} + \mathbf{q}_{mix}^{T}\right) = \\ &\rho_{mix} \mathbf{u}_{mix} \cdot \mathbf{g} + e_{mix}, \end{aligned} \tag{2.89}$$

where $\mathbf{q}_{mix} = \sum\limits_{k=1}^{2} \alpha_k \overline{\overline{\mathbf{q}_k}}$ is the mixture heat flux, $\mathbf{q}_{mix}^{Re} = \sum\limits_{k=1}^{2} \alpha_k \mathbf{q}_k^{Re}$, $\mathbf{q}_{mix}^{T} = \sum\limits_{k=1}^{2} \alpha_k \mathbf{q}_k^{T}$, and $e_{mix} = \sum\limits_{k=1}^{2} \left(\Lambda_k + W_k + \Gamma_{E,k}\right)$ is the interfacial energy source [Drew and Passman, 1999].

2.3 Evolution equations for interfacial quantities

In this Section, we analyze the evolution equations for a set of geometrical quantities that characterize the interface in two-phase flows. We assume that the interface $\Gamma(t)$ between two phases is a $d-1-$dimensional manifold in a d-dimensional Euclidean space with $d = 2, 3$. Notice that we assume that the surface $\Gamma(t)$ is closed without contact lines. Two representations of an interface in space can be considered. In the first description, the surface is seen as the zero-level of a suitable function $F(\mathbf{x}, t)$. The second representation is given by

$$\mathbf{x} = \mathbf{x}(\boldsymbol{\alpha}, t), \tag{2.90}$$

where $\boldsymbol{\alpha}$ are the surface coordinates. The velocity of a point on the surface with coordinates $\boldsymbol{\alpha}$ is defined as

$$\mathbf{v}_I = \frac{\partial \mathbf{x}}{\partial t}. \tag{2.91}$$

From now on, for the sake of simplicity, we omit the explicit dependence on space and time for the different geometric variables. Since F is identically zero for all the points located on the interface, its Lagrangian derivative at velocity $\mathbf{v}_I$ is null, which entails the following kinematic equation:

$$\frac{\partial F}{\partial t} + \mathbf{v}_I \cdot \nabla F = 0. \tag{2.92}$$

Moreover, the unit vector normal to the surface is given by:

$$\mathbf{n} = \pm \frac{\nabla F}{|\nabla F|}. \tag{2.93}$$

From (2.92) and (2.93), it follows immediately that two different interfacial velocity fields with the same normal component induce the same motion. Indeed, if we substitute (2.93) into (2.92), we obtain

$$\frac{\partial F}{\partial t} \pm (\mathbf{v}_I \cdot \mathbf{n})\, |\nabla F| = 0, \tag{2.94}$$

from which it follows that only $\mathbf{v}_I \cdot \mathbf{n}$ contributes to the evolution of the Lagrangian derivative. As discussed in [Drew and Passman, 1999, Junqua-Moullet, 2003, Morel, 2007], the characteristic function X_k follows the same dynamics (2.23) (see also Appendix A.1).

As discussed in Section 2.1, source terms are proportional to the interfacial area density. The estimate of the interfacial area is therefore a prerequisite for the correct prediction of the phase exchange terms, especially in thermodynamic non-equilibrium conditions or when chemical reactions occur. For this purpose, we aim to add to the classical set of balance laws an evolution equation for this quantity. The first step consists of deriving the local instantaneous equation for the Dirac delta distribution $\delta(\Gamma)$ with support on the interface. For this reason we take the gradient of the evolution equation of the characteristic function (2.23) and we obtain the following relation:

$$\frac{\partial \nabla X_k}{\partial t} + \nabla \left(\mathbf{v}_I \cdot \nabla X_k\right) = \mathbf{0}. \tag{2.95}$$

There are functions, like the outward unit normal vector or the interfacial velocity, whose definitions are properly meaningful only for the points on the surface Γ, as explained in [Nadim, 1996]. Therefore, for these quantities, we have to employ derivatives that are defined intrinsically on the surface. The relations for time and space derivatives for a generic scalar function f of this kind have been introduced in [Estrada and Kanwal, 1980, Estrada and Kanwal, 1985]:

$$\begin{aligned} \frac{\partial_s f}{\partial t} &= \frac{\partial \tilde{f}}{\partial t} + (\mathbf{v}_I \cdot \mathbf{n}) \left(\nabla \tilde{f} \cdot \mathbf{n}\right) && (2.96) \\ \frac{\partial_s f}{\partial x_i} &= \frac{\partial \tilde{f}}{\partial x_i} - n_i \left(\nabla \tilde{f} \cdot \mathbf{n}\right), && (2.97) \end{aligned}$$

where $\tilde{f}$ is any smooth extension of f outside Γ. In particular for a first-order tensor $\mathbf{f}$ we have

$$\nabla_{\mathrm{s}} \cdot \mathbf{f} = (\mathbf{I} - \mathbf{n} \otimes \mathbf{n}) : \nabla \tilde{\mathbf{f}} = \nabla \cdot \tilde{\mathbf{f}} - \left[\left(\nabla \tilde{\mathbf{f}}\right) \mathbf{n}\right] \cdot \mathbf{n}. \tag{2.98}$$

Here, $\mathbf{I}$ is the $d \times d$ identity tensor and we define the gradient of a first-order tensor $\tilde{\mathbf{f}}$ as the second-order tensor whose components are

$$\left[\nabla \tilde{\mathbf{f}}\right]_{ij} = \frac{\partial \tilde{f}_i}{\partial x_j}. \tag{2.99}$$

Notice that, as explained in [Estrada and Kanwal, 1985], given f defined only on Γ, we mean by $f\delta(\Gamma)$ the distribution $\tilde{f}\delta(\Gamma)$ for which

$$\nabla \tilde{f} \cdot \mathbf{n}\bigg|_{\Gamma} = 0. \tag{2.100}$$

Analogous considerations hold in the case $\mathbf{f}\delta(\Gamma)$, for which one needs

$$\left[\left(\nabla \tilde{\mathbf{f}}\right)\mathbf{n}\right]\bigg|_{\Gamma} = \mathbf{0}. \tag{2.101}$$

Thanks to (2.100) and (2.101), we avoid therefore any dependence on the value of $\tilde{f}$ or $\tilde{\mathbf{f}}$ and this allows to consider f and $\tilde{f}$ or $\mathbf{f}$ and $\tilde{\mathbf{f}}$ without distinction. On the other hand, if f or $\mathbf{f}$ are already defined and regular in the whole space-time domain $\Omega \times (0, T_f)$, one can define $f\delta(\Sigma)$ or $\mathbf{f}\delta(\Sigma)$, but this distribution will also depend on the value of $\nabla f \cdot \mathbf{n}\Big|_{\Gamma}$ or of $\left[(\nabla \mathbf{f})\,\mathbf{n}\right]\Big|_{\Gamma}$. The following relation holds:

$$\frac{\partial\left(\tilde{f}\delta(\Gamma)\right)}{\partial\square} = \frac{\partial \tilde{f}}{\partial\square}\delta(\Gamma) + \frac{\partial\delta(\Gamma)}{\partial\square}\tilde{f}, \tag{2.102}$$

which reduces to [Estrada and Kanwal, 1985]

$$\frac{\partial\left(\tilde{f}\delta(\Gamma)\right)}{\partial\square} = \frac{\partial_s f}{\partial\square}\delta(\Gamma) + \frac{\partial\delta(\Gamma)}{\partial\square}f, \tag{2.103}$$

for quantities f defined uniquely on Γ. We recall here for the sake of the convenience the relation (2.25)

$$\nabla X_k = -\mathbf{n}_k\delta(\Gamma). \tag{2.104}$$

Hence, we consider now the outward unit normal as a function defined in the whole space-time domain by means of (2.93). Applying (2.102) and (2.104) to $\frac{\partial \nabla X_k}{\partial t}$, one obtains

$$\frac{\partial \nabla X_k}{\partial t} = -\frac{\partial\left[\delta(\Gamma)\mathbf{n}_k\right]}{\partial t} = -\frac{\partial\delta(\Gamma)}{\partial t}\mathbf{n}_k - \frac{\partial \mathbf{n}_k}{\partial t}\delta(\Gamma). \tag{2.105}$$

If we substitute (2.105) into (2.95) and we compute the scalar product by $\mathbf{n}_k$ we obtain

$$-\frac{\partial\delta(\Gamma)}{\partial t} - \frac{\partial \mathbf{n}_k}{\partial t}\delta(\Gamma)\cdot\mathbf{n}_k - \nabla\cdot\left[\left(\mathbf{v}_I\cdot\mathbf{n}_k\right)\mathbf{n}_k\delta(\Gamma)\right] + \left(\mathbf{v}_I\cdot\mathbf{n}_k\right)\left(\nabla\cdot\mathbf{n}_k\right)\delta(\Gamma) = 0. \tag{2.106}$$

Since $\mathbf{n}_k \cdot \mathbf{n}_k = 1$, one can verify that $\frac{\partial \mathbf{n}_k}{\partial t} \cdot \mathbf{n}_k = 0$ and therefore (2.106) reduces to

$$\frac{\partial\delta(\Gamma)}{\partial t} + \nabla\cdot\left[\left(\mathbf{v}_I\cdot\mathbf{n}_k\right)\mathbf{n}_k\delta(\Gamma)\right] - \left(\mathbf{v}_I\cdot\mathbf{n}_k\right)\left(\nabla\cdot\mathbf{n}_k\right)\delta(\Gamma) = 0. \tag{2.107}$$

This is a well known relation and it is described in several contributions [Marle, 1982, Drew, 1990, Soria and de Lasa, 1991, Lhuillier et al., 2000, Junqua-Moullet, 2003, Morel, 2007, Essadki et al., 2019]. In (2.107), the term $\nabla\cdot\mathbf{n}_k$ is directly related to curvature effects, since the following relation holds [Drew and Passman, 1999, Morel, 2007]:

$$H = \frac{1}{2}\nabla\cdot\mathbf{n}_k, \tag{2.108}$$

where we recall here that H denotes the mean curvature. Equation (2.107) can be rewritten in other forms. First of all since $\nabla\cdot\mathbf{n}_k = \nabla_{\mathrm{s}}\cdot\mathbf{n}_k$ [Nadim, 1996], we immediately obtain

$$\frac{\partial\delta(\Gamma)}{\partial t} + \nabla\cdot\left[(\mathbf{v}_I\cdot\mathbf{n}_k)\,\mathbf{n}_k\delta(\Gamma)\right] - (\mathbf{v}_I\cdot\mathbf{n}_k)\,(\nabla_{\mathrm{s}}\cdot\mathbf{n}_k)\,\delta(\Gamma) = 0. \tag{2.109}$$

Moreover, (2.107) is equivalent to

$$\frac{\partial\delta(\Gamma)}{\partial t} + (\mathbf{v}_I\cdot\mathbf{n}_k)\,\mathbf{n}_k\cdot\nabla\delta(\Gamma) = -\delta(\Gamma)\nabla\,(\mathbf{v}_I\cdot\mathbf{n}_k)\cdot\mathbf{n}_k, \tag{2.110}$$

a relation present in [Junqua-Moullet, 2003]. Indeed, the following relation holds:

$$\begin{aligned}\nabla\cdot\left[(\mathbf{v}_I\cdot\mathbf{n}_k)\,\mathbf{n}_k\delta(\Gamma)\right] &= (\mathbf{v}_I\cdot\mathbf{n}_k)\,\mathbf{n}_k\cdot\nabla\delta(\Gamma) + \nabla\cdot\left[(\mathbf{v}_I\cdot\mathbf{n}_k)\,\mathbf{n}_k\right]\delta(\Gamma) \\ &= (\mathbf{v}_I\cdot\mathbf{n}_k)\,\mathbf{n}_k\cdot\nabla\delta(\Gamma) + (\mathbf{v}_I\cdot\mathbf{n}_k)\,\nabla\cdot\mathbf{n}_k + \nabla\,(\mathbf{v}_I\cdot\mathbf{n}_k)\cdot\mathbf{n}_k.\end{aligned} \tag{2.111}$$

If we substitute (2.111) into (2.107), we recover (2.110). The relations (2.107), (2.109) and (2.110) contain only the normal velocity $(\mathbf{v}_I\cdot\mathbf{n}_k)\,\mathbf{n}_k$. To rewrite them in order to make the complete interfacial velocity $\mathbf{v}_I$ appear, we first define the tangential velocity $\mathbf{v}_{I_t}$ as

$$\mathbf{v}_{I_t} = \mathbf{v}_I - (\mathbf{v}_I\cdot\mathbf{n}_k)\,\mathbf{n}_k = (\mathbf{I} - \mathbf{n}_k\otimes\mathbf{n}_k)\,\mathbf{v}_I. \tag{2.112}$$

Adding and subtracting $\nabla\cdot\left[\mathbf{v}_{I_t}\delta(\Gamma)\right]$ to (2.107), we obtain the following relation:

$$\frac{\partial\delta(\Gamma)}{\partial t} + \nabla\cdot\left[\mathbf{v}_I\delta(\Gamma)\right] - (\mathbf{v}_I\cdot\mathbf{n}_k)\,(\nabla\cdot\mathbf{n}_k)\,\delta(\Gamma) - \nabla\cdot\left[\mathbf{v}_{I_t}\delta(\Gamma)\right] = 0. \tag{2.113}$$

It can be proven [Marle, 1982] that

$$\nabla\cdot\left[\mathbf{v}_{I_t}\delta(\Gamma)\right] = \delta(\Gamma)\,\nabla_{\mathrm{s}}\cdot\mathbf{v}_{I_t}. \tag{2.114}$$

If we now substitute (2.114) into (2.113), we get

$$\frac{\partial\delta(\Gamma)}{\partial t} + \nabla\cdot\left[\mathbf{v}_I\delta(\Gamma)\right] - (\mathbf{v}_I\cdot\mathbf{n}_k)\,(\nabla\cdot\mathbf{n}_k)\,\delta(\Gamma) - \delta(\Gamma)\,\nabla_{\mathrm{s}}\cdot\mathbf{v}_{I_t} = 0 \tag{2.115}$$

It can be also shown [Morel, 2007] that

$$\nabla_{\mathrm{s}}\cdot\mathbf{v}_I = \nabla_{\mathrm{s}}\cdot\mathbf{v}_{I_t} + (\mathbf{v}_I\cdot\mathbf{n}_k)\,\nabla\cdot\mathbf{n}_k. \tag{2.116}$$

Exploiting this relation in (2.115) leads to the following equation [Junqua-Moullet, 2003, Lhuillier, 2003, Morel, 2007]:

$$\frac{\partial\delta(\Gamma)}{\partial t} + \nabla\cdot\left[\mathbf{v}_I\delta(\Gamma)\right] = \delta(\Gamma)\,\nabla_{\mathrm{s}}\cdot\mathbf{v}_I. \tag{2.117}$$

We can rewrite the term $\nabla\cdot(\mathbf{v}_I\delta(\Gamma))$ present in (2.117) as

$$\nabla\cdot(\mathbf{v}_I\delta(\Gamma)) = \mathbf{v}_I\cdot\nabla\delta(\Gamma) + \delta(\Gamma)\,\nabla\cdot\mathbf{v}_I \tag{2.118}$$

and, noticing that $\nabla_{\mathrm{s}}\cdot\mathbf{v}_I = \nabla\cdot\mathbf{v}_I - [(\nabla\mathbf{v}_I)\,\mathbf{n}_k]\cdot\mathbf{n}_k$, we get

$$\frac{\partial\delta(\Gamma)}{\partial t} + \mathbf{v}_I\cdot\nabla\delta(\Gamma) = -\delta(\Gamma)\,[(\nabla\mathbf{v}_I)\,\mathbf{n}_k]\cdot\mathbf{n}_k \tag{2.119}$$

or, equivalently,

$$\frac{\partial\delta(\Gamma)}{\partial t} + \mathbf{v}_I\cdot\nabla\delta(\Gamma) = -\delta(\Gamma)\mathbf{n}_k\otimes\mathbf{n}_k : \nabla\mathbf{v}_I, \tag{2.120}$$

which has been derived in [Lhuillier, 2003]. As discussed in [Junqua-Moullet, 2003], relation (2.120) is equivalent to

$$\frac{\partial\delta(\Gamma)}{\partial t} + (\mathbf{v}_I\cdot\mathbf{n}_k)\,\mathbf{n}_k\cdot\nabla\delta(\Gamma) = -\delta(\Gamma)\nabla\,(\mathbf{v}_I\cdot\mathbf{n}_k)\cdot\mathbf{n}_k. \tag{2.121}$$

One can also notice that

$$[(\nabla\mathbf{v}_I)\,\mathbf{n}_k]\cdot\mathbf{n}_k = [\nabla\cdot(\mathbf{v}_I\otimes\mathbf{n}_k)]\cdot\mathbf{n}_k - (\nabla\cdot\mathbf{n}_k)\,(\mathbf{v}_I\cdot\mathbf{n}_k)\,. \tag{2.122}$$

Hence, we can rewrite (2.119) as follows:

$$\frac{\partial\delta(\Gamma)}{\partial t} + \mathbf{v}_I\cdot\nabla\delta(\Gamma) = \delta(\Gamma)\,(\nabla\cdot\mathbf{n}_k)\,(\mathbf{v}_I\cdot\mathbf{n}_k) - \delta(\Gamma)\,[\nabla\cdot(\mathbf{v}_I\otimes\mathbf{n}_k)]\cdot\mathbf{n}_k. \tag{2.123}$$

Relation (2.123) is particularly interesting because it provides an evolution equation for $\delta(\Gamma)$ in which the complete interfacial velocity is the advecting field and a quantity related to the curvature, i.e. $\nabla\cdot\mathbf{n}_k$, appears as a forcing term. To the best of our knowledge, this novel formulation is not present in the literature we have reviewed and is presented here for the first time. Analogously, notice that

$$[(\nabla\mathbf{v}_I)\,\mathbf{n}_k]\cdot\mathbf{n}_k = \nabla\,(\mathbf{v}_I\cdot\mathbf{n}_k)\cdot\mathbf{n}_k - \nabla\cdot(\mathbf{n}_k\otimes\mathbf{n}_k)\cdot\mathbf{v}_I + (\nabla\cdot\mathbf{n}_k)\,(\mathbf{v}_I\cdot\mathbf{n}_k)\,, \tag{2.124}$$

so as to obtain

$$\begin{aligned}&\frac{\partial\delta(\Gamma)}{\partial t} + \mathbf{v}_I\cdot\nabla\delta(\Gamma) = \\ &-\delta(\Gamma)\,(\nabla\cdot\mathbf{n}_k)\,(\mathbf{v}_I\cdot\mathbf{n}_k) - \delta(\Gamma)\nabla\,(\mathbf{v}_I\cdot\mathbf{n}_k)\cdot\mathbf{n}_k + \delta(\Gamma)\,[\nabla\cdot(\mathbf{n}_k\otimes\mathbf{n}_k)]\cdot\mathbf{v}_I\end{aligned} \tag{2.125}$$

It is worthwhile to recall once more that, in all the previous relations, we have considered the outward unit normal vector and the interfacial velocity as variables already defined in the whole space-time domain $\Omega\times[0,T_f]$. Relations (2.107), (2.109), (2.110), (2.113), (2.115), (2.117), (2.120), (2.121), (2.123) and (2.125) are valid also by considering the outward unit normal vector and the interfacial velocity as functions uniquely defined on the interface Γ and then analyzing their extension, that, with a slight abuse of notation, we still denote by $\mathbf{n}_k$ and $\mathbf{v}_I$. However, in this situation, relation (2.101) allows to consider much simpler forms for the evolution equation of the interfacial area density. As reported in [Estrada and Kanwal, 1980, Estrada and Kanwal, 1985], the following relation holds:

$$\nabla\delta(\Gamma) = [\nabla\delta(\Gamma)\cdot\mathbf{n}_k]\cdot\mathbf{n}_k. \tag{2.126}$$

Moreover, thanks to (2.103), we can rewrite the term $\nabla\cdot\left[\mathbf{v}_I\delta(\Gamma)\right]$ present in (2.117) as

$$\nabla\cdot\left[\mathbf{v}_I\delta(\Gamma)\right] = \mathbf{v}_I\cdot\nabla\delta(\Gamma) + \delta(\Gamma)\,\nabla_{\mathrm{s}}\cdot\mathbf{v}_I \tag{2.127}$$

so as to obtain from (2.117)

$$\frac{\partial\delta(\Gamma)}{\partial t} + \mathbf{v}_I\cdot\nabla\delta(\Gamma) = 0 \tag{2.128}$$

or, substituting (2.126) in (2.128),

$$\frac{\partial\delta(\Gamma)}{\partial t} + \left(\mathbf{v}_I\cdot\mathbf{n}_k\right)\mathbf{n}_k\cdot\nabla\delta(\Gamma) = 0, \tag{2.129}$$

a relation present in [Delhaye, 2001]. Equation (2.129) is clearly different from (2.110). However, under the assumption that the fields involved depend only on the surface coordinates, the following relation holds [Drew, 1990, Junqua-Moullet, 2003]:

$$\delta(\Gamma)\nabla\left(\mathbf{v}_I\cdot\mathbf{n}_k\right)\cdot\mathbf{n}_k = 0 \tag{2.130}$$

and, therefore, (2.110) reduces to (2.129). It is important to notice that relations (2.128) and (2.129) are rigorously valid and are equivalent to (2.107), (2.109), (2.110), (2.113), (2.115), (2.117), (2.120), (2.121), (2.123) and (2.125), if one analyzes variables defined uniquely on the surface and then considers an extension satisfying the property (2.101). As pointed out at the beginning of the Section, all the previous relations are only valid under the assumption that the surface Γ is closed without contact lines. In case this hypothesis is not valid, we need to add an extra term which takes into account the presence of the contact lines [Marle, 1982, Junqua-Moullet, 2003]:

$$\frac{\partial\delta(\Gamma)}{\partial t} + \nabla\cdot\left[\left(\mathbf{v}_I\cdot\mathbf{n}_k\right)\mathbf{n}_k\delta(\Gamma)\right] = \left(\mathbf{v}_I\cdot\mathbf{n}_k\right)\left(\nabla\cdot\mathbf{n}_k\right)\delta(\Gamma) - \delta(\Delta)\mathbf{v}_\Delta\cdot\mathbf{t}_k. \tag{2.131}$$

Here, $\delta(\Delta)$ is the Dirac delta distribution with support on the contact lines, $\mathbf{v}_\Delta$ represents the velocity field of the contact lines and $\mathbf{t}_k$ is the unit vector tangent to the interface and directed in outward normal direction with respect to the contact lines. In the present work, we focus mainly on the interface area density. However, evolution equations for higher order statistics such as curvatures or unit normal vector can be considered. A brief overview about these supplementary relations is reported in Appendix A.2 and we also refer to [Drew and Passman, 1999] for a more exhaustive discussion.

Many physical situations are characterized by interfaces with a non trivial shape. Thus, a tracking of the interface is not feasible in practice and one needs to focus on relevant geometric features as main indicators of the topology of the interface. We present now the application of the ensemble average procedure outlined in Section 2.2 to the evolution equations of X_k and $\delta(\Gamma)$. We start from (2.23) and we set $\alpha_k = \overline{X_k}$. The ensemble average of (2.23) leads us to the following relation:

$$\frac{\partial\alpha_k}{\partial t} = \nu_k\Sigma, \tag{2.132}$$

where $\nu_k = \frac{\overline{(\mathbf{v}_I\cdot\mathbf{n}_k)\delta(\Gamma)}}{\Sigma}$ is the average scalar normal interfacial velocity and we recall that $\Sigma = \overline{\delta(\Gamma)}$ is the averaged interfacial area density. The averaging process applied to (2.109) yields [Drew and Passman, 1999]

$$\frac{\partial \Sigma}{\partial t} + \nabla\cdot\left(\overline{\mathbf{v}_{I,nk}}\Sigma\right) = \Sigma\nu_k\overline{H_k} + \Sigma S_\Sigma. \tag{2.133}$$

Here $\overline{\mathbf{v}_{I,nk}} = \frac{\overline{(\mathbf{v}_I\cdot\mathbf{n}_k)\mathbf{n}_k\delta(\Gamma)}}{\Sigma}$ is the averaged interfacial velocity projected along the normal direction and $\overline{H_k} = \frac{\overline{H_k\delta(\Gamma)}}{\Sigma}$ is the average mean curvature, with $H_k = \frac{1}{2}\nabla\cdot\mathbf{n}_k$. Moreover, S_Σ is the interfacial source term per unit area defined as $\overline{\left(H_k - \overline{H_k}\right)\mathbf{v}_I\cdot\mathbf{n}_k\delta(\Gamma)}$. As is usual for averaging processes, there is a closure problem for these equations, in particular for the term S_Σ.

2.4 Baer-Nunziato type models for two-phase flows

The full non-equilibrium two-phase Baer-Nunziato (BN) model has been proposed in [Baer and Nunziato, 1986]. It was meant originally to represent a model for detonation waves in granular explosives, but it has been widely applied also in other contexts. The model assumes that each phase is compressible and evolves with its own pressure, temperature and velocity, together with an evolution equation for the volume fraction of one of the two phases. Considering each phase as compressible can be seen as an unnecessary assumption in most of two-phase flow problems. However, there are cases in which the pressure range is such that the compressibility of both materials has to be taken into account. Moreover, it is always possible to consider materials as compressible as a general assumption [Saurel and Abgrall, 1999]. Starting from the original one, a wide set of BN-type models have been proposed, see among many others [Saurel and Abgrall, 1999, Romenski et al., 2007, Müller et al., 2016], with different modelling and closure assumptions. Reduced models have been derived by means of asymptotic expansions of the BN model [Pelanti, 2022]. We mention, among them, the so-called Kapila model [Kapila et al., 2001], which assumes velocity and pressure equilibrium, and the four equations model which considers mechanical and thermal equilibrium [Lund and Aursand, 2012, Saurel et al., 2016, Bacigaluppi et al., 2022, Demou et al., 2022], which we will briefly review in the following Section. Suitable source terms describe the coupling between the two phases. For the sake of simplicity, we do not consider dissipative effects in our description and we focus first on situations where no phase exchange occurs and the following system of partial differential equations is therefore considered:

$$
\begin{aligned}
\frac{\partial \alpha_1}{\partial t} + \mathbf{v}_I \cdot \nabla \alpha_1 &= \hat{P} \\
\frac{\partial \left(\alpha_1 \rho_1\right)}{\partial t} + \nabla \cdot \left(\alpha_1 \rho_1 \mathbf{u}_1\right) &= 0 \\
\frac{\partial \left(\alpha_1 \rho_1 \mathbf{u}_1\right)}{\partial t} + \nabla \cdot \left(\alpha_1 \rho_1 \mathbf{u}_1 \otimes \mathbf{u}_1\right) + \nabla \left(\alpha_1 p_1\right) - p_I \nabla \alpha_1 &= -\hat{\mathbf{U}} \\
\frac{\partial \left(\alpha_1 \rho_1 E_1\right)}{\partial t} + \nabla \cdot \left[\alpha_1 \left(\rho_1 E_1 + p_1\right) \mathbf{u}_1\right] - p_I \mathbf{v}_I \cdot \nabla \alpha_1 &= -p_I \hat{P} - \mathbf{v}_I \cdot \hat{\mathbf{U}} \\
\alpha_2 &= 1 - \alpha_1 \qquad (2.134) \\
\frac{\partial \left(\alpha_2 \rho_2\right)}{\partial t} + \nabla \cdot \left(\alpha_2 \rho_2 \mathbf{u}_2\right) &= 0 \\
\frac{\partial \left(\alpha_2 \rho_2 \mathbf{u}_2\right)}{\partial t} + \nabla \cdot \left(\alpha_2 \rho_2 \mathbf{u}_2 \otimes \mathbf{u}_2\right) + \nabla \left(\alpha_2 p_2\right) + p_I \nabla \alpha_1 &= \hat{\mathbf{U}} \\
\frac{\partial \left(\alpha_2 \rho_2 E_2\right)}{\partial t} + \nabla \cdot \left[\alpha_2 \left(\rho_2 E_2 + p_2\right) \mathbf{u}_2\right] + p_I \mathbf{v}_I \cdot \nabla \alpha_1 &= p_I \hat{P} + \mathbf{v}_I \cdot \hat{\mathbf{U}},
\end{aligned}
$$

for $\mathbf{x} \in \Omega, t \in (0, T_f]$, supplied with suitable initial and boundary conditions. Here T_f is the final time, $\alpha_k, \rho_k, \mathbf{u}_k, p_k, E_k$ are the volume fraction, the density, the velocity, the pressure and the total energy of phase $k = 1, 2$, respectively. Moreover, $\mathbf{v}_I$ is the interfacial velocity, whereas p_I denotes the interfacial pressure, which have both to be modelled. For the sake of simplicity, as in most standard works of two-phase flows, see e.g. [Saurel and Abgrall, 1999, Re and Abgrall, 2022], we consider a unique value for the interface variables without distinction for the specific subdomain, as done instead in (2.63). We assume the following definitions:

$$
\mathbf{v}_I = \frac{\alpha_1 \rho_1 \mathbf{u}_1 + \alpha_2 \rho_2 \mathbf{u}_2}{\alpha_1 \rho_1 + \alpha_2 \rho_2} = Y_1 \mathbf{u}_1 + Y_2 \mathbf{u}_2 \qquad p_I = \alpha_1 p_1 + \alpha_2 p_2, \tag{2.135}
$$

where

$$
Y_k = \frac{\alpha_k \rho_k}{\alpha_1 \rho_1 + \alpha_2 \rho_2} \tag{2.136}
$$

is the mass fraction. Notice that the choice of the interface variables is not unique. As reported in [Saurel and Abgrall, 1999], most authors consider the liquid phase as incompressible and, therefore, they consider uniquely the gas pressure. However, this choice leads to ill-posed problems as reported in [Saurel and Abgrall, 1999]. Other authors assume $p_I = 0$ [Powers et al., 1990]. This choice yields a hyperbolic system but it not physically justifiable. The velocity of the interface is often taken equal to the velocity of the incompressible (or less compressible) phase [Baer and Nunziato, 1986, Saurel, 1996]. Other authors [Delhaye and Bouré, 1982] have considered the velocity of the center volume, i.e. $\mathbf{v}_I = \alpha_1 \mathbf{u}_1 + \alpha_2 \mathbf{u}_2$. The estimate in (2.135) is the velocity of the center of mass and corresponds to the velocity to which the non-equilibrium system will relax [Saurel and Abgrall, 1999, Re and Abgrall, 2022]. The quantities $\hat{P}$ and $\hat{\mathbf{U}}$ represent mechanical relaxation terms and their expression reads as follows:

$$
\hat{P} = \hat{\mu} \left(p_1 - p_2\right) \tag{2.137}
$$

$$
\hat{\mathbf{U}} = \hat{\lambda} \left(\mathbf{u}_1 - \mathbf{u}_2\right), \tag{2.138}
$$

with $\hat{\mu}$ and $\hat{\lambda}$ denoting suitable relaxation parameters. The total energy can be rewritten as $\rho_k E_k = \rho_k e_k + \rho_k k_k$, where e_k is the internal energy and $k_k = \frac{1}{2}\|\mathbf{u}_k\|^2$ is the kinetic energy. We also introduce the specific enthalpy $h_k = e_k + \frac{p_k}{\rho_k}$ and remark that one can also write

$$(\rho_k E_k + p_k)\mathbf{u}_k = \left(e_k + k_k + \frac{p_k}{\rho_k}\right)\rho_k \mathbf{u}_k = (h_k + k_k)\,\rho_k \mathbf{u}_k. \tag{2.139}$$

We now proceed to derive a non dimensional formulation of equations (2.134). Hence, we introduce reference scaling values $\mathcal{L}, \mathcal{T}, \mathcal{U}_k$ for the length, time and velocity in phase k, respectively, as well as reference values $\mathcal{P}_k, \mathcal{R}_k, \Theta_k, \mathcal{E}_k, \mathcal{I}_k, \mathcal{H}_k$ for pressure, density, temperature, total energy, internal energy and enthalpy in phase m, respectively. We assume for the sake of simplicity unit Strouhal number $St_k \approx \frac{\mathcal{L}}{\mathcal{U}_k \mathcal{T}} \approx 1$ [Klein et al., 2001, Munz et al., 2003, Orlando et al., 2022a] for both phases, from which we deduce $\frac{\mathcal{U}_2}{\mathcal{U}_1} = \mathcal{O}(1)$, and we also assume that

$$\mathcal{H}_k \approx \mathcal{I}_k + \frac{\mathcal{P}_k}{\mathcal{R}_k} \qquad \mathcal{E}_k \approx \mathcal{I}_k + \mathcal{U}_k^2. \tag{2.140}$$

Thanks to (2.135), we obtain

$$\begin{aligned} \mathbf{v}_I &= \frac{\alpha_1 \rho_1 \mathbf{u}_1 + \alpha_2 \rho_2 \mathbf{u}_2 \rho_{rel}}{\alpha_1 \rho_1 + \alpha_2 \rho_2 \rho_{rel}} && (2.141)\\ p_I &= \alpha_1 p_1 + \alpha_2 p_2 p_{rel}, && (2.142) \end{aligned}$$

with $\rho_{rel} = \frac{\mathcal{R}_2}{\mathcal{R}_1}$ and $p_{rel} = \frac{\mathcal{P}_2}{\mathcal{P}_1}$. Notice that, with a slight abuse of notation, we keep the same notation to denote the non-dimensional variables. The model equations can therefore be written in non-dimensional form as follows:

$$
\begin{aligned}
\frac{\partial \alpha_1}{\partial t} + \mathbf{v}_I \cdot \nabla \alpha_1 &= \hat{\mu}\frac{\mathcal{L}}{\mathcal{U}_1}\mathcal{P}_1\left(p_1 - p_2 p_{rel}\right) \\
\frac{\partial\left(\alpha_1\rho_1\right)}{\partial t} + \nabla\cdot\left(\alpha_1\rho_1\mathbf{u}_1\right) &= 0 \\
\frac{\partial\left(\alpha_1\rho_1\mathbf{u}_1\right)}{\partial t} + \nabla\cdot\left(\alpha_1\rho_1\mathbf{u}_1 \otimes \mathbf{u}_1\right) &+ \\
\frac{\mathcal{P}_1}{\mathcal{R}_1\mathcal{U}_1^2}\nabla\left(\alpha_1 p_1\right) - \frac{\mathcal{P}_1}{\mathcal{R}_1\mathcal{U}_1^2} p_I \nabla\alpha_1 &= -\hat{\lambda}\frac{\mathcal{L}}{\mathcal{U}_1\mathcal{R}_1}\left(\mathbf{u}_1 - \mathbf{u}_2\right) \\
\frac{\partial\left(\alpha_1\rho_1 E_1\right)}{\partial t} &+ \\
\nabla\cdot\left[\alpha_1\rho_1\mathbf{u}_1\left(\frac{\mathcal{I}_1 + \frac{\mathcal{P}_1}{\mathcal{R}_1}}{\mathcal{E}_1}h_1 + \frac{\mathcal{U}_1^2}{\mathcal{E}}k_1^2\right)\right] - \frac{\mathcal{P}_1}{\mathcal{R}_1\mathcal{E}_1} p_I \mathbf{v}_I \cdot \nabla\alpha_1 &= \\
-\hat{\mu}\frac{\mathcal{L}}{\mathcal{U}_1}\mathcal{P}_1\frac{\mathcal{P}_1}{\mathcal{R}_1\mathcal{E}_1} p_I\left(p_1 - p_2 p_{rel}\right) - \hat{\lambda}\frac{\mathcal{L}}{\mathcal{U}_1\mathcal{R}_1}\frac{\mathcal{U}_1^2}{\mathcal{E}_1}\mathbf{v}_I \cdot \left(\mathbf{u}_1 - \mathbf{u}_2\right) & \\
\alpha_2 &= 1 - \alpha_1 \qquad (2.143) \\
\frac{\partial\left(\alpha_2\rho_2\right)}{\partial t} + \nabla\cdot\left(\alpha_2\rho_2\mathbf{u}_2\right) &= 0 \\
\frac{\partial\left(\alpha_2\rho_2\mathbf{u}_2\right)}{\partial t} + \nabla\cdot\left(\alpha_2\rho_2\mathbf{u}_2 \otimes \mathbf{u}_2\right) &+ \\
\frac{\mathcal{P}_2}{\mathcal{R}_2\mathcal{U}_2^2}\nabla\left(\alpha_2 p_2\right) + \frac{\mathcal{P}_2}{\mathcal{R}_2\mathcal{U}_2^2}\frac{1}{p_{rel}} p_I \nabla\alpha_1 &= \hat{\lambda}\frac{\mathcal{L}}{\mathcal{U}_1\mathcal{R}_2}\left(\mathbf{u}_1 - \mathbf{u}_2\right) \\
\frac{\partial\left(\alpha_2\rho_2 E_2\right)}{\partial t} &+ \\
\nabla\cdot\left[\alpha_2\rho_2\mathbf{u}_2\left(\frac{\mathcal{I}_2 + \frac{\mathcal{P}_2}{\mathcal{R}_2}}{\mathcal{E}_2}h_2 + \frac{\mathcal{U}_2^2}{\mathcal{E}}k_2^2\right)\right] + \frac{\mathcal{P}_2}{\mathcal{R}_2\mathcal{E}_2}\frac{1}{p_{rel}} p_I \mathbf{v}_I \cdot \nabla\alpha_1 &= \\
\hat{\mu}\frac{\mathcal{L}}{\mathcal{U}_1}\mathcal{P}_1\frac{\mathcal{P}_1}{\mathcal{R}_2\mathcal{E}_2} p_I\left(p_1 - p_2 p_{rel}\right) + \hat{\lambda}\frac{\mathcal{L}}{\mathcal{U}_1\mathcal{R}_2}\frac{\mathcal{U}_2^2}{\mathcal{E}_2}\mathbf{v}_I \cdot \left(\mathbf{u}_1 - \mathbf{u}_2\right). &
\end{aligned}
$$

Introduce now the following definitions for Mach numbers

$$
M_k^2 = \frac{\mathcal{R}_k\mathcal{U}_k^2}{\mathcal{P}_k}. \tag{2.144}
$$

The previous definition does not coincide with the classical Mach number, but it has already been used in previous works in the literature, see e.g. [Munz et al., 2003, Orlando et al., 2022a]. In view of (2.144) and of the hypothesis $\frac{\mathcal{U}_2}{\mathcal{U}_1} = \mathcal{O}(1)$, we obtain

$$
p_{rel} = \rho_{rel}\frac{M_1^2}{M_2^2}. \tag{2.145}
$$

We also assume that

$$
\mathcal{I}_k \approx \frac{\mathcal{P}_k}{\mathcal{R}_k}. \tag{2.146}
$$

Thanks to these definitions, at low and moderate Mach numbers, we obtain

$$\begin{aligned}
\frac{\mathcal{U}_k^2}{\mathcal{E}_k} &= \frac{1}{\frac{\mathcal{I}_k}{\mathcal{U}_k^2}+1} = \frac{1}{\frac{1}{M_k^2}+1} = \mathcal{O}(M_k^2) \\
\frac{\mathcal{I}_k + \frac{\mathcal{P}_k}{\mathcal{R}_k}}{\mathcal{E}_k} &= \frac{\frac{\mathcal{I}_k}{\mathcal{U}_k^2} + \frac{1}{M_k^2}}{\frac{\mathcal{I}_k}{\mathcal{U}_k^2}+1} = \mathcal{O}(1) \qquad (2.147) \\
\frac{\mathcal{I}_k}{\mathcal{E}_k} &= 1 - \frac{\mathcal{U}_k^2}{\mathcal{E}_k} = \frac{1}{1+M_k^2} = \mathcal{O}(1).
\end{aligned}$$

(2.148)

As a result, we can rewrite the following non-dimensional equations:

$$\begin{aligned}
\frac{\partial \alpha_1}{\partial t} + \mathbf{v}_I \cdot \nabla \alpha_1 &= \tilde{\mu}\left(p_1 - p_2 \rho_{rel}\frac{M_1^2}{M_2^2}\right) \\
\frac{\partial\left(\alpha_1\rho_1\right)}{\partial t} + \nabla\cdot\left(\alpha_1\rho_1\mathbf{u}_1\right) &= 0 \\
\frac{\partial\left(\alpha_1\rho_1\mathbf{u}_1\right)}{\partial t} + \nabla\cdot\left(\alpha_1\rho_1\mathbf{u}_1\otimes\mathbf{u}_1\right) &+ \\
\frac{1}{M_1^2}\nabla\left(\alpha_1 p_1\right) - \frac{1}{M_1^2} p_I \nabla\alpha_1 &= -\tilde{\lambda}\left(\mathbf{u}_1 - \mathbf{u}_2\right) \\
\frac{\partial\left(\alpha_1\rho_1 E_1\right)}{\partial t} &+ \\
\nabla\cdot\left[\alpha_1\rho_1\mathbf{u}_1\left(h_1 + M_1^2 k_1\right)\right] - p_I\mathbf{v}_I\cdot\nabla\alpha_1 &= -\tilde{\mu} p_I\left(p_1 - p_2\rho_{rel}\frac{M_1^2}{M_2^2}\right) \\
&- \tilde{\lambda} M_1^2 \mathbf{v}_I\cdot\left(\mathbf{u}_1 - \mathbf{u}_2\right) \\
\alpha_2 &= 1 - \alpha_1 \qquad (2.149) \\
\frac{\partial\left(\alpha_2\rho_2\right)}{\partial t} + \nabla\cdot\left(\alpha_2\rho_2\mathbf{u}_2\right) &= 0 \\
\frac{\partial\left(\alpha_2\rho_2\mathbf{u}_2\right)}{\partial t} + \nabla\cdot\left(\alpha_2\rho_2\mathbf{u}_2\otimes\mathbf{u}_2\right) &+ \\
\frac{1}{M_2^2}\nabla\left(\alpha_2 p_2\right) + \frac{1}{M_2^2}\frac{1}{\rho_{rel}} p_I\nabla\alpha_1 &= \frac{\tilde{\lambda}}{\rho_{rel}}\left(\mathbf{u}_1 - \mathbf{u}_2\right) \\
\frac{\partial\left(\alpha_2\rho_2 E_2\right)}{\partial t} &+ \\
\nabla\cdot\left[\alpha_2\rho_2\mathbf{u}_2\left(h_2 + M_2^2 k_2\right)\right] + \frac{M_2^2}{M_1^2}\frac{1}{\rho_{rel}} p_I\mathbf{v}_I\cdot\nabla\alpha_1 &= \frac{\tilde{\mu}}{\rho_{rel}}\frac{M_2^2}{M_1^2} p_I\left(p_1 - p_2\rho_{rel}\frac{M_1^2}{M_2^2}\right) \\
&+ \frac{\tilde{\lambda}}{\rho_{rel}} M_2^2\mathbf{v}_I\cdot\left(\mathbf{u}_1 - \mathbf{u}_2\right),
\end{aligned}$$

with $\tilde{\mu} = \hat{\mu}\frac{\mathcal{L}}{\mathcal{U}_1}\mathcal{P}_1$ and $\tilde{\lambda} = \hat{\lambda}\frac{\mathcal{L}}{\mathcal{U}_1\mathcal{R}_1}$. If phase 1 is liquid and phase 2 is gaseous, then $\rho_{rel} \ll 1$ and $\frac{M_1}{M_2} \ll 1$. In case phase exchange is considered, the system is modified as follows [De Lorenzo et al., 2019, Han et al., 2017]:

$$
\begin{aligned}
\frac{\partial \alpha_1}{\partial t} + \mathbf{v}_I \cdot \nabla \alpha_1 &= \tilde{\mu}\left(p_1 - p_2 \rho_{rel} \frac{M_1^2}{M_2^2}\right) \\
&- \tilde{\eta}\left(g_1 - g_2\right) \frac{\Sigma}{\rho_1} \\
&- \alpha_1 \tilde{\theta}\left(T_1 - T_2\right) \Sigma \\
\frac{\partial\left(\alpha_1 \rho_1\right)}{\partial t} + \nabla \cdot \left(\alpha_1 \rho_1 \mathbf{u}_1\right) &= -\tilde{\eta}\left(g_1 - g_2\right) \Sigma \\
\frac{\partial\left(\alpha_1 \rho_1 \mathbf{u}_1\right)}{\partial t} + \nabla \cdot \left(\alpha_1 \rho_1 \mathbf{u}_1 \otimes \mathbf{u}_1\right) &+ \\
\frac{1}{M_1^2} \nabla\left(\alpha_1 p_1\right) - \frac{1}{M_1^2} p_I \nabla \alpha_1 &= -\tilde{\lambda}\left(\mathbf{u}_1 - \mathbf{u}_2\right) \\
&- \tilde{\eta}\left(g_1 - g_2\right) \Sigma \mathbf{v}_I \\
\frac{\partial\left(\alpha_1 \rho_1 E_1\right)}{\partial t} &+ \\
\nabla \cdot \left[\alpha_1 \rho_1 \mathbf{u}_1\left(h_1 + M_1^2 k_1\right)\right] - p_I \mathbf{v}_I \cdot \nabla \alpha_1 &= -\tilde{\mu} p_I\left(p_1 - p_2 \rho_{rel} \frac{M_1^2}{M_2^2}\right) \\
&- \tilde{\lambda} M_1^2 \mathbf{v}_I \cdot \left(\mathbf{u}_1 - \mathbf{u}_2\right) \\
&- b_g \tilde{\eta}\left(g_1 - g_2\right) \Sigma \\
&- \tilde{\theta}\left(T_1 - T_2\right) \Sigma \\
\alpha_2 &= 1 - \alpha_1 \qquad (2.150) \\
\frac{\partial\left(\alpha_2 \rho_2\right)}{\partial t} + \nabla \cdot \left(\alpha_2 \rho_2 \mathbf{u}_2\right) &= \tilde{\eta}\left(g_1 - g_2\right) \Sigma \\
&+ \tilde{\eta}\left(g_1 - g_2\right) \Sigma \mathbf{v}_I \\
\frac{\partial\left(\alpha_2 \rho_2 \mathbf{u}_2\right)}{\partial t} + \nabla \cdot \left(\alpha_2 \rho_2 \mathbf{u}_2 \otimes \mathbf{u}_2\right) &+ \\
\frac{1}{M_2^2} \nabla\left(\alpha_2 p_2\right) + \frac{1}{M_2^2} \frac{1}{\rho_{rel}} p_I \nabla \alpha_1 &= \frac{\tilde{\lambda}}{\rho_{rel}}\left(\mathbf{u}_1 - \mathbf{u}_2\right) \\
\frac{\partial\left(\alpha_2 \rho_2 E_2\right)}{\partial t} &+ \\
\nabla \cdot \left[\alpha_2 \rho_2 \mathbf{u}_2\left(h_2 + M_2^2 k_2\right)\right] + \frac{M_2^2}{M_1^2} \frac{1}{\rho_{rel}} p_I \mathbf{v}_I \cdot \nabla \alpha_1 &= \frac{\tilde{\mu}}{\rho_{rel}} \frac{M_2^2}{M_1^2} p_I\left(p_1 - p_2 \rho_{rel} \frac{M_1^2}{M_2^2}\right) \\
&+ \frac{\tilde{\lambda}}{\rho_{rel}} M_2^2 \mathbf{v}_I \cdot \left(\mathbf{u}_1 - \mathbf{u}_2\right) \\
&+ b_g \tilde{\eta}\left(g_1 - g_2\right) \Sigma \\
&+ \tilde{\theta}\left(T_1 - T_2\right) \Sigma,
\end{aligned}
$$

where g_k represents the chemical potential, $\tilde{\theta}$ and $\tilde{\eta}$ are the relaxation parameters for temperature and chemical relaxation and Σ is the interface area density, for which possible evolution equations will be presented in Section 2.5.

2.4.1 Four-equation relaxed two-phase system

Considering non-equilibrium conditions for velocity, pressure and temperature is a modelling assumption that can be relaxed in several physical processes different from those for which the original Baer-Nunziato model has been proposed. In particular, this is valid for fluid dynamics phenomena with longer characteristic times with respect to those of the relaxation terms in (2.149). Hence, a hierarchy of relaxed models has been derived in the literature, see e.g. [Pelanti, 2022]. We focus here on a four equation model which describes a two-phase flow in kinetic, mechanic and thermal equilibrium, i.e. $\mathbf{u}_1 = \mathbf{u}_2 = \mathbf{u}, p_1 = p_2 = p$ and $T_1 = T_2 = T$, respectively. This model has been employed, among many others, in [Bacigaluppi et al., 2022, Demou et al., 2022, Saurel et al., 2016] and represents the minimal set of equations for describing phase transition. The model can be obtained from the Baer-Nunziato system in the limit of velocity, pressure and temperature equilibrium, namely considering $\tilde{\mu} \to \infty, \tilde{\lambda} \to \infty$ and $\tilde{\theta} \to \infty$. We present first the dimensional set of equations which reads as follows:

$$\begin{aligned}
\frac{\partial \alpha_1 \rho_1}{\partial t} + \nabla\cdot \left(\alpha_1 \rho_1 \mathbf{u}\right) &= -\Gamma_1 \\
\frac{\partial \alpha_2 \rho_2}{\partial t} + \nabla\cdot \left(\alpha_2 \rho_2 \mathbf{u}\right) &= \Gamma_1 \\
\frac{\partial \rho \mathbf{u}}{\partial t} + \nabla\cdot \left(\rho \mathbf{u} \otimes \mathbf{u}\right) + \nabla p &= 0 \\
\frac{\partial \rho E}{\partial t} + \nabla\cdot \left[\left(\rho E + p\right) \mathbf{u}\right] &= 0,
\end{aligned} \tag{2.151}$$

where Γ_1 is the mass transfer term. The system (2.151) is composed by two continuity equations for the two phases and by a single momentum and energy balance equation, analogous to the mixture model relations presented in Section 2.2.3. Viscous stresses, heat conduction, and gravity effects can be added, as done for instance in [Demou et al., 2022, Saurel et al., 2016], so as to obtain

$$\begin{aligned}
\frac{\partial \alpha_1 \rho_1}{\partial t} + \nabla\cdot \left(\alpha_1 \rho_1 \mathbf{u}\right) &= -\Gamma_1 \\
\frac{\partial \alpha_2 \rho_2}{\partial t} + \nabla\cdot \left(\alpha_2 \rho_2 \mathbf{u}\right) &= \Gamma_1 \\
\frac{\partial \rho \mathbf{u}}{\partial t} + \nabla\cdot \left(\rho \mathbf{u} \otimes \mathbf{u}\right) + \nabla p &= \nabla\cdot \left[\mu \left(\nabla \mathbf{u} + \nabla \mathbf{u}^T\right) - \frac{2}{3}\mu \left(\nabla \cdot \mathbf{u}\right) \mathbf{I}\right] \\
&- \rho g \mathbf{k} \\
\frac{\partial \rho E}{\partial t} + \nabla\cdot \left[\left(\rho E + p\right) \mathbf{u}\right] &= \nabla\cdot \left[\mu \left(\nabla \mathbf{u} + \nabla \mathbf{u}^T\right) \mathbf{u} - \frac{2}{3}\mu \left(\nabla \cdot \mathbf{u}\right) \mathbf{u}\right] \\
&+ \nabla\cdot \left(\kappa \nabla T\right) - \rho g \mathbf{k} \cdot \mathbf{u}
\end{aligned} \tag{2.152}$$

where μ is the dynamic viscosity, κ is the thermal conductivity, g is the modulus of the acceleration of gravity. The thermodynamic closure for (2.152) reads as follows [Saurel et al., 2016]:

$$\begin{aligned}
T_1 &= T_2 = T \\
p_1 &= p_2 = p \\
e &= Y_1 e_1 + Y_2 e_2 \\
\alpha_1 + \alpha_2 &= 1.
\end{aligned} \tag{2.153}$$

The solution of this algebraic system depends on the specific choice of the equation of state (EOS), as we will see in Section 2.6.

The dimensional analysis for (2.152) can be performed in analogy to what we did for the complete Baer-Nunziato model (see also [Orlando et al., 2022a]). We consider as reference density the one of the gaseous phase, i.e. $\mathcal{R}_2$, so that the Mach number is defined by

$$M^2 = \frac{\mathcal{R}_2\mathcal{U}^2}{\mathcal{P}}. \tag{2.154}$$

Moreover, we assume constant values for the dynamic viscosity and the thermal conductivity of the two phases and we consider as reference values μ_2 and κ_2. The resulting system of equations reads therefore as follows:

$$\begin{aligned}
\frac{\partial \alpha_1\rho_1}{\partial t} + \nabla\cdot(\alpha_1\rho_1\mathbf{u}) &= -\Gamma_1 \\
\frac{\partial \alpha_2\rho_2}{\partial t} + \nabla\cdot(\alpha_2\rho_2\mathbf{u}) &= \Gamma_1 \\
\frac{\partial \rho\mathbf{u}}{\partial t} + \nabla\cdot(\rho\mathbf{u}\otimes\mathbf{u}) + \frac{1}{M^2}\nabla p &= \frac{1}{Re}\nabla\cdot\left[\mu\left(\nabla\mathbf{u} + \nabla\mathbf{u}^T\right) - \frac{2}{3}\mu\left(\nabla\cdot\mathbf{u}\right)\mathbf{I}\right] \\
&- \frac{\rho}{Fr^2}\mathbf{k} \qquad (2.155) \\
\frac{\partial \rho E}{\partial t} + \nabla\cdot\left[\left(h + kM^2\right)\rho\mathbf{u}\right] &= \frac{M^2}{Re}\nabla\cdot\left[\mu\left(\nabla\mathbf{u} + \nabla\mathbf{u}^T\right)\mathbf{u} - \frac{2}{3}\mu\left(\nabla\cdot\mathbf{u}\right)\mathbf{u}\right] \\
&+ \frac{1}{PrRe}\nabla\cdot(\kappa\nabla T) - \rho\frac{M^2}{Fr^2}\mathbf{k}\cdot\mathbf{u},
\end{aligned}$$

where the Reynolds, Prandtl and Froude numbers are defined as

$$Re = \frac{\mathcal{R}_2\mathcal{U}\mathcal{L}}{\mu_2} \qquad \kappa_2 = \frac{c_{p_2}\mu_2}{Pr} \qquad Fr^2 = \frac{\mathcal{U}^2}{g\mathcal{L}} \tag{2.156}$$

with c_p denoting the specific heat at constant pressure. As done before, we employ with a slight abuse of notation the same symbols for the non-dimensional variables and, therefore, the following relations hold:

$$\mu = \frac{\mu_1}{\mu_2}\alpha_1 + \alpha_2 \tag{2.157}$$

$$\kappa = \frac{\kappa_1}{\kappa_2}\alpha_1 + \alpha_2. \tag{2.158}$$

2.5 Variational approach for two-phase system

In this Section, we employ the Stationary Action Principle (SAP) to derive the structure of a two-phase model with an evolution equation for the interface area density, following the contributions [Cordesse et al., 2019, Drui et al., 2019]. The SAP only provides the conservative part for our model and we shall examine suitable dissipative phenomena in the following. The relation (2.133) contains terms for which non trivial closure relations would be needed. Hence, evolution equations for the interface area density are typically derived by means of empirical approaches and considerations, see e.g. [Lhuillier, 2004]. In this Section, we analyze how to recover this kind of relations in an original way, bringing them back into a variational framework. We express the interface area density Σ as the sum of two contributions

$$\Sigma = \Sigma_0 + \tilde{\Sigma}, \tag{2.159}$$

where Σ_0 is the reference interface area density that obeys the following relation

$$\frac{\partial \Sigma_0}{\partial t} + \nabla \cdot \left(\Sigma_0 \mathbf{u} \right) = 0 \tag{2.160}$$

and $\tilde{\Sigma}$ represents the perturbation with respect to the reference value. Two phase flows which involve physical phenomena such as break-up or atomization can be described using two scales: a large scale that describes the bulk fluid and a small scale where droplets or bubbles of different size are present forming a polydisperse spray [Cordesse et al., 2019, Drui et al., 2019, Cordesse et al., 2020]. In [Drui et al., 2019], the authors derived by means of SAP a model which takes into account volume fraction variations due to small scales variables, whereas we consider here variations due to large scale quantities. We recall now for the convenience of the reader the main steps in the modelling process. Firstly, in order to the derive a system of equations, we need to define a Lagrangian energy $\mathcal{L}$ for the system. In the present work, we consider a variation of the Lagrangian functional proposed in [Drui et al., 2019]

$$\mathcal{L}\left(\rho, Y, \mathbf{u}, \alpha_L, D_t \alpha_L\right) = \frac{1}{2} \rho \mathbf{u} \cdot \mathbf{u} - \rho e \left(\rho, Y, \alpha_L\right) + \frac{1}{2} \nu \left(\alpha_L, \rho, Y\right) \left(D_t \alpha_L\right)^2, \tag{2.161}$$

with α_L denoting the large-scale volume fraction and D_t representing the material derivative. Notice that we consider immiscible fluids, so that for the volume fractions and the mass fractions the relations $\alpha_{L_1} + \alpha_{L_2} = 1$ and $Y_1 + Y_2 = 1$. For convenience in the notation, we denote $\alpha_{L,1}$ by α_L and Y_1 by Y. Moreover, ρ is the mixture density defined as $\alpha_L \rho_1 + (1 - \alpha_L) \rho_2$ and e is the mixture internal energy. The term $\frac{1}{2} \nu \left(D_t \alpha_L\right)^2$ was employed in [Drui et al., 2019] to model small-scale kinematics and is now part of the kinetic energy to model large-scale oscillations. The coefficient ν has the dimensions of $[\mathrm{kg}][\mathrm{m}]^{-1}$ and is related to inertial effects. Moreover, unlike [Drui et al., 2019], a dependence on the density ρ and on the mass fraction Y is considered for ν. The following main assumptions are made:

1. there is no mass transfer between the two phases;
2. there is kinetic equilibrium between the two phases, namely the velocities of the two phases are equal;
3. barotropic equations of state (EOS), i.e. pressure dependent only on the density, are used for both phases;
4. interfacial forces are neglected.

We also postulate additional constraints for the two-fluid system. In view of our hypotheses, the total mass and the mass fractions of each phase are conserved:

$$\frac{\partial \rho Y}{\partial t} + \nabla \cdot \left(\rho Y \mathbf{u} \right) = 0 \tag{2.162}$$

$$\frac{\partial \rho}{\partial t} + \nabla \cdot \left(\rho \mathbf{u} \right) = 0. \tag{2.163}$$

Notice that, thanks to (2.163), (2.162) is equivalent to

$$\frac{\partial Y}{\partial t} + \mathbf{u} \cdot \nabla Y = D_t Y = 0. \tag{2.164}$$

Finally, as usual, we define the Hamiltonian action by setting

$$\mathcal{A}(\zeta) = \int_\Omega \mathcal{L}\left(\rho, Y, \mathbf{u}, \alpha_L, D_t\alpha_L\right) d\mathbf{x}dt \tag{2.165}$$

and we compute the infinitesimal variation of the action

$$\delta\mathcal{A} = \int_\Omega \left[\left(\frac{\partial \mathcal{L}}{\partial \rho}\right)\delta\rho + \left(\frac{\partial \mathcal{L}}{\partial Y}\right)\delta Y + \frac{\partial \mathcal{L}}{\partial \mathbf{u}}\cdot\delta\mathbf{u} + \frac{\partial \mathcal{L}}{\partial \alpha_L}\delta\alpha_L + \frac{\partial \mathcal{L}}{\partial D_t\alpha_L}\delta D_t\alpha_L\right]. \tag{2.166}$$

We postulate, as usual, that the perturbation of all quantities vanish at the boundary of the domain and at both initial and final time. After some manipulations (see Appendix A.4), we obtain the following system

$$\begin{aligned}
&\frac{\partial \rho}{\partial t} + \nabla\cdot\left(\rho\mathbf{u}\right) = 0\\
&D_tY = 0\\
&\frac{\partial\left(\rho\mathbf{u}\right)}{\partial t} + \nabla\cdot\left(\rho\mathbf{u}\otimes\mathbf{u}\right) + \nabla P = 0\\
&\frac{\partial}{\partial t}\left[\nu\left(D_t\alpha_L\right)\right] + \nabla\cdot\left[\nu\left(D_t\alpha_L\right)\mathbf{u}\right] - \frac{1}{2}\left(D_t\alpha_L\right)^2\frac{\partial\nu}{\partial\alpha_L} + \rho\frac{\partial e}{\partial\alpha_L} = 0,
\end{aligned} \tag{2.167}$$

with $P = p + \frac{1}{2}\left(\nu - \rho\frac{\partial\nu}{\partial\rho}\right)\left(D_t\alpha_L\right)^2$ and $p = \rho^2\frac{\partial e}{\partial\rho}$. We define now the variable $\tilde{\Sigma}$ which, as aforementioned, represents the "fluctuating" part of the interfacial area density:

$$D_t\alpha_L = \xi^n\nu^m\tilde{\Sigma}, \tag{2.168}$$

with m being an arbitrary exponent to be fixed and ξ denoting a suitable physical constant whose meaning will be specified later on. This definition is inspired by the relation (2.132) obtained with the ensemble averaging approach. The system (2.167) can be therefore rewritten as

$$\begin{aligned}
&\frac{\partial \rho}{\partial t} + \nabla\cdot\left(\rho\mathbf{u}\right) = 0\\
&D_tY = 0\\
&\frac{\partial\left(\rho\mathbf{u}\right)}{\partial t} + \nabla\cdot\left(\rho\mathbf{u}\otimes\mathbf{u}\right) + \nabla P = 0\\
&\frac{\partial \Sigma_0}{\partial t} + \nabla\cdot\left(\Sigma_0\mathbf{u}\right) = 0\\
&D_t\alpha_L = \xi^n\nu^m\tilde{\Sigma}\\
&\frac{\partial\tilde{\Sigma}}{\partial t} + \nabla\cdot(\tilde{\Sigma}\mathbf{u}) = -\xi^n\nu^m\left(m+\frac{1}{2}\right)\frac{\frac{\partial\nu}{\partial\alpha_L}}{\nu}\tilde{\Sigma}^2 + (m+1)\rho\frac{\frac{\partial\nu}{\partial\rho}}{\nu}(\nabla\cdot\mathbf{u})\tilde{\Sigma} - \frac{\rho}{\nu^{m+1}\xi^n}\frac{\partial e}{\partial\alpha_L}.
\end{aligned} \tag{2.169}$$

Notice that $\tilde{\Sigma}$ has no *a priori* definite sign.

2.5.1 Dissipation and second principle of thermodynamics

In this Section, we consider the introduction of dissipative terms in the two-phase system in a way that is compatible with the second principle of thermodynamics. In the barotropic case, it is customary to consider as mathematical entropy

[Godlewski and Raviart, 1996, Drui et al., 2019]:

$$\rho\eta\left(\rho, Y, \mathbf{u}, \alpha_L, \tilde{\Sigma}\right) = \frac{1}{2}\rho\mathbf{u}\cdot\mathbf{u} + \frac{1}{2}\nu^{2m+1}\xi^{2n}\tilde{\Sigma}^2 + \rho e. \tag{2.170}$$

We seek now an entropy flux function $\mathbf{G}$ such that

$$\frac{\partial(\rho\eta)}{\partial t} + \nabla\cdot\left(\rho\eta\mathbf{u} + \mathbf{G}\right) \leq 0, \tag{2.171}$$

or, equivalently,

$$\rho D_t\eta + \nabla\cdot\mathbf{G} \leq 0. \tag{2.172}$$

We consider the following inequality, whose derivation is reported in detail in Appendix A.4

$$\begin{aligned}&\left[D_t\tilde{\Sigma} + (\nabla\cdot\mathbf{u})\tilde{\Sigma} - (m+1)\rho\frac{\frac{\partial\nu}{\partial\rho}}{\nu}(\nabla\cdot\mathbf{u})\tilde{\Sigma} + \right.\\ &\left.\frac{\rho}{\xi^n\nu^{m+1}}\frac{\partial e}{\partial\alpha_L} + \xi^n\nu^m\left(m+\frac{1}{2}\right)\frac{\frac{\partial\nu}{\partial\alpha_L}}{\nu}\tilde{\Sigma}^2\right]\tilde{\Sigma} \leq 0.\end{aligned} \tag{2.173}$$

A simple way to satisfy the inequality (2.173) is considering an equation for which we take at right-hand side $-\frac{\epsilon(\alpha_L,Y,\rho)}{\nu}\tilde{\Sigma}$, with $\epsilon > 0$ being a suitable function related to dissipation effects, so as to obtain

$$\begin{aligned}&D_t\tilde{\Sigma} + (\nabla\cdot\mathbf{u})\tilde{\Sigma} - (m+1)\rho\frac{\frac{\partial\nu}{\partial\rho}}{\nu}(\nabla\cdot\mathbf{u})\tilde{\Sigma}\\ &+ \frac{\rho}{\xi^n\nu^{m+1}}\frac{\partial e}{\partial\alpha_L} + \xi^n\nu^m\left(m+\frac{1}{2}\right)\frac{\frac{\partial\nu}{\partial\alpha_L}}{\nu}\tilde{\Sigma}^2 = -\frac{\epsilon(\alpha_L, Y, \rho)}{\nu}\tilde{\Sigma}.\end{aligned} \tag{2.174}$$

Hence, the final system reads:

$$\begin{aligned}&\frac{\partial\rho}{\partial t} + \nabla\cdot(\rho\mathbf{u}) = 0\\ &D_tY = 0\\ &\frac{\partial(\rho\mathbf{u})}{\partial t} + \nabla\cdot(\rho\mathbf{u}\otimes\mathbf{u}) + \nabla P = 0\\ &\frac{\partial\Sigma_0}{\partial t} + \nabla\cdot(\Sigma_0\mathbf{u}) = 0\\ &D_t\alpha_L = \xi^n\nu^m\tilde{\Sigma}\\ &\frac{\partial\tilde{\Sigma}}{\partial t} + \nabla\cdot(\tilde{\Sigma}\mathbf{u}) = -\xi^n\nu^m\left(m+\frac{1}{2}\right)\frac{\frac{\partial\nu}{\partial\alpha_L}}{\nu}\tilde{\Sigma}^2 + (m+1)\rho\frac{\frac{\partial\nu}{\partial\rho}}{\nu}(\nabla\cdot\mathbf{u})\tilde{\Sigma} - \frac{\rho}{\nu^{m+1}\xi^n}\frac{\partial e}{\partial\alpha_L} - \frac{\epsilon}{\nu}\tilde{\Sigma}.\end{aligned} \tag{2.175}$$

2.5.2 Analysis of eigenvalues and eigenvectors

In this Section, we study the hyperbolicity of system (2.175). This property ensures that all wave speeds are finite and that the system may be locally decoupled. Moreover, from a mathematical point of view, this property is helpful in the construction of Riemann solvers. This result is an original contribution of the thesis.

The hyperbolicity of system (2.175) can be studied in a one-dimensional setting by considering the following quasi-linear form:

$$\frac{\partial \mathbf{V}}{\partial t} + \mathbf{A}\left(\mathbf{V}\right)\frac{\partial \mathbf{V}}{\partial x} = \mathbf{0}, \tag{2.176}$$

with

$$\mathbf{V} = \begin{bmatrix} \alpha_L \\ \rho_1 \\ \rho_2 \\ \Sigma_0 \\ u \\ \tilde{\Sigma} \end{bmatrix}, \tag{2.177}$$

and the matrix $\mathbf{A}\left(\mathbf{V}\right)$ equal to

$$\begin{bmatrix} u & 0 & 0 & 0 & 0 & 0 \\ 0 & u & 0 & 0 & \rho_1 & 0 \\ 0 & 0 & u & 0 & \rho_2 & 0 \\ 0 & 0 & 0 & u & \Sigma_0 & 0 \\ \frac{p_1 - p_2}{\rho} + \tilde{a}_{u,\alpha_L} & \frac{\alpha_L c_1^2}{\rho} + \tilde{a}_{u,\rho_1} & \frac{(1-\alpha_L) c_2^2}{\rho} + \tilde{a}_{u,\rho_2} & 0 & u & \tilde{a}_{u,\tilde{\Sigma}} \\ 0 & 0 & 0 & 0 & \tilde{\Sigma} - \tilde{\Sigma}\left(m+1\right)\nu_\rho \frac{\rho}{\nu} & u \end{bmatrix}. \tag{2.178}$$

Here we set

$$\tilde{a}_{u,\alpha} = \tilde{\Sigma}_{\nu,m}\left[\nu_{\alpha_L}\tilde{m}_\nu - \nu\left(\nu_\rho\left(\rho_1 - \rho_2\right) + \rho\frac{\partial \nu_\rho}{\partial \alpha_L}\right)\right] \tag{2.179}$$

$$\tilde{a}_{u,\rho_1} = \tilde{\Sigma}_{\nu,m}\left[-2m\nu_\rho\frac{\partial \nu}{\partial \rho_1} + \nu\left(\left(1+2m\right)\frac{\partial \nu}{\partial \rho_1} - \nu_\rho \alpha_L - \frac{\partial \nu_\rho}{\partial \rho_1}\rho)\right)\right] \tag{2.180}$$

$$\tilde{a}_{u,\rho_2} = \tilde{\Sigma}_{\nu,m}\left[-2m\nu_\rho\frac{\partial \nu}{\partial \rho_2}\rho + \nu\left(\left(1+2m\right)\frac{\partial \nu}{\partial \rho_2} - \nu_\rho\left(1 - \alpha_L\right) - \frac{\partial \nu_\rho}{\partial \rho_2}\rho\right)\right], \tag{2.181}$$

with $\nu_\rho = \frac{\partial \nu}{\partial \rho}, \nu_{\alpha_L} = \frac{\partial \nu}{\partial \alpha_L}, \tilde{\Sigma}_{\nu,m} = \frac{1}{2}\nu^{2m-1}\xi^{2m}\tilde{\Sigma}^2$ and $\tilde{m}_\nu = \left(2m+1\right)\nu - 2m\rho\nu_\rho$. Notice that, for the sake of simplicity in the analysis, we consider as primary variables ρ_1 and ρ_2 instead of Y and ρ. The densities ρ_1 and ρ_2 satisfy the following conservation laws:

$$\frac{\partial\left[\alpha_L \rho_1\right]}{\partial t} + \nabla\cdot\left[\alpha_L \rho_1 \mathbf{u}\right] = 0 \tag{2.182}$$

$$\frac{\partial\left[\left(1-\alpha_L\right)\rho_2\right]}{\partial t} + \nabla\cdot\left[\left(1-\alpha_L\right)\rho_2 \mathbf{u}\right] = 0. \tag{2.183}$$

The equivalence between the system (2.176) and the system (2.175) without source terms is established taking into account that, since we are considering barotropic equations of state, $\frac{\partial p_k}{\partial \rho_k} = c_k^2$, with c_k denoting the speed of sound of phase $k = 1, 2$, and that $\frac{\partial e}{\partial \alpha_L} = \frac{p_2 - p_1}{\rho}$. Indeed the mixture internal energy is defined by the following relation:

$$\begin{aligned} e\left(\rho, Y, \alpha_L\right) &= Y e_1\left(\rho_1\right) + \left(1 - Y\right) e_2(\rho_2) \\ &= Y e_1\left(\frac{\rho Y}{\alpha}\right) + \left(1 - Y\right) e_2\left(\frac{\rho\left(1 - Y\right)}{1 - \alpha}\right), \end{aligned} \tag{2.184}$$

with $e_k, k = 1, 2$, denoting the internal energy of phase k. Hence, since $\frac{\partial \rho_1}{\partial \alpha} = -\frac{1}{\alpha^2}\rho Y$ and $\frac{\partial \rho_2}{\partial \alpha} = \frac{\rho(1-Y)}{(1-\alpha)^2}$, we obtain

$$\frac{\partial e}{\partial \alpha_L} = -\frac{Y^2}{\alpha^2}\rho\frac{\partial e_1}{\partial \rho_1} - \frac{(1-Y)^2}{(1-\alpha)^2}\rho\frac{\partial e_2}{\partial \rho_2} = -\frac{\rho}{\rho_1^2}\frac{\partial e_1}{\partial \rho_1} - \frac{\rho}{\rho_2^2}\frac{\partial e_2}{\partial \rho_2}. \tag{2.185}$$

Since $\frac{\partial e_k}{\partial \rho_k} = \frac{p_k}{\rho_k^2}$ [Vidal, 2001, Sandler, 2017], we get

$$\frac{\partial e}{\partial \alpha_L} = \frac{p_2 - p_1}{\rho}. \tag{2.186}$$

The eigenvalues of $\mathbf{A}$ are $\{u, u, u, u, u + c_{\tilde{\Sigma}}, u - c_{\tilde{\Sigma}}\}$, where:

$$c_{\tilde{\Sigma}}^2 = c_F^2 + c_\nu \tag{2.187}$$

$$c_F^2 = \frac{\alpha_L \rho_1 c_1^2 + (1-\alpha_L)\rho_2 c_2^2}{\rho} \tag{2.188}$$

$$\begin{aligned} c_\nu = \tilde{\Sigma}_{\nu,m} \Bigg[& 2(m+1)(\nu_\rho)^2 \rho + \frac{\frac{\partial \nu}{\partial \rho_1}\rho_1 \tilde{m}_\nu}{\rho} + \\ & \frac{\nu\left((2m+1)\frac{\partial \nu}{\partial \rho_2}\rho_2 + 2\nu - \rho\left(\frac{\partial \nu_\rho}{\partial \rho_1}\rho_1 + \frac{\partial \nu_\rho}{\partial \rho_2}\rho_2\right)\right)}{\rho} - \\ & \nu_\rho\left(2m\frac{\partial \nu}{\partial \rho_2}\rho_2 + 2m\nu + 5\nu\right)\Bigg]. \end{aligned} \tag{2.189}$$

Notice that in general the positivity of the quantity c_ν is not guaranteed. Conditions to guarantee that $c_\nu > 0$ in a general situation are not feasible since its expression strongly depends on the choice of ν and, therefore, on the specific physical phenomenon under consideration. We will address the issue of the positivity of c_ν for specific regimes in Section 2.5.3. Along with these eigenvalues, we have the following linearly degenerate eigenvectors:

$$\mathbf{r}_1 = \begin{bmatrix} \frac{1}{(\nu\xi)^{2m}\tilde{\Sigma}(\nu-\rho\nu_\rho)} \\ 0 \\ 0 \\ 0 \\ 0 \\ \frac{p_2-p_1-\tilde{\Sigma}_{\nu,m}\left[\nu_{\alpha_L}\tilde{m}_\nu-\nu\left(\nu_\rho(\rho_1-\rho_2)+\rho\frac{\partial\nu_{\alpha_L}}{\partial\rho}\right)\right]}{\left[(\nu\xi)^{2m}\tilde{\Sigma}(\nu-\rho\nu_\rho)\right]^2} \end{bmatrix} \tag{2.190}$$

$$\mathbf{r}_2 = \begin{bmatrix} 0 \\ 0 \\ (\nu\xi)^{2m}\,\tilde{\Sigma}\,(\nu-\rho\nu_\rho) \\ 0 \\ 0 \\ -(1-\alpha_L)\,c_2^2-\frac{1}{2}\tilde{\Sigma}_{\nu,m}\left[\frac{\partial\nu}{\partial\rho_2}\tilde{m}_\nu-\nu\nu_\rho\,(1-\alpha_L)-\nu\rho\frac{\partial\nu_\rho}{\partial\rho_2}\right] \end{bmatrix} \tag{2.191}$$

$$\mathbf{r}_3 = \begin{bmatrix} 0 \\ 0 \\ (\nu\xi)^{2m}\,\tilde{\Sigma}\left(\nu-\frac{\partial\nu}{\partial\rho}\rho\right) \\ 0 \\ 0 \\ -\alpha_L c_1^2-\tilde{\Sigma}_{\nu,m}\left[\frac{\partial\nu}{\partial\rho_1}\tilde{m}_\nu-\nu\nu_\rho\alpha_L-\nu\rho\frac{\partial\nu_\rho}{\partial\rho_1}\right] \end{bmatrix} \tag{2.192}$$

$$\mathbf{r}_4 = \begin{bmatrix} 0 \\ 0 \\ 0 \\ 1 \\ 0 \\ 0 \end{bmatrix} \tag{2.193}$$

and two truly non linear eigenvectors:

$$\mathbf{r}_5 = \begin{bmatrix} 0 \\ \rho_1 \\ \rho_2 \\ \Sigma_0 \\ -c_{\tilde{\Sigma}} \\ \tilde{\Sigma}-\tilde{\Sigma}\frac{(1+m)\rho\nu_\rho}{\nu} \end{bmatrix} \tag{2.194}$$

$$\mathbf{r}_6 = \begin{bmatrix} 0 \\ \rho_1 \\ \rho_2 \\ \Sigma_0 \\ c_{\tilde{\Sigma}} \\ \tilde{\Sigma}-\tilde{\Sigma}\frac{(1+m)\rho\nu_\rho}{\nu} \end{bmatrix} \tag{2.195}$$

The system is hyperbolic provided that the eigenvectors forms a basis. This condition is fulfilled provided that $c_\Sigma \neq 0$, since the determinant is

$$\det(\mathbf{r}_1,\mathbf{r}_2,\mathbf{r}_3,\mathbf{r}_4,\mathbf{r}_5,\mathbf{r}_6) = 2\rho c_{\tilde{\Sigma}}^3. \tag{2.196}$$

2.5.3 Submodels and limiting cases

We aim now to study some limiting cases and submodels which stem from the derived two-phase system. In particular, we will derive the conditions needed to obtain the classical pressure relaxation term [Saurel and Abgrall, 1999, Saurel and Pantano, 2018] and the evolution equation for interface area density obtained in [Lhuillier, 2004] by means of empirical considerations.

If we want to obtain the usual pressure relaxation for the transport of α_L, we need to keep the last two terms of (2.174). We consider $\epsilon = \tilde{\epsilon}\nu^{-m}$ so that, after multiplication by ν^{m+1}, we get:

$$\begin{aligned}\nu^{m+1}\left[\frac{\partial\tilde{\Sigma}}{\partial t} + \nabla\cdot\left(\tilde{\Sigma}\mathbf{u}\right)\right] &= -\xi^n\nu^{2m+1}\left(m+\frac{1}{2}\right)\frac{\frac{\partial\nu}{\partial\alpha_L}}{\nu}\tilde{\Sigma}^2 \\ &+ \nu^{m+1}\left(m+1\right)\rho\frac{\frac{\partial\nu}{\partial\rho}}{\nu}\left(\nabla\cdot\mathbf{u}\right)\tilde{\Sigma} \\ &- \frac{\rho}{\xi^n}\frac{\partial e}{\partial\alpha_L} - \tilde{\epsilon}\tilde{\Sigma}. \end{aligned} \tag{2.197}$$

We assume $\nu \to 0$ when $Y \to 0$ along with $\frac{\frac{\partial\nu}{\partial\alpha_L}}{\nu} \underset{Y\to 0}{=} O(1)$ and $\frac{\frac{\partial\nu}{\partial\rho}}{\nu} \underset{Y\to 0}{=} O(1)$. In this limit, we obtain the pressure relaxation:

$$D_t\alpha_L = -\frac{1}{\tilde{\epsilon}}\rho\frac{\partial e}{\partial\alpha_L}, \tag{2.198}$$

provided $m > -1$. In this case, $\tilde{\epsilon}$ has the role of a relaxation coefficient and the stiff source term in (2.198) drives the dissipation effects.

The present model is able also to recover the conservative and compressible contribution of Lhuillier's equation [Lhuillier, 2004]:

$$\frac{\partial\tilde{\Sigma}}{\partial t} + \nabla\cdot\left(\tilde{\Sigma}\mathbf{u}\right) = \tfrac{2}{3}\left(\nabla\cdot\mathbf{u}\right)\tilde{\Sigma} + \tilde{S}, \tag{2.199}$$

where $\tilde{S}$ collects the source terms. Comparing (2.199) and the evolution equation for $\tilde{\Sigma}$ in (2.169), one would need:

$$m = -\frac{1}{2} \qquad \left(m+1\right)\rho\frac{\frac{\partial\nu}{\partial\rho}}{\nu} = \frac{2}{3}. \tag{2.200}$$

This leads to

$$\nu(\rho, Y, \alpha_L) = C(\alpha_L, Y)\rho^{\frac{4}{3}}. \tag{2.201}$$

Going back to definition (2.168), and recalling that $[\nu] = [\mathrm{kg}][\mathrm{m}]^{-1}$, we obtain

$$[\xi^n] = [\mathrm{s}]^{-1}[\mathrm{kg}]^{\frac{1}{2}}[\mathrm{m}]^{\frac{1}{2}}, \tag{2.202}$$

and, fixing $n = \frac{1}{2}$ for the sake of simplicity in the physical interpretation of ξ, we get

$$[\xi] = [\mathrm{s}]^{-2}[\mathrm{kg}][\mathrm{m}] = [\sigma][\mathrm{m}], \tag{2.203}$$

where $[\sigma]$ denotes the units of surface tension coefficient. The relation (2.201) gives us a positive value of c_ν and therefore the system (2.176) is hyperbolic in this configuration. Indeed, taking $m = -\frac{1}{2}$ in (2.189), we obtain

$$\begin{aligned} c_\nu &= \frac{1}{2\nu^2\xi}\tilde{\Sigma}^2\left[(\nu_\rho)^2\rho + \left(\frac{\partial\nu}{\partial\rho_1}\rho_1 + \frac{\partial\nu}{\partial\rho_2}\rho_2 - 4\nu\right)\nu_\rho + \right. \\ & \qquad \left. 2\frac{\nu^2}{\rho} - \nu\left(\frac{\partial\nu_\rho}{\partial\rho_1}\rho_1 + \frac{\partial\nu_\rho}{\partial\rho_2}\rho_2\right)\right]. \end{aligned} \tag{2.204}$$

Since $\nu_\rho = \frac{\partial\nu}{\partial\rho} = \frac{4}{3}\frac{\nu}{\rho}$, we get

$$\begin{aligned} c_\nu &= \frac{1}{2\nu^2\xi}\tilde{\Sigma}^2\left[\frac{16}{9}\frac{\nu^2}{\rho} + \left(\frac{\partial\nu}{\partial\rho_1}\rho_1 + \frac{\partial\nu}{\partial\rho_2}\rho_2 - 4\nu\right)\frac{4}{3}\frac{\nu}{\rho} + 2\frac{\nu^2}{\rho} - \nu\left(\frac{\partial\nu_\rho}{\partial\rho_1}\rho_1 + \frac{\partial\nu_\rho}{\partial\rho_2}\rho_2\right)\right] \\ &= \frac{1}{2\nu^2\xi}\tilde{\Sigma}^2\left[\frac{112}{9}\frac{\nu^2}{\rho} + \left(\frac{\partial\nu}{\partial\rho_1}\rho_1 + \frac{\partial\nu}{\partial\rho_2}\rho_2\right)\frac{4}{3}\frac{\nu}{\rho} - \nu\left(\frac{\partial\nu_\rho}{\partial\rho_1}\rho_1 + \frac{\partial\nu_\rho}{\partial\rho_2}\rho_2\right)\right]. \end{aligned} \tag{2.205}$$

Moreover, we notice that the following relations hold:

$$\frac{\partial\nu_\rho}{\partial\rho_1} = \frac{\partial}{\partial\rho_1}\left(\frac{4}{3}\frac{\nu}{\rho}\right) = \frac{4}{3}\left(\frac{\partial\nu}{\partial\rho_1}\frac{1}{\rho} - \frac{\partial\rho}{\partial\rho_1}\frac{\nu}{\rho^2}\right) \tag{2.206}$$

$$\frac{\partial\nu_\rho}{\partial\rho_1} = \frac{\partial}{\partial\rho_2}\left(\frac{4}{3}\frac{\nu}{\rho}\right) = \frac{4}{3}\left(\frac{\partial\nu}{\partial\rho_2}\frac{1}{\rho} - \frac{\partial\rho}{\partial\rho_2}\frac{\nu}{\rho^2}\right). \tag{2.207}$$

Hence, (2.205) reduces to

$$c_\nu = \frac{1}{2\nu^2\xi}\tilde{\Sigma}^2\left[\frac{112}{9}\frac{\nu^2}{\rho} + \frac{4}{3}\frac{\nu^2}{\rho^2}\left(\frac{\partial\rho}{\partial\rho_1}\rho_1 + \frac{\partial\rho}{\partial\rho_2}\rho_2\right)\right]. \tag{2.208}$$

Since $\frac{\partial\rho}{\partial\rho_1} = \alpha_L$ and $\frac{\partial\rho}{\partial\rho_2} = 1 - \alpha_L$, we obtain

$$c_\nu = \frac{1}{2\nu^2\xi}\tilde{\Sigma}^2\left[\frac{112}{9}\frac{\nu^2}{\rho} + \frac{4}{3}\frac{\nu^2}{\rho}\right] = \frac{1}{2\nu^2\xi}\tilde{\Sigma}^2\frac{139}{9}\frac{\nu^2}{\rho} = \frac{139}{18}\frac{\tilde{\Sigma}^2}{\xi\rho} > 0. \tag{2.209}$$

2.6 The equation of state

In this Section, we describe the equations of state required separately for each phase to complete systems (2.143), (2.149) and (2.175). For the sake of clarity, the description and the expressions will be reported without subscripts. The most classical and simple choice is that of an ideal gas. In the non-dimensional variables introduced above, the equation that links together pressure, density and internal energy is given by

$$p = (\gamma - 1)\left(\rho E - \frac{1}{2}M^2\rho\mathbf{u}\cdot\mathbf{u}\right), \tag{2.210}$$

with γ denoting the specific heats ratio. The above relation is valid only in case of constant γ [Vidal, 2001, Sandler, 2017]. Since we aim to consider more realistic fluids, the ideal gas is not the only relation to be considered. An example of non-ideal gas equation of state is given by the general cubic equation of state, whose equation linking together internal energy, density and temperature, according to [Vidal, 2001], is given in dimensional form by

$$e = e^{\#}(T) + \frac{a(T) - T\frac{da}{dT}}{b}U(\rho, b, r_1, r_2), \tag{2.211}$$

where $e^{\#}$ denotes the internal energy of an ideal gas at temperature T. The function U and the constants r_1 and r_2 depend on the specific equation of state, whereas a and b are suitable parameters that characterize the gas behaviour. Notice that, with a slight abuse of notation, we keep in the present description the same notation for the dimensional variables. In case $c_v = \frac{de^{\#}}{dT}$ is constant, we can write

$$e = c_v T + \frac{a(T) - T\frac{da}{dT}}{b} U\left(\rho, b, r_1, r_2\right). \tag{2.212}$$

In case the previous hypothesis does not hold, we analogously define $\overline{c_v}(T) = \frac{e^{\#}(T)}{T}$, so that (2.211) reads as follows:

$$e = \overline{c_v}(T)T + \frac{a(T) - T\frac{da}{dT}}{b} U\left(\rho, b, r_1, r_2\right). \tag{2.213}$$

The quantity $\overline{c_v}(T)$ should not be understood as a real specific heat, but only as a convenient way of writing the above EOS. We consider the van der Waals EOS, for which $r_1 = r_2 = 0$ and

$$U = -b\rho \tag{2.214}$$

and the Peng-Robinson EOS, for which $r_1 = -1 - \sqrt{2}$, $r_2 = -1 + \sqrt{2}$ and

$$U = \frac{1}{r_1 - r_2} \log\left(\frac{1 - \rho b r_1}{1 - \rho b r_2}\right). \tag{2.215}$$

The link between pressure, density and temperature for the general cubic EOS in dimensional form can be expressed as follows:

$$p = \frac{\rho R_g T}{1 - \rho b} - \frac{a\rho^2}{\left(1 - \rho b r_1\right)\left(1 - \rho b r_2\right)}, \tag{2.216}$$

with R_g denoting the specific gas constant. Notice that for $a = b = 0$, the expression for the pressure of an ideal gas is retrieved. For the sake of clarity, we introduce the following non-dimensional variables

$$\tilde{R}_g = \frac{\mathcal{R}\Theta}{\mathcal{P}} R_g \qquad \tilde{a} = a\frac{\mathcal{R}^2}{\mathcal{P}} \qquad \tilde{b} = \mathcal{R}b, \tag{2.217}$$

so that (2.216) can be rewritten in non-dimensional form as

$$p = \frac{\rho \tilde{R}_g T}{1 - \rho\tilde{b}} - \frac{\tilde{a}\rho^2}{\left(1 - \rho\tilde{b}r_1\right)\left(1 - \rho\tilde{b}r_2\right)}. \tag{2.218}$$

Finally, we define $\tilde{c}_v\left(T\right) = \overline{c_v}\frac{\mathcal{R}\Theta}{\mathcal{P}}$, so that the non-dimensional version of (2.213) reads as follows:

$$e = \tilde{c}_v(T)T + \frac{\tilde{a}(T) - T\frac{d\tilde{a}}{dT}}{\tilde{b}} U\left(\rho, \tilde{b}, r_1, r_2\right). \tag{2.219}$$

Another example of non-ideal gas considered is represented by the Stiffened Gas equation of state (SG-EOS) [Le Métayer and Saurel, 2016], which is interesting for its convexity property and is given in dimensional variables by

$$p = (\gamma - 1)\left(\rho E - \frac{1}{2}\rho\mathbf{u}\cdot\mathbf{u} - \rho q_\infty\right) - \gamma\pi_\infty, \tag{2.220}$$

where q_∞ and π_∞ are parameters that determine the gas characteristics. Notice that, for this equation of state, the parameters have to be taken constant [Le Métayer and Saurel, 2016]. We define analogously to what we did for the general cubic equation of state

$$\tilde{q}_\infty = \frac{\mathcal{R}}{\mathcal{P}} q_\infty \qquad \tilde{\pi}_\infty = \frac{\pi}{\mathcal{P}}, \tag{2.221}$$

so that (2.220) reads in terms of non-dimensional variables as follows:

$$p = (\gamma - 1)\left(\rho E - \frac{1}{2} M^2 \rho \mathbf{u} \cdot \mathbf{u} - \rho \tilde{q}_\infty\right) - \gamma \tilde{\pi}_\infty. \tag{2.222}$$

Finally, the link between pressure, density and temperature for the SG-EOS can be written as:

$$T = \frac{p + \pi_\infty}{\rho (\gamma - 1) c_v}. \tag{2.223}$$

We define $\tilde{c}_v = c_v \frac{\mathcal{R}\Theta}{\mathcal{P}}$, with Θ being the reference temperature, so that the non-dimensional version of (2.223) is given by

$$T = \frac{p + \tilde{\pi}_\infty}{\rho (\gamma - 1) \tilde{c}_v}. \tag{2.224}$$

We consider the SG-EOS for the four-equation relaxed system (2.155). In this case, we need an equation of state for the mixture to link the mixture internal energy e with the pressure p, the mixture density $\rho = \alpha_1 \rho_1 + \alpha_2 \rho_2$ and the volume fractions α_1 and α_2. From (2.222), we notice that for the SG-EOS the following relation holds:

$$\rho e = \frac{p + \gamma \tilde{\pi}_\infty}{\gamma - 1} + \rho \tilde{q}_\infty. \tag{2.225}$$

Hence, we can compute the mixture internal energy as follows:

$$\rho e = \sum_{k=1}^{2} \alpha_k \rho_k e_k = \sum_{k=1}^{2} \alpha_k \left(\frac{p_k + \gamma_k \tilde{\pi}_{\infty,k}}{\gamma_k - 1} + \rho_k \tilde{q}_{\infty,k}\right). \tag{2.226}$$

Since $p_1 = p_2 = p$, we obtain

$$\rho e = \sum_{k=1}^{2} \alpha_k \rho_k e_k = p \sum_{k=1}^{2} \frac{\alpha_k}{\gamma_k - 1} + \sum_{k=1}^{2} \alpha_k \left(\frac{\gamma_k \tilde{\pi}_{\infty,k}}{\gamma_k - 1} + \rho_k \tilde{q}_{\infty,k}\right), \tag{2.227}$$

from which we also get

$$p = \frac{\rho e - \sum\limits_{k=1}^{2} \alpha_k \left(\frac{\gamma_k \tilde{\pi}_{\infty,k}}{\gamma_k - 1} + \rho_k \tilde{q}_{\infty,k}\right)}{\sum\limits_{k=1}^{2} \frac{\alpha_k}{\gamma_k - 1}}. \tag{2.228}$$

Notice that, for the sake of simplicity and as in most standard contributions, see e.g. [Saurel et al., 2016], we consider the pure thermodynamics components to compute the mixture quantities. However, as explained in [Sandler, 2017], the true mixture properties should be in principle considered, which take into account the interaction between the phases. More accurate and general equations of state are available in literature, see e.g. [Span, 2000, Lemmon and Span, 2006], but the above choices are suitable for the regimes of interest, involve already non trivial non-linearities and provide a sufficient level of complexity for the validation of the numerical scheme we will propose in the next Chapter.

For what concerns the equations (2.175), we need to consider barotropic-type equations of state, i.e. relations for which pressure depends only on the density. Possible choices are the Tait equation of state [Tait, 1965] for the liquid phase

$$p = \frac{\rho_l c_l^2}{7.15}\left[\left(\frac{\rho}{\rho_l}\right)^{7.15} - 1\right] + p_0, \tag{2.229}$$

with ρ_l denoting the density of the liquid, c_l being the speed of sound and p_0 being a reference pressure. The polytropic relation [Vidal, 2001] can be employed for the gas phase

$$p = b\rho^{\gamma}, \tag{2.230}$$

with b being a case-dependent constant and γ representing the polytropic exponent. Finally, we point out that, as discussed in [Müller et al., 2016], the reported choices of for the EOS, in combination with the definition (2.135) for the interfacial velocity and pressure, lead to a system which is compatible with the second principle of thermodynamics.

2.6.1 Analysis of isentropic processes for the general cubic equation of state

In this Section, we perform an analysis of isentropic processes which is valid for the general cubic equation of state in the case $\frac{da}{dT} = 0$ and $\frac{de^{\#}}{dT} = c_v = const.$ For the sake of simplicity, in order to avoid the influence of reference quantities, we report the computations using dimensional variables. We recall the Gibbs' relation [Vidal, 2001, Sandler, 2017]

$$de = Tds - pdv = Tds + \frac{p}{\rho^2}d\rho, \tag{2.231}$$

where s denotes the specific entropy. Dividing both sides in the previous equation by T we obtain

$$\frac{1}{T}de = ds + \frac{p}{\rho^2 T}d\rho \tag{2.232}$$

which in an isentropic process reduces to

$$\frac{1}{T}de - \frac{p}{\rho^2 T}d\rho = 0. \tag{2.233}$$

Under the specific assumptions made, we obtain

$$\frac{c_v}{T}dT + \frac{a}{b}\frac{1}{T}\frac{\partial U}{\partial \rho}d\rho - \frac{p}{\rho^2 T}d\rho = 0. \tag{2.234}$$

The EOS can be rewritten in the following form [Vidal, 2001]

$$T = \left[p + \frac{a\rho^2}{(1-\rho b r_1)(1-\rho b r_2)}\right]\frac{(1-\rho b)}{\rho R_g}. \tag{2.235}$$

If we substitute (2.235) into (2.234), we obtain

$$\frac{c_v}{T}dT + \left(\frac{a}{b}\frac{\partial U}{\partial \rho}\rho - \frac{p}{\rho}\right)\frac{R_g}{(1-\rho b)}\frac{(1-\rho b r_1)(1-\rho b r_2)}{p(1-\rho b r_1)(1-\rho b r_2) + a\rho^2}d\rho = 0. \tag{2.236}$$

In the case of van der Waals EOS, $U = -b\rho$ and $\frac{\partial U}{\partial \rho} = -b$, whereas in the case of Peng-Robinson EOS one has

$$U = \frac{1}{r_1 - r_2}\log\left(\frac{1-\rho b r_1}{1-\rho b r_2}\right) \qquad \frac{\partial U}{\partial \rho} = -\frac{b}{(1-\rho b r_1)(1-\rho b r_2)}.$$

Since, for van der Waals EOS $r_1 = r_2 = 0$, the expression

$$\frac{\partial U}{\partial \rho} = -\frac{b}{(1-\rho b r_1)(1-\rho b r_2)} \tag{2.237}$$

can be applied for both van der Waals and Peng-Robinson EOS. Hence, (2.236) reduces to

$$\frac{c_v}{T}dT - \frac{R_g}{\rho(1-\rho b)}d\rho = 0, \tag{2.238}$$

which can then be integrated to yield

$$c_v \log(T) - 2R_g \operatorname{atanh}(2\rho b - 1) = const \tag{2.239}$$

or, equivalently,

$$\log(T) - 2\frac{R_g}{c_v}\operatorname{atanh}(2\rho b - 1) = const. \tag{2.240}$$

From (2.238), it is immediate to verify that, in the non-dimensional case, we obtain

$$\beta \overset{\text{def}}{=} \log(T^*) - 2\frac{\tilde{R}_g}{\tilde{c}_v}\operatorname{atanh}\left(2\rho^*\tilde{b} - 1\right) = const, \tag{2.241}$$

where the symbol $*$ denotes non-dimensional variables. As far as we know, the variable β defined in (2.241) is a novel constant quantity for isentropic processes described by the general cubic equation of state in the case $\frac{da}{dT} = 0$ and $\frac{de^\#}{dT} = c_v = const$. In the more general case $\frac{da}{dT} \neq 0$, it can be shown that [Nederstigt, 2017]

$$\frac{p}{\rho^{\gamma_{p\rho}}} = const, \tag{2.242}$$

where

$$\gamma_{p\rho} = \frac{c^2}{M^2}\frac{\rho}{p}. \tag{2.243}$$

The evaluation of this quantity is less straightforward than that of (2.241), since it involves the computation of non trivial derivatives, see the discussions in [Nederstigt, 2017] and [Orlando et al., 2022a].

CHAPTER 3

Numerical methods for two-phase flows

In this Chapter, we describe the strategies employed to discretize the system (2.149) in space and time. The presentation will provide a clear overview of the intermediate steps developed towards this goal. After a brief general introduction of the space discretization scheme, we describe a novel filtering monotonization technique [Orlando, 2023] developed in order to reduce the spurious oscillations that arise around discontinuities using high order discretization methods. Then, we present a novel implicit DG solver for the incompressible Navier-Stokes equations [Orlando et al., 2022b] that acts as the initial building block in order to obtain a robust approach in the low Mach number limit. Afterwards, we describe its extension to the single-phase compressible Navier-Stokes equations so as to obtain a novel IMEX-DG solver [Orlando et al., 2022a] dealing also with non-ideal gases. Finally, we provide the strategy to deal with two-phase flows and with the non conservative coupling terms in (2.149).

Contents

3.1 The Discontinuous Galerkin method 44
3.2 Monotonization technique 46
3.3 Discretization for the incompressible Navier-Stokes equations . . . 49
3.4 Extension to the single-phase compressible Navier-Stokes equations 55
3.5 Two-phase system 72
    3.5.1 Discretization of the hyperbolic operator and preservation of uniform fields 73
    3.5.2 Treatment of non-conservative terms 79
    3.5.3 Discretization of four-equation relaxed system 81

3.1 The Discontinuous Galerkin method

The Discontinuous Galerkin (DG) method has become a very valuable tool over the last decades and, to an increasing extent, is applied to problems which traditionally were solved using the FV method, in particular for applications in computational fluid dynamics, see e.g. [Cockburn et al., 1989, Bassi and Rebay, 1997a, Bassi and Rebay, 1997b, Dolejší, 2004] among many others. The reason for this trend is related to the intrinsic capability of the DG method to achieve higher order accuracy at a lower computational cost. Indeed, second order FV methods are based on *ad hoc* second order reconstruction procedure that use large stencils. Their extensions to third order schemes require third order accurate reconstructions which are quite cumbersome on unstructured meshes. Higher order approximations are even more difficult to achieve on unstructured meshes. On the other hand, the order of accuracy of the DG method, for problems with a sufficiently regular solution, depends on the polynomial degree employed which can easily be increased, allowing to achieve high order accuracy on unstructured meshes in a straightforward way. A comparison between the DG method and the FV method supporting these claims has been performed in [Orlando et al., 2022b] and is recalled in Section 4.2. This guarantees flexibility in the distribution of the employed polynomial degree. Moreover, the stencil of DG methods involves only the neighbours of each element, providing a clear advantage in terms of parallelization and local mesh refinement ($h-$refinement) capabilities. Discontinuous finite element $p-$adaptive approaches were proposed, among many others, in [Hartmann and Houston, 2002, Remacle et al., 2003, Tugnoli et al., 2017, Colombo et al., 2018] and introduced in [Tumolo et al., 2013] for Numerical Weather Prediction (NWP) applications. The two adaptive techniques have been also successfully combined in several other fields, see e.g. [Houston and Süli, 2001, Toselli, 2002, Eskilsson, 2011].

We consider a decomposition of the domain Ω into a family of hexahedra $\mathcal{T}_h$ (quadrilaterals in the two-dimensional case) and denote each element by K. The skeleton $\mathcal{E}$ denotes the set of all element faces and $\mathcal{E} = \mathcal{E}^I \cup \mathcal{E}^B$, where $\mathcal{E}^I$ is the subset of interior faces and $\mathcal{E}^B$ is the subset of boundary faces. We also introduce the following finite element spaces

$$Q_r = \left\{ v \in L^2(\Omega) : v|_K \in \mathbb{Q}_r \quad \forall K \in \mathcal{T}_h \right\} \tag{3.1}$$

and

$$\mathbf{Q}_r = \left[Q_r\right]^d, \tag{3.2}$$

where $\mathbb{Q}_r$ is the space of polynomials of degree r in each coordinate direction. Notice that the above choice for the finite element spaces corresponds to that implemented in the *deal.II* library [Bangerth et al., 2007, Arndt et al., 2022], which will be employed for the numerical computation, but all the proposed approaches can in principle also be applied to tetrahedral meshes and P-spaces.

Suitable jump and average operators are defined as customary for finite element discretizations, see e.g. [Arnold et al., 2002]. A face $F \in \mathcal{E}^I$ shares two elements that we denote by K^+ with outward unit normal $\mathbf{n}^+$ and K^- with outward unit normal $\mathbf{n}^-$, whereas for a face $F \in \mathcal{E}^B$ we denote by $\mathbf{n}$ the outward unit normal. For a scalar function φ the jump is defined as

$$[[\varphi]] = \varphi^+\mathbf{n}^+ + \varphi^-\mathbf{n}^- \quad \text{if } F \in \mathcal{E}^I \qquad [[\varphi]] = \varphi\mathbf{n} \quad \text{if } F \in \mathcal{E}^B, \tag{3.3}$$

where

$$\varphi^{+} = \varphi|_{K^{+}} \qquad \varphi^{-} = \varphi|_{K^{-}}. \tag{3.4}$$

The average is defined as

$$\{\{\varphi\}\} = \frac{1}{2}\left(\varphi^{+} + \varphi^{-}\right) \quad \text{if } F \in \mathcal{E}^{I} \qquad \{\{\varphi\}\} = \varphi \quad \text{if } F \in \mathcal{E}^{B}. \tag{3.5}$$

Similar definitions apply for a vector-valued function $\boldsymbol{\varphi}$:

$$[[\boldsymbol{\varphi}]] = \boldsymbol{\varphi}^{+} \cdot \mathbf{n}^{+} + \boldsymbol{\varphi}^{-} \cdot \mathbf{n}^{-} \quad \text{if } F \in \mathcal{E}^{I} \qquad [[\boldsymbol{\varphi}]] = \boldsymbol{\varphi} \cdot \mathbf{n} \quad \text{if } F \in \mathcal{E}^{B} \tag{3.6}$$

$$\{\{\boldsymbol{\varphi}\}\} = \frac{1}{2}\left(\boldsymbol{\varphi}^{+} + \boldsymbol{\varphi}^{-}\right) \quad \text{if } F \in \mathcal{E}^{I} \qquad \{\{\boldsymbol{\varphi}\}\} = \boldsymbol{\varphi} \quad \text{if } F \in \mathcal{E}^{B}. \tag{3.7}$$

For vector-valued functions, it is also useful to define a tensor jump as:

$$\langle\langle\boldsymbol{\varphi}\rangle\rangle = \boldsymbol{\varphi}^{+} \otimes \mathbf{n}^{+} + \boldsymbol{\varphi}^{-} \otimes \mathbf{n}^{-} \quad \text{if } F \in \mathcal{E}^{I} \qquad \langle\langle\boldsymbol{\varphi}\rangle\rangle = \boldsymbol{\varphi} \otimes \mathbf{n} \quad \text{if } F \in \mathcal{E}^{B}. \tag{3.8}$$

For the sake of completeness, we outline here the development of a DG discretization for both a non-linear conservation law and an elliptic problem. A non-linear conservation law can be written as

$$\frac{\partial \Psi}{\partial t} + \nabla \cdot \mathbf{F}(\Psi) = 0, \tag{3.9}$$

where $\Psi = \Psi(\mathbf{x}, t)$ is the unknown, $\mathbf{x} \in \mathbb{R}^{d}$, and $\mathbf{F}(\Psi)$ denotes a $d-$dimensional vector field that generally depends on Ψ in a non-linear way. We multiply (3.9) by a test function Λ and, after integration by parts, we obtain the following local formulation on each element K:

$$\int_{K} \frac{\partial \Psi}{\partial t} \Lambda d\Omega - \int_{K} \mathbf{F}(\Psi) \cdot \nabla \Lambda d\Omega + \int_{\partial K} \hat{\mathbf{F}}\left(\Psi^{+}, \Psi^{-}\right) \cdot \mathbf{n} \Lambda d\Sigma = 0. \tag{3.10}$$

In the surface integral, we replace the term $\mathbf{F}(\Psi)$ with a numerical flux $\hat{\mathbf{F}}(\Psi^{+}, \Psi^{-})$, which depends on the solution on both sides of an interior face. A basic property required by the flux is to be conservative [Bassi and Rebay, 1997a], i.e. $\hat{\mathbf{F}}(\Psi^{+}, \Psi^{-}) = \hat{\mathbf{F}}(\Psi^{-}, \Psi^{+})$. An example of numerical flux is represented by the Rusanov flux [Rusanov, 1962]:

$$\mathbf{F}\left(\Psi^{+}, \Psi^{-}\right) = \{\{\mathbf{F}(\Psi)\}\} + \frac{\lambda}{2}[[\Psi]], \tag{3.11}$$

where λ is the largest eigenvalue (in absolute value) of the Jacobian $\frac{\partial \mathbf{F}}{\partial \Psi}$. Summing up over all the elements, we obtain the following formulation:

$$\sum_{K \in \mathcal{T}_h} \int_{K} \frac{\partial \Psi}{\partial t} \Lambda d\Omega - \sum_{K \in \mathcal{T}_h} \int_{K} \mathbf{F}(\Psi) \cdot \nabla \Lambda d\Omega + \sum_{F \in \mathcal{E}} \int_{F} \hat{\mathbf{F}}\left(\Psi^{+}, \Psi^{-}\right) \cdot [[\Lambda]]\, d\Sigma = 0, \tag{3.12}$$

with $\mathcal{E} = \mathcal{E}^{I} \cup \mathcal{E}^{B}$. The prototype of an elliptic problem is instead the Poisson equation

$$-\Delta \Psi = g, \tag{3.13}$$

supplied with suitable initial and boundary conditions. We proceed as we did for (3.9) so as to obtain for a single element K

$$\int_{K} \nabla \Psi \cdot \nabla \Lambda d\Omega - \int_{\partial K} \mathbf{F}^{*}\left(\nabla \Psi^{+}, \nabla \Psi^{-}\right) \cdot \mathbf{n} \Lambda d\Sigma = \int_{K} g \Lambda d\Omega, \tag{3.14}$$

where $\mathbf{F}^*$ is a suitable numerical flux. A typical choice is represented by the centered flux

$$\mathbf{F}^* = \{\{\nabla\Psi\}\}\,. \tag{3.15}$$

In the rest of the work, we consider for second order spatial operators the so-called Symmetric Interior Penalty (SIP) method [Arnold, 1982, Orlando et al., 2022b]. Hence, we obtain with the following formulation:

$$\begin{aligned}
& \sum_{K\in\mathcal{T}_h}\int_K \nabla\Psi\cdot\nabla\Lambda d\Omega \\
- & \sum_{F\in\mathcal{E}}\int_F \{\{\nabla\Psi\}\}\cdot[[\Lambda]]\,d\Sigma - \sum_{F\in\mathcal{E}}\int_F [[\Psi]]\cdot\{\{\nabla\Lambda\}\}\,d\Sigma + \sum_{F\in\mathcal{E}}\int_F \tau\,[[\Psi]]\cdot[[\Lambda]]\,d\Sigma \\
= & \sum_{K\in\mathcal{T}_h}\int_K g\Lambda d\Omega,
\end{aligned} \tag{3.16}$$

with τ being a suitable penalization constant. The extension to Navier-Stokes equations and related models will be described in the following Sections.

3.2 Monotonization technique

In this Section, we describe a novel monotonization technique for the Discontinuous Galerkin discretization of hyperbolic problems proposed in [Orlando, 2023]. It is known that spurious oscillations arise around shocks and other discontinuities when high order spatial discretizations are used. Furthermore, maintaining non negativity of the numerical solutions is essential to preserve the correct physical meaning of variables such as the volume fraction or the density. In order to address these well known issues, a number of monotonization techniques have been proposed in the literature for DG methods. In general, monotonization techniques for DG methods have been inherited from finite difference and finite volume approaches. For example, starting with [Cockburn and Shu, 1989, Cockburn et al., 1989], slope limiting techniques have been employed, while other authors have investigated Weighted Essentially Non-Oscillatory (WENO) methods [Shu, 2003, Shu, 2016] and Flux Corrected Transport (FCT) methods [Kuzmin and Turek, 2002, Restelli et al., 2006, Kuzmin et al., 2012]. In recent years, the very successful Multidimensional Optimal Order Detection (MOOD) approach has been proposed in [Dumbser et al., 2014, Loubère et al., 2014, Zanotti et al., 2015, Dumbser and Loubère, 2016], which is based on the identification of the regions of discontinuity and on the switch from a high order DG method to a monotonic first order Finite Volume method on a locally refined mesh built around the quadrature nodes used by the DG method. However, this method is strongly dependent on the choice and on the performances of a regularity indicator. We present here a method proposed in [Orlando, 2023] and inspired by the filtering approach outlined in [Bokanowski et al., 2016]. More specifically, a filter function is employed in such a way that, where the solution is regular, we keep the high order solution, whereas otherwise we switch to a low order method. While the proposed strategy is conceptually similar to that of the MOOD approach, the main novelty of the proposed method is that we do not rely on a regularity indicator and that a monotonic solution is retrieved (almost) automatically.

We consider as generic model problem the non-linear conservation law (3.9). Simple examples are the linear advection equation and the Burgers equation. Each stage of a numerical method can be represented as

$$\mathbf{u} = \mathbf{S}(\mathbf{v}), \tag{3.17}$$

where $\mathbf{u}, \mathbf{v}$ denote the new and old values, respectively, of the vector containing the discrete degrees of freedom which identify the spatial approximation to the solutions of (3.9). $\mathbf{S}$ denotes formally the solution operator associated to a specific time and space discretization. The transition from $\mathbf{v}$ to $\mathbf{u}$ can be interpreted as an advancement in time $\zeta\Delta t$ time units, where the parameter ζ depends on the details of the specific method and stage considered. We will denote by $\mathbf{S}^M$ the discrete operator associated to the monotonic, low order spatial discretization and by $\mathbf{S}^H$ that associated to a high order, not monotonic spatial discretization. We now introduce the application of the filtering approach proposed in [Bokanowski et al., 2016] in the above outlined context. First of all, a filter function $\mathcal{F}$ is introduced. This can be defined in several ways, for example

$$\mathcal{F}_1(x) = x\mathbf{1}_{|x|\leq 1} = \begin{cases} x & \text{if } |x| \leq 1 \\ 0 & \text{otherwise,} \end{cases} \tag{3.18}$$

which corresponds to the Oberman-Salvador filter function originally employed in [Oberman and Salvador, 2015] or

$$\mathcal{F}_2(x) = \operatorname{sign}(x) \max\left(1 - ||x| - 1|, 0\right), \tag{3.19}$$

the so-called Froese and Oberman filter function originally presented in [Froese and Oberman, 2013]. Figure 3.1 reports the plots of both $\mathcal{F}_1(x)$ and $\mathcal{F}_2(x)$. In

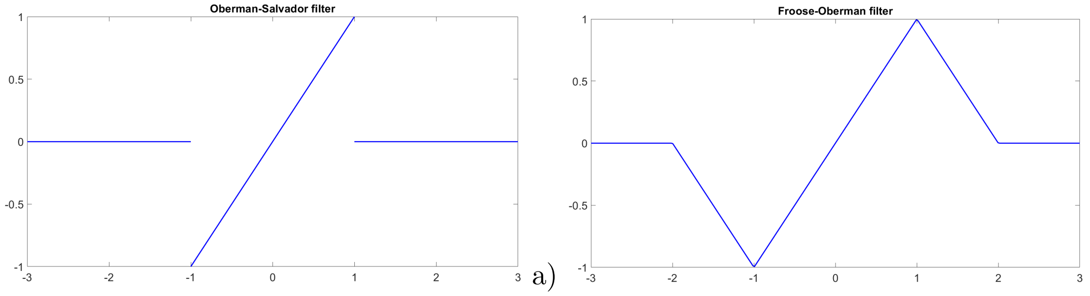

a) b)

Figure 3.1: *Plots of filter functions, a) Oberman-Salvador filter function, b) Froose-Oberman filter function.*

the simplest possible filtering approach, the filtered version of $\mathbf{u}$ can be defined as

$$\mathbf{u}^F = \mathbf{S}^M(\mathbf{v}) + \varepsilon\zeta\Delta t\mathcal{F}\left(\frac{\mathbf{S}^H(\mathbf{v}) - \mathbf{S}^M(\mathbf{v})}{\varepsilon\zeta\Delta t}\right), \tag{3.20}$$

where the low order solution $\mathbf{S}^M$ is computed on the nodes of the high order solution $\mathbf{S}^H$ and ε is a suitable parameter, depending on the time and space discretization parameters, such that

$$\lim_{(\Delta t, h)\to 0} \varepsilon(\Delta t, h) = 0, \tag{3.21}$$

with $h = \max\{\operatorname{diam}(K) | K \in \mathcal{T}_h\}$. Notice that the filter function is applied componentwise to the vector of the discrete degrees of freedom $\mathbf{v}$. In this way, as discussed in [Bokanowski et al., 2016], the high order method is actually only applied to the components i for which

$$\frac{|\mathbf{S}^H(\mathbf{v})_i - \mathbf{S}^M(\mathbf{v})_i|}{\varepsilon\zeta\Delta t} \leq 1, \quad i = 1, ..., \dim(Q_r). \tag{3.22}$$

As explained in [Bokanowski et al., 2016], ε has to be chosen in such a way that

$$\varepsilon \geq c_0 h, \tag{3.23}$$

where c_0 is a sufficiently large constant. As discussed in Section (4.1), the aforementioned approach is very dissipative and, unless a very large value of c_0 is adopted, it yields solutions that essentially coincide with the low order one. Therefore, we propose the alternative filtering strategy

$$\mathbf{u}_i^F = \mathbf{S}^M(\mathbf{v})_i + \beta\mathbf{S}^M(\mathbf{v})_i\mathcal{F}\left(\frac{\mathbf{S}^H(\mathbf{v})_i - \mathbf{S}^M(\mathbf{v})_i}{\beta\mathbf{S}^M(\mathbf{v})_i}\right), \quad i = 1, ..., \dim(Q_r), \tag{3.24}$$

where $\beta > 0$ is a suitable parameter which represents a tolerance for the componentwise relative difference $\frac{\mathbf{S}^H(\mathbf{v})_i - \mathbf{S}^M(\mathbf{v})_i}{\mathbf{S}^M(\mathbf{v})_i}$, so that when $\left|\frac{\mathbf{S}^H(\mathbf{v})_i - \mathbf{S}^M(\mathbf{v})_i}{\mathbf{S}^M(\mathbf{v})_i}\right| \leq \beta$, we resort to the high order solution. Also in this case, a too small value of β provides results that are in practice coincident with the low order solution. An extension for the Euler equations and for the two-phase flows system can be developed in a straightforward way by applying (3.24) to each unknown. For the sake of clarity, we report here the three relations to be employed for the Euler equations of the gas dynamics:

$$\begin{aligned}
\boldsymbol{\rho}_i^F &= \mathbf{S}^M(\boldsymbol{\rho})_i \\
&+ \beta_\rho\mathbf{S}^M(\boldsymbol{\rho})_i\mathcal{F}\left(\frac{\mathbf{S}^H(\boldsymbol{\rho})_i - \mathbf{S}^M(\boldsymbol{\rho})_i}{\beta_\rho\mathbf{S}^M(\boldsymbol{\rho})_i}\right), \quad i = 1, ..., \dim(Q_r) &(3.25)\\
\boldsymbol{\rho}\mathbf{u}_i^F &= \mathbf{S}^M(\boldsymbol{\rho}\mathbf{u})_i \\
&+ \beta_{\rho\mathbf{u}}\mathbf{S}^M(\boldsymbol{\rho}\mathbf{u})_i\mathcal{F}\left(\frac{\mathbf{S}^H(\boldsymbol{\rho}\mathbf{u})_i - \mathbf{S}^M(\boldsymbol{\rho}\mathbf{u})_i}{\beta_{\rho\mathbf{u}}\mathbf{S}^M(\boldsymbol{\rho}\mathbf{u})_i}\right), \quad i = 1, ..., \dim(\mathbf{Q}_r) &(3.26)\\
\boldsymbol{\rho}\mathbf{E}_i^F &= \mathbf{S}^M(\boldsymbol{\rho}\mathbf{E})_i \\
&+ \beta_{\rho E}\mathbf{S}^M(\boldsymbol{\rho}\mathbf{E})_i\mathcal{F}\left(\frac{\mathbf{S}^H(\boldsymbol{\rho}\mathbf{E})_i - \mathbf{S}^M(\boldsymbol{\rho}\mathbf{E})_i}{\beta_{\rho E}\mathbf{S}^M(\boldsymbol{\rho}\mathbf{E})_i}\right), \quad i = 1, ..., \dim(Q_r) &(3.27)
\end{aligned}$$

where $\boldsymbol{\rho}, \boldsymbol{\rho}\mathbf{u}, \boldsymbol{\rho}\mathbf{E}$ are the vectors of the degrees of freedom for the density, the momentum and the energy per unit of mass, respectively, whereas $\beta_\rho, \beta_{\rho\mathbf{u}}$ and $\beta_{\rho E}$ are the corresponding tolerance parameters, which in principle are different from each other. The choice of performing the filtering procedure for all the unknowns follows standard approaches in literature, see e.g. [Loubère et al., 2014], in which monotonization techniques are applied for all the variables. The method can be successfully combined with $h-$refinement capabilities in order to reduce the size of the region where the low order approximation is applied. The potentialities of the proposed filtering approach are shown in a number of numerical experiments in Section 4.1 and Section 4.5. We refer to [Orlando, 2023] for a complete description of the monotonization technique.

3.3 Discretization for the incompressible Navier-Stokes equations

In this Section, we present a novel discretization method for the classical unsteady incompressible Navier-Stokes equations with uniform and constant density, proposed also in [Orlando et al., 2022b]. The equations are written in non-dimensional form as:

$$\begin{aligned} \frac{\partial \mathbf{u}}{\partial t} + \nabla\cdot(\mathbf{u}\otimes\mathbf{u}) + \nabla p &= \frac{1}{Re}\Delta\mathbf{u} \\ \nabla\cdot\mathbf{u} &= 0 \end{aligned} \tag{3.28}$$

for $\mathbf{x}\in\Omega, t\in(0,T_f]$, supplied with suitable initial and boundary conditions. Here T_f is the final time, $\mathbf{u}$ is the fluid velocity, p is the pressure divided by density and Re is the Reynolds number, which is usually defined as $Re = \mathcal{U}\mathcal{L}/\nu$, where $\mathcal{U}$ denotes a reference value of the velocity magnitude, $\mathcal{L}$ a reference length scale and ν the fluid kinematic viscosity.

Projection methods [Chorin, 1968, Temam, 1969, Guermond et al., 2006] are very popular for the discretization of this problem. However, difficulties arise in the choice of the boundary conditions to be imposed for the Poisson equation which is to be solved at each time step to compute the pressure, see e.g. the discussion in [Guermond et al., 2006]. An alternative that allows to avoid (or at least to reduce) some of these problems is the so-called artificial compressibility formulation, originally introduced in [Chorin, 1967]. In this formulation, the incompressibility constraint is relaxed and a time evolution equation for the pressure is introduced, which is characterized by an artificial sound speed c, so as to obtain

$$\begin{aligned} \frac{\partial \mathbf{u}}{\partial t} + \nabla\cdot(\mathbf{u}\otimes\mathbf{u}) + \nabla p &= \frac{1}{Re}\Delta\mathbf{u} + \mathbf{f} \\ \frac{1}{c^2}\frac{\partial p}{\partial t} + \nabla\cdot\mathbf{u} &= 0. \end{aligned} \tag{3.29}$$

We introduce a discrete time step $\Delta t = T_f/N$ and discrete time levels $t^n = n\Delta t, n = 0,\dots,N$. Following then the projection approach described in [Della Rocca, 2018] and applying the TR-BDF2 method proposed in [Bank et al., 1985] and outlined in Appendix A.5 to system (3.29), the momentum predictor equation for the first stage reads as follows:

$$\begin{aligned} &\frac{\mathbf{u}^{n+\chi,*} - \mathbf{u}^n}{\chi\Delta t} - \frac{1}{2Re}\Delta\mathbf{u}^{n+\chi,*} + \frac{1}{2}\nabla\cdot\left(\mathbf{u}^{n+\chi,*}\otimes\mathbf{u}^{n+\frac{\chi}{2}}\right) = \\ &\frac{1}{2Re}\Delta\mathbf{u}^n - \frac{1}{2}\nabla\cdot\left(\mathbf{u}^n\otimes\mathbf{u}^{n+\frac{\chi}{2}}\right) - \nabla p^n \\ &\mathbf{u}^{n+\chi,*}|_{\partial\Omega} = \mathbf{u}_D^{n+\chi}. \end{aligned} \tag{3.30}$$

Notice that $\chi = 2-\sqrt{2}$ in order to guarantee L-stability and that, in order to avoid solving a non-linear system at each time step, an approximation is introduced in the non-linear momentum advection term, so that $\mathbf{u}^{n+\frac{\chi}{2}}$ is defined by extrapolation as

$$\mathbf{u}^{n+\frac{\chi}{2}} = \left(1 + \frac{\chi}{2(1-\chi)}\right)\mathbf{u}^n - \frac{\chi}{2(1-\chi)}\mathbf{u}^{n-1}. \tag{3.31}$$

Alternatively, $\mathbf{u}^{n+\frac{\chi}{2}}$ can be replaced by $\mathbf{u}^{n+\chi,*}$ in the left hand side and by $\mathbf{u}^n$ in the right-hand side of (3.30), respectively, and $\mathbf{u}^{n+\chi,*}$ can be determined by fixed point iterations. Numerical experiments show that this fully non-linear formulation is necessary to achieve accurate results for larger Courant number values [Orlando et al., 2022b]. We set then $\delta p^{n+\chi} = p^{n+\chi} - p^n$ and impose

$$\begin{aligned}
\frac{\mathbf{u}^{n+\chi} - \mathbf{u}^{n+\chi,*}}{\chi\Delta t} &= -\nabla\delta p^{n+\chi} \\
\frac{1}{c^2}\frac{\delta p^{n+\chi}}{\chi\Delta t} + \nabla\cdot\mathbf{u}^{n+\chi} &= 0.
\end{aligned} \tag{3.32}$$

Substituting the first equation into the second in (3.32), one obtains the Helmholtz equation

$$\frac{1}{c^2\chi^2\Delta t^2}\delta p^{n+\chi} - \Delta\delta p^{n+\chi} = -\frac{1}{\chi\Delta t}\nabla\cdot\mathbf{u}^{n+\chi,*}, \tag{3.33}$$

which is solved with the boundary condition $\nabla\delta p^{n+\chi}\cdot\mathbf{n}|_{\partial\Omega} = 0$. Once this equation is solved, the final velocity update for the first stage

$$\mathbf{u}^{n+\chi} = \mathbf{u}^{n+\chi,*} - \chi\Delta t\nabla\delta p^{n+\chi} \tag{3.34}$$

can be computed. Notice that the previous procedure is equivalent to introducing the intermediate update

$$\mathbf{u}^{n+\chi,**} = \mathbf{u}^{n+\chi,*} + \chi\Delta t\nabla p^n, \tag{3.35}$$

solving

$$\frac{1}{c^2}\frac{p^{n+\chi}}{\chi^2\Delta t^2} - \Delta p^{n+\chi} = -\frac{1}{\chi\Delta t}\nabla\cdot\mathbf{u}^{n+\chi,**} + \frac{1}{c^2}\frac{p^n}{\chi^2\Delta t^2} \tag{3.36}$$

and then setting

$$\mathbf{u}^{n+\chi} = \mathbf{u}^{n+\chi,**} - \chi\Delta t\nabla p^{n+\chi}. \tag{3.37}$$

The second TR-BDF2 stage is performed in a similar manner and we report it here for the sake of completeness. We first define the second momentum predictor

$$\begin{aligned}
&\frac{\mathbf{u}^{n+1,*} - \mathbf{u}^{n+\chi}}{(1-\chi)\,\Delta t} - \frac{\tilde{a}_{33}}{Re}\Delta\mathbf{u}^{n+1,*} + \tilde{a}_{33}\,\nabla\cdot\left(\mathbf{u}^{n+1,*}\otimes\mathbf{u}^{n+\frac{3}{2}\chi}\right) = \\
&\frac{\tilde{a}_{32}}{Re}\Delta\mathbf{u}^{n+\chi} - \tilde{a}_{32}\,\nabla\cdot\left(\mathbf{u}^{n+\chi}\otimes\mathbf{u}^{n+\chi}\right) + \frac{\tilde{a}_{31}}{Re}\Delta\mathbf{u}^{n} - \tilde{a}_{31}\,\nabla\cdot\left(\mathbf{u}^{n}\otimes\mathbf{u}^{n}\right) - \nabla p^{n+\chi} \\
&\mathbf{u}^{n+1,*}|_{\partial\Omega^D} = \mathbf{u}_D^{n+1},
\end{aligned} \tag{3.38}$$

where one has

$$\tilde{a}_{31} = \frac{1-\chi}{2\,(2-\chi)} \quad \tilde{a}_{32} = \frac{1-\chi}{2\,(2-\chi)} \quad \tilde{a}_{33} = \frac{1}{2-\chi}. \tag{3.39}$$

Again, in order to avoid solving a non-linear system at each time step, an approximation is introduced in the non-linear momentum advection term, so that $\mathbf{u}^{n+\frac{3}{2}\chi}$ is defined by extrapolation as

$$\mathbf{u}^{n+\frac{3}{2}\chi} = \left(1 + \frac{1+\chi}{\chi}\right)\mathbf{u}^{n+\chi} - \frac{1-\chi}{\chi}\mathbf{u}^{n}. \tag{3.40}$$

Alternatively, $\mathbf{u}^{n+\frac{3}{2}\chi}$ can be replaced by $\mathbf{u}^{n+1,*}$, which can then be determined by fixed point iteration. We set then $\delta p^{n+1} = p^{n+1} - p^{n+\chi}$ and impose

$$\begin{aligned} \frac{\mathbf{u}^{n+1} - \mathbf{u}^{n+1,*}}{(1-\chi)\Delta t} &= -\nabla \delta p^{n+1} \\ \frac{1}{c^2}\frac{\delta p^{n+1}}{(1-\chi)\Delta t} + \nabla\cdot \mathbf{u}^{n+1} &= 0. \end{aligned} \tag{3.41}$$

Substituting the first equation into the second in (3.41), one obtains the Helmholtz equation

$$\frac{1}{c^2(1-\chi)^2\Delta t^2}\delta p^{n+1} - \Delta \delta p^{n+1} = -\frac{1}{(1-\chi)\Delta t}\nabla\cdot \mathbf{u}^{n+1,*}, \tag{3.42}$$

which is solved with the boundary condition $\nabla \delta p^{n+1} \cdot \mathbf{n}|_{\partial\Omega} = 0$. Once this equation is solved, the final velocity update is computed

$$\mathbf{u}^{n+1} = \mathbf{u}^{n+1,*} - (1-\chi)\Delta t \nabla \delta p^{n+1}. \tag{3.43}$$

Also for this second stage, notice that the procedure is equivalent to setting

$$\mathbf{u}^{n+1,**} = \mathbf{u}^{n+1,*} + (1-\chi)\Delta t \nabla p^{n+\chi}, \tag{3.44}$$

solving

$$\frac{1}{c^2}\frac{p^{n+1}}{(1-\chi)^2\Delta t^2} - \Delta p^{n+1} = -\frac{1}{(1-\chi)\Delta t}\nabla\cdot \mathbf{u}^{n+1,**} + \frac{1}{c^2}\frac{p^{n+\chi}}{(1-\chi)^2\Delta t^2} \tag{3.45}$$

and then setting

$$\mathbf{u}^{n+1} = \mathbf{u}^{n+1,**} - (1-\chi)\Delta t \nabla p^{n+1}. \tag{3.46}$$

Considering the well-posedness analyses in [Toselli, 2002, Schötzau et al., 2003], the finite element spaces that will be used for the discretization of velocity and pressure are $\mathbf{V}_h = \mathbf{Q}_r$ and $W_h = Q_{r-1} \cap L^2_0(\Omega)$, respectively, where $L^2_0(\Omega) = \left\{v \in L^2(\Omega) : \int_\Omega v d\Omega = 0\right\}$ and $r \geq 2$. Notice that, while for the sake of coherence with the time discretization and for comparison with second order finite volume methods we will mostly consider the case $r = 2$, the formulation we present is completely general and also the implementation validated in Section 4.2 supports arbitrary values of r. The weak formulation of the momentum predictor equation for the first stage is obtained multiplying equation (3.30) by a test function $\mathbf{v} \in \mathbf{V}_h$, integrating over each element $K \in \mathcal{T}_h$ and applying Green's theorem. To impose the boundary conditions, we mirror the state of the adjacent internal element and we set $\left(\mathbf{u}^{n+\chi,*}\right)^- = -\left(\mathbf{u}^{n+\chi,*}\right)^+ + 2\mathbf{u}_D^{n+\chi}$ with $\left[\nabla\left(\mathbf{u}^{n+\chi,*}\right)^+\right]\cdot\mathbf{n} = \left[\nabla\left(\mathbf{u}^{n+\chi,*}\right)^-\right]\cdot\mathbf{n}$. However, analogous results are obtained by directly imposing the boundary value.

We now treat separately the discretization of the diffusion and advection contributions, respectively. The approximation of the diffusion term is based on the SIP [Arnold, 1982]. Two stabilization terms are added: a symmetrizing term corresponding to fluxes obtained after integration by parts and a penalty term imposing the weak continuity of the numerical solution. Following [Fehn et al., 2019], we set for each face F of a cell K

$$\sigma^{\mathbf{u}}_{F,K} = (r+1)^2\frac{\mathrm{diam}(F)}{\mathrm{diam}(K)} \tag{3.47}$$

and we define the penalization constant for the SIP method as

$$C_u = \frac{1}{2}\left(\sigma^{\mathbf{u}}_{F,K^+} + \sigma^{\mathbf{u}}_{F,K^-}\right) \quad \text{if } F \in \mathcal{E}^I, \qquad C_u = \sigma^{\mathbf{u}}_{F,K} \quad \text{if } F \in \mathcal{E}^B. \tag{3.48}$$

Taking into account boundary conditions as previously discussed and summing over all $K \in \mathcal{T}_h$, we can define the following bilinear form:

$$\begin{aligned}
a^{(1)}_{\mathbf{u}}(\mathbf{u},\mathbf{v}) &= \frac{1}{2Re}\sum_{K\in\mathcal{T}_h}\int_K \nabla\mathbf{u} : \nabla\mathbf{v}d\Omega \\
&- \frac{1}{2Re}\sum_{F\in\mathcal{E}^I}\int_F \{\{\nabla\mathbf{u}\}\} : \langle\langle\mathbf{v}\rangle\rangle\, d\Sigma - \frac{1}{2Re}\sum_{F\in\mathcal{E}^B}\int_F (\nabla\mathbf{u})\,\mathbf{n}\cdot\mathbf{v}d\Sigma \quad (3.49) \\
&- \frac{1}{2Re}\sum_{F\in\mathcal{E}^I}\int_F \langle\langle\mathbf{u}\rangle\rangle : \{\{\nabla\mathbf{v}\}\}\, d\Sigma - \frac{1}{2Re}\sum_{F\in\mathcal{E}^B}\int_F (\mathbf{u}\otimes\mathbf{n}) : \nabla\mathbf{v}d\Sigma \\
&+ \frac{1}{2Re}\sum_{F\in\mathcal{E}^I}\int_F C_u\,\langle\langle\mathbf{u}\rangle\rangle : \langle\langle\mathbf{v}\rangle\rangle\, d\Sigma + \frac{1}{2Re}\sum_{F\in\mathcal{E}^B}\int_F 2C_u\,(\mathbf{u}\cdot\mathbf{v})\, d\Sigma.
\end{aligned}$$

The approximation of the advection term employs the widely used Local Lax-Friedrichs (LLF) flux, see e.g. [Giraldo, 2020]. Setting

$$\lambda = \max\left(\left|\left(\mathbf{u}^{n+\frac{\chi}{2}}\right)^+ \cdot \mathbf{n}^+\right|, \left|\left(\mathbf{u}^{n+\frac{\chi}{2}}\right)^- \cdot \mathbf{n}^-\right|\right) \tag{3.50}$$

and taking into account boundary conditions, we define the trilinear form

$$\begin{aligned}
c^{(1)}(\mathbf{u}^{n+\frac{\chi}{2}},\mathbf{u},\mathbf{v}) &= -\frac{1}{2}\sum_{K\in\mathcal{T}_h}\int_K \left(\mathbf{u}\otimes\mathbf{u}^{n+\frac{\chi}{2}}\right) : \nabla\mathbf{v}d\Omega \\
&+ \frac{1}{2}\sum_{F\in\mathcal{E}^I}\int_F \left(\left\{\left\{\mathbf{u}\otimes\mathbf{u}^{n+\frac{\chi}{2}}\right\}\right\}\right) : \langle\langle\mathbf{v}\rangle\rangle\, d\Sigma \qquad (3.51) \\
&+ \frac{1}{2}\sum_{F\in\mathcal{E}^I}\int_F \frac{\lambda}{2}\,\langle\langle\mathbf{u}\rangle\rangle : \langle\langle\mathbf{v}\rangle\rangle\, d\Sigma + \frac{1}{2}\sum_{F\in\mathcal{E}^B}\int_F \lambda\,(\mathbf{u}\cdot\mathbf{v})\, d\Sigma.
\end{aligned}$$

Finally, we also define the functional

$$
\begin{aligned}
F_{\mathbf{u}}^{(1)}(\mathbf{v})^{n+\chi} = & - \frac{1}{2Re}\sum_{K\in\mathcal{T}_h}\int_K \nabla\mathbf{u}^n : \nabla\mathbf{v}d\Omega \\
& + \frac{1}{2Re}\sum_{F\in\mathcal{E}}\int_F \{\{\nabla\mathbf{u}^n\}\} : \langle\langle\mathbf{v}\rangle\rangle\, d\Sigma \\
& + \frac{1}{2}\sum_{K\in\mathcal{T}_h}\int_K \left(\mathbf{u}^n\otimes\mathbf{u}^{n+\frac{\chi}{2}}\right) : \nabla\mathbf{v}d\Omega \\
& - \frac{1}{2}\sum_{F\in\mathcal{E}}\int_F \left(\left\{\left\{\mathbf{u}^n\otimes\mathbf{u}^{n+\frac{\chi}{2}}\right\}\right\}\right) : \langle\langle\mathbf{v}\rangle\rangle\, d\Sigma \\
& + \sum_{K\in\mathcal{T}_h}\int_K p^n\,\nabla\cdot\mathbf{v}d\Omega - \sum_{F\in\mathcal{E}}\int_F \{\{p^n\}\}\,[[\mathbf{v}]]\,d\Sigma \qquad (3.52) \\
& - \frac{1}{2Re}\sum_{F\in\mathcal{E}^B}\int_F \left(\mathbf{u}_D^{n+\chi}\otimes\mathbf{n}\right) : \nabla\mathbf{v}d\Sigma \\
& + \frac{1}{2Re}\sum_{F\in\mathcal{E}^B}\int_F 2C_u\left(\mathbf{u}_D^{n+\chi}\cdot\mathbf{v}\right)d\Sigma \\
& - \frac{1}{2}\sum_{F\in\mathcal{E}^B}\int_F \left(\mathbf{u}_D^{n+\chi}\otimes\mathbf{u}^{n+\frac{\chi}{2}}\right)\mathbf{n}\cdot\mathbf{v}d\Sigma \\
& + \frac{1}{2}\sum_{F\in\mathcal{E}^B}\int_F \lambda\left(\mathbf{u}_D^{n+\chi}\cdot\mathbf{v}\right)d\Sigma,
\end{aligned}
$$

which also includes the terms representing the weak form of Dirichlet boundary conditions. It is worth to point out that in the right-hand side no penalization terms have been introduced for the variables computed at previous time-steps. Moreover, for the sake of clarity, the face integrals related to the quantities at previous time-steps are reported on the whole skeleton $\mathcal{E}$, without distinguishing between interior and boundary faces.

The complete weak formulation of the first stage velocity update reads then as follows: *given* $\mathbf{u}^{n+\frac{\chi}{2}}, \mathbf{u}^n \in \mathbf{V}_h$ *and* $p^n \in W_h$, *find* $\mathbf{u}^{n+\chi,*} \in \mathbf{V}_h$ *such that*:

$$
\begin{aligned}
& \sum_{K\in\mathcal{T}_h}\int_K \frac{1}{\chi\Delta t}\mathbf{u}^{n+\chi,*}\cdot\mathbf{v}d\Omega + a_{\mathbf{u}}^{(1)}(\mathbf{u}^{n+\chi,*},\mathbf{v}) + c^{(1)}(\mathbf{u}^{n+\frac{\chi}{2}},\mathbf{u}^{n+\chi,*},\mathbf{v}) \\
& = \sum_{K\in\mathcal{T}_h}\int_K \frac{1}{\chi\Delta t}\mathbf{u}^n\cdot\mathbf{v}d\Omega + F_{\mathbf{u}}^{(1)}(\mathbf{v})^{n+\chi} \quad \forall\mathbf{v}\in\mathbf{V}_h. \qquad (3.53)
\end{aligned}
$$

For the projection steps defined by equation (3.36) we apply again the SIP method. In order to impose homogeneous Neumann boundary conditions we prescribe $\left[\nabla\left(p^{n+\chi}\right)^-\right]\cdot\mathbf{n} = -\left[\nabla\left(p^{n+\chi}\right)^+\right]\cdot\mathbf{n}$: for this reason, no contribution from boundary faces arises. We then multiply by a test function $q \in W_h$, we apply Green's theorem and we define:

$$\begin{aligned}
a_p(p,q) &= \sum_{K\in\mathcal{T}_h}\int_K \nabla p\cdot\nabla q d\Omega - \sum_{F\in\mathcal{E}^I}\int_F \{\{\nabla p\}\}\cdot[[q]]\,d\Sigma \\
&- \sum_{F\in\mathcal{E}^I}\int_F [[p]]\cdot\{\{\nabla q\}\}\,d\Sigma + \sum_{F\in\mathcal{E}^I}\int_F C_p\,[[p]]\cdot[[q]]\,d\Sigma \qquad (3.54)\\
F_p^{(1)}(q)^{n+\chi} &= \sum_{K\in\mathcal{T}_h}\int_K \frac{1}{\chi\Delta t}\mathbf{u}^{n+\chi,**}\cdot\nabla q d\Omega \\
&- \sum_{F\in\mathcal{E}}\int_F \frac{1}{\chi\Delta t}\left\{\left\{\mathbf{u}^{n+\chi,**}\right\}\right\}\cdot[[q]]\,d\Sigma \qquad (3.55)
\end{aligned}$$

and again we set

$$\sigma^p_{F,K} = r^2\frac{\mathrm{diam}(F)}{\mathrm{diam}(K)}, \qquad (3.56)$$

while we set

$$C_p = \frac{1}{2}\left(\sigma^p_{F,K^+}+\sigma^p_{F,K^-}\right) \quad \text{if } F\in\mathcal{E}^I, \qquad C_p = \sigma^p_{F,K} \quad \text{if } F\in\mathcal{E}^B. \qquad (3.57)$$

The weak formulation of equation (3.36) reads then: *given* $p^n\in W_h$, *find* $p^{n+\chi}\in W_h$ *such that*

$$\begin{aligned}
&\sum_{K\in\mathcal{T}_h}\int_K \frac{1}{c^2\chi^2\Delta t^2}p^{n+\chi}q d\Omega + a_p(p^{n+\chi},q) = \\
&\sum_{K\in\mathcal{T}_h}\int_K \frac{1}{c^2\chi^2\Delta t^2}p^{n}q d\Omega + F_p^{(1)}(q)^{n+\chi} \qquad \forall q\in W_h. \qquad (3.58)
\end{aligned}$$

The second stage can be described in a similar manner and all the details are reported in [Orlando et al., 2022b]. We now derive the fully discrete algebraic expressions corresponding to the first stage. We denote by $\boldsymbol{\varphi}_i(\mathbf{x})$ the basis functions for the space $\mathbf{V}_h$ and by $\psi_i(\mathbf{x})$ the basis functions for the space W_h, respectively, so that the discrete approximations of $\mathbf{u}$ and p read as follows:

$$\mathbf{u}\approx\mathbf{u}_h = \sum_{j=1}^{\mathrm{dim}(\mathbf{V}_h)} u_j(t)\boldsymbol{\varphi}_j(\mathbf{x}) \qquad p\approx p_h = \sum_{j=1}^{\mathrm{dim}(W_h)} p_j(t)\psi_j(\mathbf{x}). \qquad (3.59)$$

The shape functions correspond to the products of Lagrange interpolation polynomials for the support points of $(r+1)$-order and $(r+2)$-order Gauss-Lobatto quadrature rule in each coordinate direction for $\mathbf{V}_h$ and W_h, respectively. For the first stage, we take $\mathbf{v}=\boldsymbol{\varphi}_i$, $i=1,\dots,\mathrm{dim}(\mathbf{V}_h)$ and we exploit the representation introduced above to obtain the matrices

$$\begin{aligned}
M_{ij} &= \sum_{K\in\mathcal{T}_h}\int_K \boldsymbol{\varphi}_j\cdot\boldsymbol{\varphi}_i d\Omega \qquad (3.60)\\
A_{ij}^{n+\chi} &= a_{\mathbf{u}}^{(1)}\left(\boldsymbol{\varphi}_j,\boldsymbol{\varphi}_i\right) \qquad (3.61)\\
C_{ij}\left(\mathbf{u}^{n+\frac{\chi}{2}}\right) &= c^{(1)}\left(\mathbf{u}^{n+\frac{\chi}{2}},\boldsymbol{\varphi}_j,\boldsymbol{\varphi}_i\right) \qquad (3.62)
\end{aligned}$$

After computing the integrals in the previous formulae by appropriate quadrature rules, one obtains the algebraic system

$$\left(\frac{1}{\chi\Delta t}\mathbf{M} + \mathbf{A}^{n+\chi} + \mathbf{C}\left(\mathbf{u}^{n+\frac{\chi}{2}}\right)\right)\mathbf{U}_h^{n+\chi,*} = \frac{1}{\chi\Delta t}\mathbf{M}\mathbf{U}_h^n + \mathbf{F}_{\mathbf{u}}^{n+\chi}, \tag{3.63}$$

where $\mathbf{U}_h$ denotes the vector of the discrete degrees of freedom associated to the velocity field and $\mathbf{F}_{\mathbf{u}}^{n+\chi}$ is the vector obtained evaluating $F_{\mathbf{u}}^{(1)}(\boldsymbol{\varphi}_i)^{n+\chi}, i = 1,\dots,\dim(\mathbf{V}_h)$. The same procedure can be applied for the projection step, obtaining the matrices

$$\begin{aligned} M_{ij}^p &= \sum_{K\in\mathcal{T}_h}\int_K \psi_j\psi_i d\Omega & (3.64)\\ K_{ij} &= a_p(\psi_j,\psi_j). & (3.65) \end{aligned}$$

After computing the integrals in the previous formulae by appropriate quadrature rules, one obtains the algebraic counterpart of (3.58)

$$\left(\frac{1}{c^2\chi^2\Delta t^2}\mathbf{M}^p + \mathbf{K}\right)\mathbf{P}_h^{n+\chi} = \frac{1}{c^2\chi^2\Delta t^2}\mathbf{M}^p\mathbf{P}_h^n + \mathbf{F}_p^{n+\chi}, \tag{3.66}$$

where again $\mathbf{P}_h$ denotes the vector of the discrete degrees of freedom associated to pressure and $\mathbf{F}_p^{n+\chi}$ is the vector obtained evaluating $F_p^{(1)}(\boldsymbol{\psi}_i)^{n+\chi}, i = 1,\dots,\dim(W_h)$. The derivation of the algebraic formulation for the second stage follows in a straightforward manner and is reported in [Orlando et al., 2022b]. Numerical test cases to validate the proposed method are presented in Section 4.2.

3.4 Extension to the single-phase compressible Navier-Stokes equations

In this Section, we derive an extension of the approach described in Section 3.3 to single-phase compressible flows so as to obtain a novel IMEX-DG solver, originally presented in [Orlando et al., 2022a]. We consider the following system written in non-dimensional form:

$$\begin{aligned} \frac{\partial\rho}{\partial t} + \nabla\cdot(\rho\mathbf{u}) &= 0\\ \frac{\partial\rho\mathbf{u}}{\partial t} + \nabla\cdot(\rho\mathbf{u}\otimes\mathbf{u}) + \frac{1}{M^2}\nabla p &= \frac{1}{Re}\nabla\cdot\left[\left(\nabla\mathbf{u}+\nabla\mathbf{u}^T\right) - \frac{2}{3}(\nabla\cdot\mathbf{u})\mathbf{I}\right]\\ &- \frac{\rho}{Fr^2}\mathbf{k} \qquad\qquad (3.67)\\ \frac{\partial\rho E}{\partial t} + \nabla\cdot\left[\left(h+kM^2\right)\rho\mathbf{u}\right] &= \frac{M^2}{Re}\nabla\cdot\left[\left(\nabla\mathbf{u}+\nabla\mathbf{u}^T\right)\mathbf{u} - \frac{2}{3}(\nabla\cdot\mathbf{u})\mathbf{u}\right]\\ &+ \frac{1}{PrRe}\Delta T - \rho\frac{M^2}{Fr^2}\mathbf{k}\cdot\mathbf{u} \end{aligned}$$

for $\mathbf{x}\in\Omega, t\in[0,T_f]$, along with suitable initial and boundary conditions. Here T_f is the final time, ρ is the density, $\mathbf{u}$ is the fluid velocity, p is the pressure, T is the absolute temperature, ρE is the total energy, $h = e + p/\rho$ is the specific enthalpy, with e being the internal energy, and $k = \|\mathbf{u}\|^2/2$ is the kinetic energy. Notice that these non-dimensional equations are very similar to those obtained in [Munz et al., 2003] and its derivation is rather close to the one described in Section 2.4 for the two-phase flows system. All the details are reported in [Orlando et al., 2022a]. The Reynolds, Prandtl, Mach and Froude numbers, which are the non-dimensional numbers characterizing the flow, are defined as

$$Re = \frac{\mathcal{R}\mathcal{U}\mathcal{L}}{\mu} \quad \kappa = \frac{c_p \mu}{Pr} \quad M^2 = \frac{\mathcal{R}\mathcal{U}^2}{\mathcal{P}} \quad Fr^2 = \frac{\mathcal{U}^2}{g\mathcal{L}} \tag{3.68}$$

where c_p denotes the specific heat at constant pressure, κ is the thermal conductivity, μ is the shear viscosity, g is the modulus of the acceleration of gravity, $\mathcal{U}$ is the reference velocity, $\mathcal{L}$ is the reference length, $\mathcal{R}$ is the reference density and $\mathcal{P}$ is the reference pressure. Notice that we assume to neglect the bulk viscosity and, for the sake of simplicity, we also assume constant values for both μ and κ. This choice can be justified by considering that we aim to simulate regimes with limited variations of temperature and density and, moreover, we are mainly interested in time scales where thermal effects play a less relevant role. At this stage, no specific assumptions are made on the fluid. The above equations are then completed by one of the equations of state described in Section 2.6.

In the low Mach number limit, terms proportional to $1/M^2$ in (3.67) yield stiff components of the resulting semi-discretized Ordinary Differential Equations (ODE) system. Therefore, following [Casulli and Greenspan, 1984, Dumbser and Casulli, 2016], it is appropriate to couple implicitly the energy equation to the momentum balance, while the continuity equation can be discretized in a fully explicit fashion. While this would be sufficient to yield an efficient time discretization approach for the purely hyperbolic system associated to (3.67) in absence of gravity, in regimes for which

$$Pr \approx O(1), \quad Fr \ll 1$$

thermal diffusivity and gravity terms would also have to be treated implicitly for the time discretization methods to be efficient. Straightforward application of any monolithic solver would then yield large algebraic systems with multiple couplings between discrete Degrees Of Freedom (DOF) associated to different physical variables. To avoid this, we resort to an operator splitting approach, see e.g. [LeVeque, 2002], as commonly done in numerical models for atmospheric physics. More specifically, after spatial discretization, all diffusive terms on the right-hand side of (3.67) are split from the hyperbolic part on the left hand side. The hyperbolic part is treated in a similar fashion to what outlined in [Dumbser and Casulli, 2016], while the diffusive terms are treated implicitly. For simplicity, the gravity terms will be treated explicitly in this first attempt and only a basic, first order splitting will be described, which can be easily improved to second order accuracy by the Strang splitting approach [Strang, 1968, LeVeque, 2002].

For the time discretization, an IMplicit-EXplicit (IMEX) Additive Runge Kutta (ARK) method [Kennedy and Carpenter, 2003] will be used. We refer to [Giraldo et al., 2013, Orlando et al., 2022a] and to the Appendix A.5 for a more complete description and analysis of the chosen IMEX approach. IMEX-ARK methods are represented compactly by the following two Butcher tableaux [Butcher, 2008]:

$$\begin{array}{c|c} c & A \\ \hline & b^T \end{array} \qquad \begin{array}{c|c} \tilde{c} & \tilde{A} \\ \hline & \tilde{b}^T \end{array}$$

with $A = \{A_{ij}\}, b = \{b_i\}, c = \{c_i\}, \tilde{A} = \{\tilde{a}_{ij}\}, \tilde{b} = \left\{\tilde{b}_i\right\}$ and $\tilde{c} = \{\tilde{c}_i\}$. Coefficients $a_{lm}, \tilde{a}_{lm}, c_l$ and b_l are determined so that the method is consistent of a given order. We now describe the application of the specific IMEX method and of the splitting approach outlined above to equations (3.67). Notice that, for simplicity, we first present the time semi-discretization only, while maintaining the continuous form of (3.67) with respect to the spatial variables, and the detailed description of the algebraic problems resulting from the full space and time discretization will be presented in the following. For each time step, we first consider the discretization of the hyperbolic and forcing terms. Notice that, even though we focus here on this specific second order method, the strategy we outline is applicable to a generic Diagonal Implicit Runge Kutta (DIRK) method. In particular, higher order methods could be considered for coupling to high order spatial discretization, even though the effective overall accuracy would be limited by the splitting procedure if gravity and viscous terms are present. For the first stage of the method, one simply has

$$\rho^{(n,1)} = \rho^n \qquad \mathbf{u}^{(n,1)} = \mathbf{u}^n \qquad E^{(n,1)} = E^n. \tag{3.69}$$

For the second stage, we can write formally

$$\begin{aligned} \rho^{(n,2)} &= \rho^n - a_{21}\Delta t\, \nabla\cdot\left(\rho^n \mathbf{u}^n\right) \\ \rho^{(n,2)}\mathbf{u}^{(n,2)} &+ \tilde{a}_{22}\frac{\Delta t}{M^2}\nabla p^{(n,2)} = \mathbf{m}^{(n,2)} \\ \rho^{(n,2)}E^{(n,2)} &+ \tilde{a}_{22}\Delta t\, \nabla\cdot\left(h^{(n,2)}\rho^{(n,2)}\mathbf{u}^{(n,2)}\right) = \hat{e}^{(n,2)}, \end{aligned} \tag{3.70}$$

where we have set

$$\begin{aligned} \mathbf{m}^{(n,2)} &= \rho^n \mathbf{u}^n \\ &- a_{21}\Delta t\, \nabla\cdot\left(\rho^n \mathbf{u}^n \otimes \mathbf{u}^n\right) - \tilde{a}_{21}\frac{\Delta t}{M^2}\nabla p^n - a_{21}\frac{\Delta t}{Fr^2}\rho^n \mathbf{k} \end{aligned} \tag{3.71}$$

$$\begin{aligned} \hat{e}^{(n,2)} &= \rho^n E^n \\ &- \tilde{a}_{21}\Delta t\, \nabla\cdot\left(h^n \rho^n \mathbf{u}^n\right) - a_{21}\Delta t M^2\, \nabla\cdot\left(k^n \rho^n \mathbf{u}^n\right) \\ &- a_{21}\frac{\Delta t M^2}{Fr^2}\rho^n \mathbf{k}\cdot\mathbf{u}^n. \end{aligned}$$

A slight modification for the treatment of the gravity terms has been proposed in [Orlando et al., 2023] by setting

$$\begin{aligned} \mathbf{m}^{(n,2)} &= \rho^n \mathbf{u}^n \\ &- a_{21}\Delta t\, \nabla\cdot\left(\rho^n \mathbf{u}^n \otimes \mathbf{u}^n\right) - \tilde{a}_{21}\frac{\Delta t}{M^2}\nabla p^n \\ &- \tilde{a}_{21}\frac{\Delta t}{Fr^2}\rho^n \mathbf{k} - \tilde{a}_{22}\frac{\Delta t}{Fr^2}\rho^{(n,2)}\mathbf{k} \end{aligned} \tag{3.72}$$

$$\begin{aligned} \hat{e}^{(n,2)} &= \rho^n E^n \\ &- \tilde{a}_{21}\Delta t\, \nabla\cdot\left(h^n \rho^n \mathbf{u}^n\right) - a_{21}\Delta t M^2\, \nabla\cdot\left(k^n \rho^n \mathbf{u}^n\right) \\ &- \tilde{a}_{21}\frac{\Delta t M^2}{Fr^2}\rho^n \mathbf{k}\cdot\mathbf{u}^n - \tilde{a}_{22}\frac{\Delta t M^2}{Fr^2}\rho^{(n,2)}\mathbf{k}\cdot\mathbf{u}^{(n,2)}. \end{aligned}$$

Notice that, substituting formally $\rho^{(n,2)}\mathbf{u}^{(n,2)}$ into the energy equation and taking into account the definitions $\rho E = \rho e + M^2\rho k$ and $h = e + p/\rho$, the above system can be solved by computing the solution of

$$\begin{aligned} &\rho^{(n,2)}[e(p^{(n,2)},\rho^{(n,2)}) + M^2k^{(n,2)}] \\ -\;& \tilde{a}_{22}^2\frac{\Delta t^2}{M^2}\nabla\cdot\left[\left(e(p^{(n,2)},\rho^{(n,2)}) + \frac{p^{(n,2)}}{\rho^{(n,2)}}\right)\nabla p^{(n,2)}\right] \\ +\;& \tilde{a}_{22}\Delta t\,\nabla\cdot\left[\left(e(p^{(n,2)},\rho^{(n,2)}) + \frac{p^{(n,2)}}{\rho^{(n,2)}}\right)\mathbf{m}^{(n,2)}\right] = \hat{e}^{(n,2)} \end{aligned} \tag{3.73}$$

in terms of $p^{(n,2)}$ according to the fixed point procedure described in [Dumbser and Casulli, 2016]. More specifically, setting $\xi^{(0)} = p^{(n,1)}, k^{(n,2,0)} = k^{(n,1)}$, one solves for $l = 1,\dots,L$ the equation

$$\begin{aligned} \rho^{(n,2)}e(\xi^{(l)},\rho^{(n,2)}) \;&-\; \tilde{a}_{22}^2\frac{\Delta t^2}{M^2}\nabla\cdot\left[\left(e(\xi^{(l-1)},\rho^{(n,2)}) + \frac{\xi^{(l-1)}}{\rho^{(n,2)}}\right)\nabla\xi^{(l)}\right] \\ &=\; \hat{e}^{(n,2)} - M^2\rho^{(n,2)}k^{(n,2,l-1)} \\ &-\; \tilde{a}_{22}\Delta t\,\nabla\cdot\left[\left(e(\xi^{(l-1)},\rho^{(n,2)}) + \frac{\xi^{(l-1)}}{\rho^{(n,2)}}\right)\mathbf{m}^{(n,2)}\right] \end{aligned} \tag{3.74}$$

and updates the velocity as

$$\rho^{(n,2)}\mathbf{u}^{(n,2,l)} + \frac{\tilde{a}_{22}\Delta t}{M^2}\nabla\xi^{(l)} = \mathbf{m}^{(n,2)}. \tag{3.75}$$

If one uses the definitions (3.72), the following fixed point iteration is considered:

$$\begin{aligned} \rho^{(n,2)}e(\xi^{(l)},\rho^{(n,2)}) \;&-\; \tilde{a}_{22}^2\frac{\Delta t^2}{M^2}\nabla\cdot\left[\left(e(\xi^{(l-1)},\rho^{(n,2)}) + \frac{\xi^{(l-1)}}{\rho^{(n,2)}}\right)\nabla\xi^{(l)}\right] \\ &=\; \hat{e}^{(n,2,l-1)} - M^2\rho^{(n,2)}k^{(n,2,l-1)} \\ &-\; \tilde{a}_{22}\Delta t\,\nabla\cdot\left[\left(e(\xi^{(l-1)},\rho^{(n,2)}) + \frac{\xi^{(l-1)}}{\rho^{(n,2)}}\right)\mathbf{m}^{(n,2)}\right]. \end{aligned} \tag{3.76}$$

In the case of SG-EOS, $\rho^{(n,2)}e\left(\xi^{(l)},\rho^{(n,2)}\right)$ contains a term that only depends on the density, as evident from Equation (2.222) and, therefore, it has to be properly considered in the right-hand side of (3.74). On the other hand, the general cubic EOS (2.219) contains products of quantities depending on temperature and on density. For the sake of simplicity, in order to avoid the solution of a non-linear equation for each quadrature node, in these cases we keep the temperature at the value in the previous iteration of the fixed point procedure, so as to obtain

$$
\begin{aligned}
\frac{\tilde{c}_v\left(T\left(\xi^{(l-1)},\rho^{(n,2)}\right)\right)}{\tilde{R}_g}\xi^{(l)}\left(1-\rho^{(n,2)}\tilde{b}\right) &\quad - \\
\tilde{a}_{22}^2\frac{\Delta t^2}{M^2}\nabla\cdot\left[\left(e\left(\xi^{(l-1)},\rho^{(n,2)}\right)+\frac{\xi^{(l-1)}}{\rho^{(n,2)}}\right)\nabla\xi^{(l)}\right] &\quad = \\
\hat{e}^{(n,2)}-\rho^{(n,2)}k^{(n,2,l-1)} &\quad - \\
\frac{\tilde{c}_v(T\left(\xi^{(l-1)},\rho^{(n,2)}\right))}{\tilde{R}_g}\frac{\tilde{a}\left(T\left(\xi^{(l-1)},\rho^{(n,2)}\right)\right)\left(\rho^{(n,2)}\right)^2}{\left(1-\rho^{(n,2)}\tilde{b}r_1\right)\left(1-\rho^{(n,2)}\tilde{b}r_2\right)}\left(1-\rho^{(n,2)}\tilde{b}\right) &\quad - \\
\frac{\rho^{(n,2)}}{\tilde{b}}\left[\tilde{a}\left(T\left(\xi^{(l-1)},\rho^{(n,2)}\right)\right)-T\left(\xi^{(l-1)},\rho^{(n,2)}\right)\frac{d\tilde{a}}{dT}\left(\xi^{(l-1)},\rho^{(n,2)}\right)\right]U\left(\rho^{(n,2)}\right) &\quad - \\
\tilde{a}_{22}\Delta t\,\nabla\cdot\left[\left(e\left(\xi^{(l-1)},\rho^{(n,2)}\right)+\frac{\xi^{(l-1)}}{\rho^{(n,2)}}\right)\mathbf{m}^{(n,2)}\right]. &
\end{aligned}
\tag{3.77}
$$

The same considerations as in [Dumbser and Casulli, 2016] apply concerning the favourable properties of the weakly non-linear system resulting from the discrete form of (3.74) and (3.77). Once the iterations have been completed, one sets $\mathbf{u}^{(n,2)}=\mathbf{u}^{(n,2,L)}$ and $E^{(n,2)}$ accordingly. For the third stage, one can write formally

$$
\begin{aligned}
\rho^{(n,3)} &= \rho^n-a_{31}\Delta t\,\nabla\cdot\left(\rho^n\mathbf{u}^n\right)-a_{32}\Delta t\,\nabla\cdot\left(\rho^{(n,2)}\mathbf{u}^{(n,2)}\right) \\
\rho^{(n,3)}\mathbf{u}^{(n,3)} &+ \tilde{a}_{33}\frac{\Delta t}{M^2}\nabla p^{(n,3)}=\mathbf{m}^{(n,3)} \\
\rho^{(n,3)}E^{(n,3)} &+ \tilde{a}_{33}\Delta t\,\nabla\cdot\left(h^{(n,3)}\rho^{(n,3)}\mathbf{u}^{(n,3)}\right)=\hat{e}^{(n,3)},
\end{aligned}
\tag{3.78}
$$

where the right-hand sides are defined as

$$
\begin{aligned}
\mathbf{m}^{(n,3)} &= \rho^n\mathbf{u}^n \\
&- a_{31}\Delta t\,\nabla\cdot\left(\rho^n\mathbf{u}^n\otimes\mathbf{u}^n\right)-\tilde{a}_{31}\frac{\Delta t}{M^2}\nabla p^n \qquad (3.79)\\
&- a_{32}\Delta t\,\nabla\cdot\left(\rho^{(n,2)}\mathbf{u}^{(n,2)}\otimes\mathbf{u}^{(n,2)}\right)-\tilde{a}_{32}\frac{\Delta t}{M^2}\nabla p^{(n,2)} \qquad (3.80)\\
&- a_{31}\frac{\Delta t}{Fr^2}\rho^n\mathbf{k}-a_{32}\frac{\Delta t}{Fr^2}\rho^{(n,2)}\mathbf{k}
\end{aligned}
$$

$$
\begin{aligned}
\hat{e}^{(n,3)} &= \rho^nE^n \qquad (3.81)\\
&- \tilde{a}_{31}\Delta t\,\nabla\cdot\left(h^n\rho^n\mathbf{u}^n\right)-a_{31}\Delta tM^2\,\nabla\cdot\left(k^n\rho^n\mathbf{u}^n\right) \\
&- \tilde{a}_{32}\Delta t\,\nabla\cdot\left(h^{(n,2)}\rho^{(n,2)}\mathbf{u}^{(n,2)}\right)-a_{32}\Delta tM^2\,\nabla\cdot\left(k^{(n,2)}\rho^{(n,2)}\mathbf{u}^{(n,2)}\right) \\
&- a_{31}\Delta t\frac{M^2}{Fr^2}\rho^n\mathbf{k}\cdot\mathbf{u}^n-a_{32}\Delta t\frac{M^2}{Fr^2}\rho^{(n,2)}\mathbf{k}\cdot\mathbf{u}^{(n,2)}
\end{aligned}
$$

or as follows [Orlando et al., 2023]:

$$
\begin{aligned}
\mathbf{m}^{(n,3)} &= \rho^n \mathbf{u}^n \\
&- a_{31}\Delta t\, \nabla\cdot \left(\rho^n \mathbf{u}^n \otimes \mathbf{u}^n\right) - \tilde{a}_{31}\frac{\Delta t}{M^2}\nabla p^n \\
&- a_{32}\Delta t\, \nabla\cdot \left(\rho^{(n,2)} \mathbf{u}^{(n,2)} \otimes \mathbf{u}^{(n,2)}\right) - \tilde{a}_{32}\frac{\Delta t}{M^2}\nabla p^{(n,2)} \\
&- \tilde{a}_{31}\frac{\Delta t}{Fr^2}\rho^n \mathbf{k} - \tilde{a}_{32}\frac{\Delta t}{Fr^2}\rho^{(n,2)}\mathbf{k} - \tilde{a}_{33}\Delta t \frac{\Delta t}{Fr^2}\rho^{(n,3)}\mathbf{k}
\end{aligned} \tag{3.82}
$$

$$
\begin{aligned}
\hat{e}^{(n,3)} &= \rho^n E^n \\
&- \tilde{a}_{31}\Delta t\, \nabla\cdot \left(h^n \rho^n \mathbf{u}^n\right) - a_{31}\Delta t M^2\, \nabla\cdot \left(k^n \rho^n \mathbf{u}^n\right) \\
&- \tilde{a}_{32}\Delta t\, \nabla\cdot \left(h^{(n,2)} \rho^{(n,2)} \mathbf{u}^{(n,2)}\right) - a_{32}\Delta t M^2\, \nabla\cdot \left(k^{(n,2)} \rho^{(n,2)} \mathbf{u}^{(n,2)}\right) \\
&- \tilde{a}_{31}\Delta t\frac{M^2}{Fr^2}\rho^n \mathbf{k}\cdot\mathbf{u}^n \tilde{a}_{32}\Delta t\frac{M^2}{Fr^2}\rho^{(n,2)}\mathbf{k}\cdot\mathbf{u}^{(n,2)} - \tilde{a}_{33}\Delta t\frac{M^2}{Fr^2}\rho^{(n,3)}\mathbf{k}\cdot\mathbf{u}^{(n,3)}
\end{aligned}
$$

Again, the solution of this stage is computed by substituting formally $\rho^{(n,3)}\mathbf{u}^{(n,3)}$ into the energy equation and computing the solution of

$$
\begin{aligned}
&\rho^{(n,3)}[e\left(p^{(n,3)}, \rho^{(n,3)}\right) + M^2 k^{(n,3)}] \\
-\ &\tilde{a}_{33}^2\frac{\Delta t^2}{M^2}\, \nabla\cdot \left[\left(e\left(p^{(n,3)}, \rho^{(n,3)}\right) + \frac{p^{(n,3)}}{\rho^{(n,3)}}\right)\nabla p^{(n,3)}\right] \\
+\ &\tilde{a}_{33}\Delta t\, \nabla\cdot \left[\left(e\left(p^{(n,3)}, \rho^{(n,3)}\right) + \frac{p^{(n,3)}}{\rho^{(n,3)}}\right)\mathbf{m}^{(n,3)}\right] = \hat{e}^{(n,3)}.
\end{aligned} \tag{3.83}
$$

More specifically, setting $\xi^{(0)} = p^{(n,2)}, k^{(n,3,0)} = k^{(n,2)}$, one solves for $l = 1, \ldots, L$ the equation

$$
\begin{aligned}
\rho^{(n,3)} e\left(\xi^{(l)}, \rho^{(n,3)}\right) &- \frac{\tilde{a}_{33}^2 \Delta t^2}{M^2}\, \nabla\cdot \left[\left(e(\xi^{(l-1)}, \rho^{(n,3)}) + \frac{\xi^{(l-1)}}{\rho^{(n,3)}}\right)\nabla \xi^{(l)}\right] \\
&= \hat{e}^{(n,3)} - \rho^{(n,3)} k^{(n,3,l)} \\
&- \tilde{a}_{33}\Delta t\, \nabla\cdot \left[\left(e\left(\xi^{(l-1)}, \rho^{(n,3)}\right) + \frac{\xi^{(l-1)}}{\rho^{(n,3)}}\right)\mathbf{m}^{(n,3)}\right]
\end{aligned} \tag{3.84}
$$

or, in the case of (3.82), the equation

$$
\begin{aligned}
\rho^{(n,3)} e\left(\xi^{(l)}, \rho^{(n,3)}\right) &- \frac{\tilde{a}_{33}^2 \Delta t^2}{M^2}\, \nabla\cdot \left[\left(e(\xi^{(l-1)}, \rho^{(n,3)}) + \frac{\xi^{(l-1)}}{\rho^{(n,3)}}\right)\nabla \xi^{(l)}\right] \\
&= \hat{e}^{(n,3,l-1)} - \rho^{(n,3)} k^{(n,3,l-1)} \\
&- \tilde{a}_{33}\Delta t\, \nabla\cdot \left[\left(e\left(\xi^{(l-1)}, \rho^{(n,3)}\right) + \frac{\xi^{(l-1)}}{\rho^{(n,3)}}\right)\mathbf{m}^{(n,3)}\right]
\end{aligned} \tag{3.85}
$$

and updates the velocity as

$$
\rho^{(n,3)}\mathbf{u}^{(n,3,l)} + \tilde{a}_{33}\frac{\Delta t}{M^2}\nabla \xi^{(l)} = \mathbf{m}^{(n,3)}. \tag{3.86}
$$

Once again, in case of a non-ideal gas equation of state, the expression of the term $\rho^{(n,3)}e\left(\xi^{(l)},\rho^{(n,3)}\right)$ is slightly different. For the sake of clarity, we report also for this stage the fixed point equation for the general cubic EOS:

$$
\begin{aligned}
&\frac{\tilde{c}_v\left(T\left(\xi^{(l-1)},\rho^{(n,3)}\right)\right)}{\tilde{R}_g}\xi^{(l)}\left(1-\rho^{(n,3)}\tilde{b}\right) \quad - \\
&\tilde{a}_{33}^2\frac{\Delta t^2}{M^2}\,\nabla\cdot\left[\left(e\left(\xi^{(l-1)},\rho^{(n,3)}\right)+\frac{\xi^{(l-1)}}{\rho^{(n,3)}}\right)\nabla\xi^{(l)}\right] \quad = \\
&\hat{e}^{(n,3)}-M^2\rho^{(n,3)}k^{(n,3,l)} \quad - \\
&\frac{\tilde{c}_v\left(T\left(\xi^{(l-1)},\rho^{(n,3)}\right)\right)}{\tilde{R}_g}\frac{\tilde{a}\left(T\left(\xi^{(l-1)},\rho^{(n,3)}\right)\right)\left(\rho^{(n,3)}\right)^2}{\left(1-\rho^{(n,3)}\tilde{b}r_1\right)\left(1-\rho^{(n,3)}\tilde{b}r_2\right)}\left(1-\rho^{(n,3)}\tilde{b}\right) \quad - \\
&\frac{\rho^{(n,3)}}{\tilde{b}}\left[\tilde{a}\left(T\left(\xi^{(l-1)},\rho^{(n,3)}\right)\right)-T\left(\xi^{(l-1)},\rho^{(n,3)}\right)\frac{d\tilde{a}}{dT}\left(\xi^{(l-1)},\rho^{(n,3)}\right)\right]U\left(\rho^{(n,3)}\right) \quad - \\
&\tilde{a}_{33}\Delta t\,\nabla\cdot\left[\left(e\left(\xi^{(l-1)},\rho^{(n,3)}\right)+\frac{\xi^{(l-1)}}{\rho^{(n,3)}}\right)\mathbf{m}^{(n,3)}\right]. \qquad (3.87)
\end{aligned}
$$

After the weights step (see (A.104) in Appendix A.5), one considers now the diffusive part of the Navier-Stokes equations that will be treated with an operator splitting technique. Notice that at this stage, the computation of the density is completed and, therefore, ρ^{n+1} is available. For the sake of clarity, we denote with $\sim$ the quantities computed in this part of the scheme. The discretization of the viscous terms is carried out by the implicit part of the IMEX method previously described:

$$
\begin{aligned}
\rho^{n+1}\tilde{\mathbf{u}}^{(n,2)} \quad &- \quad \tilde{a}_{22}\frac{\Delta t}{Re}\,\nabla\cdot\left[\left(\nabla\tilde{\mathbf{u}}+\nabla\tilde{\mathbf{u}}^T\right)-\frac{2}{3}(\nabla\cdot\tilde{\mathbf{u}})\mathbf{I}\right]^{(n,2)} = \tilde{\mathbf{m}}^{(n,2)} \\
\rho^{n+1}\tilde{E}^{(n,2)} \quad &- \quad \tilde{a}_{22}\frac{\Delta t M^2}{Re}\,\nabla\cdot\left[\left(\nabla\tilde{\mathbf{u}}+\nabla\tilde{\mathbf{u}}^T\right)\tilde{\mathbf{u}}-\frac{2}{3}(\nabla\cdot\tilde{\mathbf{u}})\tilde{\mathbf{u}}\right]^{(n,2)} \\
&- \quad \tilde{a}_{22}\frac{\Delta t}{PrRe}\Delta\tilde{T}^{(n,2)} = \tilde{e}^{(n,2)}, \qquad (3.88)
\end{aligned}
$$

where we have set

$$
\begin{aligned}
\tilde{\mathbf{m}}^{(n,2)} \quad &= \quad \rho^{n+1}\tilde{\mathbf{u}}^{(n,1)}+\tilde{a}_{21}\frac{\Delta t}{Re}\,\nabla\cdot\left[\left(\nabla\tilde{\mathbf{u}}+\nabla\tilde{\mathbf{u}}^T\right)-\frac{2}{3}(\nabla\cdot\tilde{\mathbf{u}})\mathbf{I}\right]^{(n,1)} \qquad (3.89) \\
\tilde{e}^{(n,2)} \quad &= \quad \rho^{n+1}\tilde{E}^{(n,1)} \\
&+ \quad \tilde{a}_{21}\frac{\Delta t M^2}{Re}\,\nabla\cdot\left[\left(\nabla\tilde{\mathbf{u}}+\nabla\tilde{\mathbf{u}}^T\right)\tilde{\mathbf{u}}-\frac{2}{3}(\nabla\cdot\tilde{\mathbf{u}})\tilde{\mathbf{u}}\right]^{(n,1)} \\
&+ \quad \tilde{a}_{21}\frac{\Delta t}{PrRe}\Delta\tilde{T}^{(n,1)}.
\end{aligned}
$$

Notice that the momentum equation in (3.88) is decoupled from the energy equation and can be solved independently, so that in a subsequent step the equation for $\tilde{E}^{(n,2)}$ can be solved using temperature as an unknown. It is worth to mention that, in case $\frac{d\tilde{a}}{dT}\neq 0$ or $\frac{d\tilde{c}_v}{dT}\neq 0$, for the cubic EOS, we end up with a non-linear equation. The following fixed point procedure is considered: setting $\xi^{(0)} = \tilde{T}^{(n,1)}$, one solves for $l = 1, \dots, L$

$$
\begin{aligned}
&\tilde{c}_v\left(\xi^{(l)}\right)\xi^{(l+1)} + \frac{\tilde{a}\left(\xi^{(l)}\right) - \xi^{(l+1)}\frac{d\tilde{a}}{dT}\left(\xi^{(l)}\right)}{\tilde{b}} \\
&-\tilde{a}_{22}\frac{\Delta t M^2}{Re}\nabla\cdot\left[\left(\nabla\tilde{\mathbf{u}} + \nabla\tilde{\mathbf{u}}^T\right)\tilde{\mathbf{u}} - \frac{2}{3}(\nabla\cdot\tilde{\mathbf{u}})\tilde{\mathbf{u}}\right]^{(n,2)} \\
&-\tilde{a}_{22}\frac{\Delta t}{Pr Re}\Delta\xi^{(l+1)} = \tilde{e}^{(n,2)}.
\end{aligned}
\tag{3.90}
$$

For the third stage, one can write formally

$$
\begin{aligned}
\rho^{n+1}\tilde{\mathbf{u}}^{(n,3)} &- \tilde{a}_{33}\frac{\Delta t}{Re}\nabla\cdot\left[\left(\nabla\tilde{\mathbf{u}} + \nabla\tilde{\mathbf{u}}^T\right) - \frac{2}{3}(\nabla\cdot\tilde{\mathbf{u}})\mathbf{I}\right]^{(n,3)} = \tilde{\mathbf{m}}^{(n,3)} \\
\rho^{n+1}\tilde{E}^{(n,3)} &- \tilde{a}_{33}\frac{\Delta t M^2}{Re}\nabla\cdot\left[\left(\nabla\tilde{\mathbf{u}} + \nabla\tilde{\mathbf{u}}^T\right)\tilde{\mathbf{u}} - \frac{2}{3}(\nabla\cdot\tilde{\mathbf{u}})\tilde{\mathbf{u}}\right]^{(n,3)} \\
&- \tilde{a}_{33}\frac{\Delta t}{Pr Re}\Delta\tilde{T}^{(n,3)} = \tilde{e}^{(n,3)},
\end{aligned}
\tag{3.91}
$$

where the right-hand sides are defined as

$$
\begin{aligned}
\tilde{\mathbf{m}}^{(n,3)} &= \rho^{n+1}\tilde{\mathbf{u}}^{(n,1)} + \tilde{a}_{31}\frac{\Delta t}{Re}\nabla\cdot\left[\left(\nabla\tilde{\mathbf{u}} + \nabla\tilde{\mathbf{u}}^T\right) - \frac{2}{3}(\nabla\cdot\tilde{\mathbf{u}})\mathbf{I}\right]^{(n,1)} \\
&+ \tilde{a}_{32}\frac{\Delta t}{Re}\nabla\cdot\left[\left(\nabla\tilde{\mathbf{u}} + \nabla\tilde{\mathbf{u}}^T\right) - \frac{2}{3}(\nabla\cdot\tilde{\mathbf{u}})\mathbf{I}\right]^{(n,2)} \\
\tilde{e}^{(n,3)} &= \rho^{n+1}\tilde{E}^{(n,1)} \\
&+ \tilde{a}_{31}\frac{\Delta t M^2}{Re}\nabla\cdot\left[\left(\nabla\tilde{\mathbf{u}} + \nabla\tilde{\mathbf{u}}^T\right)\tilde{\mathbf{u}} - \frac{2}{3}(\nabla\cdot\tilde{\mathbf{u}})\tilde{\mathbf{u}}\right]^{(n,1)} \\
&+ \tilde{a}_{32}\frac{\Delta t M^2}{Re}\nabla\cdot\left[\left(\nabla\tilde{\mathbf{u}} + \nabla\tilde{\mathbf{u}}^T\right)\tilde{\mathbf{u}} - \frac{2}{3}(\nabla\cdot\tilde{\mathbf{u}})\tilde{\mathbf{u}}\right]^{(n,2)} \\
&+ \tilde{a}_{31}\frac{\Delta t}{Pr Re}\Delta\tilde{T}^{(n,1)} + \tilde{a}_{32}\frac{\Delta t}{Pr Re}\Delta\tilde{T}^{(n,2)}.
\end{aligned}
\tag{3.92}
$$

Again, the momentum equation in (3.91) is decoupled from the energy equation and can be solved independently, so that in a subsequent step the equation for $\tilde{E}^{(n,3)}$ can be solved using temperature as an unknown. Finally, since the TR-BDF2 method is a stiffly accurate method and, therefore, the last stage is actually equal to the update solution [Burrage and Tian, 2001], one sets

$$
\mathbf{u}^{n+1} = \tilde{\mathbf{u}}^{(n,3)} \qquad E^{n+1} = \tilde{E}^{(n,3)} \tag{3.93}
$$

and the computation of the $n-$th time step is therefore completed with the update of the pressure according to the obtained density and temperature.

Let us focus now on the spatial discretization. We then denote by $\boldsymbol{\varphi}_i(\mathbf{x})$ the basis functions for the space $\mathbf{Q}_r$ and by $\psi_i(\mathbf{x})$ the basis functions for the space Q_r, the finite element spaces chosen for the discretization of the velocity and of the pressure (as well as the density), respectively.

$$
\mathbf{u} \approx \sum_{j=1}^{\dim(\mathbf{Q}_r)} u_j(t)\boldsymbol{\varphi}_j(\mathbf{x}) \qquad p \approx \sum_{j=1}^{\dim(Q_r)} p_j(t)\psi_j(\mathbf{x}). \tag{3.94}
$$

For what concerns the weak imposition of the boundary conditions, the free-slip condition for the velocity is imposed by using ghost cells on which the velocity is set as a reflection of the one inside of the wall [Abdi and Giraldo, 2016], i.e. using the so-called reflector $\mathbf{P} = \mathbf{I} - 2\mathbf{n} \otimes \mathbf{n}$. This means that the ghost state $\mathbf{u}^-$ is set equal to

$$\mathbf{u}^- = \mathbf{u}^+ - 2\left(\mathbf{u}^+ \cdot \mathbf{n}\right)\mathbf{n}. \tag{3.95}$$

However, analogous results are obtained by means of a strong imposition of the boundary condition. Given these definitions, the weak formulation for the momentum equation of the second stage (3.70) reads as follows:

$$\begin{aligned}
& \sum_{K \in \mathcal{T}_h} \int_K \rho^{(n,2)} \mathbf{u}^{(n,2)} \cdot \mathbf{v} d\Omega \\
- & \sum_{K \in \mathcal{T}_h} \int_K \tilde{a}_{22} \frac{\Delta t}{M^2} p^{(n,2)} \nabla \cdot \mathbf{v} d\Omega + \sum_{F \in \mathcal{E}} \int_F \tilde{a}_{22} \frac{\Delta t}{M^2} \left\{\left\{p^{(n,2)}\right\}\right\} [[\mathbf{v}]]\, d\Sigma \\
= & \sum_{K \in \mathcal{T}_h} \int_K \rho^n \mathbf{u}^n \cdot \mathbf{v} d\Omega - \sum_K \int_K a_{21} \frac{\Delta t}{Fr^2} \rho^n \mathbf{k} \cdot \mathbf{v} d\Omega \\
+ & \sum_{K \in \mathcal{T}_h} \int_K a_{21} \Delta t \left(\rho^n \mathbf{u}^n \otimes \mathbf{u}^n\right) : \nabla \mathbf{v} d\Omega + \sum_{K \in \mathcal{T}_h} \int_K \tilde{a}_{21} \frac{\Delta t}{M^2} p^n \nabla \cdot \mathbf{v} d\Omega \\
- & \sum_{F \in \mathcal{E}} \int_F a_{21} \Delta t \left\{\left\{\rho^n \mathbf{u}^n \otimes \mathbf{u}^n\right\}\right\} : \langle\langle \mathbf{v} \rangle\rangle\, d\Sigma \\
- & \sum_{F \in \mathcal{E}} \int_F \tilde{a}_{21} \frac{\Delta t}{M^2} \left\{\left\{p^n\right\}\right\} [[\mathbf{v}]]\, d\Sigma \\
- & \sum_{F \in \mathcal{E}} \int_F a_{21} \Delta t \frac{\lambda^{(n,1)}}{2} \langle\langle \rho^n \mathbf{u}^n \rangle\rangle : \langle\langle \mathbf{v} \rangle\rangle\, d\Sigma,
\end{aligned} \tag{3.96}$$

where

$$\lambda^{(n,1)} = \max\left(\left|\mathbf{u}^{n^+} \cdot \mathbf{n}^+\right|, \left|\mathbf{u}^{n^-} \cdot \mathbf{n}^-\right|\right). \tag{3.97}$$

One can notice that centered flux has been employed as numerical flux for the quantities defined implicitly, whereas an upwind flux has been used for the quantities computed explicitly. In view of the implicit coupling between the momentum and the energy equations, we need to derive the algebraic formulation of (3.96) in order to formally substitute the degrees of freedom of the velocity into the algebraic formulation of the energy equation. We take $\mathbf{v} = \boldsymbol{\varphi}_i$, $i = 1, \dots, \dim(\mathbf{Q}_r)$

and we exploit the representation introduced above to obtain

$$\begin{aligned}
& \sum_{K\in\mathcal{T}_h}\int_K \rho^{(n,2)}\sum_{j=1}^{\dim(\mathbf{V}_r)} u_j^{(n,2)}\boldsymbol{\varphi}_j\cdot\boldsymbol{\varphi}_i d\Omega - \sum_{K\in\mathcal{T}_h}\int_K \tilde{a}_{22}\frac{\Delta t}{M^2}\sum_{j=1}^{\dim(Q_r)} p_j^{(n,2)}\psi_j\nabla\cdot\boldsymbol{\varphi}_i d\Omega \\
+ & \sum_{F\in\mathcal{E}}\int_F \tilde{a}_{22}\frac{\Delta t}{M^2}\sum_{j=1}^{\dim(Q_r)} p_j^{(n,2)}\left\{\{\psi_j\}\right\}\left[[\boldsymbol{\varphi}_i]\right] d\Sigma \\
= & \sum_{K\in\mathcal{T}_h}\int_K \rho^n\mathbf{u}^n\cdot\boldsymbol{\varphi}_i d\Omega - \sum_{K\in\mathcal{T}_h}\int_K a_{21}\frac{\Delta t}{Fr^2}\rho^n\mathbf{k}\cdot\boldsymbol{\varphi}_i d\Omega \\
+ & \sum_{K\in\mathcal{T}_h}\int_K a_{21}\Delta t\left(\rho^n\mathbf{u}^n\otimes\mathbf{u}^n\right):\nabla\boldsymbol{\varphi}_i d\Omega + \sum_{K\in\mathcal{T}_h}\int_k \tilde{a}_{21}\frac{\Delta t}{M^2}p^n\nabla\cdot\boldsymbol{\varphi}_i d\Omega \\
- & \sum_{F\in\mathcal{E}}\int_F a_{21}\Delta t\left\{\{\rho^n\mathbf{u}^n\otimes\mathbf{u}^n\}\right\}:\langle\langle\boldsymbol{\varphi}_i\rangle\rangle d\Sigma \\
- & \sum_{F\in\mathcal{E}}\int_F \tilde{a}_{21}\frac{\Delta t}{M^2}\left\{\{p^n\}\right\}\left[[\boldsymbol{\varphi}_i]\right] d\Sigma \\
- & \sum_{F\in\mathcal{E}}\int_F a_{21}\Delta t\frac{\lambda^{(n,1)}}{2}\langle\langle\rho^n\mathbf{u}^n\rangle\rangle:\langle\langle\boldsymbol{\varphi}_i\rangle\rangle d\Sigma, \qquad (3.98)
\end{aligned}$$

which can be written in compact form as

$$\mathbf{A}^{(n,2)}\mathbf{U}^{(n,2)} + \mathbf{B}^{(n,2)}\mathbf{P}^{(n,2)} = \mathbf{F}^{(n,2)} \qquad (3.99)$$

where we have set

$$\begin{aligned}
A_{ij}^{(n,2)} &= \sum_{K\in\mathcal{T}_h}\int_K \rho^{(n,2)}\boldsymbol{\varphi}_j\cdot\boldsymbol{\varphi}_i d\Omega \qquad (3.100) \\
B_{ij}^{(n,2)} &= \sum_{K\in\mathcal{T}_h}\int_K -\tilde{a}_{22}\frac{\Delta t}{M^2}\nabla\cdot\boldsymbol{\varphi}_i\psi_j d\Omega + \sum_{F\in\mathcal{E}}\int_F \tilde{a}_{22}\frac{\Delta t}{M^2}\left\{\{\psi_j\}\right\}\left[[\boldsymbol{\varphi}_i]\right] d\Sigma \qquad (3.101)
\end{aligned}$$

with $\mathbf{U}^{(n,2)}$ denoting the vector of the degrees of freedom associated to the velocity field and $\mathbf{P}^{(n,2)}$ denoting the vector of the degrees of freedom associated to the pressure. Consider now the weak formulation for the energy equation of the second stage (3.70)

$$
\begin{aligned}
& \sum_{K \in \mathcal{T}_h} \int_K \rho^{(n,2)} E^{(n,2)} w d\Omega - \sum_{K \in \mathcal{T}_h} \int_K \tilde{a}_{22} \Delta t h^{(n,2)} \rho^{(n,2)} \mathbf{u}^{(n,2)} \cdot \nabla w d\Omega \\
+ & \sum_{F \in \mathcal{E}} \int_F \tilde{a}_{22} \Delta t \left\{\left\{ h^{(n,2)} \rho^{(n,2)} \mathbf{u}^{(n,2)} \right\}\right\} \cdot [[w]] \, d\Sigma \\
= & \sum_{K \in \mathcal{T}_h} \int_K \rho^n E^n w d\Omega - \sum_{K \in \mathcal{T}_h} \int_K a_{21} \frac{\Delta t M^2}{Fr^2} \rho^n \mathbf{k} \cdot \mathbf{u}^n w d\Omega \\
+ & \sum_{K \in \mathcal{T}_h} \int_K a_{21} \Delta t M^2 \left(k^n \rho^n \mathbf{u}^n \right) \cdot \nabla w d\Omega + \sum_{K \in \mathcal{T}_h} \int_K \tilde{a}_{21} \Delta t \left(h^n \rho^n \mathbf{u}^n \right) \cdot \nabla w d\Omega \\
- & \sum_{F \in \mathcal{E}} \int_F a_{21} \Delta t M^2 \left\{\left\{ k^n \rho^n \mathbf{u}^n \right\}\right\} \cdot [[w]] \, d\Sigma \\
- & \sum_{F \in \mathcal{E}} \int_F \tilde{a}_{21} \Delta t \left\{\left\{ h^n \rho^n \mathbf{u}^n \right\}\right\} \cdot [[w]] \, d\Sigma \\
- & \sum_{F \in \mathcal{E}} \int_F a_{21} \Delta t \frac{\lambda^{(n,1)}}{2} \left[\left[\rho^n E^n \right]\right] \cdot [[w]] \, d\Sigma. \qquad (3.102)
\end{aligned}
$$

Notice that, while the fully discrete formulation is presented here for the case of an ideal gas, in the more general case it has to be modified properly as already shown in (3.77) for the semi-discrete formulation. Take $w = \psi_i$ and consider the expansion for $\mathbf{u}^{(n,2)}$ in (3.102) to get

$$
\begin{aligned}
& \sum_{K \in \mathcal{T}_h} \int_K \rho^{(n,2)} E^{(n,2)} \psi_i d\Omega - \sum_{K \in \mathcal{T}_h} \int_K \tilde{a}_{22} \Delta t h^{(n,2)} \rho^{(n,2)} \sum_{j=1}^{\dim(\mathbf{V}_r)} u_j^{(n,2)} \boldsymbol{\varphi}_j \cdot \nabla \psi_i d\Omega \\
+ & \sum_{F \in \mathcal{E}} \int_F \tilde{a}_{22} \Delta t \sum_{j=1}^{\dim(\mathbf{V}_r)} u_j^{(n,2)} \left\{\left\{ h^{(n,2)} \rho^{(n,2)} \boldsymbol{\varphi}_j \right\}\right\} \cdot [[\psi_i]] \, d\Sigma \\
= & \sum_{K \in \mathcal{T}_h} \int_K \rho^n E^n \psi_i d\Omega - \sum_{K \in \mathcal{T}_h} \int_K a_{21} \frac{\Delta t M^2}{Fr^2} \rho^n \mathbf{k} \cdot \mathbf{u}^n \psi_i d\Omega \\
+ & \sum_{K \in \mathcal{T}_h} \int_K a_{21} \Delta t M^2 \left(k^n \rho^n \mathbf{u}^n \right) \cdot \nabla \psi_i d\Omega + \sum_{K \in \mathcal{T}_h} \int_K \tilde{a}_{21} \Delta t \left(h^n \rho^n \mathbf{u}^n \right) \cdot \nabla \psi_i d\Omega \\
- & \sum_{F \in \mathcal{E}} \int_F a_{21} \Delta t M^2 \left\{\left\{ k^n \rho^n \mathbf{u}^n \right\}\right\} \cdot [[\psi_i]] \, d\Sigma \\
- & \sum_{F \in \mathcal{E}} \int_F \tilde{a}_{21} \Delta t \left\{\left\{ h^n \rho^n \mathbf{u}^n \right\}\right\} \cdot [[\psi_i]] \, d\Sigma \\
- & \sum_{F \in \mathcal{E}} \int_F a_{21} \Delta t \frac{\lambda^{(n,1)}}{2} \left[\left[\rho^n E^n \right]\right] \cdot [[\psi_i]] \, d\Sigma, \qquad (3.103)
\end{aligned}
$$

which can be expressed in compact form as

$$
\mathbf{C}^{(n,2)} \mathbf{U}^{(n,2)} = \mathbf{G}^{(n,2)} \qquad (3.104)
$$

where we have set

$$\begin{aligned} C_{ij}^{(n,2)} &= \sum_{K\in\mathcal{T}_h}\int_K -\tilde{a}_{22}\Delta t h^{(n,2)}\rho^{(n,2)}\boldsymbol{\varphi}_j\cdot\nabla\psi_i d\Omega \\ &+ \sum_{F\in\mathcal{E}}\int_F \tilde{a}_{22}\Delta t\left\{\left\{h^{(n,2)}\rho^{(n,2)}\boldsymbol{\varphi}_j\right\}\right\}\cdot[[\psi_i]]\, d\Sigma. \end{aligned} \tag{3.105}$$

Formally we can then derive $\mathbf{U}^{(n,2)} = (\mathbf{A}^{(n,2)})^{-1}\left(\mathbf{F}^{(n,2)} - \mathbf{B}^{(n,2)}\mathbf{P}^{(n,2)}\right)$ and obtain the following relation

$$\mathbf{C}^{(n,2)}(\mathbf{A}^{(n,2)})^{-1}\left(\mathbf{F}^{(n,2)} - \mathbf{B}^{(n,2)}\mathbf{P}^{(n,2)}\right) = \mathbf{G}^{(n,2)}. \tag{3.106}$$

Taking into account that

$$\rho^{(n,2)}E^{(n,2)} = \rho^{(n,2)}e^{(n,2)}(p^{(n,2)}) + M^2\rho^{(n,2)}k^{(n,2)}, \tag{3.107}$$

we finally obtain

$$\mathbf{C}^{(n,2)}(\mathbf{A}^{(n,2)})^{-1}\left(\mathbf{F}^{(n,2)} - \mathbf{B}^{(n,2)}\mathbf{P}^{(n,2)}\right) = -\mathbf{D}^{(n,2)}\mathbf{P}^{(n,2)} + \tilde{\mathbf{G}}^{(n,2)} \tag{3.108}$$

where we have set

$$D_{ij}^{(n,2)} = \sum_{K\in\mathcal{T}_h}\int_K \rho^{(n,2)}e^{(n,2)}(\psi_j)\psi_i = \sum_{K\in\mathcal{T}_h}\int_K \frac{1}{\gamma-1}\psi_j\psi_i d\Omega \tag{3.109}$$

and $\tilde{\mathbf{G}}^{(n,2)}$ takes into account all the other terms (the one at previous stage and the kinetic energy). As mentioned above, the discrete formulation has to take into account the choice of the EOS. For the sake of clarity, we report for the present stage the expression of the entries of the matrix $\mathbf{D}$ obtained by considering the general cubic equation of state:

$$D_{ij}^{(n,2)} = \sum_{K\in\mathcal{T}_h}\int_K \left(1 - \rho^{(n,2)}\tilde{b}\right)\frac{\tilde{c}_v\left(T\left(\xi,\rho^{(n,2)}\right)\right)}{\tilde{R}_g}\psi_j\psi_i d\Omega. \tag{3.110}$$

The system (3.108) can be solved in terms of $\mathbf{P}^{(n,2)}$ according to the fixed point procedure described in [Dumbser and Casulli, 2016]. More specifically, setting $\mathbf{P}^{(n,2,0)} = \mathbf{P}^{(n,1)}, k^{(n,2,0)} = k^{(n,1)}$, for $l = 1,\dots,L$ one solves the equation

$$\begin{aligned} \left(\mathbf{D}^{(n,2,l-1)} - \mathbf{C}^{(n,2,l-1)}(\mathbf{A}^{(n,2)})^{-1}\mathbf{B}^{(n,2)}\right)\mathbf{P}^{(n,2,l)} &= \tilde{\mathbf{G}}^{(n,2,l-1)} \\ &- \mathbf{C}^{(n,2,l-1)}(\mathbf{A}^{(n,2)})^{-1}\mathbf{F}^{(n,2,l-1)} \end{aligned} \tag{3.111}$$

and updates the velocity solving

$$\mathbf{A}^{(n,2)}\mathbf{U}^{(n,2,l)} = \mathbf{F}^{(n,2,l-1)} - \mathbf{B}^{(n,2)}\mathbf{P}^{(n,2,l)}. \tag{3.112}$$

For the third stage, we proceed in a similar manner. We start with the weak formulation of the momentum equation in (3.78):

$$
\begin{aligned}
& \sum_{K\in\mathcal{T}_h}\int_K \rho^{(n,3)}\mathbf{u}^{(n,3)}\cdot\mathbf{v}d\Omega \\
- & \sum_{K\in\mathcal{T}_h}\int_K \tilde{a}_{33}\frac{\Delta t}{M^2}p^{(n,3)}\nabla\cdot\mathbf{v}d\Omega + \sum_{F\in\mathcal{E}}\int_F \tilde{a}_{33}\frac{\Delta t}{M^2}\left\{\left\{p^{(n,3)}\right\}\right\}[[\mathbf{v}]]\,d\Sigma \\
= & \sum_{K\in\mathcal{T}_h}\int_K \rho^n\mathbf{u}^n\cdot\mathbf{v}d\Omega - \sum_{K\in\mathcal{T}_h}\int_K a_{31}\frac{\Delta t}{Fr^2}\rho^n\mathbf{k}\cdot\mathbf{v}d\Omega - \sum_{K\in\mathcal{T}_h}\int_K a_{32}\frac{\Delta t}{Fr^2}\rho^{(n,2)}\mathbf{k}\cdot\mathbf{v}d\Omega \\
+ & \sum_{K\in\mathcal{T}_h}\int_K a_{31}\Delta t\left(\rho^n\mathbf{u}^n\otimes\mathbf{u}^n\right):\nabla\mathbf{v}d\Omega + \sum_{K\in\mathcal{T}_h}\int_K \tilde{a}_{31}\frac{\Delta t}{M^2}p^n\nabla\cdot\mathbf{v}d\Omega \\
+ & \sum_{K\in\mathcal{T}_h}\int_K a_{32}\Delta t\left(\rho^{(n,2)}\mathbf{u}^{(n,2)}\otimes\mathbf{u}^{(n,2)}\right):\nabla\mathbf{v}d\Omega + \sum_{K\in\mathcal{T}_h}\int_K \tilde{a}_{32}\frac{\Delta t}{M^2}p^{(n,2)}\nabla\cdot\mathbf{v}d\Omega \\
- & \sum_{F\in\mathcal{E}}\int_F a_{31}\Delta t\left\{\left\{\rho^n\mathbf{u}^n\otimes\mathbf{u}^n\right\}\right\}:\langle\langle\mathbf{v}\rangle\rangle\,d\Sigma \\
- & \sum_{F\in\mathcal{E}}\int_F \tilde{a}_{31}\frac{\Delta t}{M^2}\left\{\left\{p^n\right\}\right\}[[\mathbf{v}]]\,d\Sigma \\
- & \sum_{F\in\mathcal{E}}\int_F a_{32}\Delta t\left\{\left\{\rho^{(n,2)}\mathbf{u}^{(n,2)}\otimes\mathbf{u}^{(n,2)}\right\}\right\}:\langle\langle\mathbf{v}\rangle\rangle\,d\Sigma \\
- & \sum_{F\in\mathcal{E}}\int_F \tilde{a}_{32}\frac{\Delta t}{M^2}\left\{\left\{p^{(n,2)}\right\}\right\}[[\mathbf{v}]]\,d\Sigma \\
- & \sum_{F\in\mathcal{E}}\int_F a_{31}\Delta t\frac{\lambda^{(n,1)}}{2}\langle\langle\rho^n\mathbf{u}^n\rangle\rangle:\langle\langle\mathbf{v}\rangle\rangle\,d\Sigma \\
- & \sum_{F\in\mathcal{E}}\int_F a_{32}\Delta t\frac{\lambda^{(n,2)}}{2}\left\langle\left\langle\rho^{(n,2)}\mathbf{u}^{(n,2)}\right\rangle\right\rangle:\langle\langle\mathbf{v}\rangle\rangle\,d\Sigma, \qquad (3.113)
\end{aligned}
$$

where

$$\lambda^{(n,2)} = \max\left(\left|\mathbf{u}^{(n,2)^+}\cdot\mathbf{n}^+\right|, \left|\mathbf{u}^{(n,2)^-}\cdot\mathbf{n}^-\right|\right) \qquad (3.114)$$

is employed for the upwind flux. Now, taking $\mathbf{v} = \boldsymbol{\varphi}_i$ and exploiting the representation of $\mathbf{u}^{(n,3)}$ and $p^{(n,3)}$, we obtain the following relation:

$$
\begin{aligned}
& \sum_{K\in\mathcal{T}_h}\int_K \rho^{(n,3)} \sum_{j=1}^{\dim(\mathbf{Q}_r)} u_j^{(n,3)} \boldsymbol{\varphi}_j \cdot \boldsymbol{\varphi}_i d\Omega - \sum_{K\in\mathcal{T}_h}\int_K \tilde{a}_{33}\frac{\Delta t}{M^2} \sum_{j=1}^{\dim(Q_r)} p_j^{(n,3)} \psi_j \nabla\cdot\boldsymbol{\varphi}_i d\Omega \\
+ \quad & \sum_{F\in\mathcal{E}}\int_F \tilde{a}_{33}\frac{\Delta t}{M^2} \sum_{j=1}^{\dim(Q_r)} p_j^{(n,3)} \{\{\psi_j\}\} [[\boldsymbol{\varphi}_i]] d\Sigma \\
= \quad & \sum_{K\in\mathcal{T}_h}\int_K \rho^n \mathbf{u}^n \cdot \boldsymbol{\varphi}_i d\Omega - \sum_{K\in\mathcal{T}_h}\int_K a_{31}\frac{\Delta t}{Fr^2}\rho^n \mathbf{k}\cdot\boldsymbol{\varphi}_i d\Omega - \sum_{K\in\mathcal{T}_h}\int_K a_{32}\frac{\Delta t}{Fr^2}\rho^{(n,2)}\mathbf{k}\cdot\boldsymbol{\varphi}_i d\Omega \\
+ \quad & \sum_{K\in\mathcal{T}_h}\int_K a_{31}\Delta t \left(\rho^n \mathbf{u}^n \otimes \mathbf{u}^n\right) : \nabla\boldsymbol{\varphi}_i d\Omega + \sum_{K\in\mathcal{T}_h}\int_K \tilde{a}_{31}\frac{\Delta t}{M^2} p^n \nabla\cdot\boldsymbol{\varphi}_i d\Omega \\
+ \quad & \sum_{K\in\mathcal{T}_h}\int_K a_{32}\Delta t \left(\rho^{(n,2)}\mathbf{u}^{(n,2)} \otimes \mathbf{u}^{(n,2)}\right) : \nabla\boldsymbol{\varphi}_i d\Omega + \sum_{K\in\mathcal{T}_h}\int_K \tilde{a}_{32}\frac{\Delta t}{M^2} p^{(n,2)} \nabla\cdot\boldsymbol{\varphi}_i d\Omega \\
- \quad & \sum_{F\in\mathcal{E}}\int_F a_{31}\Delta t \{\{\rho^n \mathbf{u}^n \otimes \mathbf{u}^n\}\} : \langle\langle\boldsymbol{\varphi}_i\rangle\rangle d\Sigma \\
- \quad & \sum_{F\in\mathcal{E}}\int_F \tilde{a}_{31}\frac{\Delta t}{M^2} \{\{p^n\}\} [[\boldsymbol{\varphi}_i]] d\Sigma \\
- \quad & \sum_{F\in\mathcal{E}}\int_F a_{32}\Delta t \left\{\left\{\rho^{(n,2)}\mathbf{u}^{(n,2)} \otimes \mathbf{u}^{(n,2)}\right\}\right\} : \langle\langle\boldsymbol{\varphi}_i\rangle\rangle d\Sigma \\
- \quad & \sum_{F\in\mathcal{E}}\int_F \tilde{a}_{32}\frac{\Delta t}{M^2} \left\{\left\{p^{(n,2)}\right\}\right\} [[\boldsymbol{\varphi}_i]] d\Sigma \\
- \quad & \sum_{F\in\mathcal{E}}\int_F a_{31}\Delta t \frac{\lambda^{(n,1)}}{2} \langle\langle\rho^n \mathbf{u}^n\rangle\rangle : \langle\langle\boldsymbol{\varphi}_i\rangle\rangle d\Sigma \\
- \quad & \sum_{F\in\mathcal{E}}\int_F a_{32}\Delta t \frac{\lambda^{(n,2)}}{2} \left\langle\left\langle\rho^{(n,2)}\mathbf{u}^{(n,2)}\right\rangle\right\rangle : \langle\langle\boldsymbol{\varphi}_i\rangle\rangle d\Sigma, \qquad (3.115)
\end{aligned}
$$

which can be written in compact form as

$$
\mathbf{A}^{(n,3)}\mathbf{U}^{(n,3)} + \mathbf{B}^{(n,3)}\mathbf{P}^{(n,3)} = \mathbf{F}^{(n,3)}, \qquad (3.116)
$$

where we have set

$$
\begin{aligned}
A_{ij}^{(n,3)} &= \sum_{K\in\mathcal{T}_h}\int_K \rho^{(n,3)} \boldsymbol{\varphi}_j \cdot \boldsymbol{\varphi}_i d\Omega & (3.117) \\
B_{ij}^{(n,3)} &= \sum_{K\in\mathcal{T}_h}\int_K -\tilde{a}_{33}\frac{\Delta t}{M^2} \nabla\cdot\boldsymbol{\varphi}_i \psi_j d\Omega & \\
&+ \sum_{F\in\mathcal{E}}\int_F \tilde{a}_{33}\frac{\Delta t}{M^2} \{\{\psi_j\}\} [[\boldsymbol{\varphi}_i]] d\Sigma & (3.118)
\end{aligned}
$$

and $\mathbf{U}^{(n,3)}$ denotes the vector of the degrees of freedom associated to the velocity field, whereas $\mathbf{P}^{(n,3)}$ denotes the vector of the degrees of freedom associated to the pressure. Consider now the weak formulation for the energy equation in (3.78)

$$
\begin{aligned}
& \sum_{K\in\mathcal{T}_h}\int_K \rho^{(n,3)}E^{(n,3)}w d\Omega - \sum_{K\in\mathcal{T}_h}\int_K \tilde{a}_{33}\Delta t h^{(n,3)}\rho^{(n,3)}\mathbf{u}^{(n,3)}\cdot\nabla w d\Omega \\
+ & \sum_{F\in\mathcal{E}}\int_F \tilde{a}_{33}\Delta t \left\{\left\{h^{(n,3)}\rho^{(n,3)}\mathbf{u}^{(n,3)}\right\}\right\}\cdot[[w]]\, d\Sigma \\
= & \sum_{K\in\mathcal{T}_h}\int_K \rho^n E^n w d\Omega \\
- & \sum_{K\in\mathcal{T}_h}\int_K a_{31}\frac{\Delta t M^2}{Fr^2}\rho^n\mathbf{k}\cdot\mathbf{u}^n w d\Omega - \sum_{K\in\mathcal{T}_h}\int_K a_{32}\frac{\Delta t M^2}{Fr^2}\rho^{(n,2)}\mathbf{k}\cdot\mathbf{u}^{(n,2)} w d\Omega \\
+ & \sum_{K\in\mathcal{T}_h}\int_K a_{31}\Delta t M^2\left(k^n\rho^n\mathbf{u}^n\right)\cdot\nabla w d\Omega + \sum_{K\in\mathcal{T}_h}\int_K \tilde{a}_{31}\Delta t\left(h^n\rho^n\mathbf{u}^n\right)\cdot\nabla w d\Omega \\
+ & \sum_{K\in\mathcal{T}_h}\int_K a_{32}\Delta t M^2\left(k^{(n,2)}\rho^{(n,2)}\mathbf{u}^{(n,2)}\right)\cdot\nabla w d\Omega + \sum_{K\in\mathcal{T}_h}\int_K \tilde{a}_{32}\Delta t\left(h^{(n,2)}\rho^{(n,2)}\mathbf{u}^{(n,2)}\right)\cdot\nabla w d\Omega \\
- & \sum_{F\in\mathcal{E}}\int_F a_{31}\Delta t M^2\left\{\left\{k^n\rho^n\mathbf{u}^n\right\}\right\}\cdot[[w]]\, d\Sigma \\
- & \sum_{F\in\mathcal{E}}\int_F \tilde{a}_{31}\Delta t\left\{\left\{h^n\rho^n\mathbf{u}^n\right\}\right\}\cdot[[w]]\, d\Sigma \\
- & \sum_{F\in\mathcal{E}}\int_F a_{32}\Delta t M^2\left\{\left\{k^{(n,2)}\rho^{(n,2)}\mathbf{u}^{(n,2)}\right\}\right\}\cdot[[w]]\, d\Sigma \\
- & \sum_{F\in\mathcal{E}}\int_F \tilde{a}_{32}\Delta t\left\{\left\{h^{(n,2)}\rho^{(n,2)}\mathbf{u}^{(n,2)}\right\}\right\}\cdot[[w]]\, d\Sigma \\
- & \sum_{F\in\mathcal{E}}\int_F a_{31}\Delta t\frac{\lambda^{(n,1)}}{2}\left[\left[\rho^n E^n\right]\right]\cdot[[w]]\, d\Sigma \\
- & \sum_{F\in\mathcal{E}}\int_F a_{31}\Delta t\frac{\lambda^{(n,1)}}{2}\left[\left[\rho^n E^n\right]\right]\cdot[[w]]\, d\Sigma \\
- & \sum_{F\in\mathcal{E}}\int_F a_{32}\Delta t\frac{\lambda^{(n,2)}}{2}\left[\left[\rho^{(n,2)}E^{(n,2)}\right]\right]\cdot[[w]]\, d\Sigma. \qquad (3.119)
\end{aligned}
$$

Take now $w = \psi_i$ and consider the expansion for $\mathbf{u}^{(n,3)}$ so as to obtain

$$\begin{aligned}
&\sum_{K\in\mathcal{T}_h}\int_K \rho^{(n,3)}E^{(n,3)}\psi_i d\Omega - \sum_{K\in\mathcal{T}_h}\int_K \tilde{a}_{33}\Delta t h^{(n,3)}\rho^{(n,3)}\sum_{j=1}^{\dim(\mathbf{Q}_r)} u_j^{(n,3)}\boldsymbol{\varphi}_j\cdot\nabla\psi_i d\Omega \\
+ &\sum_{F\in\mathcal{E}^I}\int_F \tilde{a}_{33}\Delta t\sum_{j=1}^{\dim(\mathbf{Q}_r)} u_j^{(n,3)}\left\{\left\{h^{(n,3)}\rho^{(n,3)}\boldsymbol{\varphi}_j\right\}\right\}\cdot[[\psi_i]]\,d\Sigma \\
= &\sum_{K\in\mathcal{T}_h}\int_K \rho^n E^n\psi_i d\Omega \\
-&\sum_{K\in\mathcal{T}_h}\int_K a_{31}\frac{\Delta t M^2}{Fr^2}\rho^n\mathbf{k}\cdot\mathbf{u}^n\psi_i d\Omega - \sum_{K\in\mathcal{T}_h}\int_K a_{32}\frac{\Delta t M^2}{Fr^2}\rho^{(n,2)}\mathbf{k}\cdot\mathbf{u}^{(n,2)}\psi_i d\Omega \\
+ &\sum_{K\in\mathcal{T}_h}\int_K a_{31}\Delta t M^2\left(k^n\rho^n\mathbf{u}^n\right)\cdot\nabla\psi_i d\Omega + \sum_{K\in\mathcal{T}_h}\int_K \tilde{a}_{31}\Delta t\left(h^n\rho^n\mathbf{u}^n\right)\cdot\nabla\psi_i d\Omega \\
+ &\sum_{K\in\mathcal{T}_h}\int_K a_{32}\Delta t M^2\left(k^{(n,2)}\rho^{(n,2)}\mathbf{u}^{(n,2)}\right)\cdot\nabla\psi_i d\Omega + \sum_{K\in\mathcal{T}_h}\int_K \tilde{a}_{32}\Delta t\left(h^{(n,2)}\rho^{(n,2)}\mathbf{u}^{(n,2)}\right)\cdot\nabla\psi_i d\Omega \\
- &\sum_{F\in\mathcal{E}}\int_F a_{31}\Delta t M^2\left\{\left\{k^n\rho^n\mathbf{u}^n\right\}\right\}\cdot[[\psi_i]]\,d\Sigma \\
- &\sum_{F\in\mathcal{E}}\int_F \tilde{a}_{31}\Delta t\left\{\left\{h^n\rho^n\mathbf{u}^n\right\}\right\}\cdot[[\psi_i]]\,d\Sigma \\
- &\sum_{F\in\mathcal{E}}\int_F a_{32}\Delta t M^2\left\{\left\{k^{(n,2)}\rho^{(n,2)}\mathbf{u}^{(n,2)}\right\}\right\}\cdot[[\psi_i]]\,d\Sigma \\
- &\sum_{F\in\mathcal{E}}\int_F \tilde{a}_{32}\Delta t\left\{\left\{h^{(n,2)}\rho^{(n,2)}\mathbf{u}^{(n,2)}\right\}\right\}\cdot[[\psi_i]]\,d\Sigma \\
- &\sum_{F\in\mathcal{E}}\int_F a_{31}\Delta t\frac{\lambda^{(n,1)}}{2}\,[[\rho^n E^n]]\cdot[[\psi_i]]\,d\Sigma \\
- &\sum_{F\in\mathcal{E}}\int_F a_{32}\Delta t\frac{\lambda^{(n,2)}}{2}\left[\left[\rho^{(n,2)}E^{(n,2)}\right]\right]\cdot[[\psi_i]]\,d\Sigma,
\end{aligned} \tag{3.120}$$

which can be expressed in compact form as

$$\mathbf{C}^{(n,3)}\mathbf{U}^{(n,3)} = \mathbf{G}^{(n,3)}, \tag{3.121}$$

where

$$\begin{aligned}
C_{ij}^{(n,3)} &= \sum_{K\in\mathcal{T}_h}\int_K -\tilde{a}_{33}\Delta t h^{(n,3)}\rho^{(n,3)}\boldsymbol{\varphi}_j\cdot\nabla\psi_i d\Omega \\
&+ \sum_{F\in\mathcal{E}}\int_F \tilde{a}_{33}\Delta t\left\{\left\{h^{(n,3)}\rho^{(n,3)}\boldsymbol{\varphi}_j\right\}\right\}\cdot[[\psi_i]]\,d\Sigma.
\end{aligned} \tag{3.122}$$

Formally, one can derive $\mathbf{U}^{(n,3)} = (\mathbf{A}^{(n,3)})^{-1}\left(\mathbf{F}^{(n,3)} - \mathbf{B}^{(n,3)}\mathbf{P}^{(n,3)}\right)$ and obtain the following relation

$$\mathbf{C}^{(n,3)}(\mathbf{A}^{(n,3)})^{-1}\left(\mathbf{F}^{(n,3)} - \mathbf{B}^{(n,3)}\mathbf{P}^{(n,3)}\right) = \mathbf{G}^{(n,3)}. \tag{3.123}$$

Taking into account that $\rho^{(n,3)}E^{(n,3)} = \rho^{(n,3)}e^{(n,3)} + M^2\rho^{(n,3)}k^{(n,3)}$, we obtain

$$\mathbf{C}^{(n,3)}(\mathbf{A}^{(n,3)})^{-1}\left(\mathbf{F}^{(n,3)} - \mathbf{B}^{(n,3)}\mathbf{P}^{(n,3)}\right) = -\mathbf{D}^{(n,3)}\mathbf{P}^{(n,3)} + \tilde{\mathbf{G}}^{(n,3)}, \tag{3.124}$$

where

$$D_{ij}^{(n,3)} = \sum_{K\in\mathcal{T}_h}\int_K \rho^{(n,3)}e^{(n,3)}(\psi_j)\psi_i d\Omega = \int_K \frac{1}{\gamma-1}\Psi_j\Psi_i d\Omega \tag{3.125}$$

and $\tilde{\mathbf{G}}^{(n,3)}$ takes into account all the other terms (the one at previous stage and the kinetic energy). We recall once more that the reported discrete formulation depends on the EOS. As a matter of example, we obtain the following expression of the matrix $\mathbf{D}$ for the general cubic equation of state

$$D_{ij}^{(n,3)} = \sum_{K\in\mathcal{T}_h}\int_K \left(1 - \rho^{(n,3)}\tilde{b}\right)\frac{\tilde{c}_v\left(T\left(\xi, \rho^{(n,3)}\right)\right)}{\tilde{R}_g}\psi_j\psi_i d\Omega. \tag{3.126}$$

Again, the system (3.124) is solved by a fixed point procedure. More specifically, setting $\mathbf{P}^{(n,3,0)} = \mathbf{P}^{(n,2)}, k^{(n,3,0)} = k^{(n,2)}$ for $l = 1, \ldots, L$ one solves the equation

$$\begin{aligned}\left(\mathbf{D}^{(n,3,l-1)} - \mathbf{C}^{(n,3,l-1)}(\mathbf{A}^{(n,3)})^{-1}\mathbf{B}^{(n,3)}\right)\mathbf{P}^{(n,3,l)} &= \tilde{\mathbf{G}}^{(n,3,l-1)} \\ &- \mathbf{C}^{(n,3,l-1)}(\mathbf{A}^{(n,3)})^{-1}\mathbf{F}^{(n,2,l-1)}\end{aligned} \tag{3.127}$$

and then updates the velocity solving

$$\mathbf{A}^{(n,3)}\mathbf{U}^{(n,3,l)} = \mathbf{F}^{(n,3,l-1)} - \mathbf{B}^{(n,3)}\mathbf{P}^{(n,3,l)}. \tag{3.128}$$

Once the iterations have been completed, one sets $\mathbf{u}^{(n,3)} = \mathbf{u}^{(n,3,L)}$ and $E^{(n,3)}$ accordingly. After the weights step, one proceeds to the implicit discretization of the viscous terms, which, as already mentioned, is carried out by the implicit part of the IMEX method described above and is analogous to the discretization presented in Section 3.3. For the sake of completeness, we report here the weak formulation for the bilinear form of the momentum balance reported in (3.88):

$$\begin{aligned} B\left(\tilde{\mathbf{u}}, \mathbf{v}\right) &= \sum_{K\in\mathcal{T}_h}\int_K \rho^{n+1}\tilde{\mathbf{u}}\cdot\mathbf{v}d\Omega \\ &+ \tilde{a}_{22}\frac{\Delta t}{Re}\sum_{K\in\mathcal{T}_h}\int_K \left[\nabla\tilde{\mathbf{u}} + \nabla\tilde{\mathbf{u}}^T - \frac{2}{3}\left(\nabla\cdot\tilde{\mathbf{u}}\right)\mathbf{I}\right] : \nabla\mathbf{v}d\Omega \\ &- \tilde{a}_{22}\frac{\Delta t}{Re}\sum_{F\in\mathcal{E}}\int_F \left\{\left\{\nabla\tilde{\mathbf{u}} + \nabla\tilde{\mathbf{u}}^T - \frac{2}{3}\left(\nabla\cdot\tilde{\mathbf{u}}\right)\mathbf{I}\right\}\right\} : \langle\langle\mathbf{v}\rangle\rangle\, d\Sigma \\ &- \tilde{a}_{22}\frac{\Delta t}{Re}\sum_{F\in\mathcal{E}}\int_F \langle\langle\tilde{\mathbf{u}}\rangle\rangle : \left\{\left\{\nabla\mathbf{v} + \nabla\mathbf{v}^T - \frac{2}{3}\left(\nabla\cdot\mathbf{v}\right)\mathbf{I}\right\}\right\} d\Sigma \\ &+ \tilde{a}_{22}\frac{\Delta t}{Re}\sum_{F\in\mathcal{E}}\int_F \overline{C}\,\langle\langle\tilde{\mathbf{u}}\rangle\rangle : \langle\langle\mathbf{v}\rangle\rangle\, d\Sigma. \end{aligned} \tag{3.129}$$

The remaining formulations are obtained in an analogous manner. We would like to stress that the method outlined above does not require to introduce reference solutions, does not introduce inconsistencies in the splitting and only requires the solution of linear systems of a size equal to that of the number of discrete degrees of freedom needed to describe a scalar variable, as in [Dumbser and Casulli, 2016]. This contrasts with other low Mach approaches based on IMEX methods, such as e.g. the technique proposed for the Euler equations in [Zeifang et al., 2019]. The proposed approach has been validated in a number of benchmarks reported in Section 4.3 and Section 4.4.

3.5 Two-phase system

In recent years, weakly compressible two-phase flows have been finding their way in the literature with both phases governed by compressible equations and a number of numerical studies have been devoted to this configuration, see [Kuhn and Desjardins, 2021, Demou et al., 2022, Re and Abgrall, 2022]. The system (2.149) can be expressed in the following vector form

$$\frac{\partial \mathbf{Q}}{\partial t} + \nabla\cdot \mathbf{F}\left(\mathbf{Q}\right) + \mathbf{G}\left(\mathbf{Q}\right)\nabla\alpha_1 = \mathbf{S}\left(\mathbf{Q}\right), \tag{3.130}$$

with

$$\mathbf{Q} = \begin{bmatrix} \alpha_1 \\ \alpha_1\rho_1 \\ \alpha_1\rho_1\mathbf{u}_1 \\ \alpha_1\rho_1 E_1 \\ \alpha_2\rho_2 \\ \alpha_2\rho_2\mathbf{u}_2 \\ \alpha_2\rho_1 E_2 \end{bmatrix} \quad \mathbf{F}\left(\mathbf{Q}\right) = \begin{bmatrix} \mathbf{0}^T \\ \alpha_1\rho_1\mathbf{u}_1^T \\ \alpha_1\rho_1\mathbf{u}_1\otimes\mathbf{u}_1 + \frac{1}{M_1^2}\alpha_1 p_1\mathbf{I} \\ \alpha_1\rho_1\mathbf{u}_1^T\left(h_1 + M_1^2 k_1\right) \\ \alpha_2\rho_2\mathbf{u}_2^T \\ \alpha_2\rho_2\mathbf{u}_2\otimes\mathbf{u}_2 + \frac{1}{M_2^2}\alpha_2 p_2\mathbf{I} \\ \alpha_2\rho_2\mathbf{u}_2^T\left(h_2 + M_2^2 k_2\right) \end{bmatrix} \quad \mathbf{G}\left(\mathbf{Q}\right) = \begin{bmatrix} \mathbf{v}_I^T \\ \mathbf{0} \\ -\frac{1}{M_1^2}p_I\mathbf{I} \\ -p_I\mathbf{v}_I^T \\ \mathbf{0} \\ \frac{1}{M_1^2}\frac{1}{\rho_{rel}}p_I\mathbf{I} \\ \frac{M_2^2}{M_1^2}\frac{1}{\rho_{rel}}p_I\mathbf{v}_I^T \end{bmatrix}$$

and

$$\mathbf{S}\left(\mathbf{Q}\right) = \begin{bmatrix} \tilde{\mu}\left(p_1 - p_2\rho_{rel}\frac{M_1^2}{M_2^2}\right) \\ 0 \\ -\tilde{\lambda}\left(\mathbf{u}_1 - \mathbf{u}_2\right) \\ -\tilde{\mu}p_I\left(p_1 - p_2\rho_{rel}\frac{M_1^2}{M_2^2}\right) - \tilde{\lambda}M_1^2\mathbf{v}_I\cdot\left(\mathbf{u}_1 - \mathbf{u}_2\right) \\ 0 \\ \frac{\tilde{\lambda}}{\rho_{rel}}\left(\mathbf{u}_1 - \mathbf{u}_2\right) \\ \frac{\tilde{\mu}}{\rho_{rel}}\frac{M_2^2}{M_1^2}p_I\left(p_1 - p_2\rho_{rel}\frac{M_1^2}{M_2^2}\right) + \frac{\tilde{\lambda}}{\rho_{rel}}M_2^2\mathbf{v}_I\cdot\left(\mathbf{u}_1 - \mathbf{u}_2\right) \end{bmatrix}.$$

The main difference between the system (2.149) and (3.67) consists of the presence of the non-conservative terms $\mathbf{G}\left(\mathbf{Q}\right)\nabla\alpha_1$ which define the coupling between the two phases. In this Section, we provide an original extension of the IMEX scheme introduced above for system (2.149). Notice that we are considering only the hyperbolic operator for the sake of simplicity, and we give suitable strategies for the discretization of the advection equation of the volume fraction and for the numerical treatment of the non-conservatives terms. These approaches stem from an analysis to preserve uniform fields in the framework of the proposed numerical scheme.

3.5.1 Discretization of the hyperbolic operator and preservation of uniform fields

For each time step, we consider the discretization of the hyperbolic terms of system (2.149). We need to specify how to deal with the non-conservative terms and the time discretization of the advection equation for the volume fraction α_1. We will focus on the treatment of non-conservative terms in the forthcoming Section 3.5.2, whereas we discuss now the time discretization of the equation for the volume fraction. One would be tempted to consider an explicit treatment of the advection equation for α_1 in analogy to the discretization of the continuity equation in Section 3.4 so as to obtain for the second stage

$$\alpha_1^{(n,2)} = \alpha_1^n - a_{21}\Delta t \mathbf{v}_I^n \cdot \nabla \alpha_1^n. \tag{3.131}$$

However, as we will show in a while, this approach does not comply with the non-disturbance condition for velocity and pressure [Abgrall, 1996, Re and Abgrall, 2022], which prescribes that the numerical method should not induce variations in velocity and pressure in the case of spatially uniform initial data. The non-disturbance condition represents indeed an elementary form of consistency and well-balancing. Analogous analyses have been performed for other physical problems, such as free-surface models, see e.g. [Gross et al., 2002], or shallow water equations, see e.g. [Chalons and Del Grosso, 2022].

We recall here for the sake of convenience in the analysis the employed semi-discretization for the continuity equation of phase 1, which is completely analogous to those presented in (3.74) and reads as follows:

$$\alpha_1^{(n,2)}\rho_1^{(n,2)} = \alpha_1^n\rho_1^n - a_{21}\Delta t \, \nabla\cdot\left(\alpha_1^n\rho_1^n\mathbf{u}_1^n\right). \tag{3.132}$$

Since, in case of spatially uniform velocity and pressure, $p_1 = p_2 = p_I$ and $\mathbf{u}_1 = \mathbf{u}_2 = \mathbf{v}_I$, the terms $\frac{1}{M_1^2}\nabla\cdot\left(\alpha_1 p_1 \mathbf{I}\right) - \frac{1}{M_1^2} p_I \mathbf{I}\nabla\alpha_1$ and $\nabla\cdot\left(\alpha_1 p_1 \mathbf{u}_1\right) - p_I \mathbf{v}_I \cdot \nabla\alpha_1$ in the momentum and energy balance in (2.149), respectively, have to be identically equal to zero. First of all, as a result of these considerations, the semi-discretization of the momentum balance reduces to

$$\alpha_1^{(n,2)}\rho_1^{(n,2)}\mathbf{u}_1^{(n,2)} = \alpha_1^n\rho_1^n\mathbf{u}_1^n - a_{21}\Delta t \, \nabla\cdot\left(\alpha_1^n\rho_1^n\mathbf{u}_1^n \otimes \mathbf{u}_1^n\right). \tag{3.133}$$

Thanks to (3.132), it follows that $\mathbf{u}_1^{(n,2)} = \mathbf{u}_1^n$ independently on the time advancing of $\alpha_1^{(n,2)}$. We then consider the semi-discretization of the energy balance for phase 1. Recalling that $h_1 = e_1 + p_1/\rho_1$ and using the fact that $\nabla\cdot\left(\alpha_1 p_1 \mathbf{u}_1\right) - p_I \mathbf{v}_I \cdot \nabla\alpha_1 = 0$, the semi-discretization of the energy balance for phase 1 reduces to

$$\begin{aligned}
&\alpha_1^{(n,2)}\rho_1^{(n,2)}E_1^{(n,2)} + \tilde{a}_{22}\Delta t \, \nabla\cdot\left(\alpha_1^{(n,2)}\rho_1^{(n,2)}e_1^{(n,2)}\mathbf{u}_1^{(n,2)}\right) = \\
&\alpha_1^n\rho_1^n E_1^n - \tilde{a}_{21}\Delta t \, \nabla\cdot\left(\alpha_1^n\rho_1^n e_1^n\mathbf{u}_1^n\right) - a_{21}\Delta t M_1^2 \, \nabla\cdot\left(\alpha_1^n k_1^n \rho_1^n\mathbf{u}_1^n\right).
\end{aligned} \tag{3.134}$$

Recalling then that $\rho_1 E_1 = \rho_1 e_1 + M_1^2 \rho_1 k_1$, we obtain

$$\begin{aligned}
&\alpha_1^{(n,2)}\rho_1^{(n,2)}e_1^{(n,2)} + M_1^2\alpha_1^{(n,2)}\rho_1^{(n,2)}k_1^{(n,2)} + \tilde{a}_{22}\Delta t \, \nabla\cdot\left(\alpha_1^{(n,2)}\rho_1^{(n,2)}e_1^{(n,2)}\mathbf{u}_1^{(n,2)}\right) = \\
&\alpha_1^n\rho_1^n e_1^n + M_1^2\alpha_1^n\rho_1^n k_1^n - \tilde{a}_{21}\Delta t \, \nabla\cdot\left(\alpha_1^n\rho_1^n e_1^n\mathbf{u}_1^n\right) - a_{21}\Delta t M_1^2 \, \nabla\cdot\left(\alpha_1^n k_1^n \rho_1^n\mathbf{u}_1^n\right).
\end{aligned} \tag{3.135}$$

Thanks to the continuity equation (3.132) and to the assumption that the velocity field is uniform in space, we obtain

$$\begin{aligned}&\alpha_1^{(n,2)}\rho_1^{(n,2)}e_1^{(n,2)}+\tilde{a}_{22}\Delta t\,\nabla\cdot\left(\alpha_1^{(n,2)}\rho_1^{(n,2)}e_1^{(n,2)}\mathbf{u}_1^{(n,2)}\right)=\\&\alpha_1^n\rho_1^n e_1^n-\tilde{a}_{21}\Delta t\,\nabla\cdot\left(\alpha_1^n\rho_1^n e_1^n\mathbf{u}_1^n\right).\end{aligned}\tag{3.136}$$

Considering then for the sake of simplicity the equation of state of an ideal gas (2.210), we obtain from (3.136)

$$\begin{aligned}&\frac{1}{\gamma_1-1}\alpha_1^{(n,2)}p_1^{(n,2)}+\frac{\tilde{a}_{22}\Delta t}{\gamma_1-1}\,\nabla\cdot\left(\alpha_1^{(n,2)}p_1^{(n,2)}\mathbf{u}_1^{(n,2)}\right)=\\&\frac{1}{\gamma_1-1}\alpha_1^n p_1^n-\frac{\tilde{a}_{21}\Delta t}{\gamma_1-1}\,\nabla\cdot\left(\alpha_1^n p_1^n\mathbf{u}_1^n\right).\end{aligned}\tag{3.137}$$

Since we are considering a spatial uniform pressure, the terms related to the pressure can be simplified so as to obtain the following discretization for the volume fraction:

$$\alpha_1^{(n,2)}=\alpha_1^n-\tilde{a}_{22}\Delta t\mathbf{v}_I^n\cdot\nabla\alpha_1^{(n,2)}-\tilde{a}_{21}\Delta t\mathbf{v}_I^n\cdot\nabla\alpha_1^n,\tag{3.138}$$

where we exploit once more the uniformity of the velocity in order to recover the interfacial velocity. The semi-discretization (3.138) is therefore the only formulation that complies with the non-disturbance condition in contrast to (3.131) and results in a semi-implicit treatment of the volume fraction with linearization on the velocity. Finally, since we have $1/M_k^2, k=1,2$ in front of the pressure interface p_I in (2.149), we treat the non-conservative terms implicitly. Hence, for the second stage, one can write formally

$$\begin{array}{rcl}\alpha_1^{(n,2)}&=&\alpha_1^n-\tilde{a}_{22}\Delta t\mathbf{v}_I^n\cdot\nabla\alpha_1^{(n,2)}-\tilde{a}_{21}\Delta t\mathbf{v}_I^n\cdot\nabla\alpha_1^n\\ \alpha_1^{(n,2)}\rho_1^{(n,2)}&=&\alpha_1^n\rho_1^n-a_{21}\Delta t\,\nabla\cdot\left(\alpha_1^n\rho_1^n\mathbf{u}_1^n\right)\\ \alpha_1^{(n,2)}\rho_1^{(n,2)}\mathbf{u}_1^{(n,2)}&+&\tilde{a}_{22}\dfrac{\Delta t}{M_1^2}\nabla\left(\alpha_1^{(n,2)}p_1^{(n,2)}\right)-\tilde{a}_{22}\dfrac{\Delta t}{M_1^2}p_I^{(n,2)}\nabla\alpha_1^{(n,2)}=\mathbf{m}_1^{(n,2)}\\ \alpha_1^{(n,2)}\rho_1^{(n,2)}E_1^{(n,2)}&+&\tilde{a}_{22}\Delta t\,\nabla\cdot\left(\alpha_1^{(n,2)}h_1^{(n,2)}\rho_1^{(n,2)}\mathbf{u}_1^{(n,2)}\right)\\ &-&\tilde{a}_{22}\Delta tp_I^{(n,2)}\mathbf{v}_I^{(n,2)}\cdot\nabla\alpha_1^{(n,2)}=\hat{e}_1^{(n,2)}\\ \alpha_2^{(n,2)}&=&1-\alpha_1^{(n,2)}\\ \alpha_2^{(n,2)}\rho_2^{(n,2)}&=&\alpha_2^n\rho_2^n-a_{21}\Delta t\,\nabla\cdot\left(\alpha_2^n\rho_2^n\mathbf{u}_2^n\right)\\ \alpha_2^{(n,2)}\rho_2^{(n,2)}\mathbf{u}_2^{(n,2)}&+&\tilde{a}_{22}\dfrac{\Delta t}{M_2^2}\nabla\left(\alpha_2^{(n,2)}p_2^{(n,2)}\right)+\tilde{a}_{22}\dfrac{\Delta t}{M_2^2}\dfrac{1}{\rho_{rel}}p_I^{(n,2)}\nabla\alpha_1^{(n,2)}=\mathbf{m}_2^{(n,2)}\\ \alpha_2^{(n,2)}\rho_2^{(n,2)}E_2^{(n,2)}&+&\tilde{a}_{22}\Delta t\,\nabla\cdot\left(\alpha_2^{(n,2)}h_2^{(n,2)}\rho_2^{(n,2)}\mathbf{u}_2^{(n,2)}\right)\\ &+&\tilde{a}_{22}\Delta t\dfrac{M_2^2}{M_1^2}\dfrac{1}{\rho_{rel}}p_I^{(n,2)}\mathbf{v}_I^{(n,2)}\cdot\nabla\alpha_1^{(n,2)}=\hat{e}_2^{(n,2)},\end{array}\tag{3.139}$$

where we have set

$$\begin{array}{rcl}
\mathbf{m}_1^{(n,2)} & = & \alpha_1^n\rho_1^n\mathbf{u}_1^n \\
& - & a_{21}\Delta t\,\nabla\cdot\left(\alpha_1^n\rho_1^n\mathbf{u}_1^n\otimes\mathbf{u}_1^n\right) - \tilde{a}_{21}\dfrac{\Delta t}{M_1^2}\nabla\left(\alpha_1^n p_1^n\right) + \tilde{a}_{21}\dfrac{\Delta t}{M_1^2}p_I^n\nabla\alpha_1^n \\
\hat{e}_1^{(n,2)} & = & \alpha_1^n\rho_1^n E_1^n \\
& - & \tilde{a}_{21}\Delta t\,\nabla\cdot\left(\alpha_1^n h_1^n\rho_1^n\mathbf{u}_1^n\right) - a_{21}\Delta t M_1^2\,\nabla\cdot\left(\alpha_1^n k_1^n\rho_1^n\mathbf{u}_1^n\right) \\
& + & \tilde{a}_{21}\Delta t p_I^n\mathbf{v}_I^n\cdot\nabla\alpha_1^n
\end{array} \qquad (3.140)$$

$$\begin{array}{rcl}
\mathbf{m}_2^{(n,2)} & = & \alpha_2^n\rho_2^n\mathbf{u}_2^n \\
& - & a_{21}\Delta t\,\nabla\cdot\left(\alpha_2^n\rho_2^n\mathbf{u}_2^n\otimes\mathbf{u}_2^n\right) - \tilde{a}_{21}\dfrac{\Delta t}{M_2^2}\nabla\left(\alpha_2^n p_2^n\right) - \tilde{a}_{21}\dfrac{\Delta t}{M_2^2}\dfrac{1}{\rho_{rel}}p_I^n\nabla\alpha_1^n \\
\hat{e}_2^{(n,2)} & = & \alpha_2^n\rho_2^n E_2^n \\
& - & \tilde{a}_{21}\Delta t\,\nabla\cdot\left(\alpha_2^n h_2^n\rho_2^n\mathbf{u}_2^n\right) - a_{21}\Delta t M_2^2\,\nabla\cdot\left(\alpha_2^n k_2^n\rho_2^n\mathbf{u}_2^n\right) \\
& - & \tilde{a}_{21}\Delta t\dfrac{M_2^2}{M_1^2}\dfrac{1}{\rho_{rel}}p_I^n\mathbf{v}_I^n\cdot\nabla\alpha_1^n.
\end{array} \qquad (3.141)$$

In analogy to what we presented in Section 3.4, we formally substitute $\alpha_1^{(n,2)}\rho_1^{(n,2)}\mathbf{u}_1^{(n,2)}$ and $\alpha_2^{(n,2)}\rho_2^{(n,2)}\mathbf{u}_2^{(n,2)}$ into the corresponding energy balance so as to obtain the two non-linear relations for the pressures $p_1^{(n,2)}$ and $p_2^{(n,2)}$. More specifically, we obtain

$$\begin{aligned}
& \alpha_1^{(n,2)}\rho_1^{(n,2)}\left[e_1(p_1^{(n,2)},\rho_1^{(n,2)}) + M_1^2 k_1^{(n,2)}\right] \\
-\; & \tilde{a}_{22}^2\frac{\Delta t^2}{M_1^2}\nabla\cdot\left[\left(e_1(p_1^{(n,2)},\rho_1^{(n,2)}) + \frac{p_1^{(n,2)}}{\rho_1^{(n,2)}}\right)\nabla\left(\alpha_1^{(n,2)}p_1^{(n,2)}\right)\right] \\
+\; & \tilde{a}_{22}^2\frac{\Delta t^2}{M_1^2}\nabla\cdot\left[\left(e_1(p_1^{(n,2)},\rho_1^{(n,2)}) + \frac{p_1^{(n,2)}}{\rho_1^{(n,2)}}\right)p_I^{(n,2)}\nabla\alpha_1^{(n,2)}\right] \\
+\; & \tilde{a}_{22}\Delta t\,\nabla\cdot\left[\left(e_1(p_1^{(n,2)},\rho_1^{(n,2)}) + \frac{p_1^{(n,2)}}{\rho_1^{(n,2)}}\right)\mathbf{m}_1^{(n,2)}\right] = \hat{e}_1^{(n,2)}
\end{aligned} \qquad (3.142)$$

in terms of $p_1^{(n,2)}$ and

$$\begin{aligned}
& \alpha_2^{(n,2)}\rho_2^{(n,2)}\left[e_2(p_2^{(n,2)},\rho_2^{(n,2)}) + M_2^2 k_2^{(n,2)}\right] \\
-\; & \tilde{a}_{22}^2\frac{\Delta t^2}{M_2^2}\nabla\cdot\left[\left(e_2(p_2^{(n,2)},\rho_2^{(n,2)}) + \frac{p_2^{(n,2)}}{\rho_2^{(n,2)}}\right)\nabla\left(\alpha_2^{(n,2)}p_2^{(n,2)}\right)\right] \\
-\; & \tilde{a}_{22}^2\frac{\Delta t^2}{M_2^2}\nabla\cdot\left[\left(e_2(p_2^{(n,2)},\rho_2^{(n,2)}) - \frac{p_2^{(n,2)}}{\rho_2^{(n,2)}}\right)p_I^{(n,2)}\nabla\alpha_1^{(n,2)}\right] \\
+\; & \tilde{a}_{22}\Delta t\,\nabla\cdot\left[\left(e_2(p_2^{(n,2)},\rho_2^{(n,2)}) + \frac{p_2^{(n,2)}}{\rho_2^{(n,2)}}\right)\mathbf{m}_2^{(n,2)}\right] = \hat{e}_2^{(n,2)}
\end{aligned} \qquad (3.143)$$

in terms of $p_2^{(n,2)}$. The non-linear equations (3.142) and (3.143) are then solved according to the fixed point procedure introduced in Section 3.4. More in detail, setting $\xi_1^{(0)} = p_1^{(n,1)}, k_1^{(n,2,0)} = k_1^{(n,1)}$, one solves for $l = 1, \ldots, L$ the equation

$$\begin{aligned}
&\alpha_1^{(n,2)} \rho_1^{(n,2)} \left[e_1(\xi_1^{(n,2,l)}, \rho_1^{(n,2)}) + M_1^2 k_1^{(n,2)} \right] \\
&- \tilde{a}_{22}^2 \frac{\Delta t^2}{M_1^2} \nabla \cdot \left[\left(e_1(\xi_1^{(n,2,l-1)}, \rho_1^{(n,2)}) + \frac{\xi_1^{(n,2,l-1)}}{\rho_1^{(n,2)}} \right) \nabla \left(\alpha_1^{(n,2)} \xi_1^{(n,2,l)} \right) \right] \\
&+ \tilde{a}_{22}^2 \frac{\Delta t^2}{M_1^2} \nabla \cdot \left[\left(e_1(\xi_1^{(n,2,l-1)}, \rho_1^{(n,2)}) + \frac{\xi_1^{(n,2,l-1)}}{\rho_1^{(n,2)}} \right) p_I^{(n,2,l-1)} \nabla \alpha_1^{(n,2)} \right] \\
&+ \tilde{a}_{22} \Delta t \, \nabla \cdot \left[\left(e_1(\xi_1^{(n,2,l-1)}, \rho_1^{(n,2)}) + \frac{\xi_1^{(n,2,l-1)}}{\rho_1^{(n,2)}} \right) \mathbf{m}_1^{(n,2)} \right] = \hat{e}_1^{(n,2)}
\end{aligned} \tag{3.144}$$

and updates the velocity as

$$\alpha_1^{(n,2)} \rho_1^{(n,2)} \mathbf{u}_1^{(n,2,l)} + \tilde{a}_{22} \frac{\Delta t}{M_1^2} \nabla \left(\alpha_1^{(n,2)} \xi^{(l)} \right) - \tilde{a}_{22} \frac{\Delta t}{M_1^2} p_I^{(n,2,l-1)} \nabla \alpha_1^{(n,2)} = \mathbf{m}_1^{(n,2)}. \tag{3.145}$$

On the other hand, setting $\xi_2^{(0)} = p_2^{(n,1)}, k_2^{(n,2,0)} = k_2^{(n,1)}$, one solves for $l = 1, \ldots, L$ the equation

$$\begin{aligned}
&\alpha_2^{(n,2)} \rho_2^{(n,2)} \left[e_2(\xi_2^{(n,2,l-1)}, \rho_2^{(n,2)}) + M_2^2 k_2^{(n,2)} \right] \\
&- \tilde{a}_{22}^2 \frac{\Delta t^2}{M_2^2} \nabla \cdot \left[\left(e_2(\xi_2^{(n,2,l-1)}, \rho_2^{(n,2)}) + \frac{\xi_2^{(n,2,l-1)}}{\rho_2^{(n,2)}} \right) \nabla \left(\alpha_2^{(n,2)} \xi_2^{(n,2,l)} \right) \right] \\
&- \tilde{a}_{22}^2 \frac{\Delta t^2}{M_2^2} \nabla \cdot \left[\left(e_2(\xi_2^{(n,2,l-1)}, \rho_2^{(n,2)}) - \frac{\xi_2^{(n,2,l-1)}}{\rho_2^{(n,2)}} \right) p_I^{(n,2,l-1)} \nabla \alpha_1^{(n,2)} \right] \\
&+ \tilde{a}_{22} \Delta t \, \nabla \cdot \left[\left(e_2(\xi_2^{(n,2,l-1)}, \rho_2^{(n,2)}) + \frac{\xi_2^{(n,2,l-1)}}{\rho_2^{(n,2)}} \right) \mathbf{m}_2^{(n,2)} \right] = \hat{e}_2^{(n,2)}
\end{aligned} \tag{3.146}$$

and updates the velocity as

$$\alpha_2^{(n,2)} \rho_2^{(n,2)} \mathbf{u}_2^{(n,2,l)} + \tilde{a}_{22} \frac{\Delta t}{M_2^2} \nabla \left(\alpha_2^{(n,2)} \xi^{(l)} \right) + \tilde{a}_{22} \frac{\Delta t}{M_2^2} p_I^{(n,2,l-1)} \nabla \alpha_1^{(n,2)} = \mathbf{m}_2^{(n,2)}. \tag{3.147}$$

The third stage can be expressed in a similar manner. We report the semi-discretized relations for the sake of completeness:

$$\begin{aligned}
\alpha_1^{(n,3)} &= \alpha_1^n - \tilde{a}_{33}\Delta t\mathbf{v}_I^{(n,2)} \cdot \nabla\alpha_1^{(n,3)} - \tilde{a}_{32}\Delta t\mathbf{v}_I^{(n,2)} \cdot \alpha_1^{(n,2)} - \tilde{a}_{31}\Delta t\mathbf{v}_I^n \cdot \nabla\alpha_1^n \\
\alpha_1^{(n,3)}\rho_1^{(n,3)} &= \alpha_1^n\rho_1^n - a_{32}\Delta t\,\nabla\cdot\left(\alpha_1^{(n,2)}\rho_1^{(n,2)}\mathbf{u}_1^{(n,2)}\right) - a_{31}\Delta t\,\nabla\cdot\left(\alpha_1^n\rho_1^n\mathbf{u}_1^n\right) \\
\alpha_1^{(n,3)}\rho_1^{(n,3)}\mathbf{u}_1^{(n,3)} &+ \tilde{a}_{33}\frac{\Delta t}{M_1^2}\nabla\left(\alpha_1^{(n,3)}p_1^{(n,3)}\right) - \tilde{a}_{33}\frac{\Delta t}{M_1^2}p_I^{(n,3)}\nabla\alpha_1^{(n,3)} = \mathbf{m}_1^{(n,3)} \\
\alpha_1^{(n,3)}\rho_1^{(n,3)}E_1^{(n,3)} &+ \tilde{a}_{33}\Delta t\,\nabla\cdot\left(\alpha_1^{(n,3)}h_1^{(n,3)}\rho_1^{(n,3)}\mathbf{u}_1^{(n,3)}\right) \\
&- \tilde{a}_{33}\Delta t p_I^{(n,3)}\mathbf{v}_I^{(n,3)} \cdot \nabla\alpha_1^{(n,3)} = \hat{e}_1^{(n,3)} \\
\alpha_2^{(n,3)} &= 1 - \alpha_1^{(n,3)} \qquad (3.148) \\
\alpha_2^{(n,3)}\rho_2^{(n,3)} &= \alpha_2^n\rho_2^n - a_{32}\Delta t\,\nabla\cdot\left(\alpha_2^{(n,2)}\rho_2^{(n,2)}\mathbf{u}_2^{(n,2)}\right) - a_{31}\Delta t\,\nabla\cdot\left(\alpha_2^n\rho_2^n\mathbf{u}_2^n\right) \\
\alpha_2^{(n,3)}\rho_2^{(n,3)}\mathbf{u}_2^{(n,3)} &+ \tilde{a}_{33}\frac{\Delta t}{M_2^2}\nabla\left(\alpha_2^{(n,3)}p_2^{(n,3)}\right) + \tilde{a}_{33}\frac{\Delta t}{M_2^2}\frac{1}{\rho_{rel}}p_I^{(n,3)}\nabla\alpha_1^{(n,3)} = \mathbf{m}_2^{(n,3)} \\
\alpha_2^{(n,3)}\rho_2^{(n,3)}E_2^{(n,3)} &+ \tilde{a}_{33}\Delta t\,\nabla\cdot\left(\alpha_2^{(n,3)}h_2^{(n,3)}\rho_2^{(n,3)}\mathbf{u}_2^{(n,3)}\right) \\
&+ \tilde{a}_{33}\Delta t\frac{M_2^2}{M_1^2}\frac{1}{\rho_{rel}}p_I^{(n,3)}\mathbf{v}_I^{(n,3)} \cdot \nabla\alpha_1^{(n,3)} = \hat{e}_2^{(n,3)},
\end{aligned}$$

where we have set

$$\begin{aligned}
\mathbf{m}_1^{(n,3)} &= \alpha_1^n\rho_1^n\mathbf{u}_1^n \\
&- a_{31}\Delta t\,\nabla\cdot\left(\alpha_1^n\rho_1^n\mathbf{u}_1^n\otimes\mathbf{u}_1^n\right) - a_{32}\Delta t\,\nabla\cdot\left(\alpha_1^{(n,2)}\rho_1^{(n,2)}\mathbf{u}_1^{(n,2)}\otimes\mathbf{u}_1^n\right) \\
&- \tilde{a}_{31}\frac{\Delta t}{M_1^2}\nabla\left(\alpha_1^n p_1^n\right) - \tilde{a}_{32}\frac{\Delta t}{M_1^2}\nabla\left(\alpha_1^{(n,2)}p_1^{(n,2)}\right) \\
&+ \tilde{a}_{31}\frac{\Delta t}{M_1^2}p_I^n\nabla\alpha_1^n + \tilde{a}_{32}\frac{\Delta t}{M_1^2}p_I^{(n,2)}\nabla\alpha_1^{(n,2)} \\
\hat{e}_1^{(n,3)} &= \alpha_1^n\rho_1^n E_1^n \\
&- \tilde{a}_{31}\Delta t\,\nabla\cdot\left(\alpha_1^n h_1^n\rho_1^n\mathbf{u}_1^n\right) - \tilde{a}_{32}\Delta t\,\nabla\cdot\left(\alpha_1^{(n,2)}h_1^{(n,2)}\rho_1^{(n,2)}\mathbf{u}_1^{(n,2)}\right) \\
&- a_{31}\Delta t M_1^2\,\nabla\cdot\left(\alpha_1^n k_1^n\rho_1^n\mathbf{u}_1^n\right) - a_{32}\Delta t M_1^2\,\nabla\cdot\left(\alpha_1^{(n,2)}k_1^{(n,2)}\rho_1^{(n,2)}\mathbf{u}_1^{(n,2)}\right) \\
&+ \tilde{a}_{31}\Delta t p_I^n\mathbf{v}_I^n\cdot\nabla\alpha_1^n + \tilde{a}_{32}\Delta t p_I^{(n,2)}\mathbf{v}_I^{(n,2)}\cdot\nabla\alpha_1^{(n,2)}
\end{aligned} \tag{3.149}$$

$$\begin{aligned}
\mathbf{m}_2^{(n,3)} &= \alpha_2^n\rho_2^n\mathbf{u}_2^n \\
&- a_{31}\Delta t\,\nabla\cdot\left(\alpha_2^n\rho_2^n\mathbf{u}_2^n\otimes\mathbf{u}_2^n\right) - a_{32}\Delta t\,\nabla\cdot\left(\alpha_2^{(n,2)}\rho_2^{(n,2)}\mathbf{u}_2^{(n,2)}\otimes\mathbf{u}_2^n\right) \\
&- \tilde{a}_{31}\frac{\Delta t}{M_2^2}\nabla\left(\alpha_2^n p_2^n\right) - \tilde{a}_{32}\frac{\Delta t}{M_2^2}\nabla\left(\alpha_2^{(n,2)}p_2^{(n,2)}\right) \\
&- \tilde{a}_{31}\frac{\Delta t}{M_2^2}\frac{1}{\rho_{rel}}p_I^n\nabla\alpha_1^n - \tilde{a}_{32}\frac{\Delta t}{M_2^2}\frac{1}{\rho_{rel}}p_I^{(n,2)}\nabla\alpha_1^{(n,2)} \\
\hat{e}_2^{(n,3)} &= \alpha_2^n\rho_2^n E_2^n \\
&- \tilde{a}_{31}\Delta t\,\nabla\cdot\left(\alpha_2^n h_2^n\rho_2^n\mathbf{u}_2^n\right)\tilde{a}_{32}\Delta t\,\nabla\cdot\left(\alpha_2^{(n,2)}h_2^{(n,2)}\rho_2^{(n,2)}\mathbf{u}_2^{(n,2)}\right) \\
&- a_{31}\Delta t M_2^2\,\nabla\cdot\left(\alpha_2^n k_2^n\rho_2^n\mathbf{u}_2^n\right) - a_{32}\Delta t M_2^2\,\nabla\cdot\left(\alpha_2^{(n,2)}k_2^{(n,2)}\rho_2^{(n,2)}\mathbf{u}_2^{(n,2)}\right) \\
&- \tilde{a}_{31}\Delta t\frac{M_2^2}{M_1^2}\frac{1}{\rho_{rel}}p_I^n\mathbf{v}_I^n\cdot\nabla\alpha_1^n - \tilde{a}_{32}\Delta t\frac{M_2^2}{M_1^2}\frac{1}{\rho_{rel}}p_I^{(n,2)}\mathbf{v}_I^{(n,2)}\cdot\nabla\alpha_1^{(n,2)}.
\end{aligned} \tag{3.150}$$

Again, after the coupling between the momentum balances and the energy balances, we obtain the following two non-linear equations for $p_1^{(n,3)}$ and $p_2^{(n,3)}$, respectively:

$$\begin{aligned}
&\alpha_1^{(n,3)}\rho_1^{(n,3)}\left[e_1(p_1^{(n,3)},\rho_1^{(n,3)}) + M_1^2 k_1^{(n,3)}\right] \\
-\;&\tilde{a}_{33}^2\frac{\Delta t^2}{M_1^2}\,\nabla\cdot\left[\left(e_1(p_1^{(n,3)},\rho_1^{(n,3)}) + \frac{p_1^{(n,3)}}{\rho_1^{(n,3)}}\right)\nabla\left(\alpha_1^{(n,3)}p_1^{(n,3)}\right)\right] \\
+\;&\tilde{a}_{33}^2\frac{\Delta t^2}{M_1^2}\,\nabla\cdot\left[\left(e_1(p_1^{(n,3)},\rho_1^{(n,3)}) + \frac{p_1^{(n,3)}}{\rho_1^{(n,3)}}\right)p_I^{(n,3)}\nabla\alpha_1^{(n,3)}\right] \\
+\;&\tilde{a}_{33}\Delta t\,\nabla\cdot\left[\left(e_1(p_1^{(n,3)},\rho_1^{(n,3)}) + \frac{p_1^{(n,3)}}{\rho_1^{(n,3)}}\right)\mathbf{m}_1^{(n,3)}\right] = \hat{e}_1^{(n,3)}
\end{aligned} \tag{3.151}$$

$$\begin{aligned}
&\alpha_2^{(n,3)}\rho_2^{(n,3)}\left[e_2(p_2^{(n,3)},\rho_2^{(n,3)}) + M_2^2 k_2^{(n,3)}\right]\\
&-\ \tilde{a}_{33}^2\frac{\Delta t^2}{M_2^2}\nabla\cdot\left[\left(e_2(p_2^{(n,3)},\rho_2^{(n,3)}) + \frac{p_2^{(n,3)}}{\rho_2^{(n,3)}}\right)\nabla\left(\alpha_2^{(n,3)}p_2^{(n,3)}\right)\right]\\
&-\ \tilde{a}_{33}^2\frac{\Delta t^2}{M_2^2}\nabla\cdot\left[\left(e_2(p_2^{(n,3)},\rho_2^{(n,3)}) - \frac{p_2^{(n,3)}}{\rho_2^{(n,3)}}\right)p_I^{(n,3)}\nabla\alpha_1^{(n,3)}\right]\\
&+\ \tilde{a}_{33}\Delta t\,\nabla\cdot\left[\left(e_2(p_2^{(n,3)},\rho_2^{(n,3)}) + \frac{p_2^{(n,3)}}{\rho_2^{(n,3)}}\right)\mathbf{m}_2^{(n,3)}\right] = \hat{e}_2^{(n,3)}.
\end{aligned} \tag{3.152}$$

Setting $\xi_1^{(0)} = p_1^{(n,2)}, k_1^{(n,3,0)} = k_1^{(n,2)}$, one solves for $l = 1,\dots,L$ the equation

$$\begin{aligned}
&\alpha_1^{(n,3)}\rho_1^{(n,3)}\left[e_1(\xi_1^{(l-1)},\rho_1^{(n,3)}) + M_1^2 k_1^{(n,3,l-1)}\right]\\
&-\ \tilde{a}_{33}^2\frac{\Delta t^2}{M_1^2}\nabla\cdot\left[\left(e_1(\xi_1^{(l-1)},\rho_1^{(n,3)}) + \frac{\xi_1^{(l-1)}}{\rho_1^{(n,3)}}\right)\nabla\left(\alpha_1^{(n,3)}\xi_1^{(l)}\right)\right]\\
&+\ \tilde{a}_{33}^2\frac{\Delta t^2}{M_1^2}\nabla\cdot\left[\left(e_1(\xi_1^{(l-1)},\rho_1^{(n,3)}) + \frac{\xi_1^{(l-1)}}{\rho_1^{(n,3)}}\right)p_I^{(n,3,l)}\nabla\alpha_1^{(n,3)}\right]\\
&+\ \tilde{a}_{33}\Delta t\,\nabla\cdot\left[\left(e_1(\xi_1^{(l-1)},\rho_1^{(n,3)}) + \frac{\xi_1^{(l-1)}}{\rho_1^{(n,3)}}\right)\mathbf{m}_1^{(n,3)}\right] = \hat{e}_1^{(n,3)}
\end{aligned} \tag{3.153}$$

and updates the velocity as

$$\alpha_1^{(n,3)}\rho_1^{(n,3)}\mathbf{u}_1^{(n,2,l)} + \tilde{a}_{33}\frac{\Delta t}{M_1^2}\nabla\left(\alpha_1^{(n,3)}\xi^{(l)}\right) + \tilde{a}_{33}\frac{\Delta t}{M_1^2}p_I^{(n,2,l-1)}\nabla\alpha_1^{(n,3)} = \mathbf{m}_1^{(n,2)}. \tag{3.154}$$

Finally, setting $\xi_2^{(0)} = p_2^{(n,2)}, k_2^{(n,3,0)} = k_2^{(n,2)}$, one solves for $l = 1,\dots,L$ the equation

$$\begin{aligned}
&\alpha_2^{(n,3)}\rho_2^{(n,3)}\left[e_2(\xi_2^{(l-1)},\rho_2^{(n,3)}) + M_2^2 k_2^{(n,3,l-1)}\right]\\
&-\ \tilde{a}_{33}^2\frac{\Delta t^2}{M_2^2}\nabla\cdot\left[\left(e_2(\xi_2^{(l-1)},\rho_2^{(n,3)}) + \frac{\xi_2^{(l-1)}}{\rho_2^{(n,3)}}\right)\nabla\left(\alpha_2^{(n,3)}\xi_2^{(l)}\right)\right]\\
&-\ \tilde{a}_{33}^2\frac{\Delta t^2}{M_2^2}\nabla\cdot\left[\left(e_2(\xi_2^{(l-1)},\rho_2^{(n,3)}) - \frac{\xi_2^{(l-1)}}{\rho_2^{(n,3)}}\right)p_I^{(n,3,l-1)}\nabla\alpha_1^{(n,3)}\right]\\
&+\ \tilde{a}_{33}\Delta t\,\nabla\cdot\left[\left(e_2(\xi_2^{(l-1)},\rho_2^{(n,3)}) + \frac{\xi_2^{(l-1)}}{\rho_2^{(n,3)}}\right)\mathbf{m}_2^{(n,3)}\right] = \hat{e}_2^{(n,3)}.
\end{aligned} \tag{3.155}$$

and updates the velocity as

$$\alpha_2^{(n,3)}\rho_2^{(n,3)}\mathbf{u}_2^{(n,2,l)} + \tilde{a}_{33}\frac{\Delta t}{M_2^2}\nabla\left(\alpha_1^{(n,3)}\xi^{(l)}\right) + \tilde{a}_{33}\frac{\Delta t}{M_2^2}p_I^{(n,2,l-1)}\nabla\alpha_1^{(n,3)} = \mathbf{m}_2^{(n,3)}. \tag{3.156}$$

The spatial discretization of the conservative part is analogous to the one described in Section 3.4, so that we will focus in the next Section on the spatial discretization of the non-conservative terms.

3.5.2 Treatment of non-conservative terms

In this Section, we analyze the treatment of non-conservative terms for system (2.149). We start by analyzing the discretization of the term $\nabla\alpha_1$ in the advection equation for the volume fraction. Following [Bassi and Rebay, 1997a], the numerical approximation is based on a double integration by parts. We define the discrete gradient of the volume fraction as the unique element $\tilde{\nabla}\alpha_1 \in \mathbf{Q}_r$ for which:

$$\begin{aligned}
\int_K \mathbf{v}_I \cdot \tilde{\nabla}\alpha_1 \varphi d\Omega &= \int_K \nabla\cdot\left(\alpha_1 \mathbf{v}_I\right) \varphi d\Omega - \int_K \left(\nabla\cdot \mathbf{v}_I\right) \alpha_1 \varphi d\Omega \\
&= -\int_K \alpha_1 \mathbf{v}_I \cdot \nabla\varphi d\Omega + \int_{\partial K} \widehat{\alpha_1 \mathbf{v}_I} \cdot \mathbf{n}\varphi d\Sigma \\
&\quad + \int_K \mathbf{v}_I \cdot \nabla\left(\alpha_1 \varphi\right) d\Omega - \int_{\partial K} \widehat{\mathbf{v}_I}\alpha_1 \cdot \mathbf{n}\varphi d\Sigma \qquad (3.157) \\
&= \int_K \mathbf{v}_I \cdot \nabla\alpha_1 \varphi d\Omega + \int_{\partial K} \left(\widehat{\mathbf{v}_I \alpha_1} - \widehat{\mathbf{v}_I}\alpha_1\right) \cdot \mathbf{n}\varphi d\Sigma \qquad \forall \varphi \in Q_r.
\end{aligned}$$

This approach guarantees, as expected, a null contribution from the non-conservative terms in the case of uniform volume fraction, for which $\widehat{\mathbf{v}_I \alpha_1} = \widehat{\mathbf{v}_I}\alpha_1$. Hence, as observed in [Bassi and Rebay, 1997a] and remarked in [Tumolo and Bonaventura, 2015], it is possible to recast the non-conservative terms into the sum of two contributions: the first one takes into account the elementwise gradient of α_1, whereas the second one considers its jumps across the element faces. Following the same path, one defines:

$$\begin{aligned}
\int_K G_{jl} \frac{\tilde{\partial}\alpha_1}{\partial x_l} \varphi_j d\Omega &= \int_K \frac{\partial}{\partial x_l}\left(G_{jl}\alpha_1\right) \varphi_j d\Omega - \int_K \frac{\partial G_{jl}}{\partial x_l} \alpha_1 \varphi_j d\Omega \\
&= -\int_K G_{jl}\alpha_1 \frac{\partial \varphi_j}{\partial x_l} d\Omega + \int_{\partial K} \widehat{G_{jl}\alpha_1} \varphi_j n_l d\Sigma \\
&\quad + \int_K G_{jl} \frac{\partial\left(\alpha_1 \varphi_j\right)}{\partial x_l} d\Omega - \int_{\partial K} \widehat{G_{jl}}\alpha_1 \varphi_j n_l d\Sigma \qquad (3.158) \\
&= \int_K G_{jl} \frac{\partial \alpha_1}{\partial x_l} \varphi_j d\Omega + \int_{\partial K} \left(\widehat{G_{jl}\alpha_1} - \widehat{G_{jl}}\alpha_1\right) \varphi_j n_l d\Sigma.
\end{aligned}$$

We report now the algebraic formulation of the linear system associated to the advection of the volume fraction (3.138) obtained using (3.157) for the non-conservative terms. We get

$$\mathbf{L}^{(n,2)} \boldsymbol{\alpha}^{(n,2)} = \mathbf{V}^n, \qquad (3.159)$$

where

$$\begin{aligned}
L_{ij}^{(n,2)} &= \sum_{K\in\mathcal{T}_h} \int_K \left(\varphi_j + \tilde{a}_{22}\Delta t \mathbf{v}_I^n \cdot \nabla\varphi_j\right) \varphi_i d\Omega \qquad (3.160) \\
&+ \sum_{F\in\mathcal{E}} \int_F \widehat{\mathbf{v}_I^n \varphi_j} \cdot [[\varphi_i]] \, d\Sigma - \sum_{F\in\mathcal{E}} \int_F \widehat{\mathbf{v}_I^n} \cdot [[\varphi_j \varphi_i]] \, d\Sigma \\
V_i^n &= \sum_{K\in\mathcal{T}_h} \int_K \mathbf{v}_I^n \cdot \nabla\alpha_1^n \varphi_i d\Omega \qquad (3.161) \\
&+ \sum_{F\in\mathcal{E}} \int_F \widehat{\mathbf{v}_I^n \alpha_1^n} \cdot [[\varphi_i]] \, d\Sigma - \sum_{F\in\mathcal{E}} \int_F \widehat{\mathbf{v}_I^n} \cdot [[\alpha_1^n \varphi_i]] \, d\Sigma
\end{aligned}$$

and $\boldsymbol{\alpha}^{(n,2)}$ denotes the degrees of freedom associated to the discretization of the volume fraction. An alternative approach would be to consider a single integration by parts for the non-conservative terms, namely:

$$\begin{aligned}\int_K G_{jl}\frac{\tilde{\partial}\alpha_1}{\partial x_l}\varphi_j d\Omega &= -\int_K \alpha_1 \frac{\partial}{\partial x_l}\left(G_{jl}\varphi_j\right) d\Omega + \int_{\partial K} \widehat{\alpha_1} G_{jl}\varphi_j n_l d\Sigma \\ &= -\int_K \alpha_1 \frac{\partial G_{jl}}{\partial x_l}\varphi_j d\Omega - \int_K \alpha_1 G_{jl}\frac{\partial \varphi_j}{\partial x_l} d\Omega + \int_{\partial K} \widehat{\alpha_1} G_{jl}\varphi_j n_l d\Sigma.\end{aligned} \tag{3.162}$$

The relation (3.162) does not guarantee zero contribution from the non-conservative terms in the case of uniform volume fraction. However, it is consistent with the non-disturbance condition. Consider indeed the term $\frac{1}{M_1^2}\nabla\left(\alpha_1 p_1\right) - \frac{1}{M_1^2} p_I \nabla\alpha_1$, whose discretization in case of uniform pressure should be identically equal to zero. Hence, we obtain the following relation:

$$\begin{aligned} &\int_K \frac{1}{M_1^2}\nabla\left(\alpha_1 p_1\right)\cdot\boldsymbol{\varphi} d\Omega - \int_K \frac{1}{M_1^2} p_I \tilde{\nabla}\alpha_1 \cdot \boldsymbol{\varphi} = \\ -&\int_K \frac{1}{M_1^2}\alpha_1 p_1 \, \nabla\cdot\boldsymbol{\varphi} d\Omega + \int_{\partial K}\frac{1}{M_1^2}\widehat{\alpha_1 p_1}\mathbf{n}\cdot\boldsymbol{\varphi} d\Sigma \\ +&\int_K \frac{1}{M_1^2}\alpha_1 \nabla p_I \cdot\boldsymbol{\varphi} d\Omega + \int_K \frac{1}{M_1^2}\alpha_1 p_I \, \nabla\cdot\boldsymbol{\varphi} d\Omega - \int_{\partial K}\frac{1}{M_1^2}\widehat{\alpha_1} p_I \mathbf{n}\cdot\boldsymbol{\varphi} d\Sigma = 0.\end{aligned} \tag{3.163}$$

The impact of the different possibilities will be discussed along with the numerical results reported in Section 4.5.

3.5.3 Discretization of four-equation relaxed system

In this Section, we derive an extension of the IMEX scheme described in Section 3.4 for the system (2.155) without mass transfer. The mixture EOS (2.226) outlined in Section 2.6 shows that the mixture internal energy depends on the volume fraction α_1 as well as on the pressure p and the mixture density ρ. Since we consider an explicit treatment of the continuity equations, the mixture density is immediately updated, but the same is not true for the volume fraction. A straightforward way to overcome this issue consists in over-constraining system (2.155) by solving an extra equation for the volume fraction before focusing on momentum and energy balance equations. A similar over-constraining of the system for algorithmic purposes was adopted in sharp-interface formulations, see e.g. [Jemison et al., 2014]. Alternative approaches have been proposed e.g. in [Demou et al., 2022] by considering a non-conservative version of system (2.155). Hence, we consider the following system of equations:

$$
\begin{aligned}
\frac{\partial \alpha_1\rho_1}{\partial t} + \nabla\cdot\left(\alpha_1\rho_1\mathbf{u}\right) &= 0\\
\frac{\partial \alpha_2\rho_2}{\partial t} + \nabla\cdot\left(\alpha_2\rho_2\mathbf{u}\right) &= 0\\
\frac{\partial \alpha_1}{\partial t} + \mathbf{u}\cdot\nabla\alpha_1 &= 0\\
\frac{\partial \rho\mathbf{u}}{\partial t} + \nabla\cdot\left(\rho\mathbf{u}\otimes\mathbf{u}\right) + \frac{1}{M^2}\nabla p &= \frac{1}{Re}\nabla\cdot\left[\mu\left(\nabla\mathbf{u}+\nabla\mathbf{u}^T\right) - \frac{2}{3}\mu\left(\nabla\cdot\mathbf{u}\right)\mathbf{I}\right]\\
&- \frac{\rho}{Fr^2}\mathbf{k} \qquad (3.164)\\
\frac{\partial \rho E}{\partial t} + \nabla\cdot\left[\left(h+kM^2\right)\rho\mathbf{u}\right] &= \frac{M^2}{Re}\nabla\cdot\left[\mu\left(\nabla\mathbf{u}+\nabla\mathbf{u}^T\right)\mathbf{u} - \frac{2}{3}\mu\left(\nabla\cdot\mathbf{u}\right)\mathbf{u}\right]\\
&+ \frac{1}{PrRe}\nabla\cdot\left(\kappa\nabla T\right) - \rho\frac{M^2}{Fr^2}\mathbf{k}\cdot\mathbf{u}.
\end{aligned}
$$

A conservative version of (3.164) can be written as follows:

$$
\begin{aligned}
\frac{\partial \alpha_1\rho_1}{\partial t} + \nabla\cdot\left(\alpha_1\rho_1\mathbf{u}\right) &= 0\\
\frac{\partial \alpha_2\rho_2}{\partial t} + \nabla\cdot\left(\alpha_2\rho_2\mathbf{u}\right) &= 0\\
\frac{\partial \rho\alpha_1}{\partial t} + \nabla\cdot\left(\rho\alpha_1\mathbf{u}\right) &= 0\\
\frac{\partial \rho\mathbf{u}}{\partial t} + \nabla\cdot\left(\rho\mathbf{u}\otimes\mathbf{u}\right) + \frac{1}{M^2}\nabla p &= \frac{1}{Re}\nabla\cdot\left[\mu\left(\nabla\mathbf{u}+\nabla\mathbf{u}^T\right) - \frac{2}{3}\mu\left(\nabla\cdot\mathbf{u}\right)\mathbf{I}\right]\\
&- \frac{\rho}{Fr^2}\mathbf{k}\\
\frac{\partial\left(\rho E + \frac{M^2}{We}\left|\nabla\alpha_1\right|\right)}{\partial t} + \nabla\cdot\left[\left(h+kM^2\right)\rho\mathbf{u}\right] &= \frac{M^2}{Re}\nabla\cdot\left[\mu\left(\nabla\mathbf{u}+\nabla\mathbf{u}^T\right)\mathbf{u} - \frac{2}{3}\mu\left(\nabla\cdot\mathbf{u}\right)\mathbf{u}\right]\\
&+ \frac{1}{PrRe}\nabla\cdot\left(\kappa\nabla T\right) - \rho\frac{M^2}{Fr^2}\mathbf{k}\cdot\mathbf{u}.
\end{aligned}
\qquad (3.165)
$$

Preliminary numerical experiments in Section 4.5.4 have shown that the discretization of the non-conservative formulation for the advection of the volume fraction in (3.164) is less diffusive with respect to that of the conservative version in (3.165) and it is therefore preferable. Since we will resort again to an operator splitting technique, we will describe here only the discretization of the hyperbolic part and of the forcing terms. The treatment of the diffusive part is indeed completely analogous to what we already described in 3.4. Consider therefore the second stage of the IMEX time marching scheme. Following the discretization approach proposed in (3.138), one can write formally

$$\begin{aligned}
\alpha_1^{(n,2)}\rho_1^{(n,2)} &= \alpha_1^n\rho_1^n - a_{21}\Delta t\,\nabla\cdot\left(\alpha_1^n\rho_1^n\mathbf{u}^n\right)\\
\alpha_2^{(n,2)}\rho_2^{(n,2)} &= \alpha_2^n\rho_2^n - a_{21}\Delta t\,\nabla\cdot\left(\alpha_2^n\rho_2^n\mathbf{u}^n\right)\\
\alpha_1^{(n,2)} &+ \tilde{a}_{22}\Delta t\mathbf{u}^n\cdot\nabla\alpha_1^{(n,2)} = \hat{\alpha}^{(n,2)}\\
\rho^{(n,2)}\mathbf{u}^{(n,2)} &+ \tilde{a}_{22}\frac{\Delta t}{M^2}\nabla p^{(n,2)} = \mathbf{m}^{(n,2)}\\
\rho^{(n,2)}E^{(n,2)} &+ \tilde{a}_{22}\Delta t\,\nabla\cdot\left(h^{(n,2)}\rho^{(n,2)}\mathbf{u}^{(n,2)}\right) = \hat{e}^{(n,2)},
\end{aligned} \tag{3.166}$$

where we have set

$$\begin{aligned}
\hat{\alpha}^{(n,2)} &= \alpha_1^n - \tilde{a}_{21}\Delta t\mathbf{u}^n\cdot\nabla\alpha_1^n\\
\\
\mathbf{m}^{(n,2)} &= \rho^n\mathbf{u}^n\\
&- a_{21}\Delta t\,\nabla\cdot\left(\rho^n\mathbf{u}^n\otimes\mathbf{u}^n\right) - \tilde{a}_{21}\frac{\Delta t}{M^2}\nabla p^n\\
&- \tilde{a}_{21}\frac{\Delta t}{Fr^2}\rho^n\mathbf{k} - \tilde{a}_{22}\frac{\Delta t}{Fr^2}\rho^{(n,2)}\mathbf{k}\\
\\
\hat{e}^{(n,2)} &= \rho^nE^n\\
&- \tilde{a}_{21}\Delta t\,\nabla\cdot\left(h^n\rho^n\mathbf{u}^n\right) - a_{21}\Delta tM^2\,\nabla\cdot\left(k^n\rho^n\mathbf{u}^n\right)\\
&- \tilde{a}_{21}\frac{\Delta tM^2}{Fr^2}\rho^n\mathbf{k}\cdot\mathbf{u}^n - \tilde{a}_{22}\frac{\Delta tM^2}{Fr^2}\rho^{(n,2)}\mathbf{k}\cdot\mathbf{u}^{(n,2)}.
\end{aligned} \tag{3.167}$$

The third stage can be expressed in a similar manner and we report it here for the sake of completeness:

$$\begin{aligned}
\alpha_1^{(n,3)}\rho_1^{(n,3)} &= \alpha_1^n\rho_1^n\\
&- a_{31}\Delta t\,\nabla\cdot\left(\alpha_1^n\rho_1^n\mathbf{u}^n\right) - a_{32}\Delta t\,\nabla\cdot\left(\alpha_1^{(n,2)}\rho_1^{(n,2)}\mathbf{u}^{(n,2)}\right)\\
\alpha_2^{(n,3)}\rho_2^{(n,3)} &= \alpha_2^n\rho_2^n\\
&- a_{31}\Delta t\,\nabla\cdot\left(\alpha_2^n\rho_2^n\mathbf{u}^n\right) - a_{32}\Delta t\,\nabla\cdot\left(\alpha_2^{(n,2)}\rho_2^{(n,2)}\mathbf{u}^{(n,2)}\right)\\
\alpha_1^{(n,3)} &+ \tilde{a}_{33}\Delta t\mathbf{u}^{(n,2)}\cdot\nabla\alpha_1^{(n,3)} = \hat{\alpha}^{(n,3)}\\
\rho^{(n,3)}\mathbf{u}^{(n,3)} &+ \tilde{a}_{33}\frac{\Delta t}{M^2}\nabla p^{(n,3)} = \mathbf{m}^{(n,3)}\\
\rho^{(n,3)}E^{(n,3)} &+ \tilde{a}_{33}\Delta t\,\nabla\cdot\left(h^{(n,3)}\rho^{(n,3)}\mathbf{u}^{(n,3)}\right) = \hat{e}^{(n,3)},
\end{aligned} \tag{3.168}$$

where we have set

$$\begin{aligned}
\hat{\alpha}_1^{(n,3)} &= \alpha_1^n - \tilde{a}_{32}\Delta t \mathbf{u}^{(n,2)} \cdot \nabla \alpha_1^{(n,2)} - \tilde{a}_{31}\Delta t \mathbf{u}^n \cdot \nabla \alpha_1^n \\
\mathbf{m}^{(n,3)} &= \rho^n \mathbf{u}^n \\
&- a_{31}\Delta t\, \nabla\cdot \left(\rho^n \mathbf{u}^n \otimes \mathbf{u}^n\right) - \tilde{a}_{31}\frac{\Delta t}{M^2}\nabla p^n \\
&- a_{32}\Delta t\, \nabla\cdot \left(\rho^{(n,2)}\mathbf{u}^{(n,2)} \otimes \mathbf{u}^{(n,2)}\right) - \tilde{a}_{32}\frac{\Delta t}{M^2}\nabla p^{(n,2)} \\
&- \tilde{a}_{31}\frac{\Delta t}{Fr^2}\rho^n \mathbf{k} - \tilde{a}_{32}\frac{\Delta t}{Fr^2}\rho^{(n,2)}\mathbf{k} - \tilde{a}_{33}\frac{\Delta t}{Fr^2}\rho^{(n,3)}\mathbf{k} \\
\hat{e}^{(n,2)} &= \rho^n E^n \\
&- \tilde{a}_{31}\Delta t\, \nabla\cdot \left(h^n \rho^n \mathbf{u}^n\right) - a_{31}\Delta t M^2\, \nabla\cdot \left(k^n \rho^n \mathbf{u}^n\right) \\
&- \tilde{a}_{32}\Delta t\, \nabla\cdot \left(h^{(n,2)}\rho^{(n,2)}\mathbf{u}^{(n,2)}\right) - a_{32}\Delta t M^2\, \nabla\cdot \left(k^{(n,2)}\rho^{(n,2)}\mathbf{u}^{(n,2)}\right) \\
&- \tilde{a}_{31}\frac{\Delta t M^2}{Fr^2}\rho^n \mathbf{k}\cdot\mathbf{u}^n - \tilde{a}_{32}\frac{\Delta t M^2}{Fr^2}\rho^{(n,2)}\mathbf{k}\cdot\mathbf{u}^{(n,2)} - \tilde{a}_{33}\frac{\Delta t M^2}{Fr^2}\rho^{(n,3)}\mathbf{k}\cdot\mathbf{u}^{(n,3)}.
\end{aligned} \tag{3.169}$$

CHAPTER 4

Numerical simulations

In this Chapter, we validate the numerical methods and strategies outlined in Chapter 3 in a number of relevant benchmarks. Notice that, following e.g. [Tumolo et al., 2013, Tumolo and Bonaventura, 2015], we set $\mathcal{H} = \min\{\mathrm{diam}(K) | K \in \mathcal{T}_h\}$. All the proposed schemes have been implemented using the open-source numerical library *deal.II*, which is based on a matrix-free approach [Bangerth et al., 2007, Arndt et al., 2022] and provides AMR tools. All the resulting symmetric linear systems are solved with the preconditioned conjugate gradient method [Hestenes and Stiefel, 1952, Quarteroni and Valli, 2008], whereas the Generalized Minimal RESidual (GMRES) method [Saad, 1981, Quarteroni and Valli, 2008] is employed for the solution of the non symmetric linear systems (see also Appendix A.7 for some implementation details). First of all, we validate in Section 4.1 the filtering monotonization technique introduced in Section 3.2 in a number of classical test cases where discontinuities arise. Afterwards, we present the numerical results for the proposed discretization of the incompressible Navier-Stokes equations in Section 4.2, assessing the convergence properties of the method, comparing the scheme with the Finite Volume method and performing also simulations in the case of a complex geometry. Then, we focus in Section 4.3 and in Section 4.4 on single-phase compressible Navier-Stokes equations. We provide here results obtained with both ideal gas and non-ideal gas equations of state and we derive suitable refinement indicators for real gases. Finally, we present in Section 4.5 results for two-phase flows in the purely inviscid case in order to validate the IMEX method for the full non-equilibrium Baer-Nunziato model and we consider classical benchmarks for two-phase flows described by the system of equations (2.155).

Contents

4.1 Validation of the filtering monotonization technique 87
  4.1.1 Solid body rotation 87
  4.1.2 Sod shock tube problem 93
  4.1.3 Circular explosion problem 96
  4.1.4 Two-dimensional Riemann problem 99
4.2 Numerical results for the incompressible Navier-Stokes equations . 100
  4.2.1 Case tests with analytical solution 102
  4.2.2 Two-dimensional lid-driven cavity 106
  4.2.3 Three-dimensional lid-driven cavity 110
  4.2.4 Flow past a cylinder 114
  4.2.5 Complex geometry 116
4.3 Numerical results for the single-phase compressible Navier-Stokes equations with ideal gas law 119
  4.3.1 Isentropic vortex 121
  4.3.2 2D Lid-driven cavity 125
  4.3.3 Cold bubble 127
  4.3.4 Warm bubble 130
  4.3.5 Inertia-gravity waves 131
  4.3.6 Density current 133
  4.3.7 3D rising bubble 135
  4.3.8 Hydrostatic flow over a hill 138
  4.3.9 Nonhydrostatic flow over a hill 140
  4.3.10 Schär hill 144
  4.3.11 3D medium-steep bell-shaped hill 146
4.4 Numerical results for the single-phase compressible Navier-Stokes equations with non-ideal gas law 146
  4.4.1 Cold bubble 147
  4.4.2 Warm bubble 151
4.5 Numerical results for two-phase flow systems 155
  4.5.1 No mixing water-air mixture 155
  4.5.2 Pure advection test case 158
  4.5.3 Solid contact 161
  4.5.4 Rising bubble 161

4.1 Validation of the filtering monotonization technique

In this Section, we validate the filtering monotonization technique outlined in Section 3.2. Notice that the results in this Section have been obtained using dimensional variables as done in [Orlando, 2023], to which we refer for further details. Concerning the time discretization, we will consider for the purpose of validation the well known Total Variation Diminishing (TVD) Runge Kutta methods described in [Gottlieb et al., 2001, Gottlieb and Shu, 1998] (see also Appendix A.5). These are high order time discretization schemes that preserve the strong stability properties of first order explicit Euler time stepping and are known as Strong Stability Preserving (SSP) methods. We chose to employ mainly as polynomial degrees $r = 1$ and $r = 2$ in combination with the second order SSP and the third order SSP schemes, respectively. Moreover, we consider the ideal gas law (2.210) with $\gamma = 1.4$ for all the configurations and we define the Courant number

$$C = rc\Delta t/\mathcal{H}, \tag{4.1}$$

where $c = \sqrt{\gamma p/\rho}$ is the speed of sound. Applications of the filtering monotonization technique in combination with the IMEX scheme described in Section 3.4 and 3.5 will be presented in Section 4.5.

4.1.1 Solid body rotation

We consider a classical benchmark for advection schemes, the so-called solid body rotation, which has been studied in different configurations (see e.g. [Zalesak, 1979, LeVeque, 1996]). A stationary velocity field is considered, representing a rotating flow with frequency $\omega = 1\,\mathrm{s}^{-1}$ around the point $(0,0)$ on the domain $\Omega = (-0.5, 0.5)^2$. The initial datum is given by the following discontinuous function:

$$\Psi_0(\mathbf{x}) = \begin{cases} 1 & \text{if } X^2 + Y^2 \leq 1 \\ 0 & \text{otherwise,} \end{cases} \tag{4.2}$$

where $X = \frac{x - x_0}{\tilde{\sigma}}$ and $Y = \frac{y - y_0}{\tilde{\sigma}}$ with $x_0 = y_0 = \frac{1}{6}$ and $\tilde{\sigma} = 0.2$. For this first test, the computational grid is composed by 120 elements along each direction with a time step such that the maximum Courant number is $C \approx 0.1$. All the results are presented at $T_f = 2\pi\,\mathrm{s}$, when one rotation has been completed, so that the solution coincides with the initial datum. We first consider the strategy (3.20) depicted in Section 3.2 with the filter function $\mathcal{F}_1(x)$ (3.18), the Oberman-Salvador filter function, taking $\varepsilon = 5h_K$, as suggested in [Bokanowski et al., 2016]. Figure 4.1 compares the results at $t = T_f$ of the filtering approach with the Q_1 non monotonized solution and with the Q_0 one. As one can easily notice, with this choice of the parameter, too much stabilization is added and therefore the filtered solution essentially coincides with the low order one.

Increasing the value ε does not affect significantly the results until we take $\varepsilon = 10^4 h_K$: in this case, as evident from Figure 4.2, the filtering approach works quite well since it is able to provide an essentially monotonic solution, as confirmed by Table 4.1, without smoothing it too much.

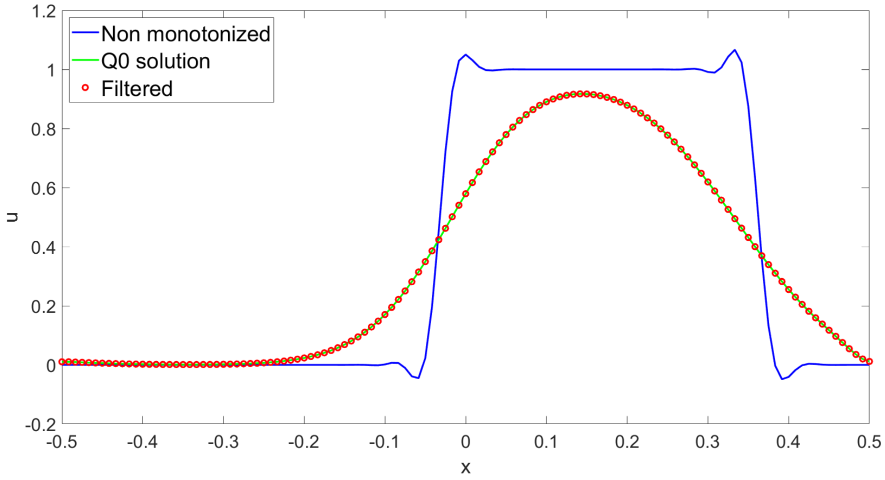

Figure 4.1: *Computational results for the solid body rotation at* $t = T_f$ *with* $r = 1$ *using filter* (3.20) *with* $\varepsilon = 5h_K$*. The red line denotes the non filtered* Q_1 *solution, the green line denotes the* Q_0 *solution, while the red dots represent the results of the simulation with the filtering approach.*

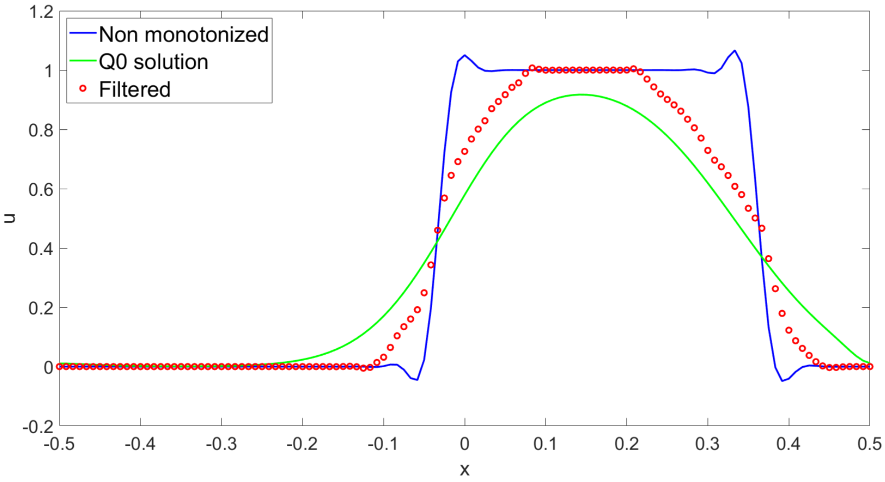

Figure 4.2: *Computational results for the solid body rotation at* $t = T_f$ *with* $r = 1$ *using filter* (3.20) *with* $\varepsilon = 10^4 h_K$*. The red line denotes the non filtered* Q_1 *solution, the green line denotes the* Q_0 *solution, while the red dots represent the results of the simulation with the filtering approach.*

The situation can be further improved using mesh adaptivity so as to start with a coarse mesh and perform refinement only in the zones where discontinuity is detected. The indicator is based on the gradient of the variable Ψ; more specifically, we define for each element K

$$\eta_K = \max_{i \in \mathcal{N}_K} |\nabla \Psi|_i \tag{4.3}$$

as local refinement indicator, where $\mathcal{N}_K$ denotes the set of nodes over the element K. The initial mesh is composed by 120 elements along each direction and we allowed up to two local refinements. Figure 4.3 shows that the results at $t = T_f$ with a time step such that the maximum Courant number is $C \approx 0.1$, using the value $\varepsilon = 10^4 h_K$ previously tested in the fixed grid configuration, compared with the full resolution Q_1 non monotonized solution and the corresponding Q_0 one.

One can easily notice that in this specific configuration the value of ε is still too small and too much dissipation is provided.

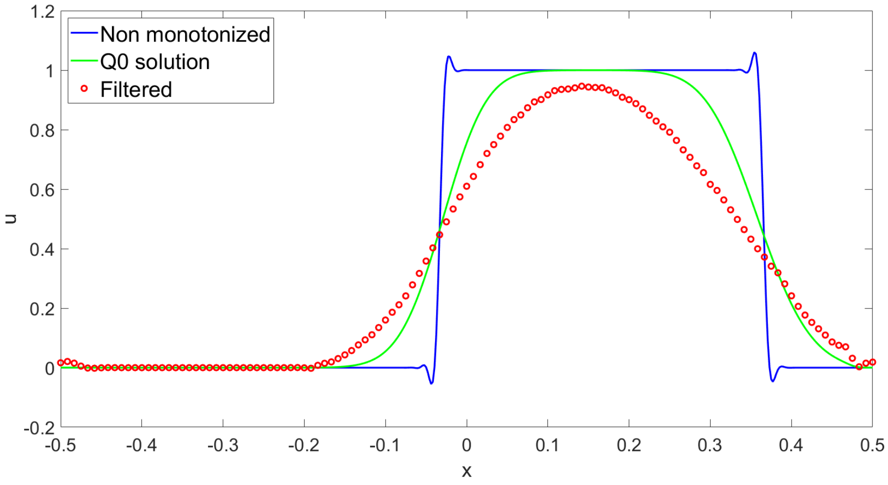

Figure 4.3: *Computational results for adaptive simulation of the solid body rotation at $t = T_f$ with $r = 1$ using filter* (3.20) *with $\varepsilon = 10^4 h_K$. The red line denotes the full resolution non filtered Q_1 solution, the green line denotes the full resolution Q_0 solution, while the red dots represent the results of the simulation with the filtering approach.*

The situation improves increasing the value of ε. Figure 4.4 shows the results using $\varepsilon = 10^5 h_K$, where an essentially monotonic solution is retrieved. The values reported in Table 4.1 confirm the better quality of the solution.

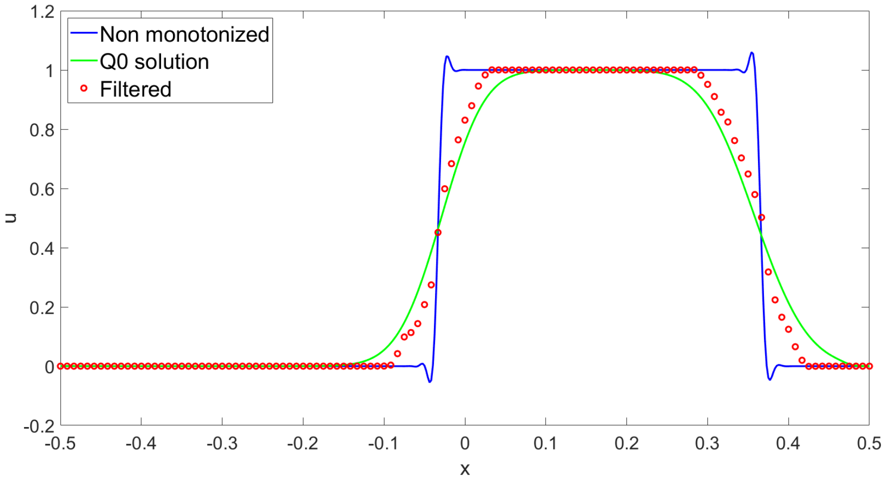

Figure 4.4: *Computational results for adaptive simulation of the solid body rotation at $t = T_f$ using filter* (3.20) *with $\varepsilon = 10^5 h_K$. The red line denotes the full resolution non filtered Q_1 solution, the green line denotes the full resolution Q_0 solution, while the red dots represent the results of the simulation with the filtering approach.*

Value of ε	**Maximum value of** Ψ	**Mininum value of** Ψ
$10^4 h_K$	$1.0 + 7.3 \times 10^{-3}$	$0.0 - 5.2 \times 10^{-3}$
$10^5 h_K$ (adaptive)	$1.0 + 1.0 \times 10^{-5}$	$0.0 - 1.9 \times 10^{-3}$

Table 4.1: *Solid body rotation, maximum and minimum values for filtering approach* (3.20) *at $t = T_f$ with $r = 1$ both in case of fixed grid and adaptive simulations.*

The very large value of ε that is necessary to achieve monotonicity suggests that the previous approach has shortcomings. We consider therefore the second strategy (3.24) outlined in Section 3.2. We start again from a fixed grid configuration, using the same mesh and the same time step previously described. After some sensitivity study, $\beta = 0.4$ seems to yield an acceptable behaviour for the solution, as evident from Figure 4.5. The discontinuity is less smeared out with respect to the Q_0 solution, while avoiding the spurious oscillations and retrieving an essentially monotonic solution, as reported in Table 4.2.

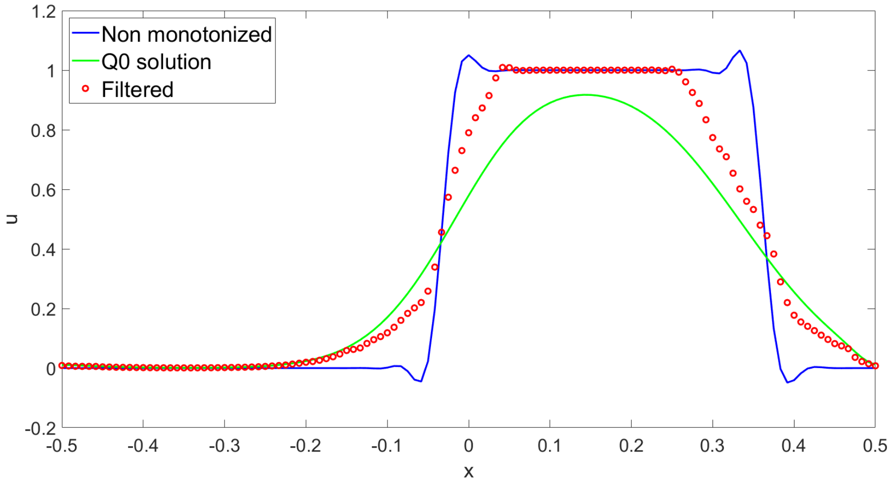

Figure 4.5: *Computational results for the solid body rotation at* $t = T_f$ *with* $r = 1$ *using filter* (3.24) *with* $\beta = 0.4$. *The red line denotes the non filtered* Q_1 *solution, the green line denotes the* Q_0 *solution, while the red dots represent the results of the simulation with the filtering approach.*

Again, the h-adaptive version of the method, using the same configuration and the same refinement criterion previously described, provides better results, as confirmed by Table 4.2. The grid at $t = T_f$ is reported in Figure 4.7 and is composed by 28119 elements.

Value of β	**Maximum value of** Ψ	**Mininum value of** Ψ
0.4	$1.0 + 9.2 \times 10^{-3}$	$0.0 + 7.6 \times 10^{-3}$
0.4 (adaptive)	$1.0 + 6.7 \times 10^{-3}$	$0.0 + 4.0 \times 10^{-4}$

Table 4.2: *Solid body rotation, maximum and minimum values for filtering approach* (3.24) *at* $t = T_f$ *both in case of fixed grid and adaptive simulations.*

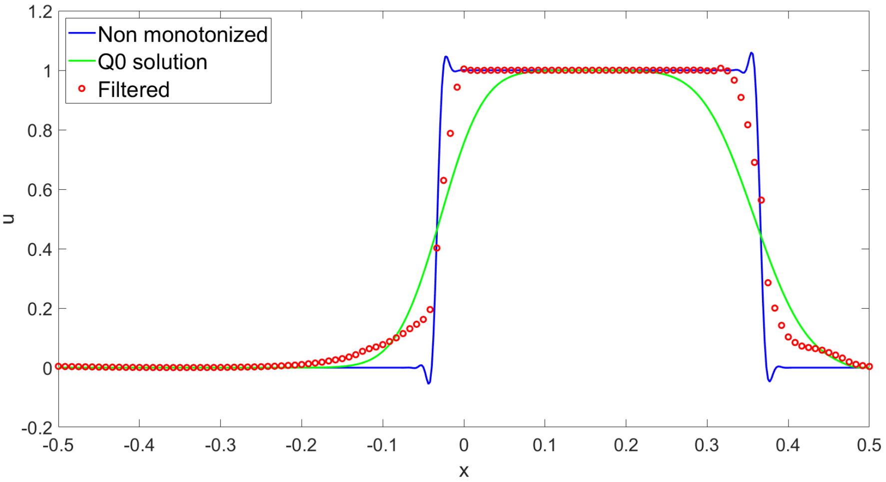

Figure 4.6: *Computational results for adaptive simulation of the solid body rotation at* $t = T_f$ *with* $r = 1$ *using filter* (3.24) *with* $\beta = 0.4$. *The red line denotes the full resolution non filtered* Q_1 *solution, the green line denotes the full resolution* Q_0 *solution, while the red dots represent the results of the simulation with the filtering approach.*

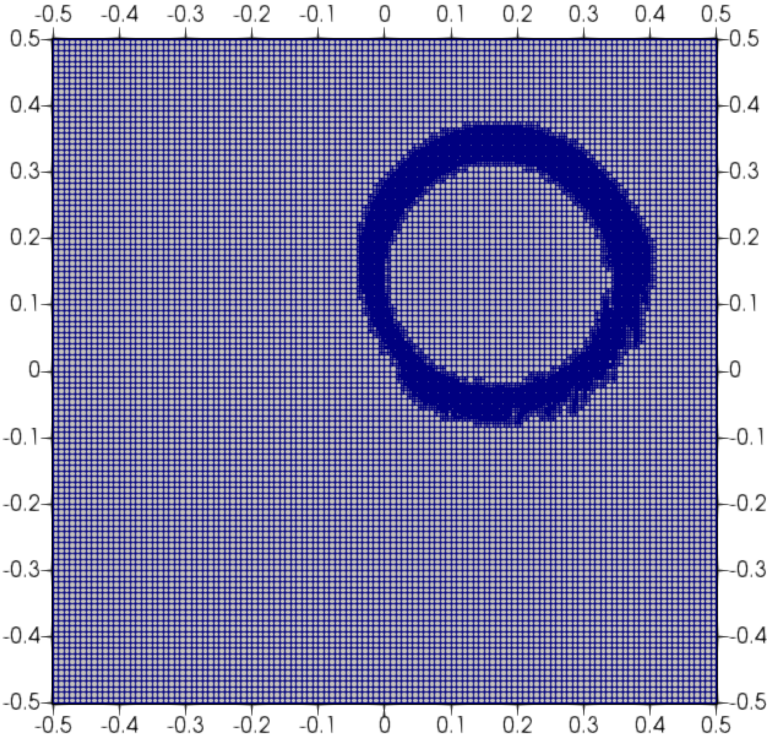

Figure 4.7: *Computational grid for adaptive simulation of the solid body rotation at* $t = T_f$ *with* $r = 1$ *using filter* (3.24) *with* $\beta = 0.4$.

The same test has been repeated using $r = 2$, i.e. Q_2 finite elements, and the third order SSP time discretization strategy. We present here only a comparison between the two strategies in case of an adaptive simulation using $\varepsilon = 10^5 h_K$ and $\beta = 0.4$, respectively. Again, we started with a mesh composed by 120 elements along each direction, we allowed up to two local refinements and the employed time step is such that the maximum Courant number is $C \approx 0.1$. Figure 4.8 shows the results with the two different approaches at $t = T_f$, compared with a full resolution Q_2 solution and the corresponding Q_0 one. One can easily notice that both strategies provide an essentially monotonic result, as confirmed by Table 4.3; moreover, the approach (3.24) is characterized by a sharper transition zone and is therefore less dissipative, allowing to apply the filter on a reduced number of elements. Moreover, as evident from Table 4.3, the filtering procedure (3.24) appears to avoid undershoots and keeps a non negative solution, which is a crucial fact in many applications in order to preserve the physical meaning of the results. Hence, it will be the one used throughout the rest of the numerical experiments.

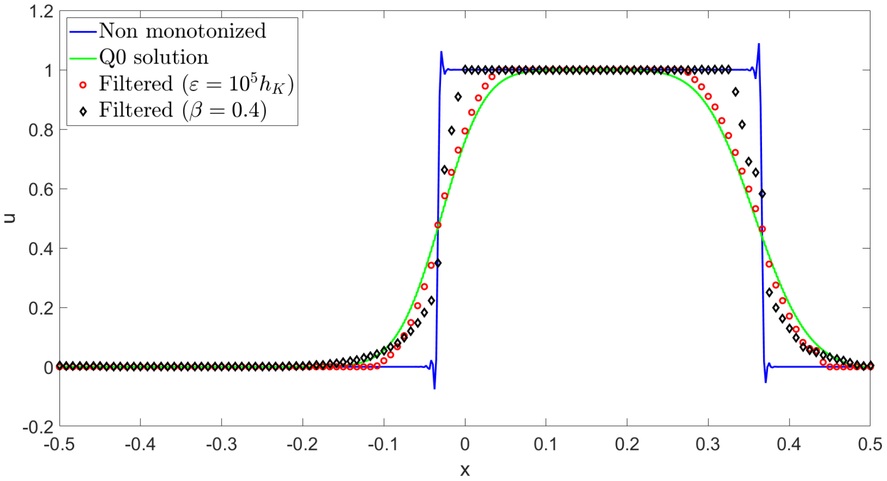

Figure 4.8: *Computational results for adaptive simulations of the solid body rotation at $t = T_f$ with $r = 2$. The red line denotes the full resolution non filtered Q_2 solution, the green line denotes the full resolution Q_0 solution, while the red dots and black diamonds represent the results of the simulation with the filtering approaches* (3.20) *and* (3.24) *using $\varepsilon = 10^5 h_K$ and $\beta = 0.4$, respectively.*

Value of the parameter	Maximum value of Ψ	Mininum value of Ψ
$\beta = 0.4$ (adaptive)	$1.0 + 1.5 \times 10^{-3}$	$0.0 + 3.8 \times 10^{-3}$
$\varepsilon = 10^5 h_K$ (adaptive)	1.0	$0.0 - 1.9 \times 10^{-4}$

Table 4.3: *Solid body rotation, maximum and minimum values comparing filtering approaches at $t = T_f$ with $r = 2$ in case of adaptive simulations.*

For the sake of completeness, we report also the results obtained using the filtering approach (3.24) with $r = 3$, $\beta = 0.4$ and a mesh composed by 240 elements along each direction. Figure 4.9 shows a comparison at $t = T_f$ between the filtering solution, the non monotonized Q_3 solution and the corresponding Q_0 one. All the considerations made so far remain valid and the overshoots are further reduced with respect to Table 4.3. The overhead with respect to the unfiltered DG scheme amounts to a factor ≈ 1.5 in terms of CPU time.

Value of the parameter	Maximum value of Ψ	Mininum value of Ψ
$\beta = 0.4$	$1.0 + 1.2 \times 10^{-4}$	$0.0 + 7.9 \times 10^{-6}$

Table 4.4: *Solid body rotation, maximum and minimum values for filtering approach* (3.20) *at $t = T_f$ with $r = 3$ in case of adaptive simulations.*

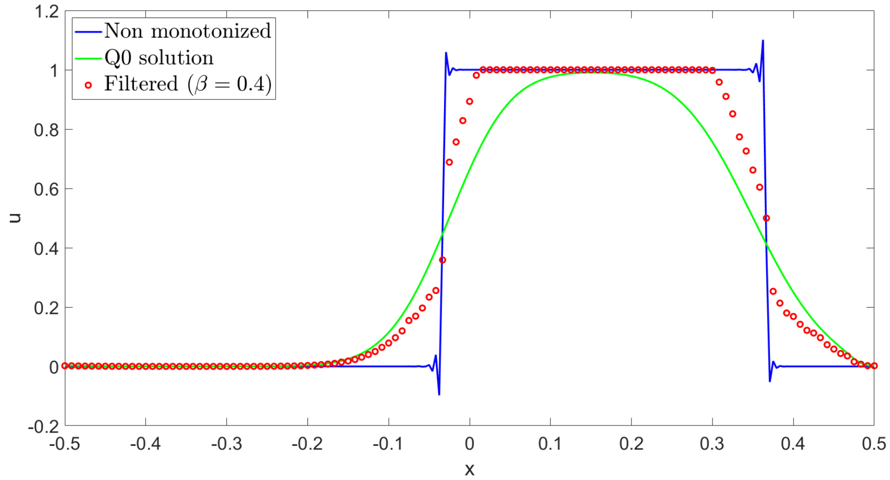

Figure 4.9: *Computational results for solid body rotation at $t = T_f$ with $r = 3$. The red line denotes the non filtered Q_3 solution, the green line denotes the Q_0 solution, while the red dots represent the results of the simulation with the filtering approaches* (3.24) *using $\beta = 0.4$.*

4.1.2 Sod shock tube problem

We consider now the classical Sod shock tube problem for the Euler equations of gas dynamics proposed by [Sod, 1978], so as to assess the capability of the filtering approach to reproduce correctly 1D waves such as shocks, contact discontinuities or rarefaction waves. It consists of a right-moving shock wave, an intermediate contact discontinuity and a left-moving rarefaction fan. The computational domain is $\Omega = (-0.5, 0.5)$, the final time is $T_f = 0.2\,\mathrm{s}$ and the initial condition is given as follows:

$$(\rho_0, u_0, p_0) = \begin{cases} (1, 0, 1) & \text{if } x < 0 \\ (0.125, 0, 1) & \text{if } x > 0, \end{cases} \tag{4.4}$$

in terms of density, velocity and pressure, respectively. Dirichlet boundary conditions are imposed. We use as numerical flux the Rusanov [Rusanov, 1962] flux. We start with a mesh composed by 100 elements, a time-step equal to $5 \cdot 10^{-4}\,\mathrm{s}$ and polynomial degree $r = 1$, yielding a maximum Courant number $C \approx 0.12$. Figure 4.10 shows the results at $t = T_f$ for the density of a simulation using $\beta_\rho = \beta_{\rho\mathbf{u}} = \beta_{\rho E} = 0.4$. One can easily notice the presence of significant under- and over-shoots. This suggests that we need to decrease the value of the parameter β_ρ in order to achieve a monotonic solution. The same considerations hold also for the velocity and the pressure. After some sensitivity study, the combination $\beta_\rho = 0.2, \beta_{\rho\mathbf{u}} = 0.15, \beta_{\rho E} = 0.2$ could be shown to provide a better quality solution with significantly reduced under- and over-shoots, as reported in Figure 4.10.

The situation can be further improved employing the Froese-Oberman filter function $\mathcal{F}_2(x)$, that is continuous and provides therefore a smoother transition between the high order and the low order solutions. This allows also to increase the values of the parameters $\beta_\rho, \beta_{\rho\mathbf{u}}$ and $\beta_{\rho E}$. Figure 4.11 shows the results at $t = T_f$ using $\beta_\rho = \beta_{\rho\mathbf{u}} = \beta_{\rho E} = 0.3$ and one can easily notice that the shock wave and the contact discontinuity are resolved in a sharper manner with only slight undershoots for density and pressure and overshoots for the velocity in the tail of the rarefaction fan. Table 4.5 reports the maximum and the minimum values

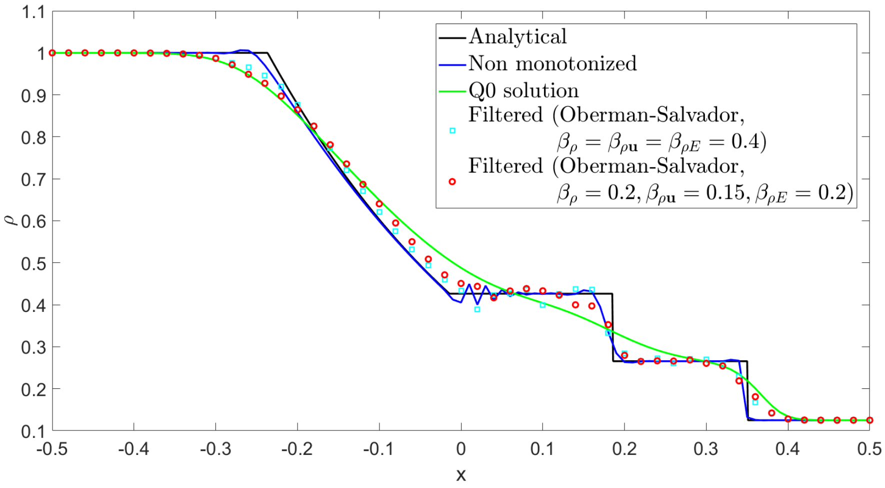

Figure 4.10: *Computational results for Sod shock tube problem at $t = T_f$ with $r = 1$. The black line reports the analytical solution, the red line denotes the non filtered Q_1 solution, the green line denotes the Q_0 solution, the cyan squares represent the results of the simulation with the filtering approach* (3.18) *using $\beta_\rho = \beta_{\rho\mathbf{u}} = \beta_{\rho E} = 0.4$, whereas the red circles represent the results of the simulation with the filtering approach* (3.18) *using $\beta_\rho = 0.2, \beta_{\rho\mathbf{u}} = 0.15, \beta_{\rho E} = 0.2$.*

for density, velocity and pressure, as well as the L^∞ norm errors, which confirm the good results of the proposed method, also in comparison with the results available in [Loubère et al., 2014] with the classical ADER-MOOD scheme. Figure 4.11 reports also the results at $t = T_f$ using 250 elements, a time step equal to $2 \cdot 10^{-4}$ s and the following parameters: $\beta_\rho = 0.6, \beta_{\rho\mathbf{u}} = 0.6, \beta_{\rho E} = 0.6$. It can be easily noticed that, as expected by increasing the resolution, the discontinuities are better retrieved. The values reported in Table 4.6 confirm the improved results.

Variable	Maximum value	Mininum value	L$^\infty$ error	L$^\infty$ error ADER-MOOD
ρ	1.0	0.125	$6.9 \cdot 10^{-2}$	$1.1 \cdot 10^{-1}$
u	$0.9275 + 5.0 \cdot 10^{-2}$	0.0	$4.8 \cdot 10^{-1}$	-
p	1.0	0.1	$8.2 \cdot 10^{-2}$	-

Table 4.5: *Computational results for Sod shock tube problem at $t = T_f$ with $r = 1$ employing Froese-Oberman filter function and using $\beta_\rho = 0.3$, $\beta_{\rho\mathbf{u}} = 0.3$ and $\beta_{\rho E} = 0.3$. Results for ADER-MOOD scheme from [Loubère et al., 2014]. Maximum and minimum values are referred to the corresponding variable declared in the left column.*

Variable	Maximum value	Mininum value	L$^\infty$ error
ρ	1.0	0.125	3.9×10^{-2}
u	$0.9275 + 4.2 \times 10^{-2}$	0.0	2.9×10^{-1}
p	1.0	0.1	$5.0 \cdot 10^{-2}$

Table 4.6: *Computational results for Sod shock tube problem at $t = T_f$ with $r = 1$ and 250 elements employing Froese-Oberman filter function and using $\beta_\rho = 0.6$, $\beta_{\rho\mathbf{u}} = 0.6$ and $\beta_{\rho E} = 0.6$. Maximum and minimum values are referred to the corresponding variable declared in the left column.*

The same test has been repeated using $r = 2$ and the third order SSP time

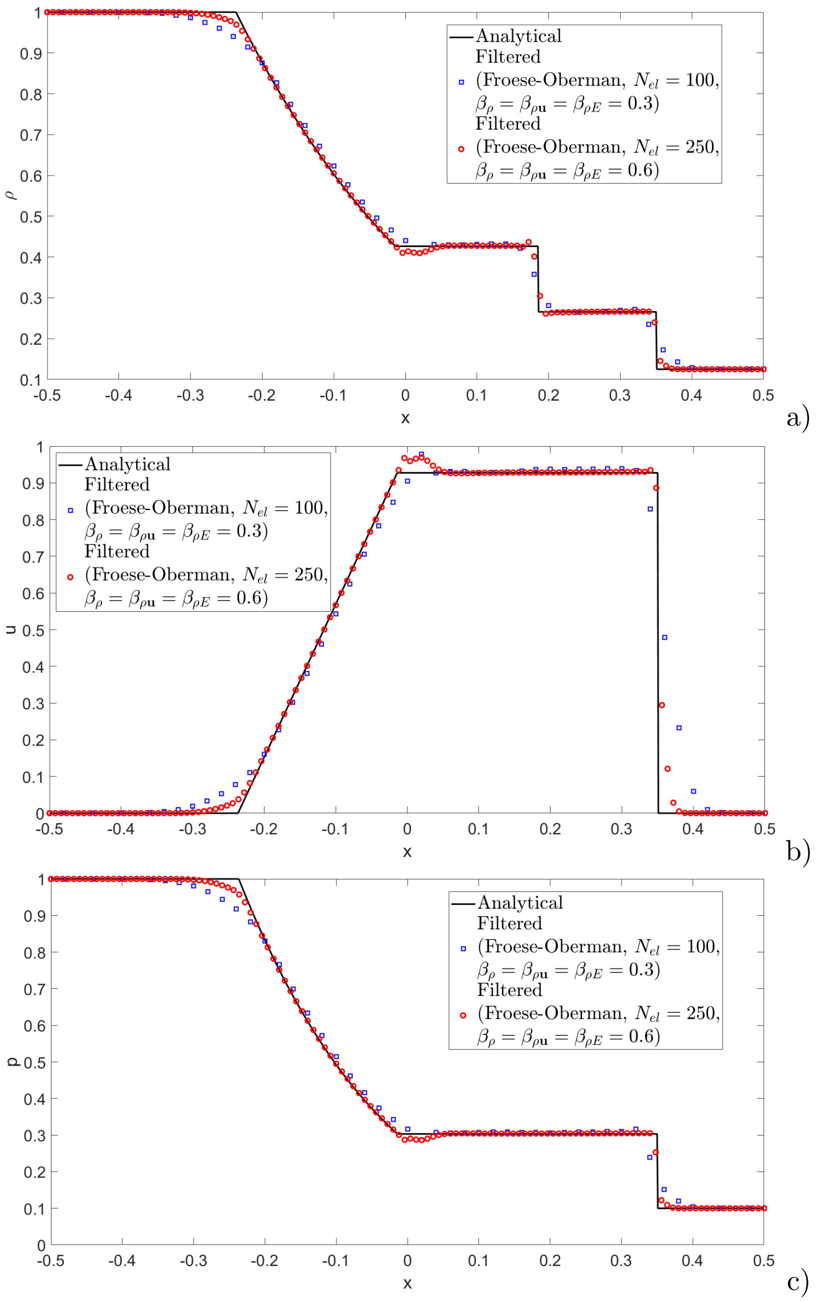

Figure 4.11: *Computational results for Sod shock tube problem at $t = T_f$ with $r = 1$, a) density, b) velocity, c) pressure. The black line reports the analytical solution, the red line denotes the non filtered Q_1 solution, the blue dots are the results employing Froese-Oberman filter function* (3.19) *and using $\beta_\rho = 0.3, \beta_{\rho\mathbf{u}} = 0.3$ and $\beta_{\rho E} = 0.3$ with 100 elements, while the red dots represent the results employing Froese-Oberman filter function* (3.19) *and using $\beta_\rho = 0.6, \beta_{\rho\mathbf{u}} = 0.6$ and $\beta_{\rho E} = 0.6$ with 250 elements.*

discretization scheme. Figure 4.12 reports the results at $t = T_f$ using 250 elements, a time step equal to $1 \cdot 10^{-4}$ s and $\beta_\rho = \beta_{\rho\mathbf{u}} = \beta_{\rho E} = 1.4$. The under- and over-shoots are significantly reduced and a good agreement with the analytical solution is established, as further confirmed by Table 4.7. The larger values of β parameters can be explained by considering that the increase of the polynomial degree leads generally to a more accurate solution with relatively large under- and over-shoots localized in a narrow region, where the low order solution has to be considered. Approximately, the filtering is applied on the 10% of the degrees of freedom and the overhead with respect to the non monotonized scheme corresponds to a factor ≈ 1.25 in terms of CPU time. Both data compare quite well with those reported in [Zanotti et al., 2015] for the ADER-WENO approach, where the 15 % of the cells was limited.

Variable	Maximum value	Mininum value	L^∞ error
ρ	$1.0 + 2.0 \times 10^{-3}$	$0.125 - 2.0 \times 10^{-4}$	1.6×10^{-2}
u	$0.9275 + 8.0 \times 10^{-3}$	$0.0 - 2.3 \times 10^{-3}$	2.2×10^{-2}
p	$1.0 + 2.8 \times 10^{-3}$	$0.1 - 2.0 \times 10^{-4}$	1.3×10^{-2}

Table 4.7: *Computational results for Sod shock tube problem at* $t = T_f$ *with 250 elements and* $r = 2$ *employing Froese-Oberman filter function and using* $\beta_\rho = 1.4$, $\beta_{\rho\mathbf{u}} = 1.4$ *and* $\beta_{\rho E} = 1.4$. *Maximum and minimum values are referred to the corresponding variable declared in the left column.*

4.1.3 Circular explosion problem

In this Section, we consider the two-dimensional explosion problem discussed in [Dumbser et al., 2014, Zanotti et al., 2015]. This test is quite relevant since it involves the propagation of waves that are not aligned with the mesh and therefore it can be used to check the ability of the proposed method to preserve physical symmetries of the problem as well as to validate it in multiple space dimensions. The computational domain is $\Omega = (-1, 1)^2$, the final time is $T_f = 0.2\,\mathrm{s}$ and the initial condition is the following:

$$(\rho_0, u_0, v_0, p_0) = \begin{cases} (1, 0, 0, 1) & \text{if } \tilde{r} \leq R \\ (0.125, 0, 0, 1) & \text{if } \tilde{r} > R, \end{cases} \tag{4.5}$$

with $R = 0.5$ denoting the radius of initial discontinuity and $\tilde{r} = \sqrt{x^2 + y^2}$ representing the radial distance. As explained in [Toro, 2009], in two dimensions we have cylindrical symmetry and a reference solution can be computed solving a one dimensional problem in the radial direction with suitable geometric source terms. Figure 4.13 shows the results obtained using $N_{el} = 200$ elements along each direction, $r = 1$ and $\beta_\rho = \beta_{\rho\mathbf{u}} = \beta_{\rho E} = 1$. One can easily notice that the discontinuities are well reproduced, even using only first order degree polynomial for the high order method, and their position is well captured with only slight undershoots and overshoots in correspondence of the rarefaction wave.

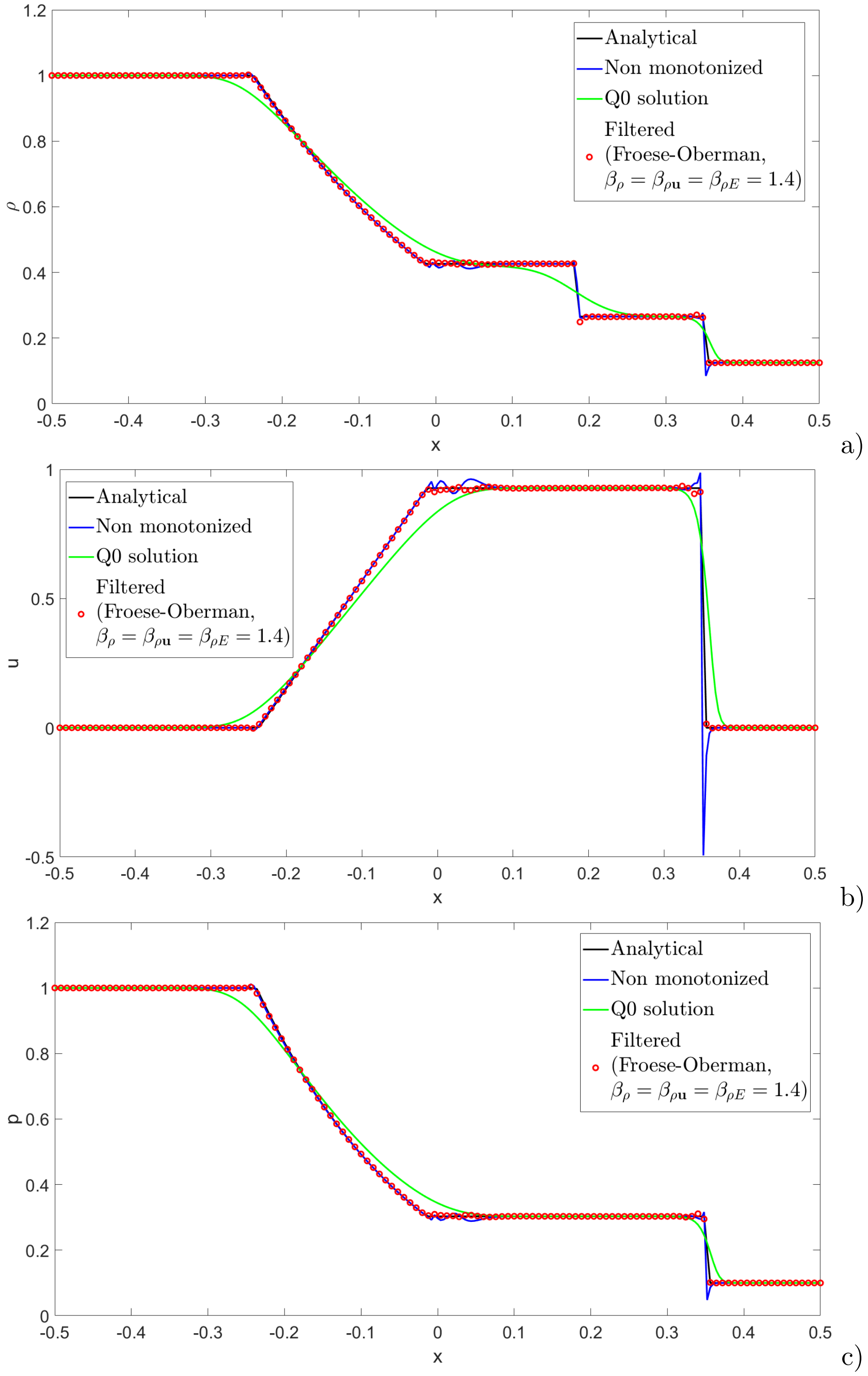

Figure 4.12: *Computational results for Sod shock tube problem at $t = T_f$ with $r = 2$, a) density, b) velocity, c) pressure. The black line reports the analytical solution, the red line denotes the non filtered Q_2 solution, the green line denotes the Q_0 solution, while the red dots represent the results of the simulation with Froese-Oberman filter function using $\beta_\rho = 1.4$, $\beta_{\rho\mathbf{u}} = 1.4$ and $\beta_{\rho E} = 1.4$.*

The same test has been repeated increasing both the spatial resolution with $N_{el} = 400$ and the high order polynomial degree with $r = 2$. Figure 4.14 reports the results obtained using $\beta_\rho = \beta_{\rho\mathbf{u}} = \beta_{\rho E} = 1.7$ and an excellent agreement

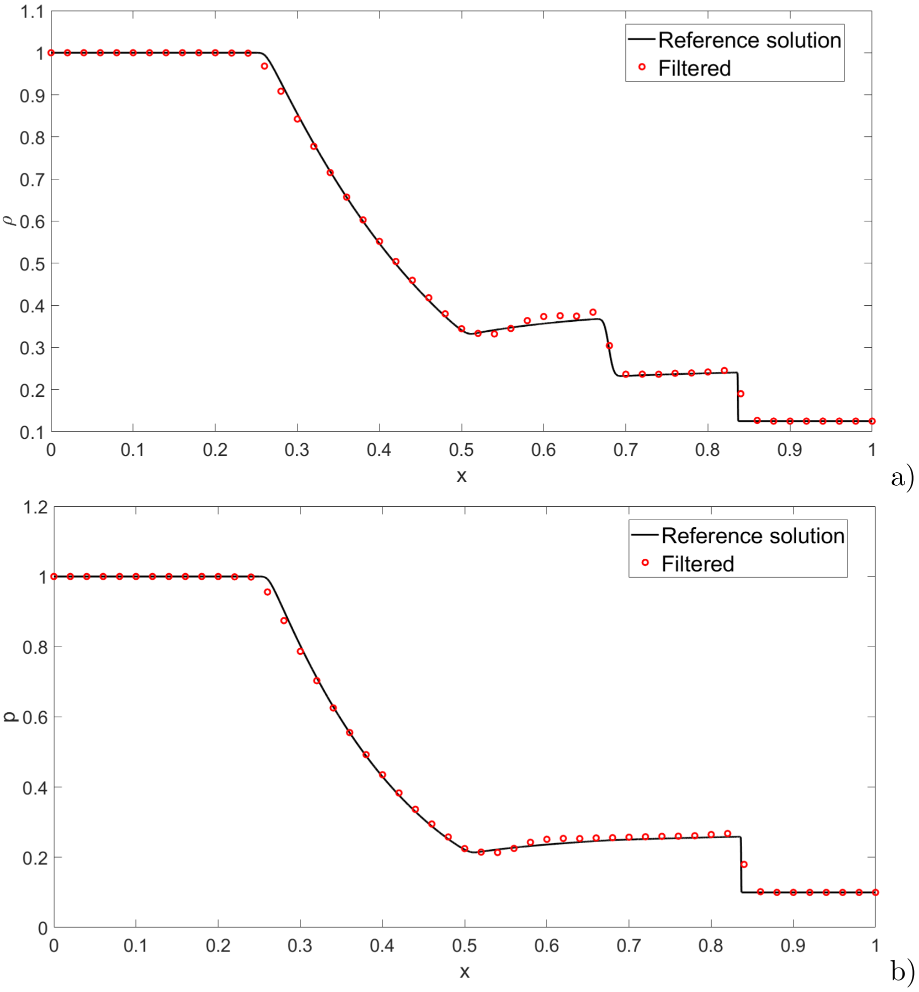

Figure 4.13: *Computational results for 2D explosion problem at $t = T_f$ with $r = 1$, a) density, b) pressure. The black line reports the reference solution computed solving the 1D problem in the radial direction, while the red dots represent the results of the simulation with Froese-Oberman filter function using $\beta_\rho = 1$, $\beta_{\rho\mathbf{u}} = 1$ and $\beta_{\rho E} = 1$.*

with the reference solution is achieved. Analogous results have been obtained in [Zanotti et al., 2015], where however polynomials of degree 9 were employed, and, for a 3D version of the problem, in [Loubère et al., 2014], with polynomials of degree 3.

Finally, we have employed the h-adaptive version of the method, starting from a coarse mesh with $N_{el} = 200$ elements along each direction and allowing up to three local refinements which would correspond to a uniform grid with $N_{el} = 1600$. The employed local indicator is based on the gradient of the density; more specifically we define for each element K

$$\eta_K = \max_{i \in \mathcal{N}_K} \left| \nabla \rho \right|_i . \tag{4.6}$$

The results for the one dimensional profiles are reported in Figure 4.15. Figure 4.16 shows the contour plot of the density and the final grid obtained at $t = T_f$ composed by 63136 elements. One can easily notice that more resolution is added in correspondence of the discontinuities.

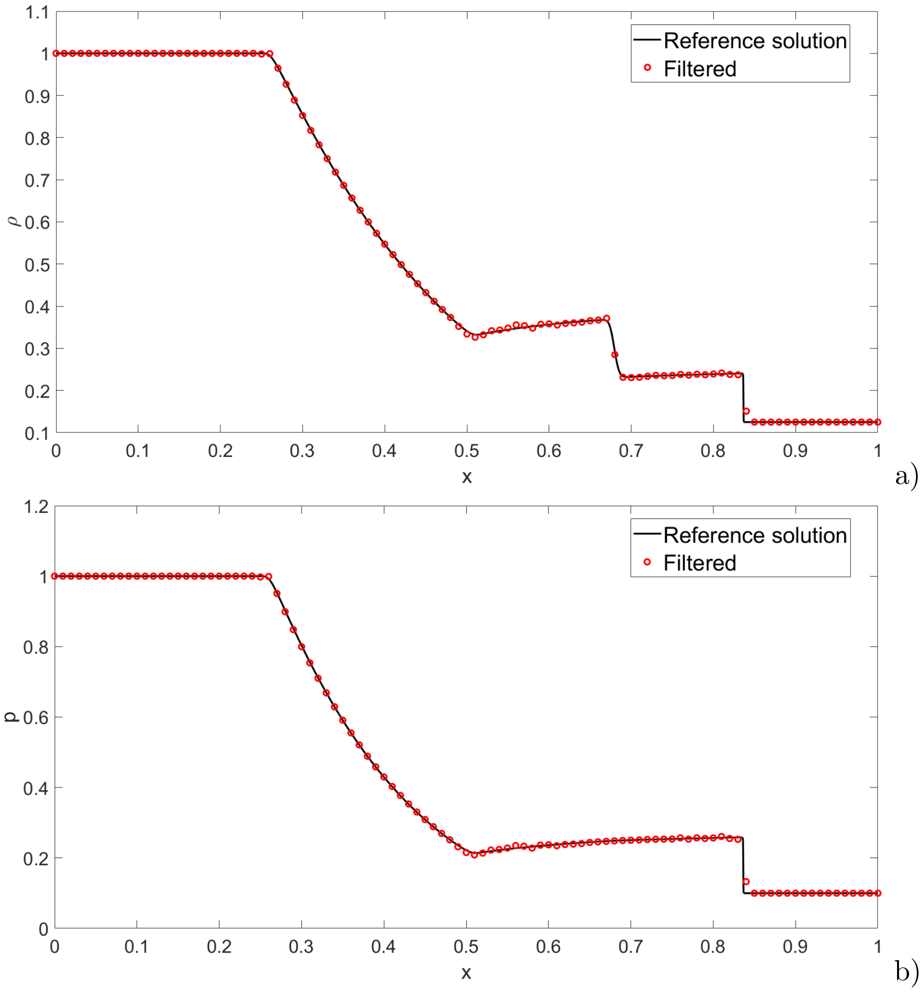

Figure 4.14: *Computational results for 2D explosion problem at* $t = T_f$ *with* $r = 2$, *a) density, b) pressure. The black line reports the reference solution computed solving the* 1*D problem in the radial direction, while the red dots represent the results of the simulation with Froese-Oberman filter function using* $\beta_\rho = 1.7$, $\beta_{\rho\mathbf{u}} = 1.7$ *and* $\beta_{\rho E} = 1.7$.

4.1.4 Two-dimensional Riemann problem

In this Section, we consider a two-dimensional Riemann problem corresponding to the Configuration 4 proposed in [Kurganov and Tadmor, 2002], which we summarize here for the convenience of the reader. The computational domain is $\Omega = (0,1)^2$ and the initial conditions are given by

$$(\rho_0, u_0, v_0, p_0) = \begin{cases} (1.1, 0, 0, 1) & \text{if } x > 0.5 \text{ and } y > 0.5 \\ (0.5065, 0.8939, 0, 0.35) & \text{if } x < 0.5 \text{ and } y > 0.5 \\ (1.1, 0.8939, 0.8939, 1.1) & \text{if } x < 0.5 \text{ and } y < 0.5 \\ (0.5065, 0, 0.8939, 0.35) & \text{if } x > 0.5 \text{ and } y < 0.5. \end{cases} \tag{4.7}$$

The final time is $T_f = 0.25\,\text{s}$. In view of the particularly challenging conditions, we employ AMR with the indicator described in (4.6) in order to enhance the resolution along strong discontinuities. The initial mesh is composed by 200 elements along each direction and we allow up to two local refinements. We consider as high order polynomial degree $r = 2$. Figure 4.17 shows the results obtained for

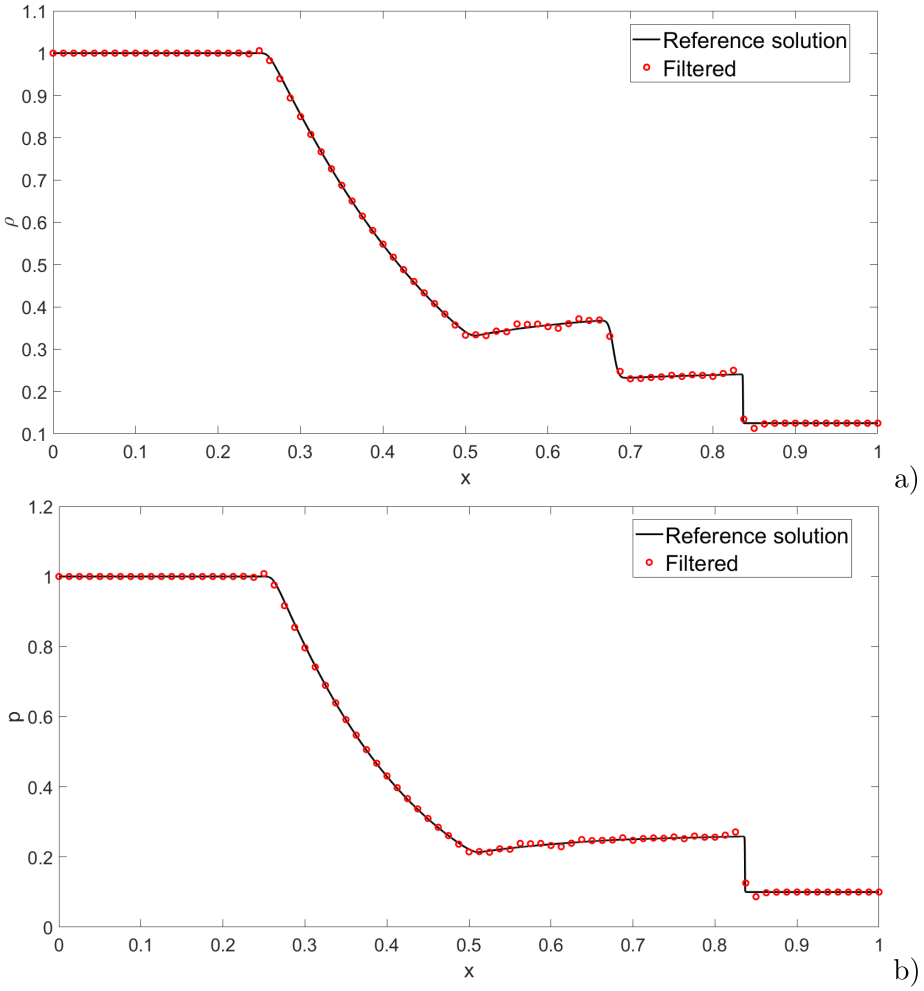

Figure 4.15: *Computational results for 2D explosion problem at $t = T_f$ with adaptive grid and $r = 2$, a) density, b) pressure. The black line reports the reference solution computed solving the $1D$ problem in the radial direction, while the red dots represent the results of the simulation with Froese-Oberman filter function using $\beta_\rho = 1.7$, $\beta_{\rho\mathbf{u}} = 1.7$ and $\beta_{\rho E} = 1.7$.*

the density using $\beta_\rho = \beta_{\rho\mathbf{u}} = \beta_{\rho E} = 0.25$. The filter tends to add more dissipation than needed, but this is necessary in order to avoid large undershoots and overshoots and more in general oscillations which completely corrupt the unfiltered solution. While not optimal, the results highlight the robustness of the proposed approach and show that the primary goal of the filter, namely avoid or at least reduce the oscillations, is achieved. Moreover, as pointed out in [Zanotti et al., 2015], the effects of Kelvin-Helmholtz instability with several small-scale features emerge at high resolution along the diagonal of the cocoon structure and this confirms that the test is particularly challenging.

4.2 Numerical results for the incompressible Navier-Stokes equations

The numerical method outlined in Section 3.3 has been validated in a number of relevant benchmarks (see also [Orlando et al., 2022b]). We define the stability

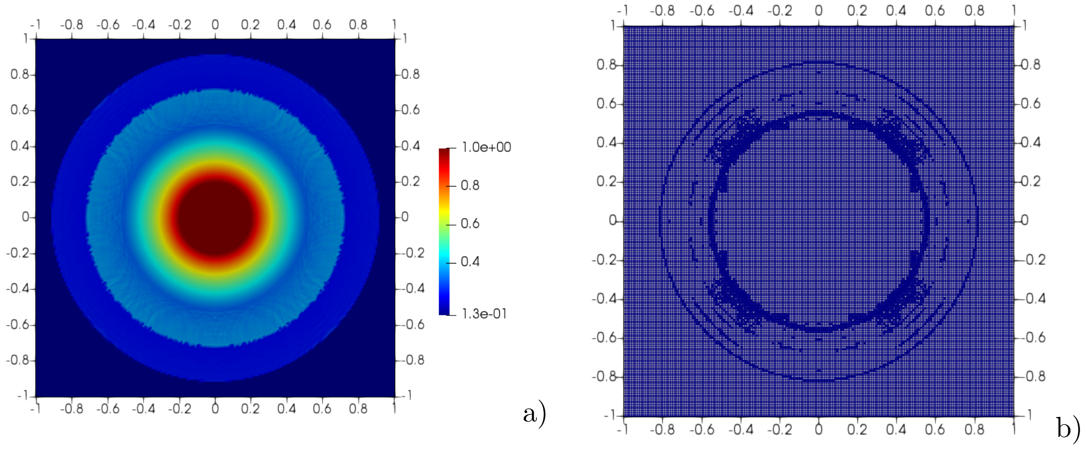

Figure 4.16: *Computational results for 2D explosion problem at $t = T_f$ with $r = 2$ and Froese-Oberman filter function using $\beta_\rho = 1.7$, $\beta_{\rho\mathbf{u}} = 1.7$ and $\beta_{\rho E} = 1.7$, a) contour plot of the density, b) adaptive grid at $t = T_f$.*

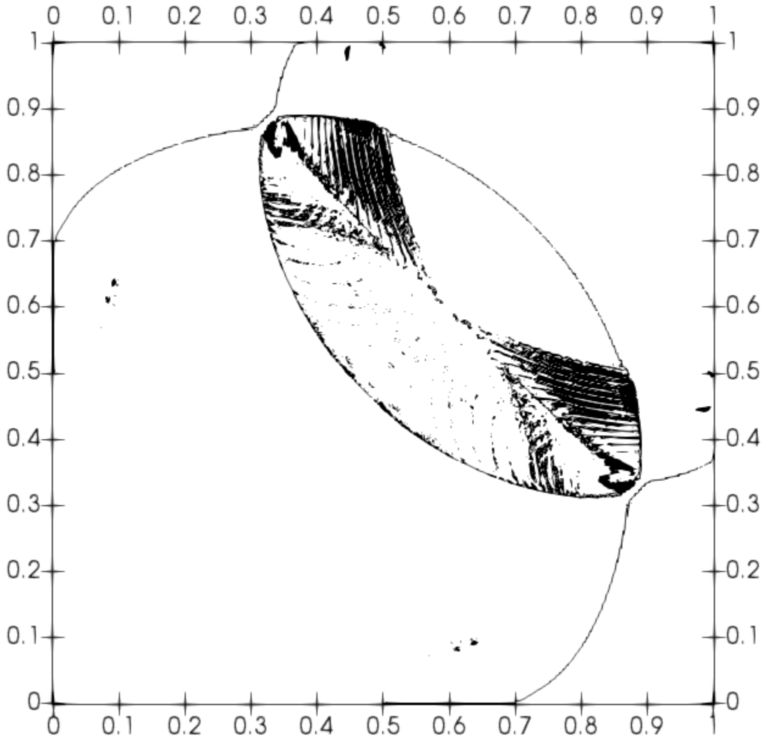

Figure 4.17: *2D Riemann problem, isolines of the density at $t = T_f$ with $r = 2$ and Froese-Oberman filter function using $\beta_\rho = 0.25$, $\beta_{\rho\mathbf{u}} = 0.25$ and $\beta_{\rho E} = 0.25$.*

parameters

$$C_u = r\mathcal{U}\Delta t/\mathcal{H}, \qquad \sigma = r^2\Delta t/(Re\mathcal{H}^2), \tag{4.8}$$

where $\mathcal{U}$ is the magnitude of a characteristic velocity and σ defines the typical stability parameter in the discretization of parabolic terms. We also recall here that r is the polynomial degree of the finite element space chosen for the discretization of the velocity. In the following tests, unless differently stated, we take the artificial speed of sound $c = 10^3$, which is the order of magnitude of the speed of sound in water.

4.2.1 Case tests with analytical solution

In order to verify the correctness of our implementation and to assess the convergence properties of the scheme, we first perform numerical convergence studies in two and three dimensions, respectively. In two dimensions, we consider as a benchmark the classical Taylor-Green vortex [Green and Taylor, 1937] in the box $\Omega = (0, 2\pi)^2$, for which an analytical solution is available:

$$\mathbf{u}(\mathbf{x}, t) = \begin{pmatrix} \cos(x)\sin(y)e^{-\frac{2t}{Re}} \\ -\sin(x)\cos(y)e^{-\frac{2t}{Re}} \end{pmatrix} \tag{4.9}$$

$$p(\mathbf{x}, t) = -\frac{1}{4}\left(\cos(2x) + \cos(2y)\right) e^{-\frac{4t}{Re}}. \tag{4.10}$$

In three dimensions, an analogous study is carried out for the Arnoldi-Beltrami-Childress (ABC) flow, see e.g. [Galloway and Frisch, 1987], whose exact solution is

$$\mathbf{u}(\mathbf{x}, t) = \begin{pmatrix} (\sin(z) + \cos(y))\, e^{-\frac{t}{Re}} \\ (\sin(x) + \cos(z))\, e^{-\frac{t}{Re}} \\ (\sin(y) + \cos(x))\, e^{-\frac{t}{Re}} \end{pmatrix}. \tag{4.11}$$

$$p(\mathbf{x}, t) = -\sin(x)\cos(z) - \sin(y)\cos(x) - \sin(z)\cos(y). \tag{4.12}$$

For the two dimensional case, we performed a convergence test at $T_f = 3.2$ for $Re = 100$ starting with an initial Cartesian mesh of 8×8 elements and doubling several times the number of elements N_{el} in each direction. The time step was chosen so as to keep $C_u = 1.63$ constant for all resolutions (hyperbolic scaling), so as to test the accuracy of the method for values of the time steps beyond the stability limit of explicit schemes but not large enough to affect the second order accuracy. The results for the $\mathbf{Q}_2 - Q_1$ and $\mathbf{Q}_3 - Q_2$ cases are reported in Tables 4.8, 4.9 and 4.10, 4.11, respectively. It can be observed that the expected convergence rates are recovered, without the necessity of employing fixed point iterations to determine the velocity in the two stages of the TR-BDF2 scheme. Analogous results are obtained, see Table 4.12, 4.13 if distorted meshes with similar characteristics are employed. As mentioned in Section 3.3, when we increase the Courant number, also the TR-BDF2 scheme requires fixed point iterations in the momentum predictor stages in order to preserve its accuracy. As it can be noticed in Tables 4.14, 4.15 that the second order convergence rate is still maintained.

For the three dimensional case, an analogous convergence test was performed again at $T_f = 3.2$ but using $Re = 1$, due to the stability characteristics of the ABC flow, see e.g. the discussion in [Galloway and Frisch, 1987]. We have considered an initial Cartesian mesh of $8 \times 8 \times 8$ elements and we have refined the mesh by doubling each time the number of elements N_{el} in each direction, while keeping $C_u = 1.63$ constant (hyperbolic scaling). The results for the $\mathbf{Q}_2 - Q_1$ and $\mathbf{Q}_3 - Q_2$ cases are reported in Tables 4.16, 4.17 and 4.18, 4.19, respectively. It can be observed that the expected convergence rates are recovered for the lower degree case, also in this case without the necessity of fixed point iterations, while less accurate results are obtained in the higher degree case. Since in this case the problem is diffusion dominated, rather than advection dominated, the loss of accuracy can be readily explained by the very large values obtained in this test for the parabolic stability parameter σ. Repeating the test at constant σ (parabolic scaling), one obtains the results displayed in Tables 4.20, 4.21 and 4.22, 4.23, which show a clear improvement both in errors and convergence rates.

We have also used the two dimensional Taylor Green benchmark at $Re = 100$ to compare our results with analogous simulations carried out using using the classical PISO method [Issa et al., 1986] as implemented in the OpenFoam package [Chen et al., 2014]. In both cases, the computation was carried out at a very small value of the Courant number, so that the spatial discretization error is dominant. We are aware of the difficulties of comparing different discretizations schemes both in space and time implemented in different frameworks and, therefore, the following analysis has to be interpreted merely as first stress test to highlight the superior flexibility of the proposed DG implementation. We have performed a test using both $\mathbf{Q}_2 - Q_1$ and $\mathbf{Q}_3 - Q_2$ elements on regular and distorted meshes. An example of the coarsest distorted mesh is shown in Figure 4.18, while the results of the convergence test for both L^2 and L^∞ norms are reported in Figure 4.19. While the OpenFoam discretization appears to outperform the $\mathbf{Q}_2 - Q_1$ DG approximation at lower resolutions, it can be seen that it is much more sensitive to the mesh distortion than DG approximations, especially with respect to L^∞ errors. Furthermore, as expected from polynomial approximation theory, the $\mathbf{Q}_3 - Q_2$ DG approximation clearly shows its faster convergence properties, which are achieved within the same mathematical and implementation framework. Instead, as also discussed in Section 3.1, higher order accuracy for finite volume formulations entails the use of complex and often *ad hoc* reconstruction procedures with large stencils.

Δt	N_{el}	σ	H^1 rel. error $\mathbf{u}$	H^1 rate $\mathbf{u}$	L^2 rel. error $\mathbf{u}$	L^2 rate $\mathbf{u}$
0.64	8	0.04	1.5×10^0		3.8×10^{-1}	
0.32	16	0.08	6.5×10^{-1}	1.22	9.5×10^{-2}	2.01
0.16	32	0.17	1.2×10^{-1}	2.45	1.6×10^{-2}	2.58
0.08	64	0.33	2.3×10^{-2}	2.38	3.1×10^{-3}	2.37

Table 4.8: *Convergence test for the Green-Taylor vortex benchmark computed at* $C_u = 1.63$ *with* $\mathbf{Q}_2 - Q_1$ *elements, relative errors for the velocity in* H^1 *and* L^2 *norms.*

Δt	N_{el}	σ	L^2 rel. error p	L^2 rate p
0.64	8	0.04	4.3×10^{-1}	
0.32	16	0.08	1.4×10^{-1}	1.60
0.16	32	0.17	4.0×10^{-2}	1.72
0.08	64	0.33	1.1×10^{-2}	1.91

Table 4.9: *Convergence test for the Green-Taylor vortex benchmark computed at* $C_u = 1.63$ *with* $\mathbf{Q}_2 - Q_1$ *elements, relative errors for the pressure in* L^2 *norm.*

Δt	N_{el}	σ	H^1 rel. error $\mathbf{u}$	H^1 rate $\mathbf{u}$	L^2 rel. error $\mathbf{u}$	L^2 rate $\mathbf{u}$
0.43	8	0.06	2.8×10^{-1}		6.2×10^{-2}	
0.21	16	0.12	3.3×10^{-2}	3.12	6.8×10^{-2}	3.18
0.11	32	0.25	4.4×10^{-3}	2.88	4.4×10^{-4}	3.93
0.053	64	0.50	5.9×10^{-4}	2.92	3.1×10^{-5}	3.85

Table 4.10: *Convergence test for the Green-Taylor vortex benchmark computed at* $C_u = 1.63$ *with* $\mathbf{Q}_3 - Q_2$ *elements, relative errors for the velocity in* H^1 *and* L^2 *norms.*

Δt	N_{el}	σ	L^2 rel. error p	L^2 rate p
0.43	8	0.06	8.7×10^{-2}	
0.21	16	0.12	1.1×10^{-2}	2.93
0.11	32	0.25	7.5×10^{-4}	3.92
0.053	64	0.50	2.9×10^{-5}	4.72

Table 4.11: *Convergence test for the Green-Taylor vortex benchmark computed at* $C_u = 1.63$ *with* $\mathbf{Q}_3 - Q_2$ *elements, relative errors for the pressure in* L^2 *norm.*

Δt	N_{el}	σ	H^1 rel. error $\mathbf{u}$	H^1 rate $\mathbf{u}$	L^2 rel. error $\mathbf{u}$	L^2 rate $\mathbf{u}$
0.52	8	0.05	1.2×10^{0}		3.2×10^{-1}	
0.22	16	0.12	5.5×10^{-1}	1.13	8.1×10^{-2}	1.96
0.11	32	0.25	1.2×10^{-1}	2.16	1.2×10^{-2}	2.77
0.052	64	0.50	2.1×10^{-2}	2.51	2.3×10^{-3}	2.41

Table 4.12: *Convergence test for the Green-Taylor vortex benchmark computed on a distorted mesh at* $C_u = 1.63$ *with* $\mathbf{Q}_2 - Q_1$ *elements, relative errors for the velocity in* H^1 *and* L^2 *norms.*

Δt	N_{el}	σ	L^2 rel. error p	L^2 rate p
0.52	8	0.05	4.3×10^{-1}	
0.22	16	0.12	7.7×10^{-2}	2.02
0.11	32	0.25	2.4×10^{-2}	1.68
0.052	64	0.50	6.4×10^{-3}	1.91

Table 4.13: *Convergence test for the Green-Taylor vortex benchmark computed on a distorted mesh at* $C_u = 1.63$ *with* $\mathbf{Q}_2 - Q_1$ *elements, relative errors for the pressure in* L^2 *norm.*

Δt	N_{el}	σ	H^1 rel. error $\mathbf{u}$	H^1 rate $\mathbf{u}$	L^2 rel. error $\mathbf{u}$	L^2 rate $\mathbf{u}$
1.18	8	0.08	1.33×10^{0}		3.9×10^{-1}	
0.59	16	0.15	6.3×10^{-1}	1.07	1.1×10^{-1}	1.79
0.29	32	0.31	1.2×10^{-1}	2.35	2.8×10^{-2}	2.02
0.15	64	0.61	2.8×10^{-2}	2.17	5.9×10^{-3}	2.23

Table 4.14: *Convergence test for the Green-Taylor vortex benchmark computed at* $C_u = 3$ *with* $\mathbf{Q}_2 - Q_1$ *elements, relative errors for the velocity in* H^1 *and* L^2 *norms.*

Δt	N_{el}	σ	L^2 rel. error p	L^2 rate p
1.18	8	0.08	4.9×10^{-1}	
0.59	16	0.15	1.3×10^{-1}	1.87
0.29	32	0.31	4.0×10^{-2}	1.60
0.15	64	0.61	1.3×10^{-2}	1.75

Table 4.15: *Convergence test for the Green-Taylor vortex benchmark computed at* $C_u = 3$ *with* $\mathbf{Q}_2 - Q_1$ *elements, relative errors for the pressure in* L^2 *norm.*

Δt	N_{el}	σ	H^1 rel. error $\mathbf{u}$	H^1 rate $\mathbf{u}$	L^2 rel. error $\mathbf{u}$	L^2 rate $\mathbf{u}$
0.32	8	2.08	1.9×10^{-2}		7.8×10^{-3}	
0.16	16	4.15	5.4×10^{-3}	1.85	2.2×10^{-3}	1.86
0.08	32	8.30	1.4×10^{-3}	1.98	5.6×10^{-4}	1.99
0.04	64	16.60	3.6×10^{-4}	1.91	1.7×10^{-4}	1.75

Table 4.16: *Convergence test for the ABC flow benchmark computed at* $C_u = 1.63$ *with* $\mathbf{Q}_2 - Q_1$ *elements, relative errors for the velocity in* H^1 *and* L^2 *norms.*

Δt	N_{el}	σ	L^2 rel. error p	L^2 rate p
0.32	8	2.08	1.0×10^{0}	
0.16	16	4.15	1.3×10^{-1}	2.93
0.08	32	8.30	3.9×10^{-2}	1.74
0.04	64	16.60	1.1×10^{-2}	1.79

Table 4.17: *Convergence test for the ABC flow benchmark computed at* $C_u = 1.63$ *with* $\mathbf{Q}_2 - Q_1$ *elements, relative errors for the pressure in* L^2 *norm.*

Δt	N_{el}	σ	H^1 rel. error $\mathbf{u}$	H^1 rate $\mathbf{u}$	L^2 rel. error $\mathbf{u}$	L^2 rate $\mathbf{u}$
0.21	8	3.11	3.6×10^{-3}		1.9×10^{-3}	
0.11	16	6.23	1.0×10^{-3}	1.80	6.8×10^{-3}	2.05
0.053	32	12.45	3.7×10^{-4}	1.5	1.4×10^{-4}	1.68

Table 4.18: *Convergence test for the ABC flow benchmark computed at* $C_u = 1.63$ *with* $\mathbf{Q}_3 - Q_2$ *elements, relative errors for the velocity in* H^1 *and* L^2 *norms.*

Δt	N_{el}	σ	L^2 rel. error p	L^2 rate p
0.21	8	3.11	2.5×10^{-1}	
0.11	16	6.23	3.3×10^{-2}	2.93
0.053	32	12.45	9.7×10^{-3}	1.72

Table 4.19: *Convergence test for the ABC flow benchmark computed at* $C_u = 1.63$ *with* $\mathbf{Q}_3 - Q_2$ *elements, relative errors for the pressure in* L^2 *norm.*

Δt	N_{el}	C_u	H^1 rel. error $\mathbf{u}$	H^1 rate $\mathbf{u}$	L^2 rel. error $\mathbf{u}$	L^2 rate $\mathbf{u}$
0.32	8	1.57	1.9×10^{-2}		7.1×10^{-3}	
0.08	16	0.79	4.5×10^{-3}	2.05	1.3×10^{-3}	2.5
0.02	32	0.39	1.2×10^{-3}	1.97	3.1×10^{-4}	2.02
0.005	64	0.20	2.9×10^{-4}	1.98	5.3×10^{-5}	2.54

Table 4.20: *Convergence test for the ABC flow benchmark computed at* $\sigma = 2$ *with* $\mathbf{Q}_2 - Q_1$ *elements, relative errors for the velocity in* H^1 *and* L^2 *norms.*

Δt	N_{el}	C_u	L^2 rel. error p	L^2 rate p
0.32	8	1.57	1.0×10^{-1}	
0.08	16	0.79	1.6×10^{-1}	2.66
0.02	32	0.39	4.2×10^{-2}	1.93
0.005	64	0.20	1.1×10^{-2}	1.94

Table 4.21: *Convergence test for the ABC flow benchmark computed at* $\sigma = 2$ *with* $\mathbf{Q}_2 - Q_1$ *elements, relative errors for the pressure in* L^2 *norm.*

Δt	N_{el}	C_u	H^1 rel. error $\mathbf{u}$	H^1 rate $\mathbf{u}$	L^2 rel. error $\mathbf{u}$	L^2 rate $\mathbf{u}$
0.14	8	1.05	2.5×10^{-3}		8.9×10^{-4}	
0.034	16	0.52	2.4×10^{-4}	2.70	1.1×10^{-4}	3.08
0.0086	32	0.26	7.1×10^{-5}	1.78	1.8×10^{-5}	2.51

Table 4.22: *Convergence test for the ABC flow benchmark computed at* $\sigma = 2$ *with* $\mathbf{Q}_3 - Q_2$ *elements, relative errors for the velocity in* H^1 *and* L^2 *norms.*

Δt	N_{el}	C_u	L^2 rel. error p	L^2 rate p
0.14	8	1.05	2.0×10^{-1}	
0.034	16	0.52	2.7×10^{-2}	2.89
0.0086	32	0.26	4.3×10^{-3}	2.65

Table 4.23: *Convergence test for the ABC flow benchmark computed at* $\sigma = 2$ *with* $\mathbf{Q}_3 - Q_2$ *elements, relative errors for the pressure in* L^2 *norm.*

4.2.2 Two-dimensional lid-driven cavity

The lid-driven cavity flow is a classical benchmark for the two-dimensional incompressible Navier-Stokes equations. Reference solutions obtained with high order techniques are reported, among many others, in [Botella and Peyret, 1998, Auteri et al., 2002, Bruneau and Saad, 2006]. For this two-dimensional problem, is it customary to represent the flow also in terms of the streamfunction Ψ, which is defined as the solution of the Laplace problem

$$\begin{aligned} -\Delta\Psi = \nabla \times \mathbf{u} = \omega \qquad \text{in } \Omega \\ \Psi|_{\partial\Omega} = 0 \end{aligned} \tag{4.13}$$

where the symbol $\nabla\times$ denotes the curl operator and the vorticity ω is therefore the scalar field defined as

$$\omega = \frac{\partial v}{\partial x} - \frac{\partial u}{\partial y}. \tag{4.14}$$

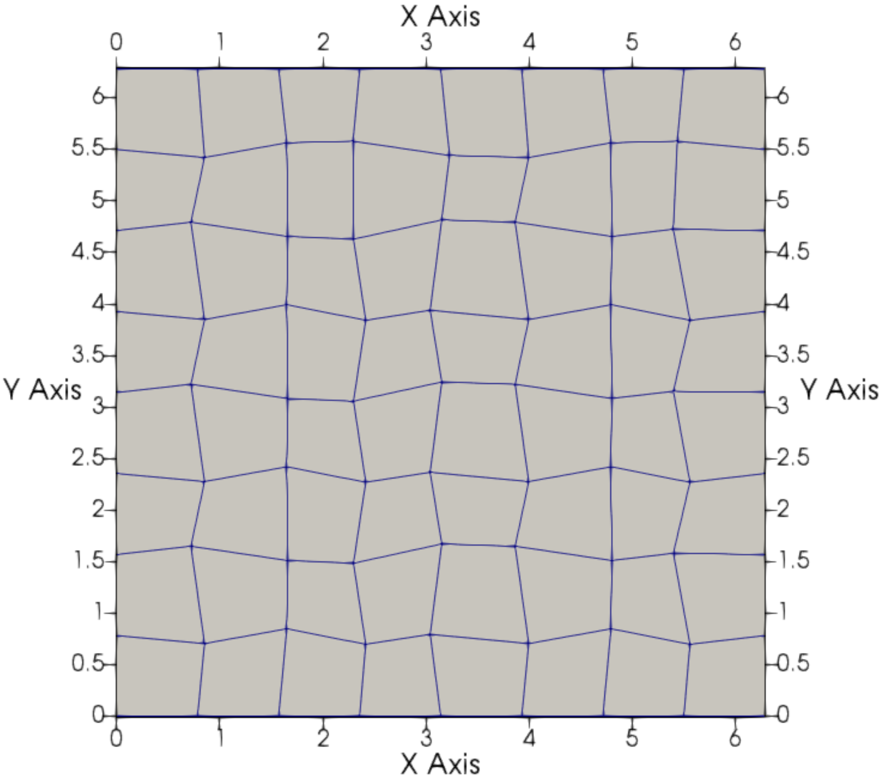

Figure 4.18: *Example of distorted mesh for the Taylor-Green vortex*

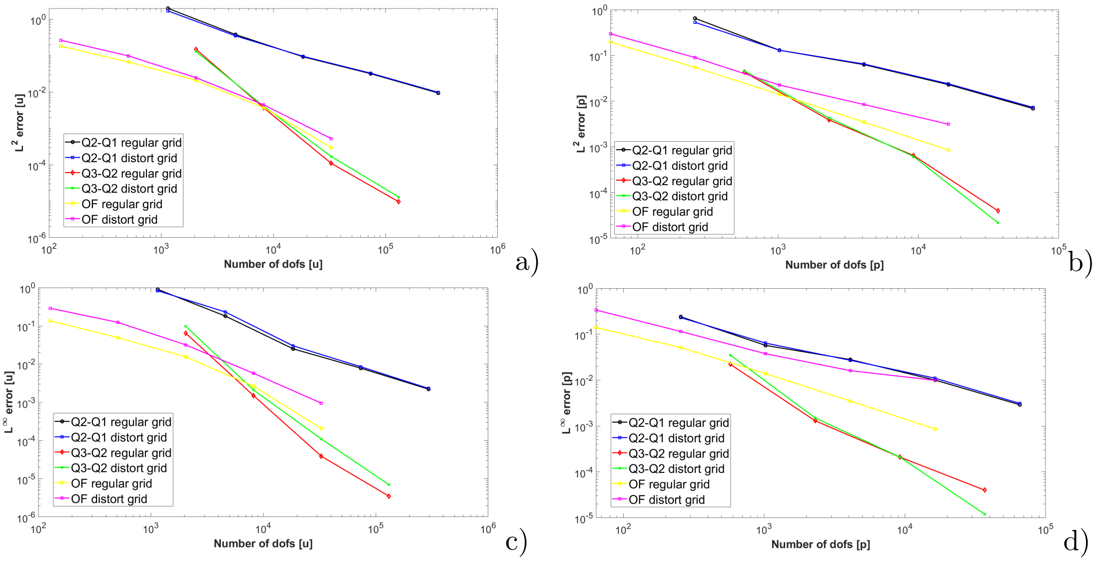

Figure 4.19: *Taylor-Green vortex at* $Re = 100$ *and* $t = 3.2$*, absolute errors as function of the number of degrees of freedom, a)* L^2 *errors for the velocity, b)* L^2 *errors for the pressure, c)* L^∞ *errors for the velocity, d)* L^∞ *errors for the pressure. The black line denotes the solution with* $\mathbf{Q}_2 - Q_1$ *on regular grids, the blue line represents the results with* $\mathbf{Q}_2 - Q_1$ *on distort grids, the red line reports the results with* $\mathbf{Q}_3 - Q_2$ *on regular grids, the green line denotes the solution with* $\mathbf{Q}_3 - Q_2$ *on distort grids, the yellow line represents the results with OpenFoam on regular grids and the magenta line represents the results with OpenFoam on distort grids.*

We consider the case $Re = 1000$ computed with $\mathbf{Q}_2 - Q_1$ elements on a Cartesian mesh composed of $N_{el} = 128$ square elements in each coordinate direction, with a time step chosen so that the Courant number C_u is approximately 1.3. The computation is performed until the steady state is reached up to a tolerance of 10^{-7}, which occurs around $T_f = 70$. The streamfunction contours at steady state are shown in Figure 4.20 using the same isoline values as in [Bruneau and Saad, 2006]. It can be observed that all the main flow structures are correctly reproduced.

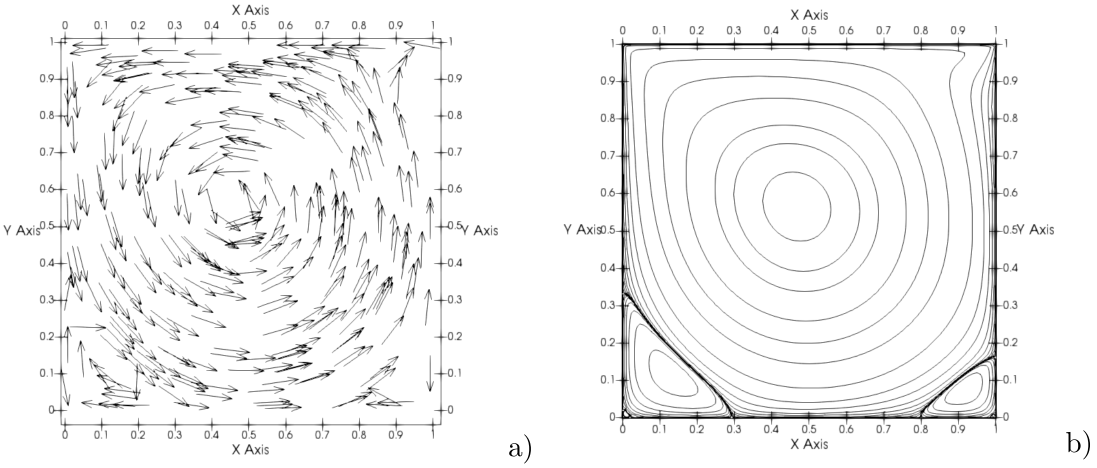

Figure 4.20: *Lid-driven cavity benchmark at* $Re = 1000$*: a) flow field, b) streamfunction contours. Contour values are chosen as in [Bruneau and Saad, 2006].*

For a more quantitative comparison, we report in Figure 4.21 the u component of the velocity and the vorticity ω along the middle of the cavity, together with the reference results of [Botella and Peyret, 1998]. Good agreement with the reference solution is achieved. The maximum horizontal velocity along the centerline was computed as $u_{max} = 0.3732$ which implies a relative error with respect to the reference solution of the order of 10^{-2}. The vorticity value at the center of the cavity was computed as $\omega_{cen} = 1.9594$, which implies again a relative error with respect to the reference solution of the order of 10^{-2}.

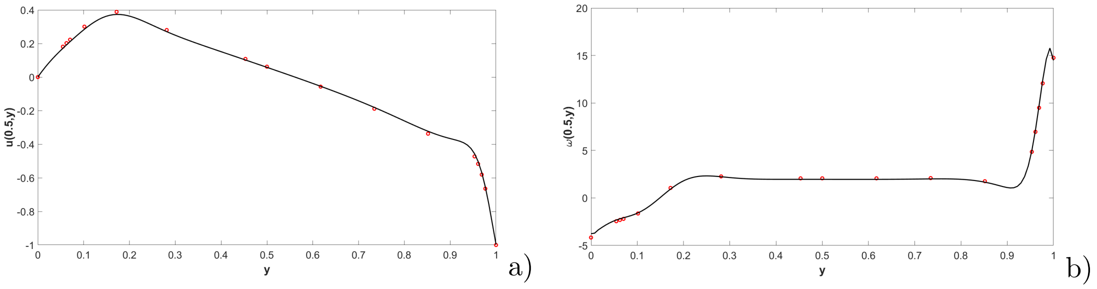

Figure 4.21: *Lid-driven cavity benchmark at* $Re = 1000$*: a) u velocity component values along the middle of the cavity, b) ω values along the middle of the cavity. The continuous line denotes the numerical solution and the dots the reference solution values from [Botella and Peyret, 1998].*

We have also repeated this test using the adaptive tools present in the *deal.II* library. In each element K we define the quantity

$$\eta_K = \mathrm{diam}(K)^2 \left\|\boldsymbol{\omega}\right\|_K^2 \tag{4.15}$$

that acts as local refinement indicator. We then started from a uniform Cartesian mesh with $N_{el} = 8$ in each coordinate direction and we allowed refinement or coarsening based on the distribution of the values of η_K, refining 10% of the elements with largest indicator values and coarsening 30% of the elements with the smallest indicator values. This remeshing procedure was carried out every 1000 time steps. However, in order to avoid using a too coarse mesh for too long in the initial stages of the simulation, every 50 time steps the maximum difference between the velocities at two consecutive time steps was checked and the remeshing was performed whenever this quantity was greater then 10^{-2}. The minimum element diameter allowed was $\mathcal{H} = \frac{1}{128}$, so as to obtain again $C_u \approx 1.3$. A maximum element diameter equal to $\frac{1}{32}$ was also required, in order to avoid an excessive reduction of the spatial resolution. The final adapted mesh and the streamline contours are reported in Figure 4.22. It can be observed that the refinement indicator allows to enhance automatically the resolution along the top boundary of the domain and in other regions of large vorticity values.

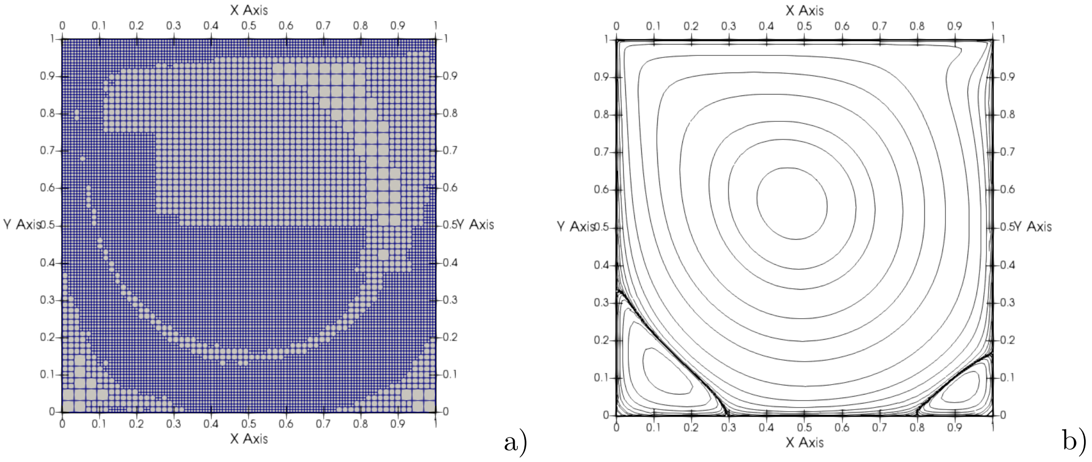

Figure 4.22: *Lid-driven cavity benchmark at Re* = 1000*, adaptive simulation: a) final mesh after adaptive refinement, b) streamfunction contours. Contour values as in [Bruneau and Saad, 2006].*

For a more quantitative point of view, we compare again in Figure 4.23 the u component of the velocity and the vorticity ω along the middle of the cavity with the reference results in [Botella and Peyret, 1998]. The maximum horizontal velocity along the centerline is now $u_{max} = 0.3739$ which implies a relative error of the order of 10^{-2}, as in the corresponding non adaptive simulation. The vorticity value at the center of the cavity is now $\omega_{cen} = 1.9652$, which also implies a relative error with respect to the reference solution of the order of 10^{-2}. In Figure 4.24, instead, the absolute difference between the velocities computed in the fixed mesh and adaptive simulations is plotted over the whole domain, showing that no substantial loss of accuracy has occurred. This result has been obtained with a reduction of about 25% of the required computational time. While showing the potential of the adaptivity procedures available in the present implementation, this is still far from optimal. Experiments with more specific error indicators and less restrictive options for the refinement parameters will be carried out in future work.

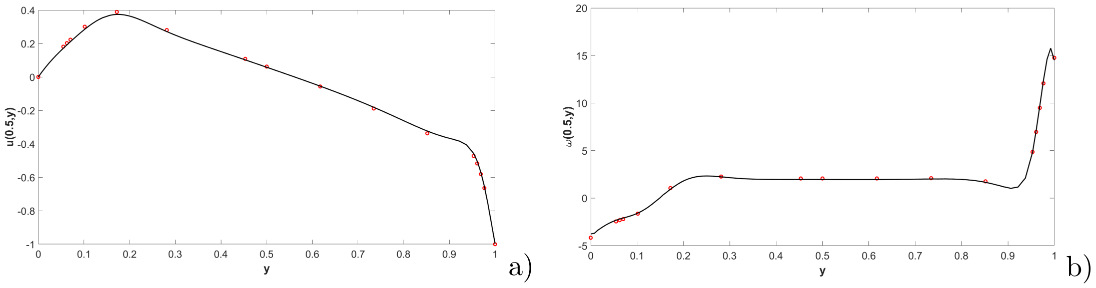

Figure 4.23: *Lid-driven cavity benchmark at* $Re = 1000$*, adaptive simulation: a)* u *velocity component values along the middle of the cavity, b)* ω *values along the middle of the cavity. The continuous line denotes the numerical solution and the dots the reference solution values from [Botella and Peyret, 1998].*

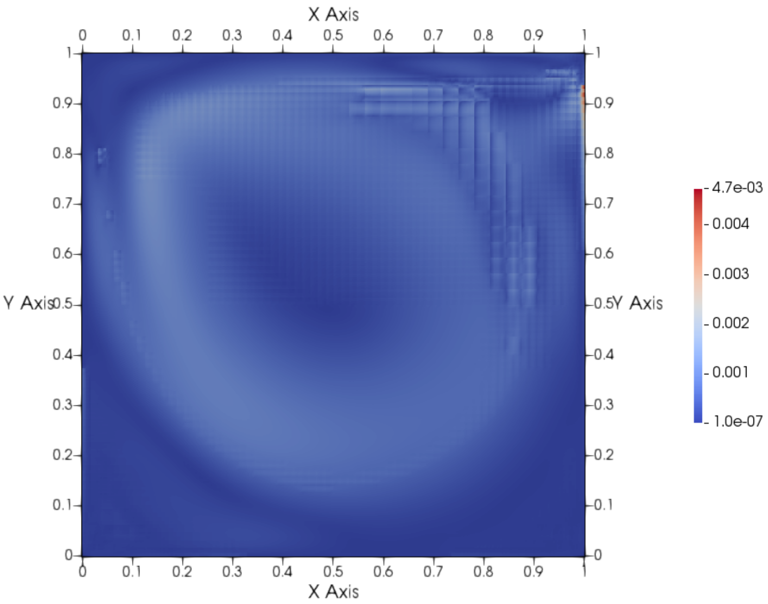

Figure 4.24: *Lid-driven cavity benchmark at* $Re = 1000$*, difference for velocity magnitude between the fixed grid simulation and the adaptive simulation (interpolated to the fixed grid).*

4.2.3 Three-dimensional lid-driven cavity

We now consider the three-dimensional analogue of the previously studied lid-driven cavity benchmark. Among several others, we consider the configuration and reference solutions provided in [Albensoeder and Kuhlmann, 2005], which we summarize here for convenience. We consider a rectangular cavity of the size $d \times h \times l$ in the x, y and z direction, respectively. The flow is driven by the wall at $x = \frac{d}{2}$, which moves tangentially in the y direction with constant velocity V. The length d is used to introduce non dimensional space variables, so that the effective computational domain is given by

$$\Omega = \left[-\frac{h}{2d}, \frac{h}{2d}\right] \times \left[-\frac{1}{2}, \frac{1}{2}\right] \times \left[-\frac{l}{2d}, \frac{l}{2d}\right].$$

We have considered here the $\frac{h}{d} = 1$, $\frac{l}{d} = 1$ case, computed with $\mathbf{Q}_2 - Q_1$ elements on a Cartesian mesh composed of $64 \times 64 \times 48$ square elements, with a time step chosen so that the Courant number is approximately 1. Notice that the same mesh was employed in [Albensoeder and Kuhlmann, 2005], in which however the authors employed a much more accurate spectral collocation method. The computation is performed until the steady state is reached up to a tolerance of 10^{-4}, which is achieved around $T_f = 40$. We take as reference results those presented in Tables 5 and 6 in [Albensoeder and Kuhlmann, 2005]. Notice that, in that paper, a different non dimensional scaling is employed, so that their results have been appropriately rescaled in order to compare them with those obtained here. In Figure 4.25 we report the results for the v velocity component values along the x axis and the u component of the velocity along the y axis, respectively. We see that, in spite of the relatively coarse mesh, a reasonable accuracy is achieved.

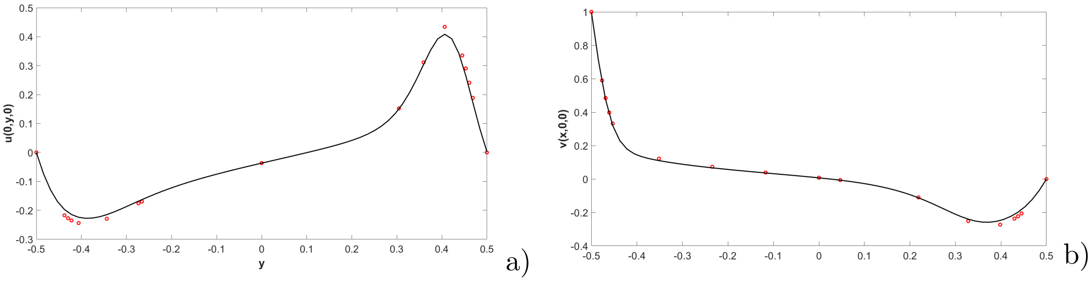

Figure 4.25: *3D lid-driven cavity benchmark at Re* $= 1000$*, fixed mesh simulation, a)* v *velocity component values along the* x *axis b)* u *velocity component values along the* y *axis. The continuous line denotes the numerical solution and the dots the reference solution values from [Albensoeder and Kuhlmann, 2005].*

In Figure 4.26 and 4.27 we show instead the velocity field on the three median plane sections of the cavity, highlighting the presence of vortices near the centerline of the cavity. The results are in good qualitative agreement with those reported in [Jiang et al., 1994].

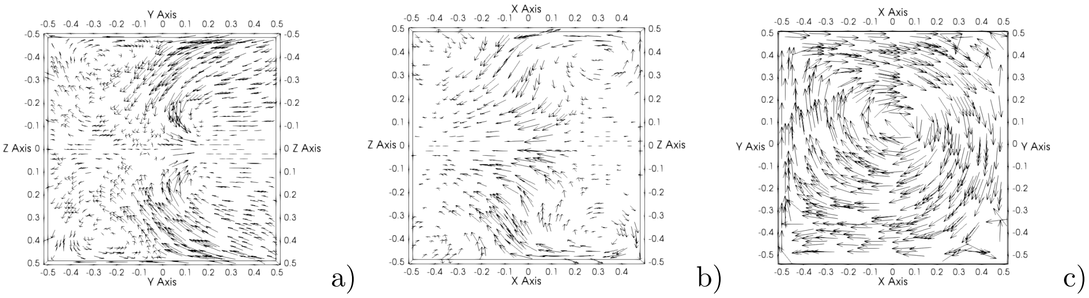

Figure 4.26: *3D lid-driven cavity benchmark at Re* $= 1000$*, a) flow field vectors for the plane* $x = 0$*, b) flow field vectors for the plane* $y = 0$*, c) flow field vectors for the plane* $z = 0$.

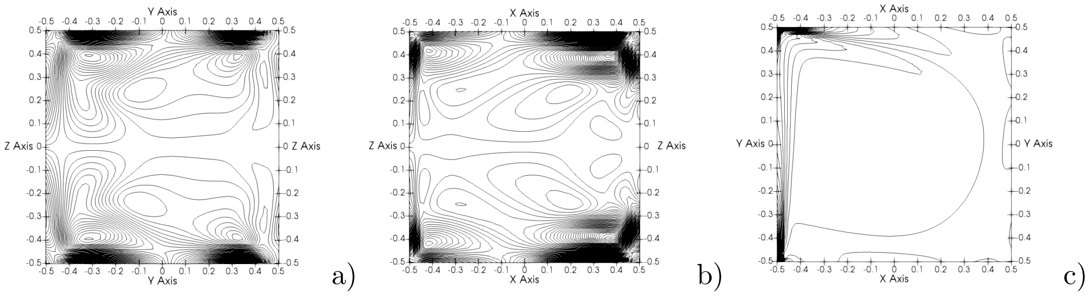

Figure 4.27: *3D lid-driven cavity benchmark at* $Re = 1000$*, a) vorticity* (ω_x) *contours at* $x = 0$*, b) vorticity* (ω_y) *contours at* $y = 0$*, vorticity* (ω_z) *contours at* $z = 0$*.*

We have also exploited again the mesh adaptivity tool provided by *deal.II* with the same refinement indicator (4.15) introduced for the two-dimensional test. In particular, we started from a coarse mesh with $N_{el} = 6$ elements along each direction and again we performed the refinement procedure on at most 10% of the elements with the largest indicator value every 1000 time steps, while coarsening on at most 30% of the elements with the smallest indicator values; moreover we have checked every 50 time steps if the refinement procedure had to be performed in advance in case the maximum difference between the velocities at two consecutive time steps was greater then 10^{-2}. The minimum element diameter allowed was $\mathcal{H} = \frac{1}{48}$ in order to obtain $C_u \approx 1$. In Figure 4.28 and in Figure 4.29 we report again the results for the v velocity component values along the x axis and the u component of the velocity along the y axis, respectively, compared with the results obtained using a fixed grid with $N_{el} = 48$ elements along each direction. One can notice very good agreement between the two simulations, while the computational time required to perform the adaptive simulation is about half of that required by the fixed grid simulation. Moreover, we have compared in Figure 4.30 the errors of the two components for the velocity for the fixed and adaptive mesh, respectively. It is clear that, in spite of the different computational time, no significant differences arise.

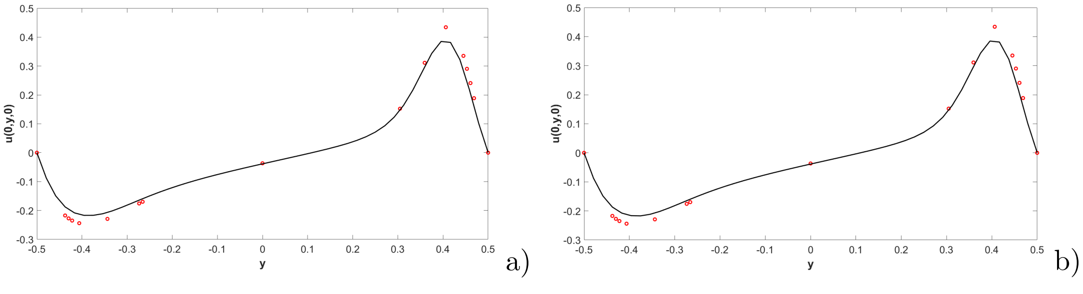

Figure 4.28: *3D lid-driven cavity benchmark at* $Re = 1000$*, a)* u *velocity component values along the* y *axis for adaptive mesh simulation, b)* u *velocity component values along the* y *axis for fixed grid simulation. The continuous line denotes the numerical solution, whereas the dots denote the reference solution values from [Albensoeder and Kuhlmann, 2005].*

The size of the configuration employed for this test (we have used 15925248 dofs for the velocity and 1572864 dofs for the pressure) makes this benchmark a good candidate for a parallel scaling test. More specifically, we have performed a strong scaling analysis executing the same simulation up to time $t = 0.6$ us-

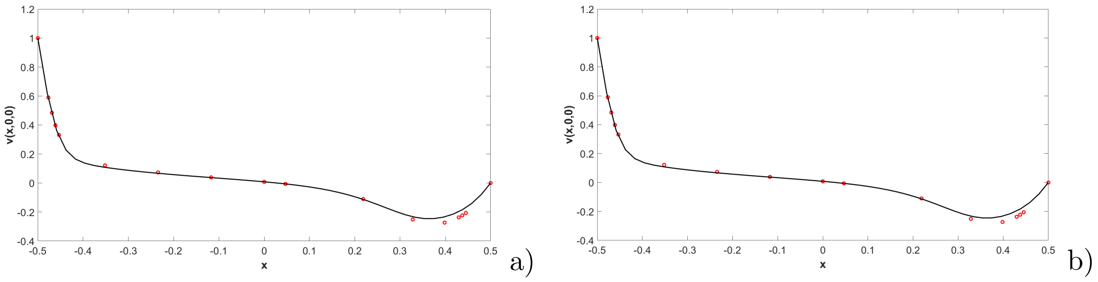

Figure 4.29: *3D lid-driven cavity benchmark at Re* $= 1000$, *a) v velocity component values along the* x *axis for adaptive mesh simulation, b) v velocity component values along the* x *axis for fixed grid simulation. The continuous line denotes the numerical solution, whereas the dots denote the reference solution values from [Albensoeder and Kuhlmann, 2005].*

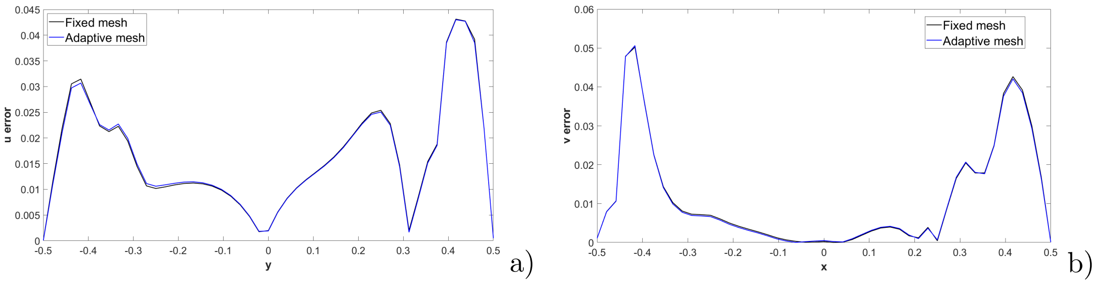

Figure 4.30: *3D lid-driven cavity benchmark at Re* $= 1000$, *a) u velocity component comparison for the plane* $x = 0, z = 0$ *with reference solution values from [Albensoeder and Kuhlmann, 2005] interpolated, b) v velocity component comparison for the plane* $y = 0, z = 0$ *with reference solution values from [Albensoeder and Kuhlmann, 2005] interpolated. The continuous black line denotes the result with fixed mesh, the blue one denotes the results with Adaptive Mesh Refinement.*

ing from 16 up to 1024 2xCPU x86 Intel Xeon Platinum 8276-8276L @ 2.4Ghz cores of the HPC infrastructure GALILEO100 at the Italian supercomputing center CINECA thanks to the computational resources made available through the ISCRA-C project SIDICoNS-HP10CLPLXI. The results, reported in Figure 4.31 and in Table 4.24, show a very good linear scaling, and even superlinear due to cache effects, up to 256 cores, while for a higher number of cores parallel performance is less optimal. A degradation of the performance for higher numbers of cores is observed, which we believe is mainly due to the fact that, given the size of the problem we were able to run, for these numbers of cores the amount of degrees of freedom owned by each core becomes very small so that the time needed by each core for computation is dominated by the time needed for communication. Indeed, using 1024 cores, the number of unknowns per core is only 15552 for the velocity and 1536 for the pressure.

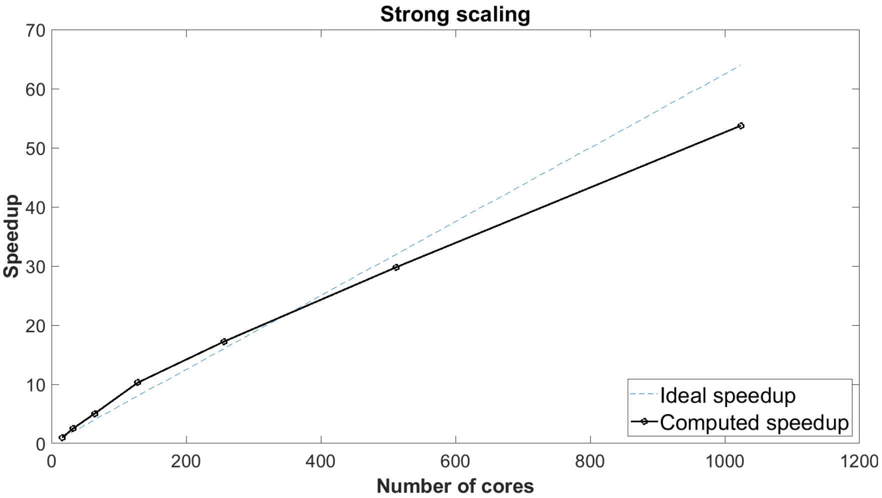

Figure 4.31: *3D lid-driven cavity benchmark at* $Re = 1000$*, strong scaling for the proposed method. The speedup is computed with respect to the time required with 16 cores.*

Number of cores	Wall-clock time TR-BDF2
16	1.86×10^3
32	7.39×10^2
64	3.69×10^2
128	1.81×10^2
256	1.08×10^2
512	6.24×10^1
1024	3.46×10^1

Table 4.24: *Wall-clock times in seconds of the different simulations performed for the strong scaling analysis.*

A weak scaling analysis has been performed using 124416 dofs per core for the velocity and 12288 dofs per core for the pressure. Figure 4.32 shows the obtained results. One can easily notice that a good parallel efficiency is maintained up to 1024 cores. The overperformance of the scheme up to 256 cores can be due to a number of factors, such as the topology of the communication network in the specific architecture employed or the handling of communications between different groups of cores.

4.2.4 Flow past a cylinder

In this Section, we consider another classical benchmark for the incompressible Navier-Stokes equations, namely the flow past a cylinder. The source code for this test case is available at [Orlando, 2022]. We use the configuration described in [Schäfer et al., 1996], that we summarize here for the convenience of the reader. More in detail, the employed geometry and boundary conditions are reported in Figure 4.33, where $H = 0.41\,\mathrm{m}$ makes the domain non-symmetric and allows the vortex shedding in the wake of the cylinder. The inflow condition is

$$\mathbf{u}(0,y) = \begin{pmatrix} 4U_m \frac{y(H-y)}{H^2} \\ 0 \end{pmatrix}, \qquad (4.16)$$

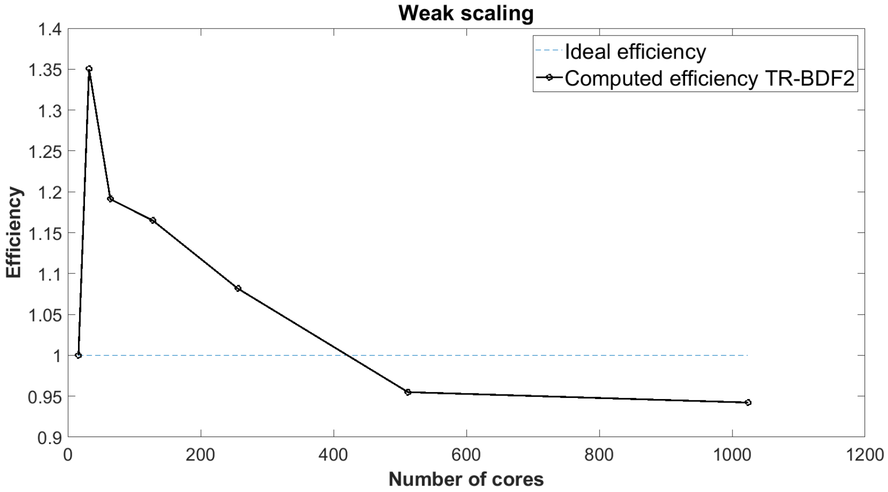

Figure 4.32: *3D lid-driven cavity benchmark at Re* = 1000*, weak scaling for the proposed method. The efficiency is computed with respect to the time required with 16 cores.*

with $U_m = 1.5\,\mathrm{m\,s^{-1}}$. Following [Schäfer et al., 1996], we consider as reference quantities the inflow velocity mean value $U = 1.0\,\mathrm{m\,s^{-1}}$, the diameter of the cylinder equal to $L = 0.1\,\mathrm{m}$ and $\nu = 0.001\,\mathrm{m^2\,s^{-1}}$, which yields $Re = 100$.

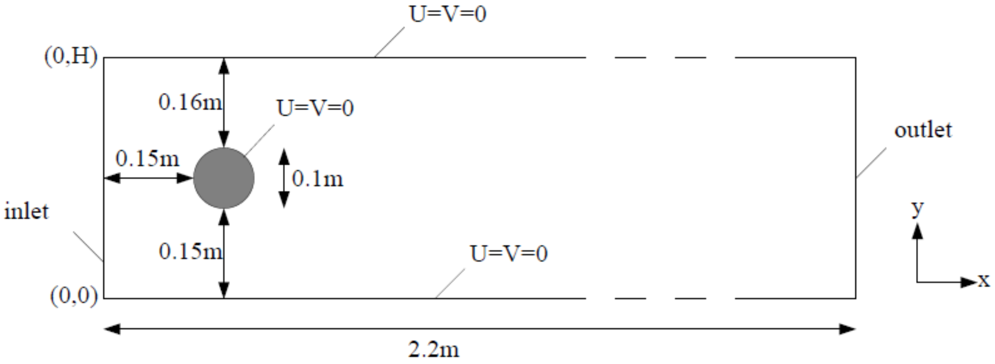

Figure 4.33: *Flow past a cylinder benchmark, geometry and boundary conditions (image from [Schäfer et al., 1996]).*

We compute the drag and lift coefficients, defined as in [Schäfer et al., 1996]. Other reference values are the pressure drop $\Delta p(t) = p(0.15, 0.2, t) - p(0.25, 0.2, t)$ and the Strouhal number $St = \frac{Df}{U}$, where f is the frequency of separation computed as a function of the lift coefficient C_L. The final time is $T_f = 400$, which corresponds to a dimensional time of 40 s, since the reference time value is $\frac{L}{U} = 0.1\,\mathrm{s}$, and allows to obtain a fully developed wake. The grid is composed by 23552 elements and the time step $\Delta t = 5 \cdot 10^{-3}$ is such that the maximum Courant number is around 1. Figure 4.34 shows the contour plot of the velocity magnitude at $t = T_f$ and one can easily notice the formation of the vortices in the wake of the cylinder. Figure 4.35 reports the evolution of the lift and drag coefficients from $t = 385$ to $t = T_f$; it can be observed that the expected periodic behaviour is retrieved. The maximum drag coefficient and the pressure drop are 3.33 and 2.60, respectively, which are slightly larger values than the intervals $[3.22, 3.24]$ and $[2.46, 2.50]$ proposed in [Schäfer et al., 1996], even though they are in the overall range of the solutions proposed in the literature. The maximum lift coefficient is 1.01, which lies in the interval $[0.99, 1.01]$ present in [Schäfer et al., 1996], while the Strouhal number is equal to 0.3, which is again in the interval $[0.295, 0.305]$ reported in [Schäfer et al., 1996].

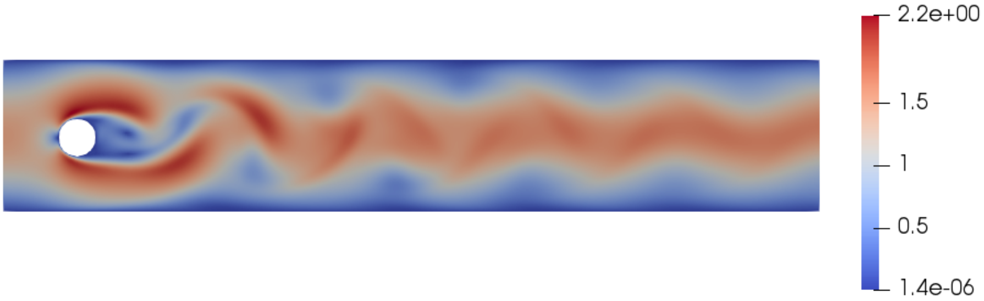

Figure 4.34: *Flow past a cylinder benchmark, contour plot of velocity magnitude at* $t = T_f$.

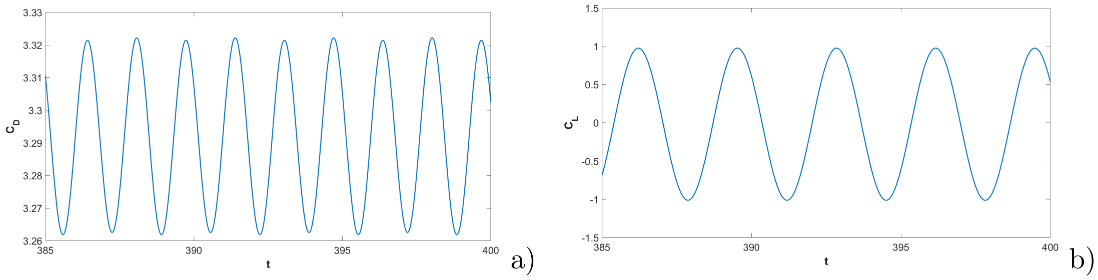

Figure 4.35: *Flow past a cylinder benchmark, a) drag coefficient, b) lift coefficient.*

The same test has been repeated using AMR with the same criterion (4.15) described in Section 4.2.2. The initial mesh is composed by 5558 elements and we allowed up to two local refinements, whereas the maximum element diameter is kept equal to the one of the initial grid. The same remeshing procedure described in 4.2.2 was applied every 5000 time steps. Figure 4.36a reports the final mesh obtained and the values of the drag and lift coefficients. One can easily notice that more resolution is added in the wake of the cylinder and on its boundary and that the behaviour of the two coefficients is analogous to that in the uniform mesh case. The final mesh consists of 11630 elements and a reduction of computational time of about 50% is achieved with respect to the uniform mesh case. Analogous results are obtained for the drag and lift coefficient in Figure 4.36b and Figure 4.36c, respectively.

4.2.5 Complex geometry

The matrix-free approach present in the *deal.II* library makes the proposed solver attractive also for industrial applications that involve a large number of degrees of freedom. For this purpose we have tested the solver on the complex geometry of an heat exchanger of industrial interest [bur, 2018]. More specifically, a four channels module of a designed checkerboard pattern heat exchanger has been considered, with the goal of simulating its pure fluid-dynamic behaviour (i.e., in absence of heat exchanges) between the inlet and the outlet. The channel is long 0.5 m.

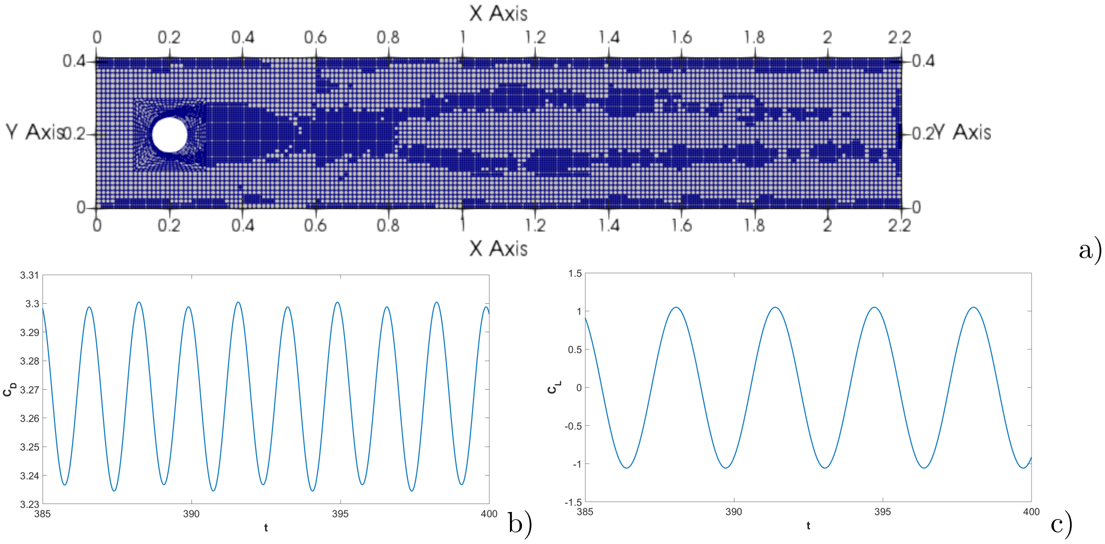

Figure 4.36: *Flow past a cylinder benchmark, adaptive simulation, a) grid at $t = T_f$, b) drag coefficient, c) lift coefficient.*

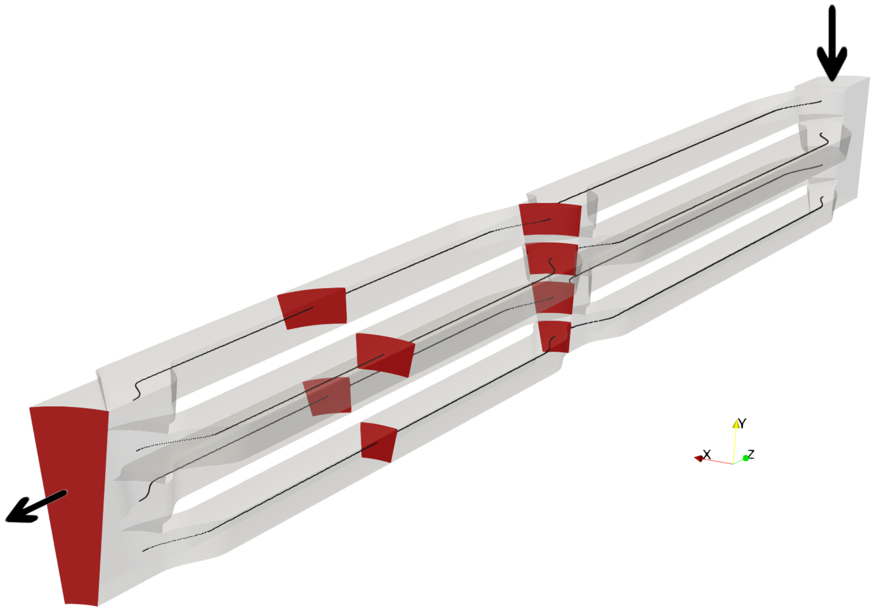

Figure 4.37: *Picture of the considered geometry*

We consider $Re = 5000$, assuming unitary inflow velocity considering the channel length as reference length. We set $c = 300$, which is of the order of magnitude of the speed of sound in air. The mesh consists of 129696 $\mathbf{Q}_2 - Q_1$ elements, which yields 10505376 degrees of freedom for the discrete velocity variables and 1037568 for the discrete pressure variables. In order to verify the results of the simulation at steady state, various simulations with an OpenFoam steady state solver have been performed. More in detail, three meshes with different resolutions have been used with the OpenFoam solver. The coarsest is the one previously described, an intermediate resolution one consists of 1382120 elements while the finest is composed by 2108119 elements. A comparison between the results obtained on each mesh is reported in Figure 4.38 for the midlines of the four channels depicted in

Figure 4.37. For the sake of simplicity, the channels are denote by A, B, C and D from bottom to top, respectively.

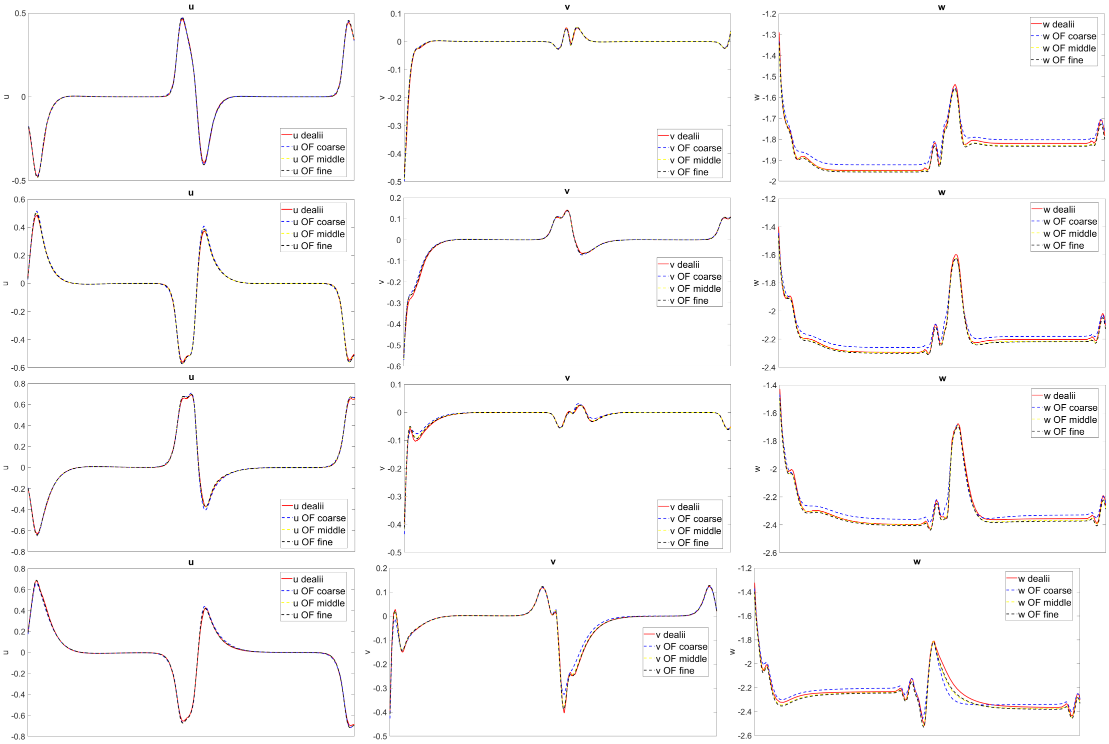

Figure 4.38: *Comparison between deal.II and OpenFOAM from line A (top) to line D (bottom) for u component of the velocity, the one along x-axis (left), v component of the velocity, the one along y-axis (center) and w component of the velocity, the one along z-axis (right).*

It can be observed that a good quantitative agreement between the two solvers has been obtained, taking into account the different features. Moreover, the solution computed with the DG approach is more similar to the results obtained with the OpenFoam solver on the finest meshes, as evident especially for the axial component w. This is further confirmed by the pressure drop computed for the four lines and reported in Table 4.25. Analogous considerations hold for the sections highlighted in Figure 4.37 where we have compared the contour of the velocity magnitude on the middle of the domain, at three-quarters of the domain and on the outlet in Figure 4.39, Figure 4.40, and Figure 4.41, respectively.

	OpenFOAM (coarse)	OpenFOAM (middle)	OpenFOAM (fine)	deal.II
line A	18.6801	18.8735	18.9112	18.7687
line B	18.5748	18.7453	18.7973	18.6780
line C	18.2494	18.4158	18.4706	18.3596
line D	17.0799	17.2534	17.3135	17.2452

Table 4.25: *Pressure drop along the four midlines of the channels for the different simulations.*

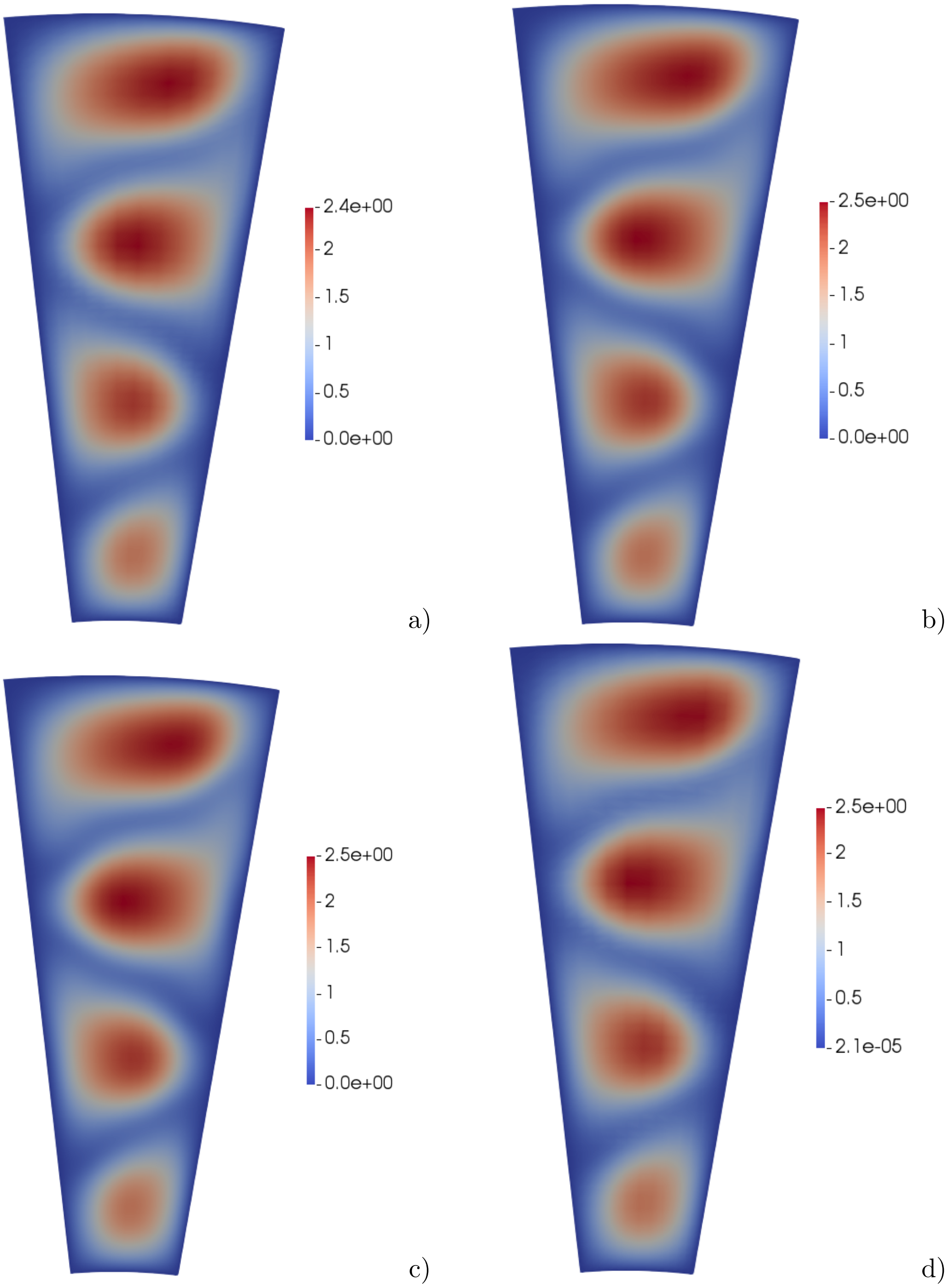

Figure 4.39: *Comparison between deal.II and OpenFOAM on the middle section, a) OpenFOAM on coarse mesh, b) OpenFOAM on middle mesh, c) OpenFOAM on fine mesh, d) deal.II.*

4.3 Numerical results for the single-phase compressible Navier-Stokes equations with ideal gas law

The numerical scheme outlined in Section 3.4 has been validated in a number of benchmarks (see also [Orlando et al., 2022a] and [Orlando et al., 2023]). In this Section, we will focus on the results obtained using the ideal gas law, while we

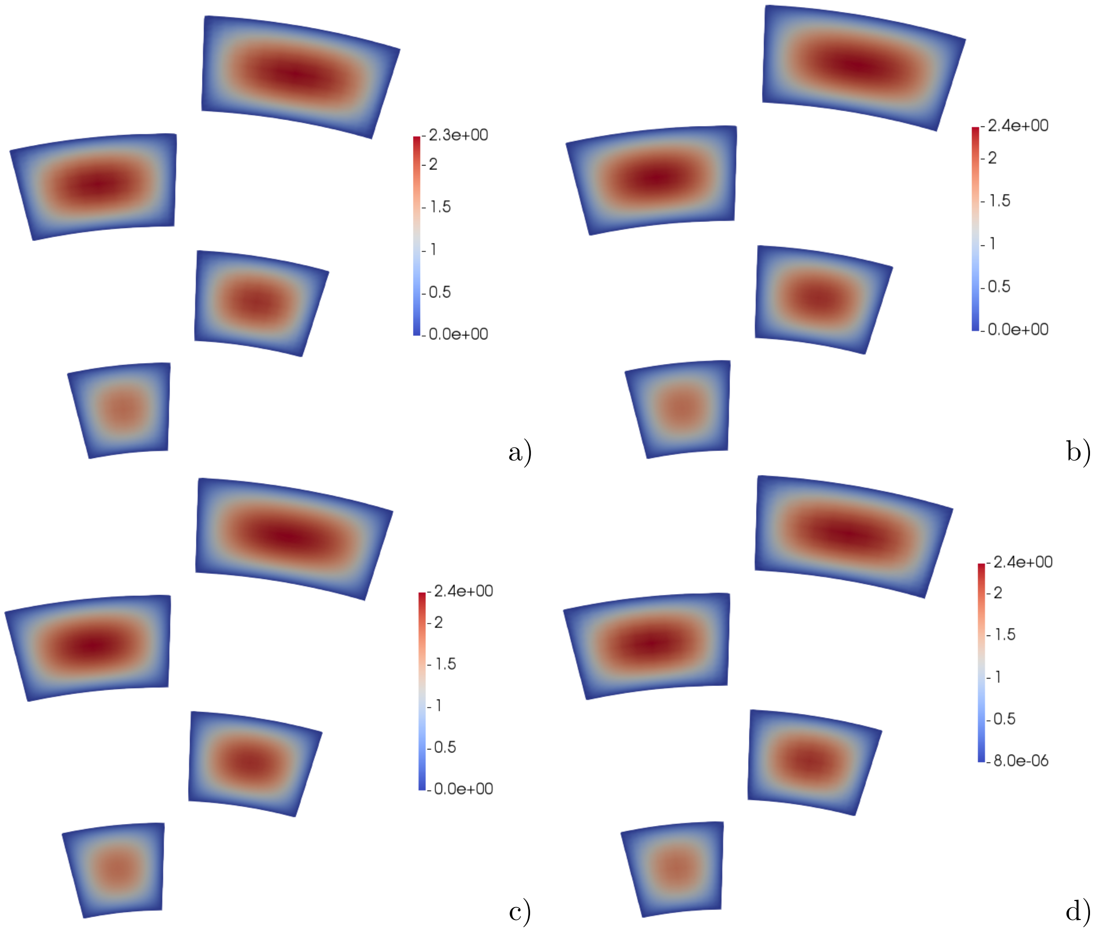

Figure 4.40: *Comparison between deal.II and OpenFOAM at three-quarters section, a) OpenFOAM on coarse mesh, b) OpenFOAM on middle mesh, c) OpenFOAM on fine mesh, d) deal.II*

will discuss benchmarks with non-ideal equations of state in the following Section. As well as the advective Courant number C_u (4.8), for which we recall here the definition for the sake of convenience, we define the acoustic number C

$$C = \frac{1}{M} rc\Delta t/\mathcal{H}, \qquad C_u = r\mathcal{U}\Delta t/\mathcal{H} \tag{4.17}$$

where c is the magnitude of the speed of sound. The factor $\frac{1}{M}$ is due to the scaling of the speed of sound, as reported in [Munz et al., 2003], for an ideal gas, and proven in [Orlando et al., 2022a] in the monodimensional case for a general equation of state (see also Appendix A.3). The fixed point loops are stopped at the l-th iteration such that the relative difference for the pressure is below 10^{-10}, namely

$$\frac{\left\|\xi^{(l)} - \xi^{(l-1)}\right\|}{\left\|\xi^{(l)}\right\|} < 10^{-10}. \tag{4.18}$$

For these tests using the ideal gas law, the value $\gamma = 1.4$ for the specific heat ratio is employed, unless differently stated.

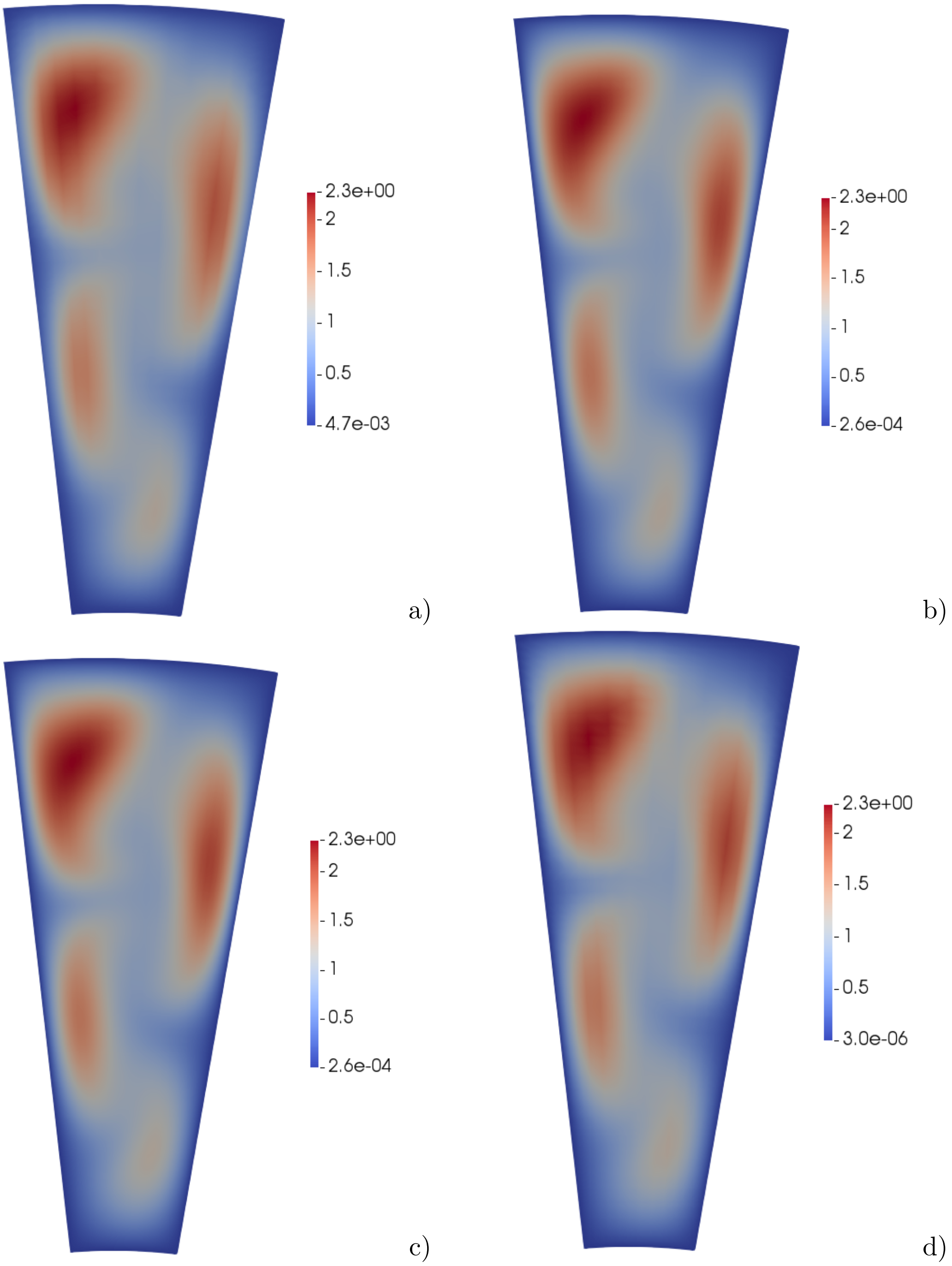

Figure 4.41: *Comparison between deal.II and OpenFOAM on the outlet, a) OpenFOAM on coarse mesh, b) OpenFOAM on middle mesh, c) OpenFOAM on fine mesh, d) deal.II*

4.3.1 Isentropic vortex

As a first benchmark, we consider the two-dimensional inviscid isentropic vortex also studied in [Tavelli and Dumbser, 2017, Zeifang et al., 2019]. For this test, an analytic solution is available, that can be used to assess the convergence properties of the scheme. The initial conditions are given as a perturbation of a reference state $(\rho_\infty, \mathbf{u}_\infty, p_\infty)$

$$\rho(\mathbf{x},0) = \rho_\infty + \delta\rho \qquad \mathbf{u}(\mathbf{x},0) = \mathbf{u}_\infty + \delta\mathbf{u} \qquad p(\mathbf{x},0) = p_\infty + \delta p \tag{4.19}$$

and the exact solution is a propagation of the initial condition at the background velocity

$$\rho(\mathbf{x},t) = \rho(\mathbf{x}-\mathbf{u}_\infty t, 0) \quad \mathbf{u}(\mathbf{x},t) = \mathbf{u}(\mathbf{x}-\mathbf{u}_\infty t, 0) \quad p(\mathbf{x},t) = p(\mathbf{x}-\mathbf{u}_\infty t, 0). \tag{4.20}$$

The typical perturbation is defined as

$$\widetilde{\delta T} = \frac{1-\gamma}{8\gamma\pi^2}\tilde{\beta}^2 e^{1-\tilde{r}^2}, \tag{4.21}$$

with $\tilde{r}^2 = (x-x_0)^2 + (y-y_0)^2$ denoting the radial coordinate and $\tilde{\beta}$ being the vortex strength. As explained in [Zeifang et al., 2019], however, in order to emphasize the role of the Mach number M, we define

$$\delta T = \frac{1-\gamma}{8\gamma\pi^2} M^2 \tilde{\beta}^2 e^{1-\tilde{r}^2} \tag{4.22}$$

and we set

$$\rho(\mathbf{x},0) = (1+\delta T)^{\frac{1}{\gamma-1}} \qquad p(\mathbf{x},0) = M^2 (1+\delta T)^{\frac{\gamma}{\gamma-1}}. \tag{4.23}$$

For what concerns the velocity, the typical perturbation is defined as

$$\widetilde{\delta\mathbf{u}} = \tilde{\beta} \begin{pmatrix} -y \\ x \end{pmatrix} \frac{e^{\frac{1}{2}\left(1-\tilde{r}^2\right)}}{2\pi} \tag{4.24}$$

and also in this case we rescale it using M so as to obtain

$$\delta\mathbf{u} = \tilde{\beta} M \begin{pmatrix} -y \\ x \end{pmatrix} \frac{e^{\frac{1}{2}\left(1-\tilde{r}^2\right)}}{2\pi}. \tag{4.25}$$

We apply the same reasoning also to the background velocity and therefore we define $\mathbf{u}_\infty = M\tilde{\mathbf{u}}_\infty$ with $\tilde{\mathbf{u}}_\infty = [10, 10]^T$. To avoid problems related to the definition of boundary conditions, we choose a sufficiently large domain $\Omega = (-10, 10)^2$ and periodic boundary conditions and we set $\rho_\infty = 1$, $p_\infty = 1$, $x_0 = y_0 = 0$, $\tilde{\beta} = 10$, the final time $T_f = 1$ and $M = 0.1$. Notice that we refrain from investigating the properties of the method in the very low Mach number regime for this test, since this entails an almost constant solution. The numerical experiments have been carried out on Cartesian meshes of square elements with N_{el} elements in each coordinate direction, choosing for each spatial resolution time steps so that the Courant numbers remained constant (hyperbolic scaling).

We first consider the original IMEX-ARK scheme with $a_{32} = \frac{7-2\chi}{6}$ for the explicit part. We observe in Tables 4.26 and 4.27 that, in general, convergence rates of at least $r + \frac{1}{2}$ are observed for $r = 1$ and for $r = 2$.

N_{el}	L^2 rel. error ρ	L^2 rate ρ	L^2 rel. error $\mathbf{u}$	L^2 rate $\mathbf{u}$	L^2 rel. error p	L^2 rate p
10	2.00×10^{-3}		1.19×10^{-2}		2.79×10^{-3}	
20	7.86×10^{-4}	1.35	3.86×10^{-3}	1.62	1.11×10^{-3}	1.33
40	2.55×10^{-4}	1.62	1.07×10^{-3}	1.84	3.61×10^{-4}	1.62
80	7.15×10^{-5}	1.83	2.67×10^{-4}	2.00	1.01×10^{-4}	1.84

Table 4.26: *Convergence test for the inviscid isentropic vortex at* $C \approx 0.01$, $C_u \approx 0.01$ *with* $r = 1$ *and* $a_{32} = \frac{7-2\chi}{6}$ *for the explicit part. Relative errors for the density, the velocity and the pressure in* L^2 *norm.* N_{el} *denotes the number of elements along each direction.*

N_{el}	L^2 rel. error ρ	L^2 rate ρ	L^2 rel. error $\mathbf{u}$	L^2 rate $\mathbf{u}$	L^2 rel. error p	L^2 rate p
10	6.38×10^{-4}		2.61×10^{-3}		9.08×10^{-4}	
20	1.18×10^{-4}	2.43	3.54×10^{-4}	2.88	1.64×10^{-4}	2.47
40	1.81×10^{-5}	2.70	4.16×10^{-5}	3.09	2.53×10^{-5}	2.70
80	2.96×10^{-6}	2.61	5.18×10^{-6}	3.00	4.13×10^{-6}	2.60

Table 4.27: *Convergence test for the inviscid isentropic vortex at* $C \approx 0.01$, $C_u \approx 0.01$ *with* $r = 2$ *and* $a_{32} = \frac{7-2\chi}{6}$ *for the explicit part. Relative errors for the density, the velocity and the pressure in* L^2 *norm.* N_{el} *denotes the number of elements along each direction.*

Analogous results are shown in Tables 4.28 and 4.29 for the modified scheme with $a_{32} = 0.5$, chosen, as discussed in [Orlando et al., 2022a] and Appendix A.5, in order to increase the region of absolute monotonicity without affecting too much stability.

N_{el}	L^2 rel. error ρ	L^2 rate ρ	L^2 rel. error $\mathbf{u}$	L^2 rate $\mathbf{u}$	L^2 rel. error p	L^2 rate p
10	2.00×10^{-3}		1.19×10^{-2}		2.79×10^{-3}	
20	7.86×10^{-4}	1.35	3.86×10^{-3}	1.62	1.11×10^{-3}	1.33
40	2.55×10^{-4}	1.62	1.07×10^{-3}	1.85	3.61×10^{-4}	1.62
80	7.15×10^{-5}	1.83	2.67×10^{-4}	2.00	1.00×10^{-4}	1.85

Table 4.28: *Convergence test for the inviscid isentropic vortex at* $C \approx 0.01$, $C_u \approx 0.01$ *with* $r = 1$ *and* $a_{32} = 0.5$ *for the explicit part. Relative errors for the density, the velocity and the pressure in* L^2 *norm.* N_{el} *denotes the number of elements along each direction.*

N_{el}	L^2 rel. error ρ	L^2 rate ρ	L^2 rel. error $\mathbf{u}$	L^2 rate $\mathbf{u}$	L^2 rel. error p	L^2 rate p
10	6.38×10^{-4}		2.61×10^{-3}		9.08×10^{-4}	
20	1.18×10^{-4}	2.43	3.54×10^{-4}	2.88	1.64×10^{-4}	2.47
40	1.81×10^{-5}	2.70	4.16×10^{-5}	3.09	2.53×10^{-5}	2.70
80	2.96×10^{-6}	2.61	5.18×10^{-6}	3.00	4.13×10^{-6}	2.60

Table 4.29: *Convergence test for the inviscid isentropic vortex at* $C \approx 0.01$, $C_u \approx 0.01$ *with* $r = 2$ *and* $a_{32} = 0.5$ *for the explicit part. Relative errors for the density, the velocity and the pressure in* L^2 *norm.* N_{el} *denotes the number of elements along each direction.*

In further numerical experiments, we have observed that the lack of absolute monotonicity strongly affects the computation of density and, as a consequence, the stability of the whole numerical scheme. For Courant number around $C \approx 0.3$ the original method becomes unstable, while the modified scheme with $a_{32} = 0.5$ is still able to recover the expected convergence rates at least in the $r = 1$ case, as evident from Table 4.30, while for $r = 2$ reported in Table 4.31 we observe a small degradation of the convergence rates due to increasing influence of the dominant second order time discretization error. In order to be able to run at slightly longer time steps we have then chosen to use the $a_{32} = 0.5$ value for the IMEX scheme for the rest of the numerical simulations carried out in this paper. We notice also that, for both schemes, the results compare well with the analogous results presented in [Tavelli and Dumbser, 2017] and with those obtained in [Zeifang et al., 2019] with a higher order IMEX method.

N_{el}	L^2 rel. error ρ	L^2 rate ρ	L^2 rel. error $\mathbf{u}$	L^2 rate $\mathbf{u}$	L^2 rel. error p	L^2 rate p
10	2.32×10^{-3}		1.19×10^{-2}		2.78×10^{-3}	
20	7.63×10^{-4}	1.60	3.88×10^{-3}	1.62	1.06×10^{-3}	1.39
40	2.43×10^{-4}	1.65	1.08×10^{-3}	1.85	3.41×10^{-4}	1.64
80	6.84×10^{-5}	1.83	2.69×10^{-4}	2.01	9.55×10^{-5}	1.84

Table 4.30: *Convergence test for the inviscid isentropic vortex at $C \approx 0.3$, $C_u \approx 0.3$ with $r = 1$ and $a_{32} = 0.5$ for the explicit part. Relative errors for the density, the velocity and the pressure in L^2 norm. N_{el} denotes the number of elements along each direction.*

N_{el}	L^2 rel. error ρ	L^2 rate ρ	L^2 rel. error $\mathbf{u}$	L^2 rate $\mathbf{u}$	L^2 rel. error p	L^2 rate p
10	6.43×10^{-4}		2.71×10^{-3}		9.15×10^{-4}	
20	1.28×10^{-4}	2.33	3.89×10^{-4}	2.80	1.68×10^{-4}	2.44
40	2.10×10^{-5}	2.61	5.78×10^{-5}	2.75	2.70×10^{-5}	2.64
80	4.08×10^{-6}	2.36	1.13×10^{-5}	2.35	$4.97 \cdot 10^{-6}$	2.44

Table 4.31: *Convergence test for the inviscid isentropic vortex at $C \approx 0.3$, $C_u \approx 0.3$ with $r = 2$ and $a_{32} = 0.5$ for the explicit part. Relative errors for the density, the velocity and the pressure in L^2 norm. N_{el} denotes the number of elements along each direction.*

For validation purposes, we have also tested in this case the $h-$adaptive version of the method. The local refinement criterion is based on the gradient of the density. More specifically, we define for each element K the quantity

$$\eta_K = \max_{i \in \mathcal{N}_K} |\nabla \rho|_i \tag{4.26}$$

that acts as local refinement indicator, where $\mathcal{N}_K$ denotes the set of nodes over the element K. Table 4.32 shows the relative errors for all the quantities on a sequence of adaptive simulations keeping the maximum Courant numbers fixed. The expected results are obtained, even though the relative errors are not significantly reduced with respect to Table 4.30 in view of the smoothness of the solution. Hence, the following results have to merely intended as a verification of the correctness of the $h-$adaptive version of the scheme. Figure 4.42 shows instead the density and the adapted mesh at $t = T_f$, from which it can be seen that the refinement criterion is able to track the vortex correctly.

N_{cells}	L^2 rel. error ρ	L^2 rel. error $\mathbf{u}$	L^2 rel. error p
241	2.04×10^{-3}	1.19×10^{-2}	2.78×10^{-3}
541	7.31×10^{-4}	3.50×10^{-3}	1.03×10^{-3}
1951	2.09×10^{-4}	9.23×10^{-4}	2.92×10^{-4}
7537	6.07×10^{-5}	2.42×10^{-4}	8.51×10^{-5}

Table 4.32: *Adaptive simulations of the inviscid isentropic vortex at different resolutions with a maximum* $C \approx 0.3$, $C_u \approx 0.3$, *relative errors for the density, the velocity and the pressure in* L^2 *norm with* $r = 1$. N_{cells} *denotes the total number of cells.*

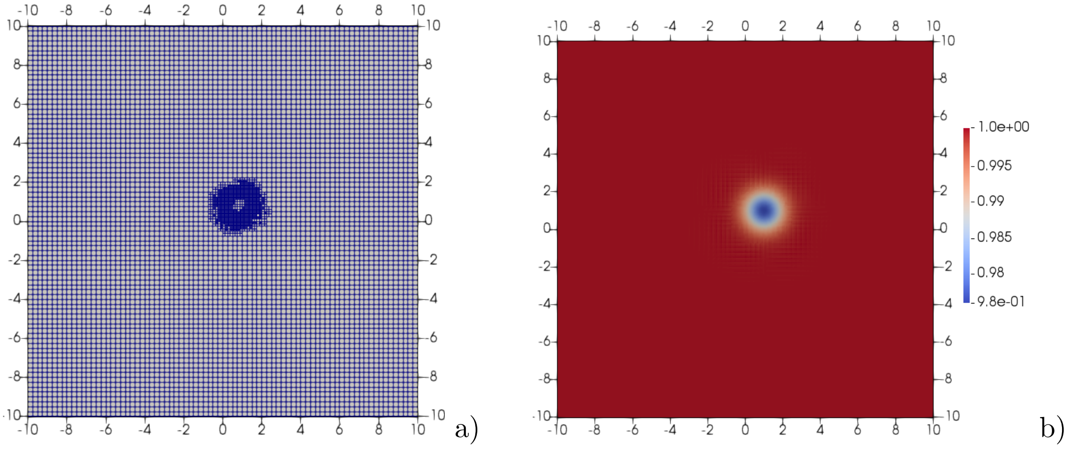

Figure 4.42: *Adaptive simulation of the inviscid isentropic vortex benchmark: a) computational mesh at* $t = T_f$, *b) contour plot of the density at* $t = T_f$.

4.3.2 2D Lid-driven cavity

We consider now the classical 2D lid-driven cavity test case already treated in Section 4.2.2. The computational domain is the box $\Omega = (0,1) \times (0,1)$ which is initialized with a density $\rho = 1$ and a velocity $\mathbf{u} = \mathbf{0}$. The flow is driven by the upper boundary, whose velocity is set to $\mathbf{u} = (1,0)^T$, while on the other three boundaries a no-slip condition is imposed. We set $Re = 100$ and $M^2 = 10^{-5}$. The advantage of the proposed scheme is that the allowed time step is more than 100 times larger than that of a fully explicit scheme. Indeed, the time-step chosen is such that the maximum advective Courant number C_u is around 0.12, while the maximum Courant number C is around 49. The streamlines are shown in Figure 4.43 and highlight the formation of the main recirculation pattern. A comparison of the horizontal component of the velocity along the vertical middle line and of the vertical component of the velocity along the horizontal middle line with the reference solutions in [Ghia et al., 1982, Tavelli and Dumbser, 2017] is also presented.

We note a reasonable agreement between the different solutions, even though there is a still visible discrepancy between our results and the reference ones. Since the solution in [Tavelli and Dumbser, 2017] is obtained using third degree polynomials, in order to further improve the results, we consider also the case $r = 2$. For this higher order approximation we note that our results fit very well both the reference solutions.

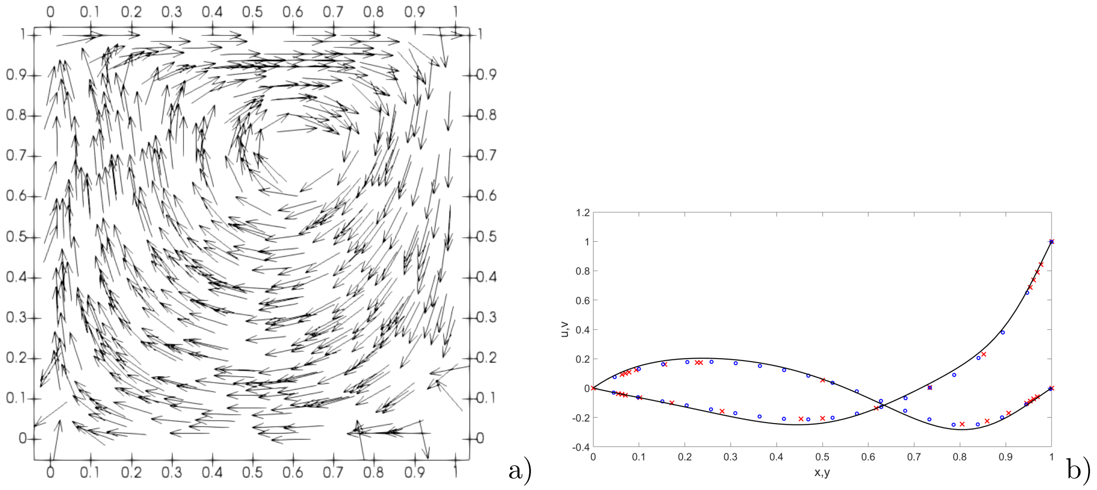

Figure 4.43: *Computational results for the 2D lid-driven cavity with* $r = 1$, *a) streamlines, b) comparison with the solutions in [Ghia et al., 1982] and in [Tavelli and Dumbser, 2017]. Blue dots denote the results in [Ghia et al., 1982], red crosses the results in [Tavelli and Dumbser, 2017] and the black line our numerical results.*

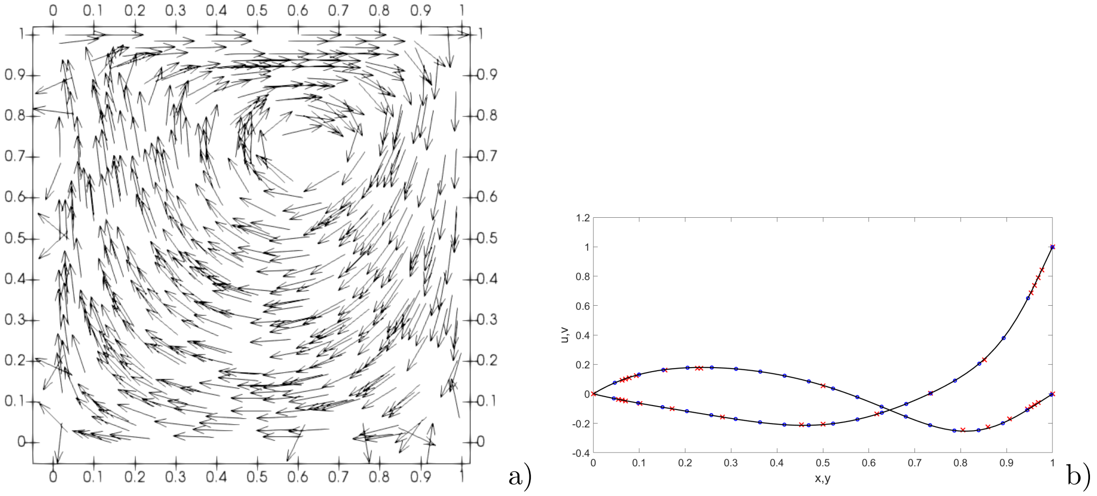

Figure 4.44: *Computational results for the 2D lid-driven cavity with* $r = 2$, *a) streamlines, b) comparison with the solutions in [Ghia et al., 1982] and in [Tavelli and Dumbser, 2017]. Blue dots denote the results in [Ghia et al., 1982], red crosses the results in [Tavelli and Dumbser, 2017] and black line our numerical results.*

We have also tested the $h-$adaptive version of the same algorithm, using the refinement criterion based on the vorticity introduced in 4.15. More specifically, we define

$$\eta_K = \operatorname{diam}(K)^2 \left\|\nabla \times \mathbf{u}\right\|_{2,K}^2 \tag{4.27}$$

as local indicator. We start from a uniform Cartesian mesh with $N_{el} = 16$ elements along each direction. We allowed refinement for 5% of the elements with largest indicator values and coarsening for 30% of the elements with the smallest indicator values. The minimum element diameter allowed is $\mathcal{H} = \frac{1}{64}$, while the maximum element diameter is $h = \frac{1}{16}$. Figure 4.45 reports the computational mesh at steady state and the computed streamlines. One can easily notice that the local refinement criterion is able to enhance automatically the resolution in the zones where vortices appear, as well as along the top boundary of the domain. For a more quantitative view, in Figure 4.46 we compare again the components of the velocity along the middle lines. Moreover, the absolute difference between the velocities of the fixed mesh and those of adaptive simulations is plotted over the whole domain, showing that no substantial loss of accuracy has occurred with a reduction of around 25% of the required computational time.

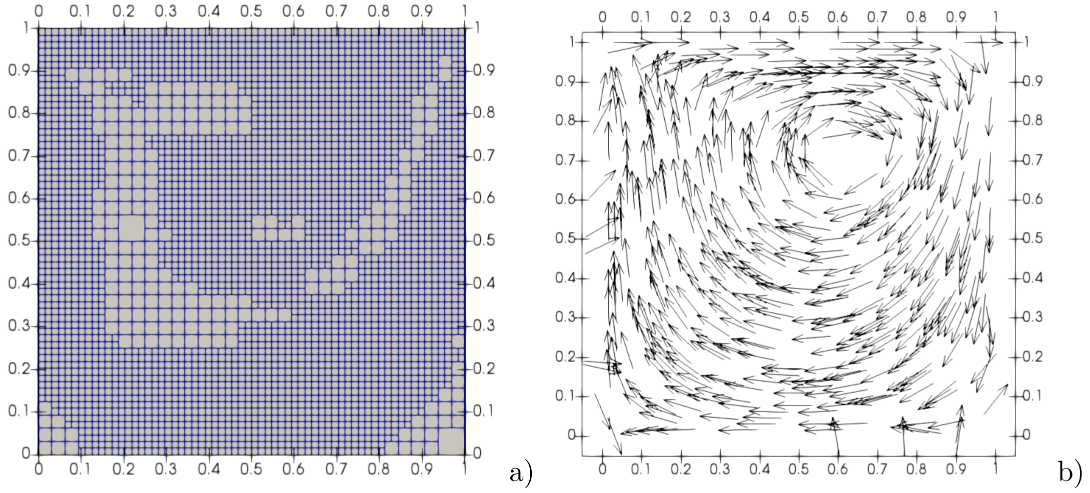

a) b)

Figure 4.45: *Adaptive simulation for the 2D lid-driven cavity, a) mesh at steady state, b) streamlines.*

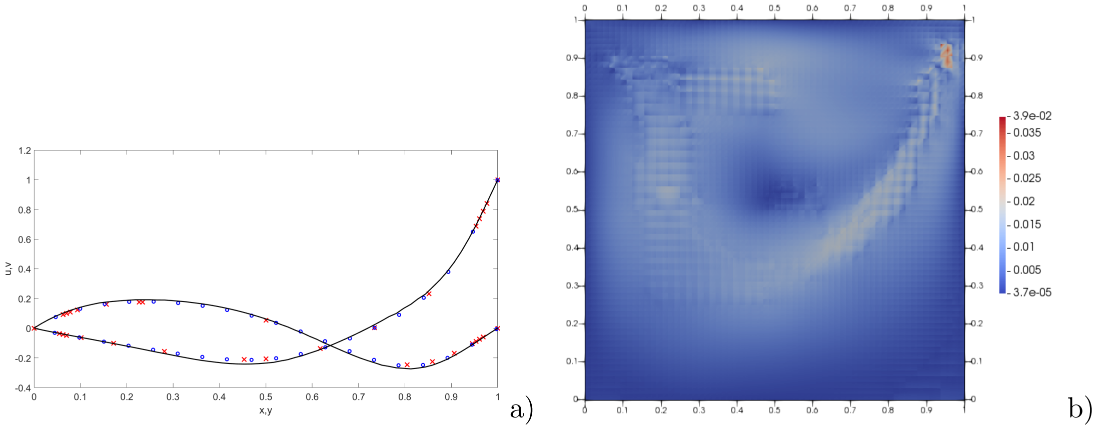

a) b)

Figure 4.46: *Adaptive simulation for the 2D lid-driven cavity, a) comparison with the solutions in [Ghia et al., 1982] and in [Tavelli and Dumbser, 2017]. Blue dots denote the results in [Ghia et al., 1982], red crosses the results in [Tavelli and Dumbser, 2017] and black line our numerical results, b) difference for velocity magnitude between the fixed grid simulation and the adaptive simulation (interpolated to the fixed grid).*

4.3.3 Cold bubble

In this Section, we consider a test case proposed in [Restelli, 2007, Restelli and Giraldo, 2009] for an ideal gas in which the gravity force is active. The computational domain is the rectangle $(0, 1000) \times (0, 2000)$ and the initial condition is represented by a thermal anomaly introduced in an isentropic background atmosphere with constant potential temperature $\theta_0 = 303$. The perturbation of potential temperature θ' defines the initial datum and it is given by

$$\theta' = \begin{cases} A & \text{if } \tilde{r} \leq r_0 \\ A \exp\left(-\frac{(\tilde{r}-r_0)^2}{\tilde{\sigma}^2}\right) & \text{if } \tilde{r} > r_0, \end{cases} \tag{4.28}$$

with $\tilde{r}^2 = (x - x_0)^2 + (y - y_0)^2$ and $x_0 = 500$, $y_0 = 1250$, $r_0 = 50$, $\tilde{\sigma} = 100$, and $A = -15$. Moreover, we set $Fr^2 = \frac{1}{9.81}$, $M^2 = 10^{-5}$, and $T_f = 50$. The expression of the Exner pressure Π is given by

$$\Pi = 1 - \frac{M^2}{Fr^2}\frac{y}{\tilde{c}_p \theta}, \tag{4.29}$$

with y denoting the vertical coordinate and $\tilde{c}_p = \frac{\gamma}{\gamma-1}\tilde{R}_g = 1.0045 \cdot 10^{-2}$ denoting the non-dimensional specific heat at constant pressure. Notice that these values are obtained by considering $\mathcal{R} = 1\,\mathrm{kg\,m^{-3}}, \Theta = 1\,\mathrm{K}$ and $\mathcal{P} = 10^5\,\mathrm{Pa}$. The same reference values will be used in Section 4.4.1. Moreover, it is to be remarked that, unlike in [Restelli, 2007], no artificial viscosity has been added to stabilize the computation. Wall boundary conditions are imposed at all the boundaries. The time step is taken to be $\Delta t = 0.08$, corresponding to a maximum Courant number $C \approx 5.6$ and a maximum advective Courant number $C_u \approx 0.18$. For the purpose of a quantitative comparison, a reference solution is computed with an explicit time discretization given by the optimal third order SSP scheme outlined in [Gottlieb et al., 2001] and recalled in Appendix A.5. Figure 4.47 shows the contour plot of the potential temperature perturbation at $t = T_f$ and one can easily notice that we are able to recover correctly the shape of the reference solution. For a more quantitative point of view, the profile of the density at $y = 1000$ is reported in Figure 4.48 and a good agreement between the reference results and those obtained with the IMEX scheme is established. The IMEX scheme allows to employ a time step 40 times larger compared to the fully explicit scheme with a computational saving of around 90%. Three fixed-point iterations were required on average for each IMEX stage.

In order to further enhance the computational efficiency, we employ again the code $h-$adaptivity capabilities. We use as refinement indicator the gradient of the potential temperature, since this quantity allows to identify the cold bubble. More specifically, we set

$$\eta_K = \max_{i \in \mathcal{N}_K} |\nabla \theta|_i \tag{4.30}$$

as local indicator, where $\mathcal{N}_K$ is defined as in (4.26), and we allow to refine when η_K exceeds 10^{-1} and to coarsen below $6 \cdot 10^{-2}$. The initial computational grid is composed by 50×100 elements and we allow up to two local refinements only, so as to keep the advective Courant number under control and to recover the same maximum resolution employed for the non adaptive mesh simulation. Notice that there is no intrinsic limitation in the maximum number of refinement levels allowed and more refinement levels will be indeed used in the following tests with non-ideal gases in Section 4.4. The only constraint is about the necessity of not having neighbouring cells with refinement levels differing by more than one. However, a maximum number of allowed local refinements has to be set depending on the chosen time step in order to fulfill the stability of the scheme. As one can easily notice from Figure 4.49, the refinement criterion is able to track the bubble and the one-dimensional density profile at $y = 1000$ in Figure 4.50 is correctly reproduced.

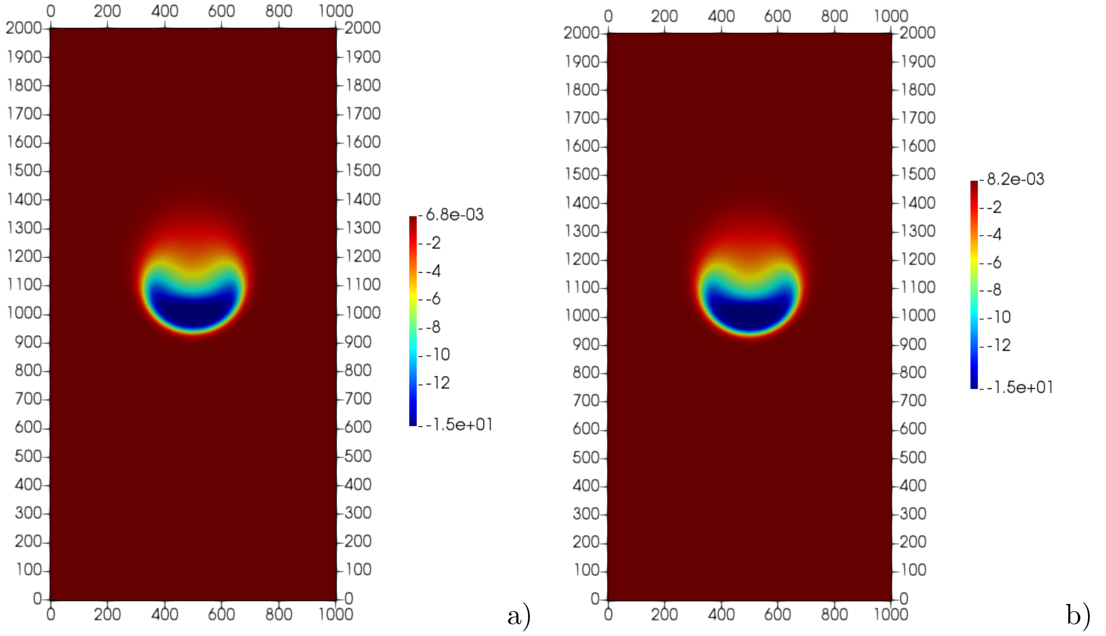

Figure 4.47: *Cold bubble test case, results at $t = T_f$, a) contour plot of potential temperature perturbation for the reference explicit simulation, b) contour plot of the potential temperature perturbation for the simulation with IMEX scheme.*

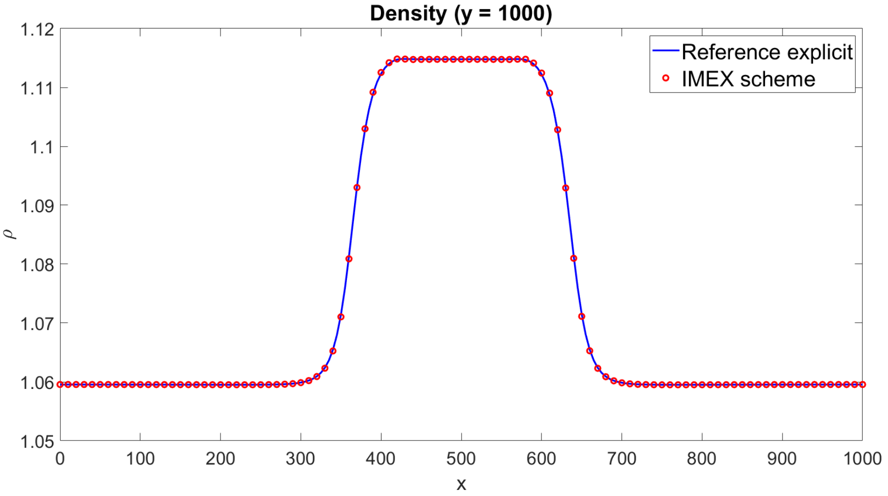

Figure 4.48: *Cold bubble test case, results at $t = T_f$, density profile at $y = 1000$. The continuous blue line represents the results for the reference explicit simulation, whereas the red dots denote the results for the IMEX scheme.*

The final mesh consists of 6914 elements instead of the 80000 elements of the full resolution mesh and a further 50% reduction in computational time is achieved. Three fixed-point iterations were required on average even with the $h-$adaptive version of the scheme and, therefore, no deterioration in the performances of the fixed-point loop occurred. We noticed instead an increase in the number of iterations required by the GMRES linear solver applied to (3.111) and to (3.127). The CPU time required for the mesh adaptation procedure represents less than 1% of the total CPU time.

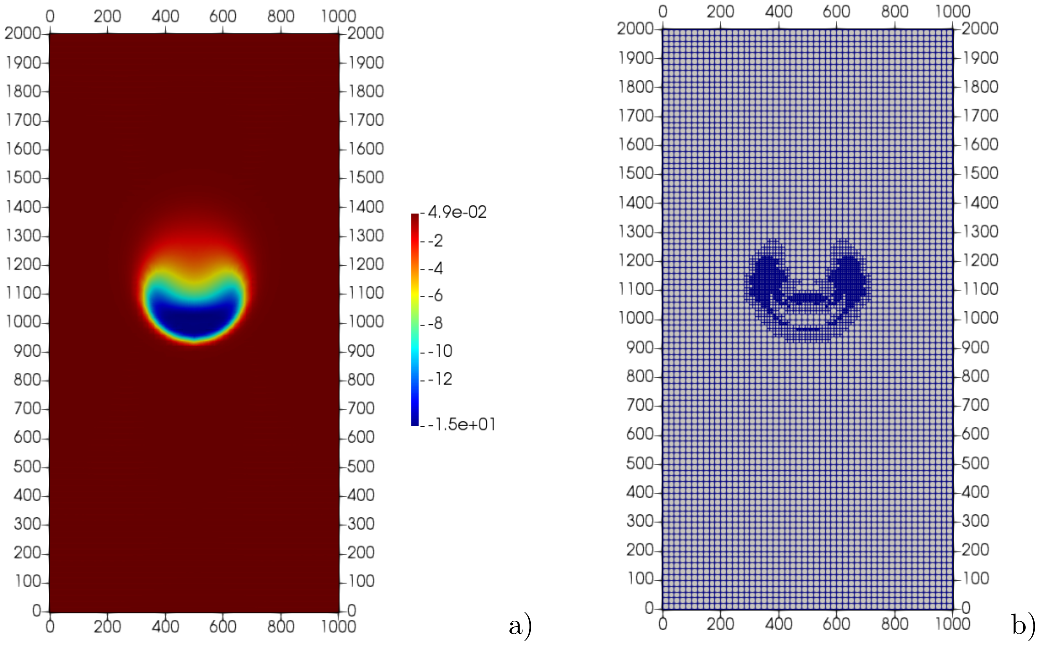

Figure 4.49: *Cold bubble test case, adaptive simulation, results at $t = T_f$, a) contour plot of potential temperature perturbation, b) computational grid.*

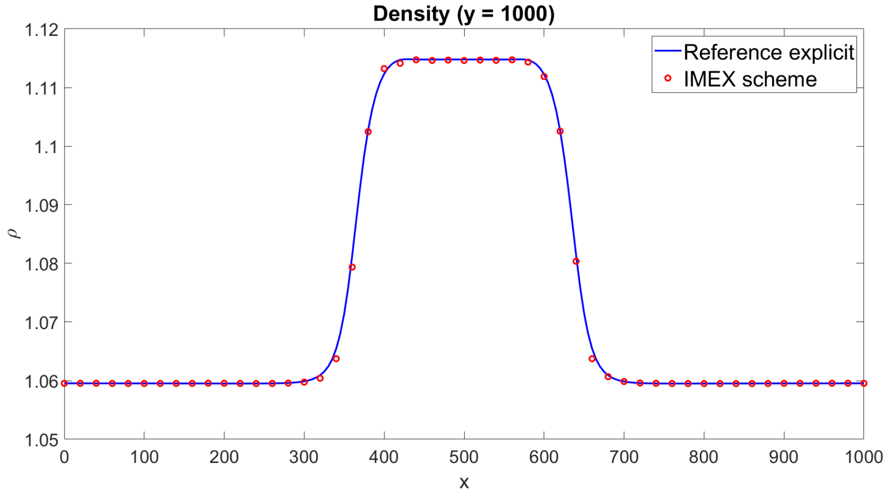

Figure 4.50: *Cold bubble test case, adaptive simulation, results at $t = T_f$, density profile at $y = 1000$. The continuous blue line represents the results for the reference explicit simulation, whereas the red dots denote the results for the IMEX scheme.*

4.3.4 Warm bubble

In order to test the method in presence of heat conduction, we now consider for an ideal gas the test case of a rising warm bubble proposed in [Busto et al., 2020]. The domain is the square box $\Omega = (-0.5, 1.5) \times (-0.5, 1.5)$ with periodic boundary conditions on the lateral boundaries and wall boundary conditions on the top and on the bottom of the domain. The initial temperature corresponds to a truncated

Gaussian profile

$$T(\mathbf{x},0) = \begin{cases} 386.48 & \text{if } \tilde{r} > r_0 \\ \dfrac{\tilde{p}_0}{\tilde{R}_{g,air}\left(1-0.1e^{\frac{\tilde{r}^2}{\tilde{\sigma}^2}}\right)} & \text{if } \tilde{r} \le r_0, \end{cases} \tag{4.31}$$

where $\tilde{r}^2 = (x-x_0)^2 + (y-y_0)^2$ is the distance from the center with coordinates $x_0 = 0.5$ and $y_0 = 0.35$, $r_0 = 0.25$ is the radius and $\tilde{\sigma} = 2$. For this test case, we consider unitary reference values for density, pressure and temperature and, therefore, we set $\tilde{p}_0 = 10^5$ and $\tilde{R}_{g,air} = 287$. The same reference values will be used in Section 4.4.2. Moreover, following [Busto et al., 2020], we consider:

$$Re = 804.9 \qquad Pr = 0.71 \qquad Fr \approx 0.004 \qquad M \approx 0.01.$$

The grid is composed by 120 elements along each direction and the time step is such that the maximum Courant number $C \approx 118$ and the maximum value of advective Courant number C_u is around 0.03. Figures 4.51, 4.52 and 4.53 show the results at $t = 10, 15, 20\,\mathrm{s}$ both in terms of contours and plots along the same specific sections along $x-$axis chosen in [Busto et al., 2020]. All the results are in good agreement with the reference ones and we are able to recover the development of the expected Kelvin-Helmholtz instability.

4.3.5 Inertia-gravity waves

The method depicted in Section 3.4 has been successfully applied to a number of idealized benchmarks for atmospheric dynamics [Orlando et al., 2023]. The model equations are the compressible Euler equations supplied with suitable initial and boundary conditions. Notice that, as in most standard presentations of this topic (see e.g [Melvin et al., 2019, Orlando et al., 2023]) and for the sake of comparison with other results in literature, we express variables and background fields using dimensional coordinates. The corresponding non-dimensional numbers can be easily computed using the reported reference quantities. Moreover, as common in the presentation of benchmark problems for atmosphere dynamics, we denote by z the vertical component also in the two-dimensional setting. We start by considering inertia-gravity waves in a two-dimensional vertical section of the atmosphere, see e.g. [Skamarock and Klemp, 1994, Bonaventura, 2000, Melvin et al., 2019]. In particular, we set the background potential temperature

$$\bar{\theta} = T_{ref} \exp\left(\frac{N^2 z}{g}\right) \tag{4.32}$$

where $N = 0.01\,\mathrm{s}^{-1}$ denotes the buoyancy frequency and $T_{ref} = 300\,\mathrm{K}$. The background density and pressure are defined as

$$\bar{p} = \exp\left\{1 - \frac{g^2}{N^2}\frac{\gamma-1}{\gamma}\frac{\rho_{ref}}{p_{ref}}\left[1 - \exp\left(-\frac{N^2 z}{g}\right)\right]\right\} \tag{4.33}$$

$$\bar{\rho} = \rho_{ref}\left(\frac{p}{p_{ref}}\right)^{\frac{1}{\gamma}} \exp\left(-\frac{N^2 z}{g}\right) \tag{4.34}$$

with $p_{ref} = 10^5\,\mathrm{Pa}$ and $\rho_{ref} = \frac{p_{ref}}{R_g T_{ref}}$. The domain is $\Omega = (0,300) \times (0,10)\,\mathrm{km}$ and we consider the following perturbation for the potential temperature

$$\theta' = 0.01 \frac{\sin\left(\frac{\pi z}{H}\right)}{1 + \left(\frac{x - x_c}{a}\right)^2} \tag{4.35}$$

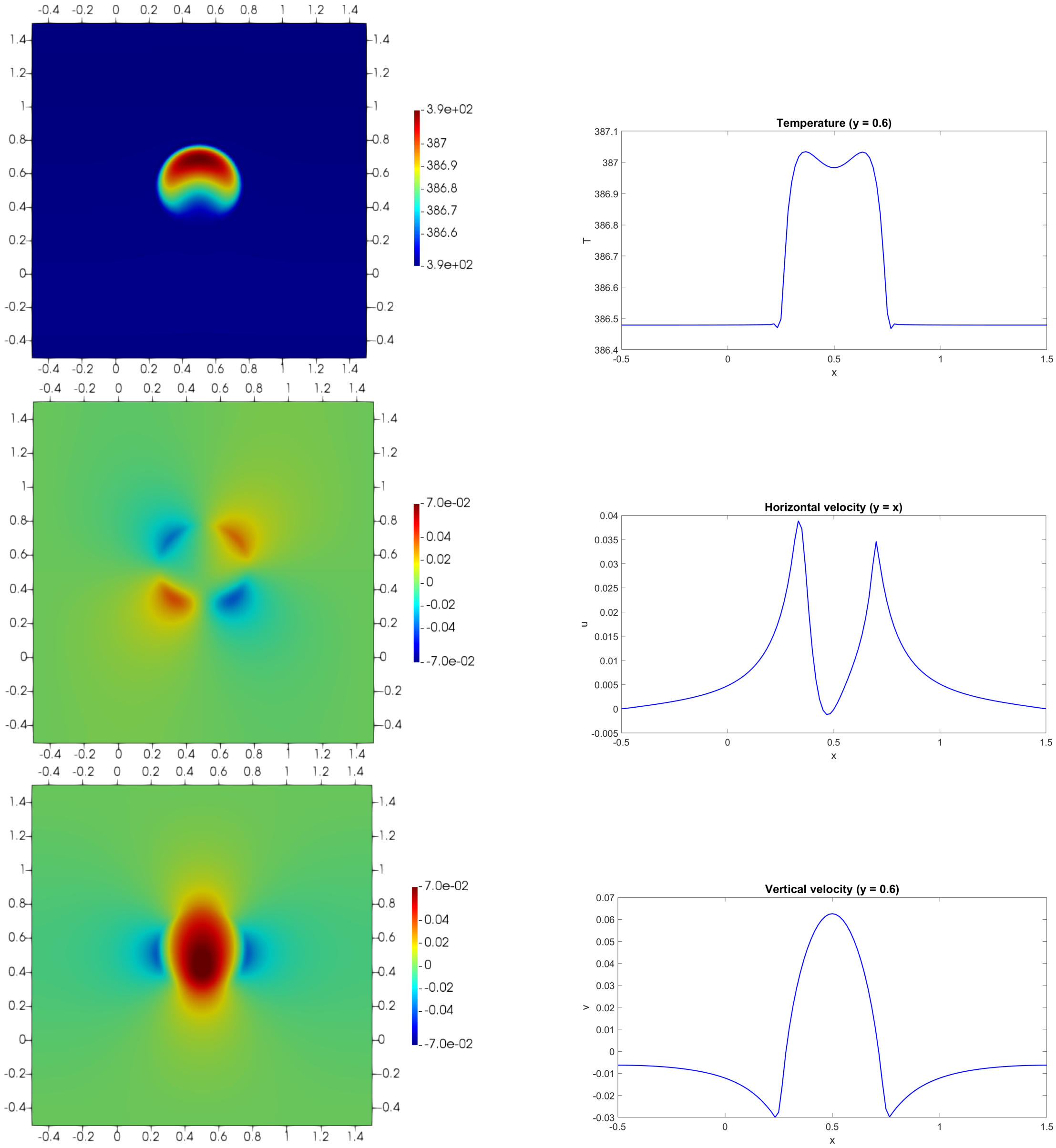

Figure 4.51: *Warm bubble test case, results at $t = 10\,\mathrm{s}$. From bottom to top: temperature, horizontal velocity and vertical velocity.*

with $x_c = 100\,\mathrm{km}, a = 5\,\mathrm{km}$ and $H = 10\,\mathrm{km}$. For what concerns the boundary conditions, we consider periodic boundary conditions for the horizontal direction and wall boundary conditions for the vertical direction. A background horizontal velocity $u = 20\,\mathrm{m\,s^{-1}}$ is imposed, leading to a Mach number $M \approx 0.068$ and a Froude number $Fr \approx 0.20$. The grid is composed by 300×10 elements with $r = 4$, while the time step is taken equal to $3\,\mathrm{s}$ yielding $C \approx 4.17$ and $C_u \approx 0.24$. Figure 4.54 shows the potential temperature perturbation at $t = 3000\,\mathrm{s}$, where one can easily notice that inertia-gravity waves propagate from the initial perturbation also reported in Figure 4.54. The results compare well with those available in the literature, see e.g. [Tumolo and Bonaventura, 2015, Melvin et al., 2019]. Figure 4.55 shows the one-dimensional profile of the potential temperature perturbation along $z = 5\,\mathrm{km}$, which is symmetric about the position $x = 160\,\mathrm{km}$ and in excellent agreement with the results reported in [Giraldo and Restelli, 2008].

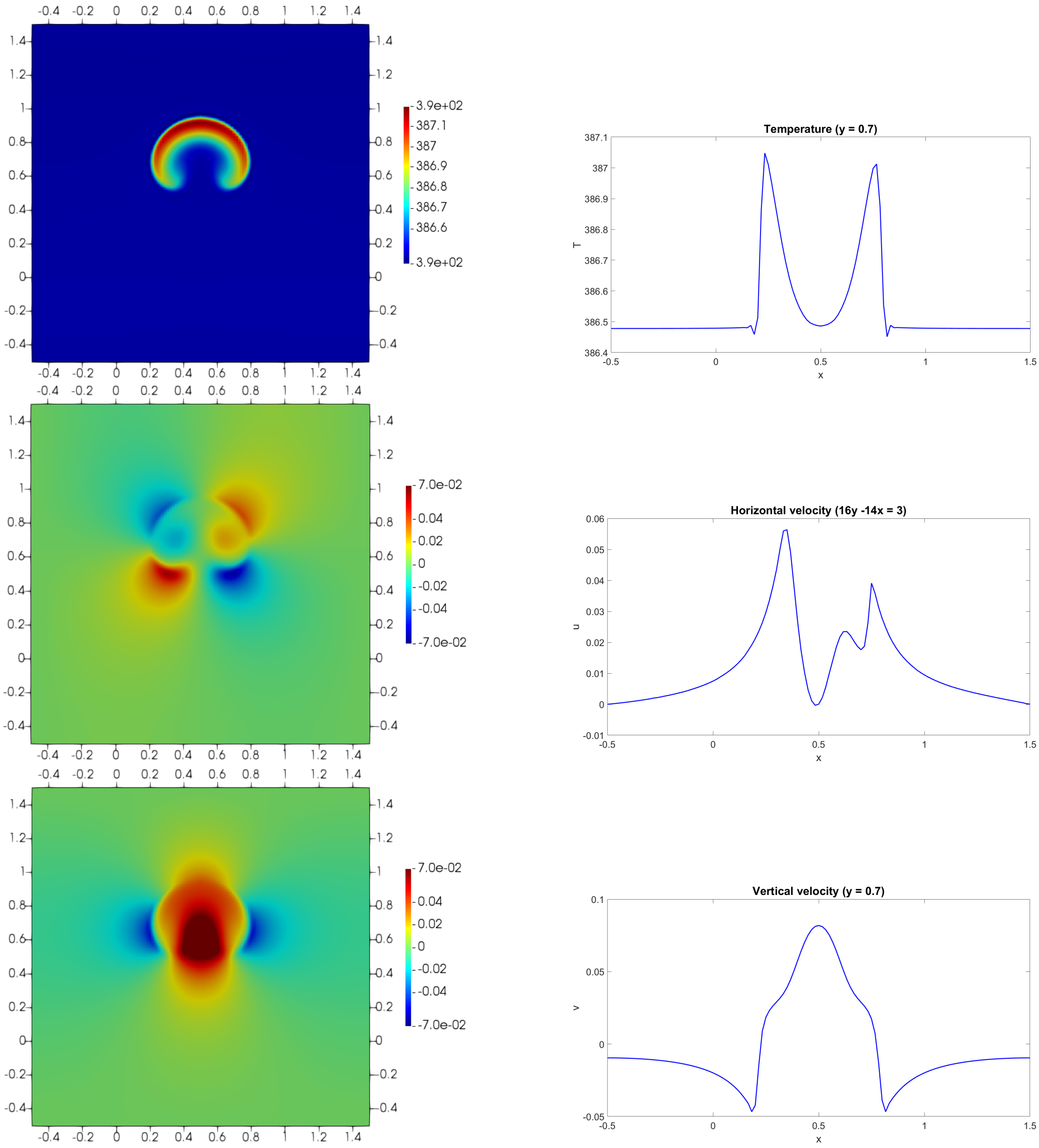

Figure 4.52: *Warm bubble test case, results at $t = 15\,\mathrm{s}$. From bottom to top: temperature, horizontal velocity and vertical velocity.*

4.3.6 Density current

In this Section, we consider the classical density current benchmark proposed in [Straka et al., 1993]. The setup consists of a negative temperature perturbation in a motionless isentropic atmosphere with background potential temperature $\bar{\theta} = 300\,\mathrm{K}$ and temperature $\bar{T} = [300 - zg\gamma R/(\gamma - 1)]\,\mathrm{K}$ on the domain $\Omega = (-25.6, 25.6) \times (0, 6.4)\,\mathrm{km}$. The temperature perturbation $T^{'}$ is defined as

$$T^{'} = \begin{cases} 0 & \text{if } \tilde{r} > 1000 \\ -15\frac{1+\cos(\pi\tilde{r})}{2} & \text{if } \tilde{r} \leq 1000, \end{cases} \tag{4.36}$$

where $\tilde{r} = \sqrt{\left[\frac{(x-x_c)}{x_r}\right]^2 + \left[\frac{(z-z_c)}{z_r}\right]^2}$, $x_c = 0\,\mathrm{m}$, $x_r = 4000\,\mathrm{m}$, $z_c = 3000\,\mathrm{m}$ and $z_r = 2000\,\mathrm{m}$. Following [Straka et al., 1993], diffusive terms are included to

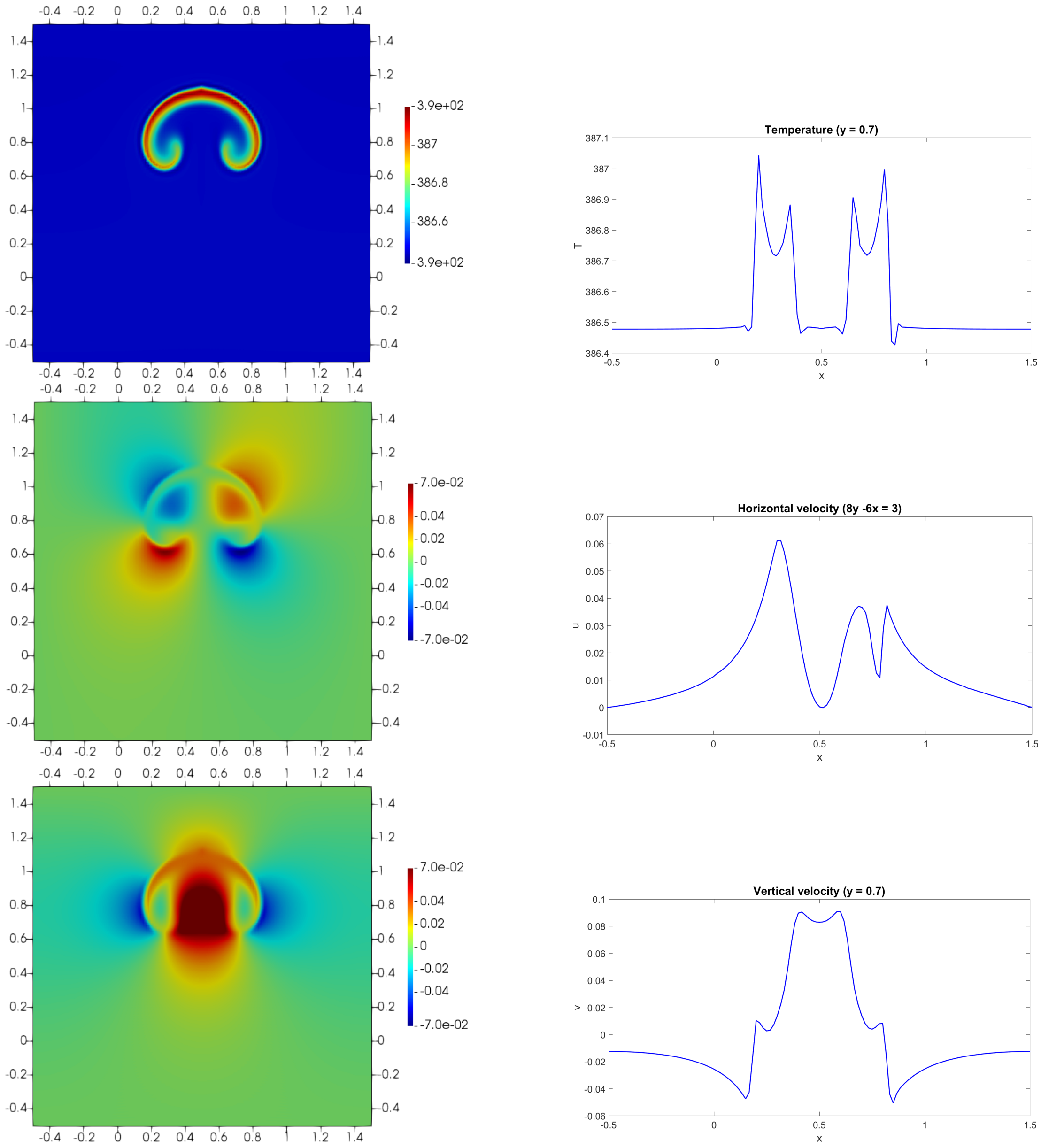

Figure 4.53: *Warm bubble test case, results at $t = 20\,\mathrm{s}$. From bottom to top: temperature, horizontal velocity and vertical velocity.*

stabilize the flow, so that the compressible Navier-Stokes equations in conservative form are considered. We consider the diffusion coefficient $\nu = 75\,\mathrm{m}^2/\mathrm{s}$ and we set the thermal conductivity value κ so that the Prandtl number is $Pr = 0.76$. The boundary conditions are periodic on the left and right boundaries and wall boundary conditions on the top and bottom boundaries. The grid is composed by 1024×128 elements with $r = 2$ leading to a resolution equal to 25 m. The time step is taken equal to 0.1 s, yielding a maximum Courant number $C \approx 1.4$ and $C_u \approx 0.15$. Figure 4.56 shows the deviation of the potential temperature with respect to the background value at different times for the subdomain $(0, 19.2) \times (0, 4.8)\,\mathrm{km}$. In view of the negative buoyancy, the structure falls and reaches the bottom boundary. It then moves to the right, developing vortices. The front location is located at $x = 15\,700\,\mathrm{m}$, in agreement with the results obtained in [Benacchio

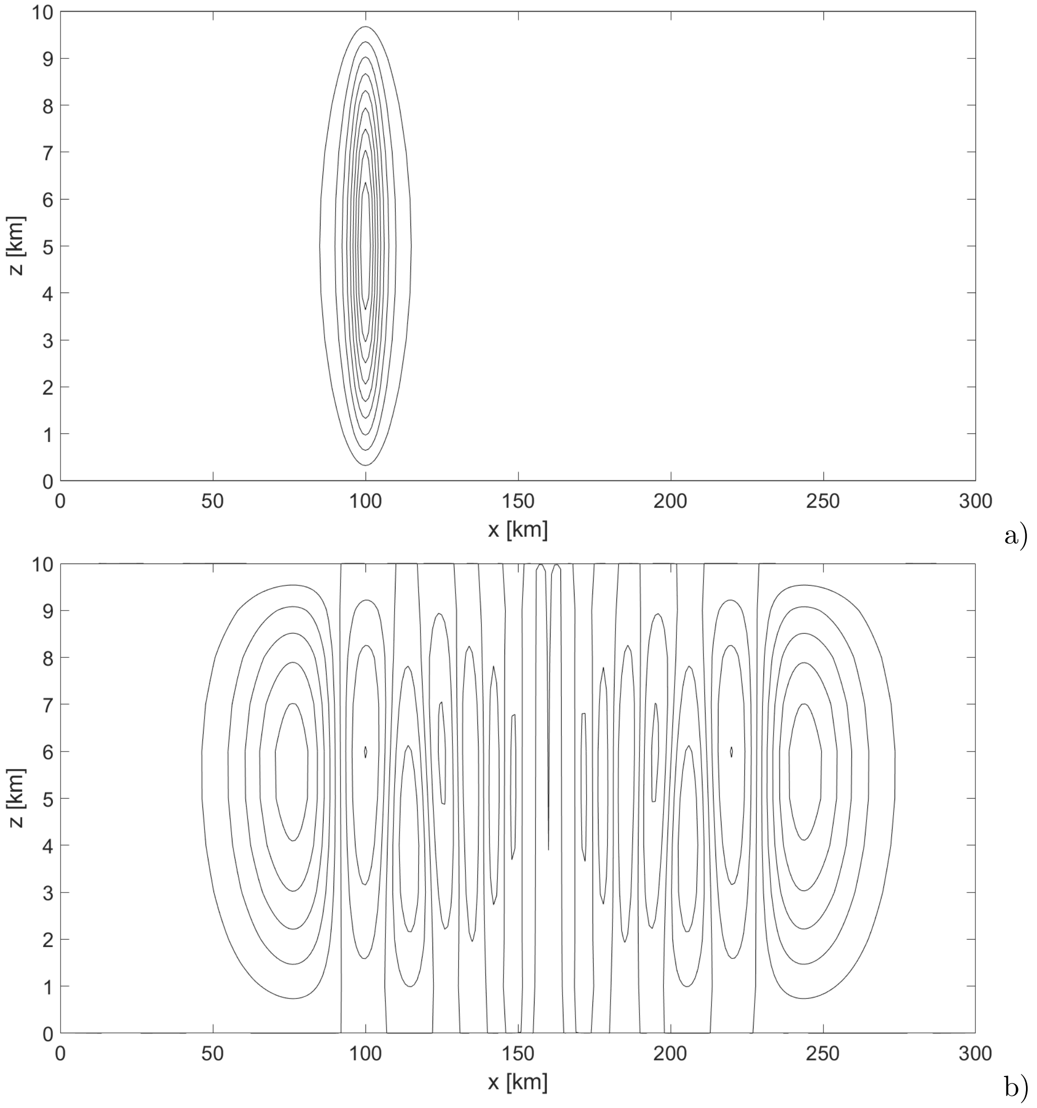

Figure 4.54: *Inertia-gravity waves benchmark, potential temperature deviation a)* $t = 0\,\mathrm{s}$*, b)* $t = 3000\,\mathrm{s}$*. Contours are plotted from* $0.001\,\mathrm{K}$ *to* $0.01\,\mathrm{K}$ *with interval equal to* $1 \times 10^{-3}\,\mathrm{K}$ *for a) and from* $-0.0015\,\mathrm{K}$ *to* $0.003\,\mathrm{K}$ *with interval equal to* $5 \times 10^{-4}\,\mathrm{K}$ *for b).*

et al., 2014, Melvin et al., 2019].

4.3.7 3D rising bubble

In this Section, we consider the 3D rising bubble benchmark proposed in [Melvin et al., 2019]. A neutrally stratified isentropic atmosphere is assumed, with $\bar{\theta} = 300\,\mathrm{K}$ in the domain $\Omega = (-500, -500, -500) \times (500, 500, 1000)\,\mathrm{m}$. A spherical perturbation θ' located at $(x_0, y_0, z_0) = (0, 0, 350)\,\mathrm{m}$ is added to the potential temperature

$$\theta' = \begin{cases} 0.25\left[1 + \cos\left(\frac{\pi r}{r_0}\right)\right] & \text{if } \tilde{r} \leq r_0 \\ 0 & \text{if } \tilde{r} > r_0, \end{cases} \tag{4.37}$$

with $\tilde{r} = \sqrt{(x - x_0)^2 + (y - y_0)^2 + (z - z_0)^2}$ and $r_0 = 250\,\mathrm{m}$. Wall boundary conditions are imposed for all the six boundaries and we take $r = 2$. In order to

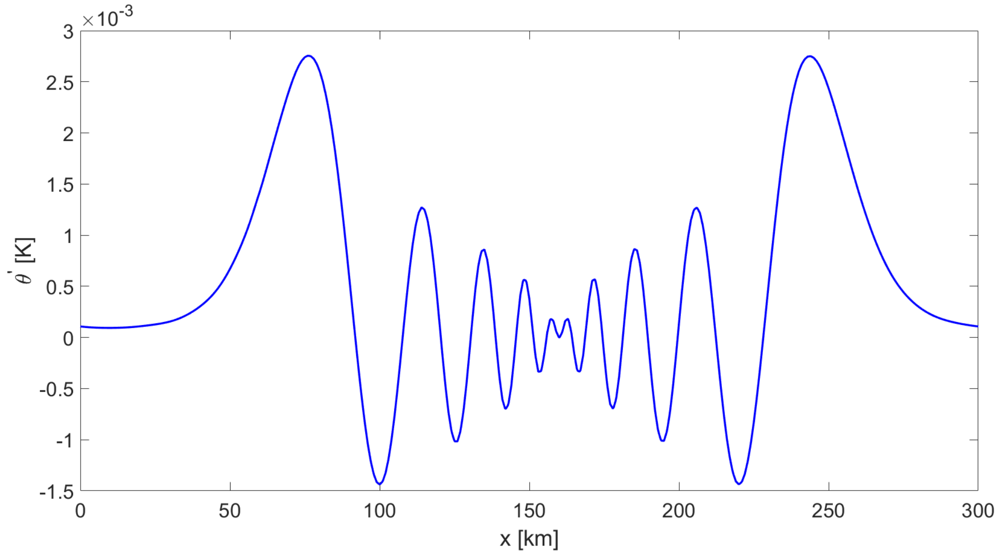

Figure 4.55: *Inertia-gravity waves benchmark, potential temperature deviation at* $t = 3000\,\mathrm{s}$ *along* $z = 5\,\mathrm{km}$ *height.*

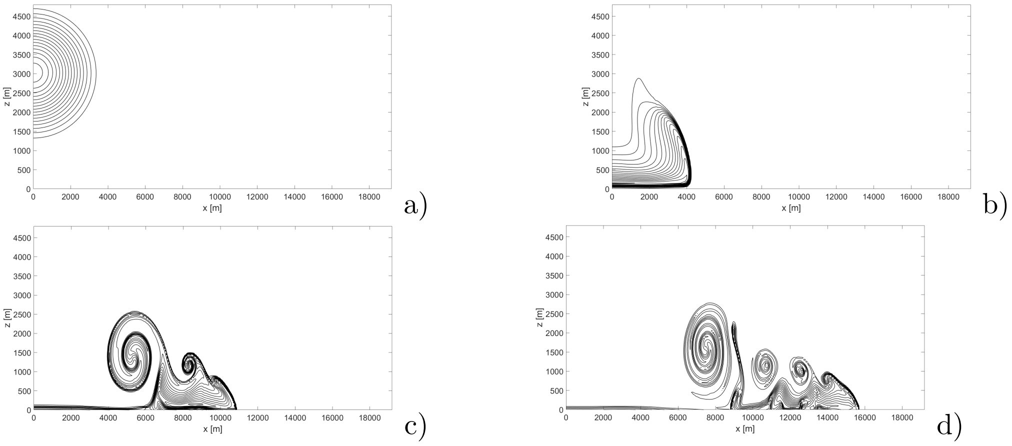

Figure 4.56: *Current density benchmark, potential temperature deviation from background at: a)* $t = 0\,\mathrm{s}$*, b)* $t = 300\,\mathrm{s}$*, c)* $t = 600\,\mathrm{s}$*, d)* $t = 900\,\mathrm{s}$*. Contours are plotted from* $-16\,\mathrm{K}$ *to* $-1\,\mathrm{K}$ *with interval equal to* $1\,\mathrm{K}$*.*

enhance the computational efficiency, we use the $h-$adaptivity capabilities, with the same refinement indicator (4.50) introduced in the Section 4.3.3, namely

$$\eta_K = \max_{i \in \mathcal{N}_K} |\nabla \theta|_i \,. \tag{4.38}$$

The initial grid is composed by $24 \times 24 \times 36$ elements and we allowed up to two local refinements which would correspond to a uniform mesh with $96 \times 96 \times 144$ elements and to a resolution around $5\,\mathrm{m}$. The time step is taken to be equal to $\Delta t = 0.4\,\mathrm{s}$, leading to a maximum acoustic Courant number $C \approx 27$ and advective Courant number $C_u \approx 0.22$. Figure 4.57 shows snapshots of the bubble at $t = 200\,\mathrm{s}$ and $t = 400\,\mathrm{s}$. At the later time, a Kelvin-Helmholtz instability starts to develop, which is however still insufficiently well resolved by the present mesh. Further refinement levels or higher polynomial degrees will have to be employed in future simulations to achieve better accuracy at the later stage. Similar issue for an analogous test case are reported in [Busto et al., 2020]. The final grid is composed by 62792 elements.

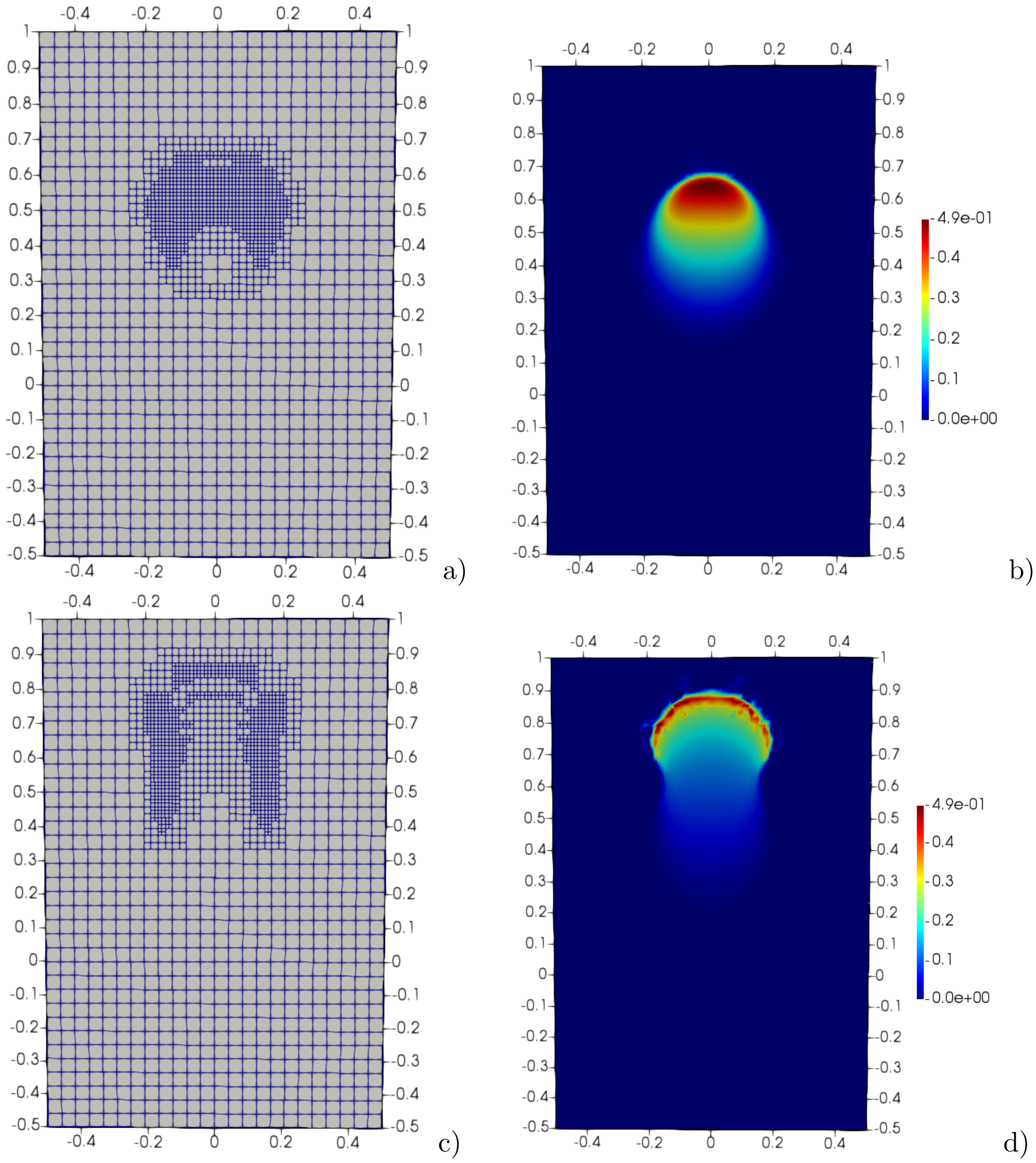

Figure 4.57: *3D rising bubble benchmark, results for* $y = 0\,\mathrm{m}$*; on the left the adaptive meshes at* $t = 200\,\mathrm{s}$ *(a) and* $t = 400\,\mathrm{s}$ *(c) are reported, whereas on the right potential temperature deviations from the background at* $t = 200\,\mathrm{s}$ *(b) and* $t = 400\,\mathrm{s}$ *(d) are reported.*

The size of this benchmark makes it a good candidate for a parallel scaling test. An initial mesh composed by 48 × 48 × 72 elements corresponding to 13436928 dofs for the velocity and 4478976 dofs for the remaining scalar variables is considered. Two configurations are employed: in the first case we keep it fixed, whereas in the second one we apply $h-$adaptivity with two local refinements, roughly doubling the number of degrees of freedom. A strong scaling analysis is performed executing the simulation up to time $t = 8\,\mathrm{s}$ and we use from 32 up to 1024 2xCPU x86 Intel Xeon Platinum 8276-8276L @ 2.4Ghz cores of the HPC infrastructure GALILEO100 at the Italian supercomputing center CINECA thanks to the computational resources made available through the ISCRA-C projects SIDICoNS-HP10CLPLXI and NUMNETF-HP10C06Y02.

The results, reported in Figure 4.58, are quite similar for the two configurations. A good linear scaling is obtained up to 128 cores, even with superlinear behaviour for the fixed mesh framework due to cache effects. Starting from 256 cores, the performance of the fixed mesh configuration exhibits a small degradation and, for a higher number of cores, the speed-up is less optimal for both configurations, due to overwhelming communication costs. The apparent better behaviour of the $h-$adaptive version is due to the fact that more degrees of freedoms are involved and, therefore, the role of communication costs is less evident. The result also highlights that the local refining procedure has no significant impact on the parallel performances and that both efficiency and scalability can be achieved in this framework. These results are also similar to those reported in Section 4.2.3.

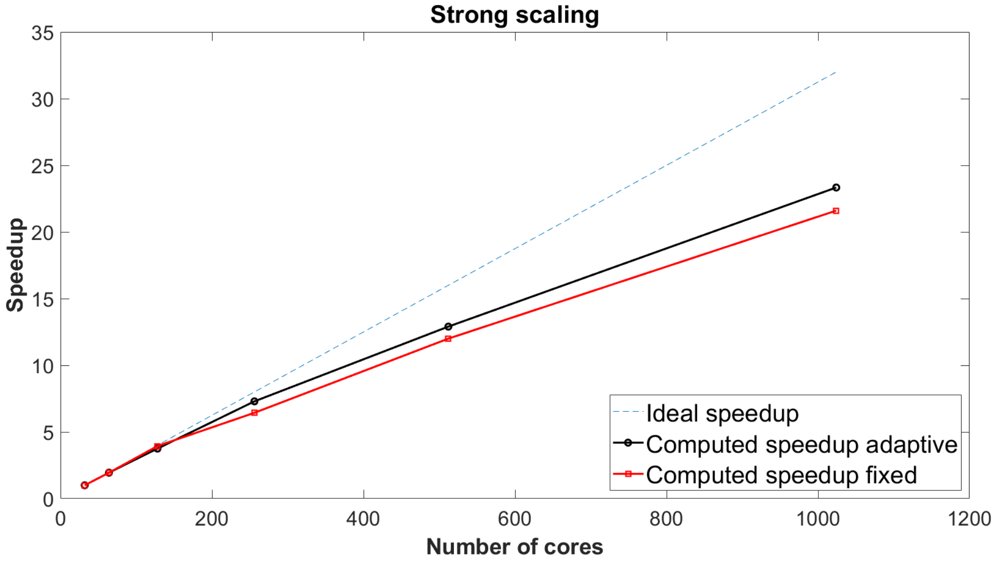

Figure 4.58: *3D rising bubble benchmark, strong scaling analysis. The speedup is computed with respect to the time required with* 32 *cores.*

4.3.8 Hydrostatic flow over a hill

We now consider a number of tests concerning idealized flows over orography, that since the seminal papers [Klemp and Durran, 1983, Klemp and Lilly, 1978] have become a standard benchmark for numerical models of atmospheric flows, see e.g. the results and discussions in [Bonaventura, 2000, Melvin et al., 2019, Pinty et al., 1995, Tumolo and Bonaventura, 2015]. In a first test, the bottom boundary is described by the function

$$h(x) = \frac{h_m}{1 + \left(\frac{x-x_c}{a_c}\right)^2}, \tag{4.39}$$

the so-called *versiera di Agnesi*, where h_m is the height of the hill and a_c is the half-width. The classical Gal-Chen height-based terrain-following coordinate [Gal-Chen and Somerville, 1975] is used to build the mapping between the reference element and the physical one and to obtain a terrain following mesh in Cartesian coordinates. We first consider the linear hydrostatic configuration presented e.g. in [Giraldo and Restelli, 2008]. The computational domain is $\Omega = (0, 240) \times (0, 30)$ km with $h_m = 1\,\mathrm{m}, x_c = 120\,\mathrm{km}$ and $a_c = 10\,\mathrm{km}$. The final time is $T_f = 45\,000\,\mathrm{s}$. The initial state of the atmosphere consists of a constant mean flow with $\overline{u} = 20\,\mathrm{m\,s^{-1}}$ and of an isothermal background profile with temperature $\overline{T} = 250\,\mathrm{K}$ leading to a Mach number $M \approx 0.075$ and a Froude number $Fr \approx 0.20$. The initial profile of the Exner pressure is given by

$$\overline{\Pi} = \left(\frac{p_0}{\overline{p}}\right)^{\frac{\gamma-1}{\gamma}} = \exp\left(-\frac{g}{c_p\overline{T}}z\right). \tag{4.40}$$

We recall that $c_p = \gamma R_g / (\gamma - 1)$ denotes the specific heat at constant pressure and that here $p_0 = 10^5\,\mathrm{Pa}$; moreover, since in an isothermal configuration the Brunt-Väisälä frequency is $N = g/\sqrt{c_p\overline{T}}$, it can be easily checked that $\frac{Na_c}{\overline{u}} >> 1$, so that this configuration corresponds to a hydrostatic regime according to the classification in [Pinty et al., 1995]. For what concerns the boundary conditions, wall boundary conditions are used for the bottom boundary and non-reflecting boundary conditions are required by the top boundary and the lateral boundaries. For this purpose, we introduce a Rayleigh damping profile following [Melvin et al., 2019]

$$\lambda = \begin{cases} 0, & \text{if } z < z_B \\ \overline{\lambda}\sin^2\left[\frac{\pi}{2}\left(\frac{z-z_B}{z-z_T}\right)\right] & \text{if } z \geq z_B, \end{cases} \tag{4.41}$$

where z_B denotes the height at which the damping starts and z_T is the top height of the considered domain. Analogous definitions apply for the two lateral boundaries. In this case, we consider $\overline{\lambda}\Delta t = 0.3$ and we apply the damping layer in the topmost 15 km of the domain and in the first and last 80 km along the horizontal direction. The grid is composed by 100×75 elements with $r = 4$, yielding a resolution of 600 m along x and 100 m along z, whereas the time-step is equal to 2.5 s, leading to $C \approx 1.84$ and $C_u \approx 0.12$. Following [Smith, 1979], we also define the vertical momentum flux as

$$m(z) = \int_{-\infty}^{\infty} \overline{\rho}(z)u^{'}(x,z)w^{'}(x,z)dx, \tag{4.42}$$

where $u^{'}$ and $w^{'}$ represent the deviation from the background state of the horizontal and vertical velocity, respectively. This is a very important diagnostic quantity in atmospheric modelling, used to check that the numerical model is correctly reproducing the orographic forcing on the main flow. From the linear theory, the analytical momentum flux is given by

$$m^H = -\frac{\pi}{4}\overline{\rho}_s\overline{u}_s N h_m^2, \tag{4.43}$$

where $\overline{\rho}_s$ and $\overline{u}_s$ denote the surface background density and velocity, respectively. Figure 4.59 shows the behaviour over time of the momentum flux normalized by its analytical value. It can be noticed that the analytical value is approached as the simulation reaches the steady state. Figure 4.60 shows instead the contour plots of both horizontal and vertical velocity deviations, which are in agreement with the reference results in [Giraldo and Restelli, 2008].

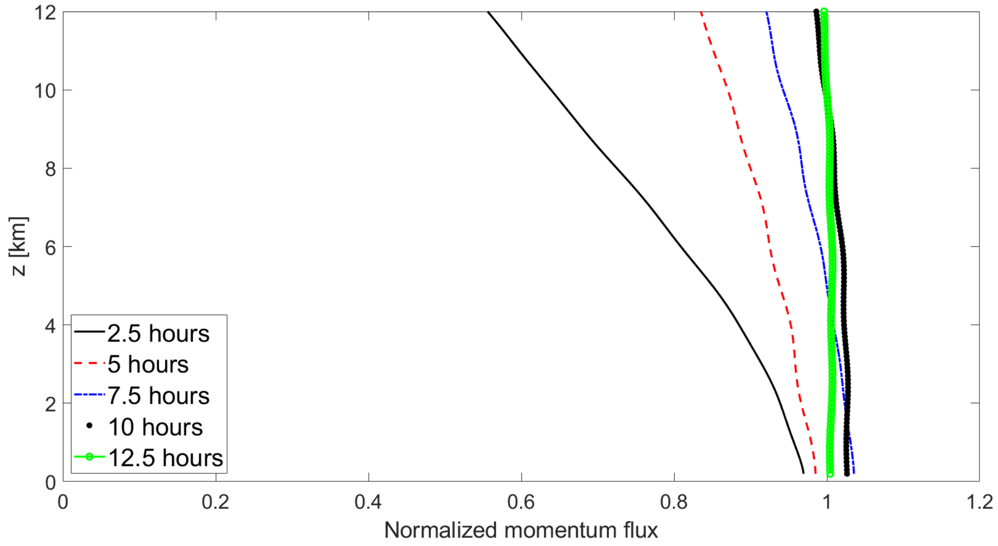

Figure 4.59: *Linear hydrostatic flow over a hill, evolution of normalized momentum flux.*

We consider now the more challenging, nonlinear hydrostatic case considered in [Bonaventura, 2000, Pinty et al., 1995]. The computational domain is $\Omega = (0, 512) \times (0, 28)$ km with $h_m = 800\,\mathrm{m}, x_c = 256\,\mathrm{km}$ and $a_c = 16\,\mathrm{km}$. The final time is $T_f = 60\,000\,\mathrm{s}$. The damping layer is applied starting from $z = 11.5\,\mathrm{km}$ and in the first and last 172 km along the horizontal direction. The background velocity is $\overline{u} = 32\,\mathrm{m\,s^{-1}}$, leading to a Mach number $M \approx 0.12$ and a Froude number $Fr \approx 0.32$, and the Brunt-Väisälä frequency N is equal to $0.02\,\mathrm{s^{-1}}$. The mesh is composed by 160×112 elements with $r = 2$, yielding a resolution of 1600 m along x and 125 m along z, whereas the time step is equal to 10 s, yielding a maximum Courant number $C \approx 1.41$ and $C_u \approx 0.25$. Figure 4.61 shows the contour plots of both the horizontal velocity perturbation and vertical velocity, which compare well with those presented e.g. in [Pinty et al., 1995]. The behaviour over time of the normalized momentum flux is reported in Figure 4.62 and its value at the surface at $t = T_f$ is approximately equal to 1.22, which is comparable to the one obtained in [Pinty et al., 1995]. The momentum flux differs from the analytical one because we are no more in a linear regime. Moreover, as explained in [Durran and Klemp, 1983], it is strongly dependent on the position of the absorbing layer. These results confirm the stability and the accuracy of the proposed numerical scheme also in presence of orography.

4.3.9 Nonhydrostatic flow over a hill

In this Section, we consider the nonhydrostatic regime, characterized by $\frac{Na_c}{\overline{u}} \approx 1$. The bottom boundary is again described by the function (4.39). We first adopt the linear nonhydrostatic configuration described e.g. in [Giraldo and Restelli, 2008]. The computational domain is $\Omega = (0, 144) \times (0, 30)$ km with $h_m = 1\,\mathrm{m}, x_c = 72\,\mathrm{km}$ and $a_c = 1\,\mathrm{km}$. The final time is $T_f = 28\,800\,\mathrm{s}$. The initial state of the atmosphere is described by the following potential temperature and Exner

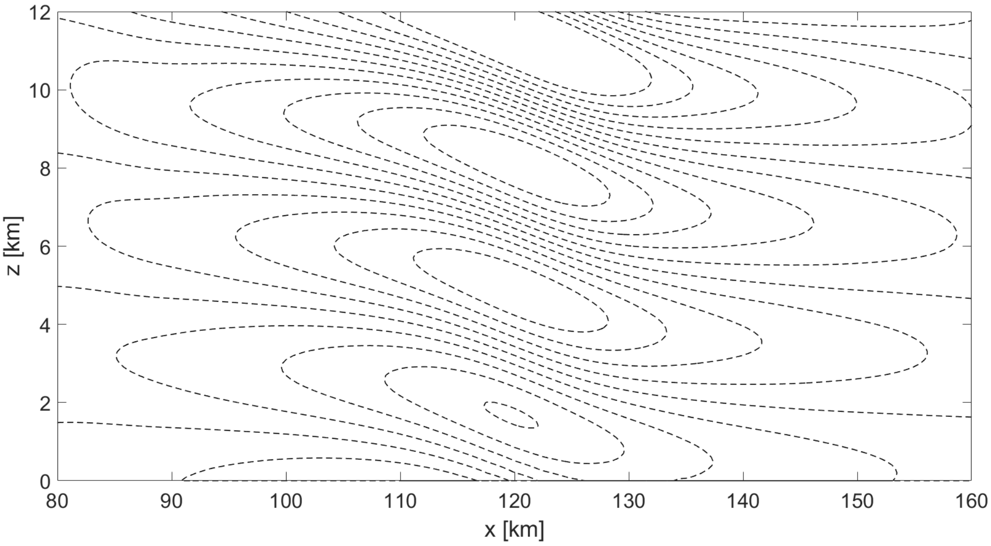

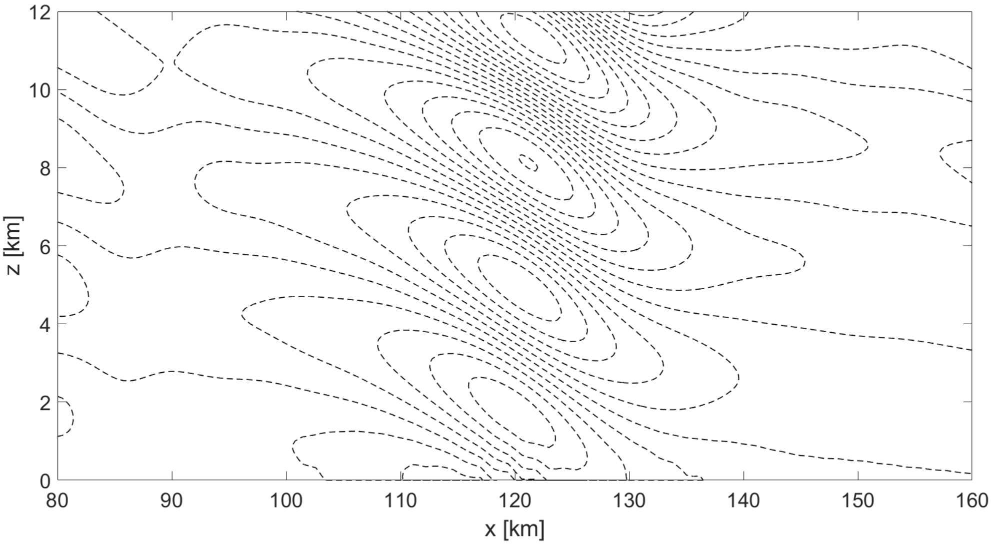

Figure 4.60: *Linear hydrostatic flow over a hill at* $t = T_f$*, a) horizontal velocity deviation. Contour values are between* $-2.5 \cdot 10^{-2}\,\mathrm{m\,s^{-1}}$ *and* $2.5 \cdot 10^{-2}\,\mathrm{m\,s^{-1}}$ *with an interval equal to* $5 \cdot 10^{-3}\,\mathrm{m\,s^{-1}}$*, b) vertical velocity. Contour values are between* $-4 \cdot 10^{-3}\,\mathrm{m\,s^{-1}}$ *and* $4 \cdot 10^{-3}\,\mathrm{m\,s^{-1}}$ *with an interval equal to* $5 \cdot 10^{-4}\,\mathrm{m\,s^{-1}}$*.*

pressure, respectively:

$$\overline{\theta} = \theta_{ref} \exp\left(\frac{N^2}{g} z\right) \qquad (4.44)$$

$$\overline{\Pi} = 1 + \frac{g^2}{c_p \theta_{ref} N^2}\left[\exp\left(-\frac{N^2}{g} z\right) - 1\right], \qquad (4.45)$$

with $\theta_{ref} = 280\,\mathrm{K}$ and $N = 0.01\,\mathrm{s^{-1}}$. The background velocity $\overline{u}$ is equal to $10\,\mathrm{m\,s^{-1}}$, leading to a Mach number $M \approx 0.035$ and a Froude number $Fr \approx 0.10$. Following [Klemp and Durran, 1983], the analytical momentum flux is given by

$$m^{NH} = 0.457 m^{H} \qquad (4.46)$$

and this value will be used to compute the normalized momentum flux for the present test case. Wall boundary conditions are applied on the bottom bound-

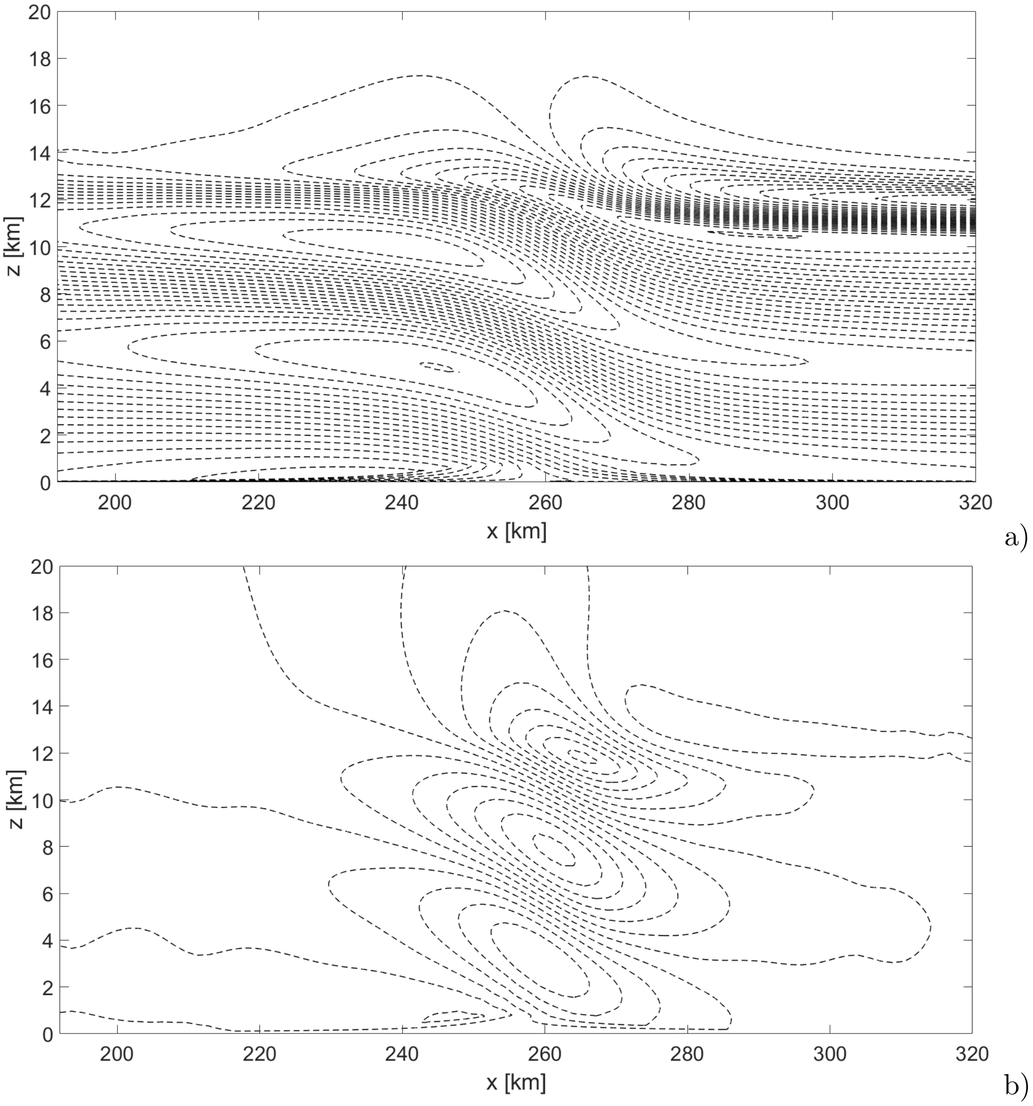

Figure 4.61: *Nonlinear hydrostatic flow over a hill at* $t = T_f$*, a) horizontal velocity deviation, values between* $-23\,\mathrm{m\,s^{-1}}$ *and* $28\,\mathrm{m\,s^{-1}}$ *with contour interval of* $2\,\mathrm{m\,s^{-1}}$*, b) vertical velocity, values between* $-3.9\,\mathrm{m\,s^{-1}}$ *and* $3.5\,\mathrm{m\,s^{-1}}$ *with contour interval of* $0.5\,\mathrm{m\,s^{-1}}$.

ary and non-reflecting boundary conditions are employed on the top and lateral boundaries with $\overline{\lambda}$ such that $\overline{\lambda}\Delta t = 0.15$. The damping layer is applied in the topmost 14 km of the domain and in the first and last 40 km along the horizontal direction. The mesh is composed by 200 × 50 elements with $r = 4$, yielding a resolution of 180 m along x and 150 m along z, whereas the time step is equal to 1 s, leading to $C \approx 2.02$ and $C_u \approx 0.06$. Figure 4.63 reports the time evolution of the normalized momentum flux and, as for the linear hydrostatic case in the previous Section, the analytical value is approached as the simulation reaches the steady state.

Finally, we consider a nonlinear nonhydrostatic case, see e.g. [Tumolo and Bonaventura, 2015]. The computational domain is $\Omega = (0, 40) \times (0, 20)$ km with $h_m = 450\,\mathrm{m}, x_c = 20\,\mathrm{km}, a_c = 1\,\mathrm{km}, T_f = 36\,000\,\mathrm{s}, N = 0.02\,\mathrm{s^{-1}}, \theta_{ref} = 273\,\mathrm{K}$ and $\overline{u} = 13.28\,\mathrm{m\,s^{-1}}$, leading to a Mach number $M \approx 0.047$ and a Froude number

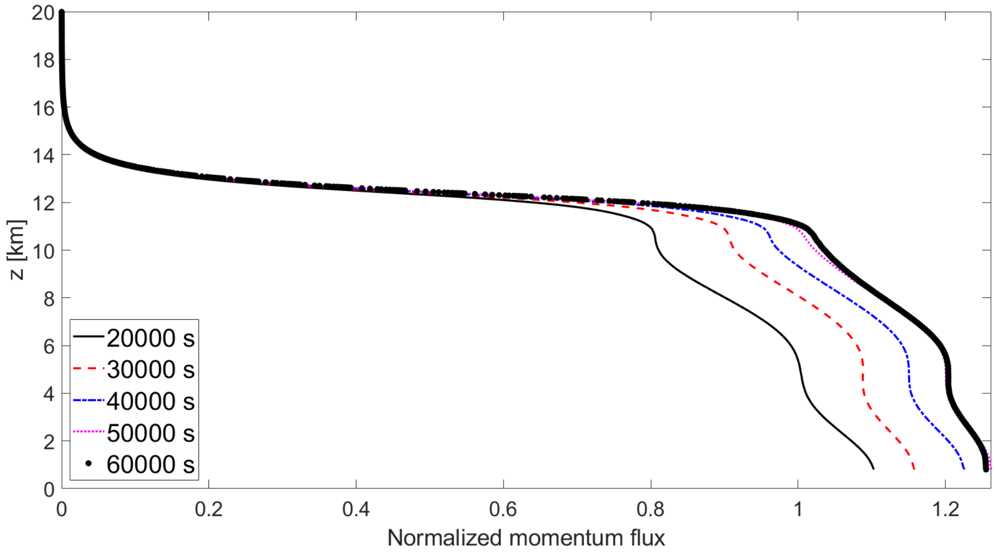

Figure 4.62: *Nonlinear hydrostatic flow over a hill, normalized momentum flux evolution*

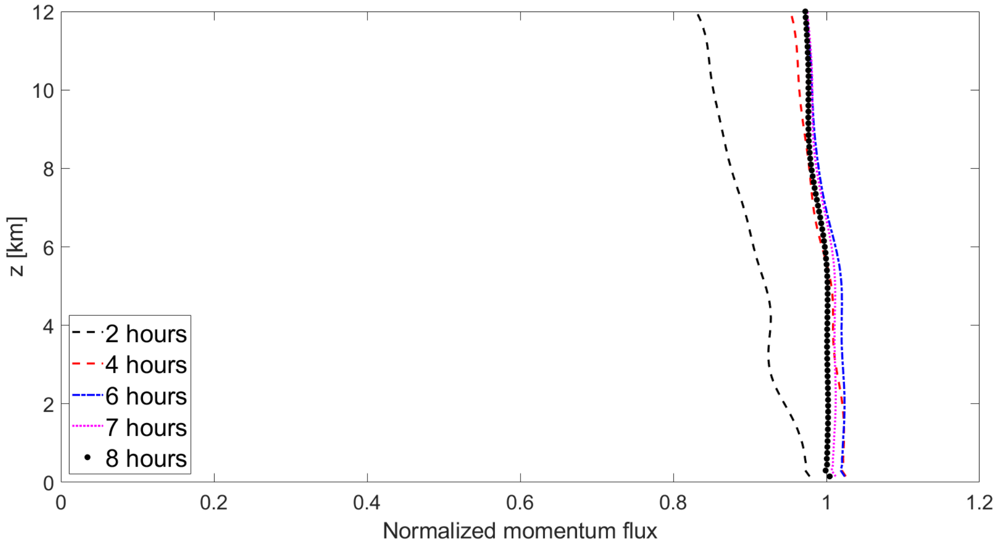

Figure 4.63: *Linear nonhydrostatic flow over a hill, evolution of normalized momentum flux.*

$Fr \approx 0.13$. The damping layer is applied in the topmost 11 km of the domain and in the first and last 10 km along the horizontal direction. The mesh is composed by 50×50 elements with $r = 4$, yielding a resolution of 200 m along x and 100 m along z. The time step is equal to 0.5 s, leading to a maximum Courant number $C \approx 1.13$ and $C_u \approx 0.08$. Figure 4.64 shows the contour plots of both horizontal velocity perturbation and vertical velocity, which are analogous to those reported in [Tumolo and Bonaventura, 2015], as well as the time evolution of the normalized vertical momentum flux. Notice that the momentum flux is normalized by the analytical value (4.43).

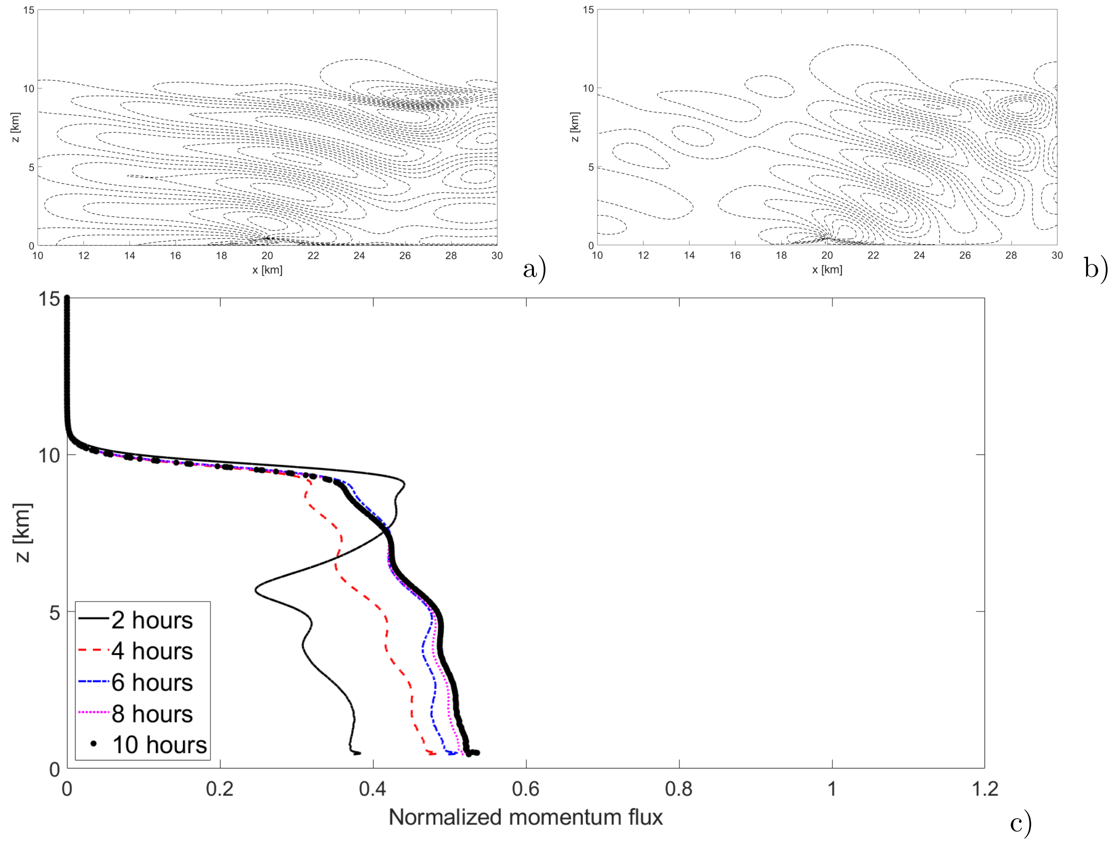

Figure 4.64: *Nonlinear nonhydrostatic flow over a hill, a) horizontal velocity deviation, values between* $-7.2\,\mathrm{m\,s^{-1}}$ *and* $9.0\,\mathrm{m\,s^{-1}}$ *with contour interval of* $1.16\,\mathrm{m\,s^{-1}}$ *at* $t = T_f$*, b) vertical velocity, values between* $-4.2\,\mathrm{m\,s^{-1}}$ *and* $4.0\,\mathrm{m\,s^{-1}}$ *with contour interval of* $0.586\,\mathrm{m\,s^{-1}}$ *at* $t = 18\,000\,\mathrm{s}$*, c) normalized momentum flux evolution.*

4.3.10 Schär hill

In this Section, we consider the well known Schär mountain test, which consists of a steady-state flow over a five-peak mountain chain [Schär et al., 2002, Melvin et al., 2019]. The domain is $\Omega = (-50, 50) \times (0, 30)$ km with surface temperature $T_{ref} = 288\,\mathrm{K}$, constant buoyancy frequency $N = 0.01\,\mathrm{s^{-1}}$ and a background wind $\bar{u} = 10\,\mathrm{m\,s^{-1}}$, leading to a Mach number $M \approx 0.035$ and a Froude number $Fr \approx 0.10$. The mountain profile is defined as

$$h(x) = h_m \exp\left[\left(-\frac{x}{a_c}\right)^2\right] \cos^2\left(\frac{\pi x}{\lambda_c}\right), \tag{4.47}$$

with $h_m = 250\,\mathrm{m}, a_c = 5\,\mathrm{km}$ and $\lambda_c = 4\,\mathrm{km}$. Notice that this test is in the hydrostatic regime, since $\frac{N a_c}{\bar{u}} > 1$. The background density and pressure have the same expression as in (4.33)-(4.34) with $\theta_{ref} = 288\,\mathrm{K}$ and the final time is $T_f = 18\,000\,\mathrm{s}$. The damping layer is applied in the topmost 10 km of the domain and in the first and last 10 km along the horizontal direction with $\overline{\lambda}\Delta t = 1.2$. The mesh is composed by 100×50 elements with $r = 4$, leading to a resolution of 250 m along x and of 150 m along z, whereas the time step is equal to 2.5 s, yielding a maximum acoustic Courant number $C \approx 2.02$ and a maximum advective Courant number $C_u \approx 0.09$. Figure 4.65 shows the contour plots of both horizontal velocity perturbation and vertical velocity, which are analogous to those reported in [Giraldo and Restelli, 2008, Melvin et al., 2019].

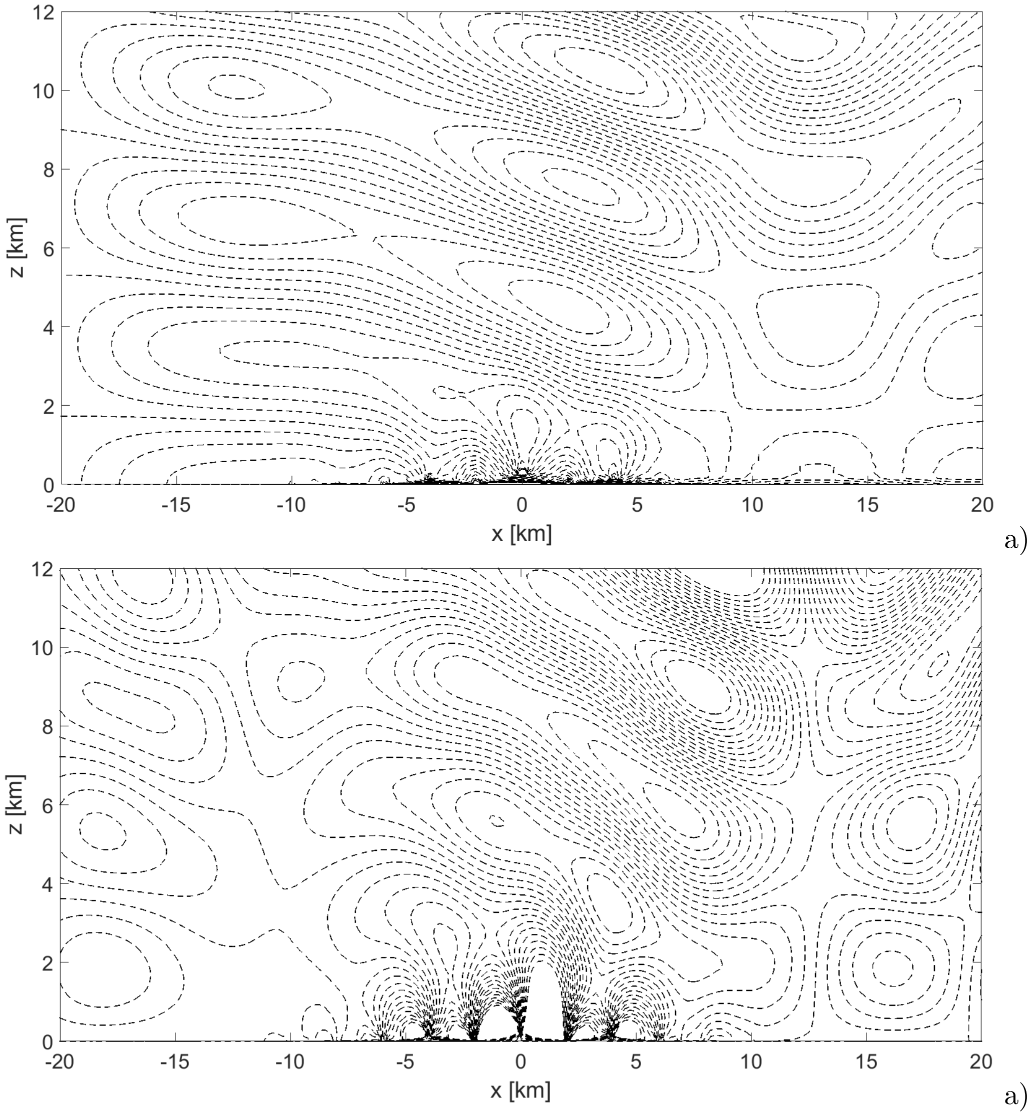

Figure 4.65: *Schär mountain test case at* $t = T_f$*, a) horizontal velocity deviation. Contour values are between* $-2\,\mathrm{m\,s^{-1}}$ *and* $2\,\mathrm{m\,s^{-1}}$ *with an interval equal to* $0.2\,\mathrm{m\,s^{-1}}$*, b) vertical velocity. Contour values are between* $-0.5\,\mathrm{m\,s^{-1}}$ *and* $0.5\,\mathrm{m\,s^{-1}}$ *with an interval equal to* $5 \cdot 10^{-2}\,\mathrm{m\,s^{-1}}$*.*

We consider now for this test case a non-conforming mesh refinement over the soil, as presented in [Orlando et al., 2023]. We apply a coarsening above $z = 2\,\mathrm{km}$, so as to obtain a resolution of $500\,\mathrm{m}$ along the horizontal direction and $300\,\mathrm{m}$ along the vertical direction. The grid is composed by 1550 elements. Figure 4.66 shows a comparison of both horizontal and the vertical velocity deviation contours between the results obtained using the non-conforming grid and those obtained with the uniform mesh. A computational saving time of around 25% is achieved by the use of the non-conforming grid and one can easily notice a good agreement of the two solutions, without spurious reflections at the interface between the two grids. This opens the way to the use of non-conforming grids for flows over orography.

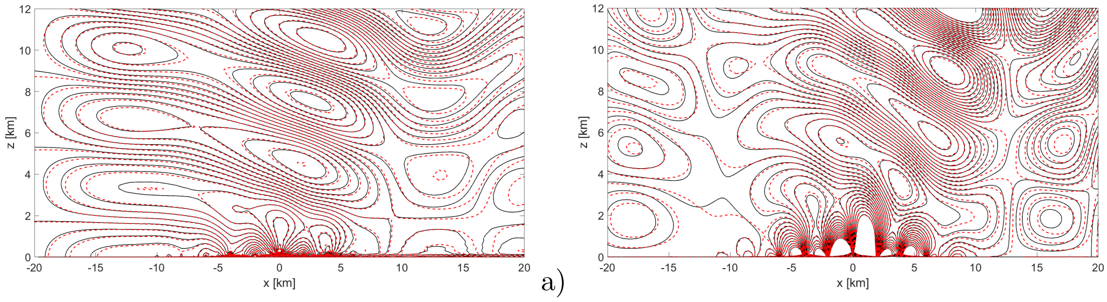

a)
b)

Figure 4.66: *Schär mountain test case at* $t = T_f$*, a) horizontal velocity deviation. Contour values are between* $-2\,\mathrm{m\,s^{-1}}$ *and* $2\,\mathrm{m\,s^{-1}}$ *with an interval equal to* $0.2\,\mathrm{m\,s^{-1}}$*, b) vertical velocity. Contour values are between* $-0.5\,\mathrm{m\,s^{-1}}$ *and* $0.5\,\mathrm{m\,s^{-1}}$ *with an interval equal to* $5 \cdot 10^{-2}\,\mathrm{m\,s^{-1}}$*. The black lines denote the solution with uniform grid, whereas the red lines denote the solution with the non-conforming grid.*

4.3.11 3D medium-steep bell-shaped hill

We finally consider the three-dimensional flow over a bell-shaped hill, see e.g. [Melvin et al., 2019]. The computation domain is $\Omega = (0, 60) \times (0, 40) \times (0, 20)$ km. The mountain profile is defined as

$$h(x, y) = \frac{h_m}{\left[1 + \left(\frac{x - x_c}{a_c}\right)^2 + \left(\frac{y - y_c}{a_c}\right)^2\right]^{3/2}}, \tag{4.48}$$

with $h_m = 400\,\mathrm{m}, a_c = 1\,\mathrm{km}, x_c = 30\,\mathrm{km}$ and $y_c = 20\,\mathrm{km}$. We consider as buoyancy frequency $N = 0.01\,\mathrm{s^{-1}}$ and a background velocity $\overline{u} = 10\,\mathrm{m\,s^{-1}}$, leading to a Mach number $M \approx 0.035$ and a Froude number $Fr \approx 0.10$. We are therefore in a nonhydrostatic regime since $\frac{Na_c}{\overline{u}} = 1$. The background density and pressure have the same expression of (4.33) and (4.34) with $\theta_{ref} = 293.15\,\mathrm{K}$ and the final time is $T_f = 3600\,\mathrm{s}$. The damping layer is applied in the topmost 6 km of the domain and in the first and last 20 km along the lateral boundaries with $\overline{\lambda}\Delta t = 1.2$. In order to increase the resolution around the hill, we consider a non-uniform grid by taking a resolution of 250 m between $x = 25\,\mathrm{km}$ and $x = 40\,\mathrm{km}$ and a resolution of 250 m between $y = 12\,\mathrm{km}$ and $y = 28\,\mathrm{km}$. A uniform resolution of 500 m is considered along the vertical direction z, as well as for the remaining part of the lateral boundaries. The mesh is composed by 8288 elements with polynomial degree $r = 4$, whereas the time step is equal to 2 s, yielding a maximum acoustic Courant number $C \approx 1.95$ and a maximum advective Courant number $C_u \approx 0.1$. The results in Figure 4.67 are in agreement with those reported in [Melvin et al., 2019].

4.4 Numerical results for the single-phase compressible Navier-Stokes equations with non-ideal gas law

We consider now a number of tests for non-ideal gases which show the potentialities of the proposed method also in this framework.

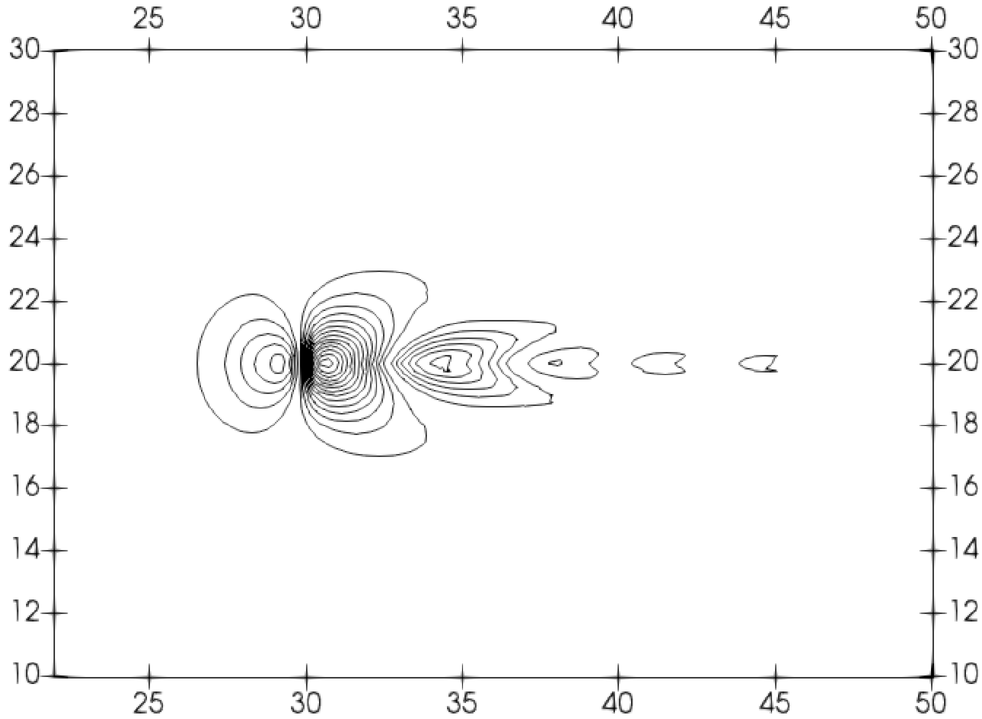

Figure 4.67: *3D mountain benchmark, $x-y$ slice at $z = 800\,\mathrm{m}$ of the vertical velocity. The values are between $-1.5\,\mathrm{m\,s^{-1}}$ and $1.3\,\mathrm{m\,s^{-1}}$ with contour interval of $0.1\,\mathrm{m\,s^{-1}}$*

4.4.1 Cold bubble

We consider first the test case in Section 4.3.3 using non-ideal equations of state. The definition of a potential temperature or of quantities with similar properties is not trivial for non-ideal gases. For an ideal gas, the definition of the potential temperature rises from the analysis of isentropic processes. Hence, we consider here, as counterpart of the potential temperature, the quantity

$$\beta = \log(T) - 2\frac{\tilde{R}_g}{\tilde{c}_v}\,\mathrm{atanh}\left(2\rho\tilde{b} - 1\right) \tag{4.49}$$

defined in (2.241), stemming from the original analysis of isentropic processes for the general cubic equation of state depicted in Section 2.6.1. We first consider the van der Waals equation with a constant $\tilde{c}_v$ given by $\tilde{c}_v = \frac{\tilde{R}_g}{\gamma-1} = 7.175 \cdot 10^{-3}, \tilde{a} = 5 \cdot 10^{-9}$ and $\tilde{b} = 5 \cdot 10^{-4}$, so that the same specific heat at constant volume with respect to the ideal gas case is obtained and $z \approx 1$. The fluid is initialized using the same pressure and the same density values as in the ideal gas case. Notice that $\frac{d\tilde{a}}{dT} = \frac{d\tilde{c}_v}{dT} = 0$ and so it is not necessary to explicitly compute the temperature for (3.77) and (3.87). We expect a behaviour similar to the ideal gas one and this is confirmed by the density profile reported in Figure 4.68.

We then consider the case with $\tilde{a} = 1.6 \cdot 10^{-1}$ and $\tilde{b} = 5 \cdot 10^{-4}$, which yield an average compressibility factor $z \approx 0.83$. In this case, we expect effects due to conditions far from the ideal ones and so we first compute a reference solution with the third order optimal SSP explicit time discretization scheme [Gottlieb et al., 2001] (see also Appendix A.5). The time step for the IMEX simulation is kept equal to $\Delta t = 0.08$, yielding a maximum Courant number $C \approx 5.3$ and a

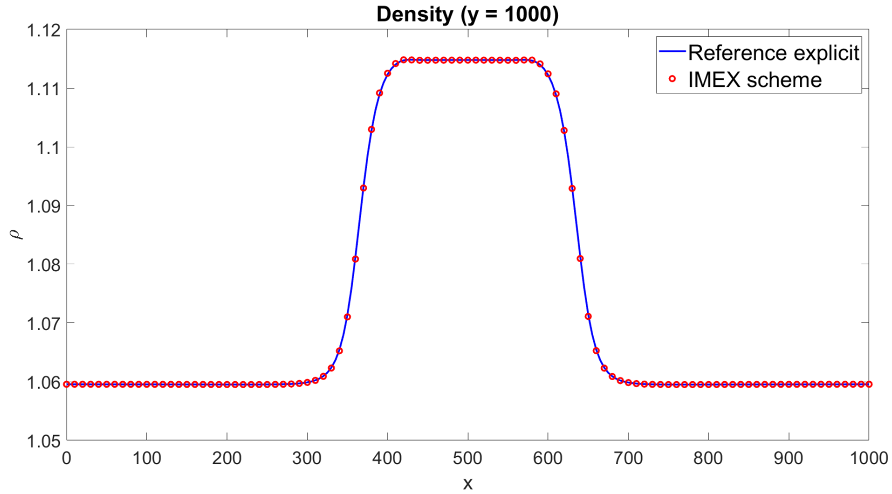

Figure 4.68: *Cold bubble test case, van der Waals EOS with* $\tilde{a} = 5 \cdot 10^{-9}$ *and* $\tilde{b} = 5 \cdot 10^{-4}$*, results at* $t = T_f$*, density profile at* $y = 1000$*. The continuous blue line represents the results for the reference explicit simulation, whereas the red dots denote the results for the IMEX scheme.*

maximum advective Courant number $C_u \approx 0.19$. Figure 4.69 shows the contour plot for β at $t = T_f$ for both the reference explicit and the IMEX simulations. The expected behaviour is retrieved and a good agreement with the reference results is established. Also in this case, a computational saving of around 90% with respect to the explicit simulation is obtained thanks to the IMEX scheme. Figure 4.70 reports the profile of the density for $y = 1000$ at $t = T_f$. One can notice the very good agreement between the IMEX results and the reference ones. Furthermore, a clear discrepancy with respect to the ideal gas can be observed. The higher density values are due to the large value of $\tilde{a}$, which means that strong forces of attraction between the gas particles are present [Nederstigt, 2017].

Concerning the adaptive simulations, since as aforementioned the quantity $\beta = \log(T) - 2\frac{\tilde{R}_g}{\tilde{c}_v} \operatorname{atanh}\left(2\rho\tilde{b} - 1\right)$ is constant in an isentropic process with $\frac{d\tilde{a}}{dT} = \frac{d\tilde{c}_v}{dT} = 0$, we define the local refinement indicator for each element as

$$\eta_K = \max_{i \in \mathcal{N}_K} |\nabla\beta|_i \,. \tag{4.50}$$

We allow to refine when η_K exceeds $4 \cdot 10^{-4}$ and to coarsen when the indicator is below $2 \cdot 10^{-4}$. The initial mesh is composed by 50×100 elements and we allow up to four local refinements. For this reason, in order to keep under control the advective Courant number, we need to reduce the time step $\Delta t = 0.02$, so as to obtain a maximum acoustic Courant number $C \approx 5.3$ and a maximum advective Courant number $C_u \approx 0.18$. Figure 4.71 confirms that β is an appropriate quantity to track the bubble and the one-dimensional density profile in Figure 4.72 shows that no significant loss in accuracy occurs. The final mesh consists of 9086 elements.

The same analysis is carried out using the Peng-Robinson EOS. Hence, we first consider $\tilde{R}_g = 2.87 \cdot 10^{-3}$, $\tilde{c}_v = 7.175 \cdot 10^{-3}$, $\tilde{a} = 5 \cdot 10^{-9}$ and $\tilde{b} = 5 \cdot 10^{-4}$, so that $z \approx 1$. The density profile reported in Figure 4.73 highlights, as expected, a behaviour entirely analogous to that of the ideal gas.

Next, we take $\tilde{a} = 1.6 \cdot 10^{-1}$ and $\tilde{b} = 5 \cdot 10^{-4}$, so that $z \approx 0.83$, and we

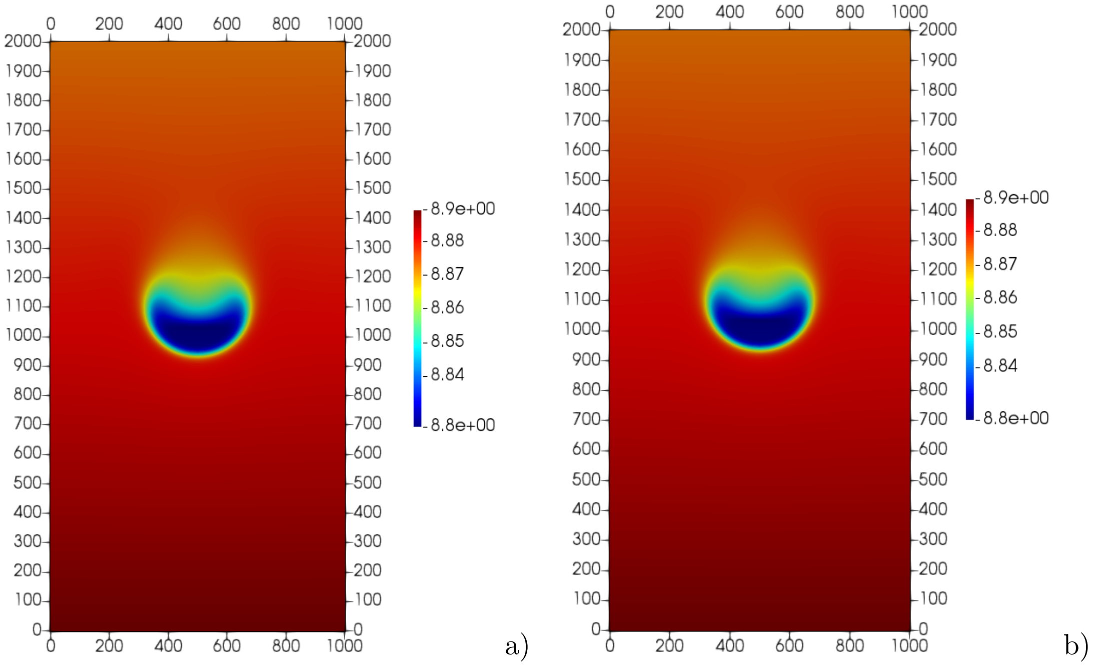

Figure 4.69: *Cold bubble test case, van der Waals EOS with $\tilde{a} = 1.6 \cdot 10^{-1}$ and $\tilde{b} = 5 \cdot 10^{-4}$, results at $t = T_f$, a) contour plot of β for the reference explicit simulation, b) contour plot of β for the simulation with IMEX scheme.*

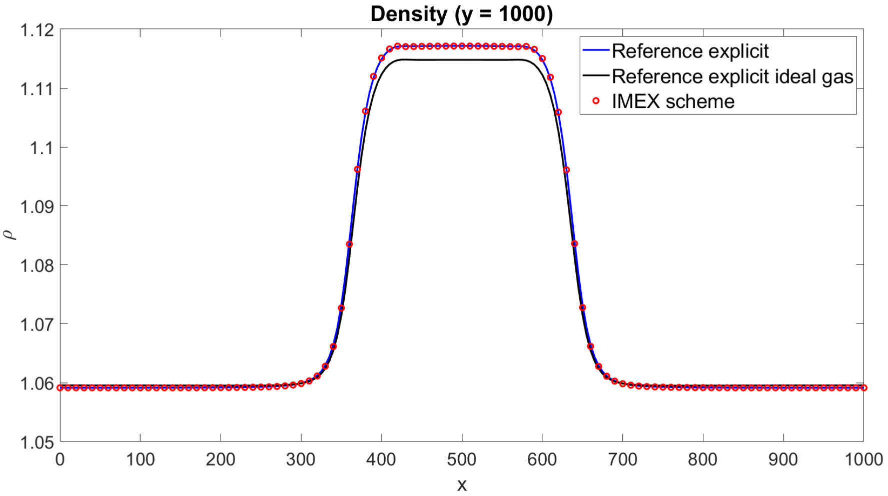

Figure 4.70: *Cold bubble test case, van der Waals EOS with $\tilde{a} = 1.6 \cdot 10^{-1}$ and $\tilde{b} = 5 \cdot 10^{-4}$, results at $t = T_f$, density profile at $y = 1000$. The continuous blue line represents the results for the full explicit simulation, the continuous black line reports the results for the reference explicit simulation with an ideal gas, whereas the red dots denote the results for the IMEX scheme.*

perform both uniform mesh and adaptive simulations, using the same parameters employed for the van der Waals EOS. The results are compared with a reference solution computed with the explicit method. Figure 4.74 shows similar contour plots for all the configurations as well as for the adaptive mesh at $t = T_f$, which consists of 9137 elements and it is able to track the bubble correctly. Figure 4.75 reports the comparison for the one-dimensional profile of the density at $y = 1000$

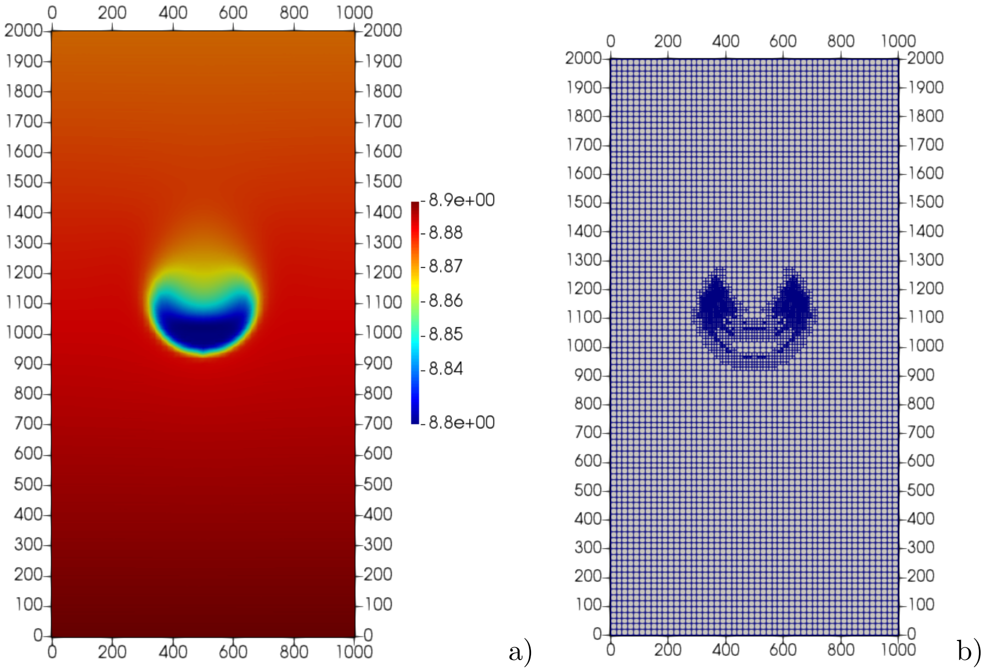

Figure 4.71: *Cold bubble test case, van der Waals EOS with* $\tilde{a} = 1.6 \cdot 10^{-1}$ *and* $\tilde{b} = 5 \cdot 10^{-4}$*, adaptive simulation, results at* $t = T_f$*, a) contour plot of* β*, b) computational grid.*

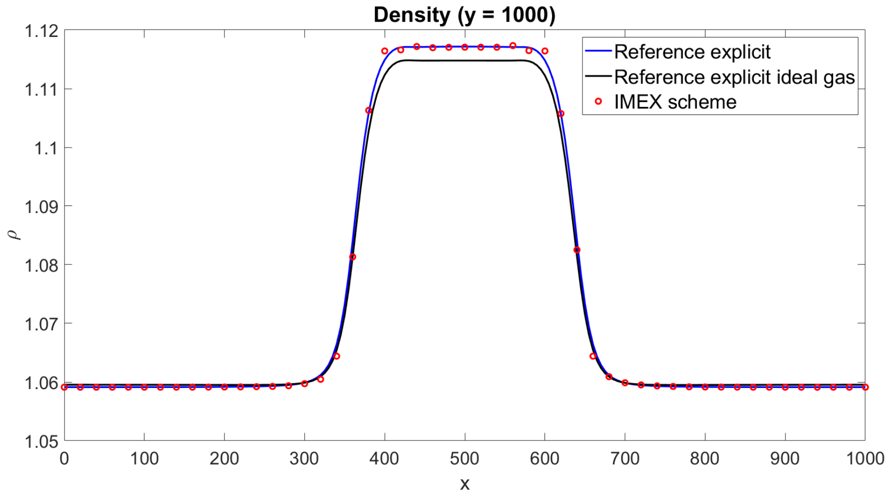

Figure 4.72: *Cold bubble test case, van der Waals EOS with* $\tilde{a} = 1.6 \cdot 10^{-1}$ *and* $\tilde{b} = 5 \cdot 10^{-4}$*, adaptive simulation, results at* $t = T_f$*, density profile at* $y = 1000$*. The continuous blue line represents the results for the reference explicit simulation, the continuous black line reports the results for the reference explicit simulation with an ideal gas, whereas the red dots denote the results for the IMEX scheme in the non-ideal case.*

and the same considerations of the van der Waals EOS are still valid. We want to test in this case the refinement indicator based on (2.242). More specifically, we set

$$\eta_K = \max_{i \in \mathcal{N}_K} \left| \nabla \left(\frac{p}{\rho^{\gamma_{p\rho}}} \right) \right|_i \tag{4.51}$$

and we allow to refine in case η_K is above $4 \cdot 10^{-4}$ and to coarsen below $2 \cdot 10^{-4}$

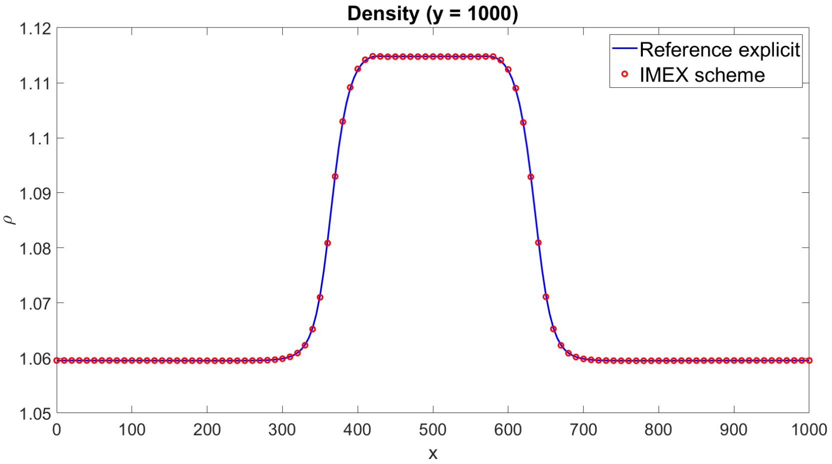

Figure 4.73: *Cold bubble test case, Peng-Robinson EOS with* $\tilde{a} = 5 \cdot 10^{-9}$ *and* $\tilde{b} = 5 \cdot 10^{-4}$*, results at* $t = T_f$*, density profile at* $y = 1000$*. The continuous blue line represents the results for the reference explicit simulation, whereas the red dots denote the results for the IMEX scheme.*

with the same remeshing procedure adopted so far for non-ideal gases. Figure 4.76 shows the contour plot of (2.242) and the computational mesh at $t = T_f$. The mesh consists of 8294 elements and one can easily notice that more resolution is added only in correspondence of the bubble.

4.4.2 Warm bubble

We repeat now the test case in Section 4.3.4 using data for nitrous oxide (N_2O) from [Lias et al., 2010], which we report here for the convenience of the reader. At temperature of 386.48 K and pressure of 10^5 Pa, $\mu = 1.8884 \cdot 10^{-5}\,\mathrm{Pa \cdot s}$ and $\kappa = 2.4855 \cdot 10^{-2}\,\mathrm{W\,m^{-1}\,K^{-1}}$, so as to obtain

$$Re \approx 716.1 \qquad Pr \approx 0.73.$$

We consider the Peng-Robinson EOS, for which the expressions of $\tilde{a}(T)$ and $\tilde{b}$ are the following [Fernandez, 2009]:

$$\begin{cases} \tilde{a}(T) & = 0.45724 \frac{\tilde{R}_g^2 \tilde{T}_c^2}{\tilde{p}_c} \alpha(T)^2 \\ \tilde{\alpha}(T) & = 1 + \tilde{\Gamma}\left(1 - \sqrt{\frac{T}{\tilde{T}_c}}\right) \\ \tilde{\Gamma} & = 0.37464 + 1.54226\omega - 0.26992\omega^2 \\ \tilde{b} & = 0.0778 \frac{\tilde{R}_g \tilde{T}_c}{\tilde{p}_c}, \end{cases} \tag{4.52}$$

where $\tilde{T}_c$ denotes the non-dimensional critical temperature, $\tilde{p}_c$ the non-dimensional critical pressure and ω the acentric factor. For what concerns N_2O, we find from [Lias et al., 2010] $\tilde{T}_c = 309.52, \tilde{p}_c = 7.2450 \cdot 10^6$ and $\omega = 0.1613$. Finally, the function $\tilde{c}_v(T)$ is computed using the following polynomial from [Lias et al., 2010]:

$$\begin{aligned} \tilde{c}_v(T) \; = \; & \frac{1}{T}\left[\left[A\frac{T}{1000} + \frac{1}{2}B\left(\frac{T}{1000}\right)^2 + \frac{1}{3}C\left(\frac{T}{1000}\right)^3 + \right.\right. \\ & \left.\left. \frac{1}{4}D\left(\frac{T}{1000}\right)^4 - E\frac{1000}{T}\right]\frac{10^6}{M_w} - \tilde{R}_{g,N_2O}T\right], \end{aligned} \tag{4.53}$$

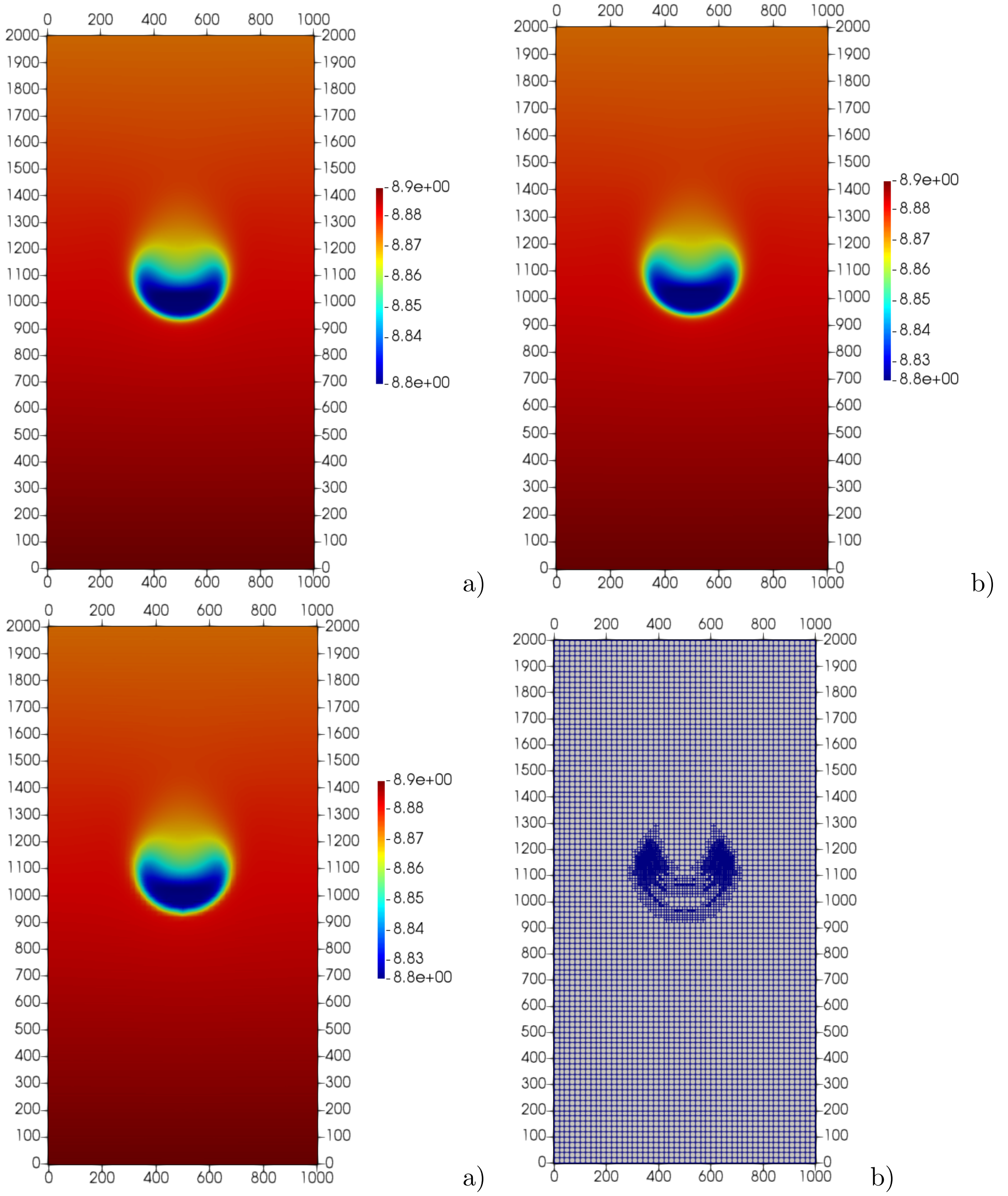

a) b) a) b)

Figure 4.74: *Cold bubble test case, Peng-Robinson EOS with* $\tilde{a} = 1.6 \cdot 10^{-1}$ *and* $\tilde{b} = 5 \cdot 10^{-4}$, *results at* $t = T_f$, *a) contour plot of* β *for the reference explicit simulation, b) contour plot of* β *for the constant mesh simulation with IMEX scheme, c) contour plot of* β *for adaptive simulation with IMEX scheme, d) adaptive mesh.*

with $\tilde{R}_{g,N_2O} = 188.91$, $M_w = 44.0128$ and A, B, C, D, E denoting suitable coefficients whose values are reported in Table 4.33. It is worth to mention once more that $\tilde{c}_v(T)$ is not a proper specific heat at constant volume, but it denotes the non-dimensional counterpart of $\frac{e^{\#}(T)}{T}$ from (2.213), as shown in (2.219). The fluid is initialized with the same temperature and the same pressure as the ideal gas test case in Section 4.3.4. The same mesh and the time step are also used, yielding to $C \approx 92$ and $C_u \approx 0.03$. Figure 4.77 shows the temperature, the horizontal and the vertical velocity at $t = 20\,\text{s}$. One can easily notice that a good

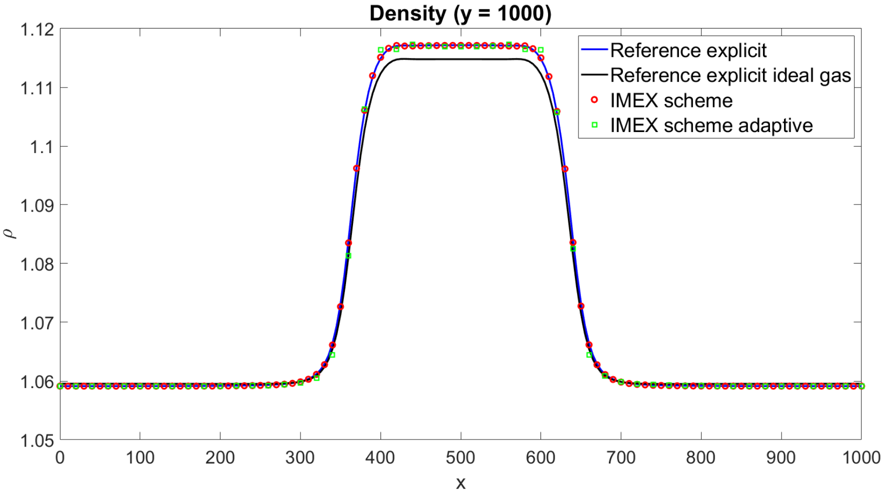

Figure 4.75: *Cold bubble test case, Peng-Robinson EOS with* $\tilde{a} = 1.6 \cdot 10^{-1}$ *and* $\tilde{b} = 5 \cdot 10^{-4}$*, adaptive simulation, results at* $t = T_f$*, density profile at* $y = 1000$*. The continuous blue line represents the results for the reference explicit simulation, the continuous black line reports the results for the reference explicit simulation with an ideal gas, the red dots denote the results for the IMEX scheme, whereas the green squares represent the results for the adaptive simulation with IMEX scheme.*

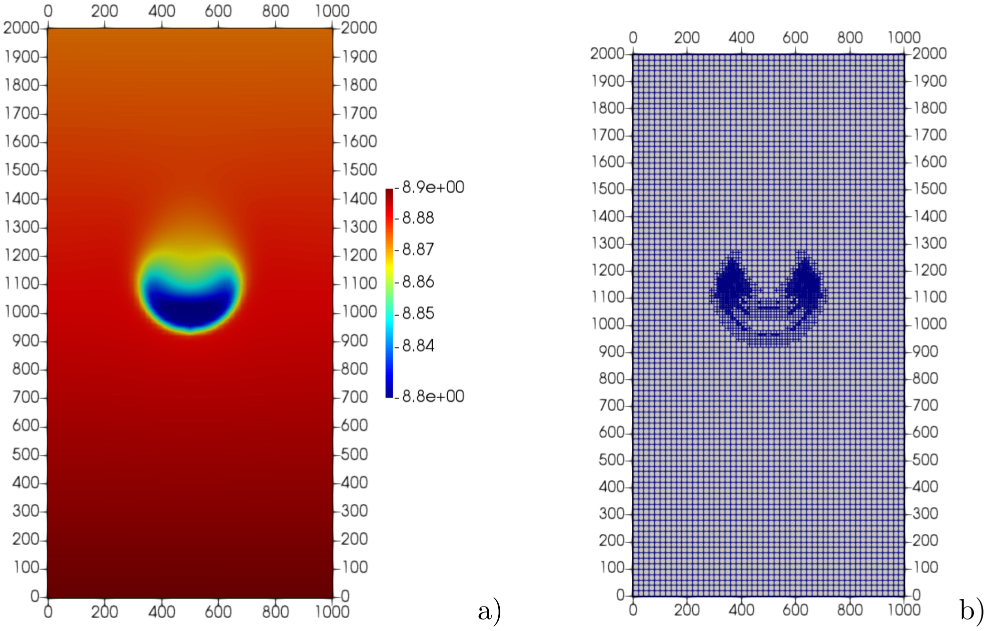

Figure 4.76: *Cold bubble test case, Peng-Robinson EOS with* $\tilde{a} = 1.6 \cdot 10^{-1}$ *and* $\tilde{b} = 5 \cdot 10^{-4}$*, adaptive simulation with criterion* (4.51)*, results at* $t = T_f$*, a) contour plot of* (2.242)*, b) adaptive mesh*

qualitative agreement compared with the results in Figure 4.53 is obtained. For a more quantitative point of view, since an explicit solution cannot be computed in view of the very large acoustic Courant number and the compressibility factor is $z \approx 0.997$, a simulation with the ideal gas law (2.210) is performed, using $\gamma = 1.2879$, which corresponds to $\frac{\tilde{c}_v(386.48)}{\tilde{R}_g} + 1$, so that the internal energy of the ideal gas at $T = 386.48$ is the same as in the case $e^{\#}(386.48)$. The temperature profile at $y = 0.8$ shown in Figure 4.78 confirms the good quality of the solution, with only slight differences due to the different equations of state.

A	27.67988
B	51.14898
C	-30.64544
D	6.847911
E	-0.157906

Table 4.33: *Values for polynomial* (4.53)

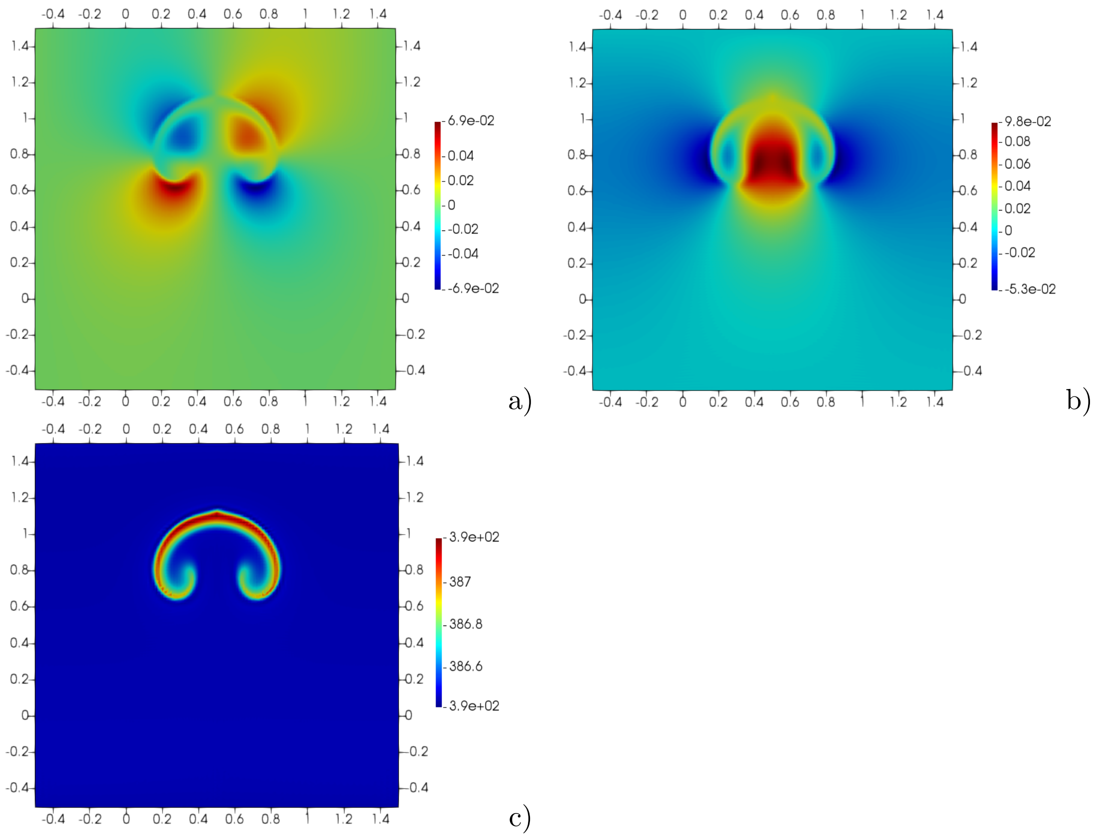

Figure 4.77: *Warm bubble test case for N_2O with Peng-Robinson EOS, results at $t = 20\,\mathrm{s}$, a) horizontal velocity, b) vertical velocity, c) temperature.*

In order to consider also non-ideal effects, we focus on conditions closer to the vapor-liquid phase equilibrium conditions, which are definitely more challenging. More in detail, we set $p = 4 \cdot 10^6$ and we consider the following temperature profile

$$T(\mathbf{x}, 0) = \begin{cases} 298 & \text{if } \tilde{r} > r_0 \\ \dfrac{\tilde{p}_0}{\tilde{R}_{g,air}\left(1 - 0.1 e^{\frac{\tilde{r}^2}{\tilde{\sigma}^2}}\right)} - 88.48 & \text{if } \tilde{r} \leq r_0, \end{cases} \tag{4.54}$$

which corresponds to a translation with respect to (4.31), yielding $z \approx 0.72$. We would like to point out that these conditions of pressure and temperature are close to the vapour-liquid phase transition curve of N_2O. The maximum

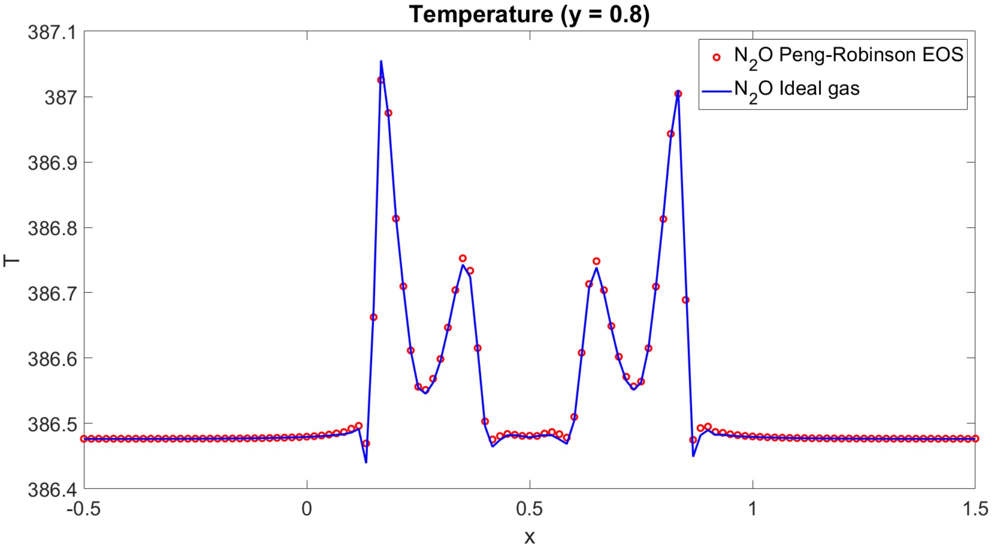

Figure 4.78: *Warm bubble test case for N_2O with Peng-Robinson EOS, temperature profile for $y = 0.8$ at $t = 20\,\mathrm{s}$.*

acoustic Courant is $C \approx 74.5$, whereas the maximum advective Courant number is $C_u \approx 0.06$. Figure 4.79 shows the contour plots of the temperature at $t = 15\,\mathrm{s}$ and $t = 20\,\mathrm{s}$. For these conditions of temperature and pressure, we obtain from [Lias et al., 2010] $\mu = 1.6680 \cdot 10^{-5}\,\mathrm{Pa \cdot s}$, $\kappa = 2.1201 \cdot 10^{-2}\,\mathrm{W\,m^{-1}\,K^{-1}}$ and $c_p = 1.5150 \cdot 10^3\,\mathrm{J\,kg^{-1}\,K^{-1}}$, so as to obtain

$$Re \approx 810.7 \quad Pr \approx 1.19$$

One can easily notice the full development of the Kelvin-Helmholtz instability with the formation of secondary vortices. The bubble reaches a higher altitude with respect to the previous case.

Finally, we consider the SG-EOS with $\gamma = 1.0936, \tilde{c}_v = 1453.91$ and $\tilde{\pi} = \tilde{q} = 0$. The values for γ and $\tilde{c}_v$ are computed using the procedure described in [Gandolfi, 2019]. The maximum acoustic Courant is $C \approx 67$, whereas the maximum advective Courant number is $C_u \approx 0.04$. Figure 4.81 shows the contour plots of the temperature at $t = 15\,\mathrm{s}$ and $t = 20\,\mathrm{s}$. The different behaviour between the two equations of state can be readily explained since, in the case of Peng-Robinson EOS, the difference between the density of the bubble and the background density is bigger with respect to SG-EOS, as evident from Figure 4.83 and, therefore, a bigger upward buoyant force is exerted on the bubble. For this reason, in the simulation with Peng-Robinson EOS reaches a higher level compared to that in the SG-EOS simulation.

4.5 Numerical results for two-phase flow systems

In this Section, we present the results in a number of benchmarks for the two-phase flow systems (2.149) and (3.164).

4.5.1 No mixing water-air mixture

The first two-phase test involves liquid water (phase 1) and air (phase 2) [Re and Abgrall, 2022]. Phase 1 is governed by SG-EOS (2.222) with $\gamma_1 = 4.4, \tilde{c}_{v,1} =$

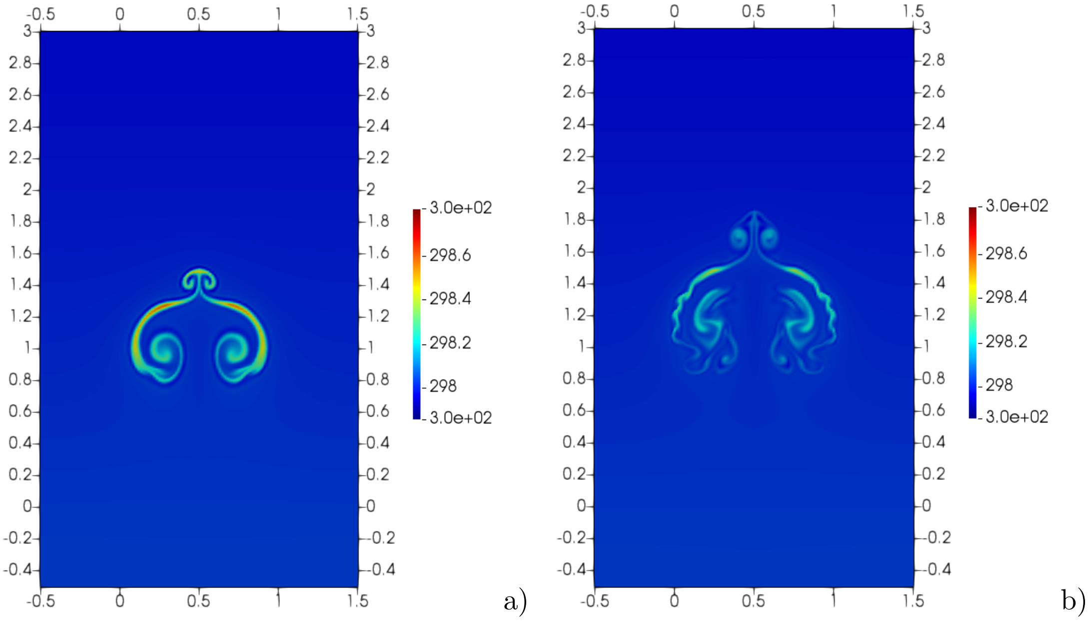

Figure 4.79: *Warm bubble test case for N_2O with Peng-Robinson EOS, a) temperature at $t = 15\,\mathrm{s}$, b) temperature at $t = 20\,\mathrm{s}$.*

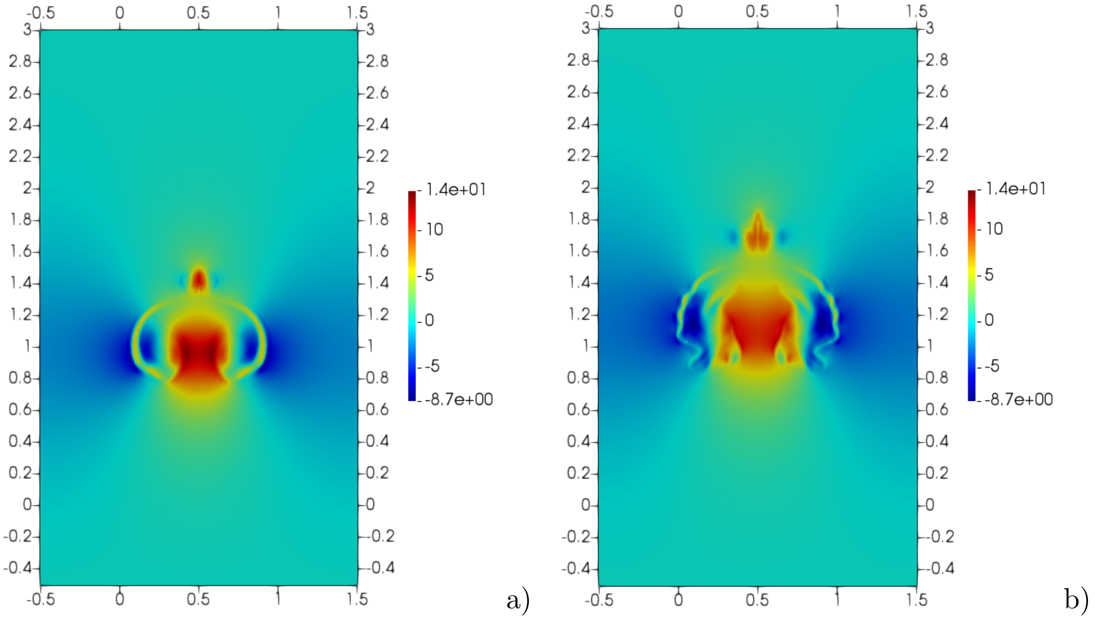

Figure 4.80: *Warm bubble test case for N_2O with Peng-Robinson EOS, a) vertical velocity at $t = 15\,\mathrm{s}$, b) vertical velocity at $t = 20\,\mathrm{s}$.*

$4.178 \cdot 10^{-2}, \tilde{\pi}_{\infty,1} = 6.8 \cdot 10^3$ and $\tilde{q}_{\infty,1} = 0$, whereas phase 2 is governed by the ideal gas law (2.210) with $\gamma_2 = 1.4$ and $\tilde{R}_{g,2} = 2.8704 \cdot 10^{-3}$. We recall once more that $\tilde{c}_v$ and $\tilde{R}_g$ are the non-dimensional counter of the specific heat at constant volume and of the specific gas constant, respectively. The previous parameters are obtained considering $\mathcal{R}_1 = \mathcal{R}_2 = 1\,\mathrm{kg\,m^{-3}}, \Theta_1 = \Theta_2 = 1\,\mathrm{K}$ and $\mathcal{P}_1 = \mathcal{P}_2 = 10^5\,\mathrm{Pa}$ so that $c_{v,1} = 4178\,\mathrm{J\,kg^{-1}\,K}, \pi_{\infty,1} = 6.8 \cdot 10^8\,\mathrm{Pa}$ and $R_{g,2} = 287.04\,\mathrm{J\,kg^{-1}\,K}$. As initial condition, the phases are uniformly dispersed with $\alpha_1 = 0.5$, in a shock tube where a mild pressure jump occurs with $p_L = 100$ and $p_R = 50$. Here,

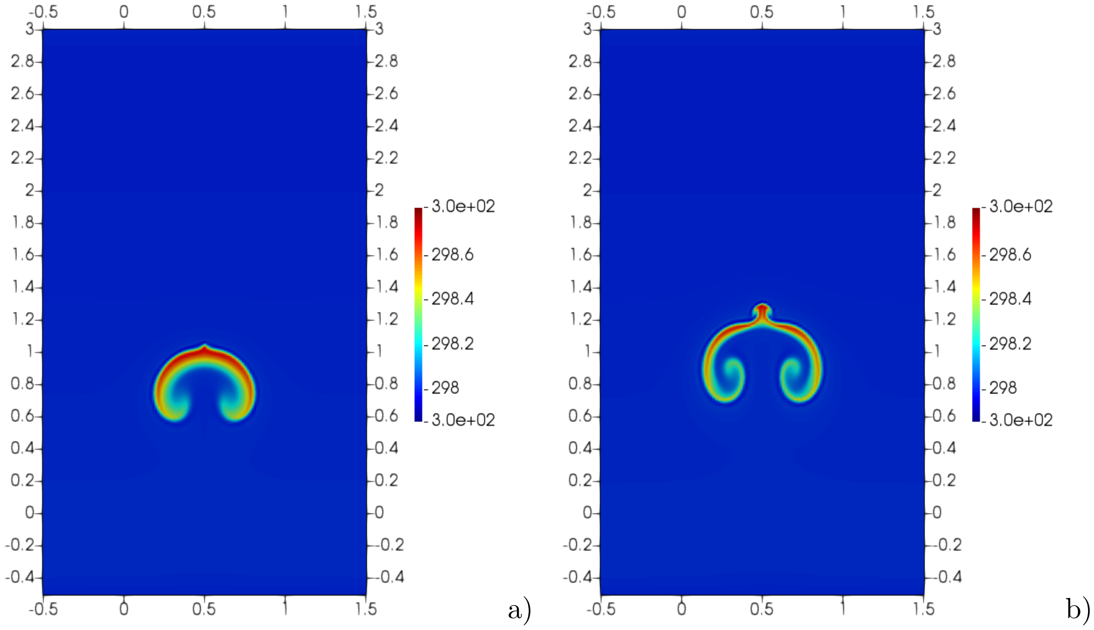

Figure 4.81: *Warm bubble test case for* N_2O *with SG-EOS, a) temperature at* $t = 15\,\mathrm{s}$*, b) temperature at* $t = 20\,\mathrm{s}$.

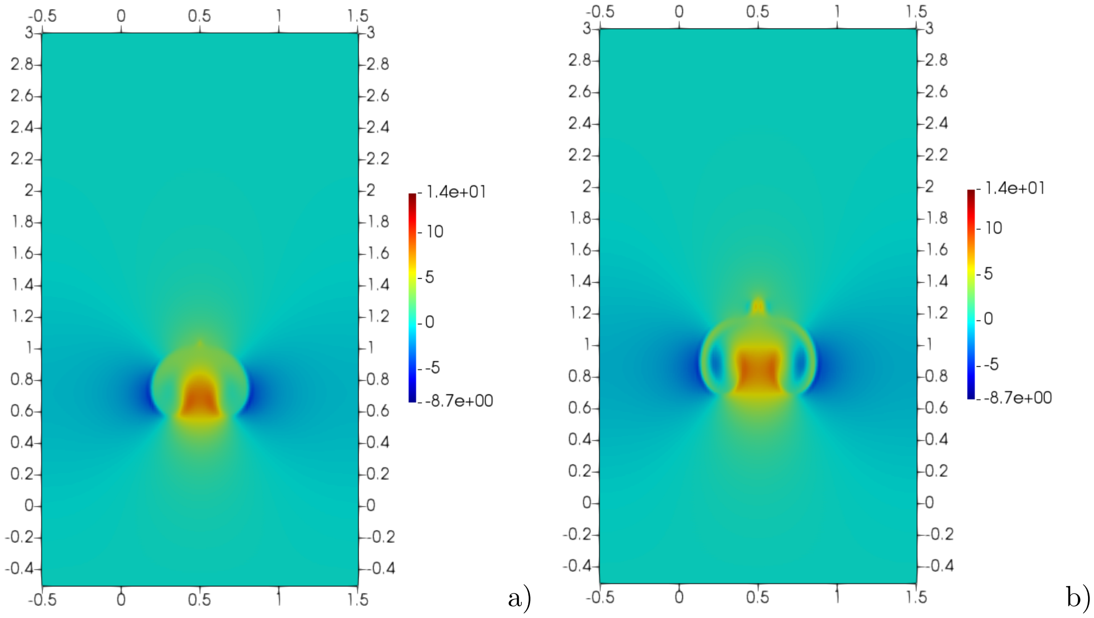

Figure 4.82: *Warm bubble test case for* N_2O *with SG-EOS, a) vertical velocity at* $t = 15\,\mathrm{s}$*, b) vertical velocity at* $t = 20\,\mathrm{s}$.

the subscripts L and R denote the left and right state, respectively. A uniform temperature $T = 270$ is assumed. The domain is $\Omega = (-1, 1)$ and the initial discontinuity is placed at $x_d = 0$. Since no volume fraction gradient is present and no relaxation is considered, each phase evolves independently from the other. The computational grid is composed by $N_{el} = 1000$ elements with polynomial degree $r = 1$, the final time is $T_f = 1.6 \cdot 10^{-4}$ and the time step is chosen in such a way that $\max(C + C_u) \approx 1.3$ for the liquid phase. First of all we point out that, as evident from Figure 4.84, using the formulation (3.158) with a double integration

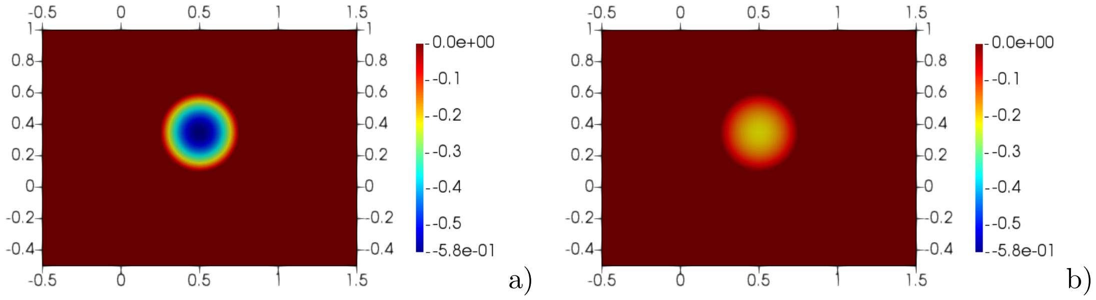

Figure 4.83: *Warm bubble test case for* N_2O*, density deviation from background state at* $t = 0$*, a) Peng-Robinson EOS, b) SG-EOS.*

by parts for all the non-conservative terms allows to preserve the uniform volume fraction, whereas the formulation (3.162) with a single integration by parts gives raise to spurious oscillations in the volume fraction. Hence, from now on we will employ the formulation (3.158) for the treatment of the non-conservative terms. We also employ the filtering monotonization technique presented in Section 3.2 to reduce the oscillations that arise using high order spatial discretization schemes. More in detail, we consider the Froese-Oberman filter function (3.19) with $\beta_{\rho\alpha} = \beta_{\mathbf{u}} = \beta_p = 0.01$ for the liquid phase and $\beta_{\rho\alpha} = \beta_{\mathbf{u}} = \beta_p = 0.1$ for the gaseous phase. Here, $\beta_{\rho\alpha}$ represents the switching parameter for the continuity equations, $\beta_{\mathbf{u}}$ is the switching parameter for the velocity fields and, finally, β_p is the switching parameter for the pressure fields. For the low order solution, we consider the Rusanov flux for both phases, whereas, for the high order solution, we consider the upwind flux for liquid phase and the Rusanov flux for the gaseous phase. The results in Figure 4.85 are analogous to those reported in [Re and Abgrall, 2022].

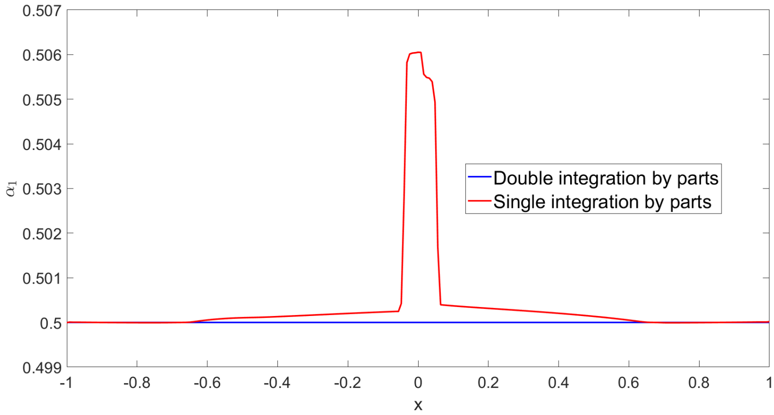

Figure 4.84: *No mixing test case, results at* $t = T_f$*. The blue line denotes the solution obtained using the formulation* (3.158)*, whereas the red line denotes the solution obtained using the formulation* (3.162)*.*

4.5.2 Pure advection test case

Here, we investigate a pure advection problem. A column of water-air mixture with a liquid volume fraction $\alpha_1 = 0.7$ initially located at $0.2 < x < 0.4$ within the domain $\Omega = (0, 1)$ is transported with unitary velocity. The volume fraction α_1 is

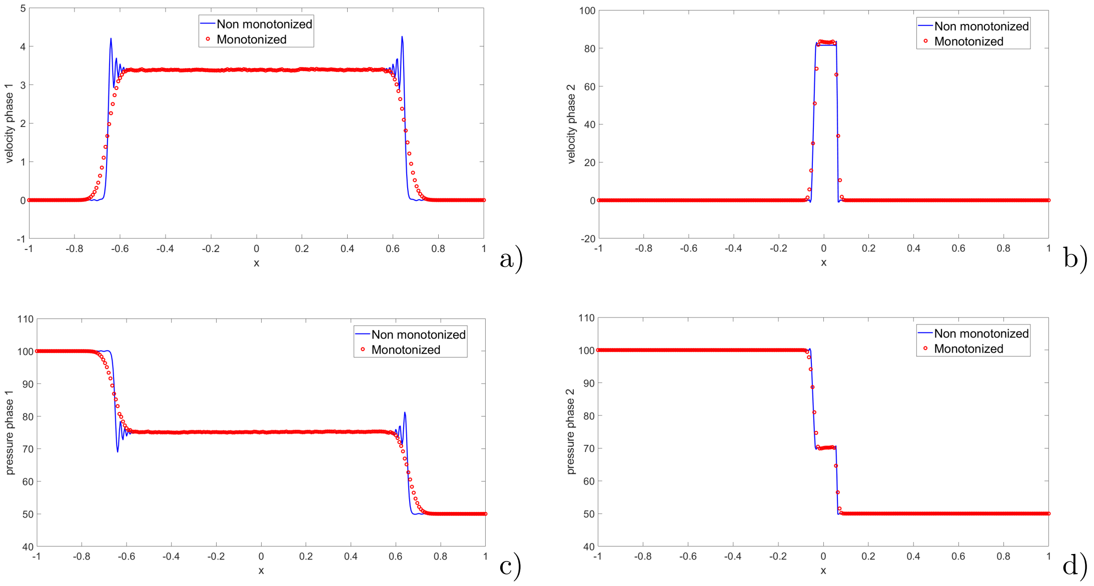

Figure 4.85: *No mixing test case, results at $t = T_f$, a) velocity of phase 1, b) velocity of phase 2, c) pressure of phase 1, d) pressure of phase 2. The blue line denotes the results with the unfiltered discretization, whereas the red dots report the results obtained using the filtering monotonization scheme.*

initialized to $\alpha_1 = 0.3$ in the rest of the domain. A uniform pressure $p_1 = p_2 = 1$ is considered and the initial temperature is $T = 270$ for both phases. The parameters for the equations of state are the same as in the previous test. The final time is $T_f = 0.3$ and we consider $r = 0$ and $r = 1$ as polynomial degree. The results in Figure 4.86 show that no spurious oscillations arise neither in pressure nor in velocity for both $r = 0$ and $r = 1$. For what concerns the volume fraction, spurious oscillations are present using $r = 1$. The application of the filtering monotonization technique for the volume fraction leads to spurious oscillations in velocity and pressure, as one can notice from Figure 4.87. This phenomenon can be readily explained as follows: since the monotonization technique is a sort of blending between the low order and the high order solution, the relation (3.138) is not satisfied at discrete level and, as a consequence, the relation (3.137) that prescribes the uniform pressure cannot be satisfied.

We perform now a convergence analysis for the employed method. For this purpose, we define the following regolarization of the volume fraction:

$$\alpha_1^0(x) = \begin{cases} 0.4\dfrac{\exp\left(-\frac{1}{(x-0.1)(0.5-x)}\right)}{\exp\left(-\frac{1}{0.04}\right)} + 0.3 & \text{if } 0.1 < x < 0.5 \\ 0.3 & \text{otherwise,} \end{cases} \tag{4.55}$$

so that the exact solution is $\alpha_1(x, t) = \alpha_1^0(x - t)$. The analysis is performed at fixed Courant number. Table 4.34 and Table 4.35 show that expected convergence rates of order $r + 1$ are achieved for both $r = 0$ and $r = 1$.

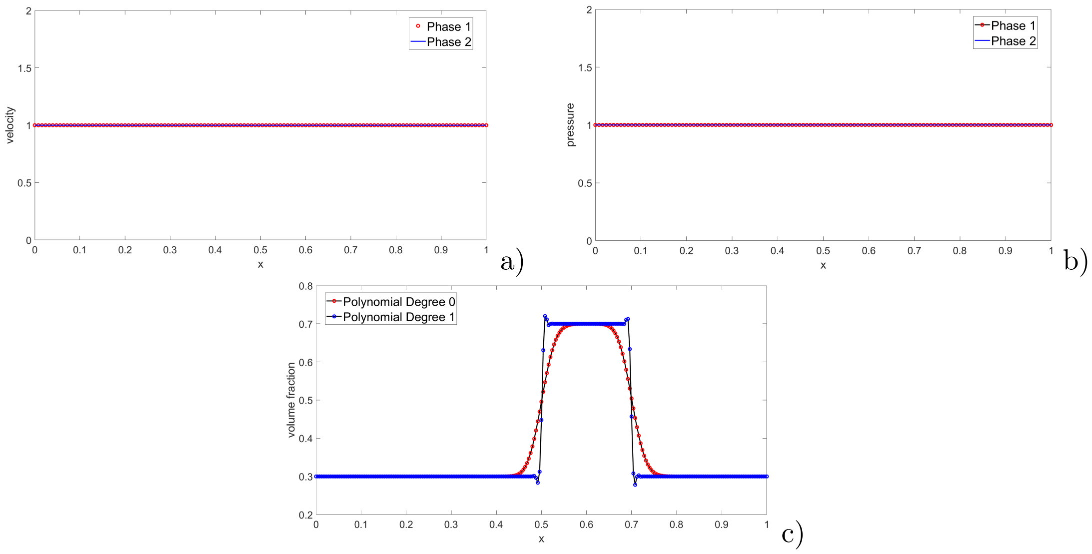

Figure 4.86: *Pure advection test case, results at $t = T_f$, a) velocity, b) pressure, c) volume fraction. For a) and b), the red dots denote the results for phase 1, whereas the blue line denotes the results for phase 2. In c), the red dots denote the results for $r = 0$, the blue dots denote the results for $r = 1$.*

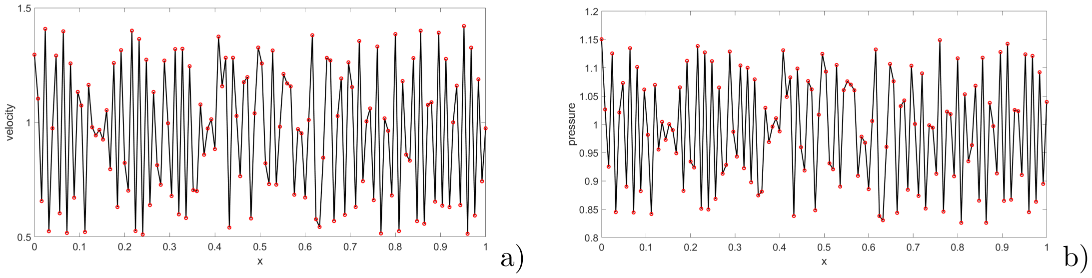

Figure 4.87: *Pure advection test case, results at $t = T_f$, a) velocity phase 1, b) pressure phase 1. The results are obtained using the filtering monotonization technique with $\beta_\alpha = \beta_{\rho\alpha} = \beta_{\mathbf{u}} = \beta_p = 0.5$.*

Δt	N_{el}	L^2 rel. error α_1	L^2 rate α_1
8×10^{-4}	125	1.31×10^{-1}	
4×10^{-4}	250	9.46×10^{-2}	0.47
2×10^{-4}	500	6.14×10^{-2}	0.62
1×10^{-4}	1000	3.62×10^{-2}	0.76
5×10^{-5}	2000	2.00×10^{-2}	0.86

Table 4.34: *Convergence test for the pure advection benchmark with polynomial degree $r = 0$, relative errors for the volume fraction in L^2 norm. N_{el} denotes the number of elements employed.*

Δt	N_{el}	L^2 rel. error α_1	L^2 rate α_1
8×10^{-4}	125	3.69×10^{-3}	
4×10^{-4}	250	7.10×10^{-4}	2.38
2×10^{-4}	500	1.49×10^{-4}	2.25
1×10^{-4}	1000	3.39×10^{-5}	2.14
5×10^{-5}	2000	8.12×10^{-6}	2.06

Table 4.35: *Convergence test for the pure advection benchmark with polynomial degree $r = 1$, relative errors for the volume fraction in L^2 norm. N_{el} denotes the number of elements employed.*

4.5.3 Solid contact

We consider now a test case known as *solid contact* [Coquel et al., 2017, Re and Abgrall, 2022]. Notice that this test does not consider a low Mach number configuration, however, it is part of a class of important and widely used test cases for the verification of discretizations of the hyperbolic operator [Re and Abgrall, 2022]. Moreover, both fluids follow (2.210) with $\gamma_1 = \gamma_2 = 1.4$ and, therefore, it is not appropriate to talk about solid, liquid or gas and we stick with the more generic notation phase 1 and phase 2. The domain is $\Omega = (-0.5, 0.5)$ and the initial discontinuity is placed at $x_d = 0$. The initial conditions are reported in Table 4.36. The computational grid is composed by $N_{el} = 1000$ elements, the final time is $T_f = 0.15$ and we employ $N_t = 200$ time steps. We take $p_I = p_1$ and $\mathbf{v}_I = \mathbf{u}_2$ for the sake of comparison with the results reported in [Coquel et al., 2017, Re and Abgrall, 2022]. For the non conservative terms, we employ an upwind flux for the advection of the volume fraction and a centered flux for the other equations, whereas, for the conservative terms, we employ an upwind flux at the interface and a Rusanov flux elsewhere. We take $\beta_\alpha = \beta_{\rho\alpha} = \beta_{\mathbf{u}} = \beta_p = 0.01$ for the filtering monotonization technique. These low values for the switching parameters are necessary in order to avoid large undershoots and overshoots and more in general oscillations which completely corrupt the unfiltered solution. The results in Figure 4.88 are in good agreement with those in [Re and Abgrall, 2022] with reduced under- and over-shoots. Moreover, one can notice that no spurious oscillations arise from the advection of the volume fraction.

	α_L	u_L	p_L	ρ_L	α_R	u_R	p_R	ρ_R
Phase 1	0.2	−0.02609	0.3	0.21430	0.7	−0.03629	0.95776	0.96964
Phase 2	0.8	0.00007	1.0	1.00003	0.3	−0.00004	1.0	0.99993

Table 4.36: *Initial conditions for the solid contact test case. The subscripts L and R denote the left and right state, respectively, with respect to the initial discontinuity location at $x_d = 0$.*

4.5.4 Rising bubble

We consider here a *rising bubble* test case for the relaxed systems (3.165) and (3.164) inspired by the well-established benchmark proposed in [Hysing et al., 2009] (see also [Demou et al., 2022]). This test case is used to assess the capability of the proposed numerical method to capture topological changes of a moving interface. The computational domain is $\Omega = (0, 2) \times (0, 4)$ and the final time is

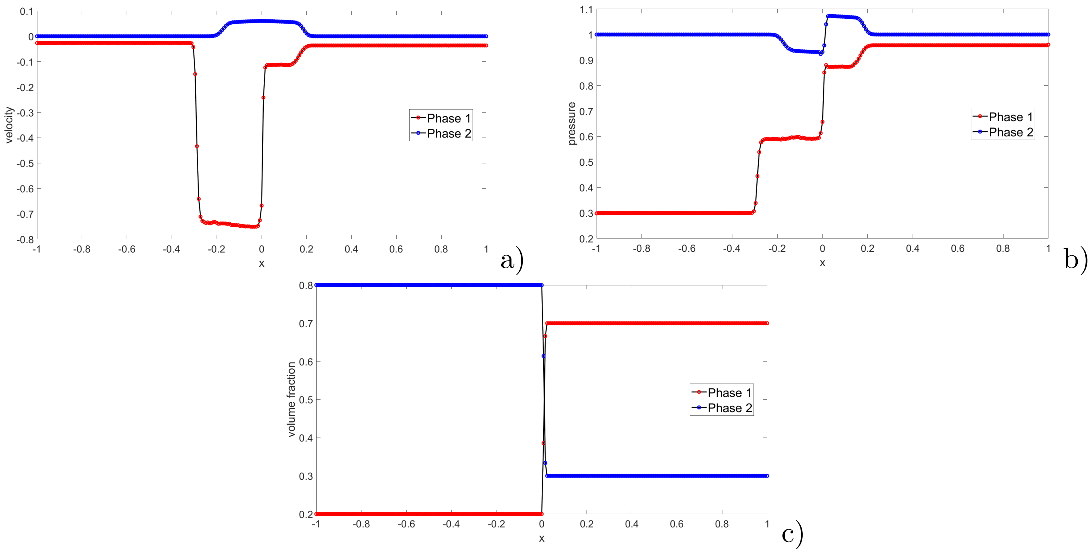

Figure 4.88: *Solid contact test case, results at* $t = T_f$*, a) velocity, b) pressure, c) volume fraction. The red dots denote the results for phase 1, whereas the blue dots denote the results for phase 2.*

$T_f = 3$. Wall boundary conditions are imposed for the top and bottom boundaries, while periodic conditions are prescribed in the horizontal directions. We set $M \approx 2.21 \cdot 10^{-3}, Re = 35, Fr = 1$ and, moreover, we set $\frac{\rho_1}{\rho_2} = 10, \frac{\mu_1}{\mu_2} = 10$. Notice that, in the original work [Hysing et al., 2009], incompressible Navier-Stokes with a level-set formulation were considered. The initial velocity field is zero and the pressure is uniform. We start by considering as polynomial degree $r = 0$ in order to investigate the discretization of the volume fraction without the presence of undershoots and overshoots that arise using high-order discretization techniques. The computational grid is composed by 128×256 elements and the chosen time step $\Delta t = 3 \cdot 10^{-4}$ yields a maximum acoustic Courant $C \approx 10$ and a maximum advective Courant number $C_u \approx 0.02$. Figure 4.89 shows a comparison between the non-conservative advection of the volume fraction present in (3.164) and the conservative version in (3.165). One can easily notice that the non-conservative formulation leads to less diffusion in the treatment of the interface. We then consider $r = 2$ as polynomial degree and a computational grid composed by 64×128 elements. As mentioned above, we need now to employ the monotonization technique to avoid spurious oscillations for the volume fraction and the density which completely corrupt the numerical solution. For this purpose, we take $\beta_\alpha = \beta_{\rho\alpha} = 0.1$. Figure 4.90 shows both the volume fraction and the mixture density with reduced undershoots and overshoots. We plan to investigate in the future the effect of the surface tension in order to avoid the development of the Kelvin-Helmholtz instability present in Figure 4.89 and Figure 4.90. Notice that the shape of the rising bubble differs between Figure 4.89 and Figure 4.90 because, using piecewise constant functions, the gradients are zero and, therefore, the diffusive terms are not acting. On the contrary, in the case of quadratic polynomials, these terms are different from zero and contribute to the smoothing of the interface.

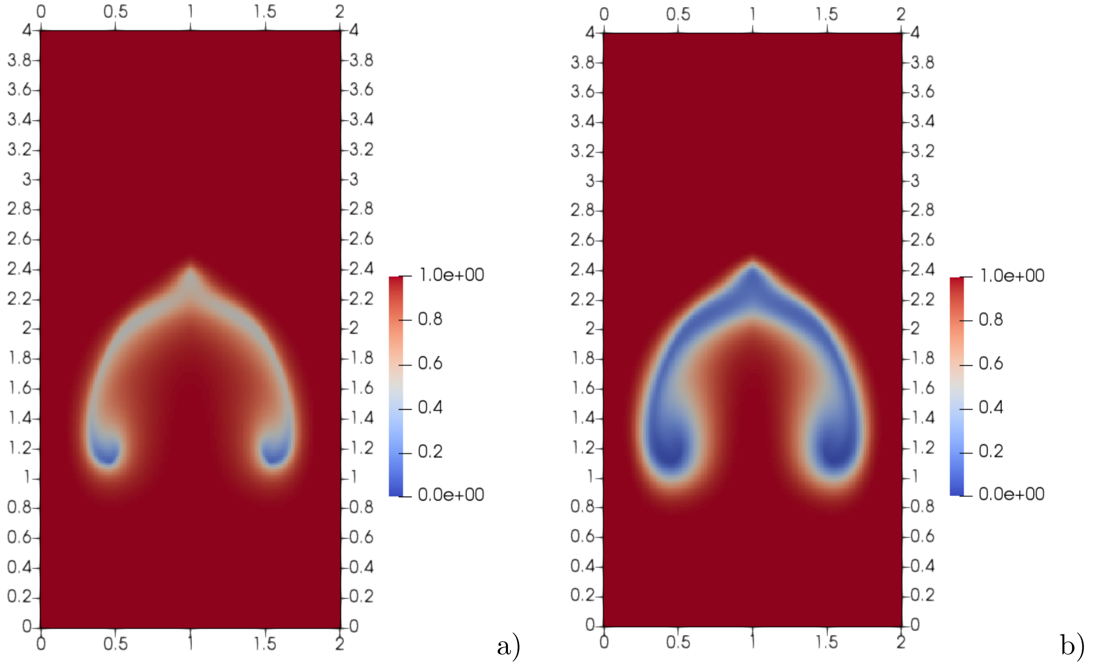

Figure 4.89: *Rising bubble test case, results at $t = T_f$ with polynomial degree $r = 0$, a) volume fraction with non-conservative advection, b) volume fraction with conservative formulation.*

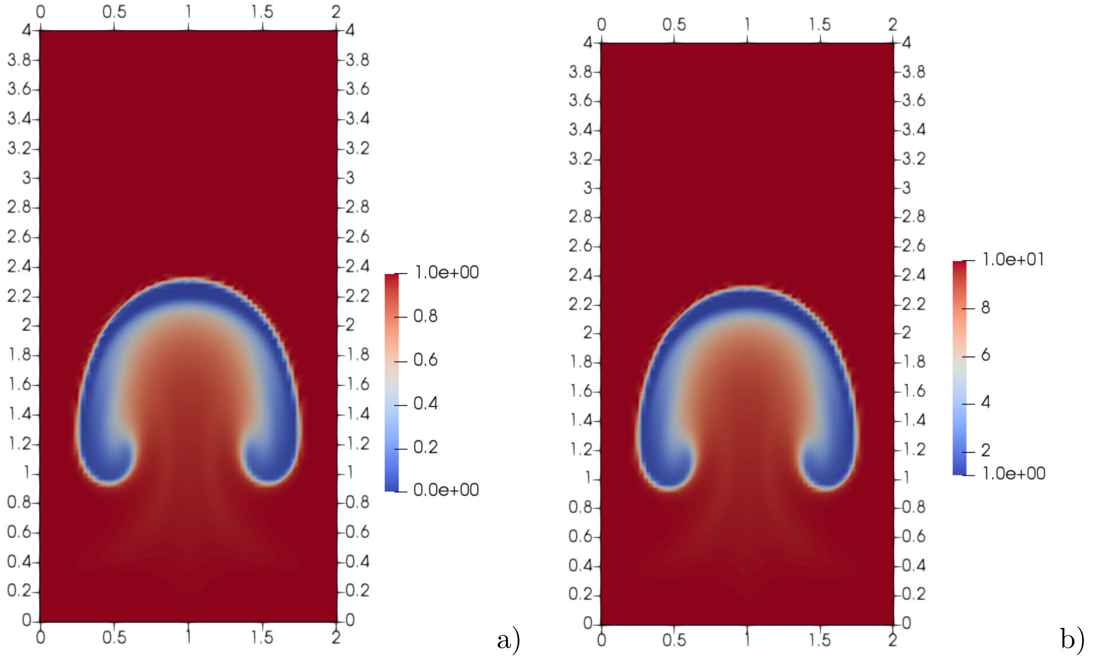

Figure 4.90: *Rising bubble test case, results at $t = T_f$ with polynomial degree $r = 2$, a) volume fraction, b) mixture density. The results are obtained using $\beta_\alpha = \beta_{\rho\alpha} = 0.1$ for the filtering monotonization technique.*

CHAPTER 5

Conclusions and further perspectives

In this Chapter, we try to draw some conclusions from the work presented in this thesis and to give some indications for future developments. This thesis was devoted to the development of models and methods for two-phase flows including geometric variables. Phase exchange terms are indeed proportional to the interface area density and the present work provides a possible approach to address the prediction of this quantity. This goal could be achieved by including a suitable evolution equation for the interface area density in classical models for two-phase flows. The relations for the interface area density are typically derived by means of empirical considerations. In this work, we first reviewed in Section 2.3 (see also Appendix A.2) the evolution equations for a set of geometrical quantities that characterize the interface in two-phase flows. In particular, we analyzed the local instantaneous equations for the Dirac delta $\delta(\Gamma)$ with support on the interface. In Section 2.5, we employed instead the Stationary Action Principle (SAP) to recover well known relations in the literature for the evolution of the interface area density which were obtained by means of empirical considerations, bringing them back into a variational framework in an original way.

For what concerns the development of an effective computational environment to perform relevant numerical simulations, we combined accurate and flexible Discontinuous Galerkin methods with a second order IMEX-ARK time discretization scheme. We first developed a novel implicit solver for the incompressible Navier-Stokes equation using an artificial compressibility formulation presented in [Orlando et al., 2022b]. The employed time discretization scheme in this framework is the TR-BDF2, which is a second order implicit method introduced as a combination of the Trapezoidal Rule method and of the Backward Differentiation Formula of order 2. The discretization method is presented in Section 3.3 and its validation is performed in Section 4.2, following the discussion already reported in [Orlando et al., 2022b]. Here, we assessed the convergence properties of the proposed scheme, comparing it also with the Finite Volume method, and we performed simulations in the case of a complex geometry as well as those of classical benchmarks for incompressible flows. An original extension to single-phase compressible flows presented in [Orlando et al., 2022a] is outlined in Section 3.4 and a number of relevant benchmarks, also reported in [Orlando et al., 2022a] and [Orlando et al., 2023], are presented in Section 4.3 and Section 4.4 to show the potentialities of the proposed approach. After a suitable dimensional analysis, following [Casulli and Greenspan, 1984, Dumbser and Casulli, 2016], we considered an implicit coupling between the momentum balance and the energy balance, so as to obtain a method particularly well suited for low Mach number applications. We employed a second order IMEX-ARK scheme for the time discretization (see also Appendix A.5 for a review of the method and for an original analysis of the explicit part in terms of absolute monotonicity). The implicit part of the IMEX method coincides with the aforementioned TR-BDF2, thus providing ample guarantees of robustness in the low Mach number limit. As discussed in Section 3.4 and also in [Orlando et al., 2022a], since we aim to describe two-phase flows using more realistic equations of state, the discretization approach provides a non straightforward extension of existing approaches in order to handle non-ideal EOS, such as the general cubic equation of state, as well as another classical convex equation of state like the SG-EOS. All the proposed schemes have been implemented in the framework of the open-source library *deal.II* [Bangerth et al., 2007, Arndt et al., 2022], which is based on a matrix-free approach and provides $h-$adaptivity capabilities. The efficiency of the various implementations has been shown with weak and strong scaling analyses reported in Section 4.2 and Section 4.3. The source code for the incompressible Navier-Stokes equations is freely available at [Orlando, 2022]. Moreover, in order to fully exploit the AMR tools, we developed suitable refinement criteria for real gases stemming from an original analysis of isentropic processes outlined in Section 2.6.1. Finally, we provided an extension to the full non-equilibrium Baer-Nunziato model in Section 3.5 and we validated it in Section 4.5 in a number of benchmarks. For this purpose, a novel filtering monotonization technique has been developed in order to avoid (or at least to reduce) the spurious oscillations that arise in presence of discontinuities using high order discretization methods. The monotonization approach is presented in Section 3.2 and [Orlando, 2023] for a scalar advection problem and then properly extended to the Euler equations of gas dynamics. It is based on a filter function that keeps the high order solution if regular, otherwise switching to a low order monotonic solution. Its validation is performed in Section 4.1 (see also [Orlando, 2023]) using second and third order SSP explicit schemes. The monotonization technique is then applied to a set of relevant two-phase flows test cases in Section 4.5 using the IMEX scheme.

Several open problems remain for the proposed approaches and several possible future developments can be envisaged. First of all, a validation of the IMEX scheme in combination with heat and mass transfer source terms should be performed. Afterwards, it would be interesting to compare the classical instantaneous relaxations towards equilibrium, like those used in [Saurel and Abgrall, 1999] and briefly recalled in Section 2.4 (see also Appendix A.6), with the model presented in Chapter 2, which employs an *ad-hoc* evolution equation for the interface area density. Finally, it is of interest to identify more general closure relations for the terms in the averaged interfacial area density evolution equation (2.133) or a more general expression for ν in the Lagrangian (2.161) defined for the SAP.

APPENDIX A

A.1 Treating Generalized Functions

Two-phase flows are characterized by discontinuities in the various properties and fields. Hence, for a generic quantity f, both $\frac{\partial f}{\partial t}$ and ∇f have to be treated as generalized functions or distributions [Estrada and Kanwal, 1980, Drew and Passman, 1999].
Consider the space-time domain $\Omega_T = \Omega \times (0, T_f)$ and denote by Φ the set of test function, namely

$$\Phi = \{\phi : \phi \in C_0^\infty(\Omega_T).\} \tag{A.1}$$

The distributional derivatives of f are defined by the following relations:

$$\int_{\Omega_T} \phi \frac{\partial f}{\partial t} d\Omega = -\int_{\Omega_T} \frac{\partial \phi}{\partial t} f d\Omega \qquad \forall \phi \in \Phi \tag{A.2}$$

$$\int_{\Omega_T} \phi \nabla f d\Omega = -\int_{\Omega_T} \nabla \phi f d\Omega \qquad \forall \phi \in \Phi. \tag{A.3}$$

An important function for which (A.2) and (A.3) hold is the characteristic function X_k (2.19), of whom we recall here its definition:

$$X_k(\mathbf{x}, t) = \begin{cases} 1, & \text{if } \mathbf{x} \text{ is in phase } k \text{ at time } t \\ 0 & \text{otherwise.} \end{cases} \tag{A.4}$$

It can be shown that

$$\frac{\partial X_k}{\partial t} + \mathbf{v}_I \cdot \nabla X_k = 0 \tag{A.5}$$

in the sense of distributions. Indeed:

$$\int_{\Omega_T} \left(\frac{\partial X_k}{\partial t} + \mathbf{v}_I \cdot \nabla X_k \right) \phi d\Omega = \int_{\Omega_T} \frac{\partial X_k}{\partial t} \phi d\Omega + \int_{\Omega_T} \nabla X_k \cdot \mathbf{v}_I \phi d\Omega. \tag{A.6}$$

If we assume that $\mathbf{v}_I$ can be extended smoothly through phase k, we obtain

$$\begin{aligned}\int_{\Omega_T}\left(\frac{\partial X_k}{\partial t}+\mathbf{v}_I\cdot\nabla X_k\right)\phi d\Omega &= -\int_{\Omega_T}\frac{\partial\phi}{\partial t}X_k d\Omega-\int_{\Omega_T}\nabla\cdot(\mathbf{v}_I\phi)X_k d\Omega \quad (A.7)\\ &= -\int_{\Omega_T}\left[\frac{\partial\phi}{\partial t}+\nabla\cdot(\mathbf{v}_I\phi)\right]X_k d\Omega \quad \forall\phi\in\Phi.\end{aligned}$$

The domain Ω_T can be split into its time and space contribution. Hence we get

$$\begin{aligned}\int_{\Omega_T}\left(\frac{\partial X_k}{\partial t}+\mathbf{v}_I\cdot\nabla X_k\right)\phi d\Omega &= -\int_0^{T_f}\left\{\int_{\Omega_k(t)}\left[\frac{\partial\phi}{\partial t}+\nabla\cdot(\mathbf{v}_I\phi)\right]d\mathbf{x}\right\}dt \qquad (A.8)\\ &= -\int_0^{T_f}\frac{d}{dt}\left[\int_{\Omega_k(t)}\phi d\mathbf{x}\right]dt=-\int_{\Omega_k(t)}\phi d\mathbf{x}\bigg|_{t=0}^{t=T_f}=0,\end{aligned}$$

where $\Omega_k(t)$ is the volume occupied by phase k at time t. It is of interest to analyze the quantity ∇X_k which often appears in the treatment of two-phase flows. One has

$$\int_\Omega \phi\nabla X_k d\Omega=-\int_\Omega X_k\nabla\phi d\Omega=-\int_{\Omega_k}\nabla\phi d\Omega \qquad \forall\phi\in\Phi. \qquad (A.9)$$

Thanks to the divergence theorem [Gurtin, 1982] we get therefore

$$\int_\Omega \phi\nabla X_k d\Omega=-\int_{\partial\Omega_k}\mathbf{n}_k\phi d\Sigma=-\int_\Omega \mathbf{n}_k\delta(\Gamma)\phi d\Omega, \qquad (A.10)$$

where $\mathbf{n}_k$ is the unit normal in direction exterior to phase k and $\delta(\cdot)$ is the Dirac delta with support on the interface Γ between the two phases. Hence we obtain

$$\nabla X_k=-\mathbf{n}_k\delta(\Gamma). \qquad (A.11)$$

Assume now that the surface Γ is expressed implicitly by an equation of the form $F(\mathbf{x},t)=0$ and that $F>0$ in phase k. Hence, according to [Estrada and Kanwal, 1980], we can relate $\delta(F)$, which with a slight abuse of notation employed also in [Estrada and Kanwal, 1980] denotes the Dirac delta distribution with support at the points where $F=0$, and $\delta(\Gamma)$ as follows:

$$\delta(\Gamma)=\delta(F)\left|\nabla F\right| \qquad (A.12)$$

Therefore we also obtain

$$\nabla X_k=-\mathbf{n}_k\delta(\Gamma)=-\mathbf{n}_k\delta(F)\left|\nabla F\right|=\delta(F)\nabla F \qquad (A.13)$$

since $\mathbf{n}_k=-\frac{\nabla F}{|\nabla F|}$. For what concerns the time derivative we exploit (A.5) to find

$$\frac{\partial X_k}{\partial t}=-\mathbf{v}_I\cdot\nabla X_k=-\mathbf{v}_I\cdot(\delta(F)\nabla F)=\delta(F)\frac{\partial F}{\partial t}. \qquad (A.14)$$

We analyze now the quantity $\nabla(X_k f)$:

$$\int_\Omega\nabla(X_k f)\phi d\Omega=-\int_\Omega X_k f\nabla\phi d\Omega=-\int_{\Omega_k}f\nabla\phi d\Omega. \qquad (A.15)$$

Assuming $f \in C^1(\Omega)$, the divergence theorem allows us to write

$$\begin{aligned} -\int_{\Omega_k} f\nabla\phi d\Omega &= -\int_\Gamma f\phi\mathbf{n}_k d\Gamma + \int_{\Omega_k} \phi\nabla f d\Omega \\ &= -\int_\Gamma f\phi\mathbf{n}_k d\Gamma + \int_\Omega X_k\phi\nabla f d\Omega \\ &= \int_\Omega f\phi\nabla X_k d\Omega + \int_\Omega X_k\phi\nabla f d\Omega. \end{aligned} \tag{A.16}$$

Hence

$$\nabla(X_k f) = f\nabla X_k + X_k\nabla f \tag{A.17}$$

Similarly one can prove that

$$\frac{\partial(X_k f)}{\partial t} = \frac{\partial X_k}{\partial t} f + X_k\frac{\partial f}{\partial t}. \tag{A.18}$$

We analyze now the behaviour of time and space derivatives for more general distributions. A function $\hat{f}$ defined on $\mathbb{R}^{p+1}$, $p \geq 1$ is called a regular singular function with respect to $\Gamma(t)$ if:

- $\hat{f}$ has derivatives of all orders outside $\Gamma(t)$
- $\hat{f}$ and all its derivatives have boundary values from both sides of $\Gamma(t)$.

The following relations hold [Estrada and Kanwal, 1980, Estrada and Kanwal, 1985]:

$$\widetilde{\nabla}\hat{f} = \nabla\hat{f} - \left[\left[\hat{f}\right]\right]\delta(\Gamma) \tag{A.19}$$

$$\frac{\widetilde{\partial}\hat{f}}{\partial t} = \frac{\partial\hat{f}}{\partial t} + \left(\mathbf{v}_I\cdot\left[\left[\hat{f}\right]\right]\right)\delta(\Gamma), \tag{A.20}$$

where $\widetilde{\nabla}$ and $\frac{\widetilde{\partial}}{\partial t}$ denote the distributional derivatives and $\left[\left[\hat{f}\right]\right]$ represents the jump across the interface already introduced in (2.14) and defined as

$$\left[\left[\hat{f}\right]\right] = \hat{f}_1\mathbf{n}_1 + \hat{f}_2\mathbf{n}_2. \tag{A.21}$$

By definition, a function $\hat{f}_k$ coincides with the value of the function itself on phase k whereas it is 0 outside. Hence it follows:

$$\left[\left[\hat{f}_k\right]\right] = \hat{f}_k\mathbf{n}_k \tag{A.22}$$

and therefore we obtain

$$\widetilde{\nabla}\hat{f}_k = \nabla\hat{f}_k - \hat{f}_k\mathbf{n}_k\delta(\Gamma) \tag{A.23}$$

$$\frac{\widetilde{\partial}\hat{f}_k}{\partial t} = \frac{\partial\hat{f}_k}{\partial t} + \hat{f}_k(\mathbf{v}_I\cdot\mathbf{n}_k)\delta(\Gamma). \tag{A.24}$$

Notice that by considering $\hat{f}_k = X_k$ in (A.23) and (A.24), we recover the relation (2.23). Thanks to (A.5) and (A.11) we obtain the following relations:

$$\widetilde{\nabla}\hat{f}_k = \nabla\hat{f}_k + \hat{f}_k\widetilde{\nabla}X_k \tag{A.25}$$

$$\frac{\widetilde{\partial}\hat{f}_k}{\partial t} = \frac{\partial\hat{f}_k}{\partial t} + \hat{f}_k\frac{\widetilde{\partial}X_k}{\partial t}. \tag{A.26}$$

If we notice that $\hat{f}_k = X_k\hat{f}_k$, $\frac{\partial \hat{f}_k}{\partial t} = X_k\frac{\partial \hat{f}_k}{\partial t}$ and $\nabla \hat{f}_k = X_k\nabla \hat{f}_k$, we derive the following relations, which are formally similar to the product rule for derivatives:

$$\begin{aligned} \widetilde{\nabla}(X_k\hat{f}_k) &= X_k\nabla\hat{f}_k + \hat{f}_k\widetilde{\nabla}X_k && \text{(A.27)}\\ \frac{\widetilde{\partial}(X_k\hat{f}_k)}{\partial t} &= X_k\frac{\partial \hat{f}_k}{\partial t} + \hat{f}_k\frac{\widetilde{\partial}X_k}{\partial t}. && \text{(A.28)} \end{aligned}$$

For the sake of simplicity we will not distinguish explicitly between classical and distributional derivatives and the appropriate definition to be employed will follow from the context. Applying the ensemble average (2.32) to (A.17) and to (A.18) leads to the so-called Gauss and Leibniz rules for the ensemble average, respectively:

$$\begin{aligned} \overline{\nabla(X_k f)} &= \overline{f\nabla X_k} + \overline{X_k\nabla f} && \text{(A.29)}\\ \overline{\frac{\partial(X_k f)}{\partial t}} &= \overline{\frac{\partial X_k}{\partial t}f} + \overline{X_k\frac{\partial f}{\partial t}}. && \text{(A.30)} \end{aligned}$$

A.2 Evolution of geometric features

In this Appendix, we provide an overview of models for the evolution of geometric features of interfaces separating the two phases in two-phase flows. The presentation follows the dissertations in [Drew, 1990, Drew and Passman, 1999] even though we do not restrict ourselves to situations where the tangential interfacial velocity is equal to zero as considered instead in [Drew, 1990, Drew and Passman, 1999]. The phase exchange terms depend indeed on the geometry of the interface and, therefore, considering higher order statistics as well as the volume fraction and the interfacial area density could significantly improve the description of such terms. We analyze the time evolution of the unit normal $\mathbf{n}$ since, as already mentioned, we can directly obtain information about the curvature from this quantity. We recall the evolution equation (2.92) of the function $F(\mathbf{x},t) = 0$ which describes implicitly the interface and the definition of the normal vector (2.93):

$$\begin{aligned} \frac{\partial F}{\partial t} + \mathbf{v}_I\cdot\nabla F &= 0 && \text{(A.31)}\\ \mathbf{n} &= \pm\frac{\nabla F}{|\nabla F|}. && \text{(A.32)} \end{aligned}$$

We will consider the definition $\mathbf{n} = \frac{\nabla F}{|\nabla F|}$, but all the computations can be extended in a straightforward manner with the opposite sign. Moreover, as already discussed in Section 2.3, relation (A.32) defines the normal vector for the whole space-time domain $\Omega_T = \Omega \times (0, T_f]$. After some manipulations, we obtain

$$\begin{aligned} \frac{\partial \mathbf{n}}{\partial t} &= \frac{1}{|\nabla F|}\frac{\partial \nabla F}{\partial t} - \frac{1}{|\nabla F|^3}\left(\nabla F\cdot\frac{\partial\nabla F}{\partial t}\right)\nabla F\\ &= \frac{1}{|\nabla F|}\left(\mathbf{I} - \mathbf{n}\otimes\mathbf{n}\right)\frac{\partial\nabla F}{\partial t}. && \text{(A.33)} \end{aligned}$$

Taking the gradient of (A.31), it follows

$$\frac{\partial \nabla F}{\partial t} = -\left(\nabla\mathbf{v}_I\right)^T\nabla F - \left[\nabla\left(\nabla F\right)\right]^T\mathbf{v}_I. \qquad \text{(A.34)}$$

Moreover, after some manipulations, it can be shown that

$$\nabla \mathbf{n} = \frac{1}{|\nabla F|}\left[\nabla\left(\nabla F\right) - \mathbf{n}\otimes\nabla\left(\nabla F\right)^T\mathbf{n}\right] = \frac{1}{|\nabla F|}\left(\mathbf{I}-\mathbf{n}\otimes\mathbf{n}\right)\nabla\left(\nabla F\right). \quad \text{(A.35)}$$

If we assume that F is sufficiently regular, thanks to the Schwarz theorem [Rudin, 1976], $\left[\nabla\left(\nabla F\right)\right]^T = \nabla\left(\nabla F\right)$ and substituting (A.35) into (A.34) we obtain the following relation:

$$\frac{\partial \nabla F}{\partial t} = -\left(\nabla \mathbf{v}_I\right)^T\nabla F - |\nabla F|\left[\left(\mathbf{I}-\mathbf{n}\otimes\mathbf{n}\right)^{-1}\left(\nabla\mathbf{n}\right)\right]\mathbf{v}_I. \quad \text{(A.36)}$$

Finally, substituting (A.36) into (A.33), we obtain

$$\frac{\partial \mathbf{n}}{\partial t} + \left(\nabla\mathbf{n}\right)\mathbf{v}_I = \left(\mathbf{n}\otimes\mathbf{n}-\mathbf{I}\right)\left(\nabla\mathbf{v}_I\right)^T\mathbf{n} \quad \text{(A.37)}$$

or equivalently

$$\frac{d\mathbf{n}}{dt} = \left(\mathbf{n}\otimes\mathbf{n}-\mathbf{I}\right)\left(\nabla\mathbf{v}_I\right)^T\mathbf{n} = \left[\left(\mathbf{n}\otimes\mathbf{n}\right):\nabla\mathbf{v}_I\right]\mathbf{n} - \left(\nabla\mathbf{v}_I\right)^T\mathbf{n}, \quad \text{(A.38)}$$

a relation derived in [Candel and Poinsot, 1990, Lhuillier, 2003]. On the other hand, substituting (A.32) into (A.31), we obtain the following relation:

$$\frac{\partial F}{\partial t} + \left(\mathbf{v}_I\cdot\mathbf{n}\right)|\nabla F| = 0. \quad \text{(A.39)}$$

Taking the gradient of (A.39), we get

$$\frac{\partial \nabla F}{\partial t} + \nabla\left(\mathbf{v}_I\cdot\mathbf{n}\right)|\nabla F| + \left(\mathbf{v}_I\cdot\mathbf{n}\right)\nabla\left(|\nabla F|\right) = \mathbf{0}. \quad \text{(A.40)}$$

Since $\nabla\left(|\nabla F|\right) = \left[\nabla\left(\nabla F\right)\right]^T\mathbf{n} = \left[\nabla\left(\nabla F\right)\right]\mathbf{n}$, we obtain from (A.40)

$$\frac{\partial \nabla F}{\partial t} = -\nabla\left(\mathbf{v}_I\cdot\mathbf{n}\right)|\nabla F| - \left(\mathbf{v}_I\cdot\mathbf{n}\right)\left[\nabla\left(\nabla F\right)\right]\mathbf{n}. \quad \text{(A.41)}$$

Substituting (A.35) into (A.41), we obtain

$$\frac{\partial \nabla F}{\partial t} = -\nabla\left(\mathbf{v}_I\cdot\mathbf{n}\right)|\nabla F| - \left(\mathbf{v}_I\cdot\mathbf{n}\right)|\nabla F|\left(\mathbf{I}-\mathbf{n}\otimes\mathbf{n}\right)^{-1}\left(\nabla\mathbf{n}\right)\mathbf{n}. \quad \text{(A.42)}$$

If we employ the previous relation into (A.33), we obtain

$$\frac{\partial \mathbf{n}}{\partial t} + \left(\mathbf{v}_I\cdot\mathbf{n}\right)\left(\nabla\mathbf{n}\right)\mathbf{n} = \left(\mathbf{n}\otimes\mathbf{n}-\mathbf{I}\right)\nabla\left(\mathbf{v}_I\cdot\mathbf{n}\right) \quad \text{(A.43)}$$

or, equivalently, thanks to (2.96) and (2.97)

$$\frac{\partial_s \mathbf{n}}{\partial t} = -\nabla_s\left(\mathbf{v}_I\cdot\mathbf{n}\right). \quad \text{(A.44)}$$

Notice that the equation (A.43) can be directly obtained from (A.37) considering only the normal component of the interfacial velocity, namely $\mathbf{v}_I = \left(\mathbf{v}_I\cdot\mathbf{n}\right)\mathbf{n}$. Notice also that, as discussed in Section 2.3, if one considers the unit normal vector and the interfacial velocity as defined uniquely on the interface and analyzes their extension, $(\nabla \mathbf{n})\,\mathbf{n} = \mathbf{0}$ and $\nabla\left(\mathbf{v}_I \cdot \mathbf{n}\right) \cdot \mathbf{n} = 0$ tanks to (2.101) and (2.100), respectively. Hence, (A.43) reduces to

$$\frac{\partial \mathbf{n}}{\partial t} = -\nabla\left(\mathbf{v}_I \cdot \mathbf{n}\right), \tag{A.45}$$

a relation present in [Drew and Passman, 1999]. Moreover, if $|\nabla F|$ is constant, the second order tensor $\nabla \mathbf{n}$ is symmetric and therefore, in this situation, (A.43) reduces to

$$\frac{\partial \mathbf{n}}{\partial t} = \left(\mathbf{n} \otimes \mathbf{n} - \mathbf{I}\right) \nabla\left(\mathbf{v}_I \cdot \mathbf{n}\right). \tag{A.46}$$

By comparing (A.37) and (A.43), we obtain the following relation:

$$(\nabla \mathbf{n})\,\mathbf{v}_{I_t} + \left(\mathbf{n} \otimes \mathbf{n} - \mathbf{I}\right)(\nabla \mathbf{n})^T \mathbf{v}_I = (\nabla \mathbf{n})\,\mathbf{v}_{I_t} + \left(\mathbf{n} \otimes \mathbf{n} - \mathbf{I}\right)(\nabla \mathbf{n})^T \mathbf{v}_{I_t} = \mathbf{0}. \tag{A.47}$$

The relation (A.47) can be also proven in the following way. We first notice that $(\nabla \mathbf{n})\,\mathbf{v}_{I_t} = (\nabla_s \mathbf{n})\,\mathbf{v}_{I_t}$. Indeed, thanks to (2.97), we get

$$\nabla_s \mathbf{n} = \nabla \mathbf{n} - (\nabla \mathbf{n})\,\mathbf{n} \otimes \mathbf{n} = \nabla \mathbf{n} - \nabla \mathbf{n}\left(\mathbf{n} \otimes \mathbf{n}\right) = \nabla \mathbf{n}\left(\mathbf{I} - \mathbf{n} \otimes \mathbf{n}\right). \tag{A.48}$$

Since $\mathbf{v}_{I_t} \cdot \mathbf{n} = 0$, it follows:

$$(\nabla_s \mathbf{n})\,\mathbf{v}_{I_t} = \nabla \mathbf{n}\left(\mathbf{I} - \mathbf{n} \otimes \mathbf{n}\right)\mathbf{v}_{I_t} = (\nabla \mathbf{n})\,\mathbf{v}_{I_t}. \tag{A.49}$$

Moreover, the second order tensor $\nabla_s \mathbf{n}$ is symmetric. Indeed, if we substitute (A.35) into (A.48), we obtain

$$\nabla_s \mathbf{n} = \frac{1}{|\nabla F|}\left(I - \mathbf{n} \otimes \mathbf{n}\right)\left[\nabla\left(\nabla F\right)\right]\left(I - \mathbf{n} \otimes \mathbf{n}\right), \tag{A.50}$$

which is a symmetric tensor if F is sufficiently regular and the Schwarz theorem holds. Hence, (A.47) reduces to

$$\begin{aligned} (\nabla \mathbf{n})\,\mathbf{v}_{I_t} + \left(\mathbf{n} \otimes \mathbf{n} - \mathbf{I}\right)(\nabla \mathbf{n})^T \mathbf{v}_{I_t} &= (\nabla_s \mathbf{n})\,\mathbf{v}_{I_t} + \left(\mathbf{n} \otimes \mathbf{n} - \mathbf{I}\right)(\nabla \mathbf{n})^T \mathbf{v}_{I_t} \\ &= (\nabla_s \mathbf{n})\,\mathbf{v}_{I_t} - (\nabla_s \mathbf{n})^T \mathbf{v}_{I_t} = \mathbf{0}. \end{aligned} \tag{A.51}$$

It is of interest to study also the behaviour of the material derivative following the surface of the normal vector. We notice two properties of the Lagrangian derivative. First of all, the convective derivative following the surface can be simplified as follows:

$$\frac{d_s \mathbf{n}}{dt} = \frac{\partial_s \mathbf{n}}{\partial t} + (\nabla_s \mathbf{n})\left[\mathbf{v}_{I_t} + \left(\mathbf{v}_I \cdot \mathbf{n}\right)\mathbf{n}\right] = \frac{\partial_s \mathbf{n}}{\partial t} + (\nabla_s \mathbf{n})\,\mathbf{v}_{I_t}, \tag{A.52}$$

since $(\nabla_s \mathbf{n})\,\mathbf{n} = \mathbf{0}$. Furthermore, thanks to (2.97), the following identity holds:

$$\begin{aligned} \frac{d_s \mathbf{n}}{dt} &= \frac{\partial_s \mathbf{n}}{\partial t} + (\nabla_s \mathbf{n})\,\mathbf{v}_I = \frac{\partial \mathbf{n}}{\partial t} + \left(\mathbf{v}_I \cdot \mathbf{n}\right)(\nabla \mathbf{n})\,\mathbf{n} + (\nabla \mathbf{n})\left(\mathbf{I} - \mathbf{n} \otimes \mathbf{n}\right)\mathbf{v}_I \\ &= \frac{\partial \mathbf{n}}{\partial t} + \left(\mathbf{v}_I \cdot \mathbf{n}\right)(\nabla \mathbf{n})\,\mathbf{n} + (\nabla \mathbf{n})\,\mathbf{v}_I - \left(\mathbf{v}_I \cdot \mathbf{n}\right)(\nabla \mathbf{n})\,\mathbf{n} \\ &= \frac{\partial \mathbf{n}}{\partial t} + (\nabla \mathbf{n})\,\mathbf{v}_I = \frac{d\mathbf{n}}{dt}. \end{aligned} \tag{A.53}$$

It is interesting to point out that an analogous relation holds for a generic scalar field f; indeed:

$$\begin{aligned}
\frac{d_s f}{dt} &= \frac{\partial_s f}{\partial t} + \mathbf{v}_I \cdot \nabla_s f = \frac{\partial f}{\partial t} + (\mathbf{v}_I \cdot \mathbf{n})(\nabla f \cdot \mathbf{n}) + \mathbf{v}_I \cdot [\nabla f - (\nabla f \cdot \mathbf{n})\,\mathbf{n}] \\
&= \frac{\partial_s f}{\partial t} + \mathbf{v}_I \cdot \nabla f + (\mathbf{v}_I \cdot \mathbf{n})(\nabla f \cdot \mathbf{n}) - (\mathbf{v}_I \cdot \mathbf{n})(\nabla f \cdot \mathbf{n}) \\
&= \frac{\partial f}{\partial t} + \mathbf{v}_I \cdot \nabla f = \frac{df}{dt}. \qquad \text{(A.54)}
\end{aligned}$$

The mean curvature H is directly linked to the outward unit normal by relation [Drew and Passman, 1999, Morel, 2007]

$$H = \frac{1}{2} \nabla\cdot \mathbf{n}. \qquad \text{(A.55)}$$

Taking the divergence of (A.37), we derive the evolution equation for the mean curvature (2.108). Notice that

$$\nabla\cdot [(\nabla \mathbf{n})\,\mathbf{v}_I] = 2\mathbf{v}_I \cdot \nabla H + \nabla \mathbf{n} : (\nabla \mathbf{v}_I)^T \qquad \text{(A.56)}$$

and that

$$\begin{aligned}
\nabla\cdot \left[(\mathbf{n} \otimes \mathbf{n} - \mathbf{I})\,(\nabla \mathbf{v}_I)^T \mathbf{n}\right] &= 2H\,(\nabla \mathbf{v}_I)\,\mathbf{n} \cdot \mathbf{n} + (\nabla \mathbf{v}_I)^T \mathbf{n} \cdot (\nabla \mathbf{n})\,\mathbf{n} \\
&+ (\mathbf{n} \otimes \mathbf{n} - \mathbf{I}) : \left[\nabla \left[(\nabla \mathbf{v}_I)^T \mathbf{n}\right]\right]^T. \qquad \text{(A.57)}
\end{aligned}$$

Hence, the evolution equation for the mean curvature reads as follows:

$$\begin{aligned}
\frac{dH}{dt} &= H\,(\nabla \mathbf{v}_I)\,\mathbf{n} \cdot \mathbf{n} - \frac{1}{2}\nabla \mathbf{n} : (\nabla \mathbf{v}_I)^T \\
&+ \frac{1}{2}(\nabla \mathbf{v}_I)^T \mathbf{n} \cdot (\nabla \mathbf{n})\,\mathbf{n} + \frac{1}{2}(\mathbf{n} \otimes \mathbf{n} - \mathbf{I}) : \left[\nabla \left[(\nabla \mathbf{v}_I)^T \mathbf{n}\right]\right]^T. \qquad \text{(A.58)}
\end{aligned}$$

Starting from (A.43), we obtain the following relation:

$$\begin{aligned}
\frac{\partial H}{\partial t} + (\mathbf{v}_I \cdot \mathbf{n})\,\mathbf{n} \cdot \nabla H &= H \nabla (\mathbf{v}_I \cdot \mathbf{n}) \cdot \mathbf{n} \qquad \text{(A.59)} \\
&+ \frac{1}{2}(\mathbf{n} \otimes \mathbf{n} - \mathbf{I}) : \nabla [\nabla (\mathbf{v}_I \cdot \mathbf{n})] \\
&- \frac{1}{2}(\nabla \mathbf{n}) : [(\mathbf{v}_I \cdot \mathbf{n})\,\mathbf{n}]^T + \frac{1}{2}(\nabla \mathbf{n})\,\mathbf{n} \cdot \nabla (\mathbf{v}_I \cdot \mathbf{n}).
\end{aligned}$$

Notice that, as already observed for (A.43) and (A.37), relation (A.59) can be directly obtained from (A.58) considering only the normal component of the interfacial velocity. We recall here the relation between the Gaussian curvature K and the unit normal vector [Weatherburn, 1930]:

$$K = \frac{1}{2} \nabla\cdot [\mathbf{n}\,(\nabla\cdot \mathbf{n}) + \mathbf{n} \times (\nabla \times \mathbf{n})]. \qquad \text{(A.60)}$$

It can be shown that (A.59) reduces to

$$\frac{\partial_s H}{\partial t} = -\left(2H^2 - K\right)(\mathbf{v}_I \cdot \mathbf{n}) - \frac{1}{2} \nabla_s\cdot [\nabla_s (\mathbf{v}_I \cdot \mathbf{n})]. \qquad \text{(A.61)}$$

In order to prove the equivalence between (A.61) and (A.59), we first notice that

$$\nabla_s(\mathbf{v}_I\cdot\mathbf{n}) = \nabla(\mathbf{v}_I\cdot\mathbf{n}) - [\nabla(\mathbf{v}_I\cdot\mathbf{n})\cdot\mathbf{n}]\,\mathbf{n} = (\mathbf{I}-\mathbf{n}\otimes\mathbf{n})\,\nabla(\mathbf{v}_I\cdot\mathbf{n}) \qquad \text{(A.62)}$$

and that

$$\begin{aligned}\nabla_s\cdot[\nabla_s(\mathbf{v}_I\cdot\mathbf{n})] &= (\mathbf{I}-\mathbf{n}\otimes\mathbf{n}):\nabla[\nabla_s(\mathbf{v}_I\cdot\mathbf{n})]\\ &= (\mathbf{I}-\mathbf{n}\otimes\mathbf{n}):\nabla[(\mathbf{I}-\mathbf{n}\otimes\mathbf{n})\,\nabla(\mathbf{v}_I\cdot\mathbf{n})]\,. \qquad \text{(A.63)}\end{aligned}$$

Since

$$\begin{aligned}\nabla[(\mathbf{I}-\mathbf{n}\otimes\mathbf{n})\,\nabla(\mathbf{v}_I\cdot\mathbf{n})] &= -\nabla\mathbf{n}\,[\nabla(\mathbf{v}_I\cdot\mathbf{n})\cdot\mathbf{n}] - \mathbf{n}\otimes[\nabla\mathbf{n}]^T\,\nabla(\mathbf{v}_I\cdot\mathbf{n})\\ &+ (\mathbf{I}-\mathbf{n}\otimes\mathbf{n})\,\nabla[\nabla(\mathbf{v}_I\cdot\mathbf{n})]\,, \qquad \text{(A.64)}\end{aligned}$$

we obtain

$$\begin{aligned}(\mathbf{I}-\mathbf{n}\otimes\mathbf{n}):\nabla[(\mathbf{I}-\mathbf{n}\otimes\mathbf{n})\,\nabla(\mathbf{v}_I\cdot\mathbf{n})] &= -H\nabla(\mathbf{v}_I\cdot\mathbf{n})\cdot\mathbf{n} \qquad \text{(A.65)}\\ &+ (\mathbf{I}-\mathbf{n}\otimes\mathbf{n}):\nabla[\nabla(\mathbf{v}_I\cdot\mathbf{n})]\,.\end{aligned}$$

If we substitute into (A.61), we obtain

$$\begin{aligned}\frac{\partial_s H}{\partial t} &= -\left(2H^2-K\right)(\mathbf{v}_I\cdot\mathbf{n}) + H\nabla(\mathbf{v}_I\cdot\mathbf{n})\cdot\mathbf{n} \qquad \text{(A.66)}\\ &+ \frac{1}{2}(\mathbf{n}\otimes\mathbf{n}-\mathbf{I}):\nabla[\nabla(\mathbf{v}_I\cdot\mathbf{n})]\,.\end{aligned}$$

Comparing (A.66) with (A.59), since $\frac{\partial_s H}{\partial t} = \frac{\partial H}{\partial t} + (\mathbf{v}_I\cdot\mathbf{n})\,\mathbf{n}\cdot\nabla H$, we notice that the equivalence between (A.61) and (A.59) is established if

$$\frac{1}{2}(\nabla\mathbf{n})\,\mathbf{n}\cdot\nabla(\mathbf{v}_I\cdot\mathbf{n}) - \frac{1}{2}\nabla\mathbf{n}:\nabla[(\mathbf{v}_I\cdot\mathbf{n})\,\mathbf{n}]^T = -\left(2H^2-K\right)(\mathbf{v}_I\cdot\mathbf{n})\,. \qquad \text{(A.67)}$$

Starting from (A.60), we notice that

$$K = 2H^2 + \mathbf{n}\cdot\nabla H + \frac{1}{2}|\nabla\times\mathbf{n}|^2 - \frac{1}{2}\mathbf{n}\cdot[\nabla\times(\nabla\times\mathbf{n})] \qquad \text{(A.68)}$$

and, therefore, we get

$$\begin{aligned}-\left(2H^2-K\right)(\mathbf{v}_I\cdot\mathbf{n}) &= (\mathbf{v}_I\cdot\mathbf{n})\,\mathbf{n}\cdot\nabla H + \frac{1}{2}(\mathbf{v}_I\cdot\mathbf{n})\,|\nabla\times\mathbf{n}|^2\\ &- \frac{1}{2}(\mathbf{v}_I\cdot\mathbf{n})\,\mathbf{n}\cdot[\nabla\times(\nabla\times\mathbf{n})]\,. \qquad \text{(A.69)}\end{aligned}$$

Hence, (A.66) reduces to

$$\begin{aligned}\frac{\partial H}{\partial t} &= H\nabla(\mathbf{v}_I\cdot\mathbf{n})\cdot\mathbf{n} + \frac{1}{2}(\mathbf{n}\otimes\mathbf{n}-\mathbf{I}):\nabla[\nabla(\mathbf{v}_I\cdot\mathbf{n})]\\ &+ \frac{1}{2}(\mathbf{v}_I\cdot\mathbf{n})\,|\nabla\times\mathbf{n}|^2 - \frac{1}{2}(\mathbf{v}_I\cdot\mathbf{n})\,\mathbf{n}\cdot[\nabla\times(\nabla\times\mathbf{n})]\,. \qquad \text{(A.70)}\end{aligned}$$

Since

$$\nabla\times(\nabla\times\mathbf{n}) = \nabla(\nabla\cdot\mathbf{n}) - \nabla\cdot(\nabla\mathbf{n}) = 2\nabla H - \nabla\cdot(\nabla\mathbf{n}) \qquad \text{(A.71)}$$

and

$$|\nabla\times\mathbf{n}|^2 = -[\nabla\cdot(\nabla\mathbf{n})]\cdot\mathbf{n} - \nabla\mathbf{n}:(\nabla\mathbf{n})^T\,, \qquad \text{(A.72)}$$

we obtain

$$\begin{aligned}\frac{\partial H}{\partial t} + (\mathbf{v}_I \cdot \mathbf{n})\, \mathbf{n} \cdot \nabla H &= H \nabla (\mathbf{v}_I \cdot \mathbf{n}) \cdot \mathbf{n} + \frac{1}{2} (\mathbf{n} \otimes \mathbf{n} - \mathbf{I}) : \nabla \left[\nabla (\mathbf{v}_I \cdot \mathbf{n}) \right] \\ &- \frac{1}{2} (\mathbf{v}_I \cdot \mathbf{n})\, \nabla \mathbf{n} : (\nabla \mathbf{n})^T . \end{aligned} \tag{A.73}$$

Finally, since

$$(\mathbf{v}_I \cdot \mathbf{n})\, \nabla \mathbf{n} : (\nabla \mathbf{n})^T = \nabla \mathbf{n} : \left[(\mathbf{v}_I \cdot \mathbf{n})\, \mathbf{n} \right]^T - (\nabla \mathbf{n})\, \mathbf{n} \cdot \nabla (\mathbf{v}_I \cdot \mathbf{n}) , \tag{A.74}$$

we recover (A.59). Relation (A.61) represents an extension of the evolution equation derived in [Drew and Passman, 1999], which we report here for the convenience of the reader:

$$\frac{\partial H}{\partial t} = -\left(2H^2 - K \right) (\mathbf{v}_I \cdot \mathbf{n}) - \frac{1}{2} \nabla \cdot \left[\nabla (\mathbf{v}_I \cdot \mathbf{n}) \right] . \tag{A.75}$$

Relation (A.75) reduces to (A.61) if all the variables are uniquely defined on the interface and one considers extensions which satisfy the properties (2.100) and (2.101). Analogously, starting from (A.60), one can show that the evolution for the Gaussian curvature reads as follows:

$$\frac{\partial_s K}{\partial t} = 2HK (\mathbf{v}_I \cdot \mathbf{n}) + 2H\, \nabla_s \cdot \left[\nabla_s (\mathbf{v}_I \cdot \mathbf{n}) \right] . \tag{A.76}$$

A.3 Eigenvalues of 1D Euler equations

In this Appendix, we compute the eigenvalues for the Euler equations in non-dimensional form for a general equation of state. For the sake of simplicity, we focus on 1D case and so the equations can be written as follows:

$$\begin{aligned}\frac{\partial \rho}{\partial t} + \frac{\partial}{\partial x} (\rho u) &= 0 \\ \frac{\partial \rho u}{\partial t} + \frac{\partial}{\partial x} \left(\rho u^2 \right) + \frac{1}{M^2} \frac{\partial p}{\partial x} &= 0 \\ \frac{\partial \rho E}{\partial t} + \frac{\partial}{\partial x} \left[(\rho E + p)\, u \right] &= 0. \end{aligned} \tag{A.77}$$

This is equivalent to

$$\begin{aligned}\frac{\partial \rho}{\partial t} + u \frac{\partial \rho}{\partial x} + \rho \frac{\partial u}{\partial x} &= 0 \\ \frac{\partial \rho}{\partial t} u + \frac{\partial u}{\partial t} \rho + u^2 \frac{\partial \rho}{\partial x} + 2 \rho u \frac{\partial u}{\partial x} + \frac{1}{M^2} \frac{\partial p}{\partial x} &= 0 \\ \frac{\partial \rho}{\partial t} E + \frac{\partial E}{\partial t} \rho + (\rho E + p) \frac{\partial u}{\partial x} + u \left(\frac{\partial \rho}{\partial x} E + \frac{\partial E}{\partial x} \rho + \frac{\partial p}{\partial x} \right) &= 0. \end{aligned} \tag{A.78}$$

Thanks to the continuity equation and to the relation $E = e + \frac{1}{2} M^2 u^2$, we obtain

$$\begin{aligned}\frac{\partial \rho}{\partial t} + u \frac{\partial \rho}{\partial x} + \rho \frac{\partial u}{\partial x} &= 0 \\ \frac{\partial u}{\partial t} + u \frac{\partial u}{\partial x} + \frac{1}{\rho M^2} \frac{\partial p}{\partial x} &= 0 \\ \frac{\partial e}{\partial t} + \frac{p}{\rho} \frac{\partial u}{\partial x} + u \frac{\partial e}{\partial x} &= 0. \end{aligned} \tag{A.79}$$

In general $e = e(p, \rho)$, so that

$$\frac{\partial e}{\partial t} = \frac{\partial e}{\partial \rho}\frac{\partial \rho}{\partial t} + \frac{\partial e}{\partial p}\frac{\partial p}{\partial t}$$

and

$$\frac{\partial e}{\partial x} = \frac{\partial e}{\partial \rho}\frac{\partial \rho}{\partial x} + \frac{\partial e}{\partial p}\frac{\partial p}{\partial x}.$$

Hence, the system reduces to

$$\begin{aligned} \frac{\partial \rho}{\partial t} + u\frac{\partial \rho}{\partial x} + \rho\frac{\partial u}{\partial x} &= 0 \\ \frac{\partial u}{\partial t} + u\frac{\partial u}{\partial x} + \frac{1}{\rho M^2}\frac{\partial p}{\partial x} &= 0 \\ \frac{\partial p}{\partial t} + \frac{\left(\frac{p}{\rho} - \rho\frac{\partial e}{\partial \rho}\right)}{\frac{\partial e}{\partial p}}\frac{\partial u}{\partial x} + u\frac{\partial p}{\partial x} &= 0, \end{aligned} \tag{A.80}$$

which can be rewritten in vector notation as $\frac{\partial \mathbf{Q}}{\partial t} + \mathbf{A}\frac{\partial \mathbf{Q}}{\partial x} = \mathbf{0}$ with

$$\mathbf{Q} = \begin{bmatrix} \rho \\ u \\ p \end{bmatrix} \tag{A.81}$$

and

$$\mathbf{A} = \begin{bmatrix} u & \rho & 0 \\ 0 & u & \frac{1}{\rho M^2} \\ 0 & \frac{\left(\frac{p}{\rho} - \rho\frac{\partial e}{\partial \rho}\right)}{\frac{\partial e}{\partial p}} & u \end{bmatrix}. \tag{A.82}$$

The eigenvalues of (A.82) are $u - \frac{1}{M}\frac{1}{\rho}\sqrt{\frac{p - \frac{\partial e}{\partial \rho}\rho^2}{\frac{\partial e}{\partial p}}}$, u and $u + \frac{1}{M}\frac{1}{\rho}\sqrt{\frac{p - \frac{\partial e}{\partial \rho}\rho^2}{\frac{\partial e}{\partial p}}}$. The first law of thermodynamics, already recalled in Section 2.6.1, provides us the following relation:

$$Tds = de - \frac{p}{\rho^2}d\rho = \left(\frac{\partial e}{\partial \rho} - \frac{p}{\rho^2}\right)d\rho + \frac{\partial e}{\partial p}dp, \tag{A.83}$$

or, equivalently,

$$dp = \frac{\frac{p}{\rho^2} - \frac{\partial e}{\partial \rho}}{\frac{\partial e}{\partial p}}d\rho + \frac{T}{\frac{\partial e}{\partial p}}ds. \tag{A.84}$$

Hence, following [Vidal, 2001], we have

$$c^2 = \left.\frac{\partial p}{\partial \rho}\right|_s = \frac{\frac{p}{\rho^2} - \frac{\partial e}{\partial \rho}}{\frac{\partial e}{\partial p}} \tag{A.85}$$

and, therefore, the eigenvalues of (A.82) are

$$u - \frac{c}{M} \quad u \quad u + \frac{c}{M}$$

also for a generic equation of state, and not only in the case of an ideal gas, as already discussed in [Munz et al., 2003]. This justifies the definition (4.17) also in the case of non-ideal gases.

A.4 Derivation of the two-phase model

In this Appendix, we report the computations needed to obtain the system of equations (2.169) reported in Section 2.5. The infinitesimal variations for density, mass fraction and velocity, respectively, are given by

$$\begin{aligned}\delta\rho &= -\nabla\cdot(\rho\boldsymbol{\eta}) &\text{(A.86)}\\ \delta Y &= -\boldsymbol{\eta}\cdot\nabla Y &\text{(A.87)}\\ \delta\mathbf{u} &= D_t\boldsymbol{\eta}-(\nabla\mathbf{u})\,\boldsymbol{\eta}. &\text{(A.88)}\end{aligned}$$

Hence, after some manipulations, the action is given by

$$\begin{aligned}\delta\mathcal{A} &= -\int\frac{\partial(\rho\mathbf{u})}{\partial t}\cdot\boldsymbol{\eta}-\int[\nabla\cdot(\rho\mathbf{u}\otimes\mathbf{u})]\cdot\boldsymbol{\eta}-\int\nabla\left(\rho^2\frac{\partial e}{\partial\rho}\right)\cdot\boldsymbol{\eta}\\ &- \int\rho\frac{\partial e}{\partial\alpha_L}\nabla\alpha_L\cdot\boldsymbol{\eta}-\int\frac{1}{2}\frac{\partial\nu}{\partial\rho}(D_t\alpha_L)^2\nabla\cdot(\rho\boldsymbol{\eta})\\ &+ \int\frac{1}{2}\frac{\partial\nu}{\partial\alpha_L}(D_t\alpha_L)^2\delta\alpha_L+\int\nu(D_t\alpha_L)\,\delta(D_t\alpha_L)\\ &- \int\rho\frac{\partial e}{\partial\alpha_L}\delta\alpha_L &\text{(A.89)}\end{aligned}$$

Since $\delta(D_t\alpha_L)=D_t\delta\alpha_L+\delta\mathbf{u}\cdot\nabla\alpha_L$, we get

$$\begin{aligned}\delta\mathcal{A} &= -\int\frac{\partial(\rho\mathbf{u})}{\partial t}\cdot\boldsymbol{\eta}-\int[\nabla\cdot(\rho\mathbf{u}\otimes\mathbf{u})]\cdot\boldsymbol{\eta}-\int\nabla\left(\rho^2\frac{\partial e}{\partial\rho}\right)\cdot\boldsymbol{\eta}\\ &- \int\rho\frac{\partial e}{\partial\alpha_L}\nabla\alpha_L\cdot\boldsymbol{\eta}+\int\nabla\left[\frac{1}{2}\frac{\partial\nu}{\partial\rho}(D_t\alpha_L)^2\right]\rho\cdot\boldsymbol{\eta}\\ &+ \int\frac{1}{2}\frac{\partial\nu}{\partial\alpha_L}(D_t\alpha_L)^2\delta\alpha_L\\ &+ \int\nu(D_t\alpha_L)\,D_t\delta\alpha_L+\int\nu(D_t\alpha_L)\,\nabla\alpha_L\cdot\delta\mathbf{u}\\ &- \int\rho\frac{\partial e}{\partial\alpha_L}\delta\alpha_L. &\text{(A.90)}\end{aligned}$$

After a new integration by parts, we obtain

$$\begin{aligned}\delta\mathcal{A} &= -\int\frac{\partial(\rho\mathbf{u})}{\partial t}\cdot\boldsymbol{\eta}-\int[\nabla\cdot(\rho\mathbf{u}\otimes\mathbf{u})]\cdot\boldsymbol{\eta}-\int\nabla\left(\rho^2\frac{\partial e}{\partial\rho}\right)\cdot\boldsymbol{\eta}\\ &- \int\rho\frac{\partial e}{\partial\alpha_L}\nabla\alpha_L\cdot\boldsymbol{\eta}+\int\nabla\left[\frac{1}{2}\frac{\partial\nu}{\partial\rho}(D_t\alpha_L)^2\right]\rho\cdot\boldsymbol{\eta}\\ &- \int\frac{\partial[\nu(D_t\alpha_L)\nabla\alpha_L]}{\partial t}\cdot\boldsymbol{\eta}-\int\{\nabla\cdot[\nu(D_t\alpha_L)\nabla\alpha_L\otimes\mathbf{u}]\}\cdot\boldsymbol{\eta}\\ &- \int\nu(D_t\alpha_L)(\nabla\mathbf{u})^T\nabla\alpha_L\cdot\boldsymbol{\eta} &\text{(A.91)}\\ &- \int\frac{\partial}{\partial t}[\nu(D_t\alpha_L)]\,\delta\alpha_L-\int\nabla\cdot[\nu(D_t\alpha_L)\,\mathbf{u}]\,\delta\alpha_L\\ &+ \int\frac{1}{2}\frac{\partial\nu}{\partial\alpha_L}(D_t\alpha_L)^2\delta\alpha_L\\ &- \int\rho\frac{\partial e}{\partial\alpha_L}\delta\alpha_L.\end{aligned}$$

The momentum equation associated to the volume fraction reads therefore as follows:

$$\frac{\partial}{\partial t}\left[\nu\left(D_t\alpha_L\right)\right]+\nabla\cdot\left[\nu\left(D_t\alpha_L\right)\mathbf{u}\right]-\frac{1}{2}\left(D_t\alpha_L\right)^2\frac{\partial\nu}{\partial\alpha_L}+\rho\frac{\partial e}{\partial\alpha_L}=0. \tag{A.92}$$

Thanks to the previous relation, we find

$$\begin{aligned}
& \frac{\partial\left[\nu\left(D_t\alpha_L\right)\nabla\alpha_L\right]}{\partial t}+\nabla\cdot\left[\nu\left(D_t\alpha_L\right)\nabla\alpha_L\otimes\mathbf{u}\right] \\
+ \quad & \nu\left(D_t\alpha_L\right)\left(\nabla\mathbf{u}\right)^T\nabla\alpha_L+\rho\frac{\partial e}{\partial\alpha_L}\nabla\alpha_L= \\
& \nabla\alpha_L\left[\frac{1}{2}\left(D_t\alpha_L\right)^2\frac{\partial\nu}{\partial\alpha_L}-\rho\frac{\partial e}{\partial\alpha_L}\right]+\nu\left(D_t\alpha_L\right)\left[\frac{\partial\nabla\alpha_L}{\partial t}+\nabla\left(\nabla\alpha_L\right)\mathbf{u}\right] \\
+ \quad & \nu\left(D_t\alpha_L\right)\left(\nabla\mathbf{u}\right)^T\nabla\alpha_L+\rho\frac{\partial e}{\partial\alpha_L}\nabla\alpha_L= \\
& \frac{1}{2}\nabla\alpha_L\left(D_t\alpha_L\right)^2\frac{\partial\nu}{\partial\alpha_L}+\nu\left(D_t\alpha_L\right)\nabla\left(D_t\alpha_L\right)
\end{aligned} \tag{A.93}$$

Notice that

$$\begin{aligned}
\nabla\left(\frac{1}{2}\nu\left(D_t\alpha_L\right)^2\right) &= \frac{1}{2}\left(D_t\alpha_L\right)^2\nabla\nu+\frac{1}{2}\nu\nabla\left(D_t\alpha_L\right)^2 \\
&= \frac{1}{2}\left(D_t\alpha_L\right)^2\frac{\partial\nu}{\partial\alpha_L}\nabla\alpha_L+\frac{1}{2}\left(D_t\alpha_L\right)^2\frac{\partial\nu}{\partial\rho}\nabla\rho \\
&+ \nu\left(D_t\alpha_L\right)\nabla\left(D_t\alpha_L\right),
\end{aligned} \tag{A.94}$$

so as to obtain

$$\begin{aligned}
& \frac{\partial\left[\nu\left(D_t\alpha_L\right)\nabla\alpha_L\right]}{\partial t}+\nabla\cdot\left[\nu\left(D_t\alpha_L\right)\nabla\alpha_L\otimes\mathbf{u}\right] \\
+ \quad & \nu\left(D_t\alpha_L\right)\left(\nabla\mathbf{u}\right)^T\nabla\alpha_L+\rho\frac{\partial e}{\partial\alpha_L}\nabla\alpha_L-\nabla\left[\frac{1}{2}\frac{\partial\nu}{\partial\rho}\left(D_t\alpha_L\right)^2\right]\rho= \\
& \nabla\left[\frac{1}{2}\left(\nu-\rho\frac{\partial\nu}{\partial\rho}\right)\left(D_t\alpha_L\right)^2\right].
\end{aligned} \tag{A.95}$$

We provide now the computations performed in order to consider dissipative effects. First, we notice that

$$\rho D_t\eta=\rho\frac{\partial\eta}{\partial\rho}D_t\rho+\rho\frac{\partial\eta}{\partial Y}D_tY+\rho\frac{\partial\eta}{\partial\mathbf{u}}\cdot D_t\mathbf{u}+\rho\frac{\partial\eta}{\partial\alpha_L}D_t\alpha_L+\rho\frac{\partial\eta}{\partial\tilde{\Sigma}}D_t\tilde{\Sigma} \tag{A.96}$$

and that

$$\begin{aligned}
\frac{\partial\eta}{\partial\rho} &= \left(m+\frac{1}{2}\right)\frac{\nu^{2m}\xi^{2n}\tilde{\Sigma}^2}{\rho}\frac{\partial\nu}{\partial\rho}-\frac{1}{2}\frac{\nu^{2m+1}\xi^{2n}\tilde{\Sigma}^2}{\rho^2}+\frac{\partial e}{\partial\rho} \\
\frac{\partial\eta}{\partial\mathbf{u}} &= \mathbf{u} \\
\frac{\partial\eta}{\partial\alpha_L} &= \left(m+\frac{1}{2}\right)\frac{\nu^{2m}\xi^{2n}\tilde{\Sigma}^2}{\rho}\frac{\partial\nu}{\partial\alpha_L}+\frac{\partial e}{\partial\alpha_L} \\
\frac{\partial\eta}{\partial\tilde{\Sigma}} &= \frac{\nu^{2m+1}\xi^{2n}}{\rho}\tilde{\Sigma}.
\end{aligned} \tag{A.97}$$

Moreover, thanks to the system (2.169), the following relations hold:

$$D_t\rho = -\rho\left(\nabla\cdot\mathbf{u}\right) \qquad D_t\mathbf{u} = -\frac{1}{\rho}\nabla P. \tag{A.98}$$

Hence, we get

$$\begin{aligned}
\rho D_t\eta \;&=\; -\rho^2\left(\nabla\cdot\mathbf{u}\right)\left(\frac{\partial e}{\partial\rho} + \left(\delta+\frac{1}{2}\right)\frac{\nu^{2m}\xi^{2n}\tilde{\Sigma}^2}{\rho}\frac{\partial\nu}{\partial\rho} - \frac{1}{2}\frac{\nu^{2m+1}\xi^{2n}\tilde{\Sigma}^2}{\rho^2}\right) - \mathbf{u}\cdot\nabla P \\
&+\; \rho\left(\frac{\partial e}{\partial\alpha_L} + \left(m+\frac{1}{2}\right)\frac{\nu^{2m}\xi^{2n}\tilde{\Sigma}^2}{\rho}\frac{\partial\nu}{\partial\alpha_L}\right)\xi^n\nu^m\tilde{\Sigma} \qquad\qquad (\text{A.99}) \\
&+\; \left(\nu^{2m+1}\xi^{2n}\tilde{\Sigma}\right)D_t\tilde{\Sigma}.
\end{aligned}$$

After a few manipulations, we obtain

$$\begin{aligned}
\rho D_t\eta = &-\nabla\cdot\left(P\mathbf{u}\right) + \left(\nabla\cdot\mathbf{u}\right)\left[\left(\nu-(\delta+1)\,\rho\frac{\partial\nu}{\partial\rho}\right)\xi^{2n}\nu^{2m}\tilde{\Sigma}^2\right] \\
&+\rho\left[\frac{\partial e}{\partial\alpha_L} + \left(m+\frac{1}{2}\right)\frac{\nu^{2m}\xi^{2n}\tilde{\Sigma}^2}{\rho}\frac{\partial\nu}{\partial\alpha_L}\right]\xi^n\nu^m\tilde{\Sigma} \qquad\qquad (\text{A.100}) \\
&+\left(\nu^{2m+1}\xi^{2n}\tilde{\Sigma}\right)D_t\tilde{\Sigma}.
\end{aligned}$$

The second principle of thermodynamics reduces therefore to

$$\begin{aligned}
&\nabla\cdot\left(\mathbf{G}-P\mathbf{u}\right) + \left(\nabla\cdot\mathbf{u}\right)\left[\left(\nu-(m+1)\,\rho\frac{\partial\nu}{\partial\rho}\right)\left(\xi^{2n}\tilde{\nu}^{2m}\tilde{\Sigma}^2\right)\right] \\
+\;&\rho\left[\frac{\partial e}{\partial\alpha_L} + \left(m+\frac{1}{2}\right)\frac{\nu^{2m}\xi^{2n}\tilde{\Sigma}^2}{\rho}\frac{\partial\nu}{\partial\alpha_L}\right]\xi^n\nu^m\tilde{\Sigma} \\
+\;&\left(\nu^{2m+1}\xi^{2n}\tilde{\Sigma}\right)D_t\tilde{\Sigma} \le 0. \qquad\qquad (\text{A.101})
\end{aligned}$$

Taking $\mathbf{G} = P\mathbf{u}$ and dividing by $\nu^{2m+1}\xi^n$, which is positive since both ν and ξ are assumed to be positive, we recover (2.173).

A.5 Time discretization methods

In this Appendix, we review the time discretization methods employed throughout the thesis. The TR-BDF2 method is a second order implicit scheme, originally introduced in [Bank et al., 1985] as a combination of the Trapezoidal Rule (or Crank-Nicholson) method and of the Backward Differentiation Formula method of order 2. For a generic time dependent problem $\boldsymbol{u}' = \mathcal{N}(\boldsymbol{u})$, the incremental form of the TR-BDF2 method can be described in terms of two stages, the first from t^n to $t^{n+\chi} = t^n + \chi\Delta t$ and the second from $t^{n+\chi}$ to t^{n+1}:

$$\begin{aligned}
\frac{\boldsymbol{u}^{n+\chi}-\boldsymbol{u}^n}{\chi\Delta t} &= \frac{1}{2}\mathcal{N}\left(\boldsymbol{u}^{n+\chi}\right) + \frac{1}{2}\mathcal{N}\left(\boldsymbol{u}^n\right) \qquad\qquad (\text{A.102}) \\
\frac{\boldsymbol{u}^{n+1}-\boldsymbol{u}^{n+\chi}}{(1-\chi)\,\Delta t} &= \frac{1}{2-\chi}\mathcal{N}\left(\boldsymbol{u}^{n+1}\right) + \frac{1-\chi}{2\,(2-\chi)}\mathcal{N}\left(\boldsymbol{u}^{n+\chi}\right) + \frac{1-\chi}{2\,(2-\chi)}\mathcal{N}\left(\boldsymbol{u}^n\right).
\end{aligned}$$

Here, $\boldsymbol{u}^n$ denotes the approximation at time $n = 0, ..., N$. Notice that, in order to guarantee L-stability, one has to choose $\chi = 2-\sqrt{2}$. The TR-BDF2 scheme has been fully analyzed in [Hosea and Shampine, 1996], where the method was shown to be an L-stable Explicit Singly Diagonal Impicit Runge Kutta (ESDIRK) method. The TR-BDF2 has been shown to be stiffly accurate in [Hosea and Shampine, 1996] and has been very successfully employed in simulations of low Mach number flows with gravity in [Tumolo and Bonaventura, 2015]. Unconditionally strong stability preserving extensions of TR-BDF2 have been derived in [Bonaventura and Della Rocca, 2017]. Explicit methods that complement TR-BDF2 as second order IMEX pairs have been introduced in [Giraldo et al., 2013] and successfully employed in [Bonaventura et al., 2018, Garres-Díaz and Bonaventura, 2021, Orlando et al., 2022a]. These methods are useful for time dependent problems that can be formulated as $\boldsymbol{u}^{'} = \boldsymbol{f}_S(\boldsymbol{u}, t) + \boldsymbol{f}_{NS}(\boldsymbol{u}, t)$, where the S and NS subscripts denote the stiff and non-stiff components of the system, to which the implicit and explicit companion methods are applied, respectively. If $\boldsymbol{v}^n \approx \boldsymbol{u}(t^n)$, the generic $s-$stage IMEX-ARK method can be defined as

$$\begin{aligned}
\boldsymbol{v}^{(n,l)} = \boldsymbol{v}^n \quad &+ \quad \Delta t \sum_{m=1}^{s-1} \Big(a_{lm} \boldsymbol{f}_{NS}(\boldsymbol{v}^{(n,m)}, t + c_m \Delta t) \\
&+ \quad \tilde{a}_{lm} \boldsymbol{f}_S(\boldsymbol{v}^{(n,m)}, t + c_m \Delta t) \Big) \\
&+ \quad \Delta t \, \tilde{a}_{ll} \, \boldsymbol{f}_S(\boldsymbol{v}^{(n,l)}, t + c_l \Delta t),
\end{aligned} \tag{A.103}$$

where $l = 1, \dots, s$. After computation of the intermediate stages, $\boldsymbol{v}^{n+1}$ is computed as

$$\boldsymbol{v}^{n+1} = \boldsymbol{v}^n + \Delta t \sum_{l=1}^{s} b_l \left[\boldsymbol{f}_{NS}(\boldsymbol{v}^{(n,l)}, t + c_l \Delta t) + \boldsymbol{f}_S(\boldsymbol{v}^{(n,l)}, t + c_l \Delta t) \right]. \tag{A.104}$$

Coefficients $a_{lm}, \tilde{a}_{lm}, c_l$ and b_l are determined so that the method is consistent of a given order. In particular, in addition to the order conditions specific to each submethod, the coefficients should respect coupling conditions. Here, we consider a variant of the IMEX method proposed in [Giraldo et al., 2013], whose coefficients are presented in the Butcher tableaux reported in Tables A.1 and A.2 for the explicit and implicit method, respectively, where $\chi = 2 - \sqrt{2}$. The coefficients of the explicit method were proposed in [Giraldo et al., 2013], while the implicit method, also employed in the same paper, coincides indeed for the above choice of χ with the TR-BDF2 method, thus providing ample guarantees the robustness of the proposed approach in the low Mach number limit.

$$\begin{array}{c|ccc}
0 & 0 & & \\
\chi & \chi & 0 & \\
1 & 1 - a_{32} & a_{32} & 0 \\
\hline
 & \frac{1}{2} - \frac{\chi}{4} & \frac{1}{2} - \frac{\chi}{4} & \frac{\chi}{2}
\end{array}$$

Table A.1: *Butcher tableaux of the explicit ARK2 method*

Notice that, as discussed in [Giraldo et al., 2013], the choice of the coefficients

$$a_{32} = \frac{7 - 2\chi}{6} \qquad 1 - a_{32} = \frac{2\chi - 1}{6}$$

$$
\begin{array}{c|ccc}
0 & 0 & & \\
\chi & \frac{\chi}{2} & \frac{\chi}{2} & \\
1 & \frac{1}{2\sqrt{2}} & \frac{1}{2\sqrt{2}} & 1-\frac{1}{\sqrt{2}} \\
\hline
 & \frac{1}{2}-\frac{\chi}{4} & \frac{1}{2}-\frac{\chi}{4} & \frac{\chi}{2}
\end{array}
$$

Table A.2: *Butcher tableaux of the implicit ARK2 method*

in the third stage of the explicit part of the method is arbitrary. In [Giraldo et al., 2013], the above value of a_{32} was chosen with the aim of maximizing the stability region of the method, but this coefficient is indeed a free parameter and can also be chosen in different ways, as long as stability is not compromised. We study now the stability and monotonicity of the explicit part of the IMEX scheme. In order to identify possible alternative choices, we perform an analysis using the concepts introduced in [Kraaijevanger, 1991, Ferracina and Spijker, 2004, Higueras, 2004] (see also the review in [Gottlieb et al., 2001]). A similar analysis for the implicit part of the IMEX scheme was carried out in [Bonaventura and Della Rocca, 2017], to which we refer for a summary of the related theoretical results. We then define

$$
A = \begin{bmatrix} 0 & 0 & 0 \\ \chi & 0 & 0 \\ 1-a_{32} & a_{32} & 0 \end{bmatrix} \qquad b^T = \begin{bmatrix} \frac{1}{2}-\frac{\chi}{4} & \frac{1}{2}-\frac{\chi}{4} & \frac{\chi}{2}. \end{bmatrix} \tag{A.105}
$$

We define for $\xi \in \mathbb{R}$ the quantities

$$
\begin{aligned}
A(\xi) &= A\left(I-\xi A\right)^{-1} & b^T(\xi) &= b^T\left(I-\xi A\right)^{-1} \\
e(\xi) &= \left(I-\xi A\right)^{-1} e & \varphi(\xi) &= 1+\xi b^T\left(I-\xi A\right)^{-1} e
\end{aligned} \tag{A.106}
$$

where I is the 3×3 identity matrix and e is a vector whose all components are equal to 1. Therefore, for the specific scheme, we obtain

$$
A(\xi) = \begin{bmatrix} 0 & 0 & 0 \\ \chi & 0 & 0 \\ 1+a_{32}\left(\chi\xi-1\right) & a_{32} & 0 \end{bmatrix} \tag{A.107}
$$

$$
b^T(\xi) = \begin{bmatrix} \frac{1}{4}\left[2+\chi\left(-1+\xi\left(4-\chi+2a_{32}\left(\chi\xi-1\right)\right)\right)\right] \\ \frac{1}{4}\left[2+\chi\left(2a_{32}\xi-1\right)\right] \\ \frac{\chi}{2} \end{bmatrix} \tag{A.108}
$$

$$
e(\xi) = \begin{bmatrix} 1 \\ 1+\chi\xi \\ 1+\xi+a_{32}\chi\xi^2 \end{bmatrix} \tag{A.109}
$$

$$
\varphi(\xi) = 1+\xi+\frac{\xi^2}{2}+\left(3-2\sqrt{2}\right)a_{32}\xi^3. \tag{A.110}
$$

A method with tableaux $\left(A, b^T\right)$ is absolutely monotone at $\xi \in \mathbb{R}$ if $A(\xi) \geq 0$, $b^T(\xi) \geq 0$, $e(\xi) \geq 0$ and $\varphi(\xi) \geq 0$ elementwise; moreover the radius of absolute monotonicity is defined for all ξ in $-r \leq \xi \leq 0$ as

$$
R(A,b) = \sup\left[r | r \geq 0, A(\xi) \geq 0, b^T(\xi) \geq 0, e(\xi) \geq 0, \varphi(\xi) \geq 0\right]. \tag{A.111}
$$

Figure A.1 shows the behaviour of the radius of absolute monotonicity as a_{32} varies, along with the behaviour of the stability region along the imaginary axis. As already mentioned before, $a_{32} = \frac{7-2\chi}{6}$ was chosen originally to maximize the stability region, but in this case $R = \frac{2\sqrt{2}-3}{2+\sqrt{2}} \approx 0.05$, so that the region of absolute monotonicity is quite small. It can be shown that the region of absolute stability is given by

$$S = \left\{ z \in \mathbb{C} : \left| 1 + z + a_{32}\chi z^2 \right| < 1 \right\}. \tag{A.112}$$

The alternative value $a_{32} = 0.5$ maximizes the region of absolute monotonicity without compromising too much the stability and yields a novel way in the choice of the coefficients for the explicit part as proposed in [Orlando et al., 2022a]. The impact of this alternative choice on numerical results is discussed in Sections 4.3 and 4.4.

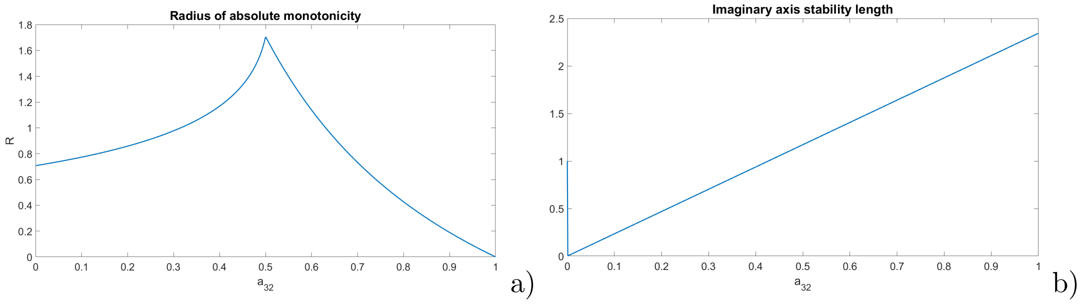

Figure A.1: *Analysis of the explicit part of IMEX scheme: a) Radius of absolute monotonicity as function of a_{32}, b) Size of stability region along the imaginary axis as a_{32} varies.*

We briefly recall here also the second order and the third order optimal SSP Runge-Kutta methods derived in [Gottlieb and Shu, 1998] for ordinary differential equations which have been employed in Section 4.1 and Section 4.3. The second order scheme reads as follows:

$$\boldsymbol{v}^{(1)} = \boldsymbol{v}^n + \Delta t \mathcal{N}(\boldsymbol{v}^n) \tag{A.113}$$

$$\boldsymbol{v}^{n+1} = \frac{1}{2}\boldsymbol{v}^n + \frac{1}{2}\boldsymbol{v}^{(1)} + \frac{1}{2}\Delta t \mathcal{N}(\boldsymbol{v}^{(1)}). \tag{A.114}$$

The third order method is given instead by:

$$\boldsymbol{v}^{(1)} = \boldsymbol{v}^n + \Delta t \mathcal{N}(\boldsymbol{v}^n) \tag{A.115}$$

$$\boldsymbol{v}^{(2)} = \frac{3}{4}\boldsymbol{v}^n + \frac{1}{4}\boldsymbol{v}^{(1)} + \frac{1}{4}\Delta t \mathcal{N}(\boldsymbol{v}^{(1)}) \tag{A.116}$$

$$\boldsymbol{v}^{n+1} = \frac{1}{3}\boldsymbol{v}^n + \frac{2}{3}\boldsymbol{v}^{(2)} + \frac{2}{3}\Delta t \mathcal{N}(\boldsymbol{v}^{(2)}). \tag{A.117}$$

A.6 Relaxation operator

In this Appendix, we describe some possible strategies to deal with the relaxation source terms for the system (2.149). According to the standard operator splitting procedure, the system of ordinary differential equations associated with the mechanical relaxation terms is the following:

$$
\begin{aligned}
\frac{d\alpha_1}{dt} &= \tilde{\mu}\left(p_1 - p_2\rho_{rel}\frac{M_1^2}{M_2^2}\right)\\
\frac{d\alpha_1\rho_1}{dt} &= 0\\
\frac{d\alpha_1\rho_1\mathbf{u}_1}{dt} &= -\tilde{\lambda}\left(\mathbf{u}_1 - \mathbf{u}_2\right)\\
\frac{d\alpha_1\rho_1 E_1}{dt} &= -\tilde{\mu}p_I\left(p_1 - p_2\rho_{rel}\frac{M_1^2}{M_2^2}\right) - \tilde{\lambda}M_1^2\mathbf{v}_I\cdot\left(\mathbf{u}_1 - \mathbf{u}_2\right)\\
\frac{d\alpha_2\rho_2}{dt} &= 0 \qquad\qquad (A.118)\\
\frac{d\alpha_2\rho_2\mathbf{u}_2}{dt} &= \frac{\tilde{\lambda}}{\rho_{rel}}\left(\mathbf{u}_1 - \mathbf{u}_2\right)\\
\frac{d\alpha_2\rho_2 E_2}{dt} &= \frac{\tilde{\mu}}{\rho_{rel}}\frac{M_2^2}{M_1^2}p_I\left(p_1 - p_2\rho_{rel}\frac{M_1^2}{M_2^2}\right) + \frac{\tilde{\lambda}}{\rho_{rel}}M_2^2\mathbf{v}_I\cdot\left(\mathbf{u}_1 - \mathbf{u}_2\right).
\end{aligned}
$$

We immediately notice that the partial densities remain constant. This system is characterized by a high degree of stiffness [Re and Abgrall, 2022, Pelanti, 2022] since the relaxation coefficients $\tilde{\mu}$ and $\tilde{\lambda}$ assume typically large values. Hence, we consider the implicit part of the IMEX scheme for its time integration. For the sake of clarity, we report the second stage of the time discretization that reads as follows

$$
\begin{aligned}
\alpha_1^{(n,2)} &= \alpha_1^{(n,1)} \\
&+ \tilde{a}_{22}\Delta t\tilde{\mu}\left(p_1^{(n,2)} - p_2^{(n,2)}\rho_{rel}\frac{M_1^2}{M_2^2}\right) + \tilde{a}_{21}\Delta t\tilde{\mu}\left(p_1^{(n,1)} - p_2^{(n,1)}\rho_{rel}\frac{M_1^2}{M_2^2}\right) \\
\alpha_1^{(n,2)}\rho_1^{(n,2)} &= \alpha_1^{(n,1)}\rho_1^{(n,1)} \\
\alpha_1^{(n,2)}\rho_1^{(n,2)}\mathbf{u}_1^{(n,2)} &= \alpha_1^{(n,1)}\rho_1^{(n,1)}\mathbf{u}_1^{(n,1)} \\
&- \tilde{a}_{22}\Delta t\tilde{\lambda}\left(\mathbf{u}_1^{(n,2)} - \mathbf{u}_2^{(n,2)}\right) - \tilde{a}_{21}\Delta t\tilde{\lambda}\left(\mathbf{u}_1^{(n,1)} - \mathbf{u}_2^{(n,1)}\right) \\
\alpha_1^{(n,2)}\rho_1^{(n,2)}E_1^{(n,2)} &= \alpha_1^{(n,1)}\rho_1^{(n,1)}E_1^{(n,1)} \\
&- \tilde{a}_{22}\Delta t\tilde{\mu}p_I^{(n,2)}\left(p_1^{(n,2)} - p_2^{(n,2)}\rho_{rel}\frac{M_1^2}{M_2^2}\right) \\
&- \tilde{a}_{21}\Delta t\tilde{\mu}p_I^{(n,1)}\left(p_1^{(n,1)} - p_2^{(n,1)}\rho_{rel}\frac{M_1^2}{M_2^2}\right) \\
&- \tilde{a}_{22}\Delta t\tilde{\lambda}M_1^2\mathbf{v}_I^{(n,2)}\cdot\left(\mathbf{u}_1^{(n,2)} - \mathbf{u}_2^{(n,2)}\right) \\
&- \tilde{a}_{21}\Delta t\tilde{\lambda}M_1^2\mathbf{v}_I^{(n,1)}\cdot\left(\mathbf{u}_1^{(n,1)} - \mathbf{u}_2^{(n,1)}\right) \\
\alpha_2^{(n,2)}\rho_2^{(n,2)} &= \alpha_2^{(n,1)}\rho_2^{(n,1)} \qquad\qquad (A.119) \\
\alpha_2^{(n,2)}\rho_2^{(n,2)}\mathbf{u}_2^{(n,2)} &= \alpha_2^{(n,1)}\rho_2^{(n,1)}\mathbf{u}_2^{(n,1)} \\
&+ \tilde{a}_{22}\Delta t\frac{\tilde{\lambda}}{\rho_{rel}}\left(\mathbf{u}_1^{(n,2)} - \mathbf{u}_2^{(n,2)}\right) + \tilde{a}_{21}\Delta t\frac{\tilde{\lambda}}{\rho_{rel}}\left(\mathbf{u}_1^{(n,1)} - \mathbf{u}_2^{(n,1)}\right) \\
\alpha_2^{(n,2)}\rho_2^{(n,2)}E_2^{(n,2)} &= \alpha_2^{(n,1)}\rho_2^{(n,1)}E_2^{(n,1)} \\
&+ \tilde{a}_{22}\Delta t\frac{\tilde{\mu}}{\rho_{rel}}\frac{M_2^2}{M_1^2}p_I^{(n,2)}\left(p_1^{(n,2)} - p_2^{(n,2)}\rho_{rel}\frac{M_1^2}{M_2^2}\right) \\
&+ \tilde{a}_{21}\Delta t\frac{\tilde{\mu}}{\rho_{rel}}\frac{M_2^2}{M_1^2}p_I^{(n,1)}\left(p_1^{(n,1)} - p_2^{(n,1)}\rho_{rel}\frac{M_1^2}{M_2^2}\right) \\
&+ \tilde{a}_{22}\Delta t\frac{\tilde{\lambda}}{\rho_{rel}}M_2^2\mathbf{v}_I^{(n,2)}\cdot\left(\mathbf{u}_1^{(n,2)} - \mathbf{u}_2^{(n,2)}\right) \\
&+ \tilde{a}_{21}\Delta t\frac{\tilde{\lambda}}{\rho_{rel}}M_2^2\mathbf{v}_I^{(n,1)}\cdot\left(\mathbf{u}_1^{(n,1)} - \mathbf{u}_2^{(n,1)}\right).
\end{aligned}
$$

Thanks to the continuity equations, we can rewrite the momentum equations as follows:

$$
\begin{aligned}
\mathbf{u}_1^{(n,2)} &= \mathbf{u}_1^{(n,1)} - \frac{\tilde{a}_{22}\Delta t\tilde{\lambda}}{\alpha_1^{(n,1)}\rho_1^{(n,1)}}\left(\mathbf{u}_1^{(n,2)} - \mathbf{u}_2^{(n,2)}\right) - \frac{\tilde{a}_{21}\Delta t\tilde{\lambda}}{\alpha_1^{(n,1)}\rho_1^{(n,1)}}\left(\mathbf{u}_1^{(n,1)} - \mathbf{u}_2^{(n,1)}\right) \qquad (A.120) \\
\mathbf{u}_2^{(n,2)} &= \mathbf{u}_2^{(n,1)} + \frac{\tilde{a}_{22}\Delta t\tilde{\lambda}}{\alpha_2^{(n,1)}\rho_2^{(n,1)}\rho_{rel}}\left(\mathbf{u}_1^{(n,2)} - \mathbf{u}_2^{(n,2)}\right) + \frac{\tilde{a}_{21}\Delta t\tilde{\lambda}}{\alpha_2^{(n,1)}\rho_2^{(n,1)}\rho_{rel}}\left(\mathbf{u}_1^{(n,1)} - \mathbf{u}_2^{(n,1)}\right),
\end{aligned}
$$

from which we obtain the following relation for $\mathbf{u}_1^{(n,2)} - \mathbf{u}_2^{(n,2)}$:

$$
\mathbf{u}_1^{(n,2)} - \mathbf{u}_2^{(n,2)} = \frac{\left[1 - \tilde{a}_{21}\Delta t\hat{\lambda}\left(\frac{1}{\alpha_1^{(n,1)}\rho_1^{(n,1)}} - \frac{1}{\alpha_2^{(n,1)}\rho_2^{(n,1)}}\right)\right]}{\left[1 + \tilde{a}_{22}\Delta t\hat{\lambda}\left(\frac{1}{\alpha_1^{(n,1)}\rho_1^{(n,1)}} - \frac{1}{\alpha_2^{(n,1)}\rho_2^{(n,1)}}\right)\right]}\left(\mathbf{u}_1^{(n,1)} - \mathbf{u}_2^{(n,1)}\right) \qquad (A.121)
$$

and the corresponding relations for the velocity which are, therefore, known at this point. The remaining equations form a system of non-linear equations, namely

$$
\begin{aligned}
\alpha_1^{(n,2)} &= \alpha_1^{(n,1)} \\
&+ \tilde{a}_{22}\Delta t\tilde{\mu}\left(p_1^{(n,2)} - p_2^{(n,2)}\rho_{rel}\frac{M_1^2}{M_2^2}\right) + \tilde{a}_{21}\Delta t\tilde{\mu}\left(p_1^{(n,1)} - p_2^{(n,1)}\rho_{rel}\frac{M_1^2}{M_2^2}\right) \\
\alpha_1^{(n,2)}\rho_1^{(n,2)} &= \alpha_1^{(n,1)}\rho_1^{(n,1)} \\
E_1^{(n,2)} &= E_1^{(n,1)} \\
&- \frac{\tilde{a}_{22}\Delta t\tilde{\mu}p_I^{(n,2)}\left(p_1^{(n,2)} - p_2^{(n,2)}\rho_{rel}\frac{M_1^2}{M_2^2}\right)}{\alpha_1^{(n,1)}\rho_1^{(n,1)}} \\
&- \frac{\tilde{a}_{21}\Delta t\tilde{\mu}p_I^{(n,1)}\left(p_1^{(n,1)} - p_2^{(n,1)}\rho_{rel}\frac{M_1^2}{M_2^2}\right)}{\alpha_1^{(n,1)}\rho_1^{(n,1)}} \\
&- \frac{\tilde{a}_{22}\Delta t\tilde{\lambda}M_1^2\mathbf{v}_I^{(n,2)}\cdot\left(\mathbf{u}_1^{(n,2)} - \mathbf{u}_2^{(n,2)}\right)}{\alpha_1^{(n,1)}\rho_1^{(n,1)}} \\
&- \frac{\tilde{a}_{21}\Delta t\tilde{\lambda}M_1^2\mathbf{v}_I^{(n,1)}\cdot\left(\mathbf{u}_1^{(n,1)} - \mathbf{u}_2^{(n,1)}\right)}{\alpha_1^{(n,1)}\rho_1^{(n,1)}} \\
\alpha_2^{(n,2)}\rho_2^{(n,2)} &= \alpha_2^{(n,1)}\rho_2^{(n,1)} \qquad\qquad \text{(A.122)} \\
E_2^{(n,2)} &= E_2^{(n,1)} \\
&+ \frac{\tilde{a}_{22}\Delta t\frac{\tilde{\mu}}{\rho_{rel}}\frac{M_2^2}{M_1^2}p_I^{(n,2)}\left(p_1^{(n,2)} - p_2^{(n,2)}\rho_{rel}\frac{M_1^2}{M_2^2}\right)}{\alpha_2^{(n,1)}\rho_2^{(n,1)}} \\
&+ \frac{\tilde{a}_{21}\Delta t\frac{\tilde{\mu}}{\rho_{rel}}\frac{M_2^2}{M_1^2}p_I^{(n,1)}\left(p_1^{(n,1)} - p_2^{(n,1)}\rho_{rel}\frac{M_1^2}{M_2^2}\right)}{\alpha_2^{(n,1)}\rho_2^{(n,1)}} \\
&+ \frac{\tilde{a}_{22}\Delta t\frac{\tilde{\lambda}}{\rho_{rel}}M_2^2\mathbf{v}_I^{(n,2)}\cdot\left(\mathbf{u}_1^{(n,2)} - \mathbf{u}_2^{(n,2)}\right)}{\alpha_2^{(n,1)}\rho_2^{(n,1)}} \\
&+ \frac{\tilde{a}_{21}\Delta t\frac{\tilde{\lambda}}{\rho_{rel}}M_2^2\mathbf{v}_I^{(n,1)}\cdot\left(\mathbf{u}_1^{(n,1)} - \mathbf{u}_2^{(n,1)}\right)}{\alpha_2^{(n,1)}\rho_2^{(n,1)}}.
\end{aligned}
$$

The previous system can be rewritten as follows

$$
\begin{aligned}
\alpha_1^{(n,2)} &= \alpha_1^{(n,1)} \\
&+ \tilde{a}_{22}\Delta t\tilde{\mu}\left(p_1^{(n,2)} - p_2^{(n,2)}\rho_{rel}\frac{M_1^2}{M_2^2}\right) + \tilde{a}_{21}\Delta t\tilde{\mu}\left(p_1^{(n,1)} - p_2^{(n,1)}\rho_{rel}\frac{M_1^2}{M_2^2}\right) \\
\alpha_1^{(n,2)}\rho_1^{(n,2)} &= \alpha_1^{(n,1)}\rho_1^{(n,1)} \\
e_1^{(n,2)} &+ \frac{\tilde{a}_{22}\Delta t\tilde{\mu}p_I^{(n,2)}\left(p_1^{(n,2)} - p_2^{(n,2)}\rho_{rel}\frac{M_1^2}{M_2^2}\right)}{\alpha_1^{(n,1)}\rho_1^{(n,1)}} = \hat{e}_1 \\
\alpha_2^{(n,2)}\rho_2^{(n,2)} &= \alpha_2^{(n,1)}\rho_2^{(n,1)} \qquad\qquad \text{(A.123)} \\
e_2^{(n,2)} &- \frac{\tilde{a}_{22}\Delta t\frac{\tilde{\mu}}{\rho_{rel}}\frac{M_2^2}{M_1^2}p_I^{(n,2)}\left(p_1^{(n,2)} - p_2^{(n,2)}\rho_{rel}\frac{M_1^2}{M_2^2}\right)}{\alpha_2^{(n,1)}\rho_2^{(n,1)}} = \hat{e}_2,
\end{aligned}
$$

with

$$\begin{aligned}
\hat{e}_1 &= E_1^{(n,1)} - \frac{\tilde{a}_{21}\Delta t\tilde{\mu}p_I^{(n,1)}\left(p_1^{(n,1)} - p_2^{(n,1)}\rho_{rel}\frac{M_1^2}{M_2^2}\right)}{\alpha_1^{(n,1)}\rho_1^{(n,1)}} \\
&- \frac{\tilde{a}_{22}\Delta t\tilde{\lambda}M_1^2\mathbf{v}_I^{(n,2)}\cdot\left(\mathbf{u}_1^{(n,2)} - \mathbf{u}_2^{(n,2)}\right)}{\alpha_1^{(n,1)}\rho_1^{(n,1)}} - \frac{\tilde{a}_{21}\Delta t\tilde{\lambda}M_1^2\mathbf{v}_I^{(n,1)}\cdot\left(\mathbf{u}_1^{(n,1)} - \mathbf{u}_2^{(n,1)}\right)}{\alpha_1^{(n,1)}\rho_1^{(n,1)}} \\
&- \frac{1}{2}M_1^2\mathbf{u}_1^{(n,2)}\cdot\mathbf{u}_1^{(n,2)} \qquad \text{(A.124)}
\end{aligned}$$

$$\begin{aligned}
\hat{e}_2 &= E_2^{(n,1)} + \frac{\tilde{a}_{21}\Delta t\frac{\tilde{\mu}}{\rho_{rel}}\frac{M_2^2}{M_1^2}p_I^{(n,1)}\left(p_1^{(n,1)} - p_2^{(n,1)}\rho_{rel}\frac{M_1^2}{M_2^2}\right)}{\alpha_2^{(n,1)}\rho_2^{(n,1)}} \\
&+ \frac{\tilde{a}_{22}\Delta t\frac{\tilde{\lambda}}{\rho_{rel}}M_2^2\mathbf{v}_I^{(n,2)}\cdot\left(\mathbf{u}_1^{(n,2)} - \mathbf{u}_2^{(n,2)}\right)}{\alpha_2^{(n,1)}\rho_2^{(n,1)}} + \frac{\tilde{a}_{21}\Delta t\frac{\tilde{\lambda}}{\rho_{rel}}M_2^2\mathbf{v}_I^{(n,1)}\cdot\left(\mathbf{u}_1^{(n,1)} - \mathbf{u}_2^{(n,1)}\right)}{\alpha_2^{(n,1)}\rho_2^{(n,1)}} \\
&- \frac{1}{2}M_2^2\mathbf{u}_2^{(n,2)}\cdot\mathbf{u}_2^{(n,2)}.
\end{aligned}$$

We rewrite now the previous system of equation in order to analyze it in terms of the unknowns $\left(\alpha_1^{(n,2)}, \rho_1^{(n,2)}, p_1^{(n,2)}, \rho_2^{(n,2)}, p_2^{(n,2)}\right)$

$$\begin{aligned}
\alpha_1^{(n,2)} - \tilde{a}_{22}\Delta t\tilde{\mu}\left(p_1^{(n,2)} - p_2^{(n,2)}\rho_{rel}\frac{M_1^2}{M_2^2}\right) &= \alpha_1^{(n,1)} \\
&+ \tilde{a}_{21}\Delta t\tilde{\mu}\left(p_1^{(n,1)} - p_2^{(n,1)}\rho_{rel}\frac{M_1^2}{M_2^2}\right) \\
\alpha_1^{(n,2)}\rho_1^{(n,2)} &= \alpha_1^{(n,1)}\rho_1^{(n,1)} \\
e_1^{(n,2)}\left(p_1^{(n,2)}, \rho_1^{(n,2)}\right) &+ \\
\frac{\tilde{a}_{22}\Delta t\tilde{\mu}p_I^{(n,2)}\left(p_1^{(n,2)} - p_2^{(n,2)}\rho_{rel}\frac{M_1^2}{M_2^2}\right)}{\alpha_1^{(n,1)}\rho_1^{(n,1)}} &= \hat{e}_1 \\
\left(1 - \alpha_1^{(n,2)}\right)\rho_2^{(n,2)} &= \alpha_2^{(n,1)}\rho_2^{(n,1)} \qquad \text{(A.125)} \\
e_2^{(n,2)}\left(p_2^{(n,2)}, \rho_2^{(n,2)}\right) &- \\
\frac{\tilde{a}_{22}\Delta t\frac{\tilde{\mu}}{\rho_{rel}}\frac{M_2^2}{M_1^2}p_I^{(n,2)}\left(p_1^{(n,2)} - p_2^{(n,2)}\rho_{rel}\frac{M_1^2}{M_2^2}\right)}{\alpha_2^{(n,1)}\rho_2^{(n,1)}} &= \hat{e}_2.
\end{aligned}$$

We notice that

$$\frac{\partial p_I^{(n,2)}}{\partial \alpha_1^{(n,2)}} = p_1^{(n,2)} - p_2^{(n,2)}\rho_{rel}\frac{M_1^2}{M_2^2} \qquad \text{(A.126)}$$

$$\frac{\partial p_I^{(n,2)}}{\partial p_1^{(n,2)}} = \alpha_1^{(n,2)} \qquad \text{(A.127)}$$

$$\frac{\partial p_I^{(n,2)}}{\partial p_2^{(n,2)}} = \left(1 - \alpha_1^{(n,2)}\right)\rho_{rel}\frac{M_1^2}{M_2^2}. \qquad \text{(A.128)}$$

Denote by $\tilde{\Delta}p$ the quantity $p_1^{(n,2)} - p_2^{(n,2)}\rho_{rel}\frac{M_1^2}{M_2^2}$. Hence, we obtain the following Jacobian matrix for the system (A.125):

$$\begin{bmatrix} 1 & 0 & -\tilde{a}_{22}\Delta t\tilde{\mu} & 0 & \tilde{a}_{22}\rho_{rel}\frac{M_1^2}{M_2^2} \\ \rho_1^{(n,2)} & \alpha_1^{(n,2)} & 0 & 0 & 0 \\ 0 & \frac{\partial e_1^{(n,2)}}{\partial \rho_1^{(n,2)}} & \frac{\partial e_1^{(n,2)}}{\partial \rho_1^{(n,2)}} + \frac{\tilde{a}_{22}\Delta t\tilde{\mu}}{\alpha_1^{(n,1)}\rho_1^{(n,1)}} p_{I,\alpha_1}^{(n,2)} & 0 & \frac{\tilde{a}_{22}\Delta t\tilde{\mu}}{\alpha_1^{(n,1)}\rho_1^{(n,1)}} p_{I,\alpha_2}^{(n,2)} \\ -\rho_2^{(n,2)} & 0 & 0 & 1-\alpha_1^{(n,2)} & 0 \\ 0 & 0 & -\frac{\tilde{a}_{22}\Delta t\frac{\tilde{\mu}}{p_{rel}}}{\alpha_2^{(n,1)}\rho_2^{(n,1)}} p_{I,\alpha_1}^{(n,2)} & \frac{\partial e_2^{(n,2)}}{\partial \rho_2^{(n,2)}} & \frac{\partial e_2^{(n,2)}}{\partial \rho_2^{(n,2)}} - \frac{\tilde{a}_{22}\Delta t\frac{\tilde{\mu}}{p_{rel}}}{\alpha_2^{(n,1)}\rho_2^{(n,1)}} p_{I,\alpha_2}^{(n,2)} \end{bmatrix} \tag{A.129}$$

with $p_{I,\alpha_1}^{(n,2)} = \left[\alpha_1^{(n,2)}\tilde{\Delta}p + p_I^{(n,2)}\right]$ and $p_{I,\alpha_2}^{(n,2)} = \left[\tilde{\Delta}p\left(1-\alpha_1^{(n,2)}\right) - p_I^{(n,2)}\right] p_{rel}$. Several alternatives have been proposed in literature in order to mitigate the issue of the non-linearity. We describe here some of them and, for the sake of clarity in the notation, we report the dimensional counterpart. First of all, we mention the approach proposed in [De Lorenzo et al., 2019], that assumes an exponential decrease in time for the pressure disequilibrium:

$$\frac{d\left(p_1 - p_2\right)}{dt} = -\frac{p_1 - p_2}{\mathcal{T}^p}, \tag{A.130}$$

with $\mathcal{T}^p$ denoting the characteristic time of the pressure relaxation. The previous equation admits the following analytical solution

$$\left(p_1 - p_2\right)(t) = \left(p_1 - p_2\right)|_{t=0} e^{-\frac{t}{\mathcal{T}^p}}, \tag{A.131}$$

which is always positive and guarantees that the pressure perturbation never changes its sign. The characteristic time has to be set to a very small value so as to model an infinitely fast process and, therefore, it is adequate only when a very fast relaxation towards the equilibrium is considered. A more recent alternative has been presented in [Pelanti, 2022], starting, basically, from the following system

$$\begin{aligned} \frac{d\alpha_1}{dt} &= \hat{\mu}\left(p_1 - p_2\right) \\ \frac{d\alpha_1\rho_1}{dt} &= 0 \\ \frac{dp_1}{dt} &= \hat{\mu}\frac{1}{\alpha_1}\left[\left.\left(\frac{\partial p_1}{\partial\left(\rho_1 e_1\right)}\right)\right|_{\rho_1}\left(\rho_1 e_1 + p_I\right) + \left.\left(\frac{\partial p_1}{\partial \rho_1}\right)\right|_{\rho_1 e_1}\rho_1\right]\left(p_2 - p_1\right) \\ \frac{d\alpha_2\rho_2}{dt} &= 0 \\ \frac{dp_2}{dt} &= -\hat{\mu}\frac{1}{\alpha_2}\left[\left.\left(\frac{\partial p_2}{\partial\left(\rho_2 e_2\right)}\right)\right|_{\rho_2}\left(\rho_2 e_2 + p_I\right) + \left.\left(\frac{\partial p_2}{\partial \rho_2}\right)\right|_{\rho_2 e_2}\rho_2\right]\left(p_2 - p_1\right). \end{aligned} \tag{A.132}$$

Denote by ξ_m the quantity whose inverse multiply the pressure difference, namely

$$\frac{1}{\xi_m} = \frac{1}{\alpha_m}\left[\left.\left(\frac{\partial p_m}{\partial \rho_m e_m}\right)\right|_{\rho_m}\left(\rho_m e_m + p_I\right) + \left.\left(\frac{\partial p_m}{\partial \rho_m}\right)\right|_{\rho_m e_m}\rho_m\right]. \tag{A.133}$$

Hence, we obtain the following system of ordinary differential equations to be solved

$$\begin{aligned}
\frac{d\alpha_1}{dt} &= \hat{\mu}\left(p_1 - p_2\right) \\
\frac{d\alpha_1\rho_1}{dt} &= 0 \\
\frac{dp_1}{dt} &= \hat{\mu}\frac{1}{\xi_1}\left(p_2 - p_1\right) \\
\frac{d\alpha_2\rho_2}{dt} &= 0 \\
\frac{dp_2}{dt} &= -\hat{\mu}\frac{1}{\xi_2}\left(p_2 - p_1\right).
\end{aligned} \tag{A.134}$$

It is assumed that ξ_m is constant over time, namely $\xi_m = \xi_m^0$. Taking the difference of the two pressure equations, we get

$$\frac{d\left(p_2 - p_1\right)}{dt} = -\hat{\mu}\left(\frac{1}{\xi_1^0} + \frac{1}{\xi_2^0}\right)\left(p_2 - p_1\right), \tag{A.135}$$

which admits an exact solution

$$\left(p_2 - p_1\right)(t) = \left(p_2 - p_1\right)|_{t=0}e^{-K_p t}, \tag{A.136}$$

with $K_p = \hat{\mu}\left(\frac{1}{\xi_1^0} + \frac{1}{\xi_2^0}\right)$. From here, we obtain

$$\alpha_1 = \alpha_1^0 - \frac{\left(p_2 - p_1\right)|_{t=0}}{\left(\frac{1}{\xi_1^0} + \frac{1}{\xi_2^0}\right)}\left(1 - e^{-K_p t}\right). \tag{A.137}$$

This procedure is for arbitrary rate and not only in the case of very fast relaxation towards the equilibrium [Pelanti, 2022].

A.7 HPC framework and implementation issues

The numerical discretization methods presented in Chapter 3 have been implemented using the numerical library *deal.II* [Bangerth et al., 2007, Arndt et al., 2022], which is based on a matrix-free approach. As a consequence, no global sparse matrix is built and only the action of the linear operators on a vector is actually implemented. Matrix-free methods avoid the storage of big global sparse matrices and compute the underlying weak forms on the fly. Since the memory transfer, i.e. the speed at which the data can be read from RAM memory, is nowadays the most relevant bottleneck in HPC environment both in terms of time and energy [Mehonic and Kenyon, 2022], it is important to reduce the amount and the exchange of data involved in the computations. A matrix-free evaluation that reads less data can be therefore advantageous even if it does more computations. Another feature of the library employed during the numerical simulations is the mesh adaptation capability, as shown in the presentation of the results. We report here a call to the routine that performs mesh refinement

```
GridRefinement::refine_and_coarsen_fixed_number(triangulation,
    estimated_error_per_cell, 0.1, 0.3);
```

```
for(const auto& cell: triangulation.active_cell_iterators()) {
  if(cell->refine_flag_set() && cell->level() == max_loc_refinements)
    cell->clear_refine_flag();
  if(cell->coarsen_flag_set() && cell->level() == min_loc_refinements)
    cell->clear_coarsen_flag();
}
triangulation.prepare_coarsening_and_refinement();
triangulation.execute_coarsening_and_refinement(); /*--- Effectively
    perform the remeshing ---*/
```

The preconditioned conjugate gradient method implemented in the function *SolverCG* of the *deal II* library is employed to solve the symmetric linear systems, like the one obtained in (3.66), while the GMRES solver for non symmetric linear systems, like the one in (3.63), is implemented in the function *SolverGMRES* of the same library. A Jacobi preconditioner is used for non symmetric linear systems, whereas a Geometric Multigrid preconditioner is employed for the symmetric linear systems using the procedure described in [Janssen and Kanschat, 2011], which allows us to express all the stages of the Geometric MultiGrid (GMG) in terms of matrix-vector multiplications, thus reformulating it as a matrix-free method. All one needs to do in order to employ the GMG in a matrix free framework is to find a smoother that is based on matrix-vector products rather than all the matrix entries. One such candidate would be a damped Jacobi iteration that requires access only to the matrix diagonal, but this is often not sufficiently good in damping all high-frequency errors. This issue can be overcome by iterating with the so-called Chebyshev iteration, see e.g. [Adams et al., 2003].
A way to enhance the computational efficiency is to reduce the amount of data involved in the computation, the number of operations performed and to limit the use of double precision only to the algorithmic steps for which it is absolutely essential, see e.g. [Ackmann et al., 2022]. For this reason, the preconditioners are computed using single precision data instead of double precision data, as evident for instance below for the GMG preconditioner.

```
PreconditionMG<dim,
LinearAlgebra::distributed::Vector<float>,
MGTransferMatrixFree<dim, float>> preconditioner(dof_handler_pressure, mg,
    mg_transfer);
```

A complete version of the code for the incompressible Navier-Stokes equations is publicly available at [Orlando, 2022].

Bibliography

[bur, 2018] (2018). RFCS (Research Fund for Coal and Steel) research project “Burner 4.0, Development of a new burner concept: Industry 4.0 technologies applied to the best available combustion system for the Steel Industry”, project ID 847237. Technical report.

[Abdi and Giraldo, 2016] Abdi, D. and Giraldo, F. (2016). Efficient construction of unified continuous and discontinuous Galerkin formulations for the 3D Euler equations. *Journal of Computational Physics*, 320:46–68.

[Abgrall, 1996] Abgrall, R. (1996). How to Prevent Pressure Oscillations in Multicomponent Flow Calculations: A Quasi Conservative Approach. *Journal of Computational Physics*, 125:150–160.

[Ackmann et al., 2022] Ackmann, J., Dueben, P., Palmer, T., and Smolarkiewicz, P. (2022). Mixed-precision for linear solvers in global geophysical flows. *Journal of Advances in Modeling Earth Systems*, 14:e2022MS003148.

[Adams et al., 2003] Adams, M., Brezina, M., Hu, J., and Tuminaro, R. (2003). Parallel multigrid smoothing: polynomial versus Gauss-Seidel. *Journal of Computational Physics*, 188:593–610.

[Albensoeder and Kuhlmann, 2005] Albensoeder, S. and Kuhlmann, H. (2005). Accurate three-dimensional lid-driven cavity flow. *Journal of Computational Physics*, 206:536–558.

[Arndt et al., 2022] Arndt, D., Bangerth, W., Feder, M., Fehling, M., Gassmöller, R., Heister, T., Heltai, L., Kronbichler, M., Maier, M., Munch, P., Pelteret, J.-P., Sticko, S., Turcksin, B., and Wells, D. (2022). The deal II library, version 9.4. *Journal of Numerical Mathematics*, 30:231–246.

[Arnold, 1982] Arnold, D. (1982). An interior penalty finite element method with discontinuous elements. *SIAM Journal of Numerical Analysis*, 19:742–760.

[Arnold et al., 2002] Arnold, D., Brezzi, F., Cockburn, B., and Marini, L. (2002). Unified analysis of Discontinuous Galerkin methods for elliptic problems. *SIAM Journal of Numerical Analysis*, 39:1749–1779.

[Auteri et al., 2002] Auteri, F., Parolini, N., and Quartapelle, L. (2002). Numerical investigation on the stability of singular driven cavity flow. *Journal of Computational Physics*, 183:1–25.

[Bacigaluppi et al., 2022] Bacigaluppi, P., Carlier, J., Pelanti, M., Congedo, P., and Abgrall, R. (2022). Assessment of a non-conservative four-equation multiphase system with phase transition. *Journal of Scientific Computing*, 90:1–28.

[Baer and Nunziato, 1986] Baer, M. and Nunziato, J. (1986). A two-phase mixture theory for the deflagration-to-detonation transition (DDT) in reactive granular materials. *International Journal of Multiphase Flow*, 12:861–889.

[Bangerth et al., 2007] Bangerth, W., Hartmann, R., and Kanschat, G. (2007). deal II: a general-purpose object-oriented finite element library. *ACM Transactions on Mathematical Software (TOMS)*, 33:24–51.

[Bank et al., 1985] Bank, R., Coughran, W., Fichtner, W., Grosse, E., Rose, D., and Smith, R. (1985). Transient Simulation of Silicon Devices and Circuits. *IEEE Transactions on Electron Devices.*, 32:1992–2007.

[Bassi et al., 2015] Bassi, F., Botti, L., Colombo, A., Ghidoni, A., and Massa, F. (2015). Linearly implicit Rosenbrock-type Runge–Kutta schemes applied to the Discontinuous Galerkin solution of compressible and incompressible unsteady flows. *Computers & Fluids*, 118.

[Bassi et al., 2007] Bassi, F., Crivellini, A., Di Pietro, D., and Rebay, S. (2007). An implicit high-order discontinuous Galerkin method for steady and unsteady incompressible flows. *Computers & Fluids*, 36:1529–1546.

[Bassi and Rebay, 1997a] Bassi, F. and Rebay, S. (1997a). A High-order accurate discontinuous finite element method for the numerical solution of the compressible Navier-Stokes equations. *Journal of Computational Physics*, 131:267–279.

[Bassi and Rebay, 1997b] Bassi, F. and Rebay, S. (1997b). High-order accurate discontinuous finite element solution of the 2d Euler equations. *Journal of Computational Physics*, 138:251–285.

[Benacchio et al., 2014] Benacchio, T., O'Neill, W., and Klein, R. (2014). A blended soundproof-to-compressible numerical model for small- to mesoscale atmospheric dynamics. *Monthly Weather Review*, 142:4416–4438.

[Bokanowski et al., 2016] Bokanowski, O., Falcone, M., and Sahu, S. (2016). An efficient filtered scheme for some first order time-dependent Hamilton-Jacobi equations. *SIAM Journal on Scientific Computing*, 38:A171–A195.

[Bonaventura, 2000] Bonaventura, L. (2000). A Semi-Implicit, Semi-Lagrangian Scheme Using the Height Coordinate for a Nonhydrostatic and Fully Elastic Model of Atmospheric Flows. *Journal of Computational Physics*, 158:186–213.

[Bonaventura and Della Rocca, 2017] Bonaventura, L. and Della Rocca, A. (2017). Unconditionally strong stability preserving extensions of the TR-BDF2 method. *Journal of Scientific Computing*, 70:859–895.

[Bonaventura et al., 2018] Bonaventura, L., Fernández-Nieto, E., Garres-Díaz, J., and Narbona-Reina, G. (2018). Multilayer shallow water models with locally variable number of layers and semi-implicit time discretization. *Journal of Computational Physics*, 364:209–234.

[Bonaventura et al., 2012] Bonaventura, L., Redler, R., and Budich, R. (2012). *Earth System Modelling 2: Algorithms, Code Infrastructure and Optimisation.* Springer-Verlag.

[Boscheri and Pareschi, 2021] Boscheri, W. and Pareschi, L. (2021). High order pressure-based semi-implicit IMEX schemes for the 3D Navier-Stokes equations at all Mach numbers. *Journal of Computational Physics*, 434:110206.

[Botella and Peyret, 1998] Botella, O. and Peyret, R. (1998). Benchmark spectral results on the lid-driven cavity flow. *Computers and Fluids*, 27:421–433.

[Bruneau and Saad, 2006] Bruneau, C. and Saad, M. (2006). The 2D lid-driven cavity flow revisited. *Computers and Fluids*, 35:326–348.

[Burrage and Tian, 2001] Burrage, K. and Tian, T. (2001). Stiffly accurate Runge-Kutta methods for stiff stochastic differential equations. *Computer Physics Communications*, 142:186–190.

[Busto et al., 2020] Busto, S., Tavelli, M., Boscheri, W., and Dumbser, M. (2020). Efficient high order accurate staggered semi-implicit discontinuous Galerkin methods for natural convection problems. *Computers & Fluids*, 198:104399.

[Butcher, 2008] Butcher, J. (2008). *Numerical Methods for Ordinary Differential Equations.* Wiley, 2 edition.

[Candel and Poinsot, 1990] Candel, S. and Poinsot, T. (1990). Flame stretch and the balance equation for the flame area. *Combustion Science and Technology*, 70:1–15.

[Casulli and Greenspan, 1984] Casulli, V. and Greenspan, D. (1984). Pressure method for the numerical solution of transient, compressible fluid flows. *International Journal for Numerical Methods in Fluids*, 4:1001–1012.

[Chalons and Del Grosso, 2022] Chalons, C. and Del Grosso, A. (2022). A second-order well-balanced Lagrange-projection numerical scheme for shallow water Exner equations in 1d and 2d. *Communications in Mathematical Sciences*, 20:1839–1873.

[Chen et al., 2014] Chen, G., Xiong, Q., Morris, P., Paterson, E., Sergeev, A., and Wang, Y. (2014). OpenFOAM for computational fluid dynamics. *Notices of the AMS*, 61:354–363.

[Chiodi et al., 2014] Chiodi, F., Claudin, P., and Andreotti, B. (2014). A two-phase flow model of sediment transport: transition from bedload to suspended load. *Journal of Fluid Mechanics*, 755:561–581.

[Chorin, 1967] Chorin, A. (1967). A numerical method for solving incompressible viscous flow problems. *Journal of Computational Physics*, 2:12–26.

[Chorin, 1968] Chorin, A. (1968). Numerical solution of the Navier-Stokes equations. *Mathematics of Computation*, 22:745–762.

[Cockburn et al., 1989] Cockburn, B., Lin, S., and Shu, C. (1989). TVB Runge-Kutta local projection discontinuous Galerkin finite element method for conservation laws. III. One-dimensional systems. *Journal of Computational Physics*, 84:90–113.

[Cockburn and Shu, 1989] Cockburn, B. and Shu, C. (1989). TVB Runge-Kutta local projection discontinuous Galerkin finite element method for conservation laws. II. General framework. *Mathematics of Computation*, 52:411–435.

[Colombo et al., 2018] Colombo, A., Manzinali, G., Ghidoni, A., Noventa, G., Franciolini, M., Crivellini, A., and Bassi, F. (2018). A p-adaptive implicit discontinuous Galerkin method for the under-resolved simulation of compressible turbulent flows. In *7nd European Conference on Computational Fluid Dynamics*.

[Coquel et al., 2017] Coquel, F., Hérard, J., and Saleh, K. (2017). A positive and entropy-satisfying finite volume scheme for the Baer-Nunziato model. *Journal of Computational Physics*, 330:401–435.

[Cordesse et al., 2020] Cordesse, P., Di Battista, R., Chevalier, Q., Matuszewski, L., Ménard, T., Kokh, S., and Massot, M. (2020). A diffuse interface approach for disperse two-phase flows involving dual-scale kinematics of droplet deformation based on geometrical variables. *ESAIM: Proceedings and Surveys*, 69:24–46.

[Cordesse et al., 2019] Cordesse, P., Kokh, S., Di Battista, R., and Massot, M. (2019). Derivation of a two-phase flow model with two-scale kinematics and surface tension by means of variational calculus. In *10th International Conference on Multiphase Flow (ICMF 2019)*.

[Cullen, 1990] Cullen, M. (1990). A test of a semi-implicit integration technique for a fully compressible non-hydrostatic model. *Quarterly Journal of the Royal Meteorological Society*, 116:1253–1258.

[De Lorenzo et al., 2019] De Lorenzo, M., Lafon, P., and Pelanti, M. (2019). A hyperbolic phase-transition model with non-instantaneous EoS-independent relaxation procedures. *Journal of Computational Physics*, 379:279–308.

[Delhaye, 2001] Delhaye, J. (2001). Some issues related to the modeling of interfacial areas in gas-liquid flows I. the conceptual issues. *Comptes Rendus de l'Académie des Sciences - Series IIB - Mechanics*, 329:397–410.

[Delhaye and Bouré, 1982] Delhaye, J. and Bouré, J. (1982). *Handbook of Multiphase Systems*, chapter General equations and two-phase flow modeling, pages 36–95. Hemisphere.

[Della Rocca, 2018] Della Rocca, A. (2018). *Large-Eddy Simulations of Turbulent Reacting Flows with Industrial Applications*. PhD thesis, Politecnico di Milano. `http://hdl.handle.net/10589/137775`.

[Demou et al., 2022] Demou, A., Scapin, N., Pelanti, M., and Brandt, L. (2022). A pressure-based diffuse interface method for low-Mach multiphase flows with mass transfer. *Journal of Computational Physics*, 448:110730.

[Di Battista, 2021] Di Battista, R. (2021). *Towards a unified Eulerian modeling framework for two-phase flows: geometrical small scale phenomena and associated flexible computing strategies*. PhD thesis, Institut Polytechnique de Paris. `https://www.theses.fr/2021IPPAX055`.

[Dolejší, 2004] Dolejší, V. (2004). On the discontinuous Galerkin method for the numerical solution of the Navier-Stokes equations. *International Journal for Numerical Methods in Fluids*, 45:1083–1106.

[Drew, 1990] Drew, D. (1990). Evolution of geometric statistics. *SIAM Journal on Applied Mathematics*, 50:649–666.

[Drew and Passman, 1999] Drew, D. and Passman, S. (1999). *Theory of Multicomponent Fluids*. Applied Mathematical Sciences, vol. 135, Springer.

[Drui et al., 2019] Drui, F., Larat, A., Kokh, S., and Massot, M. (2019). Small-scale kinematics of two-phase flows: identifying relaxation processes in separated- and disperse-phase flow models. *Journal of Fluid Mechanics*, 876:326–355.

[Dumbser and Casulli, 2016] Dumbser, M. and Casulli, V. (2016). A conservative, weakly nonlinear semi-implicit finite volume scheme for the compressible Navier-Stokes equations with general equation of state. *Applied Mathematics and Computation*, 272:479–497.

[Dumbser and Loubère, 2016] Dumbser, M. and Loubère, R. (2016). A simple robust and accurate a posteriori sub-cell finite volume limiter for the discontinuous Galerkin method on unstructured meshes. *Journal of Computational Physics*, 319:163–199.

[Dumbser et al., 2014] Dumbser, M., Zanotti, O., Loubère, R., and Diot, S. (2014). A posteriori subcell limiting of the discontinuous galerkin finite element method for hyperbolic conservation laws. *Journal of Computational Physics*, 278:47–75.

[Durran and Klemp, 1983] Durran, D. and Klemp, J. (1983). A Compressible Model for the Simulation of Moist Mountain Waves. *Monthly Weather Review*, 111:2341–2361.

[Eskilsson, 2011] Eskilsson, C. (2011). An *hp*−adaptive discontinuous Galerkin method for shallow water flows. *International Journal for Numerical Methods in Fluids*, 67:1605–1623.

[Essadki et al., 2019] Essadki, M., Drui, F., de Chaisemartin, S., Larat, A., Ménard, T., and Massot, M. (2019). Statistical modeling of the gas-liquid interface using geometrical variables: Toward a unified description of the disperse and separated phase flows. *International Journal of Multiphase Flow*, 120:103084.

[Estrada and Kanwal, 1980] Estrada, R. and Kanwal, R. (1980). Applications of distributional derivatives to wave propagation. *IMA Journal of Applied Mathematics*, 26:39–63.

[Estrada and Kanwal, 1985] Estrada, R. and Kanwal, R. (1985). Distributional analysis for discontinuous fields. *Journal of Mathematical Analysis and Applications*, 105:478–490.

[Fehn et al., 2019] Fehn, N., Kronbichler, M., Lehrenfeld, C., Lube, G., and Schroeder, P. (2019). High-order DG solvers for under-resolved turbulent incompressible flows: A comparison of l^2 and $h(div)$ methods. *International Journal of Numerical Methods in Fluids*, 91:533–556.

[Fernandez, 2009] Fernandez, M. (2009). Propellant tank pressurization modeling for a hybrid rocket. Master's thesis, Rochester Institute of Technology. `https://scholarworks.rit.edu/theses/7111/`.

[Ferracina and Spijker, 2004] Ferracina, L. and Spijker, M. (2004). Stepsize restrictions for the Total-Variation-Diminishing property in general Runge-Kutta methods. *SIAM Journal of Numerical Analysis*, 42:1073–1093.

[Froese and Oberman, 2013] Froese, B. and Oberman, A. (2013). Convergent filtered schemes for the Monge-Ampère partial differential equation. *SIAM J. Numer. Anal.*, 51:423–444.

[Gal-Chen and Somerville, 1975] Gal-Chen, T. and Somerville, R. (1975). On the use of a coordinate transformation for the solution of the Navier-Stokes equations. *Journal of Computational Physics*, 17:209–228.

[Galloway and Frisch, 1987] Galloway, D. and Frisch, U. (1987). A note on the stability of a family of space-periodic Beltrami flows. *Journal of Fluid Mechanics*, 158:557–564.

[Gandolfi, 2019] Gandolfi, M. (2019). Baer-Nunziato type models for the simulation of hybrid rockets self-pressurizing tanks. Master's thesis, Politecnico di Milano. `http://hdl.handle.net/10589/149428`.

[Garnier et al., 2009] Garnier, E., Adams, N., and Sagaut, P. (2009). *Large eddy simulation for compressible flows.* Springer Science & Business Media.

[Garres-Díaz and Bonaventura, 2021] Garres-Díaz, J. and Bonaventura, L. (2021). Flexible and efficient discretizations of multilayer models with variable density. *Applied Mathematics and Computation*, 402:126097.

[Ghia et al., 1982] Ghia, U., Ghia, K., and Shin, C. (1982). High-Re solutions for incompressible flow using the Navier-Stokes equations and a multigrid method. *Journal of Computational Physics*, 48:387–411.

[Giraldo, 2020] Giraldo, F. (2020). *An Introduction to Element-Based Galerkin Methods on Tensor-Product Bases.* Springer Nature.

[Giraldo et al., 2013] Giraldo, F., Kelly, J., and Constantinescu, E. (2013). Implicit-explicit formulations of a three-dimensional nonhydrostatic unified model of the atmosphere (NUMA). *SIAM Journal of Scientific Computing*, 35:1162–1194.

[Giraldo and Restelli, 2008] Giraldo, F. and Restelli, M. (2008). A study of spectral element and discontinuous Galerkin methods for the Navier-Stokes equations in nonhydrostatic mesoscale atmospheric modeling: Equation sets and test cases. *Journal of Computational Physics*, 227:3849–3877.

[Giraldo et al., 2010] Giraldo, F., Restelli, M., and Läuter, M. (2010). Semi-implicit formulations of the Navier-Stokes equations: Application to nonhydrostatic atmospheric modeling. *SIAM Journal on Scientific Computing*, 32:3394–3425.

[Godlewski and Raviart, 1996] Godlewski, E. and Raviart, P. (1996). *Numerical Approximation of Hyperbolic Systems of Conservation Laws.* Springer Science & Business Media.

[Gottlieb and Shu, 1998] Gottlieb, S. and Shu, C. (1998). Total variation diminishing Runge-Kutta schemes. *Mathematics of Computation*, 67:73–85.

[Gottlieb et al., 2001] Gottlieb, S., Shu, C. W., and Tadmor, E. (2001). Strong stability-preserving high-order time discretization methods. *SIAM Review*, 43:89–112.

[Green and Taylor, 1937] Green, A. and Taylor, G. (1937). Mechanism of the production of small eddies from large ones. *Proceedings of The Royal Society A: Mathematical, Physical and Engineering Sciences*, 158:499–521.

[Gross et al., 2002] Gross, E., Bonaventura, L., and Rosatti, G. (2002). Consistency with continuity in conservative advection schemes for free-surface models. *International Journal for Numerical Methods in Fluids*, 38:307–327.

[Guermond et al., 2006] Guermond, J., Minev, P., and Shen, J. (2006). An overview of projection methods for incompressible flows. *Computer methods in applied mechanics and engineering*, 195:6011–6045.

[Gurtin, 1982] Gurtin, E. (1982). *An introduction to continuum mechanics.* Academic press.

[Han et al., 2017] Han, E., Hantke, M., and Müller, S. (2017). Efficient and robust relaxation procedures for multi-component mixtures including phase transition. *Journal of Computational Physics*, 338:217–239.

[Hartmann and Houston, 2002] Hartmann, R. and Houston, P. (2002). Adaptive discontinuous Galerkin finite element methods for the compressible Euler equations. *Journal of Computational Physics*, 183:508–532.

[Hestenes and Stiefel, 1952] Hestenes, M. and Stiefel, E. (1952). Methods of conjugate gradients for solving linear systems. *Journal of research of the National Bureau of Standards*, 49(6):409–436.

[Hibiki and Ishii, 2002] Hibiki, T. and Ishii, M. (2002). Interfacial area concentration of bubbly flow systems. *Chemical Engineering Science*, 57:3967–3977.

[Higueras, 2004] Higueras, I. (2004). On Strong Stability Preserving Time Discretization Methods. *Journal of Scientific Computing*, 21:193–223.

[Hosea and Shampine, 1996] Hosea, M. and Shampine, L. (1996). Analysis and implementation of TR-BDF2. *Applied Numerical Mathematics*, pages 21–37.

[Houston and Süli, 2001] Houston, P. and Süli, E. (2001). *hp*-adaptive discontinuous Galerkin finite element methods for first-order hyperbolic problems. *SIAM Journal on Scientific Computing*, 23:1226–1252.

[Hysing et al., 2009] Hysing, S.-R., Turek, S., Kuzmin, D., Parolini, N., Burman, E., Ganesan, S., and Tobiska, L. (2009). Quantitative benchmark computations of two-dimensional bubble dynamics. *International Journal for Numerical Methods in Fluids*, 60:1259–1288.

[Ishii, 1975] Ishii, M. (1975). *Thermo-fluid Dynamics of Two-Phase Flows.* Eyrolles, Paris.

[Issa et al., 1986] Issa, R., Ahmadi-Befrui, B., Beshay, K., and Gosman, A. (1986). Solution of the implicitly discretised reacting flow equations by operator-splitting. *Journal of Computational Physics*, 62:388–410.

[Jamet et al., 2001] Jamet, D., Lebaigue, O., Coutris, N., and Delhaye, J. (2001). The second gradient method for the direct numerical simulation of liquid-vapor flows with phase change. *Journal of Computational Physics*, 169(2):624–651.

[Janssen and Kanschat, 2011] Janssen, B. and Kanschat, G. (2011). Adaptive multilevel methods with local smoothing for H^1- and H^{curl}-conforming high order finite element methods. *SIAM Journal on Scientific Computing*, 33:2095–2114.

[Jemison et al., 2014] Jemison, M., Sussman, M., and Arienti, M. (2014). Compressible, multiphase semi-implicit method with moment of fluid interface representation. *Journal of Computational Physics*, 279:182–217.

[Jiang et al., 1994] Jiang, B., Lin, T., and Povinelli, L. (1994). Large-scale computation of incompressible viscous flow by least-squares finite element method. *Computer Methods in Applied Mechanics and Engineering*, 114:213–231.

[Junqua-Moullet, 2003] Junqua-Moullet, A. (2003). *Détermination expérimentale et modélisation de la concentration d'aire interfaciale en écoulement stratifié horizontal.* PhD thesis.

[Kapila et al., 2001] Kapila, A., Menikoff, R., Bdzil, J., Son, S., and Stewart, D. (2001). Two-phase modeling of deflagration-to-detonation transition in granular materials: Reduced equations. *Physics of fluids*, 13:3002–3024.

[Karniadakis and Sherwin, 2005] Karniadakis, G. and Sherwin, S. (2005). *Spectral hp−Element Methods for Computational Fluid Dynamics.* Oxford University Press.

[Kennedy and Carpenter, 2003] Kennedy, C. and Carpenter, M. (2003). Additive Runge-Kutta schemes for convection-diffusion-reaction equations. *Applied Numerical Mathematics*, 44:139–181.

[Klein et al., 2001] Klein, R., Botta, N., Schneider, T., Munz, C.-D., Roller, S., Meister, A., Hoffmann, L., and Sonar, T. (2001). Asymptotic adaptive methods for multi-scale problems in fluid mechanics. *Journal of Engineering Mathematics*, 39:261–343.

[Klemp and Durran, 1983] Klemp, J. and Durran, D. (1983). An upper boundary condition permitting internal gravity wave radiation in numerical mesoscale models. *Monthly Weather Review*, 111:430–444.

[Klemp and Lilly, 1978] Klemp, J. and Lilly, D. (1978). Numerical simulation of hydrostatic mountain waves. *Journal of the Atmospheric Sciences*, 35:78–107.

[Kolev, 2002] Kolev, N. (2002). *Multiphase flow dynamics 1- Fundamentals.* Berlin, Germany: Springer-Verlag GmbH, 2002.

[Kraaijevanger, 1991] Kraaijevanger, J. (1991). Contractivity of Runge-Kutta methods. *BIT*, 31:482–528.

[Kuhn and Desjardins, 2021] Kuhn, M. and Desjardins, O. (2021). An all-Mach, low-dissipation strategy for simulating multiphase flows. *Journal of Computational Physics*, 445:110602.

[Kurganov and Tadmor, 2002] Kurganov, A. and Tadmor, E. (2002). Solution of two-dimensional Riemann problems for gas dynamics without Riemann problem solvers. *Numerical Methods for Partial Differential Equations*, 18.

[Kuzmin et al., 2012] Kuzmin, D., Löhner, R., and Turek, S. (2012). *Flux-corrected transport: principles, algorithms, and applications.* Springer Verlag.

[Kuzmin and Turek, 2002] Kuzmin, D. and Turek, S. (2002). Flux correction tools for finite elements. *Journal of Computational Physics*, 175:525–558.

[Le Métayer and Saurel, 2016] Le Métayer, O. and Saurel, R. (2016). The Noble-Abel Stiffened-Gas equation of state. *Physics of Fluids*, 28:046102.

[Lebas et al., 2009] Lebas, R., Menard, T., Beau, P., Berlemont, A., and Demoulin, F. (2009). Numerical simulation of primary break-up and atomization: Dns and modelling study. *International Journal of Multiphase Flow*, 35:247–260.

[Lemmon and Span, 2006] Lemmon, E. and Span, R. (2006). Short fundamental equations of state for 20 industrial fluids. *Journal of Chemical & Engineering Data*, 51:785–850.

[LeVeque, 1996] LeVeque, R. (1996). High-resolution conservative algorithms for advection in incompressible flow. *SIAM Journal on Numerical Analysis*, 33:627–665.

[LeVeque, 2002] LeVeque, R. (2002). *Finite volume methods for hyperbolic problems.* Cambridge University Press.

[Lhuillier, 2003] Lhuillier, D. (2003). Dynamics of interfaces and rheology of immiscible liquid-liquid mixtures. *Comptes Rendus Mécanique*, 331:113–118.

[Lhuillier, 2004] Lhuillier, D. (2004). Evolution of the volumetric interfacial area in two-phase mixtures. *Comptes Rendus Mecanique*, 332:103–108.

[Lhuillier et al., 2000] Lhuillier, D., Morel, C., and Delhaye, J. (2000). Bilan d'aire interfaciale dans un mélange diphasique : approche locale vs approche particulaire. *Comptes Rendus De L'Academie Des Sciences Serie II Fascicule B-Mecanique Physique Astronomie*, 328:143–149.

[Lias et al., 2010] Lias, S., Bartmess, J., Liebman, J., Holmes, J., Levin, R., and Mallard, G. (2010). NIST chemistry webbook standard reference database number 69. *National Institute of Standards Technology.*

[Loubère et al., 2014] Loubère, R., Dumbser, M., and Diot, S. (2014). A new family of high order unstructured MOOD and ADER finite volume schemes for multidimensional systems of hyperbolic conservation laws. *Communications in Computational Physics*, 16:718–763.

[Lund and Aursand, 2012] Lund, H. and Aursand, P. (2012). Two-phase flow of CO2 with phase transfer. *Energy Procedia*, 23:246–255.

[Marle, 1982] Marle, C. (1982). On macroscopic equations governing multiphase flow with diffusion and chemical reactions in porous media. *International Journal of Engineering Science*, 20:643–662.

[McGraw, 1997] McGraw, R. (1997). Description of aerosol dynamics by the quadrature method of moments. *Aerosol Science and Technology*, 27:255–265.

[Mehonic and Kenyon, 2022] Mehonic, A. and Kenyon, A. (2022). Brain-inspired computing needs a master plan. *Nature*, 604:255–260.

[Melvin et al., 2019] Melvin, T., Benacchio, T., Shipway, B., Wood, N., Thuburn, J., and Cotter, C. (2019). A mixed finite-element, finite-volume, semi-implicit discretization for atmospheric dynamics: Cartesian geometry. *Quarterly Journal of the Royal Meteorological Society*, 145:2835–2853.

[Morel, 2007] Morel, C. (2007). On the surface equations in two-phase flows and reacting single-phase flows. *International Journal of Multiphase Flow*, 33:1045–1073.

[Mortensen and Bilger, 2009] Mortensen, M. and Bilger, R. (2009). Derivation of the conditional moment closure equations for spray combustion. *Combustion and Flame*, 156:62–72.

[Müller et al., 2016] Müller, S., Hantke, M., and Richter, P. (2016). Closure conditions for non-equilibrium multi-component models. *Continuum Mechanics and Thermodynamics*, 28:1157–1189.

[Munz et al., 2003] Munz, C., Roller, S., Klein, R., and Geratz, K. (2003). The extension of incompressible flow solvers to the weakly compressible regime. *Computers and Fluids*, 32:173–196.

[Nadim, 1996] Nadim, A. (1996). A concise introduction to surface rheology with application to dilute emulsions of viscous drops. *Chemical Engineering Communications*, 148-150:391–407.

[Nederstigt, 2017] Nederstigt, P. (2017). Real Gas Thermodynamics: and the isentropic behavior of substances. Master's thesis, Delft University of Technology. `http://resolver.tudelft.nl/uuid:ee16f7e5-4251-4629-9192-8f4a2e3d599b`.

[Nigmatulin, 1970] Nigmatulin, R. (1970). Methods of mechanics of a continuous medium for the description of multiphase mixtures. *Journal of Applied Mathematics and Mechanics*, 34:1033–1049.

[Oberman and Salvador, 2015] Oberman, A. and Salvador, T. (2015). Filtered schemes for Hamilton-Jacobi equations: A simple construction of convergent accurate difference schemes. *J. Comput. Phys.*, 284:367–388.

[Orlando, 2022] Orlando, G. (2022). `https://www.dealii.org/current/doxygen/deal.II/code_gallery_NavierStokes_TRBDF2_DG.html`. Technical report.

[Orlando, 2023] Orlando, G. (2023). A filtering monotonization approach for DG discretizations of hyperbolic problems. *Computers & Mathematics with Applications*, 129:113–125.

[Orlando et al., 2022a] Orlando, G., Barbante, P., and Bonaventura, L. (2022a). An efficient IMEX-DG solver for the compressible Navier-Stokes equations for non-ideal gases. *Journal of Computational Physics*, 471:111653.

[Orlando et al., 2023] Orlando, G., Benacchio, T., and Bonaventura, L. (2023). An IMEX-DG solver for atmospheric dynamics simulations with adaptive mesh refinement. *Journal of Computational and Applied Mathematics*, 427:115124.

[Orlando et al., 2022b] Orlando, G., Della Rocca, A., Barbante, P., Bonaventura, L., and Parolini, N. (2022b). An efficient and accurate implicit DG solver for the incompressible Navier-Stokes equations. *International Journal for Numerical Methods in Fluids*, 94:1484–1516.

[Pelanti, 2022] Pelanti, M. (2022). Arbitrary-rate relaxation techniques for the numerical modeling of compressible two-phase flows with heat and mass transfer. *International Journal of Multiphase Flow.*

[Pinty et al., 1995] Pinty, J., Benoit, R., Richard, E., and Laprise, R. (1995). Simple tests of a semi-implicit semi-Lagrangian model on 2D mountain wave problems. *Monthly Weather Review*, 123:3042–3058.

[Powers et al., 1990] Powers, J., Stewart, D., and Krier, H. (1990). Theory of two-phase detonation-part i: modeling. *Combustion and Flame*, 80:264–279.

[Quarteroni and Valli, 2008] Quarteroni, A. and Valli, A. (2008). *Numerical approximation of partial differential equations*, volume 23. Springer Science & Business Media.

[Ramos, 1995] Ramos, J. (1995). One-dimensional, time-dependent, homogeneous, two-phase flow in volcanic conduits. *International journal for numerical methods in fluids*, 21:253–278.

[Re and Abgrall, 2022] Re, B. and Abgrall, R. (2022). A pressure-based method for weakly compressible two-phase flows under a Baer-Nunziato type model with generic equations of state and pressure and velocity disequilibrium. *International Journal for Numerical Methods in Fluids*, 94:1183–1232.

[Remacle et al., 2003] Remacle, J., Flaherty, J., and Shephard, M. (2003). An adaptive discontinuous Galerkin technique with an orthogonal basis applied to compressible flow problems. *SIAM review*, 45:53–72.

[Restelli, 2007] Restelli, M. (2007). *Semi-Lagrangian and Semi-Implicit Discontinuous Galerkin Methods for Atmospheric Modeling Applications*. PhD thesis, Politecnico di Milano.

[Restelli et al., 2006] Restelli, M., Bonaventura, L., and Sacco, R. (2006). A semi-Lagrangian Discontinuous Galerkin method for scalar advection by incompressible flows. *Journal of Computational Physics*, 216:195–215.

[Restelli and Giraldo, 2009] Restelli, M. and Giraldo, F. (2009). A conservative Discontinuous Galerkin semi-implicit formulation for the Navier-Stokes equations in nonhydrostatic mesoscale modeling. *SIAM Journal of Scientific Computing*, 31:2231–2257.

[Robert, 1982] Robert, A. (1982). A semi-Lagrangian and semi-implicit numerical integration scheme for the primitive meteorological equations. *Journal of the Meteorological Society of Japan*, 60:319–325.

[Romenski et al., 2007] Romenski, E., Resnyansky, A., and Toro, E. (2007). Conservative hyperbolic formulation for compressible two-phase flow with different phase pressures and temperatures. *Quarterly of applied mathematics*, 65:259–279.

[Rudin, 1976] Rudin, W. (1976). *Principles of mathematical analysis*, volume 3. McGraw-hill New York.

[Rusanov, 1962] Rusanov, V. (1962). The calculation of the interaction of non-stationary shock waves and obstacles. *USSR Computational Mathematics and Mathematical Physics*, 1:304–320.

[Saad, 1981] Saad, Y. (1981). Krylov subspace methods for solving large unsymmetric linear systems. *Mathematics of computation*, 37(155):105–126.

[Sandler, 2017] Sandler, S. (2017). *Chemical, biochemical, and engineering thermodynamics*. John Wiley & Sons.

[Saurel, 1996] Saurel, R. (1996). Numerical analysis of a ram accelerator employing two-phase combustion. *Journal of propulsion and power*, 12:708–717.

[Saurel and Abgrall, 1999] Saurel, R. and Abgrall, R. (1999). A Multiphase Godunov Method for Compressible Multifluid and Multiphase Flows. *Journal of Computational Physics*, 150:425–467.

[Saurel et al., 2016] Saurel, R., Boivin, P., and Le Métayer, O. (2016). A general formulation for cavitating, boiling and evaporating flows. *Computers & Fluids*, 128:53–64.

[Saurel and Pantano, 2018] Saurel, R. and Pantano, C. (2018). Diffuse-Interface Capturing Methods for Compressible Two-Phase Flows. *Annual Review of Fluid Mechanics*, 50:105–130.

[Schäfer et al., 1996] Schäfer, M., Turek, S., Durst, F., Krause, E., and Rannacher, R. (1996). *Benchmark Computations of Laminar Flow Around a Cylinder*, pages 547–566. Vieweg+Teubner Verlag, Wiesbaden.

[Schär et al., 2002] Schär, C., Leuenberger, D., Fuhrer, O., Lüthi, D., and Girard, C. (2002). A new terrain-following vertical coordinate formulation for atmospheric prediction models. *Monthly Weather Review*, 130:2459–2480.

[Schötzau et al., 2003] Schötzau, D., Schwab, C., and Toselli, A. (2003). Stabilized DGFEM for incompressible flows. *Mathematical Models and Methods in Applied Sciences*, 13:1413–1436.

[Séro-Guillaume and Rimbert, 2005] Séro-Guillaume, O. and Rimbert, N. (2005). On thermodynamic closures for two-phase flow with interfacial area concentration transport equation. *International journal of multiphase flow*, 31:897–920.

[Shu, 2003] Shu, C. (2003). High-order finite difference and finite volume WENO schemes and discontinuous Galerkin methods for CFD. *International Journal of Computational Fluid Dynamics*, 17:107–118.

[Shu, 2016] Shu, C. (2016). High order WENO and DG methods for time-dependent convection-dominated PDEs: A brief survey of several recent developments. *Journal of Computational Physics*, 316:598–613.

[Skamarock and Klemp, 1994] Skamarock, W. and Klemp, J. (1994). Efficiency and accuracy of the Klemp-Wilhelmson time-splitting technique. *Monthly Weather Review*, 122:2623–2630.

[Slattery et al., 2007] Slattery, J., Sagis, L., and Oh, E.-S. (2007). *Interfacial transport phenomena*. Springer Science & Business Media.

[Smith, 1979] Smith, R. (1979). The influence of mountains on the atmosphere. *Advances in Geophysics*, 21:87–230.

[Sod, 1978] Sod, G. (1978). A survey of several finite difference methods for systems of nonlinear hyperbolic conservation laws. *Journal of Computational Physics*, 27:1–31.

[Soria and de Lasa, 1991] Soria, A. and de Lasa, H. (1991). Averaged transport equations for multiphase systems with interfacial effects. *Chemical Engineering Science*, 46:2093–2111.

[Span, 2000] Span, R. (2000). *Multiparameter Equations of State*. Springer.

[Straka et al., 1993] Straka, J., Wilhelmson, R., Wicker, L., Anderson, J., and Droegemeier, K. (1993). Numerical solutions of a non-linear density current: A benchmark solution and comparisons. *International Journal for Numerical Methods in Fluids*, 17:1–22.

[Strang, 1968] Strang, G. (1968). On the construction and comparison of difference schemes. *SIAM Journal on Numerical Analysis*, 5:506–517.

[Tait, 1965] Tait, P. (1965). *Report on some of the physical properties of fresh water and of sea water.* Johnson Reprint Corporation.

[Tavelli and Dumbser, 2017] Tavelli, M. and Dumbser, M. (2017). A pressure-based semi-implicit space-time discontinuous Galerkin method on staggered unstructured meshes for the solution of the compressible Navier-Stokes equations at all Mach numbers. *Journal of Computational Physics*, 341:341–376.

[Temam, 1969] Temam, R. (1969). Sur l'approximation de la solution des équations de Navier-Stokes par la méthode des pas fractionnaires (II). *Archive for Rational Mechanics and Analysis*, 33:377–385.

[Toro, 2009] Toro, E. (2009). *Riemann Solvers and Numerical Methods for Fluid Dynamics: A Practical Introduction.* Springer.

[Toselli, 2002] Toselli, A. (2002). *hp* Discontinuous Galerkin approximations for the Stokes problem. *Mathematical Models and Methods in Applied Sciences*, 12:1565–1597.

[Trusdell and Toupin, 1960] Trusdell, C. and Toupin, R. (1960). *The classical field theories.* Springer Verlag, Berlin.

[Tugnoli et al., 2017] Tugnoli, M., Abbà, A., Bonaventura, L., and Restelli, M. (2017). A locally p-adaptive approach for Large Eddy Simulation of compressible flows in a DG framework. *Journal of Computational Physics*, 349:33–58.

[Tumolo and Bonaventura, 2015] Tumolo, G. and Bonaventura, L. (2015). A semi-implicit, semi-Lagrangian discontinuous Galerkin framework for adaptive numerical weather prediction. *Quarterly Journal of the Royal Meteorological Society*, 141:2582–2601.

[Tumolo et al., 2013] Tumolo, G., Bonaventura, L., and Restelli, M. (2013). A semi-implicit, semi-Lagrangian, $p-$adaptive discontinuous Galerkin method for the shallow water equations. *Journal of Computational Physics*, 232:46–67.

[Vallet et al., 2001] Vallet, A., Burluka, A., and Borghi, R. (2001). Development of a Eulerian model for the "atomization" of a liquid jet. *Atomization and sprays*, 11:619–642.

[Vidal, 2001] Vidal, J. (2001). *Thermodynamics: Applications to chemical engineering and petroleum industry.* Editions Technip.

[Weatherburn, 1930] Weatherburn, C. (1930). *Differential Geometry of Three Dimensions, Volume II.* Cambridge University Press.

[Whitaker, 1986] Whitaker, S. (1986). Flow in porous media II: The governing equations for immiscible, two-phase flow. *Transport in porous media*, 1:105–125.

[Williams, 1958] Williams, F. (1958). Spray combustion and atomization. *Physics of Fluids*, 1:541–545.

[Zalesak, 1979] Zalesak, S. (1979). Fully multidimensional flux-corrected transport algorithms for fluids. *Journal of Computational Physics*, 31:335–362.

[Zanotti et al., 2015] Zanotti, O., Fambri, F., Dumbser, M., and Hidalgo, A. (2015). Space-time adaptive ADER discontinuous Galerkin finite element schemes with a posteriori sub-cell finite volume limiting. *Computers & Fluids*, 118:204–224.

[Zeifang et al., 2019] Zeifang, J., Schütz, J., Kaiser, K., Beck, A., Lukáčová-Medvid'ová, M., and Noelle, S. (2019). A Novel Full-Euler Low Mach Number IMEX Splitting. *Communications in Computational Physics*, 27:292–320.